UNIVERSITÀ DELLA CALABRIA

UNIVERSITÀ DELLA CALABRIA

DIPARTIMENTO DI FISICA

DOTTORATO DI RICERCA IN
SCIENZE E TECNOLOGIE FISICHE, CHIMICHE E DEI MATERIALI

CICLO
XXX

MEASUREMENTS OF DIFFERENTIAL CROSS SECTIONS OF TOP QUARK PAIR PRODUCTION IN ASSOCIATION WITH JETS IN *pp* COLLISIONS AT $\sqrt{s}$=13 TEV USING THE ATLAS DETECTOR

SETTORE SCIENTIFICO DISCIPLINARE FIS/01

COORDINATORE: PROF. VINCENZO CARBONE

Vincenzo Carbone

SUPERVISORE: PROF.SSA LAURA LA ROTONDA

Laura La Rotonda

CO-SUPERVISORE: DOTT. MICHELE FAUCCI GIANNELLI

Michele Fauci Giannelli

DOTTORANDA: DOTT.SSA SERENA PALAZZO

Serena Palazzo

Abstract

In this thesis the measurements of differential cross sections of top quark pair production in association with jets are presented. Data collected by the ATLAS experiment at the LHC during the 2015 corresponding to an integrated luminosity of 3.2 fb^{-1} were used. The top quark pair events are selected in the lepton (electron or muon) + jets channel. Several variables are selected because are sensitive to additional jets: the top quark tranverse momentum, the transverse momentum of the top quark anti-top quark system and of the out-of-plane transverse momentum. The measured cross sections are compared to several theoretical Monte Carlo predictions and allow detailed studies of the top quark production.

In this thesis the work on the new MicroMegas tracking chambers which will be installed in the Muon Spectrometer during the Phase-1 Upgrade of the ATLAS detector, is also presented. The performances of the first chamber prototype built by the INFN Italian collaboration and tested on beam at CERN on June 2016 are reported.

Abstract

In questa tesi sono presentate le misure delle sezioni d'urto differentiali di produzione di coppie di top quark in associazione a jets. Per effettuare le misure sono stati usati i dati raccolti dall'esperimento ATLAS a LHC nel 2015 che corrispondono a una luminosità integrata di 3.2 fb^{-1}. Gli eventi di coppie di top quark sono selezionati nel canale leptone (elettrone o muone) + jets. Diverse osservabili sono selezionate perchè sono sensitive a jets addizionali: il momento trasverso del top quark, il momento transverso del sistema top quark anti-top quark e il momento transverso out-of-plane. Le sezioni d'urto misurate sono comparate a diverse predizioni teoriche Monte Carlo e permettono studi dettagliati della produzione di top quark.

Nella tesi è anche presentato il lavoro sulle nuove camere di tracciamento MicroMegas che verranno installate nello Spettrometro per Muoni durante l'Upgrade di Fase-1 del detector ATLAS. Sono riportate le performance del primo prototipo di camera MicroMegas costruita dalla collaborazione Italiana INFN e testata su fascio al CERN a Giugno del 2016.

Contents

List of Figures

List of Tables

Introduction

This thesis is focused on data analysis and on detectors upgrade of the ATLAS experiment at CERN. Measurements of the differential cross sections of top quark pairs production in association with jets are reported. In addition, relatively to the Phase-1 Upgrade program of the ATLAS detector, studies of the MicroMegas tracking chambers are shown.

The large number of top quark pair ($t\bar{t}$) events produced at the Large Hadron Collider (LHC) allow detailed studies of the charecteristics of $t\bar{t}$ production as functions of several kinematic variables. The measurements of the differential cross sections in different bins of jets multiplicity provide high sensitivity to study in detail the effects related to QCD radiation; these effects are hidden in inclusive measurements due to the higher jet multiplicity. Data used in the analysis have been collected by the ATLAS detector in 2015 corresponding to an integrated luminosity of 3.2 fb^{-1}.

After the LHC shutdown (2019-2020) the luminosity will be increased up to 2-3 $\cdot$ 10^{34} cm^{-2} s^{-1}. While high luminosity will provides more data, it is essential that the ATLAS subdetectors are still able to operate in the higher background environment maintaining their performances as good as that at lower luminosities. To obtain this, some of the subdetectors that are located nearest to the beam pipe have to be replaced.

The MicroMegas chambers will substitute the MDT chambers in the forward regions. It is therefore important to certify the chambers before the installation on the Muon Spectrometer. In this thesis performances of the first MicroMegas chamber prototype built by the INFN Italian collaboration, are reported. The setup installation at LNF to test the MicroMegas chamber produced in Italy and the development of part of the relative reconstruction code have been the arguments of my qualification task.

This thesis is divided in ten chapters:

- In Chapter 1 an overview of the Standard Model of particles physic togheter with an overview of the top quark physics and of its properties are reported;

- In Chapter 2 an overview of the LHC collider and the timeline of its planed upgrade as well as a general view of the ATLAS detector and of the Phase-1 Upgrade of its Muon Spectrometer are described;
- In Chapter 3 my work relative to the MicroMegas chambers performances is presented.

The second part of my work relative to the measurements of the differential cross sections of top quark pair in the lepton + jets channel, is reported from Chapter 4 ongoing where the motivations of the analysis are explained. The analysis in detail is presented in the following Chapters:

- In Chapter 5 the data and Monte Carlo samples used in the analysis are described;
- In Chapter 6 the methods used by the ATLAS collaboration to reconstruct and identify the detector level objects are described and the particle level definition is reported;
- In Chapter 7 the event selection and the background sources determination are described;
- In Chapter 8 the unfolding method used to obtain the measured distributions is described;
- In Chapter 9 all the systematic uncertainties sources are reported;
- In Chapter 10 the results distribution differential cross sections are presented.

Finally, in the conclusions, the summary of the analysis, as well as the open issues and plans for the future, are presented.

Appendices, relative to the top quark data analysis, are reported at the end of the thesis. In Appendix A the systematic uncertainties tables are reported. In Appendix B and C the closure and stress tests plots, concerning the validation of the unfolding procedure, are respectively shown. In Appendix D the covariance and correlation matrices are presented. In Appendix E the plots obtained by the rivet routine are shown. Finally, in Appendix F studies on the stability of the unfolding iterations are presented.

Chapter 1

The Standard Model

In this Chapter an overview of the Standard Model of particles physic is presented in Sections 1.1. The fundamental interactions are briefly discussed in Sections 1.2–1.5. At last the top quark physic is discussed in Sections 1.6–1.13.

1.1 The Standard Model of particles physic

The Standard Model (SM), formulated in the 1970s, is a theory of interacting fields. This theory includes, in a coherent scheme, all the known subnuclear particles (and antiparticles) and their interactions. Only the gravitational force is not included in the theory.

The SM is a gauge fiekd theory based on symmetry laws and the mathematic of symmetry is provided by the group theory; it is based on the gauge symmetries $\mathrm{SU(3)}_C \otimes \mathrm{SU(2)}_L \otimes \mathrm{U(1)}_Y$.

According to the SM, all matter is constituted by a small number of fundamental particles, spin $\frac{1}{2}$ Dirac *fermions*: six *leptons* and six *quarks* and the corresponding anti-particles.

Leptons and quarks are divided in three generations. The charged *leptons* are *electrons* (e), *muons* (μ) and *tauos* (τ). They carry integral negative electric charge. The other three leptons, called *neutrinos*, are neutral and are denoted by the generic symbol ν. A neutrino's flavour matchs the flavour of charged leptons as indicated by the subscript.

In the SM neutrinos are supposed to be massless but, recent observations suggest that this hypothesis is not true; neutrinos can oscillate and in this case neutrinos have mass.

The electron is the only stable charged lepton; muons and tauons are both unstables, in fact the mean lifetime is $\tau = 2.2 \times 10^{-6}\ s$ for the muons, and $\tau = 2.9 \times 10^{-13}\ s$ for the tauons.

Quarks, just as leptons, are grouped into pairs. They carry fractional electric charges of $\frac{2}{3}|e|$ and $-\frac{1}{3}|e|$. The quark type or flavour is denoted by a symbol: u for *up*, d for *down*, s for *strange*, c for *charmed*, t for *top* and b for *bottom*.

In Table 1.1 a scheme of fermions, quarks and their electric charge is reported. Going from left to right in the table, the lepton masses increase, just as they do for quarks.

Particle	Flavour	$\frac{Q}{\lvert e\rvert}$
Leptons	e μ τ	-1
	ν_e ν_μ ν_τ	0
Quarks	u s t	$+\frac{2}{3}$
	d c b	$-\frac{1}{3}$

TABLE 1.1: Fermions flavour and their electric charge.

The quarks have a further degree of freedom respect to leptons: the *colour* (blue, green and red). Quarks cannot be observed isolated due to an effect called "*confinement*" that is caused by the strong force.

The term *hadron* is generically used for a quark system: the *baryons* are constitute of three quarks and the *mesons* are constituted of a quark and an antiquark. In particular, protons and neutrons are baryons made up by a combination of quarks u and d.

The common material of the known universe is constituted of the e lepton and d and u quarks. The heavier quarks s, c, t, b also combine to form particles; these particles are unstables and decay in typically 10^{-13} s to u, d combinations, just as the heavy leptons decay to electrons.

The SM also comprises the interactions among particles. Quarks interact via strong, weak and electromagnetic forces; leptons only by the electromagnetic and weak ones and neutrinos interact only via weak force [**Perkins:396126**].

The interactions are described in terms of the exchange of *gauge bosons* between the fermions constituents. These bosons mediators are particles of integral spin. The fundamental interactions or fields are:

- **Electromagnetic interaction**: responsible for all the phenomena in extranuclear physics. This interaction is mediated by a massless particle, *photon*. It is based on an Abelian gauge theory with an U(1) gauge group;
- **Strong interaction**: responsible for binding the quarks in neutron and proton, and the neutrons and protons within nucleus. This force is mediated by a massless particle, *gluon*. It is based on the gauge group $SU(3)_C$;
- **Weak interaction**: responsible for hadron instability. This is the only force that involves neutrinos and that can change the flavours of particles. The mediators of the weak interactions are the $W^{\pm}$ and Z^0 bosons, with masses of order 100 times the proton mass. It is based on a non-abelian gauge theory with a symmetry group SU(2).

The three fundamental interactions just itemised are briefly described in Sections 1.2, 1.3 and, 1.4, respectively.

In the 1970s, thanks to the work of Glashow, Weinberg, Salam and other physicists, the electromagnetic and weak forces had been unified. The main problem of this theory is in describing as massless the weak interaction mediators, because of it has been observed that have a large mass. A solution was proposed in 1964 by Anderson, Higgs, Englert and Brout. They added to the SM Lagrangian a scalar field that permeated the vacuum. Through the spontaneous symmetry breaking of the Lagrangian, this field could give mass to W and Z bosons; incidentally it also describes how the other particles in the SM could have a mass. This mechanism is described in Section 1.5.

The theory includes also a massive, chargeless boson (Higgs boson) that is the quantum of the vacuum field just introduced. In Figure 1.1 a complete scheme of SM particles and interaction mediators is shown:

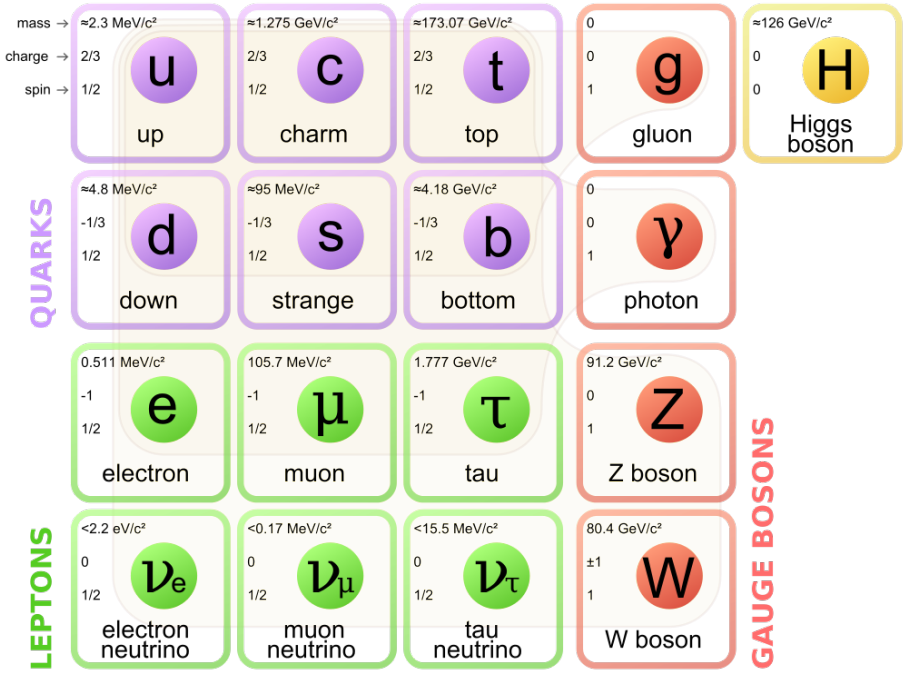

FIGURE 1.1: SM fermions and gauge bosons interaction mediators.

1.2 Quantum Electrodynamic (QED)

Quantum Electrodynamics (QED) is an Abelian gauge field theory with the symmetry gauge group U(1). This theory describes phenomena involving charged particles and their interactions through the electromagnetic force. The mediator of the electromagnetic interaction is a massless gauge boson, the *photon*. The QED Lagrangian is:

$$\mathcal{L} = i\bar{\psi}\gamma^{\mu}D_{\mu}\psi - m\bar{\psi}\psi - \frac{1}{4}F_{\mu\nu}F^{\mu\nu}, \tag{1.1}$$

where ψ is the Dirac field, γ^μ are the Dirac matrices, m is the mass of the electron or positron, D_μ is the *covariant derivative* defined by:

$$D_\mu = \partial_\mu - iA_\mu(x), \tag{1.2}$$

and $F_{\mu\nu}$ is the electromagnetic tensor:

$$F_{\mu\nu} = \partial_\mu A_\nu - \partial_\nu A_\mu. \tag{1.3}$$

The local gauge invariance of the QED Lagrangian requires the presence of the 4-potential vector of the electromagnetic field A_μ and the introduction of D_μ in the Lagrangian. This yields the Lagrangian to be invariant under the local gauge transformations:

$$\psi = e^{i\alpha(x)}\psi, \tag{1.4}$$

$$A_\mu \rightarrow A'_\mu = A_\mu + \frac{1}{e}\partial_\mu \alpha(x), \tag{1.5}$$

where $\alpha(x)$ is an arbitrary gauge field. The expression of the Lagrangian is:

$$\mathcal{L}_{QED} = -\frac{1}{4}F_{\mu\nu}F^{\mu\nu} - \overline{\psi}(\gamma^\mu\partial_\mu + m)\psi + ieA_\mu\overline{\psi}\gamma^\mu\psi. \tag{1.6}$$

The first term describes the free propagation of the A_μ field (photons), the second term the free propagation of the ψ field (charged particles) and the third term describes the elementary interaction between photons and charged particles.

1.3 Quantum Chromodynamic (QCD)

Quantum chromodynamics (QCD) is the gauge theory of strong interactions (Yang-Mills theory [1]). The name Chromodynamics is due to the introduction of a new quantum number, the so called *color*.

In QCD, quarks cannot be observed as free states but they can be only found in colorless confined states (baryons or mesons).

As the QED theory, it is based on a gauge principle; the symmetry gauge group is the colour $SU(3)_C$. The QCD Lagrangian is:

$$\mathcal{L}_{QCD} = -\frac{1}{4}F^a_{\mu\nu}F^{a\mu\nu} + \overline{\psi}(i\gamma^\mu D_\mu - m)\psi, \tag{1.7}$$

where ψ is the fermion field with mass m.

Respect to the quantum electrodynamic, which has one gauge field, the QCD has eight gauge fields. These gauge fields correpond to the 8 generators (T^a) of the SU(3)$_C$ group. They have to satisfy the commutation relations:

$$[T^a, T^b] = if^{abc}T^c, \tag{1.8}$$

where f^{abc} are the structure constants characterising the algebra.

The Lagrangian is invariant under the non-Abelian local gauge transformation introducing a covariant derivative of the form:

$$D_\mu = \partial_\mu - igT^a A^a_\mu, \tag{1.9}$$

where A^a_μ are the gauge fields and g is the *gauge coupling constant*. As in the case of the QED Abelian theory, the QCD Lagrangian contains a term describing the dynamics of free gauge fields A^a_μ.

In the not-Abelian case, the $F^a_{\mu\nu}$ term has the form:

$$F^a_{\mu\nu} = \partial_\mu A^a_\nu - \partial_\nu A^a_\mu + g f^{abc} A^b_\mu A^c_\nu. \tag{1.10}$$

The term $g f^{abc} A^b_\mu A^c_\nu$ in $F^a_{\mu\nu}$ describes the interactions among the gauge fields A^a_μ [2]. This feature was not present in the case of electrodynamic. This difference with the QED is due to the charge of the mediators: in QCD each gluon carries a combination of color and anticolor, instead in the QED, photons are chargeless.

The self interaction of the gauge fields leads to a strange behavior of the strong coupling costant.

The QCD strong coupling costant is defined, in a leading-logarithm approximation, as follows [3]:

$$\alpha_s(Q_2) = \frac{\alpha_s(Q_0^2)}{1 + B\alpha_s(Q_0^2) ln(\frac{Q^2}{Q_0^2})}. \tag{1.11}$$

As $Q_2 \to \infty$ the coupling $\alpha \to 0$ and quarks behave as free particles. This phenomenon is the so called *asymptotic freedom*. Instead, as the distances increase, $Q_2 \to 0$ and the coupling $\alpha \to \infty$. In this case the confinement of the quarks becomes more energetically convenient respect to the free particles state. For this reason, the perturbative theories can be used only at high energies. The behaviour of the coupling costant as function of the energy is shown in Figure 1.2.

1.4 The Weak interaction

The observed lifetimes of pions and muons are longer than those of particles which decay through strong or electromagnetic interactions. The lifetime of the pion decay ($\pi^- \to \mu^- \overline{\nu}_\mu$) is about $\sim 10^{-8}\ s$ and the lifetime of the muon decay ($\mu^- \to e^- \overline{\nu}_e \nu_\mu$) is of the order of $\sim 10^{-6}\ s$. On the other hand, particles decay through color interactions in $\sim 10^{-23}\ s$ and by electromagnetic interactions in $\sim 10^{-16}\ s$. Since the lifetimes are inversely related to the coupling strenght, the longer lifetime of the π reflect the fact that $\alpha \ll \alpha_s$.

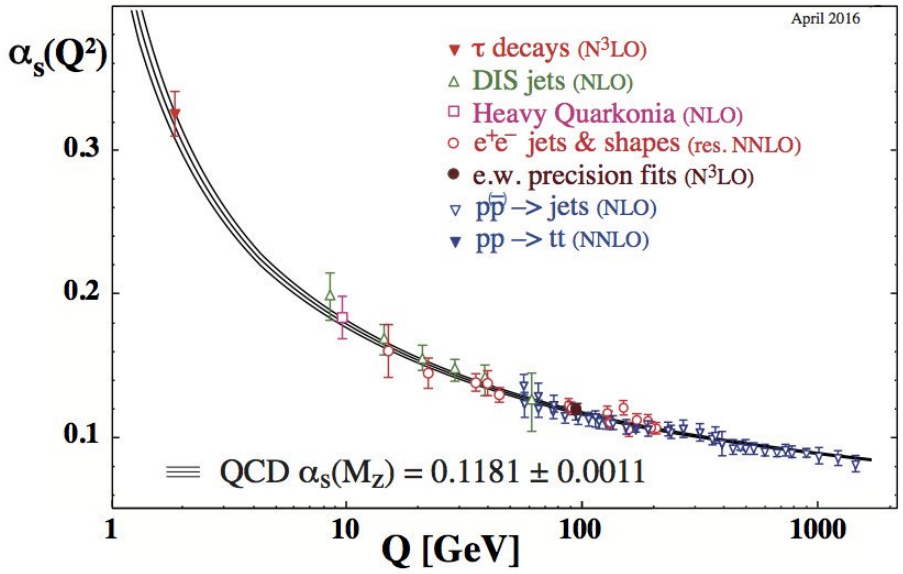

FIGURE 1.2: Strong running coupling constant distribution (α_s) with respect to the momentum transfer.

Pions and muons decays are evidence for another type of interaction, the *weak interaction*.

The two weak decays shown above involve neutrinos which can only interact via weak interactions. Hadrons and leptons can undergo weak decays but they are often hidden by the much more rapid strong or electromagnetic decays. However, $\pi^{\pm}$ and μ cannot decay via the latter two interactions. Whereas the neutral pion (π^0) can decays into photons, the charged pions cannot. The fact that the $\pi^{\pm}$ decay modes into photons is not observed is an evidence for *conserved lepton numbers*: the electron number (L_e), the muon number (L_μ) and the tauon number (L_τ). Known reactions conserve these three numbers separately.

The weak interaction field is invariant under $SU(2)_L$ transformations and its gauge group is not-Abelian. The subscript L on $SU(2)$ reminds that the weak interaction couples only left-handed fermions.

This force has a V-A (vector-axial) structure, i.e. the weak field ψ can be decomposed into two components: the left-handed $\psi_L = \frac{1}{2}(1-\lambda_5)\psi$ component and the right-handed $\psi_R = \frac{1}{2}(1-\lambda_5)\psi$ component [3, 4].

This force has two unique characteristics:

- it is the only fundamental interaction that breaks parity-symmetry and charge-parity-symmetry;
- it allows for quarks to swap their flavour for another.

The transition probability for a quark to change its flavour is described by the Cabibbo-Kobayashi-Maskawa matrix (CKM) and it is proportional to the

square of the V_{CKM} matrix element [5, 6] $|Vqq'|^2$:

$$V_{CKM} = \begin{bmatrix} V_{ud} & V_{us} & V_{ub} \\ V_{cd} & V_{cs} & V_{cb} \\ V_{td} & V_{ts} & V_{tb} \end{bmatrix} \Rightarrow$$

$$\begin{bmatrix} 0.97427 \pm 0.00015 & 0.22534 \pm 0.00065 & 0.00351^{+0.00015}_{-0.00014} \\ 0.22520 \pm 0.00065 & 0.97343 \pm 0.00016 & 0.0412^{+0.00011}_{-0.00005} \\ 0.00867^{+0.00029}_{-0.00031} & 0.0404^{+0.0011}_{-0.0005} & 0.999146^{+0.000021}_{-0.000046} \end{bmatrix}. \quad (1.12)$$

There are two types of weak interactions. The first type is called *charged-current interaction* and it is mediated by particles that carry an electric charge (the W^+ or W^- bosons). The second type is called *neutral-current interaction* and it is mediated by a neutral particle, the Z^0 boson.

Respect to the QED and QCD theories, the weak force mediator bosons have mass ($\sim 90GeV/c^2$). The presence of massive gauge bosons suggests that there must be a mechanism which give mass to these particles.

1.5 The Electroweak unification and Higgs mechanism

In the 1960s Weinberg, Salam and Glashow proposed the *electroweak theory* including both electromagnetic and weak interactions. They postulated the existence of four massless mediating bosons, organised in a *weak isospin* triplet I and in a *weak hypercharge* singlet Y. Three of the bosons, denoted $W_\mu = W_\mu^{(1)}, W_\mu^{(2)}, W_\mu^{(3)}$, are the components of an $I = 1$ triplet of the $SU(2)$ group of weak isospin, while the fourth B_μ is an isoscalar $I = 0$ of the $U(1)$ group of weak hypercharge. The symmetry group of this theory is therefore a not-Abelian $SU(2) \times U(1)$ group.

To give mass to the bosons of the electroweak theory a process called *spontaneous symmetry breaking* acts. This happens through a $I = \frac{1}{2}$ doublet of complex fields called *Higgs scalars* which generate mass as results of their self-interactions.

As result of this mechanism the massive bosons are $W_\mu^+, W_\mu^-, Z_\mu^0$ while the photon A_μ remains massless. Thus, it is possible to define:

$$W_\mu^\pm = \frac{1}{\sqrt{2}}[W_\mu^{(1)} \pm iW_\mu^2], \quad (1.13)$$

$$W_\mu^{(3)} = \frac{gZ_\mu^0 + g'A_\mu}{\sqrt{g^2 + 2'^2}}, \quad (1.14)$$

$$B_\mu = \frac{-g'Z_\mu^0 + gA_\mu}{\sqrt{g^2 + 2'^2}}. \quad (1.15)$$

As shown in Eq. 1.14-1.15, $W_\mu^{(3)}$ and B_μ are linear combinations of the states A_μ and Z_μ^0.

The resulting electroweak Lagrangian is:

$$L = \frac{g}{\sqrt{2}}(J_\mu^- W_\mu^+ + J_\mu^+ W_\mu^-) + \frac{g}{\cos\theta_W}(J_\mu^{(3)} - \sin^2\theta_W J_\mu^{em})Z_\mu + g\sin\theta_W J_\mu^{em} A_\mu. \tag{1.16}$$

The Lagrangian contains the weak charge-changing current (first term), the weak neutral current (second term) and the electromagnetic neutral current (third term) [3]. The electroweak coupling constants g, g', e and the θ_W angle (Weak or Weinberg angle) are related, as shown, in the equations 1.17,1.18:

$$\frac{g}{g'} = \tan\theta_W, \tag{1.17}$$

$$e = g\sin\theta_W. \tag{1.18}$$

In the SM, the Higgs field is a doublet in $SU(2)$:

$$\phi = \begin{pmatrix} \phi^+ \\ \phi^0 \end{pmatrix}, \tag{1.19}$$

where ϕ^+ and ϕ^0 are the following complex fields:

$$\phi^+ = \frac{\phi_1 + i\phi_2}{\sqrt{2}}, \phi^0 = \frac{\phi_3 + i\phi_4}{\sqrt{2}}. \tag{1.20}$$

The contribution to the SM Lagrangian from the Higgs sector is:

$$\mathcal{L}_{Higgs} = (D_\mu\phi)^\dagger(D_\mu\phi) - V(\phi), \tag{1.21}$$

where D^μ is the covariant derivative of the form:

$$D^\mu = \partial^\mu + ig\overrightarrow{T}\cdot\overrightarrow{W}^\mu + i\frac{g'}{2}YB^\mu, \tag{1.22}$$

and $V(\phi)$ is the so-called Higgs potential and has the form:

$$V(\phi) = +\mu^2|\phi|^2 + \lambda|\phi|^4, \tag{1.23}$$

where the first term contains mass $m = \sqrt{-\mu^2}$ and the second term corresponds to the self-interaction among the scalar fields.

The minimum value of the field ϕ occurs when $\frac{\partial V}{\partial\phi} = 0$.

If $\mu^2 > 0$, the minimum value of ϕ is 0, i.e. the normal situation with $V = 0$. If $\mu^2 < 0$, the minimum ϕ value is:

$$\phi = \pm\sqrt{\frac{-\mu^2}{\lambda}} \equiv \nu, \tag{1.24}$$

where ν is called *vacuum expectation value* of the Higgs field ϕ.

Therefore in the case of $\mu^2 < 0$, $V(\phi)$ has two minima. Possible solutions for the Higgs potential, satisfying the relation, are infinite:

$$(\phi_1^2 + \phi_2^2 + \phi_3^2 + \phi_4^2) = -\frac{\mu^2}{2\lambda}. \tag{1.25}$$

A possible choice is:

$$\phi_1 = \phi_2 = \phi_4 = 0, \phi_3 = -\frac{\mu^2}{\lambda} = \nu^2. \tag{1.26}$$

The corresponding vacuum state is:

$$\phi_0 = \frac{1}{\sqrt{2}} \begin{pmatrix} 0 \\ \nu \end{pmatrix}. \tag{1.27}$$

It is necessary to expand the scalar field ϕ around the minimum to obtain a convergent solution:

$$\phi(x) = \frac{1}{\sqrt{2}} \begin{pmatrix} 0 \\ \nu + h(h) \end{pmatrix}, \tag{1.28}$$

$V(\phi)$ is no more invariant under the $SU(2)_L \times U(1)_Y$ symmetry which is therefore broken.

According to the Goldstone theorem [7], which predicts four scalar fields and three broken symmetries, there are three Goldstone bosons and an Higgs boson with mass:

$$m_H = \sqrt{2\lambda\nu}. \tag{1.29}$$

The Higgs boson discovery was announced by the ATLAS [8] and CMS [9] experiments on July 4, 2012. Combining the ATLAS and CMS measurements[10] the Higgs mass is:

$$m_H = 125.09 \pm 0.21(stat.) \pm 0.11(scale) \pm 0.02(other) \pm 0.01(theory) GeV. \tag{1.30}$$

Considering this mechanism within the electroweak field the SM scheme is completed.

1.6 A special component of the SM: the top quark

The top quark is a special particle because of several reasons; as it is shown in Figure 1.1, with a mass of m_t = 173.34 $\pm$ 0.27 (stat.) $\pm$ 0.71 (syst.) GeV [11], it is the heaviest of the foundamental particles known, significantly heavier than the other quark in its generation, the bottom quark.

Contrary to the lighter quarks, which are confined in bound states (hadrons), the top quark has a very short lifetime ($\tau_{\mathrm{t}} \sim 0.5 \cdot 10^{-24}\ s$) and decays before to hadronize. This peculiarity offers an unique opportunity to study the properties of a bare quark.

Once the existence of the bottom quark was experimentally confirmed in 1977, the existence of a quark with a 2/3 charge, in the third generation was expected; it was in fact discovered at the FermiLab Tevatron, a proton-antiproton ($p\overline{p}$) collider at a center of mass energy ($\sqrt{s}$) of 1.8 TeV, in 1995 by the CDF [12] and D∅ [13] experiments.

The top quark production is now studied by the experiments of the LHC accelerator which is considered a *top quark factory* because of its high rate of top quark production.

The top quark production is a backgrounds in many searches for physics beyond the SM; for this reason a precise understanding of the top quark signal is crucial to claim new physics. In addition, its very large mass implies a large coupling with the Higgs boson.

1.7 Top quark production and decay

The top quark can be produced in pairs via strong interactions and as single particle in electroweak processes. The strong processes have a higher cross section, whereas the electroweak cross section production is less likely.

The cross section production for top quarks, both in pairs and as single quark, strongly depends on the collision energy reached in the accelerators. Since the top quark decays before hadronizing, detectors can only be able to measure its decay products.

The probability for each type of the down-type quarks to occur as decay product is given by the CKM matrix elements involving top quarks. The top quark decays almost exclusively into a W boson and a bottom quark ($t \to W^+$ and $\bar{t} \to W^-$) since the CKM element V_{tb} is close to 1. This can be written in terms of branching ratio and can be measured experimentally.

$$R_b = \frac{\mathcal{BR}(t \to Wb)}{\mathcal{BR}(t \to Wq)} = \frac{|V_{tb}|^2}{|V_{tb}|^2 + |V_{ts}|^2 + |V_{td}|^2} \approx 1. \tag{1.31}$$

The $t \to Wb$ process is shown in the Feynman diagram in Figure 1.3.

The decay signatures of the top quark or the anti-top quark are categorised according to the decay of the W boson, leptonic or hadronic. In the leptonic decay mode, the W boson decays into a lepton (anti-lepton) and in its associated neutrino (anti-neutrino). Whereas, in the hadronic decay mode, the W boson decays into a $q\overline{q}$ pair.

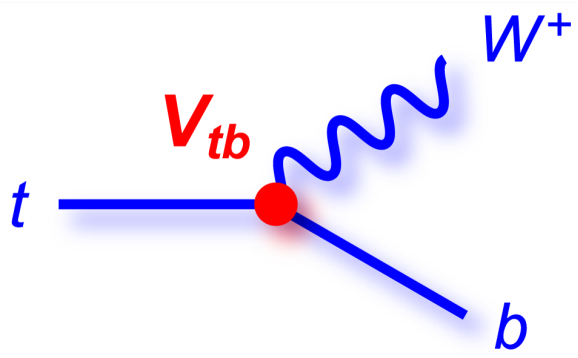

FIGURE 1.3: Feynman diagram of the top quark decays chain.

The $t\bar{t}$ events are therefore classified according to the decay modes of the two W bosons. When both the W bosons decay hadronically, the event is defined *fully hadronic*. This is the decay channel with the highest branching ratio ($\approx 46\%$) but it has also the largest background. When both the W bosons decay leptonically, the channel decay mode is called *dilepton* and it has the lowest branching ratio ($\approx 10\%$) but it is the cleanest channel. The last channel is the ℓ + jets, namely semileptonic, characterised by the decay of one W boson leptonically and by the other one hadronically.

In the analysis described in this thesis, leptonic decays of the τ are also considered; cases where both top quarks decay semileptonically into τ leptons which then decay hadronically, are rejected and considered as background. This channel has a branching ratio of ($\approx 44\%$) and a moderate background.

The top quark pairs decay channels and its branching ratio are shown in Figure 1.4(a),1.4(b). The Feynman diagrams of the three channel decay modes are shown in Figure 1.5 for the dilepton channel 1.5(a), ℓ + jets channel 1.5(b) and fully hadronic channel 1.5(c) respectively.

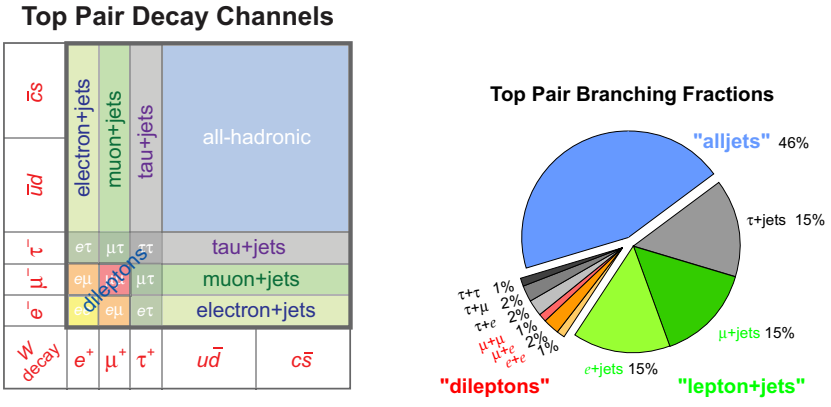

FIGURE 1.4: Top quark decay channels (a) and (b) branching ratio.

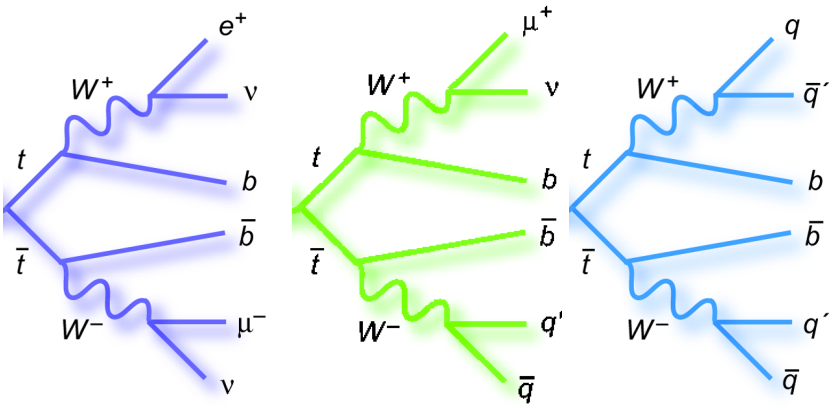

FIGURE 1.5: Feynman diagram of top quark decay modes: (a) Dilepton channel, (b) ℓ + jets channel and (c) fully hadronic channel.

1.8 Top quark pair production

At leading order (LO), the first perturbative order of α_s, top quark pairs can be produced in two ways: gluon-gluon fusion and $q\bar{q}$ annihilation.

At the Tevatron collider, in $p\bar{p}$ collisions, the dominat process was the $q\bar{q}$ annihilation, whereas, at the LHC, in proton-proton (pp) collisions, the dominant production process is the gluon-gluon fusion. The Feynman diagram of both the processes, at LO, are shown in Figure 1.6. At next-to-leading order (NLO), second perturbative order of α_s, the processes are also a mixture of quark-gluon (qg) or antiquark-gluon ($\bar{q}$g). Some examples of the Feynman diagrams of these NLO processes are shown in Figure 1.7.

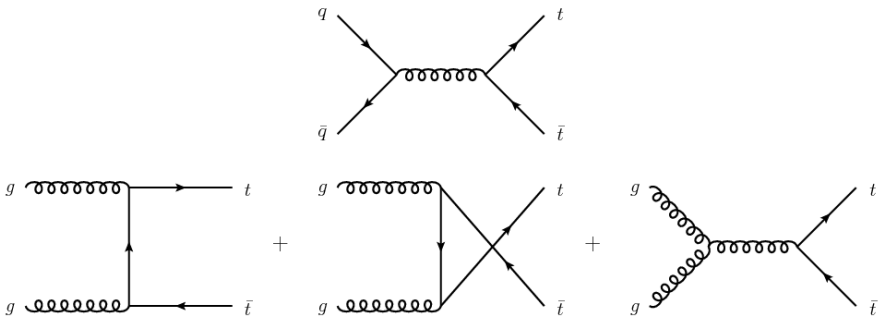

FIGURE 1.6: Top quark pairs production Feynman diagram at LO. The two production processes are the gluon-gluon fusion and the $q\bar{q}$ annihilation.

The fact that at the LHC the gluon-gluon fusion production process is the dominant one is due to two reasons: the higher $\sqrt{s}$ and that pp beams collide at LHC.

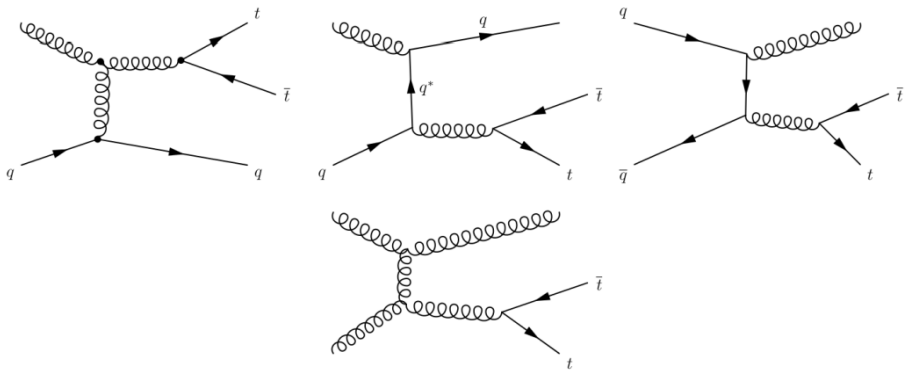

FIGURE 1.7: Top quark pairs production Feynman diagram at NLO. The two production processes are the quark-gluon and antiquark-gluon.

First of all, $q\bar{q}$ annihilation are disfavored in general in pp collisions respect to in the $p\bar{p}$ ones. In addition, at the Tevatron collider the partons partecipating in the collisions have to carry a high fraction of the proton's momentum. At high values of x, the up and down valence quarks from the proton dominate, making $q\bar{q}$ annihilation more likely respect to gluon-gluon fusion, at the Tevatron $\sqrt{s}$=1.96 TeV.

At the LHC energies, partons with small fraction of x are able to produce top quark pairs. Since gluons dominate the parton distribution function of the proton up to high x, the gluon gluon fusion becomes the dominating processes.

To quantify the production of top quark pairs ($t\bar{t}$), it is necessary to measure the cross section of the process. Classically, the cross section is a quantity describing the process of interaction between two bodies and it has the dimension of an area measured in barn b.

The total inclusive cross section of a process considers all the possible scattering processes that occur during collisions, for example, between protons at the LHC. The most general cross section expression, for a collider is given by:

$$\sigma = \frac{N_{events}}{\epsilon L}, \tag{1.32}$$

where N_{events} is the number of observed events, ϵ is the efficiency of the detector and L is the integrated luminosity, defined as:

$$L = \int \mathcal{L} dt, \tag{1.33}$$

i.e, the integral of the instantaneus luminosity in time, here defined:

$$\mathcal{L} = \frac{1}{4\pi} \frac{n_1 \cdot n_2}{\sigma_x \cdot \sigma_y} f_k, \tag{1.34}$$

where f is the collision frequency, k is the number of bunches that circulate simultaneously, n_1 and n_2 correpond to the number of particles contained in each bunch and, σ_x and σ_y correspond to the distributions of the particles contained in the beams along the orthogonal axes with respect to the beam direction.

The factorisation theorem

At the $\sqrt{s}$ reached at the LHC, quarks and gluons in the protons can be considered as quasi-free particles and, therefore, the processes involved in the pp collisions can be described in terms of interactions between the costituent partons.

This process implies the use of the parton model which is schematically described in Figure 1.8. The Figure shows the collision of two energetic protons P_1 and P_2 with momentum p_1 and p_2 respectively.

The hard scattering process of two protons can be seen as interaction between the constituents partons of the protons. The probability density to find a parton i (j) inside a proton P_1 (P_2) carrying a fraction x_i (x_j) of the proton's momentum is described by $f_{i/P_1}(x_i, \mu_F^2)$ and $f_{j/P_2}(x_j, \mu_F^2)$, the parton distribution functions (PDFs).

The PDFs are not predicted by the theory but are determined from fits to Deep-Inelastic-Scattering (DIS) cross section measurements performed by various experiments, HERA in particular. The PDFs are required to calculate the production cross section in all Monte Carlo (MC) generators. Therefore, in order to allow the community to use the PDF fits, theorists package these informations in software tools.

Commonly the MRST [14] and CTEQ PDF fits [15] are used.

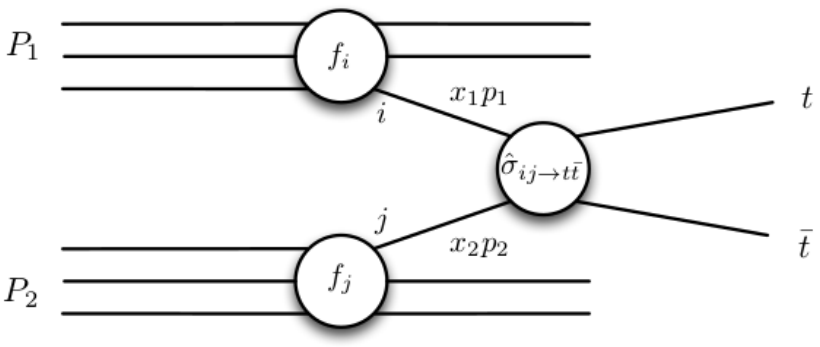

FIGURE 1.8: The top quark pair production of a hard scattering process in the parton model.

The inclusive production cross section of the process $pp \to t\bar{t}$ can be calculated using the *factorisation theorem* [16] exploiting the main features of the

QCD, confinement and asymptotic freedom (discussed in Section 1.3) separating short and long distances processes.

The cross section is convoluted with the PDFs. In such a way, the cross section of any QCD process can be written as a convolution between calculable parts (hard scattering coefficients) and not-calculable parts (PDFs), as follows:

$$\sigma_{P_1P_2} = \int dx_i dx_j f_{i/P_1}(x_i, \mu_F^2) f_{j/P_2}(x_j, \mu_F^2) \hat{\sigma}(x_i, x_j, \alpha_s(\mu_R^2), \mu_F^2, \mu_R^2), \quad (1.35)$$

where $\hat{\sigma}$ is the factorized hard parton-parton cross section, α_s is the strong coupling constant and μ_R and μ_F are the renormalisation and factorisation scales, respectively.

The partonic cross section $\hat{\sigma}$ can be expanded in fixed order series in α_s as:

$$\hat{\sigma}_{ij\to t\bar{t}} = \alpha_s^2[\hat{\sigma}^{(0)}_{ij\to t\bar{t}} + \alpha_s \hat{\sigma}^{(1)}_{ij\to t\bar{t}} + 0(2)] \quad (1.36)$$

where the first term is the contribution at LO, $\hat{\sigma}(1)$ is the contribution at NLO and so on.

The PDFs and $\hat{\sigma}$ have a residual dependence on the factorisation and renormalisation scales, due to uncalculated high orders.

The PDFs are evaluated at the factorisation scale μ_F^2 and α_s at the renormalisation scale μ_R^2 and accounts for divergences coming from loop diagrams. These two scales are chosen to be equal and, in the case of the top quark production, μ is set to be equal to the top quark mass ($\mu = m_t$).

1.8.1 The inclusive $t\bar{t}$ pair cross sections

The $t\bar{t}$ inclusive cross section has been experimentally measured for the first time at Tevatron by the CDF [17] and D∅ [18] collaborations. The value of the cross section, combining the results obtainted by the two experiments, is:

$$\sigma_{t\bar{t}}^{Tevatron}(p\overline{p}\ 1.96\ TeV) = 7.08 \pm 0.36\ pb. \quad (1.37)$$

The inclusive $t\bar{t}$ cross section has been also measured by the ATLAS and CMS experiments at $\sqrt{s}$ of 7, 8 and 13 TeV.

Because of the strong dependence on $\sqrt{s}$, the theoretical and experimental $t\bar{t}$ production cross sections are much bigger respect to the Tevatron ones.

The latest experimental measurments of the $t\bar{t}$ cross sections were obtained by the ATLAS and CMS collaborations at a $\sqrt{s}$ of 13 TeV and with 3.2 fb^{-1} of data collected.

The cross section theoretical prediction for the energies reached by the LHC up to now was calculated, at next-to-next-leading-order (NNLO) including

the resumation of next-to-next-leading-logarithm (NNLL), using the *top++2.0* program [19] and assuming m_t = 172.5 GeV:

$$\sigma_{t\bar{t}}^{LHC}(pp\ 13\ TeV) = 832^{40}_{-46}\ pb. \tag{1.38}$$

The ATLAS [20] and CMS [21] experiments, have measured, respectively:

$$\sigma_{t\bar{t}}^{ATLAS}(pp\ 13\ TeV) = 818 \pm 8(stat) \pm 27(syst) \pm 19(lumi) \pm 12(beam)\ pb, \tag{1.39}$$

$$\sigma_{t\bar{t}}^{CMS}(pp\ 13\ TeV) = 815 \pm 9(stat) \pm 38(syst) \pm 19(lumi)\ pb, \tag{1.40}$$

both the measurements were performed in the dilepton channel and are in good agreement with the SM predictions.

A complete picture of the LHC and Tevatron top quark pair inclusive cross sections is shown in Figure 1.9 where the cross sections are reported as a function of $\sqrt{s}$ and compared with the latest NNLO+NNLL predictions.

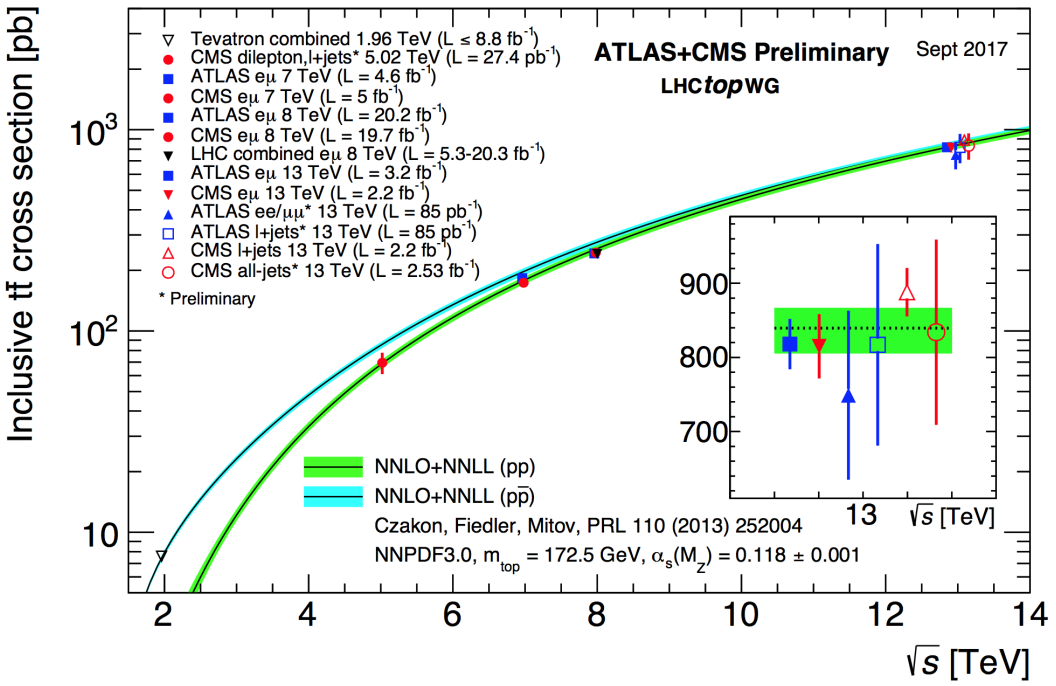

FIGURE 1.9: Summary of LHC and Tevatron measurements of the top-pair production cross section as a function of the $\sqrt{s}$ compared to the NNLO QCD calculation complemented with NNLL resummation.

1.8.2 The differential $t\bar{t}$ pair cross sections

The differential measurements are defined as cross sections as functions of kineamtic observables. The measurement of the differential cross section

is an important test of the SM predictions and a sensitive channel for new physics.

The differential cross sections can be measured either at *parton level* or at *particle level*. The parton level is referred to the case where in the measurement are considered objects at the level after the radiation but before decay, while, the particle level is referred to objects after decay, parton shower and hadronisation.

In the analysis reported in this thesis measurements at particle level have been done; a *fiducial phase space*, where the measurements are performed, is defined in Section 6.6.

The first experimental results of differential top quark pair cross sections have been obtained at Tevatron by the CDF and D∅ collaborations, as functions of the mass of the $t\bar{t}$ system [22] and of the top quark transverse momentum [23], respectively.

Several differential cross section measurements with increasing statistic, have been performed also by the ATLAS and CMS collaborations at LHC with a $\sqrt{s}$ of 7, 8 and 13 TeV in the dilepton, ℓ + jets and in the fully hadronic channels at both particle and parton levels.

1.9 The single-top quark production

As already said in Section 1.7, the single-top quark production occurs via electroweak interaction during the hard scattering process. Only one top quark is produced and for this reason it is referred to as *single-top quark* production.

The single-top quark production was observed for the first time at Tevatron by the CDF and D∅ experiments in 2009 [24]. At the Tevatron energies, the single-top quark cross sections were very low, therefore, the contribution of the single-top quark production was not significant. Instead for this kind of production large cross sections correspond to the energies reached at the LHC.

Depending on the way the W boson is involved in the interaction, the single-top quark production can be categorised into three production modes: t-channel, s-channel and Wt-channel. In Figure 1.10, the Feynman diagrams, at LO, for the single-top quark production are reported for the t-channel 1.10(a), Wt-channel 1.10(b) and s-channel 1.10(c), respectively.

In the t-channel process, the top quark is produced via the exchange of a virtual space-like W boson which decays leptonically and the final objects are one b-quark from the top quark, one charged letpon, one neutrino, one light quark and one additional b-quark. In the s-channel process, the top quark is produced by the exchange of a virtual time-like W boson which produces one high-p_T bottom quark, one charged lepton, one neutrino and one single-top

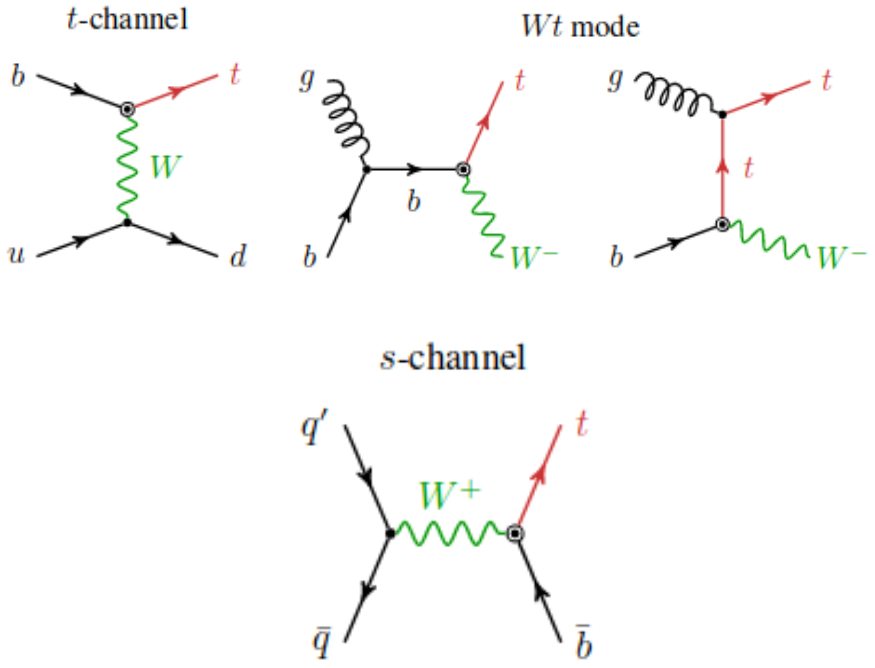

FIGURE 1.10: Feynman diagram at LO of single-top quark production: t-channel (a), Wt-channel (b) and s-channel (c).

quark. Searching for s-channel is more difficult than the t-channel beacuse of the very small cross section. The third mechanism of single-top quark production is the Wt channel where the top quark is produced in association with a real W boson. At the LHC this is the channel with major contribution in terms of cross section.

1.10 Top quark mass

The mass of the top quark, is a parameter of the SM and has been experimentally measured (m_t = 173.34 $\pm$ 0.27 (stat.) $\pm$ 0.71 (syst.) GeV).

In Figure 1.11 the recent direct measurements of the top quark mass, obtained by the ATLAS detector, are reported. As can be seen from the Figure, the results are compared with the Tevatron and the Tevatron + LHC top quark mass combinations.

The indirect determination of the m_t simultaneous togheter with the determination of the m_W is an important consistency test of the SM and can be obtained from precision measurements of the electroweak theory's parameters. The mass of the W boson is:

$$m_W^2 = \frac{\pi\alpha(M_Z^2)/\sqrt{2}G_F}{sin^2\theta_W \cdot (1-\delta_r)}, \tag{1.41}$$

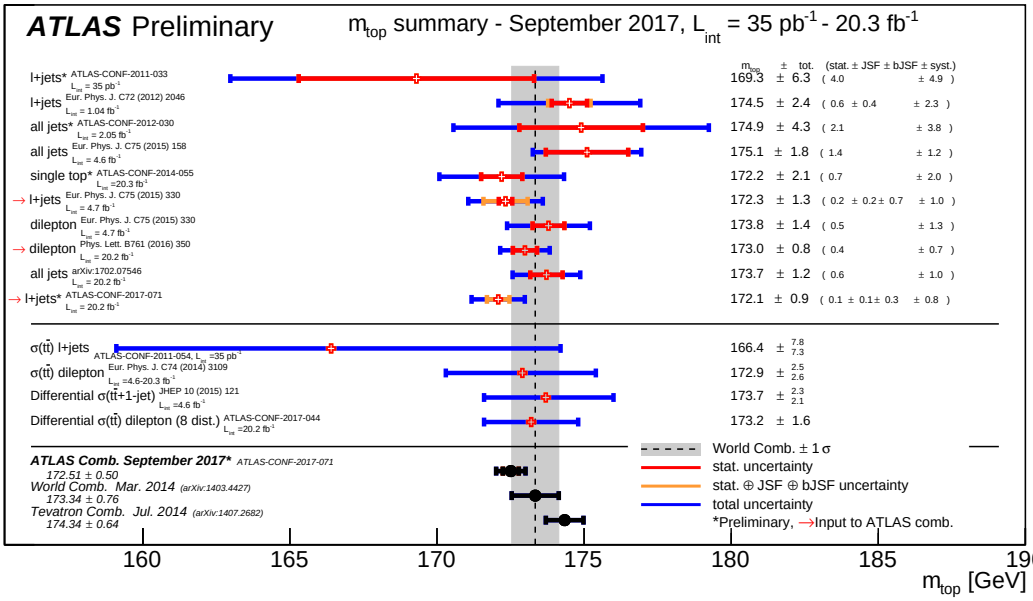

FIGURE 1.11: Summary of the ATLAS top quark mass measurements compared with the Tevatron and the Tevatron + LHC combinations.

where α is the electromagnetic coupling constant, G_F is the Fermi constants, θ_W is the electroweak angle determined as $\sin^2\theta_W \equiv 1 - m_W^2/m_Z^2$ and the term δ_r, which contains contributions from higher order electroweak loop and depends quadratically on m_t, is defined as:

$$\delta_r = -\frac{\approx 3G_F}{8\sqrt{2}\pi^2 \tan^2\theta_W} m_t^2. \tag{1.42}$$

The most recent indirect constraint on the m_t based on the electroweak precision measurements is $m_t = 179.7^{+11.7}_{-8.7}$ GeV [25]; this value is in good agreement with the direct measurements. Since the δ_r term also containts contributions from loop diagrams involving the Higgs boson, with a logarithmically dependence on the m_H, it is possible to obtain direct constraints on m_H from global electroweak fits which include direct measurements of the m_t.

1.11 Top quark decay width

The large mass of the top quark has as result a short lifetime. Hence, its decay width is the largest of all SM fermions.

The decay width evaluated at LO calculation corresponding to a top quark mass of 172.5 GeV is Γ_t = 1.33 GeV, while, the recent NLO calculation predicts a Γ_t = 1.322 GeV for a m_t=172.5 GeV.

A direct measurement of Γ_t was performed at Tevatron by the CDF collaboration.

The direct measurements of the width are limited by the experimental resolution of the top quark mass spectrum and are significatively less precise respect to the indirect measurements but allow to avoid model dependent assumptions.

The last measurement of the top quark width has been performed by the ATLAS collaboration using at $\sqrt{s}$=8 TeV [26]. The measurement is direct and consists of an extraction of the width by using $t\bar{t}$ events in the ℓ+jets channel. The decay width has been measured to be $\Gamma_{\rm t}$ = 1.76 $\pm$ 0.33 (stat.)$^{+0.79}_{-0.68}$(syst.) GeV for $m_{\rm t}$=172.5 GeV.

1.12 Top quark charge asymmetry

In pp collisions, the difference in rapidity between top quarks and anti-top quarks is called charge asymmetry $A_{\rm C}$ and is defined as:

$$A_{\rm C} = \frac{N^{\Delta|y|>0} - N^{\Delta|y|<0}}{N^{\Delta|y|>0} + N^{\Delta|y|<0}}, \tag{1.43}$$

using the difference of the absolute value of the rapidities of the top quark and anti-top quark, $\Delta|y| = |y_{\rm t}| - |y_{\bar{\rm t}}|$.

The number of events with $\Delta|y|$ that take positive and negative values, is given by the expressions $N^{\Delta|y|>0}$ and $N^{\Delta|y|<0}$, respectively.

The SM predicts $A_{\rm C}$ to be of the order of one percent. The interest of the ATLAS [27] and CMS [28] collaborations to measure the $A_{\rm C}$ has grown after that the CDF and D$\varnothing$ collaborations reported measurements of $A_{\rm FB}$ forward-backward asymmetry, which is significatively larger respect to the SM predictions.

Both the ATLAS and CMS have measured the charge asymmetry at 7 and 8 TeV and the last measurement of the $A_{\rm C}$ have been performed by both the collaborations in the single lepton channel using data of the LHC with a $\sqrt{s}$ of 8 TeV.

The charge asymmetry measured by the ATLAS collaboration is $A_{\rm C}$ = 0.008 $\pm$ 0.005 (stat.) + 0.003 (syst.) while the measure performed by the CMS collaboration is $A_{\rm C}^{\rm y}$ = 0.003 $\pm$ 0.006 (stat) $\pm$ 0.003 (syst.) which are compatible with the SM prediction $A_{\rm C}$ = 0.0064 $\pm$ 0.0003.

The combination of the measurement of $A_{\rm C}$ of both the ATLAS and CMS collaborations, in several channels, corresponding to data collected at 8 TeV is shown in Figure 1.12, where the measurements are compared to the theoretical predictions.

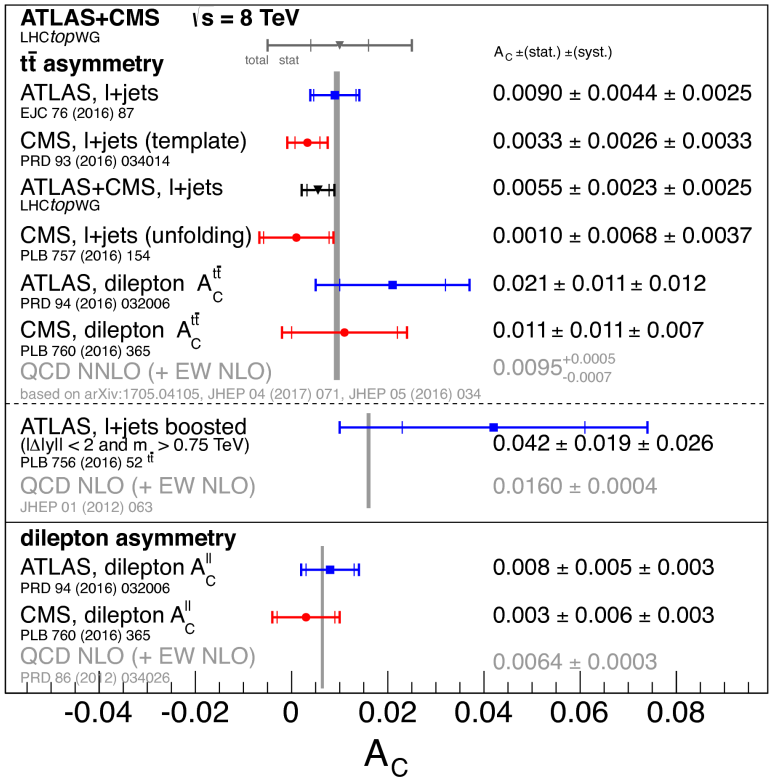

FIGURE 1.12: Summary of the combined ATLAS and CMS top quark charge asymmetry measurements.

1.13 Top quark spin

Quarks and gluons of the initial state are unpolarised which means that their spin is not preferentially aligned with any given direction.

The spins of top quark and anti-top quark produced are correlated with a strenght depending on the spin quantisation axis and on the production process. The spin information is not decorrelated by the hadronisation and therefore the spin information is transferred to the decay products.

It is therefore possible to measure the top quark pair's spin structure using angular observables of the decay products.

The last measurements performed on the spin correlation by the ATLAS detector use data collected with a $\sqrt{s}$ of 8 TeV [29]; the measurement has been performed with dilepton events in the final state.

The spin correlation between the axis a and b is expressed as:

$$C(a,b) = -9 < \cos\theta_+^a \cos\theta_-^b > . \tag{1.44}$$

The resulting value obtained is C(a,b) = 0.296 $\pm$ 0.093 [$\pm$ 0.037 (mass)] in agreement with the SM predictions C(a,b) = 0.318$\pm$ 0.003.

Chapter 2

The LHC and the ATLAS detector

In this Chapter, the Large Hadron Collider (LHC) and the ATLAS experiment with its subdetectors are described in Sections 2.1 and 2.2, respectively. Also, in Section 2.3 the LHC and the ATLAS program Phase-1 Upgrade are reported, focusing for what concern the ATLAS Upgrade, on the Muon subdetector.

2.1 The Large Hadron Collider

The Large Hadron Collider (LHC) [30, 31] is the world's largest and most powerful collider; it is a superconducting pp collider. An overwiev of the LHC is shown in Figure 2.1.

The LHC is a 27-kilometer in circumference ring placed at a mean depth of $100\ m$ below the Franco-Swiss border near Geneva, built by the European Organization for Nuclear Reasearch (CERN).

FIGURE 2.1: The Large Hadron Collider (LHC) ring.

The LHC is a complex machine made of many components. The two main elements are magnets and RF cavities that respectively bend and accelerate the beams.

Inside the accelerator two high-energy particle beams travel at close to the speed of light before they are made to collide. The beams travel in opposite directions, in separate beam pipes. The two tubes are kept at ultrahigh vacuum. The beams are guided around the accelerator ring by a magnetic field up to $8.33\ T$ maintained by superconducting electromagnets chilled to $-271.3°C$. The first beams circulated on September 10, 2008.

Fundamental parameters to determine the performances of the collider are luminosity and $\sqrt{s}$.

The luminosity is a parameter that depends only on the characteristics of the accelerator; the instantaneus and integrated luminosity have been defined in Section 1.8 in Eq. 1.34 and in Eq. 1.33.

The nominal luminosity of the LHC is $10^{34} cm^{-2} s^{-1}$, has been improved to $1.58 \cdot 10^{34} cm^{-2} s^{-1}$ in summer 2017 and will reach the value of $5 \cdot 10^{34} cm^{-2} s^{-1}$ at the end of 2023.

The LHC is opertating at a $\sqrt{s}$ = 13TeV. In particular during the 2011 year, the LHC reached a $\sqrt{s}$ of 7 TeV and an integrated luminosity (L) of $4.6\ fb^{-1}$. In the following year, in 2012, $\sqrt{s}$ has increased up to $8\ TeV$ achieving L = 20.3 fb^{-1}. Then, from 2015, the LHC reached $\sqrt{s} = 13\ TeV$ and a L = 35.6 fb^{-1} at the end of 2016.

Now, the LHC is operating, collecting data maintaining $\sqrt{s} = 13\ TeV$. In Figure 2.2 the acceleration system of the particles is shown.

The LHC is only the last accelerator in a long chain of machines. The proton source is a simple bottle of hydrogen gas. An electric field is used to strip hydrogen atoms of their electrons to yield protons. In the first step of the chain, protons are accelerated by a linear accelerator, *Linac2*, to the energy of $50\ MeV$. Then, the beam passes into the *Proton Synchrotron Booster* (PSB) where the protons reach an energy of $1.4\ GeV$. Subsequently, the *Proton Synchrotron* (PS) leads them to an energy of $26\ GeV$, and finally the Super Proton Synchrotron (SPS) accelerates them to $450\ GeV$.

Reached the energy of $450\ GeV$, the protons are injected to the two beam pipes into the LHC. The beam in one of the pipes circulates clockwise while, the beam in the other pipe circulates anticlockwise. Simultaneously up to 3600 bunches of protons circulate in the ring, at a frequency of revolution of $1.1 \cdot 10^4\ Hz$, thus obtaining an interaction every $25\ ns$.

The number of events in the time unit ($\frac{dN}{dt}$), generated in collisions, is given by the following relation:

$$\frac{dN}{dt} = L_{ins} \cdot \sigma_{event}, \tag{2.1}$$

where σ_{event} is the total interaction cross section of the event.

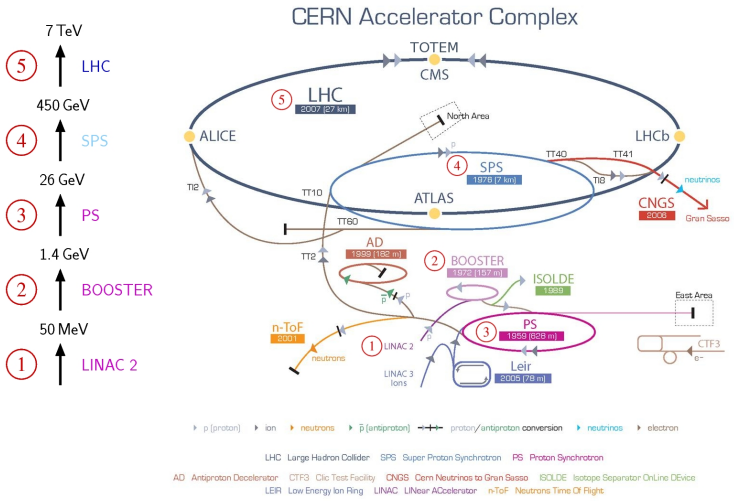

FIGURE 2.2: Overwiev of the LHC accelerator complex.

2.1.1 The LHC's experiments

Seven experiments analyse the events produced by collisions in the LHC. The beams inside the LHC are made to collide at four locations (interaction points (IP)). Around each of them an experiment is placed, as shown in Figure 2.3 located in a large cavern created to host it.

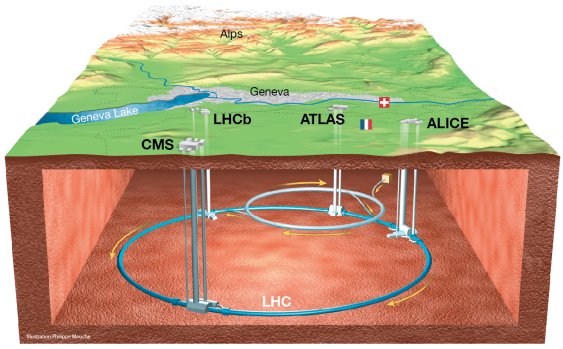

FIGURE 2.3: The LHC ring and its experiments at the IP.

The experiments located around the IPs are:

- **ALICE** [32]: it is a heavy-ion detector designed to study matter behavior at high energy and densities;
- **ATLAS** [33]: it is the largest experiment at CERN with a $25\ m \times 46\ m \times 26\ m$ volume and a weight of $7000\ tons$. It is one of the two general purpose detectors to investigate the larger range of physics possible;
- **CMS** [34]: it is the heaviest detector ($14000\ tons$) at LHC and as ATLAS, it is a general purpose detector to perform precision measurements and

to search new particles; it can generates a field of $4\ T$ and respect to the ATLAS experiment it uses a different magnet-system design;

- **LHCb** [35]: it is specialised to perform dedicated studies on physics of B-meson and on CP violation.

Other three smaller experiments are located further away the interaction point in the LHC tunnel: **TOTEM** [36], **LHCf** [37] and **MoEDAL** [38]. These experiments focus on events with a small scattering angle, commonly defined "forward physics".

2.1.2 The Worldwide LHC Computing Grid (WLCG)

The WLCG is a global computing infrastructure whose mission is to provide computing resources to store, distribute and analyse the data generated by the LHC.

The WLCG is the largest computing grid in the world. It is composed of four levels (0, 1, 2 and 3), called "Tiers". Each Tier is made up of severals computer centers and provides a specific set of services.

The services of the different Tiers, are listed below:

- **Tier 0**: it is the CERN Data Center (CDC). All the LHC's data pass through this central hub. It provides less then 20% of the Grid's total computing capacity. It distributes raw data and reconstructed output to Tier 1 and when the LHC is not running, reprocesses data;
- **Tier 1**: it consists of 13 computers centers and it is large enough to store all the LHC data. Tier 1 is responsible for reprocess and distribute outputs to the Tier 2 centers;
- **Tier 2**: these types of Tiers are typically universities and scientific institutes that can store sufficient quantity of data and can provide adequate computing power for specific analysis tasks. There are 155 Tier 2 around the world;
- **Tier 3**: they are local computing resources accessible by individual scientists.

2.2 The ATLAS experiment

The ATLAS (A Toroidal LHC ApparatuS) experiment is a general purpose detector. It is able to study all the processes predicted by the SM, as well as to detect signals of "new physics".

The detector was designed to fulfill the requirements that LHC imposes for high multiplicity and high rate of bunch crossing.

The ATLAS layout is based on the traditional onion-shell structure used in collider experiments; it is about $45\ m$ long, more than $25\ m$ high, and weighs about $7000\ tons$. The detector is constituted by a central part, **barrel**, and two side parts, **endcaps**.

In detail, it is composed by a toroidal magnetic system and five main subdetectors: going from the inner part to the external one, the ATLAS detector is composed of the Inner Detector (ID), the Electromagnetic Liquid Argon Calorimeter (LAr), the Hadronic Calorimeter (Tile), the Muon Spectrometer (MS) and the forward detectors (Lucid and BCM).

Each subdetector has a different task: the ID is a tracking system, the calorimeters measure particle energy and the MS, the most external part of the ATLAS detector is a tracking system to detect muons.

The magnet system is designed to bend the charged particle trajectory and, therefore, to measure the particles momentum. At last, the forward detectors measure the luminosity.

Figure 2.4 shows a tridimensional image of the whole apparatus and the subdetectors [39] are briefly discussed in the following Sections 2.2.1–2.2.5.

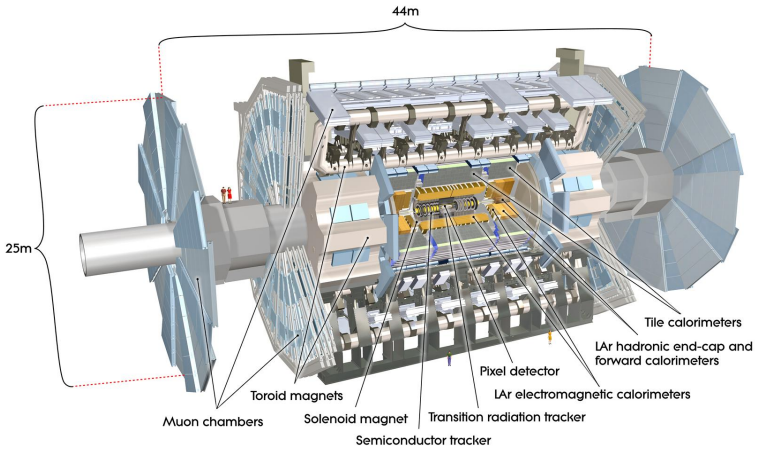

FIGURE 2.4: Overwiev of the ATLAS detector and its subdetectors.

The detector is built at the IP-1; it has a cylindrical symmetry respect to the beam line. ATLAS uses a right-handed coordinate system defined taking the IP as origin. The beam direction defines the z-axis and the x-y plane is transverse to the beam direction. The x-axis is defined as pointing from the IP to the center of the LHC ring while, the y-axis is defined pointing upwards.

Given the symmetry of the detector, a system of cylindrical coordinates (R, ϕ, θ) can be used. The azimuthal angle ϕ is measured around the beam axis and the polar angle θ is the angle from the beam axis.

A graphical representation of the pseudorapidity is shown in Figure 2.5 and it is defined as:

$$\eta = -ln \tan \frac{\theta}{2}. \tag{2.2}$$

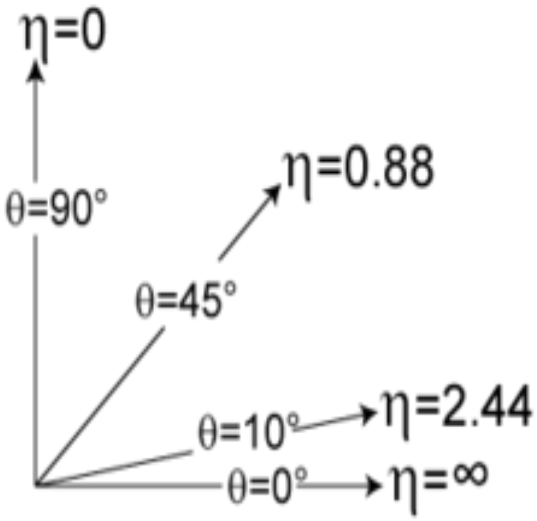

FIGURE 2.5: Pseudorapidity (η) values with polar angle (θ) values.

The transverse momentum (p_{T}), the transverse energy (E_T) and the missing transverse energy ($E_{\mathrm{T}}^{\mathrm{miss}}$) are defined in the x-y plane.

The distance ΔR in the $\eta - \phi$ angle space is defined as:

$$\Delta R = \sqrt{\Delta\eta^2 + \Delta\phi^2}. \tag{2.3}$$

2.2.1 Magnet system

To determine the momentum of a charged particle, the curvature of its trajectory through the detector is measured. It is therefore necessary to place the tracking detectors in a magnetic field in such a way the trajectory of the particle is bended.

The ATLAS detector has a magnet system which consists of four large superconducting magnets. The ATLAS magnet system layout is shown in Figure 2.6.

This system consists of:

- a **Solenoid** which is aligned on the beam axis and provides a $2\ T$ axial magnetic field. It is placed around the ID cavity and it has a diameter of $2.4\ m$ with a lenght of $5.3\ m$;
- a **Barrel Toroid** and two **End-Cap Toroids**, that provides a $4\ T$ magnetic field. The barrel toroid has an outer diameter of 20.1 m and a lenght of

25.3 m. The end-cap toroids have an outer diameter of 10.3 m and an axial lenght of 5 m.

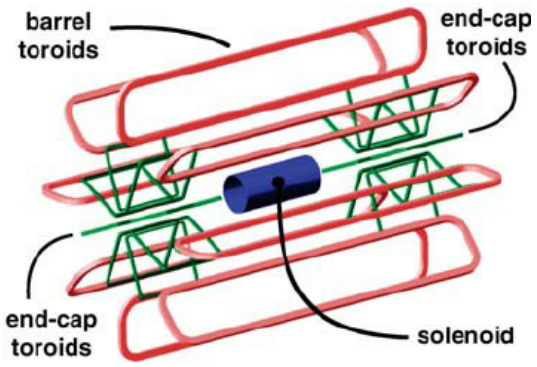

FIGURE 2.6: Layout of the ATLAS magnet system.

2.2.2 The Inner Detector (ID)

The ATLAS ID [40] is placed in the most inner part of the ATLAS detector and it is the closest part to the beam line. The ID occupies the cylindrical cavity and it is bounded by cryostats of the electromagnetic calorimeter and surround the beam-pipe.

It is a $7\ m$ long and $1.15\ m$ of radius cylinder and is immersed in a solenoid magnetic field parallel to the axis of the beam with intensity of $2\ T$. The ID layout is shown in Figure 2.7.

The acceptance in pseudorapidity is $|\eta| < 2.5$ for particles coming from the LHC beam-interaction region, with a full coverage in ϕ.

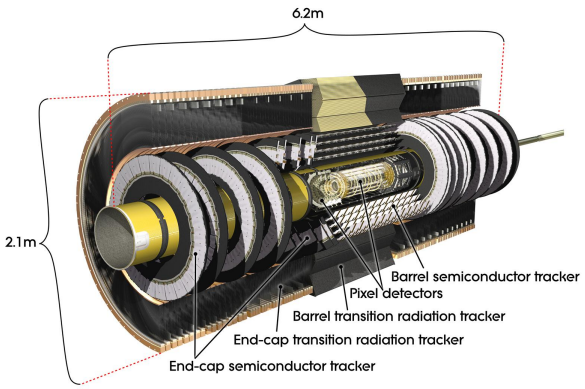

FIGURE 2.7: The ATLAS ID general layout.

The detector was designed to provide pattern recognition, transverse momentum resolution and vertex reconstruction for charged tracks above a given p_T threshold of $0.5\ GeV$ and within the pseudorapidity range $|\eta| < 2.5$. It also provides electron identification over $|\eta| < 2$ and in a range of energy between $0.5\ GeV$ and $150\ GeV$.

Due to the high number of tracks per events, the discrimination between tracks and the recognition of vertices is possible only with high granularity of the detector. Vertices and tracks of charged particles are reconstructed by using different techniques.

The ID is organized in different levels of indipendent sub-detectors: the first level is the Insertable B-Layer (IBL), the second level is the semiconductor Pixel Detector, the third level is the Semi-Conductor Tracker (SCT) and then in the last level there is the Transition Radiation Tracker (TRT). A detailed view of the ID subdetectors is shown in Figure 2.8.

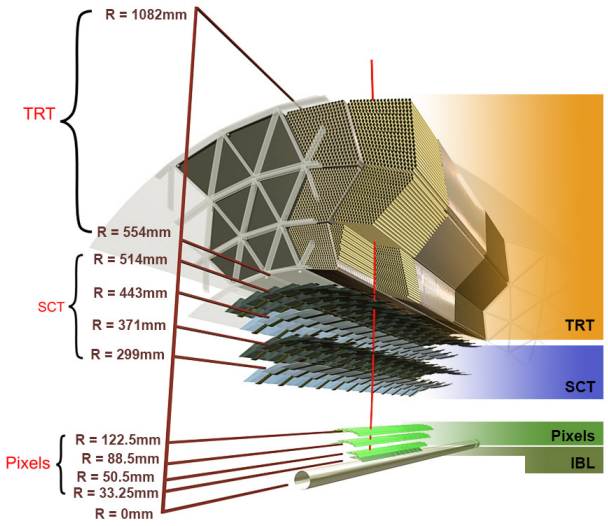

FIGURE 2.8: View of the ATLAS ID subdetectors.

The Insertable B-Layer (IBL)

The IBL was inserted at a radius of $3.3\ cm$ between the beam line and the ID, before the start of the Run-2 data tacking period, during the LHC shut-down in 2013 (Phase-0). It consists of a cylindrical layer of full lenght of $3.5\ m$.

The IBL insertation has increased the efficiency in reconstructing secondary vertices. It improves tracking by providing an additional measurement point and mitigates the possible loss of hits in the 3 layers due to the LHC luminosity increasing and to radiation damage [41].

The Pixel Detector

The ATLAS Pixel Detector provides a very high granularity, high precision set of measurements as close as possible to the IPs.

The system provides three precision measurements points for tracks with pseudorapidity $|\eta| < 2.5$ and it has a full ϕ coverage. Its function is to measure the particle impact parameter resolution and has the ability to find short lived particles such as B-Hadrons.

The system consists of three barrel layers placed at the radii of $5\ cm$, $9\ cm$, and $12\ cm$ respectively, centered around the beam axis (z) and 2 endcaps. Each end-cap has three disk layers.

The full detector has 1744 modules and the total number of the pixels is 80 millions. The 80 millions pixels cover an area of $1.7\ m^2$. Each module is $62.4\ mm$ long and $21.4\ mm$ wide, with 46080 pixel elements readout by 16 chips.

The Semi-Conductor-Tracker (SCT)

The SCT [42] is designed to provide track precision measurements in the intermediate radial region and contributes to the measure of momentum, impact parameters and vertex position. It is constituted of modules of silicon-strip detectors. The system consists of four concentric barrels with a total of 2112 modules and two endcaps. Each endcap has nine disk layers and 988 modules.

The layout of the detector is shown in Figure 2.9. The barrel modules have strips approximately parallel to the magnetic field and beam axis. Each module consists of four rectangular silicon-strip sensors; the strips has a constant pitch of $80\ \mu m$.

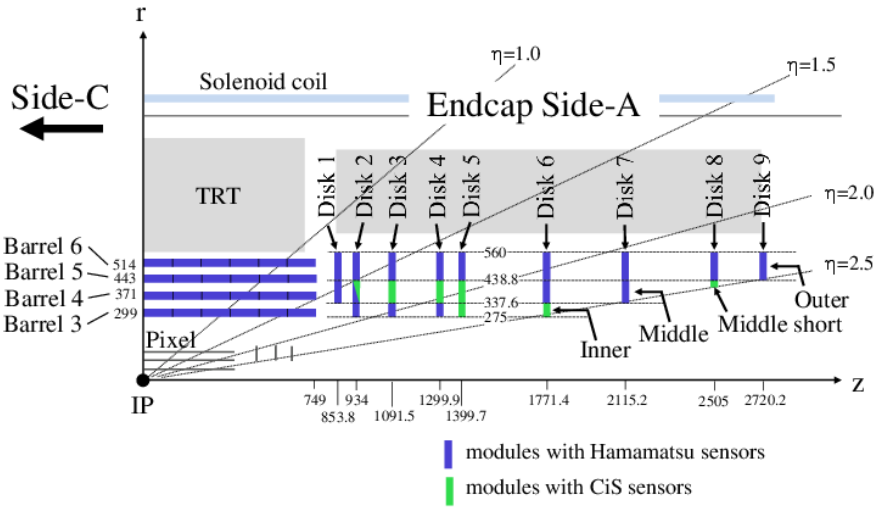

FIGURE 2.9: Layout of the SCT detector.

The Transition Radiation Tracker (TRT)

The ATLAS TRT [43] is the outermost system of the ID. It provides electron identification capability through the detection of transition radiation X-ray photons. The detector is a strawtube tracker; it consists of drift tubes (straws) with a diameter of $4\ mm$ made of Kapton and carbon fibres.

Each tube has at its center a tungsten wire of $31\ \mu m$ of diameter. The tubes are filled with a gas mixture of $70\%\ Xe$, $27\%\ CO_2$ and $3\%\ O_2$. The TRT barrel region is organised in three cylindrical layers and has a total of 52544 straw tubes of $1.5\ m$ lenght, parallel to the beam axis. They cover a pseudorapidity range of $|\eta| < 1$. Each side of the endcap consists of 122880 straws with a pseudorapidity range of $1 < |\eta| < 2$.

When a charged particle traverses the TRT, it ionises the gas inside the straws. The resulting free electrons drift towards the wire, where they are amplified and readout.

2.2.3 Calorimetry

The ATLAS calorimetry[33] consists of electromagnetic and hadronic calorimeters with full ϕ coverage around the beam axis and with coverage of pseudorapidity range up to $\eta < 4.9$.

In Figure 2.10 an overview of the ATLAS calorimeters is shown. The Electro-Magnetic calorimeters (EM) is based on liquid Argon technology only while, the hadronic calorimeters also use scintillating tiles technology.

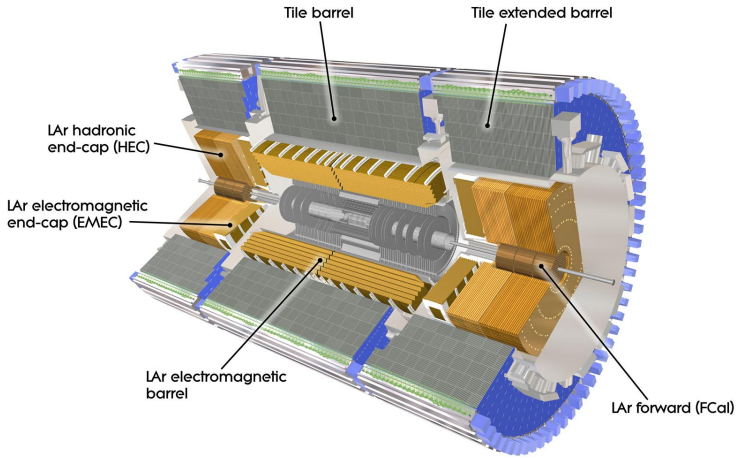

FIGURE 2.10: Overview of the ATLAS calorimetry system.

The Electromagnetic Calorimetry (EM)

The main part of the ATLAS EM calorimeter is a Liquid-Argon (LAr) detector mantained at T=88 K. This detector was designed with an accordion geometry. Such geometry provides a full coverage in ϕ and leads to a very uniform performance in terms of linearity and resolution as a function of ϕ.

It consists of a barrel part with an $|\eta|$ coverage up to 1.475 and two endcaps with the pseudorapidity range $1.375 < |\eta| < 3.2$, each part with its own cryostat.

Each endcap is divided into two coaxial wheels: an outer wheel covering $1.375 < |\eta| < 2.5$ and an inner wheel with a coverage of $2.5 < |\eta| < 3.2$. There are three longitudinal samplings for $|\eta| < 2.5$ and two for $2.5 < |\eta| < 3.2$. One of the reasons to have this particular geometry is that ensures a complete ϕ symmetry.

The transition region between the barrel and endcap EM calorimeters, $1.37 < |\eta| < 1.52$, is expected to have a poorer performance because of the higher amount of passive material in front; it is referred to this region as *crack region*. Electrons which are detected in that region are not considered in this analysis.

In the forward region ($3.1 < |\eta| < 4.9$), the calorimeter is made up by another type of LAr calorimeter: the Forward Calorimeter (FCAL). This part consists of copper rods inside an outer tube with $250\ \mu m$ liquid Argon gap in between. This matrix is parallel to the beam axis.

The Hadronic Calorimetry

The Hadronic Calorimetry consists of an iron-scintillating tile calorimeter, a liquid Argon hadronic endcap calorimeter (HEC) and a liquid Argon forward calorimeter (FCal).

The tile calorimeter is located in the pseudorapidity region of $|\eta| < 1.7$ behind the LAr EM calorimeter and is subdivided into a central barrel, $5.8\ m$ in lenght and two extended barrels $2.6\ m$ in lenght. The region between the barrel and the extended barrels is instrumented with special modules that allow to partially recover the energy lost in the crack regions.

The Hadronic End-Cap Calorimeter (HEC) is a copper/liquid Argon sampling calorimeter which covers the pseudorapidity range $1.5 < |\eta| < 3.2$. This calorimeter shares the liquid Argon endcap cryostats with the Electromagnetic endcap (EMEC) and forward (FCal) calorimeters.

The HEC consists of two wheels in each endcap cryostat: a front wheel (HEC1) and a rear wheel (HEC2). The wheels closest to the IP are built with $25\ mm$ parallel copper plates, while the other wheels use $50\ mm$ copper plates. The FCal provides coverage of $3.1 < |\eta| < 4.9$.

Because of the FCal modules are located at high η, they are exposed to high particle fluxes. For this reason an electrode structure of small diameter rods, centered in tubes parallel to the beam axis, has been used. This has resulted in a design with small liquid Argon gaps which provide the highest possible density.

2.2.4 The Muon Spectrometer

The Muon Spectrometer (MS) is the outer part of the ATLAS detector and in volume is the bigger part of the detector. An overview of the MS layout is

shown in Figure 2.11.

The detector consists of separated trigger and high precision tracking chambers. The main purpose of the MS is the measurement of the muon momentum in the pseudorapidity range $|\eta| < 2.7$ by means of the deflection of muon tracks in large superconductive toroidal magnets.

This configuration provides a magnetic field that is mostly orthogonal to the muon trajectories, minimizing the deterioration in resolution due to multiple scattering. In the barrel region ($|\eta|$<1), muon tracks are measured in chambers arranged in three concentric cylindrical layers (stations) around the beam axis, with a $5\ m$, $7.5\ m$ and $10\ m$ radius respectively (inner, medium and outer stations).

In the two endcap regions ($1.0 < |\eta| < 2.7$) the chambers are arranged into four large wheels, perpendicular to the z-axis, at the distance of $\approx 7.4\ m$, $10.8\ m$, $14\ m$ and $21.5\ m$ from the IP.

The first station of the ATLAS muon endcap system Small Wheel (SW), will need to be replaced in order to benefit from the expected high luminosity performance that will be provided by the Phase-I upgraded LHC, as described in Section 2.3. The MS consists of: Monitored Drift Tubes (MDT), Catode Strip Chambers (CSC), Resistive Plate Chambers (RPC) and Thin Gap Chambers (TGC).

A detailed description of the four different types of muon chambers is reported in the follow sections.

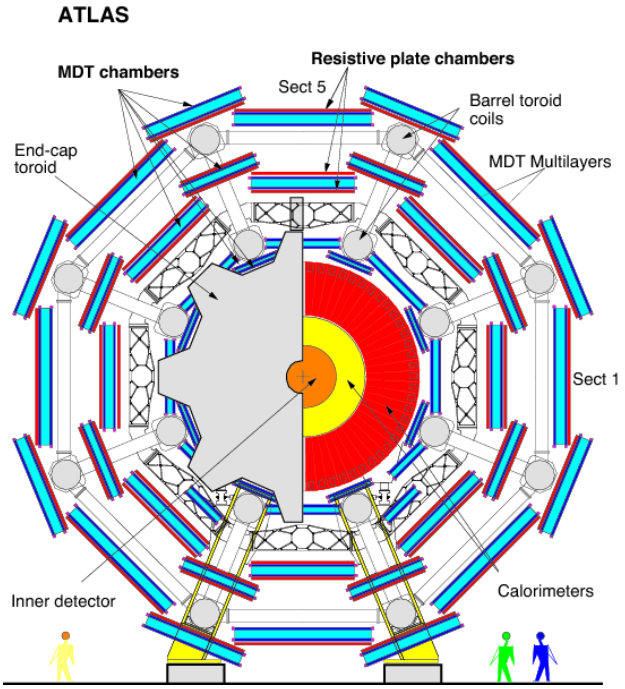

FIGURE 2.11: Overview of the ATLAS MS.

Monitored Drift Tubes (MDT)

The main role of the MDT chambers is the precision momentum measurement. They cover the pseudorapidity range $|\eta| < 2.7$. These chambers consists of three to eight layers of drift tubes.

A tube is made of aluminium with an outer diameter of $3\ cm$ and an anodic central wire held at high voltage. They operate with a mixture of $Ar(93\%)$ and $CO_2(7\%)$ at $3\ bar$ absolute pressure. The anodic wire is a gold plated tungsten and rhenium with a $50\ \mu m$ diameter. With this system of tubes assembly, a high level of operation reliability can be expected because the failure of a single tube does not affect the performances of most of the other tubes. One more advantage is that a cylindrical shape leads in a radial electric field, proportional to the inverse of the distance from the anode: $E \propto \frac{1}{r}$.

A muon crossing the MDT, ionizes the gas along its track creating electron-ion pairs. The electrons drift toward the wire in the electric field and are multiplied, due to the high field, in an avalanche process only close to the wire, as shown in Figure 2.12. In this way it is avoided that the number of electrons is dependent on the distance at which the particle is passed from the anode wire.

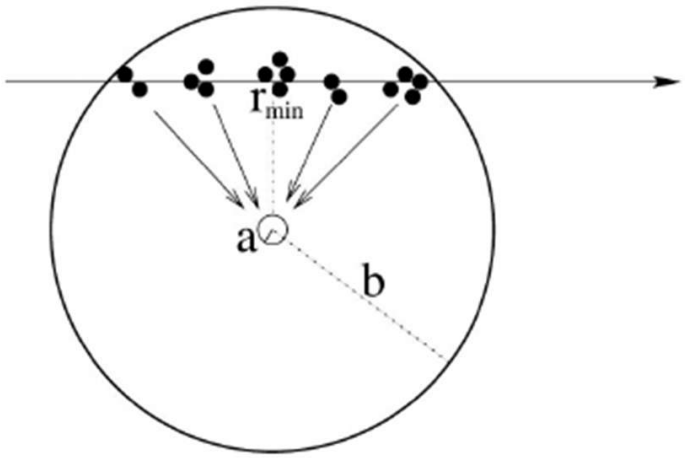

FIGURE 2.12: Crossing of a particle in a drift tube of the MDT chambers.

The amount of charge collected is proportional to the energy deposited by the particle, the gas pressure and the potential of the wire. The measured drift time is converted to the drift distance using the $r - t$ relation of the mixture.

Each MDT chamber consists of two multilayers of tubes fixed at a support structure. A multilayer is composed of 3 or 4 layers depending on the location of the chamber in ATLAS.

A representation of the MDT structure is shown in Figure 2.13. The chambers are currently used in the MS, both in the barrel and in the endcaps.

In the barrel the MDT chambers are rectangular and arranged on three cylinders (Inner, Middle, Outer) concentric with the axis of the beam. They are divided into large and small, depending on the length of the tubes that is between $1.8\ m$ and $5.2\ m$. In the endcaps, instead, are of trapezoidal shape and arranged on three coaxial disks perpendicular to the beam.

These chambers have a high spatial resolution ($80\ \mu m$) and a typical drift time of $700\ ns$. As is shown is Section 2.3, such drift time is a limiting factor at high luminosity.

For this reason, new precision trackers, the MicroMegas chambers, will substitute the MDT chambers in the first station of the MS in the endcaps regions, i.e. the Small Wheel, as is explained in the next Sections 2.3.1.

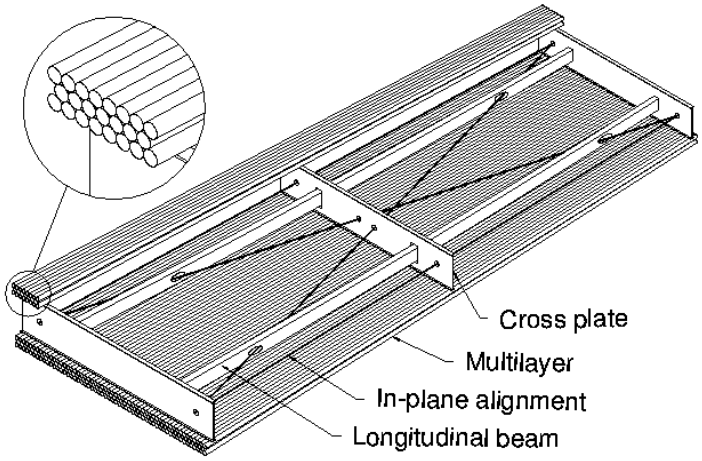

FIGURE 2.13: Layout of a MDT chamber of the ATLAS MS.

Catode Strip Chambers (CSC)

The Catode Strip Chambers (CSC) are used in the pseudorapidity range $2.0 < |\eta| < 2.7$ of the first station of the endcap MS. The whole CSC system consists of two disks each with eight chambers (eight smalls and eight larges).

Each chamber contains four CSC planes. The CSCs are multiwire proportional chambers and consist of arrays of positively-charged "anode" wires crossed with negatively-charged copper "cathode" strips within a gas volume.

When muons pass through, they knock electrons off the gas atoms, which flock to the anode wires creating an avalanche of electrons. Positive ions move away from the wire and towards the copper cathode, also inducing a charge pulse in the strips, at right angles to the wire direction. Since the

strips and the wires are perpendicular, for each passing particle two position coordinates are measured.

Resistive Plate Chambers (RPC)

The Resistive Plate Chambers (RPC) are located in the barrel region and are used as trigger chambers. The RPCs are fast gaseous detectors and consist of two parallel plates, a positively-charged anode and a negatively-charged cathode, both made of a very high resistivity plastic material and separated by a gas volume.

When a muon passes through the chamber, electrons are knocked out of gas atoms. These electrons turn hit other atoms causing an avalanche of electrons. The electrons are picked up by external metallic strips after a small but precise time delay. A RPC trigger chamber consists of two rectangular detector layers, each one readout by two orthogonal series of pick-up strips: the η-strips are parallel to the MDT wires and provide the bending view of the trigger detector, the ϕ-strips are orthogonal to the MDT wires and provide the second-coordinate measurement. RPCs combine a good spatial resolution with a time resolution of just $1\ ns$.

Thin Gap Chambers (TGC)

The Thin Gap chambers (TGC) are used for the muon trigger system of the endcaps MS. A TGC chamber consists of a plane of closely spaced wires maintained at positive high voltage, sandwiched between resistive grounded cathode planes. The spacing between the wires is $1.8\ mm$ and the anode-cathode spacing is $1.4\ mm$. The operational gas is a mixture of $55\%\ CO_2$ and $45\%\ n - C_5H_{12}$ (n-pentane). The anode wires, arranged parallel to the MDT wires, provide trigger signal together with readout strips arranged orthogonal to the wires. The TGCs can provide spatial resolution better than $100\ \mu m$.

2.2.5 The Luminosity detectors

The most exteral part of the ATLAS detector is constitute by system used to measure the luminosity.

Three different detectors provide good coverage in the very forward region and help in the determination of the luminosity.

The one closest to the IP is LUCID (Luminosity measurement using Cerenkov Integrating Detector). The LUCID main purpose is to detect inelastic pp scattering in the forward direction. In this way it can both measure the integrated luminosity and provide online monitoring of the instantaneous luminosity. It is the main luminosity monitor and it is located at a distance of $\pm 17\ m$ from

the IP covering a pseudorapidity range $5.6 < |\eta| < 6.0$. For the beam monitoring, another detector has been inserted: BCM (Beam Condition Monitor).

The second detector is ZDC (Zero-Degree Calorimeter), placed at a distance of $\pm 140\ m$ from the IP. The primary purpose of this system is to detect forward neutrons in heavy-ion collisions.

The last detector is ALFA (Absolute Luminosity For ATLAS), a scintillating fiber tracker located inside roman pots at a distance of $\pm 240\ m$ from the IP.

2.2.6 The Trigger and Data Acquisition system

An important system of the ATLAS detector is the trigger and data acquisition system (DAQ); this system provides the selection and the saving of interesting physics processes for the offline analysis.

Because of the increase of the luminosity, after the LHC long shutdown (2013-2014), the ATLAS trigger system was upgraded to reduce the amount of data [44]. To do this reduction, the ATLAS Trigger and DAQ system identify the events potentially containing interesting physics and discards the remaining majority.

This mechanism is built on a hardware-based first Level trigger (Level-1) and a software-based High Level Trigger (HLT). Each step of the system selects events with requirements and cuts in such a way to reduce the rate. A schematic overwiev of the ATLAS Run-2 trigger system is shown in Figure 2.14

Level-1 trigger

Level-1 trigger uses granularity informations from the muon chambers and from calorimeters and forward detectors. There are therefore two types of Level-1 triggers: calorimeter Level-1 and muon Level-1.

The Level-1 calorimeter trigger receives data from the electromagnetic and hadronic calorimeters. The Level-1 muon trigger receives inputs from the muon trigger detectors: RPCs in the barrel region (η < 1.05) and TGCs in the endcaps region (1.05<η<2.4).

The Level-1 trigger has a decision time of $2.5\ \mu m$. It uses an electronic system to determine Regions-of-Interest (RoI) in the detector and reduces the event rate from the LHC bunch crossing rate of approximately 30 MHz to 100 kHz.

The High Level Trigger

The HLT reconstruction is based on energy from calorimeters and tracking informations from the ID and MS. It is used to refine the Level-1 decision and to do a selection of the event to reduce the rate. In such a way, the

RoI determined by the Level-1 trigger are sent to HLT whom reduces the rate from the Level-1 output of 100 kHz to approximately 1kHz within a processing time of $\sim 200\ ms$.

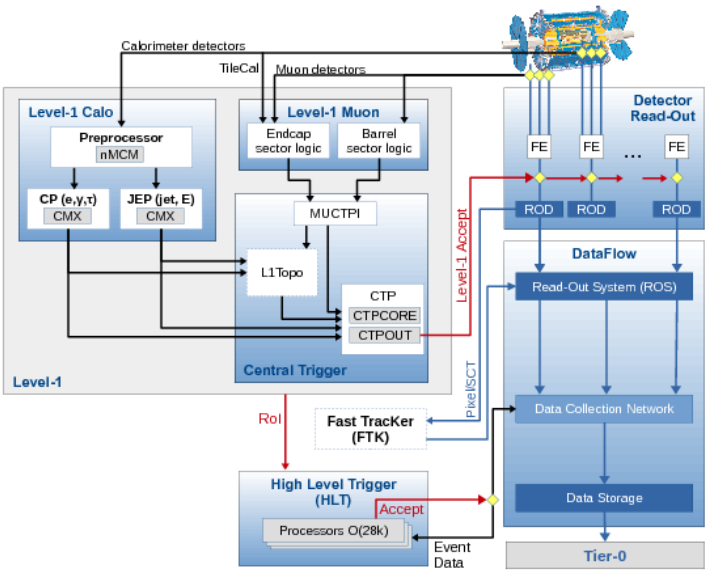

FIGURE 2.14: Overwiev of the ATLAS Run-2 trigger system.

Trigger used in the analysis

For the analysis described in this thesis, electrons are selected at the HLT using a likelihood based criteria which takes as input electromagnetic shower shape and tracking informations.

For the electrons, the triggers HLT_e24_lhmedium_L1EM20VH, HLT_e60_lhmedium and HLT_e120_lhloose are used. For MC HLT_e24_lhmedium_L1EM18VH instead of HLT_e24_lhmedium_L1EM20VH is used because the latter is not included in the simulation. For the muons, the HLT_mu20_iloose_L1MU15 and HLT_mu50 triggers are used [44].

These triggers require an electron candidate with $E_{\mathrm{T}}^{\mathrm{miss}} > 24$ GeV and $E_{\mathrm{T}}^{\mathrm{miss}} > 60$ GeV satisfying the *lhmedium* identification and an electron candidate $E_{\mathrm{T}}^{\mathrm{miss}} > 120$ GeV satisfying the *lhloose* selection, respectively. They are seeded by the Level-1 triggers L1EM20VH which apply a E_{T} dependent veto against energy deposit in the hadronic calorimeter.

The efficiencies are measured with a tag-and-probe method using a $Z \rightarrow ee$ decays. The reconstruction of the muons, at the HLT level, combines information from the MS and the ID.

The L1MU15 trigger requires that candidates pass the 15 GeV threshold requirements of the Level-1 muon trigger system. The HLT_mu20_iloose trigger is seeded with the L1MU15 trigger and is required to satisfy the 20 GeV

threshold and to pass the loose selection. The HLT_mu50_iloose trigger is seeded with the L1MU20 trigger and is required to satisfy the 50 GeV.

In Figure 2.15 the efficiency of the single electron trigger as a function of E_{T} 2.15(a) and the efficiency of the single muon trigger as a function of the p_{T} of the offline muon candidate in the barrel 2.15(b), are shown .

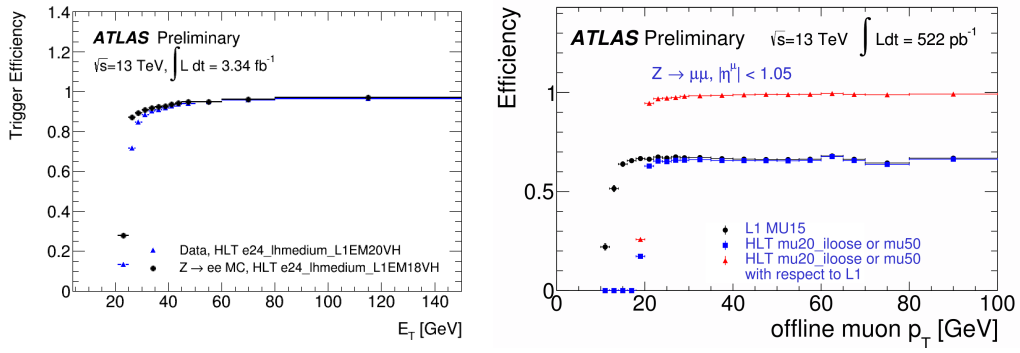

(a) (b)

FIGURE 2.15: Efficiency of the single electron trigger as a function of E_{T} 2.15(a) and the efficiency of the single muon trigger as a function of the p_{T} of the offline muon candidate in the barrel 2.15(b).

2.3 The LHC and ATLAS experiment Phase–1 Upgrades

The LHC complex will be upgraded in several phases [45]. During 2013-2014 there was the first long shutdown (LS1). A second long shutdown (LS2) for the LHC is planned at the end of 2018. During this shutdown Linac4 will be integrate into the injector complex to increase the energy of the PS Booster, to reduce the beam emittance and to upgrade the collider collimation system.

After this long shutdown, the peak luminosity is expected to reach $2 - 3 \cdot 10^{34} cm^{-2} s^{-1}$. Phase-I upgrade will allow collection of an integrated luminosity of $300 fb^{-1}$. A subsequent upgrade step at the end of 2023 is planned which will make significant improvements to other parts of the accelerator complex. These improvements will result in the luminosity increasing to $5 \cdot 10^{34} cm^{-2} s^{-1}$. This upgrade will allow to collect an integrated luminosity of $3000 fb^{-1}$ at $\sqrt{s} = 14\ TeV$ entering in the High-Luminosity-LHC era. Figure 2.16 shows an approximate timeline for the planned LHC upgrades.

During the LHC upgrades, also the LHC's experiments will be upgraded and in the uncoming one (Phase-I), for what concern the ATLAS experiment, the installation of the New Small Wheels (NSW) in the muon ATLAS detector, will take place.

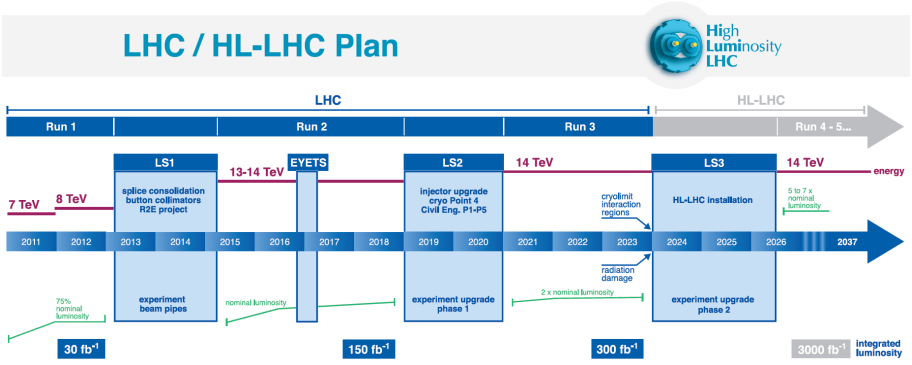

FIGURE 2.16: Timeline of the planned LHC phases upgrade.

2.3.1 New Small Wheel project

After the LS2, the expected high luminosity will provide more data but a higher background too (up to $15kHz/cm^2$). So it is essential that the ATLAS detector is still able to operate in the higher background enviroment, while maintaining its performances as good as at lower luminosity.

To obtain this the first endcap station of the MS, Small Wheels (SW), will be replaced by the NSW able to operate in the higher background enviroment while reconstructing muon tracks with high precision as well as furnishing information for the Level-1 trigger.

The precision reconstruction of tracks requires a spatial resolution of about $100\ \mu m$ per detector layer and the Level-1 trigger track segments have to be reconstructed online with angular resolution of approximately $1\ mrad$.

The NSW will have a new chamber technology: the Micro-MEsh Gaseous Structures (Micromegas detectors, MM) dedicated to precision tracking. The MM have exceptional precision tracking capabilities due to their small gap ($5\ mm$) and strips pitch ($\sim\ 500\mu m$). This precision level is fundamental to maintain the current ATLAS muon momentum resolution in the high background enviroment. The MicroMegas chambers layout and operation principles are described in Section 3.1. In addition, the current small-strip Thin Gap Chambers (sTGC) primarly devoted to the Level-1 trigger function, will be upgraded.

2.3.2 New Small Wheel layout

The NSW consist of 16 detector planes in two multilayers [46]. In each multilayer there are 4 sTGC and 4 MicroMegas detector planes. The detectors are arranged in such a way (sTGC-MM-MM-sTGC) to maximize the distance between the sTGC. With eight planes per detector, tracks will be reconstructed reliably and with high precision and will ensure an overall efficiency close to $100\ \%$ both for online and offline track reconstruction. In Figure 2.17 an overview of the NSW is reported.

For what concern the MM chambers, each sector is segmented in two parts of different sizes, each covering a different $|\eta|$ region. This results in four kinds of chambers: SM1 and SM2 for the small sectors and LM1 and LM2 for large sectors. The chamber sizes are $\sim 2\ m^2$ for SM1 and SM2 and $\sim 3\ m^2$ for LM1 and LM2.

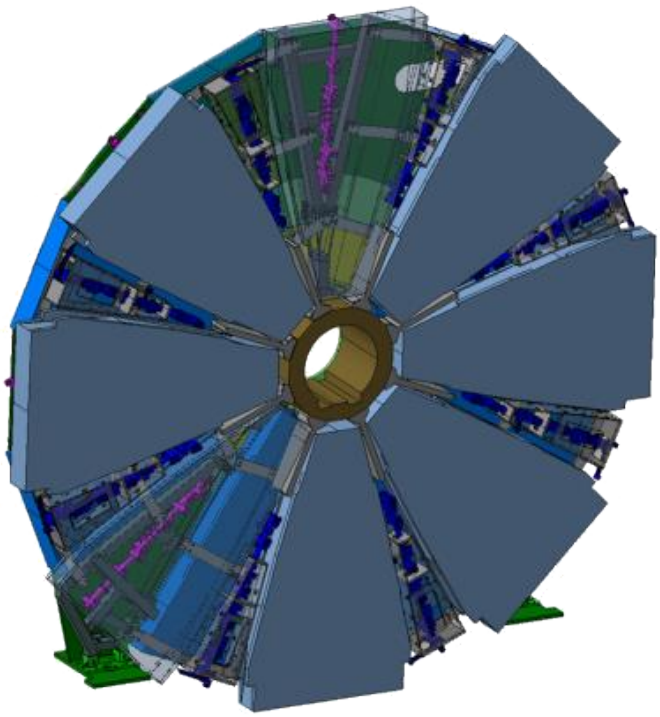

FIGURE 2.17: View of the NSW structure.

Chapter 3

MicroMegas chambers and their performances

3.1 MicroMegas chambers

The MicroMegas (Micro-MEsh GAseous Structure) chambers (MM) [47] were developed to provide very good position resolution independent on the particle incident angle and good two track separation.

The MicroMegas detectors (see Figure 3.1) are arranged in two regions: the conversion or drift region and the amplification region.

The conversion region is large $5\ mm$; it is bounded by a plan electrode (drift) on a side and by a metal mesh on the other side. The amplification zone, instead, is bounded by the metallic mesh on a side and by a plane of copper readout strips on the other side. The thickness of this zone is usually about $100 - 150\ \mu m$. This thickness is kept constant by cylindrical spacers (pillars) of $200\ \mu m$ of diameter placed every $2\ mm$.

The two regions are filled with ionisation gas. The ATLAS-MM operate with $Ar - CO_2$ $93\% : 7\%$ mixture.

A PCB, printed circuit board $0.5\ mm$ thickness, carries the readout strips. The strips have a thickness of $18\ \mu m$ and a pitch in the range of $100 - 500\ \mu m$. An electric field of $\sim 600 V/cm$ in the drift region and a field of $40 - 50 kV/cm$ in the amplification region are applied, respectively.

Charged particles crossing the drift region ionise the gas. The resulting ionisation electrons drift towards the mesh with a drift velocity of $\sim 47\ \mu m/ns$.

Since the electric field in the amplification region is $50 - 100$ times stronger than in the drift field, the mesh is transparent to more than 95% of the electrons. The electron avalanche takes place in the thin amplification region, immediately above the readout electrodes.

The drift time of the electrons in the conversion region, depending on the drift gas, the drift distance and the drift field, is of the order of several tens of nanoseconds (up to $\sim 100\ ns$). On the other hand the amplification process happens in few nanoseconds resulting in a fast pulse on the readout strips.

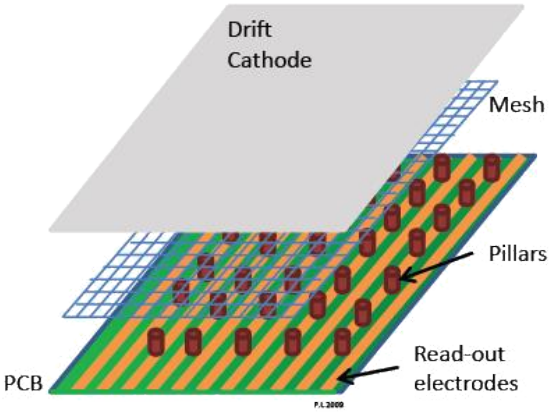

FIGURE 3.1: Structure of a MicroMegas chamber.

The ions that are produced in the avalanche process move in the opposite direction of the electrons, back to the amplification mesh. Most of the ions are produced in the last avalanche step and therefore close to the readout strips.

Given the relatively low drift velocity of the ions, it takes them about $100\ ns$ to reach the mesh. The fast evacuation of the positive ions makes the MM chambers particularly suited to operate at very high particle fluxes.

An illustration of the basic principle of a MicroMegas detector is shown in Figure 3.2.

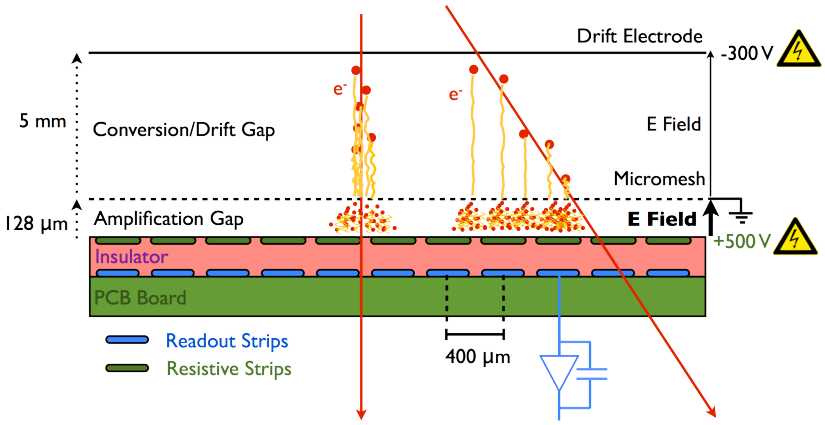

FIGURE 3.2: Illustration of a basic principle of a MicroMegas detector. The incident particles ionize gas-atoms and the resulting secondary electrons drift to the mesh. Once passing the mesh, the electrons cause a secondary electron cascade, leading to a signal amplification factor of several thousand.

3.1.1 Track reconstruction method

Tracks of crossing particles are reconstructed by the charge signal of the readout strips. The MM chambers can provide a position measurement by using two methods:

- Cluster with centroid of charge;
- μTPC method.

The first method is applied in case of about orthogonal tracks respect to the chamber. The second one allows accurate measurements in case of tracks bended (> 10°). In the first case a few strips collect the charge, while number of strips increases as angle increases.

Method of the charge centroid

When a particle crosses perpendicularly through an MM chamber usually more than one strip accumulates enough charge to overcome the threshold signal. This effect is due mainly to the multiple scattering of the ionisation electrons in the gas.

Other phenomena that can contribute to enlarge the cluster, negligible respect to the multiple scattering, are the diffusion during the amplification process and the induction of the charge from the resistive strips to the readout ones.

The reconstruction algorithm search contiguous *fired* strips and connect them in groups called *clusters*. A representation of this method is shown in Figure 3.3. The spatial coordinate, defined as the weighted sum of the charged

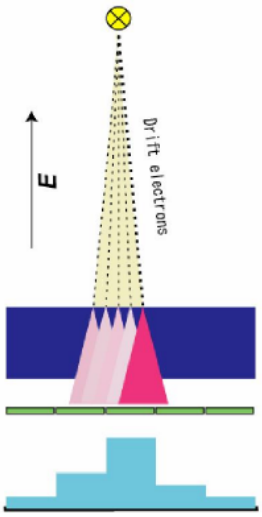

FIGURE 3.3: Schematic representation of the centroid of charge track reconstruction method.

strips, is described by the follow expression:

$$x_{clu} = \frac{\sum_{k=1}^{N} x_k \cdot q_k}{\sum_{k=1}^{N} q_k}, \tag{3.1}$$

where N is the number of strips in a cluster, x_k is k-position in the cluster and q_k is the charge measured on the k-strip.

The μTPC method

The micro Time Projection Chamber (μTPC) method allows to reconstruct a segment of track within the drift region in the case of incident particles with angle greater than of 10° respect to the perpendicular to the chamber.

This method uses the arrival time of the electron on the strip and the large segmentation of the readout electrode. In fact, the electrons from the bended tracks deposite signals on all the strips that intersect along the x coordinate. The position of each strip determines the x-coordinate, while the z-coordinate, orthogonal to the plane of the strips, can be reconstructed from the arrival time by the relation ($z = v_{drift} \times t$).

The drift velocity can be directly measured using the spectrum of the times. The lowest spectrum of times corresponds to the primary ionized electrons close to the mesh, while the highest one corresponds to electrons released close to the cathode. Therefore by measuring the width of this distributions the time required for an electron to traverse the thickness of 5 mm of the drift region is obtained.

For each event, the coordinates (x_i, z_i) are assigned to each hit and a linear fit of these points is done. The best measure of the position x_{half} is obtained from the intersection of the straight line with the median plane of the area of drift (z_{half}), as shown in Figure 3.4.

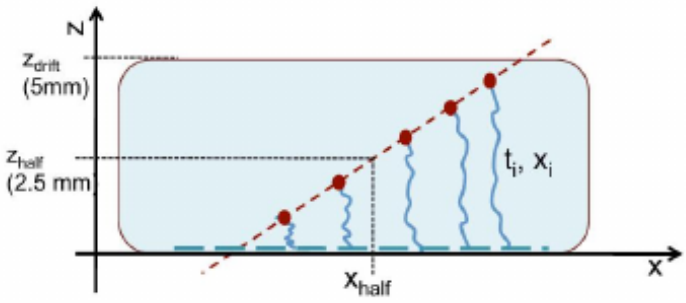

FIGURE 3.4: Schematic representation of the μTPC track reconstruction method.

3.2 The INFN SM1 Module-0 MicroMegas chamber

To the INFN consortium has been assigned the construction of the 32 SM1 quadruplete chambers; the produced chambers will be tested at LNF laboratories under cosmic rays.

The first full size MicroMegas prototype chamber, for the ATLAS MS phase-I Upgrade was built by the INFN collaboration.

The construction of the SM1 Module-0 prototype started in late October 2015 and was completed in April 2016. Its performances have been checked during the construction and in a test-beam at CERN in June 2016.

My contribution to the test beam has been relative to the implementation of the chambers layout in the reconstruction code and to the data analysis; about the last item, the most significative results are reported in the following.

During the assembling I was involved in measuring the panels alignment of the SM1 module-0 at LNF.

I have also implemented a Monte Carlo code to simulate the response of the experimental setup at LNF devoted to certify the produced chambers.

3.2.1 SM1 Module-0 design

The SM1 Module-0 chamber is constitute of four MicroMegas layers assembled in a quadruplete as a sandwich. The structure of the layers are described in Section 3.1.

A scheme of the quadruplet chamber assembled is shown in Figure 3.5 and in Figure 3.6 the four layers are shown.

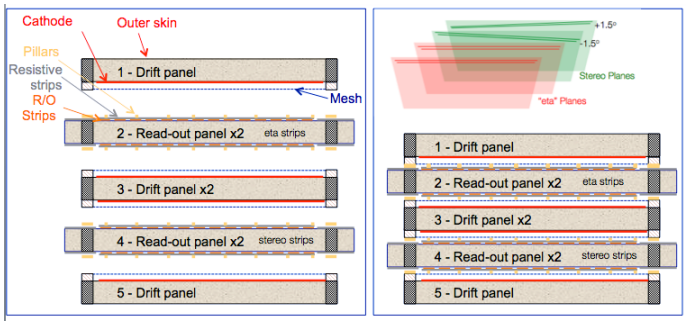

FIGURE 3.5: Scheme of the SM1 Module-0 chamber assembled. Quadruplet component (left), stereo and eta strips representation (top right), quadruplet assemblet (bottom right).

The four active gaps including the meshes are bounded by five $\sim 11\ mm$ thick panels. In the external part of the quadruplet there are two single drift

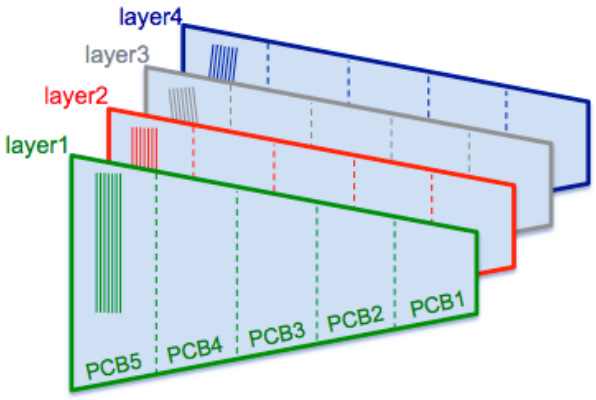

FIGURE 3.6: MM quadruplate layers.

cathode panels. In the central part there is one double drift panel, enclosed by one double readout η panel and one double readout stereo panel.

The so called η panels are equipped with the (η strips). These strips are parallel to the bases of the trapezoids and to the resistive strips and provide precision coordinate measurement. Instead, the stereo panels are equipped with the stereo strips (ϕ strips) inclinated $\pm 1.5°$ respect to the resistive strips. These strips provide the second coordinate measurement.

3.3 Cern test beam on SM1 Module-0 prototype

The SM1 Module-0 prototype was tested for the first time at CERN in June 2016 during a test beam at H4 beam line of the SPS. The purpose of the test beam was to certify the produced prototype respect to the project requirements.

A 180 GeV/c π^+ beam with a rate of 1 KHz to $\sim$ 0.5 MHz and with a beam spot of about 1×1 cm^2 hits was used. The experimental setup was composed by a detector arrays of which SM1 Module-0 is a part as shown in Figure 3.7. Five T_{mm} small dimension MM chambers, with X and Y coordinate readout, were used as references.

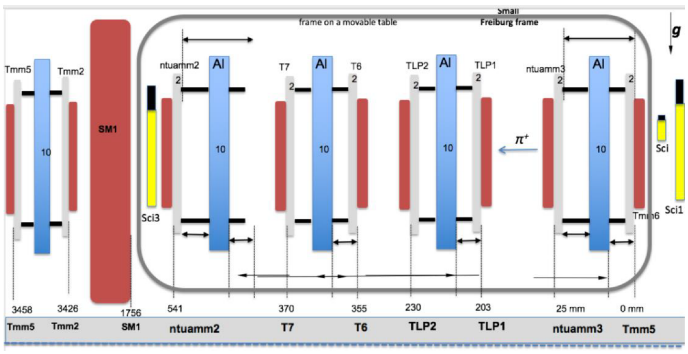

FIGURE 3.7: Test beam setup.

To perform position scans the SM1 module-0 chamber was placed on a movable platform. In such way, to obtain the X coordinate position scan, the table was horizontally moved and it was vertically moved to obtain the Y position scan. This platform has allowed also to rotate the chamber respect to the beam axis, up to 20° degree.

In Figure 3.8 the Module-0 prototype mounted on this platform, is shown.

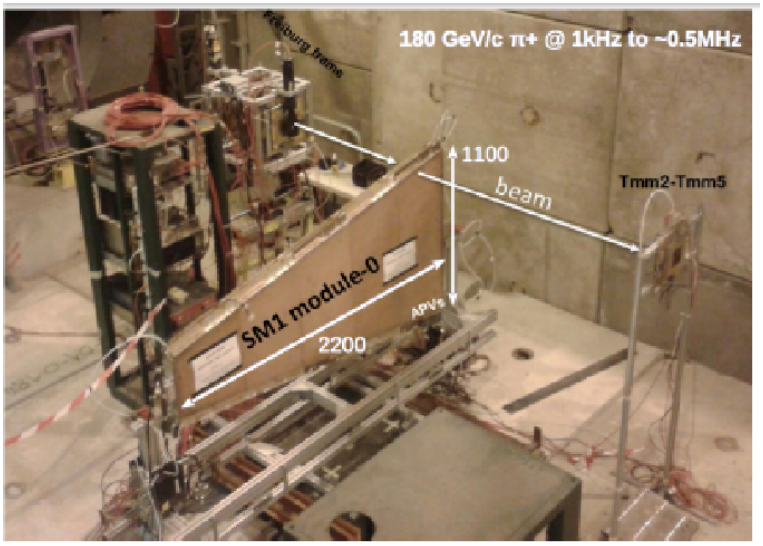

FIGURE 3.8: SM1 Module–0 on platform

3.3.1 Data reconstruction

The layers were filled with a Ar:CO_2 (93:7) gas mixture with a flux rate of 20 l/h. APV25+SRS provide the readout; the APV is not the final electronic that will be used in the experiment; the final electronic (VMM modules) is currently under tests. The APV25 is a 128 channel chip. The output data structure consists of values in charge of the individual samples. The total structure consists of 18 samples, one every $25\ ns$, for each channel of the APV25. Therefore the acquisition time window is $450\ ns$.

The APV25 signal rising edge is fitting with a Fermi-Dirac function. The only important parameter from the fit is the starting time of the signal t_0 used in the μTPC position reconstruction method.

Raw data, pedestal subtracted, have been processed by a C++ code to remove cross-talk events. Then the reconstruction code, C++ based, provides the final rootples. The code allows to reconstruct the track by the centroid or the μTPC reconstruction methods.

Both the quality of the single layers and the quality of their assembling have been tested. To test the SM1 Module-0 response X and Y scans have been performed on PCB3 and PCB5. Data have been collected at different HV amplification values from $550\ V$ to $590\ V$. The HV drift baseline was set at $300\ V$ but data have been collected also at $200\ V$ and $400\ V$.

3.3.2 Measurement results

In the following Sections the most significative measurements to show the good agreement between the required and obtained performances, are reported.

Spatial resolution

The spatial resolution of the PCB5 SM1 Module-0 layers have been evalueted for the precision (η) coordinate and for the second coordinate (ϕ). Data have been collected at 0° and 20°.

The centroid method or the μTPC method, depending from the angle, have been applied in track reconstruction. Data have been preselected, to estimate the spatial resolution: at 0° to estimate the spatial resolution of the precision coordinate of SM1 Module-0, residuals between the precision coordinates of the two layers of SM1 Module-0, divided by $\sqrt{2}$ have been evalueted.

As example a fit with a bi-gaussian function is shown in Figure 3.9(a), the core gaussian is 81 μm, the weighted average of the widths of the gaussians is 160 μm.

To evaluate the spatial resolution of the second coordinate, the difference between the second coordinate position reconstructed on the stereo layers and the position extrapolated from the first layer of the chamber, has been calculated.

A fit with a bi-gaussian function is shown in Figure 3.9(b), the core gaussian is 2.3 mm and the weighted average of the widths of the gaussians is 3.2 mm.

In Figure 3.10 the obtained spatial resolution (260 μm) at 20° is shown.

Strips alignment

A measurement of the displacement of strips as a function of a position Y scan, for different layers of both PCB5 and PCB3 has been performed. This kind of measurement could be an indication of layer-to-layer rotation or strip pattern global deformation.

The measurements for the displacement at 0° of the precision and second coordinates are performed, as a function of the Y scanned positions, by taking the mean of gaussian fits of residuals calculated as described above for the measurement of the resolutions.

In Figure 3.11(a) the results obtained on PCB5 and in Figure 3.11(b) for PCB3 are shown .

The displacements reported for both PCB5 and PCB3 are within $\pm$ 80 μm.

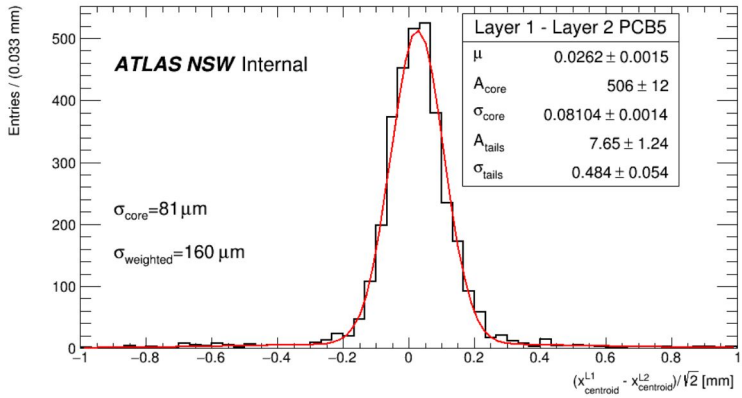

(a)

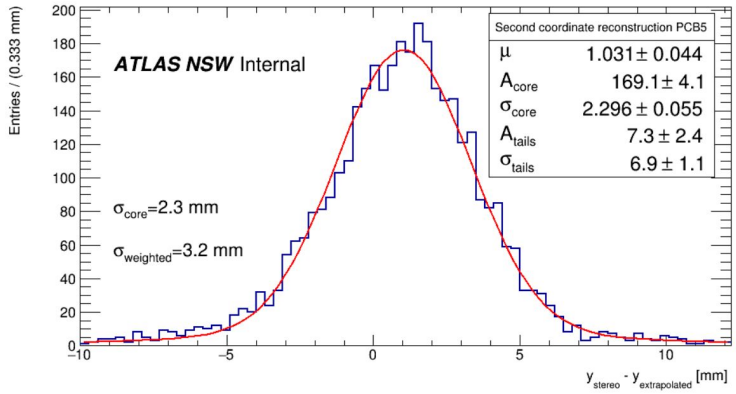

(b)

FIGURE 3.9: Spatial resolution of the η precision coordinate (a) and spatial resolution of the second coordinate ϕ (b), at 0°.

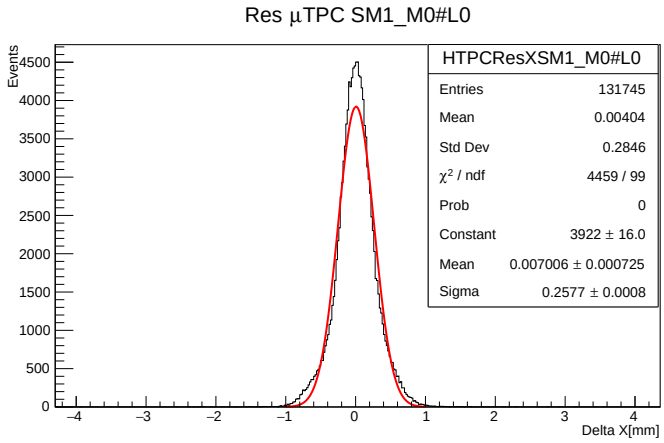

FIGURE 3.10: Spatial resolution of the η precision coordinate at 20°.

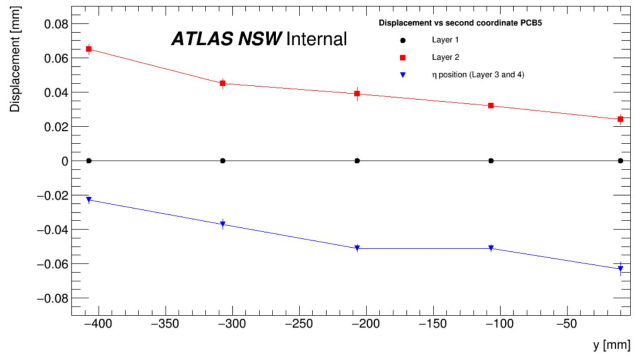

(a)

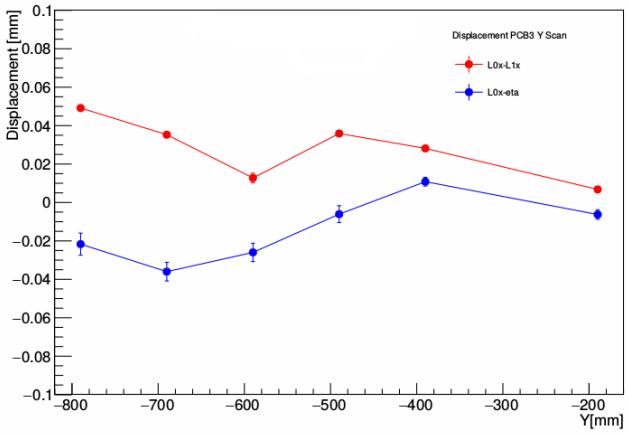

(b)

FIGURE 3.11: Layers displacement as a function of the scanned Y positions on PCB5 (a) and layers displacement as a function of the scanned Y positions on PCB3 (b).

Software efficiency of SM1 Module-0 layers

The homogeneity and the efficiency of the SM1 Module-0 chamber response have been studied. To calculate the software efficiency, a fiducial region that take into account cut selections, has been defined. The software efficiency is defined as the ratio:

$$\frac{Evts_{in}}{Evts_{tot}}, \tag{3.2}$$

where $Evts_{in}$ are the events with at least one cluster within $1.5\ mm$ from the extrapoleted position and $Evts_{tot}$ are the total events that pass the cut selections in the fiducial region.

In Figure 3.12 the software efficiency as a function of the beam position is shown for one layer. The obtained value ($\sim 96\%$) is the same for the other layers.

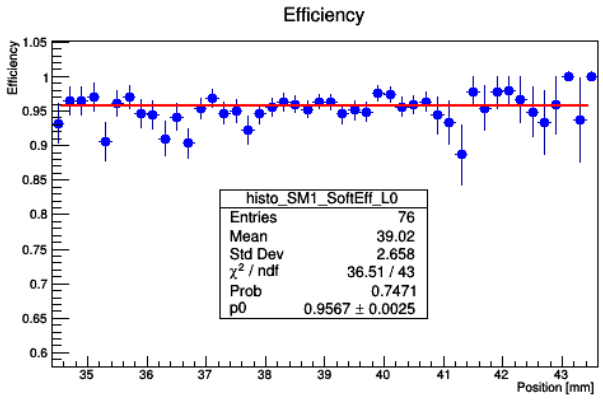

FIGURE 3.12: Software efficiency as a function of the beam position.

The software efficiency as a function of the HV amplification voltage for all the SM1 layers using data collected on PCB5 is shown in Figure 3.13.

The first layer of the chamber has better efficiency, for each value of the HV considered. For the other layers the dipendence of the efficiency on HV values is clear.

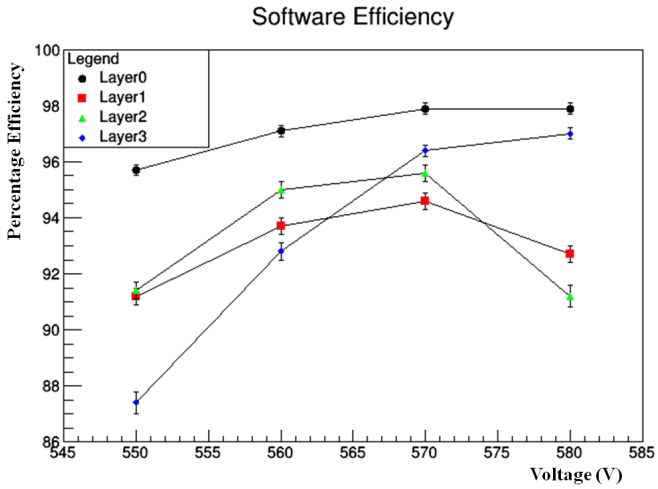

FIGURE 3.13: Software efficiency as a function of the HV amplification voltage.

Chapter 4

Motivations for the analysis

From this Chapter ongoing, the results of my research, one of the most recent analysis of the ATLAS collaboration, are presented. In Section 4.1 the kinematic observables used to perform the differential cross section measurements are described. In Sections 4.1.1 and 4.1.2 comparison between measurements performed in the dilepton and in the ℓ+jets channels are presented for the $p_{\mathrm{T}}^{t,had}$ and $p_{\mathrm{T}}^{t\bar{t}}$ observables, respectively. Finally the measurement perfomed on the $|\,p_{\mathrm{out}}^{t\bar{t}}\,|$ observable with data collected at $\sqrt{s}$ = 8 TeV in the inclusive ℓ+jets is shown in Section 4.1.3. For all these measurements, an inclusive selection was applied.

The motivation of the analysis are reported here.

The top quark plays a special role in the SM and in some theories of physics beyond the SM; in fact, measurements of top quark provide an important test of the SM and any observed deviation from the SM predictions could indicate the presence of new physics. The large top quark mass and the large $t\bar{t}$ pair production cross section in pp collisions make top quark production at the LHC a unique laboratory frame for study the behaviour of QCD at the highest accessible energy scales. In addition, some of the measured distributions can be used to improve our understanding of parton distribution functions (PDFs). Moreover, the $t\bar{t}$ production constitute a background source for some measurements, therefore, it is important to well model this kind of production.

Measurements of the top quark pair differential cross sections, in different bins of jet multiplicity, as functions of different kinematic variables are the object of the analysis.

Since the top quark decays almost always to a W boson and a b-quark, the decay of a top quark pair produces six particles in the final state. The decay channel considered is characterised by the leptonic decay of one W boson and the hadronic decay of the other W boson and it is common to refer to as semileptonic decay mode or ℓ+jets. The final state contains one lepton (electron or muon), one neutrino giving rise to missing transverse momentum ($E_{\mathrm{T}}^{\mathrm{miss}}$) and four jets, two of which originated from b-quarks. More jets can be produced in the final state, i.e., jets not originating from the decay

of top quark and anti-top quark but arising from quark and gluon radiation produced in association with the $t\bar{t}$ system.

The uncertainties associated with these processes are significant in precision measurements, such as the measurement of the top quark mass and the inclusive $t\bar{t}$ production cross sections.

It is therefore important to study the differential cross sections in bins of jet multiplicity to investigate in detail the effect of QCD radiation on kinematic variables which cannot be seen in inclusive differential measurements. In the inclusive measurements, at least 4 jets are selected, therefore some effects are hidden due to higher multiplicity.

Measurements of differential cross sections as functions of several kinematic variables [48–51] and as function of the number of additional jets [52–54] were pusblished by the ATLAS collaboration with data collected at $\sqrt{s}$ of 7, 8 and 13 TeV; the measurements were performed in differents $t\bar{t}$ topologies. Some of the results, in comparison, are shown in the next sections.

The results here presented combine these two types of measurements to provide further informations about top quark production and explore the effect of the QCD radiation on kinematic variables. The CMS collaboration published a similar measurement [55].

To study the dependence of the observables on the QCD emission, three orthogonal configurations are defined depending on the number of additional jets: the "4-jet exclusive configuration" where no additional jets are selected, the "5-jet exclusive configuration", where only one additional jet is required and the "6-jet inclusive configuration", where two or more additional jets are required.

4.1 Kinematic observables

The kinematic observables studied, are the transverse momentum of the $t\bar{t}$ system ($p_{\mathrm{T}}^{t\bar{t}}$), the transverse momentum of the hadronic top quark ($p^{\mathrm{t,had}}$) and the absolute value of the out-of-plane momentum ($|\, p_{\mathrm{out}}^{t\bar{t}} \,|$), defined as:

$$|p_{\mathrm{out}}^{t\bar{t}}| = \left| \overrightarrow{p}^{\,t,had} \cdot \frac{\overrightarrow{p}^{\,t,lep} \times \hat{z}}{|\overrightarrow{p}^{\,t,lep} \times \hat{z}|} \right|, \tag{4.1}$$

where $\overrightarrow{p}^{\,t,lep}$ and $\overrightarrow{p}^{\,t,had}$ are the momenta of the leptonically and hadronically decaying top quark, respectively, and $\hat{z}$ represents the beam axis.

This variable was chosen because it was found to be one of the most sensitive variable to emission of additional radiation associated to the production of the top quark pair [56].

Measure the three defined observables, in particular the $p_{\mathrm{T}}^{t\bar{t}}$ and $|p_{\mathrm{out}}^{t\bar{t}}|$ which are more sensitive to the jets activity, helps the improvement of the tune of

next generation of MC samples; the measurements show that is possible to further constraint the behaviour of the parton shower and that the settings of these generators can be improved.

4.1.1 Measurements of $p_{\mathrm{T}}^{t,had}$

Comparison between the measurements of the $p_{\mathrm{T}}^{t,had}$ are shown in Figures 4.1. The measurements were performed in the dilepton channel 4.1(a) and in the ℓ+jets channel 4.1(b) using data collected at $\sqrt{s}$ = 13 TeV.

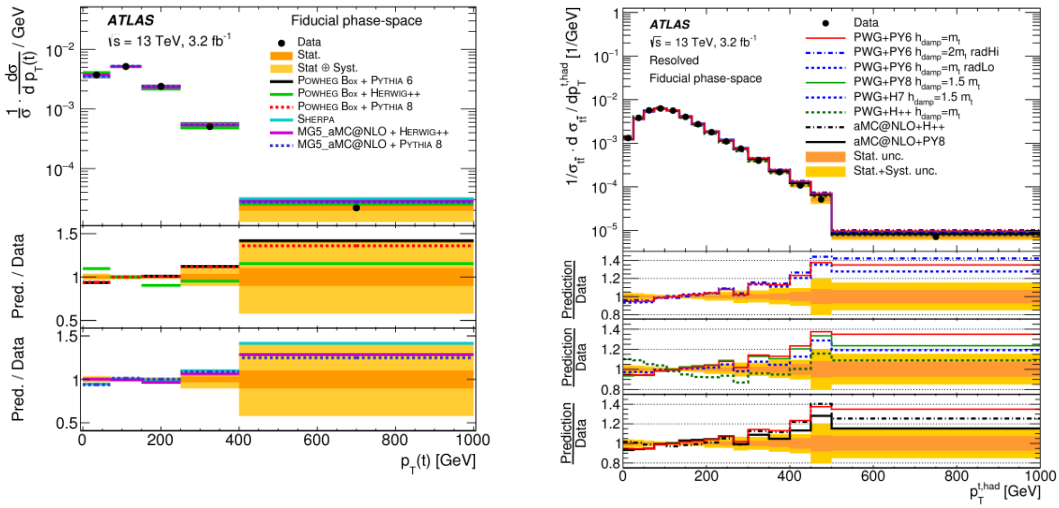

(a) (b)

FIGURE 4.1: Normalised differential cross section in the fiducial phase at particle level as a function of the $p_{\mathrm{T}}^{t,had}$ in the dilepton channel (a) and for the ℓ+jets channel (b) with an inclusive selection without considering additional jets.

In both the measurements, a tendency of all the predictions to overestimate data at high value of p_{T} is shown. This tendency is also observed in the measurements reported in this thesis in Chapter 10 in all the three configurations of additional jets.

4.1.2 Measurements of $p_{\mathrm{T}}^{t\bar{t}}$

An analogus comparison is reported in this Section for the $p_{\mathrm{T}}^{t\bar{t}}$ observable. The measurements of this variable, in two different channels of the $t\bar{t}$ topology, is shown in Figures 4.2. The measurements were performed in the dilepton channel 4.2(a) and in the ℓ+jets channel 4.2(b) using data collected at $\sqrt{s}$ = 13 TeV; also in these measurements an inclusive selection was applied.

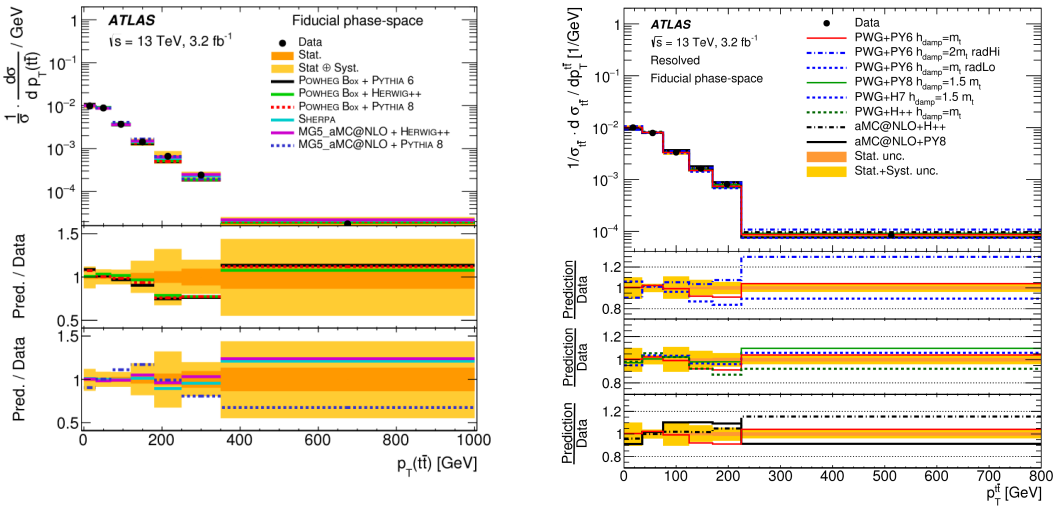

(a) (b)

FIGURE 4.2: Normalised differential cross section in the fiducial phase at particle level as a function of the $p_{\mathrm{T}}^{t\bar{t}}$ in the dilepton channel (a) and for the ℓ+jets channel (b) with an inclusive selection without considering additional jets.

This variable is sensitive to additional radiations as already mentioned and as is shown in Chapter 10. For the dilepton measurement shown in Figure 4.2(a), almost all the predictions tend to overestimate data at high value of the p_{T} but are consistent within the uncertainties. In the ℓ+jet channel distribution, shown in Figure 4.2(b), can be clearly observed that the 'radHi' and 'radLo' predictions bracket the nominal sample.

4.1.3 Measurements of $|p_{\mathrm{out}}^{t\bar{t}}|$

The $|p_{\mathrm{out}}^{t\bar{t}}|$ observable was already studied in the $t\bar{t}$ in the differential analysis performed using data collected at 8 TeV [51] in the ℓ+jets channel. The result of this measurements is shown in Figure 4.3 where data are compared with different MC predictions.

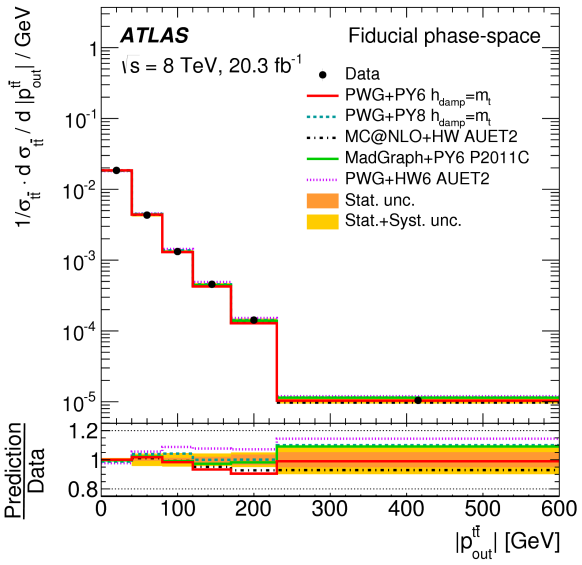

FIGURE 4.3: Normalised differential cross section in the fiducial phase at particle level as a function of the $p_{\mathrm{out}}^{t\bar{t}}$ from the 8 TeV measurements.

Chapter 5

Data and Monte Carlo samples

Data and Monte Carlo samples used in the analysis are briefly described. In Section 5.1 data samples are described. In Section 5.2 the Monte Carlo simulation and the event simulation processes are described. The latter consists of the event generation and of the detector simulation as reported in Sections 5.2.1 and 5.2.2, respectively. Finally, in Sections 5.3 and 5.4 the signal and background simulated samples are described, respectively.

A summary of the MC samples used and described below is reported in Table 5.1.

5.1 Data samples

The data used were recorded with the ATLAS detector at a $\sqrt{s}$ of 13 TeV in 2015 and correspond to an integrated luminosity of 3.2 fb^{-1}; the corresponding samples were collected in several data-tacking periods characterised by different beam and detector conditions. Only data taken under stable beam conditions and with the full operation of the relevant subdetectors, included IBL, are considered. In Figure 5.1 the total integrated luminosity versus time, is shown.

The luminosity calibrations is performed from Van der Meer scans, following techniques similars to those descibed in Ref. [57] and the relative uncertainty, for data used in this analisys, is 2.1%.

5.2 Monte Carlo simulations

The MC samples have been generated according to both theoretical predictions and phenomenological models. These samples simulate processes resulting from hard interactions.

The event simulation process consists of severals parts: the event generation is performed by using software applications such as POWHEG [58] and MC@NLO [59] while the parton shower is performed by using samples such

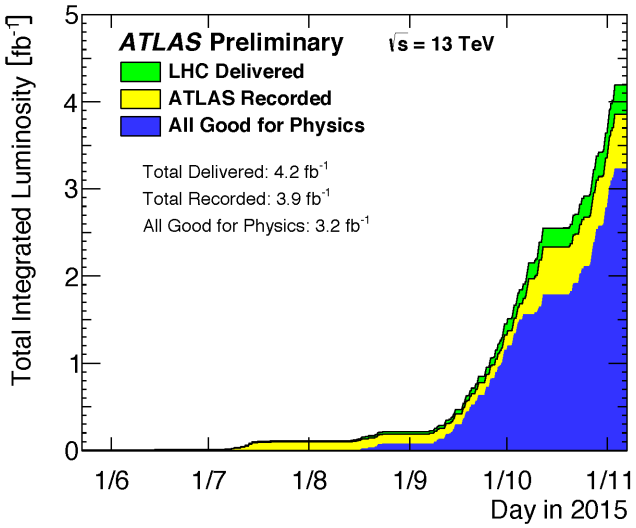

FIGURE 5.1: Cumulative luminosity versus time:delivered by the LHC (yellow), recorded by the ATLAS detector (green) and all good for physics (blue).

as PYTHIA [60] and HERWIG [61]; the detector simulation is carried out by applications such as GEANT4 [62] or ATLFAST2 [63].

5.2.1 Event generators

The event generators are software applications which simulate high energy physics events production. The generators are based on theoretical models and the parameters can be modified to make distributions compatible with data.

An event generator simulate all the processes from pp interactions to final state particles; these processes are characterised by several steps:

- Hard process;
- parton shower;
- hadronisation;
- multiple parton interactions and beam remnants (minimum bias collisions).

These steps are schematically reported in Figure 5.2 and explained in detailed below.

Hard process

The first step of the event generation is the hard scattering process, involving partons from each proton. In this process, the scattering probability of

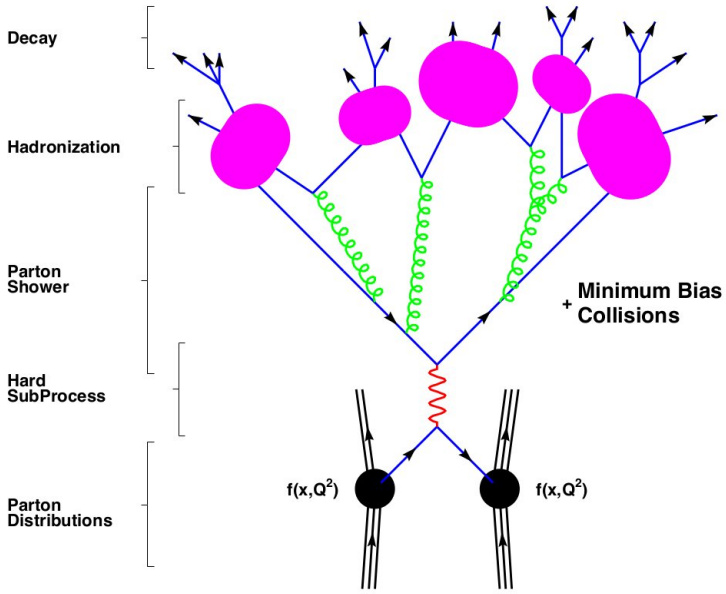

FIGURE 5.2: Workflow of the Monte Carlo event generation steps.

the hard process is simulated with fixed-order perturbative Matrix Elements (ME).

All the generators used are NLO calculations and are more complex to be calculated, respect to the LO calculations, because take into account the first order of emission.

Parton shower (PS) and Hadronisation

The next steps are the *parton shower* and *hadronisation* processes. One of the software used to simulate both the processes is PYTHIA. The partons partecipating in the hard process, involve large momentum transfers and therefore, are wildly accelerated. These accelerated partons emit virtual gluons which, since carry colour charges, can further emit gluons or produce quark-antiquark pairs.

During this process two states occur; one of the states is the initial-state radiation (ISR) which is developed on an incoming parton of the hard process; the incoming particles emit radiation before the interaction with other particles reducing therefore the beam energy prior to the momentum transfer. It is a space-like process.

The other state is the final-state radiation (FSR) which is a time-like process where particles lose energy and virtuality until the splitting of the primary particle and all the discendent partons is terminated.

The hadronisation process is non-perturbative and leads to the generation of observed final-state hadrons. It is only described by phenomenological models.

The common models are the *Lund string model* [64] on which is based PYTHIA and the *cluster model* [65] for SHERPA [66] and HERWIG.

- **Lund string model**: in this model, gluons are treated as field lines, attracted to each other. This idea comes from the observation that, at large distances, the potential energy of colour sources increases linearly with their separation. This effect leads to an actractive force independent from the distance. This phenomenon is due to the gluon self-interaction;
- **Cluster model**: this model is based on the so-called *preconfinement* property of QCD. This phenomenon explains that, at evolution scales much small than the hard process scales ($q \ll Q$), the partons in a shower are clustered in groups to which corresponds an invariant mass distribution asymptotically independent on the hard subprocess scale and type.

The representation of these models is shown in Figure 5.3(a), 5.3(b).

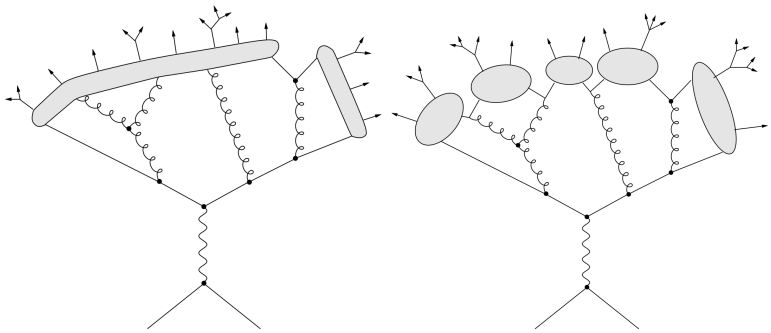

(a) (b)

FIGURE 5.3: Models of hadronisation process: string model 5.3(a) and cluster model 5.3(b).

Underlying events and additional processes

In hadron collider interactions there is extra activity which superimposes the hard scattering process. These kind of activities are the underlying events, minimum-bias events and pile-up.

The underlying events arise from collisions between those partons of the incoming hadrons that not produce the hard scattering.

The minimum-bias events, are due to collisions that are not ascribed to hard processes.

Both the underlying and minimum bias events are modelled by the introduction of Multiple Parton Interactions (MPI) in the event generators.

The additional pp interactions in the bunch-crossing that do not produce hard scattering are named *in time pile-up*.

Pile-up includes also other events such effects as beam halo, beam gas, cavern background, as well as overlapping detector responses from interactions of neighboring bunch crossings, called *out-of-time pile-up*.

5.2.2 Detector simulation

The simulation of the detector response is performed by the toolkit GEANT4. It provides a model for the interaction of particles through matter. It is therefore important a detailed description of the detector geometry, the materials involved and of the trigger system.

The detailed simulation performed with GEANT4 requires a significant amount of time. In order to simulate all the events required in the analysis some samples are simulated with a fast simulation, called *ATLASFastII* (AFII), in which the calorimeter showers are generated with a parametrisation.

5.3 Signal Monte Carlo samples

In this Section the different MC employed to generate the $t\bar{t}$ signal events and the modeling $t\bar{t}$ samples, are described; the modeling uncertainties are described in details in Section 9.1 [67].

- **POWHEG +PYTHIA6**: this is the nominal sample, i.e. the sample used as reference. This sample is generated using the POWHEG generator [68] with the CT10 PDF sets [69], both at NLO.

  The NLO matrix element of the POWHEG generator simulates the hard scattering process. The resummation damping factor (h_{damp}) is set to the top quark mass and it is one of the parameters that controls the ME and PS matching in POWHEG and regulates the high-p_{T} raditions.

  Parton showers and underlying events are simulated by PYTHIA (version 6.427) [70] with the Perugia 2012 tune [71] and the LO CTEQ6L1 PDFs [72].

  The hard process renormalisation μ_r and factorisation μ_f scales are set to the default generator value:

  $$\mu = \sqrt{m_{\mathrm{top}}^2 + p_{\mathrm{T}}^2}, \tag{5.1}$$

  where m_{top} is the top quark mass and p_{T} is the top quark transverse momentum evaluated before the Born configuration, i.e. before QCD radiation;

Additional POWHEG+PYTHIA6 samples, with variations on the hadronisation and factorisation scales and on the h_{damp} parameter, produce the effect of more or less radiation [67]:

- the factorisation and hadronisation scales are varied by a factor of 0.5 and simultaneously, the h_{damp} parameter is increased to $2m_{\mathrm{top}}$. The 'radHi' tune variation from the P2012 tune is used;
- the factorisation and hadronisation scales are varied by a factor of 2.0, while, the h_{damp} parameter remains unchanged. The 'radLo' tune variation from the P2012 tune is used.

- **POWHEG + HERWIG++**: this sample is generated with the same setup used for POWHEG in the nominal sample. In this case, the PS, hadronisation and the UE events are simulated using HERWIG++ (version 2.7.1) with the UE-EE-5 tune [73] and the corrisponding CTEQ6L1 PDFs;
- **MADGRAPH5_MC@NLO + HERWIG++**: this sample is generated with the version 2.2.1 of the MadGraph5_aMC@NLO event generator [59]. For the $t\bar{t}$ hard scattering process a NLO ME and CT10 PDF sets are used. The renormalisation and factorisation scales are set to the mass of the top quark.

$$\mu = \sqrt{m_{\mathrm{t}}^2 + 0.5 \cdot (p_{\mathrm{T,t}}^2 + p_{\mathrm{T,\bar{t}}}^2)}. \tag{5.2}$$

Also in this sample, the PS, hadronisation and UE events are modeled using the HERWIG++ (version 2.7.1) generator with the UE-EE-5 tune and the corrisponding CTEQ6L1 PDFs.

Additional $t\bar{t}$ samples [56, 74] are the followings:

POWHEG + PYTHIA8 which is generated using the same settings for POWHEG as for the nominal sample but the PS, hadronisation and UE events are simulated by PYTHIA8 (version 8.183) with A14 tune and the corresponding CTEQ6L1 PDFs.

Two samples with different values of the h_{damp} parameter are considered: one with $h_{\mathrm{damp}} = m_{\mathrm{t}}$ and the other one with $h_{\mathrm{damp}} = 1.5\ m_{\mathrm{t}}$.

Two POWHEG + PYTHIA8 samples similar to the two POWHEG + PYTHIA6, described above, but with the h_{damp} parameter set to $3\ m_{\mathrm{t}}$, for the 'radHi' tune variation and to $1.5\ m_{\mathrm{t}}$ for the 'radLo' tune variation.

Two MADGRAPH5_AMC@NLO + PYTHIA8 samples. These are generated using the version 2.2.1 of MADGRAPH5_AMC@NLO but the PS, hadronisation and UE events are simulated by PYTHIA8(version 8.183) with A14 tune and the corresponding NNPDF2.3LO PDF. These two samples have two different factorisation scales. One has the scale set to $H_{\mathrm{T}}/2$ (H_{T} is defined as the scalar sum of the transverse momenta of the two top quarks) and the other one to $\sqrt{m_T^2 + p_T^2}$.

The last two samples used are a POWHEG+HERWIG7 generated with the h_{damp} parameter set to $1.5\ m_{\mathrm{t}}$ and using the H7-UE-MMHT tune and a SHERPA sample (version 2.2.1) with MEPS@NLO setup; the events are generated with a $t\bar{t}$ matrix element plus zero and one parton simulated at NLO and two, three and four partons at LO. The CT10 PDFs were used and the PS, hadronisation and UE events are simulated using the default SHERPA settings.

All the samples described are normalised to $\sigma_{t\bar{t}} = 832^{+20}_{-29}(scale)^{+35}_{-35}(PDF)\ pb$ as calculated with the TOP++2.0 program NNLO in perdurbative QCD including soft-gluon resummation to (NNLL), and assuming a top quark mass $m_{\mathrm{t}} = 172.5\ GeV$.

The uncertainties of this cross section are due to the independent variation of the factorisation and renormalisation scales, μ_{F} and μ_{R} (scale term) and to variations in the PDF and α_{S} (PDF term).

5.4 Background Monte Carlo samples

The $t\bar{t}$ signal selection is affected by background events. The background could be due to other physics processes producing the same final state or due to mis-reconstruction of a lepton. Both types of events need to be evauated as described in Chapter 7 (in Section 7.2) and substracted from data, using the unfolding procedure to calculate the top quark pair cross sections.

The first kind of background source is characterised by the similarity of the decay products with the signal events. The other kind of background is characterised by a misidentification of objects by the detector.

The processes considered are the single top quark production, V+jets production (W+jets and Z+jets), diboson final states and $t\bar{t}$ producted in association with weak bosons, $t\bar{t} + WZ/WW$ to which is referred to as $t\bar{t}V$.

Single-top quark

The generation of single-top quark production events for the Wt and s channel samples was done with the configuration of the POWHEG-BOX V2 event generator with the CT10 PDF set matrix element calculations, as done for the nominal $t\bar{t}$ sample described above.

To avoid the overlap between the Wt and $t\bar{t}$ samples, the diagram removal scheme [75] is used.

The electroweak t-channel single-top quark events are simulated using the POWHEG-BOX V1 generator.

For the t- and s-channels, the single-top quark cross sections are normalised to their NLO predictions, while, for the Wt-channel the cross section is normalised to its NLO+NNLL prediction [76–78].

V+jets

To simulate the background of single W or Z, in association with jets, the SHERPA 2.2.1 generator is used.

Matrix elements are calculated for up to two partons at NLO and for up to four partons at LO using the Comix [79] and OpenLoop [80] matrix element event generators.

The two ME event generators are merged with the SHERPA parton shower sample.

The matching occur using the ME+PS@NLO prescription. The CT10 PDF set is used in conjunction with dedicated parton shower tuning developed by the authors of SHERPA.

The Z+jets events are normalised to the NNLO cross sections [81], while, the normalisation of the W+jets is obtained with a data-driven technique.

Diboson

In the diboson background events one of the boson decaying hadronically and the other one leptonically. This background is simulated using the SHERPA V2.1.1 event generator. Matrix elements are calculated for up one (ZZ) or zero (WW,WZ) additional partons at NLO and up to three additional partons at LO using the Comix and OpenLoops matrix element event generator. These event generators are merged with SHERPA parton shower using the ME+PS@NLO prescription.

The CT10 PDF set is used in conjunction with dedicated parton shower tuning developed by the authors of SHERPA. In this case, for the normalisation, the event generator cross sections, already evaluated at NLO accurancy, are used.

$t\bar{t}V$

The $t\bar{t}$ events, in association with weak bosons ($t\bar{t}$ + W/Z or WW), are simulated using MADGRAPH_AMC@NLO event generator at LO interfaced to the PYTHIA8 parton shower model.

The matrix elements are simulated with up to two ($t\bar{t}$ + W), one ($t\bar{t}$ + Z) or zero ($t\bar{t}$ + WW) extra partons. The ATLAS UE A14 tune is used together with the NNPDF2.3LO PDF set. For the normalisation of the events their respective NLO cross sections are used [59].

Physics process	Generator	Cross section normalisation	PDF set for hard process	Parton shower	Tune
$t\bar{t}$ signal	POWHEG-BOX v2	NNLO+NNLL	CT10	PYTHIA6.428	Perugia2012
$t\bar{t}$ PS syst.	POWHEG-BOX v2	NNLO+NNLL	CTEQ6L1	HERWIG++ 2.7.1	UE-EE-5
$t\bar{t}$ ME syst.	MADGRAPH5_aMC@NLO	NLO	CT10	HERWIGPP 2.7.1	UE-EE-5
$t\bar{t}$ rad. syst.	POWHEG-BOX v2	NNLO+NNLL	CT10	PYTHIA 6.428	'radHi/Lo'
Single top: t-channel	POWHEG-BOX v1	NLO	CT10f4	PYTHIA 6.428	Perugia2012
Single top: s-channel	POWHEG-BOX v2	NLO	CT10	PYTHIA 6.428	Perugia2012
Single top: Wt-channel	POWHEGBOX v2	NLO+NNLL	CT10	PYTHIA 6.428	Perugia2012
$t\bar{t}$+$W/Z/WW$	MADGRAPH5_aMC@NLO	NLO	NNPDF2.3LO	PYTHIA 8.186	A14
$W(\to \ell\nu)$+ jets	SHERPA 2.1.1	NNLO	CT10	SHERPA	SHERPA
$Z(\to \ell\bar{\ell})$+ jets	SHERPA 2.1.1	NNLO	CT10	SHERPA	SHERPA
$Z(\to \ell\bar{\ell})$+ jets	SHERPA 2.1.1	NNLO	CT10	SHERPA	SHERPA
WW, WZ, ZZ	SHERPA 2.1.1	NLO	CT10	SHERPA	SHERPA

TABLE 5.1: Summary of MC samples, showing the generator for the hard-scattering process, cross-section normalisation precision, PDF choice as well as the parton shower and the corresponding tune used in the analysis.

Chapter 6

Objects reconstruction and definition

In this Chapter the reconstruction of physics objects collected by the ATLAS detector, are described. In Figure 6.1 a Feynman diagram at LO corresponding to the semileptonic $t\bar{t}$ topology is reported; only objects which characterise this topology and used in the analysis are considered and described.

Electrons and muons objects are described in Sections 6.1, 6.2, respectively. Jets objects are detailed described in Section 6.3. The missing transverse energy and overlap removal criterion are described in Sections 6.4 and 6.5, respectively. Finally, the particle level definition is described in Section 6.6.

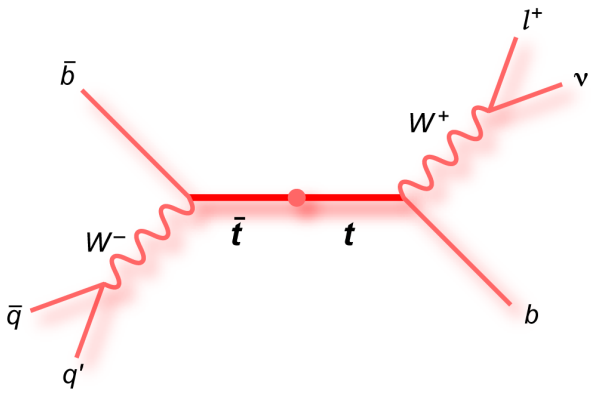

FIGURE 6.1: Leading order Feynman diagram for the ℓ + jets $t\bar{t}$ topology.

6.1 Electrons

It is important to efficiently reconstruct and identify electrons over the full acceptance of the detector. To achieve this, the ATLAS detector exploits a powerful detector technologies: silicon detectors and transition tracker to identify the track of the electron, longitudinally layered electromagnetic calorimeters to measure the electron's energy and hadronic calorimeters which are used as veto for particles giving rise a significant hadronic activity [82, 83].

6.1.1 Electron reconstruction

The standard electron reconstruction procedure, in the central region of the ATLAS detector ($|\eta|$<2.47), is based on three steps: the first step is the identification of the energy deposit in the EM calorimeter, the second step is the association of the tracks in the ID with the clusters of energy generated in the EM calorimeter. The last step is the reconstruction of the electron candidate.

Cluster recontruction

Electron reconstruction begins with the creation of EM clusters. These clusters are seeded from energy deposits with the total transverse energy above 2.5 GeV and are generated using a sliding-window algorithm with window size of 3×5 in units of 0.025×0.025 in (η,ϕ) space.

Track association with cluster

In the region of the tracker detectors ($|\eta| < 2.5$), an electron is defined by the existence of one or more reconstructed tracks matched to a seed cluster. Tracks are extrapolated from their last measured point to the second layer of the EM calorimeter. Then the extrapolated η and ϕ coordinates of the impact point, are compared to the coordinates of the cluster in the layer.

The track and the cluster are considered matched if the distance between the track impact point and the EM cluster barycentre is $|\Delta\eta| < 0.05$.

To account for the breamsstrahlung loss effects, on the azimuthal distance, the size of the $\Delta\phi$ track-cluster matching window is 0.1 in the region where the extrapolated track bends as it transverses the solenoidal magnetic field.

An electron candidate is considered to be reconstructed if at least one track is matched with a cluster. In case two tracks have the same number of hits, the one better matching the cluster is chosen. In case of absence of matching between cluster and tracks, the candidate is identified as *uncoverted* photon candidate.

Electrons are distinguished by converted photons if there is presence of two close tracks originated from a vertex displaced from the interaction point and by verifying the location of the first hit along the path of the single track.

Reconstructed electron candidate

After a successful track-cluster matching, the cluster sizes are optimaised to take into account the overall energy distribution in the different regions of the EM calorimeter. In the EM barrel region the size of the cluster is 3×7 in units of 0.025×0.025 in (η,ϕ) space, while in the EM endcaps regions the size is icreased to 5×5.

The total reconstructed electron candidate energy is determined from the sum of four contributions: the estimated energy deposit in the material in front the EM calorimeter, the measured energy deposit in the cluster, the estimated energy deposit outside the cluster and the estimated deposit of energy in the region beyond the EM calorimeter.

6.1.2 Electron identification

To determine whether the reconstructed electron candidates are effectively electrons, algorithm for electron identification (ID) are applied. The baseline ID algorithm is the likelihood (LH) based method. It is a multivariate analysis (MVA) technique that simultaneously evaluates several properties of the electron candidates while making a selection decision. This method provides a good separation between signal electrons (isolated) and jets (fakes electrons). The re-optimisation of the ID algorithm for Run-2 is based on MC simulation samples. Electron candidates from MC simulations of $Z \rightarrow ee$ are used. The identification criteria for electron candidates is based on sequential cuts on calorimeter, tracking and on combined track-cluster variables.

Three sets of cuts, with increasing power of background rejection have been chosen identifying *loose*, *medium*, *tight* electrons. These criteria are designed in a hierarchical way; them provide increasing background-rejection power while decreasing in the same time the identification efficiency.

The increasing of the background-rejection occurs adding variables in each step. The performance of the identification algorithm is illustrated in Figure 6.2.

Loose selection

The loose selection uses shower-shape variables in both the first and the second layers of the EM calorimeter. Additional requirements on the quality of the electron track and track-cluster matching improve the rejection of the hadronic background of a factor ~ 5 in the E_{T} range 30 to 40 GeV while maintaining a high identification efficiency.

Medium selection

The medium selection adds discriminanting variables to the loose selection, by requiring the presence of a measured hit in the innermost layer of the pixel detector, applying a loose selection requirement on the transverse impact parameter $|d_0|$ and identifying transition radiation in the TRT, when available.

Tight selection

The tight selection achieves a rejection power higher by a factor two respect to the medium selection. On the ratio between the cluster energy over the track momentum, in addition to the requirements on medium selection discriminant variables, stricter requirements are applied on track quality when a track extention is present in the TRT detector.

A veto is also applied on reconstructed photon conversion vertices associated with the cluster.

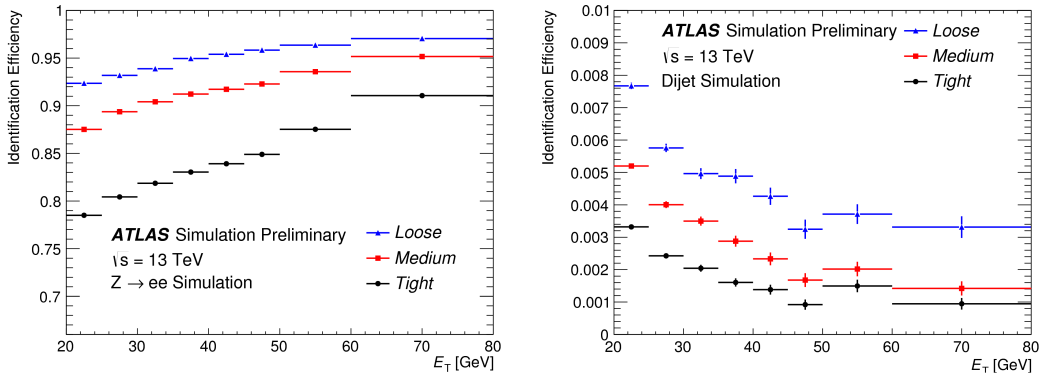

(a) (b)

FIGURE 6.2: The efficiency to identify electrons from $Z \rightarrow ee$ decays 6.2(a) estimated using simulated dijet samples and the efficiency to identify hadrons 6.2(b) as electrons estimated using dijet samples.

6.1.3 Electron isolation

In addition to the identification criteria, electrons are required to be isolated to further discriminate between signal and background. Two discriminant criteria are used: a calorimeter isolation discriminator and a tracking based discriminator, briefly described below.

Calorimeter isolation discriminator

This discriminator is defined as the sum of the transverse energies of topological clusters, within a cone of $\Delta R = 0.2$ around the cluster of the candidate electron, where the energy of the electron itself is excluded.

Tracking based discriminator

It is defined as the sum of scalar p_{T} of tracks within a cone of ΔR= 0.2 around the track of the candidate electron and originating from the reconstructed primary vertex of hard collisions, excluding the electron associated track.

The considered tracks quality requirements are:

- $p_{\mathrm{T}} > 1\ GeV$;
- 1 hit in the innermost pixel detector layer;
- $\geq$ 7 hits in silicon detectors;
- transverse (d_0) and longitudinal (z_0) impact parameters < $1\ mm$.

6.1.4 Electron efficiency measurements

The experimentally determined electron spectra must be corrected for inefficiencies related to trigger, isolation, identification and reconstruction [84].

To estimate these inefficiencies the so-called *tag-and-probe* method is used. The method uses $Z \rightarrow e^+e^-$ samples to select unbiased samples of electrons (probes) by using strict selection requirements on the second object produced from the particle's decay (tags).

The efficiency to find and select an electron is not measured in a single quantity but is composed by several quantities, namely, reconstruction, identification, isolation and trigger efficiencies.

The total efficiency ϵ_{tot} for a single electron can be written as:

$$\epsilon_{\mathrm{tot}} = \epsilon_{\mathrm{reconstruction}} \times \epsilon_{\mathrm{identification}} \times \epsilon_{\mathrm{isolation}} \epsilon_{\mathrm{trigger}}. \tag{6.1}$$

Since the efficiency depends on E_{T} and η, the measurements are performed in two dimensional bins in (E_{T},η).

The efficiency is of 90 % for electron with p_{T} of 25 GeV and 99 % for electrons with p_{T} of 60 GeV; these efficiencies have been obtained applying the two isolation discriminant criteria for calorimeter and tracking, described above.

6.2 Muons

As for the electrons, it is important to efficiently reconstruct and identify muons. The following sections describe the techniques used to reconstruct and identify muons.

6.2.1 Muon reconstruction

The first step of the reconstruction is performed independently in the ID and MS subdetectors. Then, the muon candidates are identified by matching the tracks in the ID and tracks in the MS, forming the muon tracks used in physics analyses.

In the ID, muons are reconstructed like any other charged particles, as described for example previously for the reconstruction of the electrons.

Here the reconstruction of the muons in the MS and the combined muon reconstruction [85], are described.

Muon reconstruction in the MS

In the MS the reconstruction starts by searching hit patterns to form segments inside each muon chamber. The MDT chambers of the MS are used to search for hits which are aligned on a trajectory in the bending plane of the detectors. A Hough transform [86] is used to perform this search. The RPC or TGC hits measure the coordinate orthogonal to the bending plane. In the CSC chambers, segments are build searching in the η and ϕ planes.

After the separated search in each component of the MS, the muon track candidates are built by fitting together, hits of segments of different layers. At least two matching segments are required to build a track, except in the barrel-endcap transition region where a single high-quality segment with η and ϕ information can be used to build a track.

To ensure high efficiency for close-by muons, all tracks with segments in three different layers of the MS are kept when they are identical in two of the three layers but share no hits in the outermost layer.

6.2.2 Combined muon reconstruction ID-MS

To combine the ID and MS muon reconstructions several algorithms based on the informations provided by the ID, MS and calorimeters are used. Four muon type of algorithms, depending on which subdetector is used in the reconstruction, are defined, as follows:

- **Combined muon (CB)**: the track reconstruction is performed independently in the ID and MS, and a combined track is formed with a global fit that uses the hits from both the ID and MS subdetectors. To improve the fit quality, during the global fit procedure, MS hits may be added to the track or removed;
- **Segment-tagged muons (ST)**: a track in the ID is classified as a muon if, once extrapolated to the MS, it is associated with at least one track segment in the MDT or CSC chambers. The ST muons are used when

muons cross only one layer of MS chambers, either because of their low p_{T} or because they fall in regions with reduced MS acceptance;

- **Calorimeter-tagged muons (CT)**: a track in the ID is identified as a muon if it can be matched to an energy deposit in calorimeters. This type of muon candidate has the lowest purity of all the muon types. The identification criteria for CT muons are optimised for regions with $|\eta|$<0.1 and a momentum range of 15<p_{T}<100 GeV;
- **Extrapolated muons (ME)**: the muon trajectory reconstruction is based only on the MS track and a loose requirement on compatibility with originating from the IP. In general, the muon is required to traverse at least two layers of MS chambers to provide a track measurement,but three layers are required in the forward region. ME muons are mainly used to extend the acceptance for muon reconstruction into the region 2.5< $|\eta|$<2.7, which is not covered by the ID.

A rapresentation of the reconstruction with the 4 different algorithms is shown in Figure 6.3.

Overlaps between different muon types are resolved before producing the muons used in physics analyses. When two muon types share the same ID track, preference is given to CB muons, then to ST, and finally to CT muons. The overlap with ME muons in the muon system is resolved by analyzing the track hit content and selecting the track with better fit quality and larger number of hits.

The use of a Hough transform to identify the hit patterns makes the reconstruction faster and more robust against misidentification of hadrons, thus providing better background rejection.

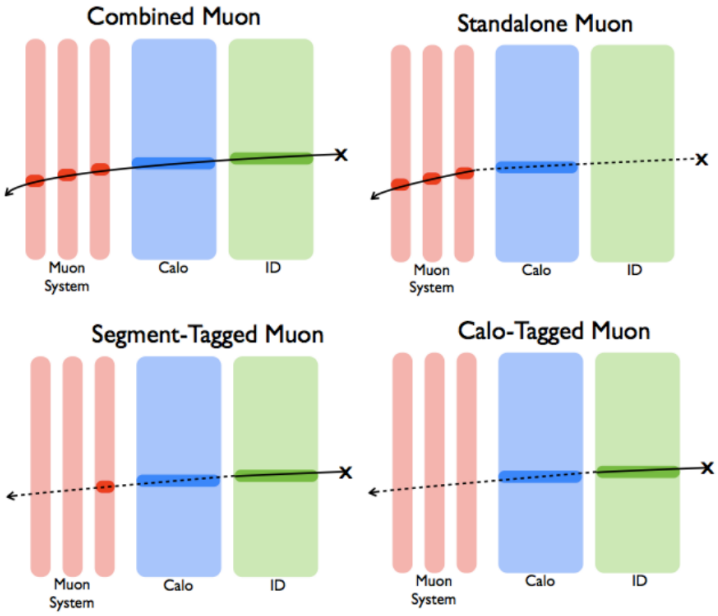

FIGURE 6.3: Reconstruction of the muons using four different algorithms, namely, CB, ST, CT, ME.

6.2.3 Muon identification

Muon identification is performed by applying quality requirements that suppress background, mainly from pions decays, while selecting prompt muons with high efficiency and ensuring a robust momentum measurement.

Several variables offer a good separation between promt muons and pions. These variables are studied in simulated $t\bar{t}$ events.

To ensure a robust momentum measurement, specific requirements on the number of hits in the ID and MS are used. In the ID at least one hit in the Pixel, 5 hit in the SCT and less than three holes in Pixel or SCT are required and that at least 10% of the TRT hits are included in the final fit.

Four muon identification selections, namely *medium*, *loose*, *tight* and *high-*p_{T} are defined.

- **Loose muons**: this selection is optimised to maximise the reconstruction efficiency while providing good quality muon tracks. All muon types are used;
- **Medium muons**: this is the default selection in the ATLAS detector. It uses only CB and ME tracks. At least 3 hits in at least two MDT layers are required, except in the region of $|\eta|$<0.1 where track with at least one MDT layer and no more than one MDT hole layer, are allowed;
- **Tight muons**: this selection is optimise to maximise the purity of muons at the cost of efficiency. Only CB muons with hits in at least two stations of the MS are considered and have also to satisfy the medium selection creteria;
- **High-**p_{T}: the aim of this selection is to maximise the momentum resolution for tracks with transverse momentum greater than 100 GeV. Only CB muons having at least three hits in three MS stations and passing the medium criteria selection are selected.

6.2.4 Muon isolation

The measurement of the detector activity around a muon candidate is a powerful tool for background rejection in many analyses.

As for the electron isolation, two variables are defined to asses the muon isolation: a track-based variable and a calorimeter-based isolation variable.

- **Track-based isolation**: the track-based isolation variable $p_{\mathrm{T}}^{varcone30}$ is defined as the scalar sum of the transverse momenta of the tracks in a cone of size $\Delta R > 0.3$, around the muon p_{T}^{μ}, excluding the muon track itself;

- **Calorimeter-based isolation**: the calorimeter-based isolation variable, $E_{\mathrm{T}}^{topocone20}$, is defined as the sum of the transverse energy of the topological cluster in a cone of $\Delta R > 0.3$ around the muon, with the muon's energy loss substracted.

6.2.5 Muon reconstruction efficiency

Seven isolation working points are defined each one optimised for different physics analyses. The efficiencies for each isolation working points are measured in data and simulation in $Z \rightarrow \mu\mu$ decay using the tag-and-probe method.

To avoid muons close to jets, the angular separation ΔR is required to be greater than 0.4. In addition, the two muons originated from the decay of the Z are required to be separated of $\Delta R > 0.3$.

6.3 Jets

Hadronic particles deposit energy mainly in the hadronic calorimeter system. These deposits are grouped into objects called jets.

The basic structures of the jet reconstruction process in ATLAS are the topological clusters (topo-clusters), built from calorimeter's cells. Jets are reconstructed with anti-k_{t} algorithm [87] with a Δ R = 0.4.

To reduce the number of jets originating from pile-up, an additional selection criterion based on "jet-vertex tagging" (JVT) technique is applied. The JVT is a likelihood discriminant that combines information from several track-based variables and this criterion is only applied to jets wth p_{T} < 60 GeV and $|\eta|$ < 2.4 [88].

6.3.1 Jet reconstruction algorithms

The functionality of the anti-k_{t} algorithm can be understood by considering very well separated hard particles with transverse momentum p_{ti} producing many soft particles.

The distance d_{ij} between entities (particles (i) and pseudojets (j)) and the distance d_{iB} between the particle i and the beam (B) are introduced.

The clustering proceeds by identifying the smallest of the distances:

- If the minimum value is d_{ij} i and j are combined in a single object, i.e. a pesudo jet;
- if the minimum value is d_{iB} i is considered as a single jet and it is removed from the list of entities.

The definition of the distances are:

$$d_{ji} = min(1/p_{tj}^{2k}, 1/p_{ti}^{2k})\Delta R_{ji}^2/R^2, \tag{6.2}$$

$$d_{iB} = 1/p_{\mathrm{ti}}^{2k}, \tag{6.3}$$

and:

$$\Delta_{ij}R^2 = (\phi_i + phi_j)^2 + (y_i + y_j)^2, \tag{6.4}$$

where R is the dimension of the jet, ϕ_i and y_i are the azimuthal angle and the rapidity of the object i, respectively, and k_{ti} is the transverse momentum of i.

The parameter k has been introduced to govern the relative power of the energy versus geometrical scales ($\Delta_{ij}R$).

In this analysis, jet reconstructed by the anti-k_{t} algorithm are used. This algorithm has the k parameter egual to -1. This choice favours the clusterisation around hard particles rather than soft ones. The other options are the k_{t} algorithm ($k = 1$) and the Cambridge/Achen (C/A) algorithm ($k = 0$).

Among the three algorithms, the anti-k_{t} provides stable and robust jets. The disadvantage of the anti-k_{t} algorithm, with respect to the other two algorithms, is that it doesn't provides informations about the history of the jets.

6.3.2 Jet energy calibration

The ATLAS hadronic calorimeters are non compensating and the energy of the hadronic particles is underestimated. In order to correctly reconstruct the energy of the jets, a calibration procedure [89] is needed.

The reconstructed jets are calibrated using a sequential scheme consisting of several steps. This procedure is shown schematically in Figure 6.4.

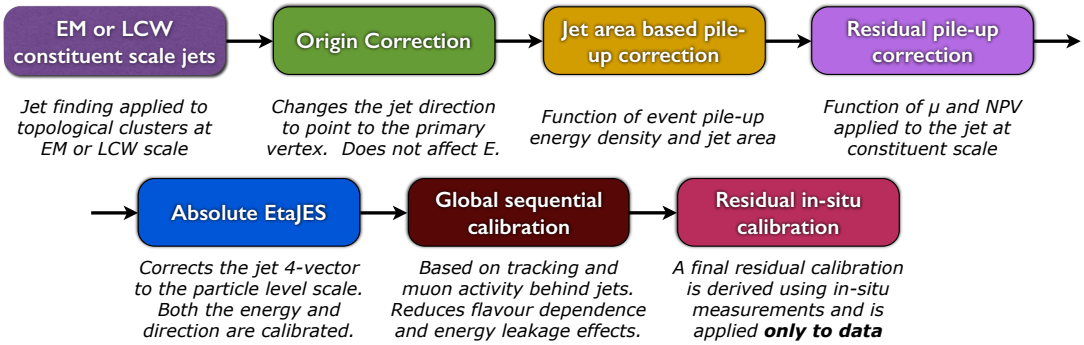

FIGURE 6.4: The stages used in the calibration of EM and LCW jets.

First a jet is corrected to point back to the correct primary vertex. Since the ATLAS calorimeters measure the energy of the particles, the assignment of a direction to the topological clusters is required to complete their 4-vector.

The default direction choice is the center of the detector but, the better assumption is that they are originated from the position of the first primary vertex. This procedure results in a significant improvement in the η resolution of the jets due to the lenght of the beam spot along the beamline.

The following step consists in the pile-up correction. The pile-up generates additional particles that contaminate jets and this contamination is proportional to the area of the jet. To reduce the effect of the pile-up an area based substraction method it is used . This removes the effect of pile-up by using the pile-up density per each event in the $\phi \times \eta$ plane ρ, and the area of the jet in this plane, A.

The density ρ provides an estimation of the global pile-up activity in each event and the area is the measure of the predisposition of the jets to pile-up.

The pile-up energy substraction is computed as an additive correction on the p_{T} of the jets, as shown in Eq. 6.5:

$$p_{\mathrm{T}}^{\mathrm{corr}} = p_{\mathrm{T}}^{\mathrm{jet}} - \rho \times A^{\mathrm{jet}}. \tag{6.5}$$

The pile-up energy density of each event is calculated using jets reconstructed in the central ($|\eta| < 2.0$) region. After the application of the jet areas subtraction, a residual small pile-up dependence on the jet energy remains. A residual pileup correction is applied after 6.5 to account for all these effects.

The follow step consists on the jet energy scale (JES) calibration which is derived as a correction that relates the reconstructed jet energy to the truth jet energy. The JES factors are derived from isolated jets using an inclusive jet Monte Carlo sample after the previous corrections have been applied. The JES has a strong η dependence.

Since the jet energy scale calibration is derived in inclusive dijets events, a mixture of quark and gluon jets in the sample is presented. The jet response for individual quark or gluon which initiate jets is different due to the differences in jet fragmentation and particle composition. The different response leads to an effect known as *flavor-dependence* of the jet response and is a major source of the JES systematic uncertainty.

The following step of the jet energy calibration, the Global Sequential Calibration (GSC), consists in a track-based post-calibration correction that attempts to reduce the difference in response between quark and gluon jets. The GSC includes a *punch-through* correction to correct high p_{T} jets whose energy is not fully contained within the calorimeter.

The corrections applied depend of the topology of energy deposits in the calorimeter, the tracking information and the MS informations. Corrections are applied sequentially in such a way the average jet energy response is left unchanged.

The last step of the jet energy calibration consists on residual *in situ* calibrations. This correction is only applied to jets in data. It consists of three different corrections. Firstly, dijet events are used to derive an η-intercalibration where the response of forward jets are calibrated to the response of jets in the central region. The purpose of this intercalibration is to remove any residual pseudorapidity difference in the jet response following the MC calibration. Next, an absolute p_{T} calibration is derived for the central region using the balance of γ and Z bosons recoiling against jets. Finally, high-p_{T} jets are calibrated using events in which a system of low-p_{T} jets recoils against a single high-p_{T} jet.

6.3.3 Jet vertex tagging

The jet-vertex-tagger (JVT) [90] is a likelihood discriminant used to reject fake jets originated from pile-up flactuations. It is built by the combination of two variables, corrJVF and R_{pT}, using simulated di-jet events and provides informations to separate hard scatter from pile-up jets. Figure 6.5 shows the fake rate versus efficiency curves comparing the performance of the four variables JVF, corrJVF, R_{pT}, and JVT when selecting a sample of jets with 20<p_{T}<50 GeV, $|\eta|$ <2.4 in simulated di-jet events.

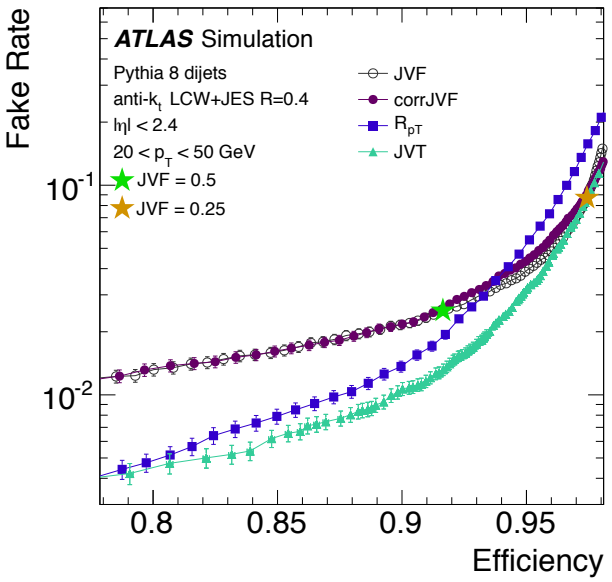

FIGURE 6.5: Fake rate from pile-up jets versus hard-scatter jet efficiency curves for JVF, corrJVF, R_{pT}, and JVT.

The reconstruction algorithm is a multivariate (MVA) technique called *k-Nearest Neighbourhood* method (k-NN). In the JVT method, for each point in the two-dimensional corrJVF-R_{pT} plane, the relative probability for a jet to be of "signal type" (produced from a hard scatter vertex) is computed as the

ratio of the number of hard scatter jets to the number of hard scatter plus pile-up jets found in a local neighbourhood around the point.

6.3.4 Jet energy resolution

The measurement of the jet energy resolution (JER) in data is a multi-step process. To measure the jet energy resolution, for the majority of the jet p_{T} spectrum, the width of the distributions of the balance between jets and well measured photons or reconstructed Z bosons is used. In addition, the balance between di-jet events can be used to extend these measurments to higher $|\eta|$ and p_{T} spectrum.

6.3.5 *b*-tagging algorithms

The identification of b-quarks jets, referred to as b-tagging, plays an important role for the ATLAS experiment [91].

The basic input required for b-tagging are the charged particle tracks reconstructed in the ID.

The aim of the b-tagging algorithms is to identify jets containting b-flavoured hadrons.

Tracks are first associated to jet and then required to pass a quality selection. The ATLAS detector uses three different algorithms which provide complementary information:

- Impact parameter based algorithms: IP2D, IP3D;
- inclusive secondary vertex reconstruction algorithm: SV;
- decay chain multi-vertex reconstruction algorithm: JetFitter;

The algorithm used in the analysis is the MV1 which is a multivariate discriminant combining the output of these algoritm and provides the best separation between different jet flavours.

The association of tracks to calorimeter jets is based on their angular separation ΔR (track, jet). A track can only be associated to a jet; if more than one jet is compatible, the closest in Δ R is chosen.

The selection of tracks depends on each algorithm; for the impact parameter algorithm, a tight selection is applied which has as most important requirement, a track with $p_{\mathrm{T}} > 1$ GeV and at least two hits in the pixel detector.

In the secondary vertex based algorithm a looser selection is used; this includes requiring track p_{T} above 700-800 MeV and looser requirements on the impact parameter and track quality. The b-tagging algorithms are briefly described below.

Impact parameter based algorithms: IP2D, IP3D

The IP2D and IP3D algorithms operation is based on the signed impact parameter significance of the tracks matched to a jet. The sign is defined positive if the distance of closest approach of the track is in front to the primary vertex with respect to the jet direction and negative if is behind it.

The difference between the two algorithms is that IP3D uses both the d_0 and z_0 impact parameters taking into account their correlations, while IP2D only uses the transverse impact parameters.

Comparing the two algorithms, IP2D is more robust against the effects of pile-up, as it does not take into account the z_0 significance, which typically is large for tracks from pi-leup jets.

Figure 6.6 shows the d_0 6.6(a) and z_0 6.6(b) impact parameters distributions for tracks from b- c- and light-flavour jets.

The component of tracks from pile-up, is seen in the tail of the longitudianal distribution 6.6(b), for light-jets and it is symmetric around zero.

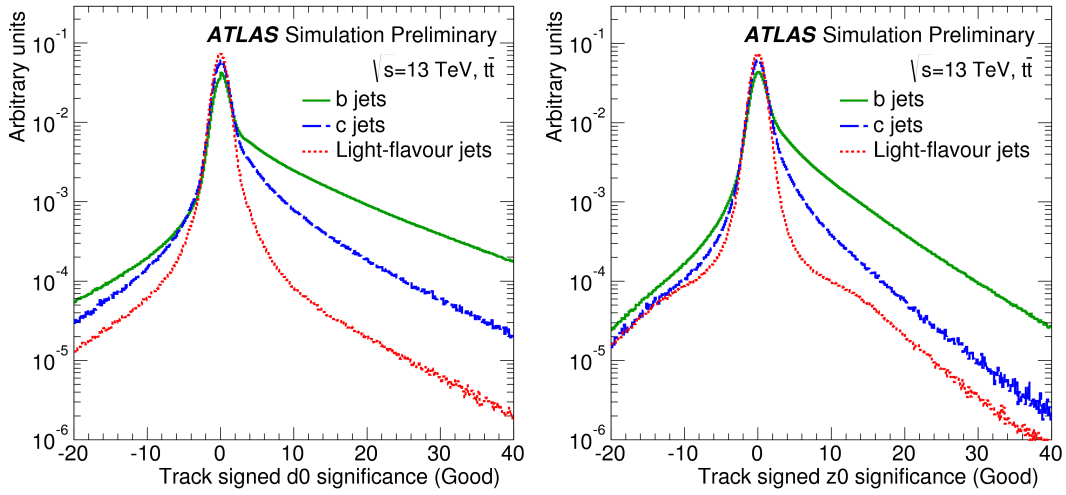

(a) (b)

FIGURE 6.6: The d_0 6.6(a) and z_0 6.6(b) signed impact parameters significance of tracks in the $t\bar{t}$ events associated with b (solid green), c (dashed blue) and light-flavour (dotted red) jets for the good category tracks used by IPD2 and IPD3 algorithms.

Secondary vertex finding algorithm: SV

The purpose of the secondary vertex based algorithm is to reconstruct an inclusive displaced secondary vertex within the jet. It uses the inclusive vertex formed by the decay products of the b-hadron, including the products of eventual subsequent c-hadron decay.

The first step is the build of two tracks that form a good vertex, using only tracks associated to the jet and far enough from the primary vertex.

All tracks coming from the decay of long-lived particles, photon conversion or hadronic interaction with the detector material, are rejected.

A single vertex is then reconstructed using the tracks that survive the preselection; an iterative procedure to remove the worst tracks is used.

Decay chain multi-vertex algorithm: JetFitter

The JetFitter algorithm exploits the topological structure of weak b- and c-hadron decays inside the jet trying to reconstruct the full decay chain.

A*Kalman filter* is used to find a common line on which the primary vertex and the bottom and charm vertices lie, giving an approximating b-hadron flight path as well as their positions.

The discrimination between b-, c- and light jets is based on a likelihood which uses the masses, momenta, flight-length significances and track multiplicities of the reconstructed vertices as inputs.

Multivariate algorithm: MV2

The input variables obtained from the three algorithms described above, are combined using a boosted decision tree (BDT) algorithm to discriminate b-jets from light (u, d, s -quark or gluon jets) and c-jets.

The MV2c20 algorithm is defined as the output of a BDT algorithm, with a training, assigning b-jets as signal and a mixture of 80% light-flavour jets and 20% c-jets as background.

The MV2c20 output distribution is shown in Figure 6.7 for b- c- and light-flavour jets. The performance for several background mixtures of c- and light-flavour jets in the training has been compared and the mixture adopted in MV2c20 gave the best compromise between light- and c-jet rejection.

The operating points are defined by a single cut value on the MV2 output distribution and are chosen to provide a specific b-jet efficiency on a $t\bar{t}$ sample.

The operating point used in the analysis corresponds to an overall 77% b-tagging efficiency, with a corresponding rejection of c-quark jets and light-flavour jets by a factor of 4.5.

Figure 6.8 shows the b-jet efficiency for the four operating points of MV2c20 tagger. The best efficiency is obtatined for the working point with value 85%.

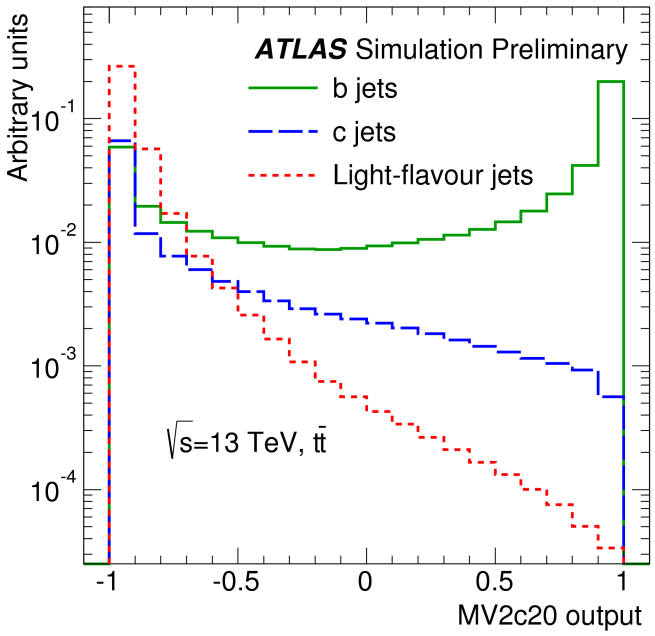

FIGURE 6.7: The MV2c20 output for b- (solid green), c- (dashed blue) and light-flavour (dotted red) jets in $t\bar{t}$ events.

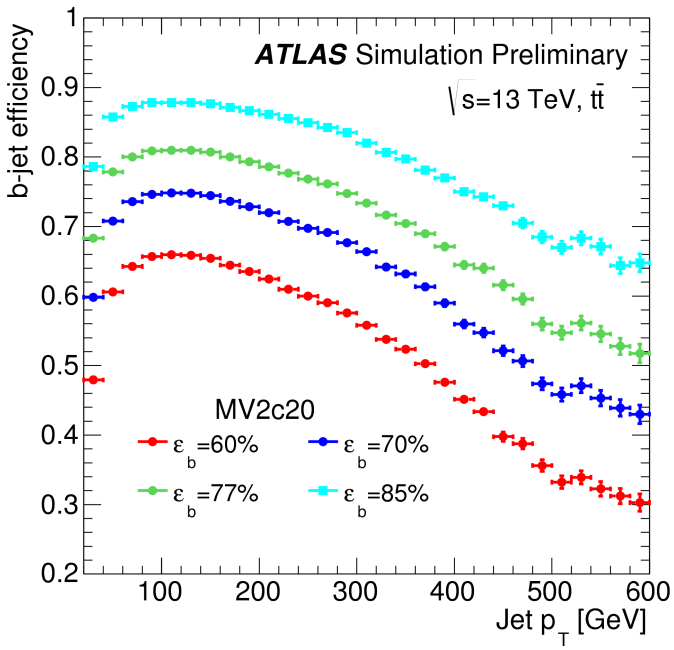

FIGURE 6.8: The b-jet efficiency for the four operating points of the MV2c20 tagger: 60% (red), 70% (blue), 77% (green) and 85% (light blue). Efficiencies are shown as a function of the jet p_{T}.

6.4 Missing transverse energy

Momentum conservation transverse to the beam axis implies that the transverse momenta of all particles in the final state should sum to zero. Any imbalance in the sum of the transverse momenta is known as *missing transverse momentum* ($E_{\mathrm{T}}^{\mathrm{miss}}$) [92] and indicates the presence of undetectable particles such as neutrinos or new particles which are not detected.

The $E_{\mathrm{T}}^{\mathrm{miss}}$ is reconstructed as the negative vector sum of the transverse momenta (p_{T}) of all the detected particles.

The measured $E_{\mathrm{T}}^{\mathrm{miss}}$ strongly depends on the energy scale and resolution of the reconstructed physics objects (electrons, photons, hadronically decaying τ leptons, jets and muons).

Several algorithms have been developed to quantify the $E_{\mathrm{T}}^{\mathrm{miss}}$, utilizing a combination of calorimeter signals and tracks in the ID.

The algorithms differs in the informations used to reconstruct the p_{T} of the particles, using either the energy deposits in the calorimeters, tracks reconstructed in the ID or both.

The $\mathrm{E}_{\mathrm{T}}^{\mathrm{miss}}$ of an event is calculated as the sum of a number of components:

$$E_{\mathrm{x(y)}}^{\mathrm{miss}} = E_{\mathrm{x(y)}}^{\mathrm{miss,e}} + E_{\mathrm{x(y)}}^{\mathrm{miss},\gamma} + E_{\mathrm{x(y)}}^{\mathrm{miss},\tau} + E_{\mathrm{x(y)}}^{\mathrm{miss,jets}} + E_{\mathrm{x(y)}}^{\mathrm{miss},\mu} + E_{\mathrm{x(y)}}^{\mathrm{miss,soft}}. \tag{6.6}$$

The terms for jets, charged leptons, and photons are the negative sum of the momenta for the respective calibrated objects.

The "soft" term is reconstructed from the transverse momentum deposited in the detector but not associated with any reconstructed hard object.

It can be reconstructed either by calorimeter-based methods, known as Calorimeter Soft Term (CST), or track-based methods, known as Track Soft Term (TST). The methods are briefly described below.

From the components $\mathrm{E}_{\mathrm{x(y)}}^{\mathrm{miss}}$, the $\mathrm{E}_{\mathrm{T}}^{\mathrm{miss}}$ is calculated as:

$$E_{\mathrm{T}}^{\mathrm{miss}} = \sqrt{(E_{\mathrm{x}}^{\mathrm{miss}})^2 + (E_{\mathrm{y}}^{\mathrm{miss}})^2}. \tag{6.7}$$

- **Calorimeter soft term (CST)**: this reconstruction algorithm uses information mainly from the calorimeter, energy deposits in calorimeter cells grouped into topoclusters. These are not matched with the high-p_{T} physics objects used in the $\mathrm{E}_{\mathrm{T}}^{\mathrm{miss}}$. The $\mathrm{E}_{\mathrm{T}}^{\mathrm{miss}}$ calculated using a calorimeter soft term is known as "CST $\mathrm{E}_{\mathrm{T}}^{\mathrm{miss}}$".
- **Track soft term (TST)**: it is built from ID tracks not matched to any reconstructed object. The algorithm allows excellent vertex matching for the soft terms. Tracks associated with jets using the ghost-association technique are removed. The $\mathrm{E}_{\mathrm{T}}^{\mathrm{miss}}$ calculated using the track soft term is known as "TST $\mathrm{E}_{\mathrm{T}}^{\mathrm{miss}}$";

- **Track E_T^{miss}**: this method uses track information in the E_T^{miss} hard terms and takes advantage of the excellent vertex resolution of the ATLAS detector. For Track E_T^{miss}, the soft term is reconstructed from ID tracks not matched to either electrons or muons.

The performances of E_T^{miss} reconstruction may be quantified by the observed width of the E_T^{miss} distribution. The performance of the reconstructed E_T^{miss} is influenced by the method used for the reconstruction.

Figure 6.9 shows the resolution of the reconstructed E_T^{miss} in a $t\bar{t}$ events, comparing the three reconstruction methods described above.

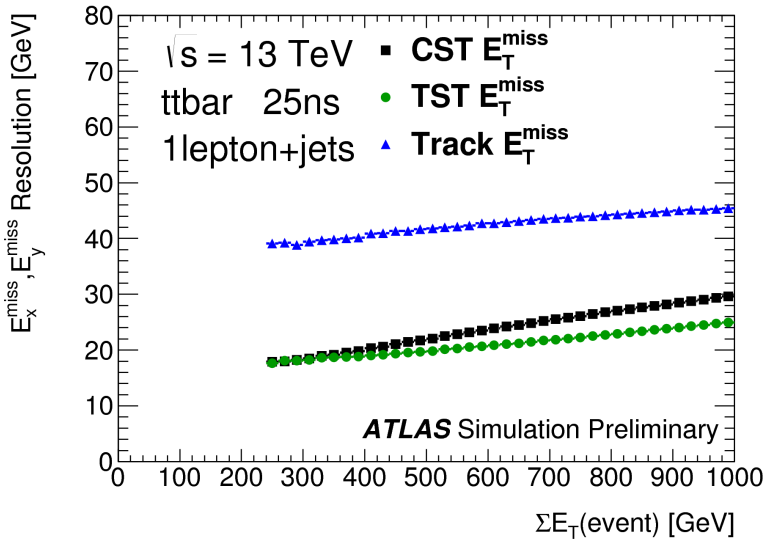

FIGURE 6.9: Comparison of the performance of TST E_T^{miss}, CST E_T^{miss} and Track E_T^{miss}, as quantified by the resolution (RMS of E_x^{miss}, E_y^{miss}) as a function of CST $\sum$ ET in tt events

.

6.5 Overlap removal

Since reconstructed electrons might also be reconstructed as jets in the calorimeter, a procedure called *overlap removal* is applied in that case, to assign objects to a unique hypothesis, to prevent a double counting of electron energy deposits as jets.

If a selected electron shares a track with a selected muon, the electron is removed. If a jet is within $\Delta R < 0.2$ of a reconstructed electron, it is removed.

Subsequently, to reduce the impact of non-prompt leptons, if an electron is within $\Delta R < 0.4$ of a jet, then that electron is removed. If a jet has less than three tracks and is within $\Delta R < 0.4$ of a muon, the jet is removed. Finally the muon is removed if it is within $\Delta R < 0.4$ of a jet which has greater or equal to three tracks.

6.6 Particle level objects definition

Particle level objects are defined from stable MC particles to closely match the reconstructed objects. Only stable particles, i.e., particles with a mean lifetime $\tau > 30$ ps are used.

Stable electrons and muons are required not to come from a hadron in the MC event record, either directly or through a τ decay. This ensures that the lepton come from the decay of a real W-boson, without requiring a direct W-boson match. The four momenta of bare leptons are then *dressed* by adding the four momenta of all stable photons within ΔR=0.1, and not originating from hadron decays.

Neutrinos and charged leptons from hadron decays, either directly or via a τ decay, are included in particle level jets.

Particle level jets are clustered using the anti-k_{t} algorithm, as for the detector level objects, with a radius parameter of R = 0.4, starting from all stable particles.

A jet is considered b-jet if a hadron containing a b-quark, is matched to the jet through ghost-matching techniques; the hadron must have $p_{\mathrm{T}} > 5$ GeV. Particle level $E_{\mathrm{T}}^{\mathrm{miss}}$ is calculated from the four-vector sum of the selected neutrinos from W-boson decays. At particle level, no overlap removal is applied between the different objects.

Chapter 7

Event selection and background determination

The event selection of the $t\bar{t}$ events is described in Section 7.1. The background determination of all the sources is described in Section 7.2. In Section 7.3 the procedure to combine the e and μ channels, before to perform the unfolding, is explained. Then, in Section 7.4 the plots of the comparison between Data/MC at detector level are reported. Finally, in Section 7.5, the pseudo top quark algorithm to reconstruct the kinematic of the two top quark involved in the ℓ+jets topology and the plots of comparison Data/MC of the kinematic reconstructed objects are presented.

7.1 Event selection

A fiducial phase-space is defined applying a series of cuts to particle level objects, analogous to those applied for the reconstructed objects.

Data used in the measurements described in this thesis were collected using a logical OR of three triggers in the e+jets channel and two triggers in the μ+jets channel, as described in Section 2.2.6.

Each event is required to be triggered and to contain a reconstructed primary vertex with five or more associated tracks and no electromagnetic or hadronic calorimeter corrupted data and exactly one good electron or muon. The offline leptons must also match the trigger objects. Dressed leptons are required to have p_{T}>25 GeV and $|\eta| < 2.5$.

Dilepton $t\bar{t}$ events, with exactly one lepton (e or μ) satisfying the fiducial selection, as described above, are by definition, included in the fiducial particle selection. Four jets are required at particle level and must have $p_{\mathrm{T}} > 25$ GeV, $|\eta| < 2.5$. Finally, at least two b-tagged jets are required.

These criteria are sufficient to give a highly pure $t\bar{t}$ sample; the top quark pair signal is more than 85% of the total prediction. Events used in the analysis here described come from the electron and muon channels and in the following steps the combination of the two channels as described in Section 7.3, is used.

After the selection, to study in detail the effect of QCD radiation on kineamtic variables, three configurations with increasing number of additional jets, are defined; this further selection offers an unique opportunity to study the effects of QCD radiation on differential cross section which are otherwhise hidden in the inclusive selections.

Each event is therefore unequivocally assigned to orthogonal configurations, namely, 4-jet exclusive, 5-jet exclusive or 6-jet inclusive, respectively, depending on the number of reconstructed additional jets.

The events selection at both the detector level and particle level, are reported on Table 7.1 for all the objects defined previously.

Object definition	Detector level		Particle level
	e+jets	μ+jets	
Leptons	$\lvert d_0^{BL}\text{sign.}\rvert < 5$ and $\lvert\Delta z_0^{BL}\sin\theta\rvert < 0.5$ mm Track-Calo-based Isolation $\lvert\eta\rvert$ <1.37 or 1.52< $\lvert\eta\rvert$ <2.47 $E_{\mathrm{T}} > 25$ GeV	$\lvert d_0^{BL}\text{sign.}\rvert < 3$ and $\lvert\Delta z_0^{BL}\sin\theta\rvert < 0.5$ mm Track-Calo-based Isolation $\lvert\eta\rvert$ <2.5 $p_{\mathrm{T}} > 25$ GeV	$\lvert\eta\rvert$ <2.5 $p_{\mathrm{T}} > 25$ GeV
Anti-k_t $R = 0.4$ jets	$p_{\mathrm{T}} > 25$ GeV $\lvert\eta\rvert$ <2.5 JVT cut (if $p_{\mathrm{T}} < 50$ GeV and $\lvert\eta\rvert < 2.4$) b-tagging: ≥ 2 jets with MV2c20 at 77%		$\lvert\eta\rvert$ <2.5 $p_{\mathrm{T}} > 25$ GeV b-tagging: ghost-matched B-hadron
Overlap removal	if $\Delta R(e, \text{jet}_{R=0.4})$ <0.2: jet removed if $\Delta R(e, \text{jet}_{R=0.4})$ <0.4: e removed	if $\Delta R(\mu, \text{jet}_{R=0.4,ntrk<3})$ <0.4: jet removed if $\Delta R(\mu, \text{jet}_{R=0.4,ntrk\geq 2})$ <0.4: μ removed	none

TABLE 7.1: Summary of event selections for detector level and MC-generated particle level events.

7.2 Background determination

After the event selection described in Section 7.1, various backgrounds still contribute to the event yields. The several constributions of background and their estimation are explained in the following sections for each source and are estimated by using both MC simulations and data-driven techniques.

The latter technique is used in the case where the MC simulations are not adequate, as in the case of W-boson production in association with jets and for the estimation of the non-prompt and fake leptons background.

The explanation of the background source and the MC samples used to simulate them, were discussed in Section 5.4.

7.2.1 Monte Carlo-based background

The background sources estimated with the MC-based techniques are the single-top quark, Z+jets and dibosons.

The background from electroweak single-top quark production is the largest background contribution in all the configurations considered. It amounts to 15% to the total event yield and 30% of the total background estimated. This background is modelled with MC simulation and the event yields are normalised to calculations of their cross sections. The normalisation and the MC samples used to estimate the single-top quark background are described in section 5.4.

The background contributions coming from Z+jets, $t\bar{t}V$ and diboson events, are obtained using MC based techniques too. The events yields are normalised to the theoretical calculations of their cross sections. The total contribution from these processes is about 1-2% of the total event yield and about 11-14% of the total background.

7.2.2 Data-driven background

W+jets background

The shape of the W+jets background is obtained with the SHERPA MC samples described in Section 5.4, whereas, its normalisation is partially data-driven [93].

The vector boson production, as the W boson, occur at the LHC via $q\overline{q}$ annilihation processes. Therefore, a positively charged W-boson (W^+) can be produced from a process like $u\overline{d} \rightarrow W^+$ or $c\overline{s} \rightarrow W^+$. In the same way, a negatively charged W-boson (W^-) can be produced from the conjugated processes, i.e $\overline{u}d \rightarrow W^-$ or $\overline{c}s \rightarrow W^-$.

Both the processes depend on the corresponding PDF products $u(x_1)\overline{d}(x_2)$ and $\overline{u}(x_1)d(x_2)$ repectively, with the relative momentum fraction x_i.

Since in the LHC collide pp beams and proton's valence is composed of 2 quark of up type and one of down type, it is more likely to have an up quark partecipating in an interaction, which produces W^+ bosons, respect to a down quark which contrariwise produces W^- bosons.

For this reason, there is an asymmetry in the production of W-bosons at the LHC; indeed many more positive W-bosons (W^+) are produced.

The ratio of the production of positive and negative W-bosons is:

$$r_{\mathrm{MC}} = \frac{\sigma(pp \rightarrow W^+)}{\sigma(pp \rightarrow W^-)}, \tag{7.1}$$

which is well understood and predicted with a higher precision. The W+jet normalisation can therefore be obtained from the measurement of the charge asymmetry.

The approach described here consists of two steps. In the first step, the number of W+jets events N_{j} is estimated after a specific selection without including b-tagging requirements ($W^{N_{\mathrm{j}}}_{\mathrm{pretag}}$). In the second step, needeed for the estimation of the W+jets background in b-tagged samples, the pretag estimate is extrapolated by multiplying the $W^{N_{\mathrm{j}}}_{\mathrm{pretagged}}$ selection for a factor $f^{\mathrm{N_j}}_{\mathrm{tag}}$ (W-tagging rate):

$$W^{N_{\mathrm{j}}}_{\mathrm{tagged}} = W^{N_{\mathrm{j}}}_{\mathrm{pretag}} \cdot f^{\mathrm{N_j}}_{\mathrm{tag}}. \tag{7.2}$$

The equation used to extract the charge asymmetry is:

$$N_{W^+} + N_{W^-} = \frac{N^{\mathrm{MC}}_{W^+} + N^{\mathrm{MC}}_{W^-}}{N^{\mathrm{MC}}_{W^+} - N^{\mathrm{MC}}_{W^-}}(D^+ - D^-) \quad = (\frac{r_{\mathrm{MC}}+1}{r_{\mathrm{MC}}-1})(D^+ + D^-), \tag{7.3}$$

where D represents the positive/negative yields from data after the substraction of the charge asymmetry backgrounds and r_{MC} is the ratio defined above.

The charge asymmetry normalisation is obtained by a comparison of the W+jets event yields in MC and data samples:

$$CA = \frac{N_{\mathrm{Data,W}}}{N_{\mathrm{MC,W}}}. \tag{7.4}$$

The normalisation weights obtained applying the charge asymmetry method, are reported in Table 7.2.

Channel	2j ex	3j ex	4j incl
e+jets (pretag)	0.933 ± 0.001	0.795 ± 0.001	0.926 ± 0.001
μ+jets (pretag)	1.018 ± 0.001	0.911 ± 0.001	0.910 ± 0.001
e+jets (tagged)	1.181 ± 0.014	1.007 ± 0.015	1.173 ± 0.025
μ+jets (tagged)	1.269 ± 0.014	1.135 ± 0.016	1.135 ± 0.018

TABLE 7.2: The W+jets scale factors derived via the charge asymmetry method in separate jet multiplicity bins, including their statistical uncertainties.

In addition to the weights of the overall normalisation, heavy flavour (HF) scale factors are derived for $W_{\mathrm{b\bar{b}}}$, $W_{\mathrm{c\bar{c}}}$, W_{c} and W_{light} jets for each bin of the b-tagged events.

By definition, these scale factors do not change the normalisation of W+jets yield in the pretag region and are extracted simultaneously with the normalisation weights by using an iterative procedure. These weights are obtained in a region with two additional jets and are then extrapolated for regions with higher jet bins.

The procedure to extract the scale factors starts by solving the follow system equation:

$$\begin{pmatrix} CA \cdot (N^{\mathrm{b\bar{b}}}_{\mathrm{MC,W^-}} + N^{\mathrm{c\bar{c}}}_{\mathrm{MC,W^-}}) & CA \cdot N^{\mathrm{c}}_{\mathrm{MC,W^-}} & CA \cdot N^{\mathrm{light}}_{\mathrm{MC,W^-}} \\ (f_{\mathrm{b\bar{b}}} + f_{\mathrm{c\bar{c}}}) & f_{\mathrm{c}} & f_{\mathrm{light}} \\ CA \cdot (N^{\mathrm{b\bar{b}}}_{\mathrm{MC,W^+}} + N^{\mathrm{c\bar{c}}}_{\mathrm{MC,W^+}}) & CA \cdot N^{\mathrm{c}}_{\mathrm{MC,W^+}} & CA \cdot N^{\mathrm{light}}_{\mathrm{MC,W^+}} \end{pmatrix} \cdot \begin{pmatrix} W_{\mathrm{b\bar{b},c\bar{c}}} \\ W_{\mathrm{c}} \\ W_{\mathrm{light}} \end{pmatrix} \begin{pmatrix} D_{W^-} \\ 1.0 \\ D_{W^+} \end{pmatrix}, \tag{7.5}$$

where $D_{W^\pm}$ represents the number of b-tagged W+jets events in data after background events substraction from it:

$$D_{W^\pm} = D^{\pm}_{\mathrm{Data}} - N^{\pm}_{\mathrm{bkg}}. \tag{7.6}$$

Also, in equation 7.5, the term $N^{\mathrm{i}}_{\mathrm{MC,W^{+(-)}}}$ represents the tagged W+jets yield of events with charge $+(-)$ and flavour i; f_i represents the fraction of W+jets events for a given flavour at the pretag level:

$$f_{\mathrm{i}} = \frac{N^{i,pretag}_{MC,W}}{N^{pretag}_{MC,W}}. \tag{7.7}$$

Then, the second row of the equation 7.5 represents the requirement on the total sum of all flavour fractions, to remain constant:

$$(f_{\mathrm{bb}} + f_{\mathrm{c\bar{c}}}) \cdot W_{\mathrm{b\bar{b},c\bar{c}}} + f_{\mathrm{c}} \cdot W_{\mathrm{c}} + f_{\mathrm{light}} \cdot W_{\mathrm{light}} = 1.0. \tag{7.8}$$

Finally, the first and third rows of the equation represent the adaption of the MC yields to the data yields, by applying both the scaling factor and the charge asymmetry normalisation.

The linear equation system 7.5 is solved for the vector $(W^{\mathrm{b\bar{b},c\bar{c}}}, W_{\mathrm{c}}, W_{\mathrm{light}})$ by using an iterative process, as said above.

The procedure consists in applying the scaling factors to the pretagging yields after each iteration and then recalculating the charge asymmetry normalisation. The procedure converges to a stable result after about 10 iterations.

To do this process the 2 jets exclusive multiplicity bin has been choosen because in this region a most stable behaviour with the smallest systematic uncertainties was shown.

The scheme consists of four steps and starts with the default value W_{i} = 1.0:

1. Apply scaling factors W_{i} to MC pretag yields used for the calculation of CA;
2. calulate charge asymmetry normalisation CA;
3. build and solve the linear equation system 7.5;
4. go back to the first step.

The W+jets background represents the third largest background contributing approximately to 2-3% of the total yields.

QCD Multijets background

QCD multijets events constitute an important background source in some regions of the phase space. This source is constituted of mis-identified leptons called "fake leptons". The dominant source of fake leptons are long living mesons (i.e. $\pi^{\pm}$ or $K^{\pm}$), semi-leptonic B-hadrons decay, electrons from photons conversion or direct photons and mis-identifided hadronic jets. The multijet background contributes to the total yield at the level of about 4%.

The probability of a multijet events to pass the selection is very low, but the production cross section of multijets events is higher than the $t\bar{t}$ events cross section.

Data-driven techniques are the most appropriate to estimate this kind of background source. The data driven method used in this analysis is the Matrix method (MM) [94]. This method has been already extensively used at LHC by both the ATLAS and CMS collaborations.

With the matrix method, data samples are classified in two levels of lepton selection requirements: the number of events with one tight lepton (N^{t}), used in the nominal selection and the number of events with one loose lepton (N^{l}) with less stringent identification and isolation requirements. Differences between the two selections are summarised in Table 7.3.

These selections can be expressed as linear combination of the number of events with a real or a non-promt or fake lepton:

$$N^{\mathrm{l}} = N^{\mathrm{l}}_{\mathrm{r}} + N^{\mathrm{l}}_{\mathrm{f}}, \tag{7.9}$$

$$N^{\mathrm{t}} = N^{\mathrm{t}}_{\mathrm{r}} + N^{\mathrm{t}}_{\mathrm{f}}. \tag{7.10}$$

ϵ_{r} is the fraction of real leptons in the loose selection that also passes the tight selection, namely *real efficiency* defined as:

$$\epsilon_{\mathrm{r}} = \frac{N^{\mathrm{l}}_{\mathrm{r}}}{N^{t}_{r}}, \tag{7.11}$$

and ϵ_{f} is the fraction of non-promt and fake lepton backgrounds in the loose selection that also passes the tight one, namely *fake efficiency*, defined as:

$$\epsilon_{\mathrm{f}} = \frac{N^{\mathrm{l}}_{\mathrm{f}}}{N^{t}_{f}}. \tag{7.12}$$

So, the equation of the number of events passing the tight selection can be rewritten as:

$$N^{\mathrm{t}} = \epsilon_{\mathrm{r}} N^{\mathrm{l}}_{\mathrm{r}} + \epsilon_{\mathrm{f}} N^{\mathrm{l}}_{\mathrm{f}}. \tag{7.13}$$

The efficiecies ϵ_{r} and ϵ_{f} are measured in data control regions dominated by real and fake lepton events, respectively.

In order to estimate the tight events coming from non-promt or fake lepton backgrounds, the following expression is defined:

$$N_{\mathrm{f}}^{\mathrm{t}} = \frac{\epsilon_{\mathrm{f}}}{\epsilon_{\mathrm{r}} - \epsilon_{\mathrm{f}}}(\epsilon_{\mathrm{r}} N^{\mathrm{l}} - N^{\mathrm{t}}). \tag{7.14}$$

The efficiencies ϵ_{r} and ϵ_{f} depend on lepton kinematics and event characteristics, such as number of jets or b-jets.

Therefore, to cover this dependence, an event weight is computed from the efficiencies; these are parametrised as a function of various object kinematics.

The expression of this defined event weight is:

$$w_{\mathrm{i}} = \frac{\epsilon_{\mathrm{f}}}{\epsilon_{\mathrm{r}} - \epsilon_{\mathrm{f}}}(\epsilon_{\mathrm{r}} - \delta_{\mathrm{i}}), \tag{7.15}$$

where δ_{i} is equals to unity if the loose event i passes the tight selection and equals to 0 otherwise.

	Loose selection	**Tight selection**
Electron identification level	MediumLH	TightLH
Muon identification level	Medium	Medium
Lepton isolation requirement	None	Gradient

TABLE 7.3: Definition of loose and tight lepton selection requirements.

- **Measurement and parametrisation of the fake efficiency**: The fake efficiencies ϵ_{f} are measured in data control regions dominated by non-promt and fake lepton background events.

  These control regions, namely CR_{f} are selected requiring:

  - exactly one loose or tight lepton;
  - at least one jet;
  - in the e+jets channel: $E_{\mathrm{T}}^{\mathrm{miss}} < 30$ GeV and $m_{\mathrm{T}}^{\mathrm{W}} < 50$ GeV;
  - in the μ+jets channel: muon with $|d_0^{\mathrm{sig}}| > 5$.

  The contributions of the residual event yields, from other processes, containing promt leptons, such as Z+jets, W+jets, $t\bar{t}$, single-top quark and diboson, are determined using MC simulations.

  The fake efficiency is measured as functions of these observables:

  - p_{T}^{ℓ} transverse momentum of the lepton;
  - η^{ℓ} lepton pseudorapidity;
  - $E_{\mathrm{T}}^{\mathrm{miss}}$ transverse missing energy;

- $\Delta\phi$ azimuthal angle difference between the lepton and the $E_{\mathrm{T}}^{\mathrm{miss}}$;
- N_{j} jet multiplicity;
- N_{b}, b-jet multiplicity;
- $p_{\mathrm{T}}^{\mathrm{jet1}}$ leading jet transverse momentum;
- ΔR distance between the lepton and the closest jet.

The amount of residual yields is summarised in Table 7.4.

		ttbar	**Single top**	**W+jets**	**Z+jets**	**Total**
e+jets	loose + tight	0.21%	0.06%	7.19%	6.39%	13.85%
	tight	0.48%	0.13%	16.63%	19.29%	36.53%
μ+jets	loose + tight	0.14%	0.03%	1.64%	0.54%	2.35%
	tight	0.37%	0.07%	4.80%	1.62%	6.86%

TABLE 7.4: Residual amount of events from other processes in the control region, where the fake efficiency is measured.

The calculation of the fake efficiencies is different in the e+jets and μ+jets channels.

In the e+jets channel the fake efficiency is calculated as a geometric mean of three double-differential measurements:

$$\epsilon_{\mathrm{f}} = \sqrt[3]{\epsilon_{\mathrm{f}}^{\mathrm{2D}}(p_{\mathrm{T}}^{\ell}, N_{\mathrm{p}}) \times \epsilon_{\mathrm{f}}^{\mathrm{2D}}(\Delta\phi, \eta^{\ell}) \times \epsilon_{\mathrm{f}}^{\mathrm{2D}}(\Delta\phi, p_{\mathrm{T}}^{\ell})}. \tag{7.16}$$

In the μ+jets channel, the fake efficiency is calculated with two parametrisations, for low and high p_{T} values.

In case of the low p_{T}^{ℓ} parametrisation, the efficiency is a geometrical mean of the double differential measurements in $\Delta\phi$ and p_{T}^{ℓ} and a one-dimensional measurement of $E_{\mathrm{T}}^{\mathrm{miss}}$:

$$\epsilon_{\mathrm{f}}^{\mathrm{L}} = \sqrt{\epsilon_{\mathrm{f}}^{\mathrm{2D}}(\Delta\phi, p_{\mathrm{T}}^{\ell}) \cdot \epsilon_{\mathrm{f}}(E_{\mathrm{T}}^{\mathrm{miss}})}. \tag{7.17}$$

Whereas the high p_{T}^{ℓ} efficiency is only dependent on the measurement of p_{T}^{ℓ}:

$$\epsilon_{\mathrm{f}}^{\mathrm{H}} = \epsilon_{\mathrm{f}}(p_{\mathrm{T}}^{\ell}). \tag{7.18}$$

The two parametrisations are then combined with a Fermi function around 60 GeV with 10 GeV of width:

$$\epsilon_{\mathrm{f}} = (1 - f) \times \epsilon_{\mathrm{f}}^{\mathrm{L}} + f \times \epsilon_{\mathrm{f}}^{\mathrm{H}}, \tag{7.19}$$

$$f = f(p_{\mathrm{T}}^{\ell}) = \left(1 + exp(-\frac{p_{\mathrm{T}}^{\ell} - 60GeV}{10GeV})\right)^{-1}. \tag{7.20}$$

- **Measurement and parametrisation of the real efficiency**: To measure the real efficiency the Z $\rightarrow \ell\ell$ tag-and-probe method is used. For this parametrisation the same observables as for the fake efficiency are used.

  The selection contains a pair of same-flavour opposite-sign loose or tight leptons and at least one jet.

  The invariant mass of the system composed by the two leptons is required to be between 60 and 120 GeV. One of the two leptons is considered tag if it passes the tight lepton requirements, whereas, the other lepton is considered a probe.

  Therefore, in the efficiency expression, the denominator contains all the probe leptons and the numerator consists of all the numbers of probe leptons which pass the tight criteria.

  In case of the real efficiency, the fake leptons in the selection are originated mostly from $t\bar{t} \rightarrow \ell$+jets events with an additional fake lepton. Also for this parametrisation it is necessary to correct the measurement for residual amount of fake leptons and a method based on $m_{\ell\ell}$ fit is used.

  The method considers each bin of an observable x, where the efficiency is measured. In each of these bin, a fit of $m_{\ell\ell}$ is performed using a signal+background model which includes events coming only from the considered bin.

  The signal model is a convolution of two different distributions, Breit-Wigner and Crystal Ball, whereas, the model of the background is a linear function. The signal, i.e. $Z \rightarrow \ell\ell$, is then calculated substracting from the number of events within the range of 80-100 GeV the integral of the background function over this range. This procedure is computed separately both for the numerator and denominator of the efficiency.

  The resulting numbers are then divided obtaining the value of the real efficiency in a given bin of an observable x considered.

  As for the fake efficiency, the real efficiency has two different parametrisations for the e+jets and μ+jets channels, respectively.

  In the e+jets channel, the real efficiency is parametrised only as a function of the real transverse momentum:

  $$\epsilon_{\mathrm{r}} = \epsilon_{\mathrm{r}}(p_{\mathrm{T}}^{\ell}). \tag{7.21}$$

  In the μ+jets channel, as for the fake efficiency parametrisation, is performed a p_{T}^{ℓ}-splitting, using the same merging function and calculating the corresponding components:

  $$\epsilon_{\mathrm{r}}^{\mathrm{L}} = \sqrt{\epsilon_{\mathrm{r}}(\Delta\phi) \cdot \epsilon_{\mathrm{r}}(p_{\mathrm{T}}^{\ell})}, \tag{7.22}$$

$$\epsilon_{\mathrm{r}}^{\mathrm{H}} = \epsilon_{\mathrm{r}}(p_{\mathrm{T}}^{\ell}). \tag{7.23}$$

7.3 Combination of the channels

Before applying the unfolding procedure, the individual muon and electron channels, which have very similar corrections and give compatible results, are combined by adding togheter the events of the two channels, after the selection cuts. To do the combination between channels it is important to take care of the systematics. The correlated uncertainties, i.e. for example, the JES which affect the two channels in the same way, will be added linearly to the other uncertainties while, uncorrelated uncertainties, as electron scale factors, will enter only in one of the channels and will be added in quadrature to the other uncertainties sources. Since the largest uncertainties are common between the channels, after the combination, the relative uncertainty is similar respect to the one observed in the single channel.

7.4 Data Monte Carlo comparison at detector level

The event yield in the three configurations is summarised in Table 7.5 for data, signal and various backgrounds.

4-jet exclusive	
Sample	Yield
$t\bar{t}$	61400^{+3300}_{-3400}
W+jets	2200^{+1400}_{-1600}
Z+jets	840^{+630}_{-620}
Diboson	140^{+100}_{-100}
Single top	3600^{+360}_{-360}
Multijet	3300^{+1700}_{-1800}
$t\bar{t}V$	103^{+17}_{-17}
Total prediction	71600^{+4800}_{-5000}
Data	75768
Data/prediction	1.06 ± 0.07

5-jet exclusive	
Sample	Yield
$t\bar{t}$	36900^{+3700}_{-3700}
W+jets	890^{+600}_{-680}
Z+jets	340^{+330}_{-330}
Diboson	100^{+100}_{-100}
Single top	1730^{+240}_{-240}
Multijet	1460^{+770}_{-780}
$t\bar{t}V$	132^{+21}_{-21}
Total prediction	41600^{+4000}_{-4300}
Data	46243
Data/prediction	1.11 ± 0.11

6-jet inclusive	
Sample	Yield
$t\bar{t}$	25400^{+4700}_{-4400}
W+jets	540^{+400}_{-450}
Z+jets	160^{+100}_{-100}
Diboson	110^{+57}_{-57}
Single top	980^{+210}_{-200}
Multijet	920^{+500}_{-500}
$t\bar{t}V$	224^{+40}_{-40}
Total prediction	28400^{+4900}_{-4900}
Data	33582
Data/prediction	1.2 ± 0.2

TABLE 7.5: Event yields in the 4-jet exclusive (left), 5-jet exclusive (centre) and 6-jet inclusive (right) configurations.

The comparison between data and various background contributions have been done for different distributions in the three configurations.

Several of these distributions are displayed in Figures 7.1–7.4 for the combined ℓ+jets channel (combination of electron and muon channels), showing the jet, b-jet and lepton transverse momentum and missing transverse energy. In all plots, data distributions are compared to predictions using the nominal sample as the $t\bar{t}$ signal model.

The predictions from different processes are displayed in different colours and stacked together in such a way they can be compared with data.

The hashed area indicates the combined statistical and systematic uncertainties in the total prediction, excluding systematic uncertainties related to the modelling of the $t\bar{t}$ system.

In Figure 7.5 the distribution of the jet multiplicity is shown indicating that the difference in the normalisation between data and prediction can be attributed to the difference observed at high jet multiplicity.

Nevertheless, in all distributions shown a good agreement between data and predictions can be seen and therefore they are compatible within the total uncertainties.

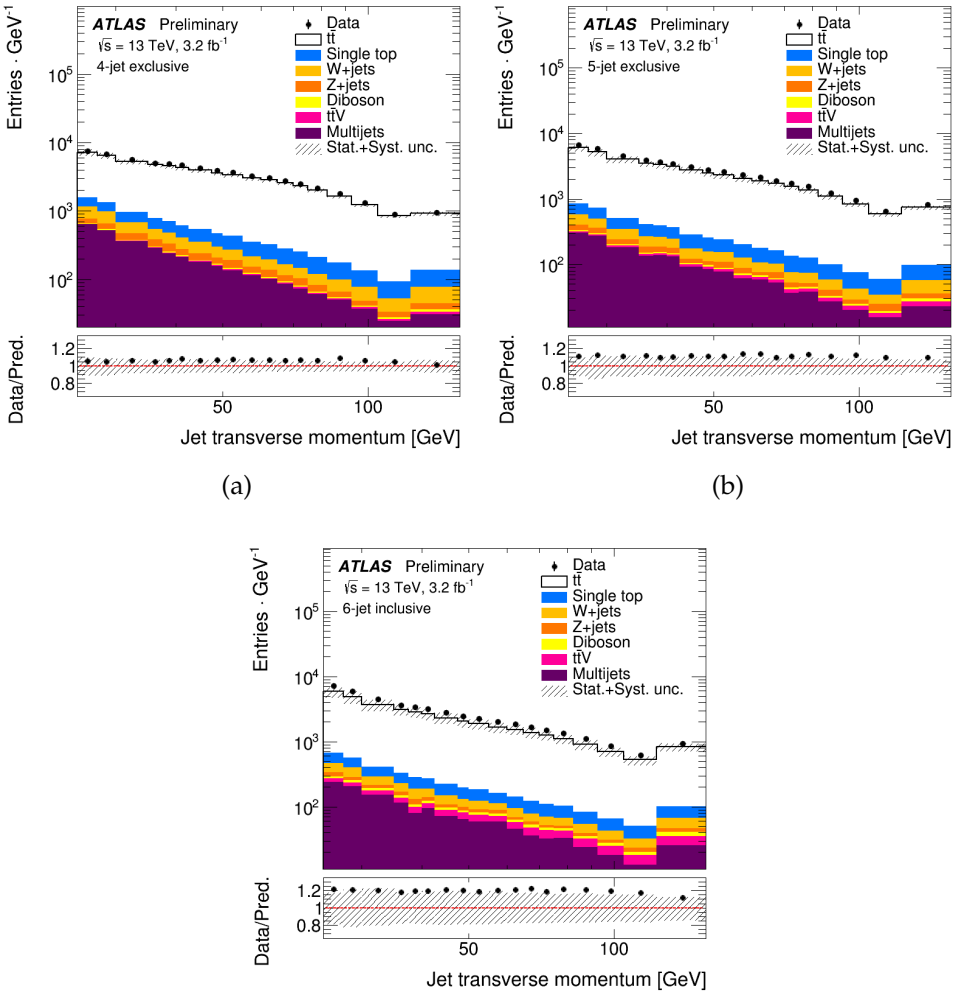

FIGURE 7.1: Kinematic distributions of the transverse momentum of the selected jet at reconstruction level in the 4-jet exclusive configuration (a), 5-jet exclusive configuration (b) and 6-jet inclusive configuration (c).

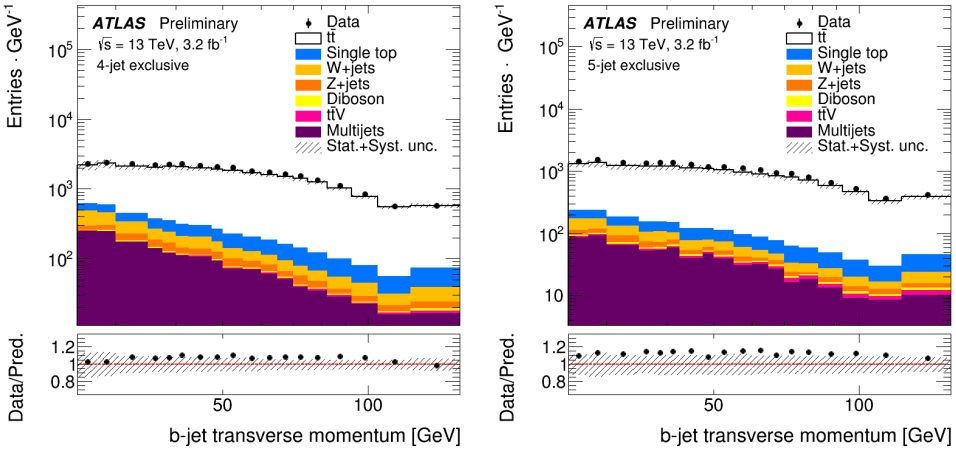

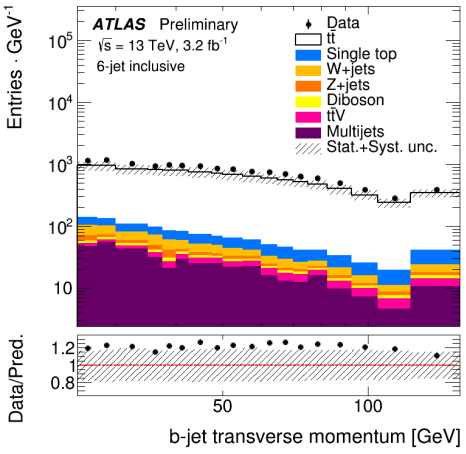

FIGURE 7.2: Kinematic distributions of the transverse momentum of the selected b-jet at reconstruction level in the 4-jet exclusive configuration (a), 5-jet exclusive configuration (b) and 6-jet inclusive configuration (c).

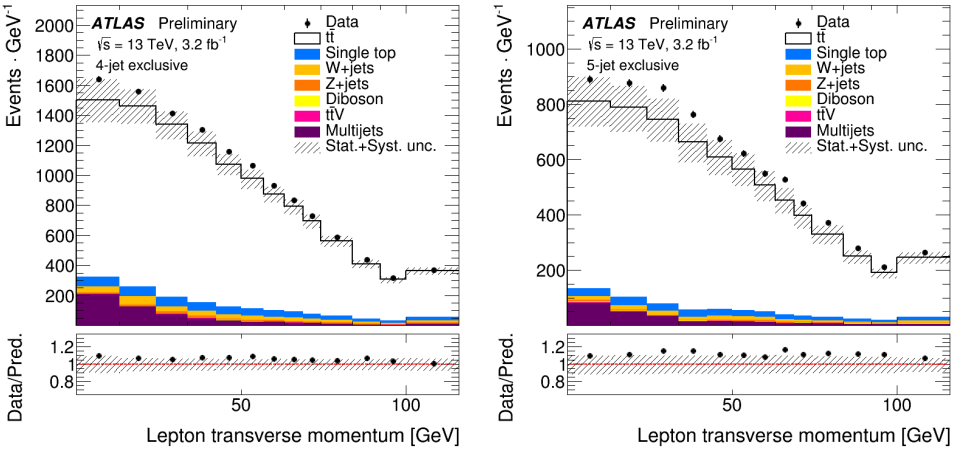

(a) (b)

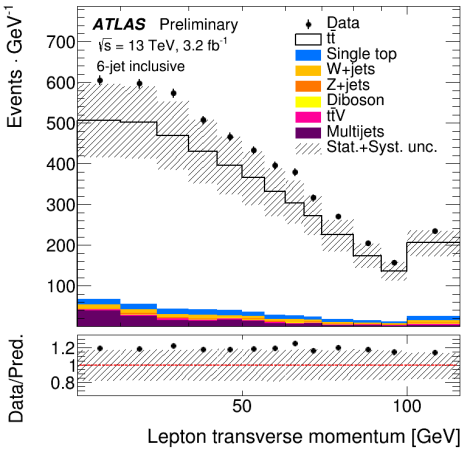

(c)

FIGURE 7.3: Kinematic distributions of the lepton transverse momentum at reconstruction level in the 4-jet exclusive configuration (a), 5-jet exclusive configuration (b) and 6-jet inclusive configuration (c).

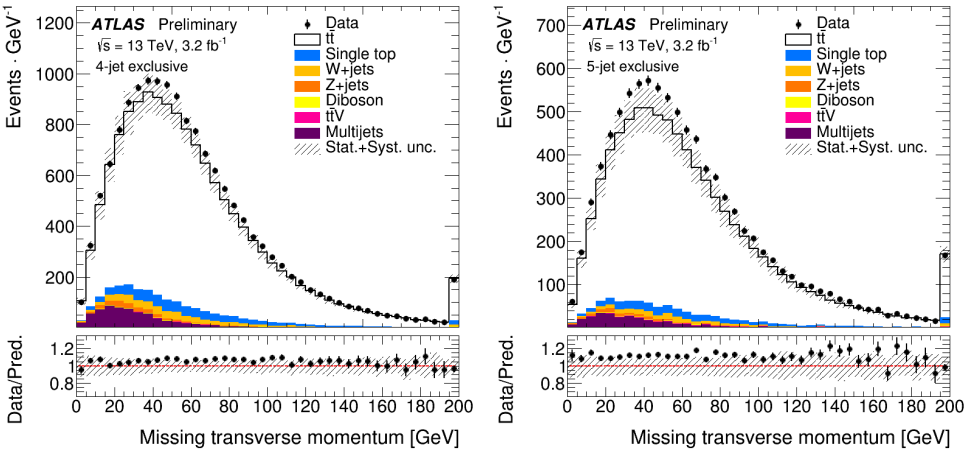

(a) (b)

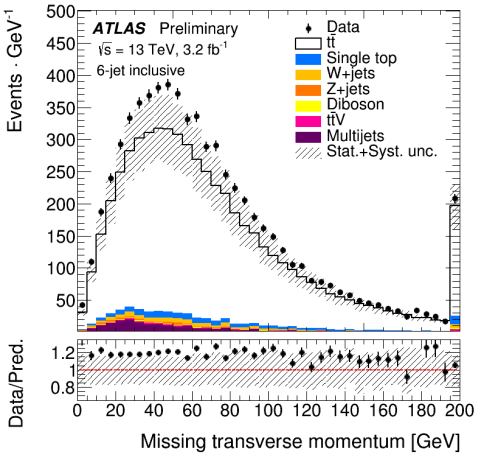

(c)

FIGURE 7.4: Kinematic distributions of the missing transverse momentum $E_{\mathrm{T}}^{\mathrm{miss}}$ at reconstruction level in the 4-jet exclusive configuration (a), 5-jet exclusive configuration (b) and 6-jet inclusive configuration (c).

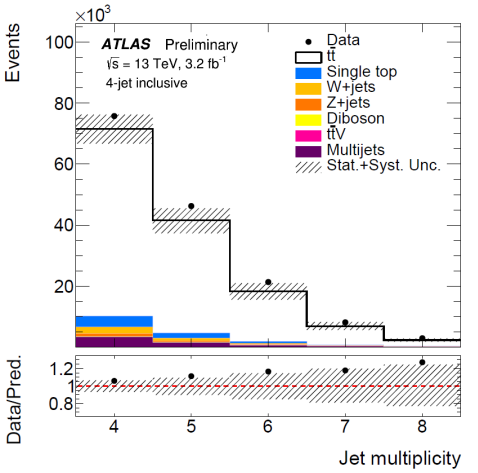

FIGURE 7.5: Distribution of the jet multiplicity.

7.5 Reconstruction of top quark kinematic properties

The two top quarks involved in the process are reconstructed from their decay products. The leptonic top quark refers to a leptonic decay W boson and hadronic is referred to a hadronic decay W boson, as described in Chapter 4.

The differential cross sections can be measured as function of observables involving the top quark and the $t\bar{t}$ system.

To reconstruct the top quarks, the pseudo-top algorithm [95] is used. In brief, this algorithm reconstructs the four momenta of the top quarks together with the complete decay chain from final state objects, namely the charged lepton which could be an electron or a muon, missing transverse energy and four jets two of which are b-tagged.

A fraction of the selected events contains more than two candidates b-jets. In that case, the two with the highest transverse momentum are selected, as coming from top quarks.

The algorithm reconstructs both the leptonic top quark and the hadronic top quark, as described below:

- **leptonic top quark reconstruction**: the leptonically decay W boson is constructed from the lepton and the neutrino;

  The reconstruction procedure starts from the determination of the z-component of the neutrino momentum using the constraint of the W boson mass. Neglecting the neutrino mass, the $p_{\mathrm{z},\nu}$ component of the neutrino is taken from the solution of the resulting quadratic equation:

  $$p_{\mathrm{z},\nu} = \frac{-b \pm \sqrt{b^2 - 4ac}}{2a}, \tag{7.24}$$

  where

  $$a = E_\ell^2 - p_{z,\ell}^2 \quad b = -2kp_{\mathrm{z},\ell} \quad c = E_\ell^2 p_{T,\nu}^2 - k^2, \tag{7.25}$$

  and

  $$k = \frac{m_W^2 - m_\ell^2}{2} + (p_{x,\ell}p_{x,\nu} + p_{y,\ell}p_{y,\nu}). \tag{7.26}$$

  If the resulting quadratic equation has two real solutions, the smallest absolute value of $p_{\mathrm{z},\nu}$ is chosen.

  Otherwise, if the determinant is negative the immaginary part of the solution with smallest $p_{\mathrm{z},\nu}$ is dropped.

  The components of the four momentum of the neutrino in the (p_{x}, p_{y}, p_{z}, m) representation are given by:

  $$p^\nu = (E_{\mathrm{x}}^{\mathrm{miss}}, E_{\mathrm{y}}^{\mathrm{miss}}, E_{\mathrm{z}}^{\mathrm{miss}}, 0). \tag{7.27}$$

The leptonic W boson is reconstructed from the sum of the charged lepton and the neutrino.

Finally, the leptonic top quark is reconstucted from the sum of the leptonic W and the b-tagged jet closest in ΔR to the charged lepton.

- **hadronic top quark reconstruction**: the hadronic decaying W boson is constructed from the sum of the remaining non b-tagged jets whose invariant mass is the closest to the mass of the W. Then, the hadronic top quark is reconstructed from the sum of the hadronic W boson and the remaining b-jet.

The performance of the pseudo-top quark algorithm was studied in each of the three configurations. It was demostrated that the algorithm reconstructs the top quarks with a very little dependency on the number of additional jets; this demostration was done by comparing the masses of the hadronic top quark in the three configurations and by doing a Gaussian fit in the peak regions to evaluate the mass and the width.

The performed fits of this study are shown in Figure 7.6 and the results in Table 7.6. From the fits is clear that the mass of the top quark and the width do not depend on the increasing of the jet multiplicity.

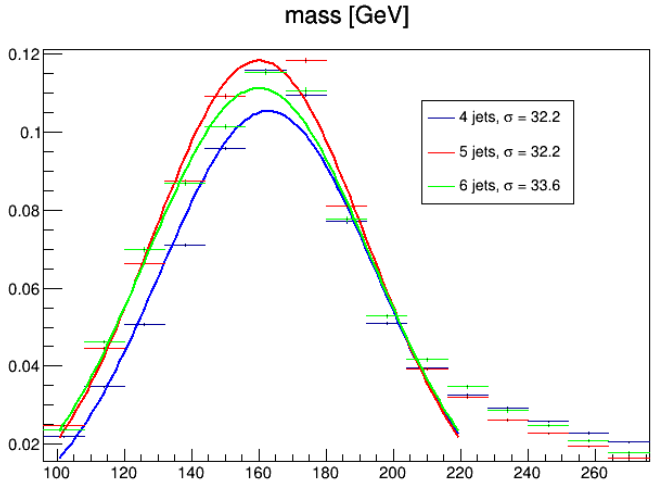

FIGURE 7.6: Result of the Gaussian fit to the mass distribution in the different configurations of additional jets.

	4-jet	5-jet	6-jet
Normalisation	0.1054 ± 0.0002	0.1184 ± 0.0002	0.1113 ± 0.0003
Mass	162.76 ± 0.06	160.05 ± 0.06	159.91 ± 0.09
Width	32.20 ± 0.06	32.24 ± 0.07	33.6 ± 0.1

TABLE 7.6: Result of the Gaussian fit of the top quark masses in different configurations of jet multiplicity.

The comparison between data and MC for the reconstructed kinematic variables was done; in the distributions the difference between MC and data is covered by the uncertainties.

Figures 7.7–7.9 show these distributions. Starting from Figure 7.7 the $p_{\mathrm{T}}^{\mathrm{t\bar{t}}}$ distributions for the three configurations are shown. This observable strongly depends on QCD radiation, hence, if additional jets are produced, the p_{T} takes larger values.

Figure 7.8 shows the distributions of the $p_{\mathrm{T}}^{\mathrm{t,had}}$ in the three configurations. In the ratio plots of these distributions is observed that the predictions tend to underestimate the data at low value of $p_{\mathrm{T}}^{\mathrm{t,had}}$ and to overestimate them at high value of $p_{\mathrm{T}}^{\mathrm{t,had}}$.

Finally, the $|p_{\mathrm{out}}^{t\bar{t}}|$ distributions are shown in Figure 7.9 where the shape of the three distributions shows a small dependence on the number of additional jets.

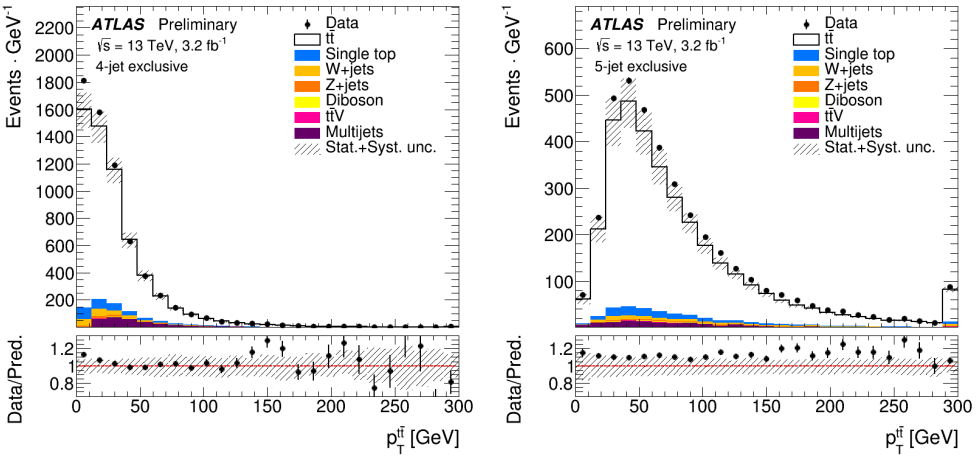

(a) (b)

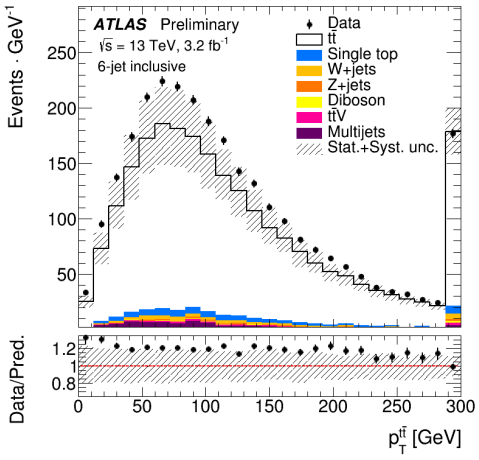

(c)

FIGURE 7.7: Distributions of $p_{\mathrm{T}}^{\mathrm{t\bar{t}}}$ at reconstruction level: (a) 4-jet exclusive, (b) 5-jet exclusive and (c) 6-jet inclusive configurations.

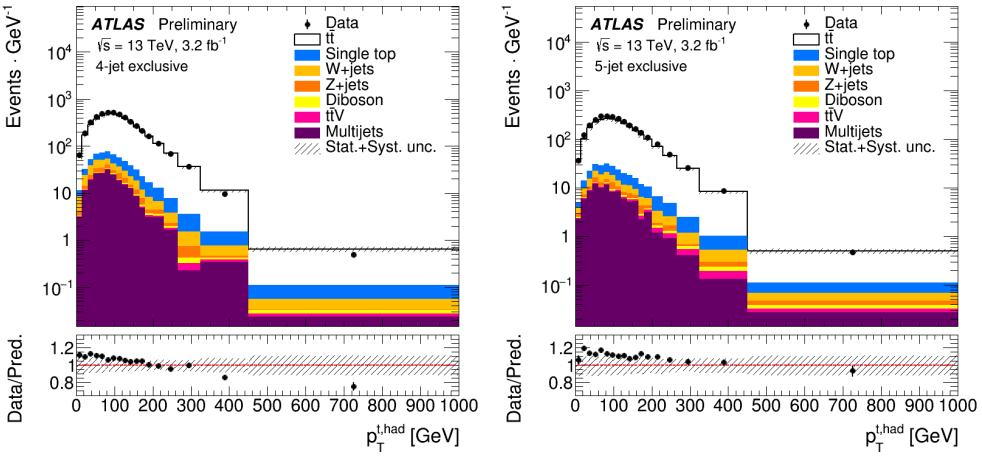

FIGURE 7.8: Distributions of $p_{\mathrm{T}}^{\mathrm{t,had}}$ at reconstruction level: (a) 4-jet exclusive, (b) 5-jet exclusive and (c) 6-jet inclusive configurations. Data distributions are compared to predictions.

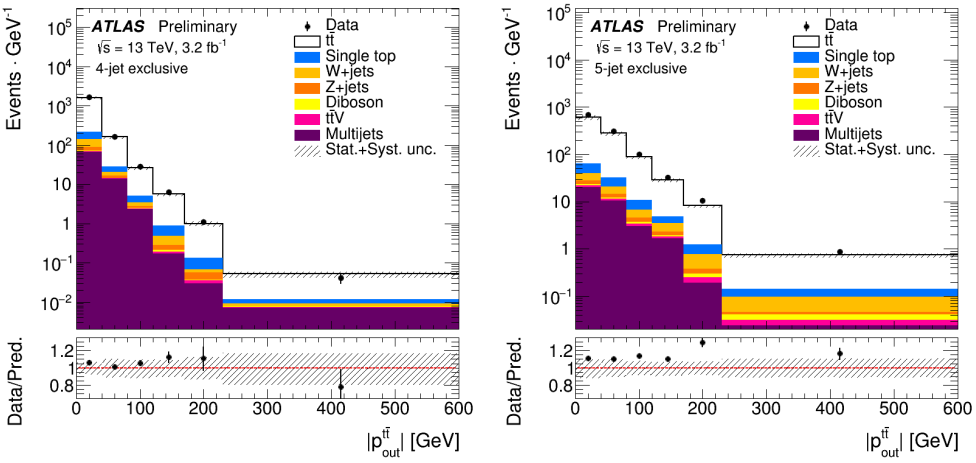

(a) (b)

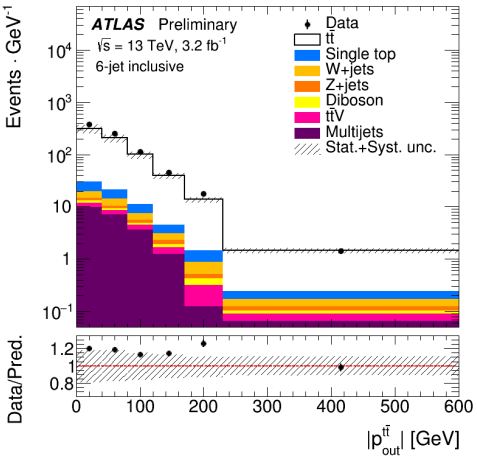

(c)

FIGURE 7.9: Distributions of $|\,p_{\mathrm{out}}^{\mathrm{t\bar{t}}}\,|$ at reconstruction level: (a) 4-jet exclusive, (b) 5-jet exclusive and (c) 6-jet inclusive configurations.

Chapter 8

Unfolding

In this Chapter, the unfolding step of the analysis is described. The definition and all the unfolding methods are explained in Section 8.1. In Section 8.2 the binning choice is explained. The unfolding corrections are described in Section 8.3. Finally, the unfolding procedure and validation of the method used in the analysis are described in Sections 8.4 and 8.5, respectively.

8.1 Unfolding definition and method

The measurements of physical observables performed in high energy physics are subject to distortion, due to detector effects. For this reason, the measured distributions can't be directly compared with the theoretical predictions. It is first necessary to correct data from these detector effects, before the comparison; a procedure called *unfolding* is applied.

A certain quantity x and its distribution $f(x)$, which could be measured in an ideal detector, are related to an experimental quantity y and its distribution $f(y)$ which are results of a real detector. The latter, is different with respect to the true distribution because of the distortion due to the detector effects.

The effects due to the detector are a limited acceptance and a limited resolution of the observed quantities. The acceptance of the detector is defined as the probability to observe a given event. It depends on the true physical quantity x.

A limited detector acceptance means that not all the events can be used to measure a physical quantity. A finite resolution means that it is impossible to measure a physical quantity with an infinite accurancy.

The measured quantity y is smeared out due to the finite resolution of the detector, therefore, there is a difference between the $f(y)$ distribution and the true distribution; the only relation between them is statistical.

The relation which link the two distributions is the folding integral:

$$g(y) = \int A(y,x) f(x) dx + b(y), \tag{8.1}$$

called *Fredholm integral of the first kind*.

In this equation the distribution $b(y)$ represents a background contribution to the measured distribution $g(y)$. The term $A(y, x)$ is a resolution function and represents the smearing effects on the measurements.

Therefore the unfolding consists in the determination of the real distribution $f(x)$ from the measured distributions $g(y)$; it is called inverse problem and to calculate the inverse of the resolution function $A(y, x)$ must be solved.

To estimate the resolution function, MC simulations are used which allow to predict detector effects of the known distribution $f(x)$ and to determine a relation between the $g(y)$ quantity and the true one $f(x)$.

To have a numerical solution of the equation 8.1, discrete quantities x and y are used; the distributions $f(x)$ and $f(y)$ are represented by histograms.

The resolution function is represented by a matrix equation:

$$y = Ax + b, \tag{8.2}$$

where the vector y (and b) with n elements represents histograms of the reconstructed quantity y, the vector x is associated to the distribution $f(x)$ and has m elements and A is a n-by-m matrix which represents the transition from x to y.

A is called *response matrix* and contains informations on the acceptance and smearing of the reconstruction process.

Usually, the response matrix A is not diagonal, because of some events generated in a bin j could be reconstructed in bins where $i \neq j$; this phenomenon is called *migration*.

From the response matrix is therefore possible to generate a *migration matrix*:

$$M_{\mathrm{ij}} = \frac{1}{E_{\mathrm{j}}} A_{\mathrm{ij}}, \tag{8.3}$$

where E_{j} is the efficiency of the reconstruction in the true j-th bin.

The migration matrix represents the probability that events generated into a bin j migrate and are reconstructed into a bin i.

There are various approaches of the unfolding methods:

- *bin-per-bin* method;
- *simple matrix inversion* method;
- *Single value decomposition* (SVD) method;
- *Iterative Bayesian* method.

The unfolding method used in the analysis is the Iterative Bayesian described below.

8.1.1 Iterative Bayesian

This procedure is based on the Bayes theorem [96] which can be interpreted in terms of a "cause and effect" procedure. Causes (C_i) correspond to events in truth bins while, effects (E_j) correspond to events in the reconstructed bins. While the effects are measured, it is impossible to determine unequivocally the causes, which have to be estimated. Infact, each cause can produce a single effect but the exact corresponding cause of an effect is not known.

A probability for a cause to generate a specific effect P($E_\mathrm{j}|C_\mathrm{i}$) can be therefore defined. It is evaluated by assuming an a-priori knowledge of the migration matrix and a measured efficiency and resolution calculated from MC simulations. This probability, given by the Bayes theorem, can be espressed as:

$$P(C_\mathrm{i}|E_\mathrm{j}) = \frac{P(C_\mathrm{i}|E_\mathrm{j}) \cdot P_0(C_\mathrm{i})}{\sum_{\mathrm{l}=1}^{n_\mathrm{C}} P(E_\mathrm{j}|C_\mathrm{i}) \times P_0(C_\mathrm{i})}, \tag{8.4}$$

while the number of events assignable to each of the causes is:

$$\widehat{n}(C_\mathrm{i}) = \frac{1}{\epsilon_\mathrm{i}} \sum_{\mathrm{j}=1}^{\mathrm{n_E}} P(C_\mathrm{i}|E_\mathrm{j}) n(E_\mathrm{j}), \tag{8.5}$$

where $n(E_\mathrm{j})$ represents the number of events assigned to the effect bin j, $P_0(C_\mathrm{i})$ is an a-priori probability of the cause C_i and ϵ_i is the efficiency of the selection in the bin i.

The number of events in the cause bins can be written in terms of the *unfolding matrix* M:

$$\widehat{n}(C_\mathrm{i}) = \sum_{\mathrm{j}=1}^{n_\mathrm{E}} M_\mathrm{ij}^{-1} n(E_\mathrm{j}), \tag{8.6}$$

where M_ij^{-1} is not the algebric inverse of the migration matrix M_ij but is defined as:

$$M_{ij}^{-1} = \frac{P(E_\mathrm{j}|C_\mathrm{i}) \cdot P_0(C_\mathrm{i})}{\sum_{\mathrm{l}=1}^{n_\mathrm{E}} P(E_\mathrm{l}|C_\mathrm{i}) \sum_{\mathrm{l}=1}^{n_\mathrm{C}} P(E_\mathrm{j}|C_\mathrm{l}) \cdot P_0(C_\mathrm{l})}. \tag{8.7}$$

It is then possible to evaluate an a-posterior probability of each cause C_i as:

$$\widehat{P}(C_\mathrm{i}) = \frac{\widehat{n}(C_\mathrm{i})}{\sum_\mathrm{j} \widehat{n}(C_\mathrm{j})}. \tag{8.8}$$

To obtain a stable solution, the bayesian method is repeated iteratively. This procedure consists in a polinomyal fit of the posterior solution which is used in the next iteration as prior solution. In each iteration the estimation will be better. The algorithm reachs a stability when the result is quite similar to the previous one.

The number of iterations used to perform the results are 4.

Studies to check the stability of the unfolding with respect to the number of iterations were done and are reported in Appendix F.

8.2 Binning choice and optimisation

The binning used in the measurements performed and reported in this thesis was optimised respect to the precedent differential cross sections measurements in the ℓ+jets channel.

The binning choice must account for severals physical effects:

- to reduce the fluctuations at least in the dominant systematic;
- to pass the closure tests (shown in Appendix B);
- to pass the stress tests (shown in Appendix C);
- to guarantee good statistic in each bin;

The bin choice are reported in Tables 8.1–8.3, for the $p_{\mathrm{T}}^{\mathrm{t,had}}$, $|\,p_{\mathrm{out}}^{\mathrm{t\bar{t}}}\,|$ and $p_{\mathrm{T}}^{\mathrm{t\bar{t}}}$ in the three configurations respectively.

P_T topH Bin edges [GeV]	
4je2bi 5je2bi 6ji2bi	0–15 15–30 30–45 45–60 60–75 75–90 90–105 105–120 120–135 135–150 150–165 165–180 180–200 200–230 230–265 265–325 325–450 450–1000

TABLE 8.1: Table of the binning choice for the $|\,p_{\mathrm{T}}^{t,had}\,|$ observable.

P_T $t\bar{t}$ Bin edges [GeV]	
4je2bi	0–15 15–35 35–75 75–125 125–170 170–800
5je2bi 6ji2bi	0–35 35–75 75–125 125–170 170–225 225–800

TABLE 8.2: Table of the binning choice for the $|\,p_{\mathrm{T}}^{t\bar{t}}\,|$ observable.

$\lvert P_{out}^{t\bar{t}} \rvert$ Bin edges [GeV]	
4je2bi 5je2bi 6ji2bi	0–40 40–80 80–120 120–170 170–230 230–600

TABLE 8.3: Table of the binning choice for the $|\,p_{\mathrm{out}}^{t\bar{t}}\,|$ observable.

8.3 Unfolding corrections

A fiducial phase-space is defined with the selection criteria presented in Section 6.6 where the measurements are performed.

First of all, for each of the distributions, the non-$t\bar{t}$ background contamination is substracted from the observed events in data. In the next single step, the matching and acceptance corrections, are applied respectively. The matching has the task to correct for badly reconstructed signal events. It improves the diagonality of the migration matrix. It is used a geometric ΔR algorithm which angularly matchs the detector level objects to the corresponding particle level objects forming the pseudo top quark at particle level and satysfing the fiducial requirements.

The reconstructed leptons are matched to the particle level with ΔR<0.02.

The same thing is required for the jets; a particle level jet must be geometrically matched to the closest reconstructed jet within ΔR<0.35. The acceptance correction consists in a factor, applied bin-by-bin, which corrects for reconstructed events at detector level, which are not reconstructed at the particle level. Both the two corrections, acceptance and matching are obtained using MC simulations.

The matching correction $f^{\mathrm{j}}_{\mathrm{match}}$ is defined as the ratio of the events passing the detector level, particle level and matching selections over the events that pass both detector level and particle level selections:

$$f^{\mathrm{j}}_{\mathrm{match}} \equiv \left(\frac{N_{\mathrm{reco}\wedge\mathrm{part}\wedge\mathrm{matched}}}{N_{\mathrm{reco}\wedge\mathrm{part}}} \right)^{\mathrm{j}}. \tag{8.9}$$

The expression of the acceptance correction $f^{\mathrm{j}}_{\mathrm{acc}}$ is the ratio of the number of events which pass both the detector and particle level selections over the number of events which pass only the detector level selection:

$$f^{\mathrm{j}}_{\mathrm{acc}} \equiv (\frac{N_{\mathrm{reco}\wedge\mathrm{part}}}{N_{\mathrm{reco}}})^{\mathrm{j}}. \tag{8.10}$$

Then, the combination of the two correction factors is:

$$f^{\mathrm{j}}_{\mathrm{acc}\wedge\mathrm{match}} \equiv \left(\frac{N_{\mathrm{reco}\wedge\mathrm{part}\wedge\mathrm{matched}}}{N_{\mathrm{reco}}} \right)^{\mathrm{j}} = f^{\mathrm{j}}_{\mathrm{acc}} \cdot f^{\mathrm{j}}_{\mathrm{match}}, \tag{8.11}$$

i.e the number of events which pass the detector level, particle level and matched selections over the number of all the events passing the detector level selection.

The corrections plots for all the observables and configurations are reported, in Figures 8.1(a)–8.3(c) for the matching and in Figures 8.4(a)–8.6(c) for the acceptance. These correction distributions are not identical in all configurations of additional jets. For example in the 4-jet exclusive configuration the distribution of matching is higher respect to the other configurations where decreases with the number of additional jets. It is in general more likely that, a pair of jets doesn't match. In the 4-jet exclusive configuration too a perfect matching is not obtained. In fact, in the 4-jet exclusive configuration it is not guarantee a 100% matching; this is due to the fact that if at reco/particle

level, 4-jets are selected from the top quark and at reco/particle level only 3 of the 4 jets are selected from the top quark and the remaining jet comes from underlying events, it is likely that they don't match.

The behaviour of the acceptance is opposite. It is low in the 4-jet exclusive configuration and increases with the number of additional jets.

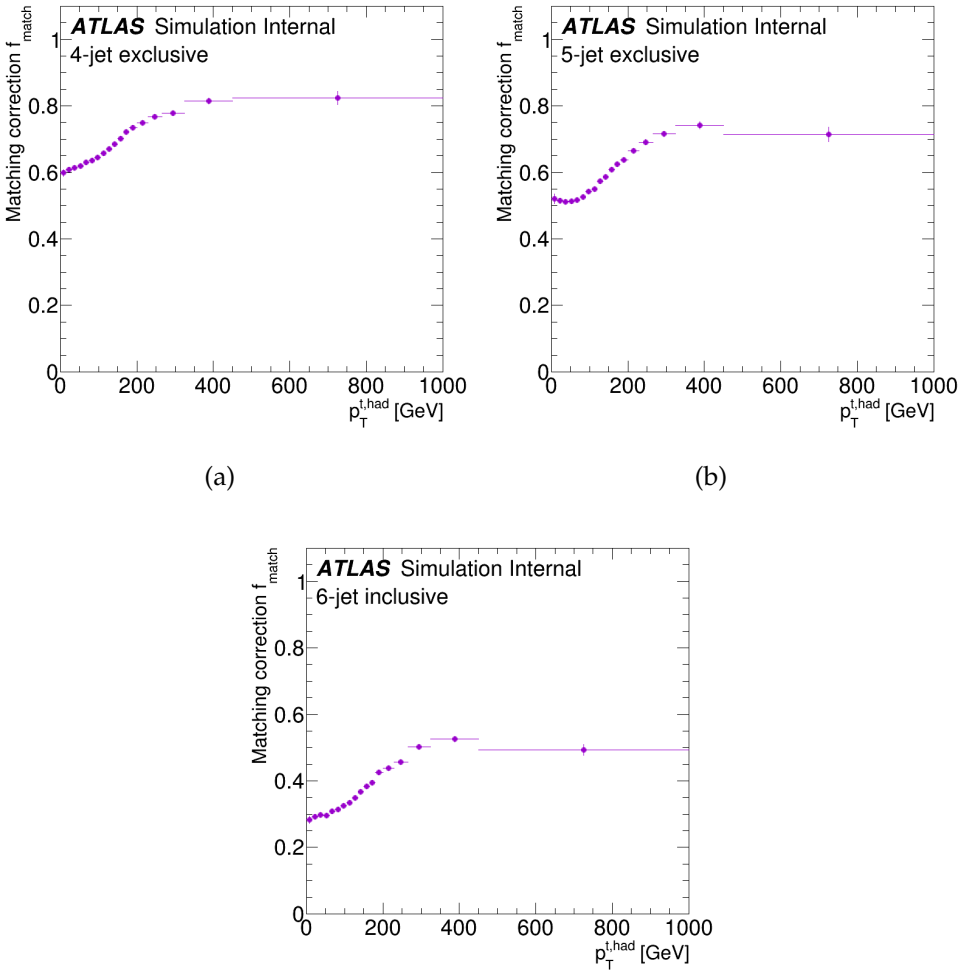

FIGURE 8.1: Matching corrections as a function of $p_{\mathrm{T}}^{\mathrm{t,had}}$ in the (a) 4-jet exclusive, (b) 5-jet exclusive, and (c) 6-jet inclusive configurations.

8.3.1 Migration matrix and efficiency corrections

After the distributions have been corrected for acceptance, matching and background, they are unfolded at particle level using the iterative Bayesian unfolding method described in Section 8.1.1.

The method requires as input the response matrix between the particle level and the measured distribution. For each distribution, the response matrix is

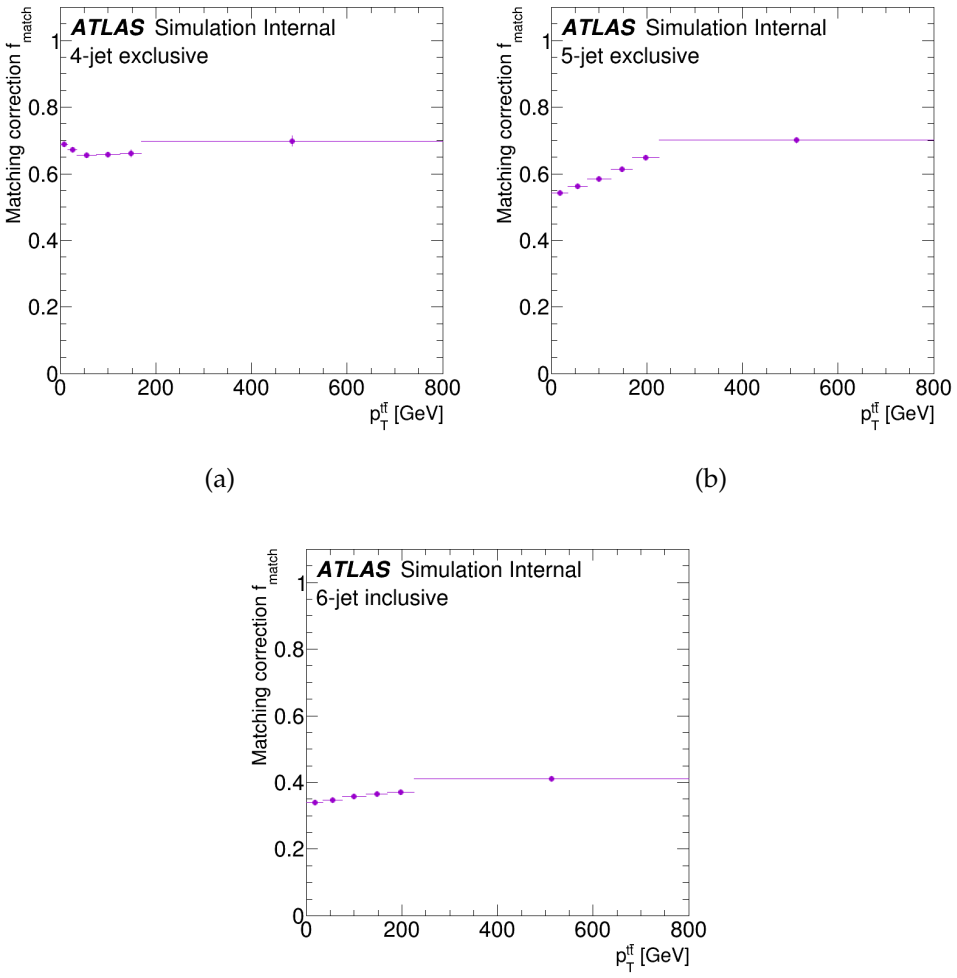

FIGURE 8.2: Matching corrections as a function of $p_{\mathrm{T}}^{\mathrm{t\bar{t}}}$ in the (a) 4-jet exclusive, (b) 5-jet exclusive, and (c) 6-jet inclusive configurations.

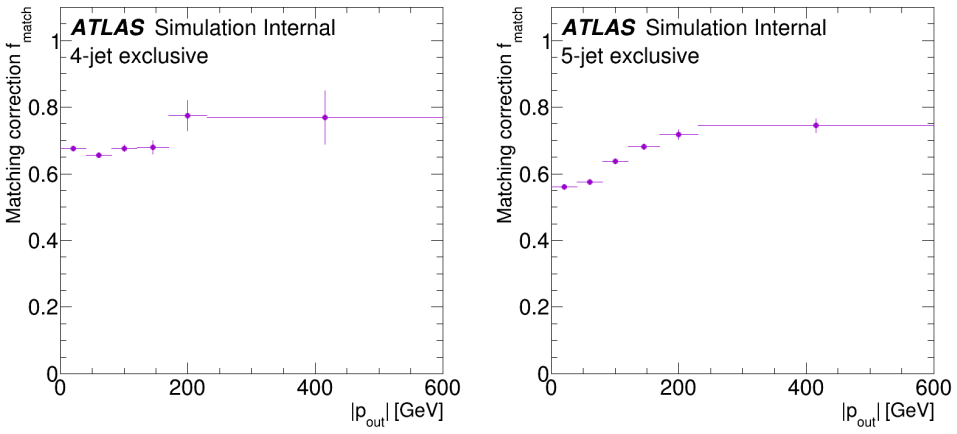

(a) (b)

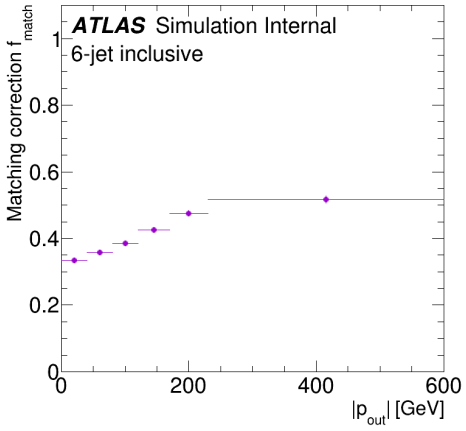

(c)

FIGURE 8.3: Matching corrections as a function of $|p_{\mathrm{out}}^{\mathrm{t\bar{t}}}|$ in the (a) 4-jet exclusive, (b) 5-jet exclusive, and (c) 6-jet inclusive configurations.

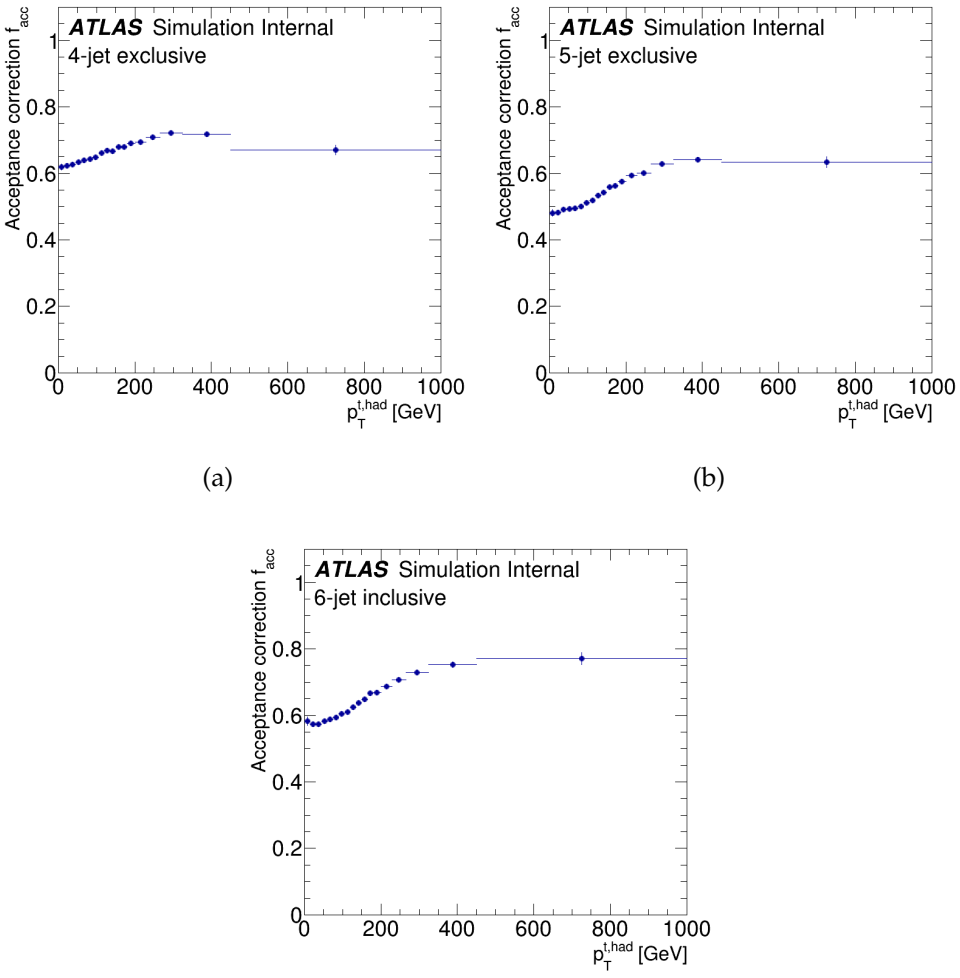

FIGURE 8.4: Acceptance corrections as a function of $p_{\mathrm{T}}^{\mathrm{t,had}}$ in the (a) 4-jet exclusive, (b) 5-jet exclusive, and (c) 6-jet inclusive configurations.

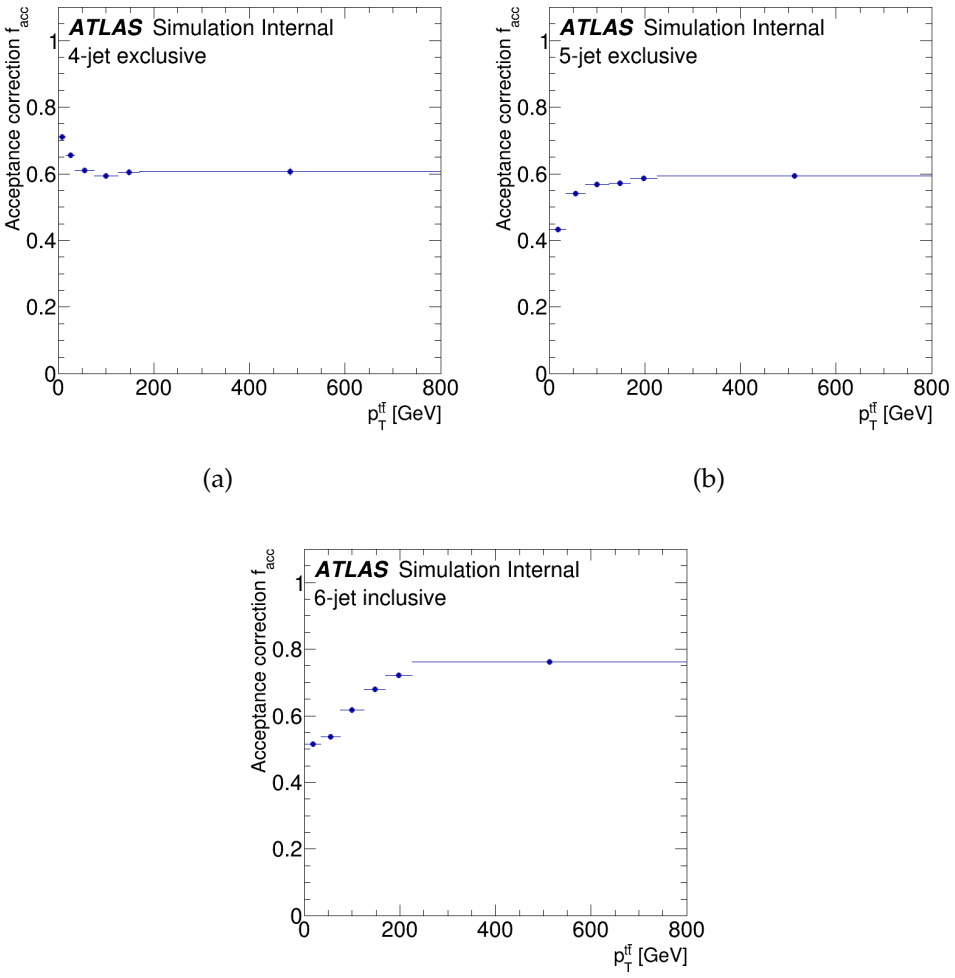

FIGURE 8.5: Acceptance corrections as a function of $p_{\mathrm{T}}^{\mathrm{t\bar{t}}}$ in the (a) 4-jet exclusive, (b) 5-jet exclusive, and (c) 6-jet inclusive configurations.

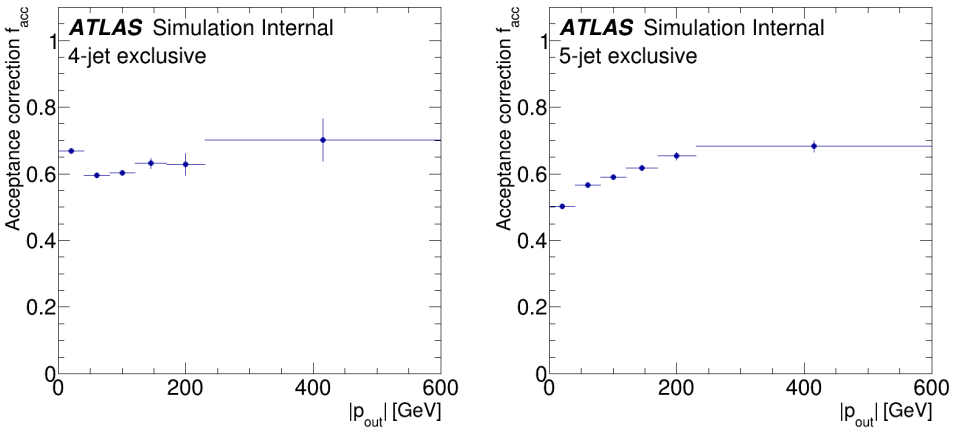

(a) (b)

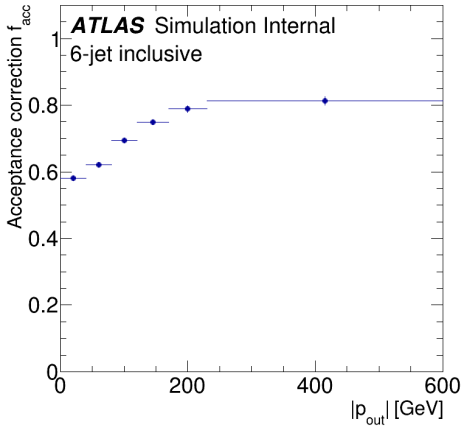

(c)

FIGURE 8.6: Acceptance corrections as a function of $|p_{\mathrm{out}}^{\mathrm{t\bar{t}}}|$ in the (a) 4-jet exclusive, (b) 5-jet exclusive, and (c) 6-jet inclusive configurations.

constructed from all events that pass both the particle level and detector level selection and the matching condition. To reconstruct the response matrix the nominal $t\bar{t}$ sample is used. Then, the migration matrix is estrapolated from the response matrix as described in Section 8.1.1.

The migration matrices for all the distributions in the three configurations of additional jets are shown in Figures 8.7(a)–8.9(c).

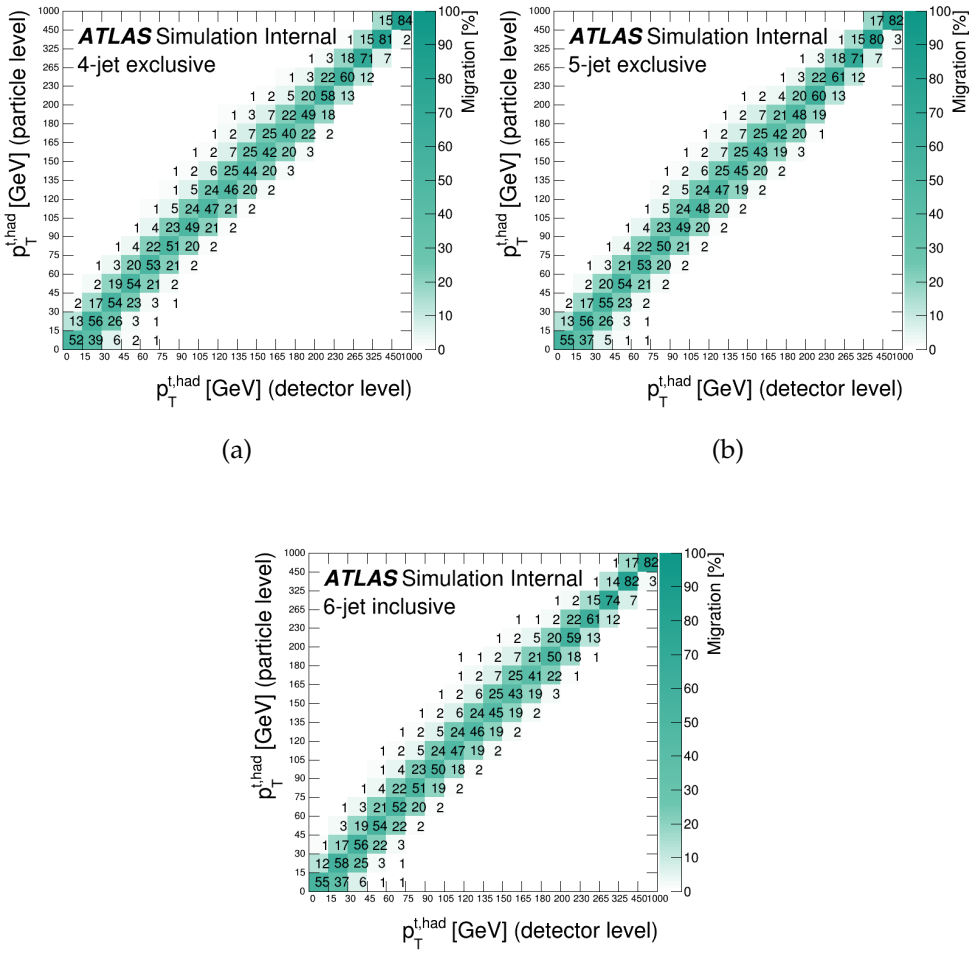

(a) (b)

(c)

FIGURE 8.7: Migration matrices as a function of $p_{\mathrm{T}}^{\mathrm{t,had}}$ in the (a) 4-jet exclusive, (b) 5-jet exclusive, and (c) 6-jet inclusive configurations.

Finally, the efficiency correction ϵ is applied to the unfolded distributions correcting the results by using a bin-by-bin factor to the fiducial phase space. It is used for events which pass the particle level selection but are not reconstructed at the detector level.

The efficiency correction is defined as the ratio of the events wich pass the reconstructed particle and matching selections over the number of events

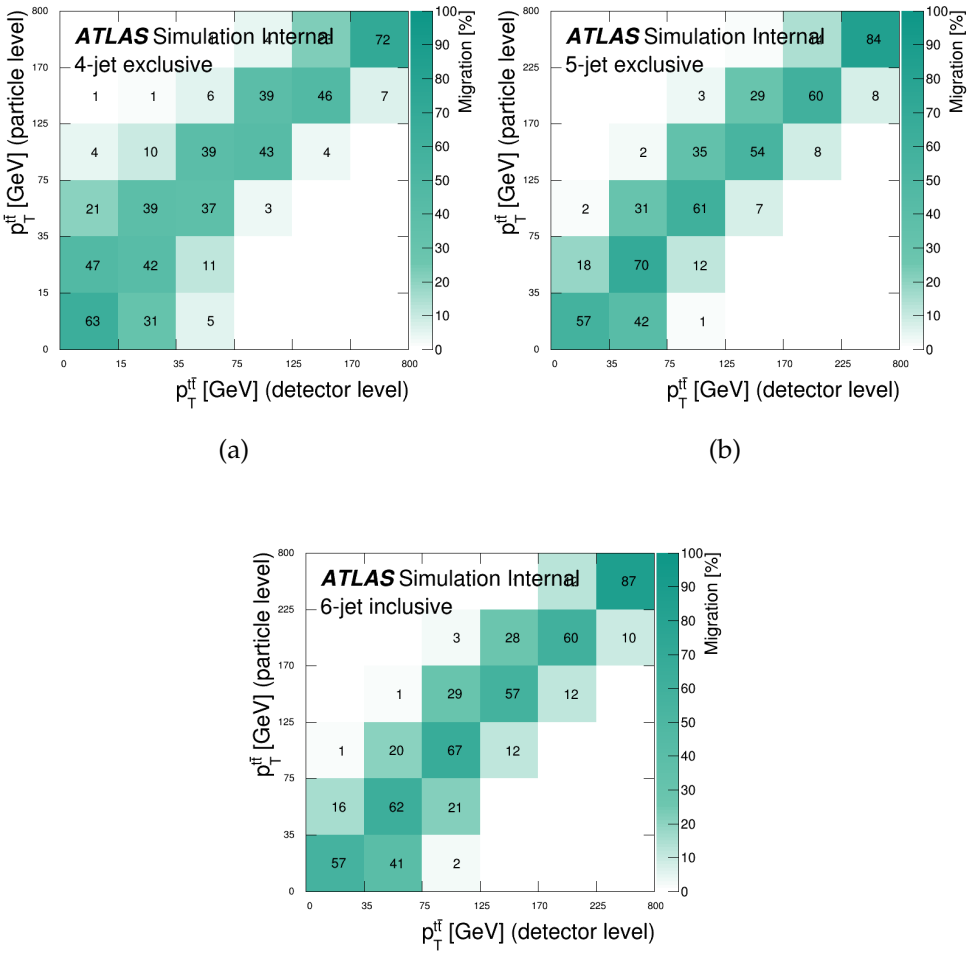

(a) (b)

(c)

FIGURE 8.8: Migration matrices as a function of $p_{\mathrm{T}}^{\mathrm{t\bar{t}}}$ in the (a) 4-jet exclusive, (b) 5-jet exclusive, and (c) 6-jet inclusive configurations.

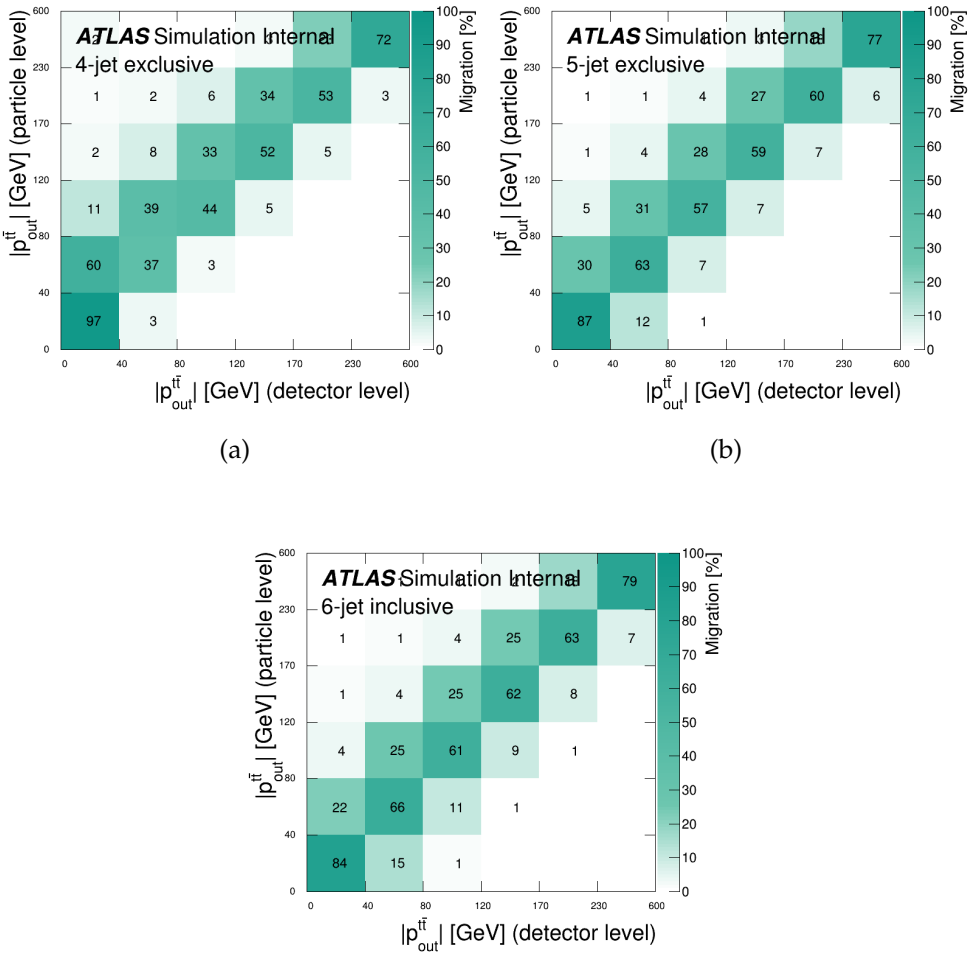

(a) (b)

(c)

FIGURE 8.9: Migration matrices as a function of $|\,p_{\mathrm{out}}^{\mathrm{t\bar{t}}}\,|$ in the (a) 4-jet exclusive, (b) 5-jet exclusive, and (c) 6-jet inclusive configurations.

which pass the particle level selection:

$$\epsilon \equiv \left(\frac{N_{\text{reco}\wedge\text{part}\wedge\text{matched}}}{N_{\text{part}}} \right)^{\text{i}} . \tag{8.12}$$

The efficiency tends to decrease with the number of additional jets in the combined ℓ+jets channel. The efficiency for all the spectra in the three configurations of additional jets is shown in Figures 8.10–8.12.

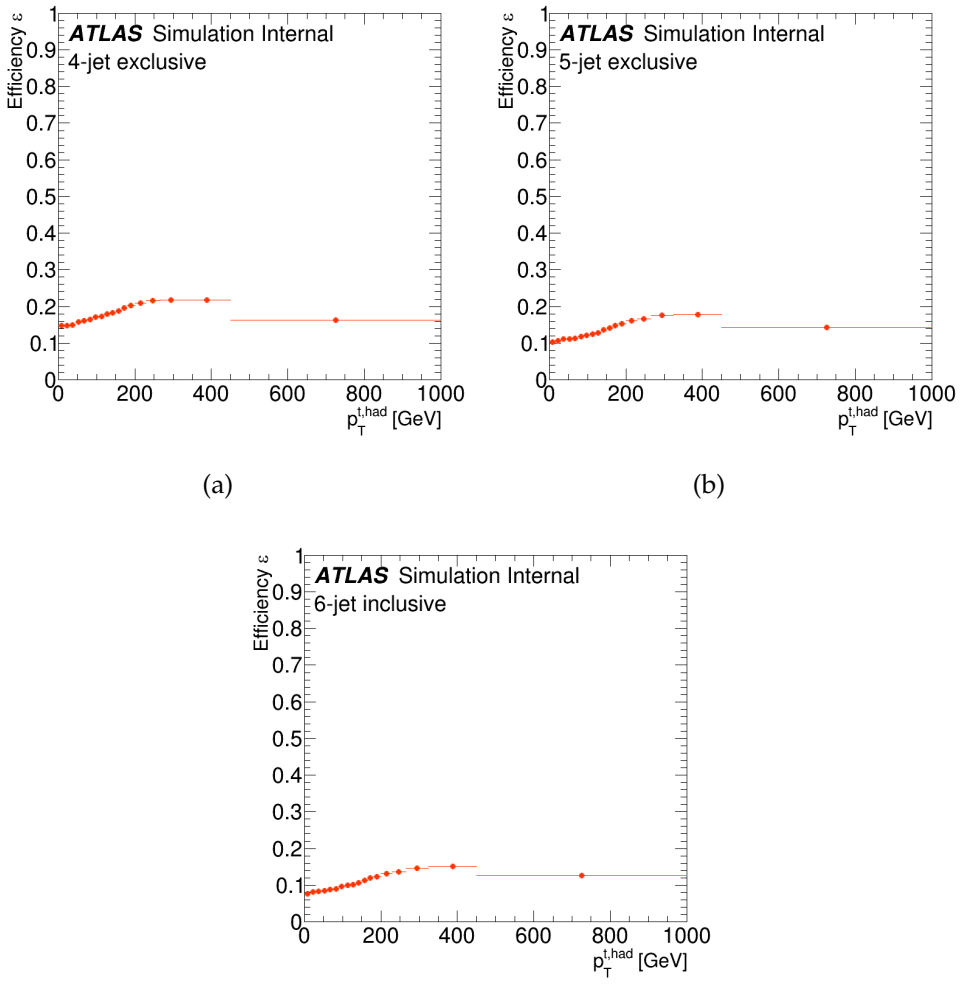

FIGURE 8.10: Efficiency as a function of $p_{\text{T}}^{\text{t,had}}$ in the (a) 4-jet exclusive, (b) 5-jet exclusive, and (c) 6-jet inclusive configurations.

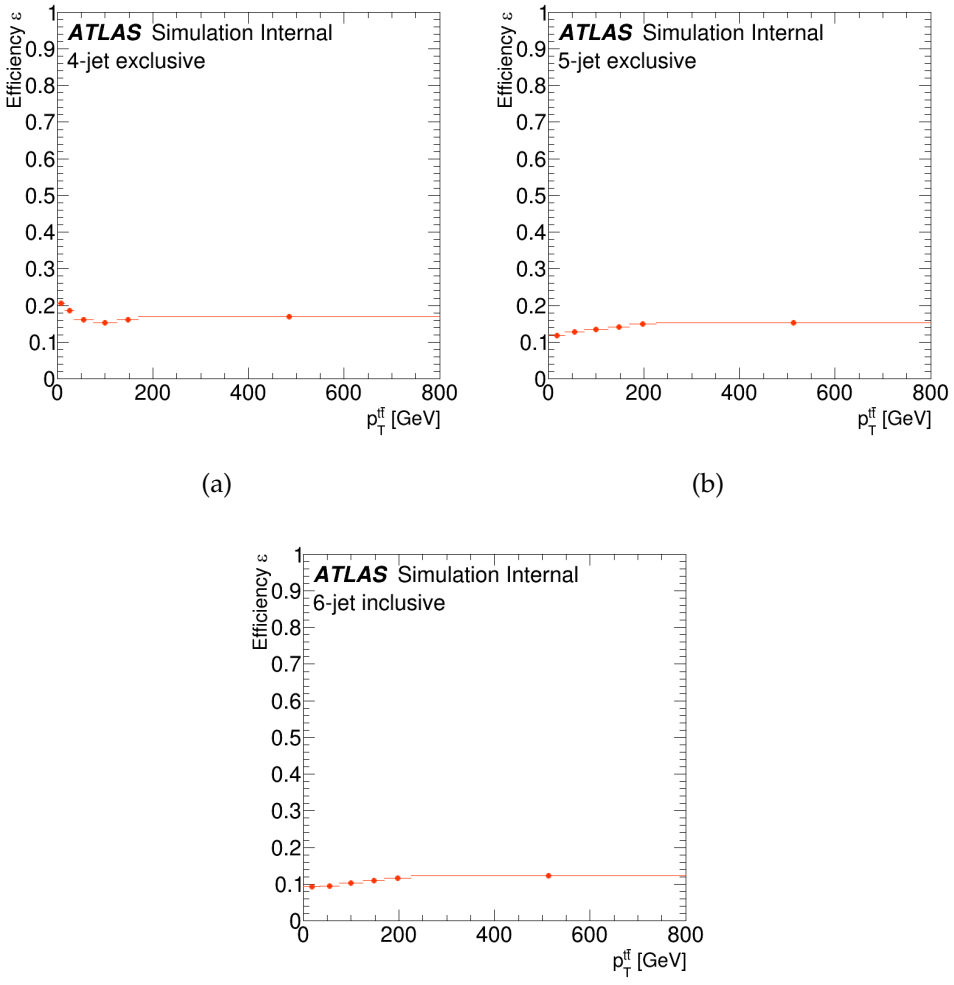

FIGURE 8.11: Efficiency as a function of $p_{\mathrm{T}}^{\mathrm{t\bar{t}}}$ in the (a) 4-jet exclusive, (b) 5-jet exclusive, and (c) 6-jet inclusive configurations.

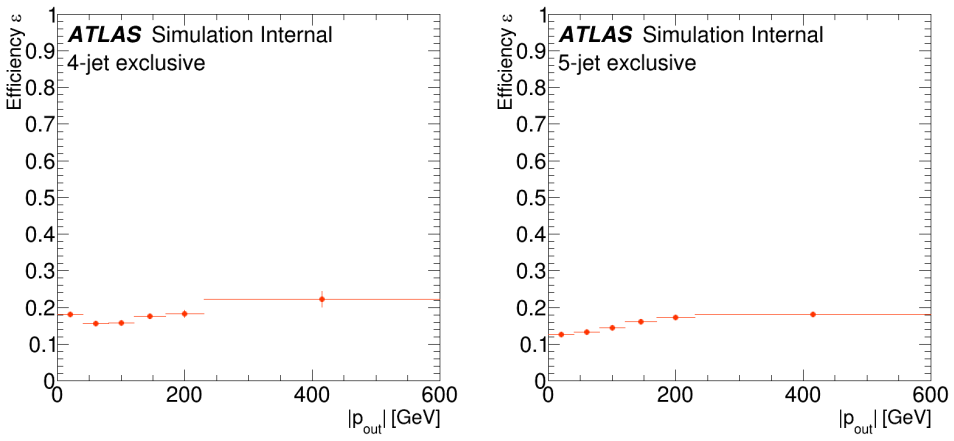

(a)

(b)

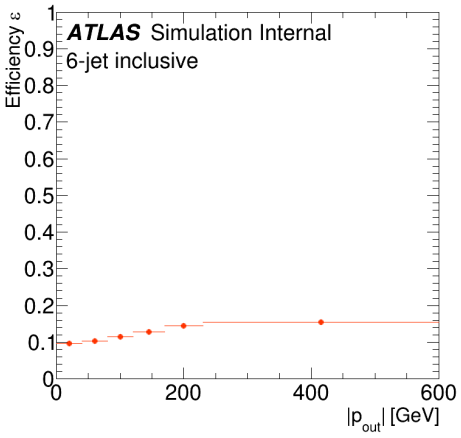

(c)

FIGURE 8.12: Efficiency as a function of $|p_{\mathrm{out}}^{\mathrm{t\bar{t}}}|$ in the (a) 4-jet exclusive, (b) 5-jet exclusive, and (c) 6-jet inclusive configurations.

8.4 Unfolding procedure

The full unfolding procedure can be summarised with the following formula:

$$x^{\mathrm{i}}_{\mathrm{part}} \equiv \frac{1}{\epsilon} \cdot \sum_{\mathrm{j}} \mathcal{M}^{-1}_{\mathrm{ij}} \cdot f^{\mathrm{j}}_{\mathrm{match}} \cdot f^{\mathrm{j}}_{\mathrm{acc}} \cdot (N^{\mathrm{j}}_{\mathrm{reco}} - N^{\mathrm{j}}_{\mathrm{bkg}}), \tag{8.13}$$

where the indices i and j represent the detector level bins and particle level bins, respectively, $\mathcal{M}^{-1}_{\mathrm{ij}}$ is the inversion of the migration matrix and symbolises the Bayesian unfolding.

At last, to pass from the unfolding results to the differential cross sections, the unfolding formula is divided by the integrated luminosity and the bin width:

$$\frac{d\sigma^{\mathrm{fid}}}{dX^{\mathrm{i}}} \equiv \frac{1}{\mathcal{L} \cdot \Delta X^{\mathrm{i}}} \cdot \frac{1}{\epsilon} \cdot \sum_{\mathrm{j}} \mathcal{M}^{-1}_{\mathrm{ij}} \cdot f^{\mathrm{j}}_{\mathrm{match}} \cdot f^{\mathrm{j}}_{\mathrm{acc}} \cdot (N^{\mathrm{j}}_{\mathrm{reco}} - N^{\mathrm{j}}_{\mathrm{bkg}}), \tag{8.14}$$

where ΔX^{i} represents the bin width.

The unfolded differential coss section is integrating over the bins of the unfolded differential cross sections to obtain the total fiducial cross section; the normalised differential cross section is defined as:

$$\frac{1}{\sigma^{\mathrm{fid}}} \frac{d\sigma^{\mathrm{fid}}}{dX^{\mathrm{i}}}. \tag{8.15}$$

8.5 Unfolding validation

The unfolding procedure needs to be validate in order to assess the reliability and stability of the chosen unfolding method. In the analysis described in this thesis, the validation of the unfolding is carried out by two different kind of tests: closure and stress tests. The procedure and the results of these tests are reported respectively in Appendices B–C.

Chapter 9

Systematic uncertainties

In this Chapter the techniques used to estimate the systematic uncertainties affecting the measurements which are shown in Chapter 10 are described.

In Sections 9.1, 9.2 and 9.3 the signal modeling, background and detector level uncertainties are respectively described. Finally, in Section 9.4 the summary sistematic uncertainies plots are shown. The systematic uncertainties tables are reported in Appendix A

The measured differential cross sections are affected by several sources of systematic uncertainties which impact on the precision of the measurements. These systematics uncertanties are related both to detector effects and to the modeling of the signal and background MC components. The latter were found to be the most relevant ones.

Each of the systematic uncertainties is evaluated after the unfolding procedure. The procedure used to evalute these uncertainties consists of a variation bin-per-bin of the nominal distribution by one standard deviation on the total effect generated by the considered error source; this procedure leads, usually, to two shifted distributions each of one representing a shift respect to the nominal distribution. Some of the uncertainties have a single variation, in this case the uncertainty is evaluated by symmetrising the single deviation.

This evaluation of the systematics uncertainties is performed for each observable independently, after the event selection and the unfolding procedure; before this evaluation, the electron and muon channels are combined.

9.1 Signal modeling uncertainties

In this Section the sources of signal modeling systematics uncertainties are discussed. The samples used to evaluate the signal modeling uncertainties were described in Section 5.3.

9.1.1 Monte Carlo generator: matrix element and parton shower models

The choice of the MC generator used in the signal modeling affects the kinematic properties of the simulated $t\bar{t}$ events and reconstruction efficiencies. Therefore to asses the impact of different NLO matrix element calculations and parton shower models, different settings of POWHEG and AMC@NLO with various parton showers, have been used.

The effect due to the choice of the ME generator is estimated by unfolding the sample MADGRAPH5_MC@NLO + HERWIG++ with the POWHEG + HERWIG++ sample and using corrections and migration matrices taken from the latter sample.

Then, the unfolded result is compared to its particle level spectrum of the MADGRAPH5_MC@NLO + HERWIG++; the difference is used as systematic uncertainty of the hard scatter generation modeling.

For the estimation of the effect of the PS and hadronisation, the POWHEG + HERWIG++ sample is unfolded with the nominal sample, using corrections and response matrices taken from it.

The unfolded results is then compared with its particle level spectrum of the POWHEG + HERWIG++ sample and the difference is used as systematic uncertainty of the parton shower. The resulting systematic uncertainty is in the range 3-15% and strongly depends on the observable measured and its bins.

The effect of additional radiation is studied using the samples described in Section 5.3. The spectrum unfolded with the nominal sample is compared with the particle level spectrum of the corresponding generator sample ('radHi'/'radLo') and its uncertainty is used as systematic uncertainty of the initial- and -final state radiation.

9.1.2 Parton distribution functions

To evaluate the impact of the uncertainty of the PDF a $t\bar{t}$ sample generated with MADGRAPH5_AMC@NLO interfeced to HERWIG++ is used; an event-by-event reweighting procedure is applied using the 30 PDF set of the PDF4LHC15 presciption [97] as well as using the central value of the CT10 PDF. The uncertainty on the PDFs obtained, are defined intra-PDF and inter-PDF and reported below.

The choice of different PDF sets, has impact on the efficiency, acceptance and also response matrix, i.e, on the correction factors used to unfold the central MADGRAPH5_AMC@NLO+HERWIG++ sample.

Unfolded results are then compared with the known central particle level spectrum.

The total uncertainties obtained are the intra-PDF variations added in quadrature to define the relative uncertainty as:

$$\delta_{\text{intra}} \equiv \frac{\sqrt{\sum_{i\epsilon\text{sets}}(U_{\text{i}} \cdot R_0 - T_0)^2}}{T_0}. \tag{9.1}$$

In addition to this relative uncertainty, there is an inter-PDF uncertainty between the central PDF4LHC15 and CT10, evaluated in a similar way and added in quadrature:

$$\delta_{\text{inter}} \equiv \frac{U_{\text{CT10}} \cdot R_0 - T_0}{T_0}, \tag{9.2}$$

where the subscript 0 denote the PDF4LHC15 central PDF set and i the variations; R represents the distribution at the detector level and T the distribution at particle level. Finally, the factor U represents the unfolding and its subscript symbolizes the PDF set used to evaluate the spectrum or the corrections.

The resulting uncertainties are found to be at the level of sub percent, with the exception of few bins with low statistic where the uncertainty is up to 2%.

A summary of the modeling systematic uncertainties is shown in Table 9.1.

Source of Uncertainty	Samples
Nominal	POWHEG+PYTHIA6
Parton shower and Hadronisation model	POWHEG+HERWIG++ vs. MADGRAPH_MC@NLO + HERWIG++
Scales and additional radiation	POWHEG+PYTHIA6 variations
PDF	MADGRAPH_MC@NLO + HERWIG++ vs. 30 PDF set of PDF4LHC15

TABLE 9.1: Summary of the modeling systematic uncertainties for the $t\bar{t}$ events.

9.2 Background uncertainties

In this Section the systematic uncertainties affecting the backgrounds evaluated with MC simulations are shown.

The individual experimental and theoretical uncertainties are used to calculate the uncertainty of the background

9.2.1 Single-top quark, diboson and Z+jets backgrounds

The uncertainty on the single-top quark background is evaluated by assigning an uncertainty associated with its normalisation of 15%. The overall impact of this normalisation uncertainty, on the measured cross section, is less

than 0.5%.

The uncertainty related to both the Z+jets and diboson backgrounds, include a contribution from the overall normalisation of the cross-sections as well as an extra 24% for additional jet [98], added in quadrature for each reconstructed jet.

Therefore, 48%, 72% and 96% for the three configurations (4-jet, 5-jet, 6-jet), respectively.

The overall impact, of these uncertainties, on the measured cross-sections is less than 1%, and the largest contribution is due to the Z+jets background.

9.2.2 W+jet uncertainty

The W+jets background has been estimated with a data-driven technique, using the charge asymmetry method, as explained in Section 7.2.2. With the charge asymmetry method normalisation weights were extracted.

In addition to them heavy flavour scale factors ($W_{\mathrm{b\bar{b}}}$, $W_{\mathrm{c\bar{c}}}$, W_{c}, W_{light}), were derived.

To estimate the W-jets systematic uncertainty, these CA and HF scale factors are re-derived from data.

With this procedure, additional uncertainties are obtained by varying one scale factor per time within its statistical uncertainty and re-deriving the other scale factors by using the iterative procedure described in Section 7.2.2.

This results in three additional uncertainties:

- The CA weights are varied up and down and also the HF are calculated accordly;
- The HF scale factors $W_{\mathrm{b\bar{b}}}/W_{\mathrm{c\bar{c}}}$ are varied up and down and simultaneously also the W_{c} scale factors, while, the W_{light} scale factors are modified in such a way the normalisation remain constant at the pretag level;
- The W_{light} scale factors are varied up and down while the other HF scale factors are modified in such a way the normalisation remain constant at the pretag level.

The overall impact of these uncertainties is 2%. In addition to this uncertainty, the same configuration dependent modelling uncertainty described for the Z+jets sample is applied. This uncertainty has an impact of about 2%.

In addition, an extra 50% normalisation uncertainty is applied to this background to account for the remaining mis-modeling observed in various control regions. This systematic uncertainty also includes the impact of the normalisation on the estimation of the W+jets background.

9.2.3 QCD uncertainty

Componentes of systematic uncertainty for non-promt and fake lepton background are evaluated. The systematic uncertainty due to the fake and real efficiency, in the final cross section measurement, is related to the statistical uncertainty coming from to the amount of data in the control region and the MC used to substract the residual background.

The uncertainty is evaluated by varying the definition of loose leptons, changing the selection used to form the control region and propagating the statistical uncertainty of parameterizations of the efficiency to pass the tighter lepton requirements for real and fake leptons.

The definition of the fake efficiency control region is varied once per channel. The efficiency is therefore recalculated in the alternative control region. The new efficiency is used to produce the varied background yields. The final uncertainty is obtained as the difference between the nominal yields and the varied ones and then symmetrised.

9.3 Detector level uncertainties

9.3.1 Leptons uncertainties

For both muons and electrons, uncertainties related to the MC modeling of the lepton trigger, identification, reconstruction and selection efficiencies are estimated.

To correct from the MC mis-modeling scale factors derived from measurements of the efficiency in data are used.

$Z \rightarrow \mu\mu$ ($Z \rightarrow ee$ $W \rightarrow e\nu$) decays were used to obtain scale factors, as functions of the lepton kinematics.

The uncertainties are obtained by varying the lepton and signal selections and from the uncertainty in the evaluation of the backgrounds.

A similar procedure is also used to correct the lepton energy scale or momentum scale and resolution [99, 100].

These uncertainties are relatively small and dominated by the lepton identification in the e+jets channel and the muon triggering efficiency in the μ+jets channel. Because of these uncertainties are specific of each lepton flavour, there isn't correlation between the channels.

9.3.2 Missing transverse energy uncertainties

The uncertainty associated with the $E_{\mathrm{T}}^{\mathrm{miss}}$ is determined by a propagation of the energy scale and resolution uncertaitnies to all jets and leptons in the $E_{\mathrm{T}}^{\mathrm{miss}}$ calculation [101].

Additional sources of uncertainties come from energy deposits not associated to any reconstructed objects. These uncertainties take into account the impact of the generator and undelying-event modeling as well as effects from pile-up.

9.3.3 Jet uncertainties

Regarding the uncertainties related to the jets, the JES systematic uncertainty is estimated using a combination of simulation, test beam data and *in situ* measurements [102].

It takes into account several sources, like the effect of dead material, the known area where the calorimeters are affected by hardware problems, but also the effect of the different behaviour of jets at different energies. The overall uncertainty results in 19 eigenvector subcomponents.

The JER systematic uncertainty is obtained with an in situ measurement of the jet response in dijet events [103]. It is due to the difference in jet-energy resolution between data and MC events. The evaluation consists in a smearing of the MC jet transverse momentum according to the jet resolution as a function of the jet p_{T} and η.

The uncertainty due to the jet reconstruction efficiency was estimated by using minimum bias QCD events randomly discarding jets according to the difference in jet reconstruction efficiency between data and MC. The total jet reconstruction systematic uncertainties are for all the $t\bar{t}$ differential cross-sections at the level of $5 - 10\%$

9.3.4 b-tagging

The systematic uncertainties associated with the tagging of the jets by the b-quarks, are divided into three categories, the efficiency of the tagging algorithm, namely b-quark tagging efficiency, the efficiency of jets which are originated from c-quark but pass the b-tag requirements (c-quark tagging efficiency) and the efficiency which corresponds to the rate at which light-flavour jets are tagged, namely misidentified tagging efficiency.

All the three efficiencies are parametrised as a function of p_{T} and η. In each of these categories, scale factors to correct for the residual difference between data and simulation are used.

From these scale factors systematic uncertainties arise, which are computed splitted into eigenvector components. The uncertainty associated to the b-tagging efficiency is a large contribution, about 10% of the overall systematic uncertainty.

9.3.5 Luminosity uncertainty

The luminosity was measured from Van Der Meer scans, as mentioned in Section 5.1. This uncertainty is applied on all not-normalized differential cross section measurements. The total luminosity error is obtained by adding the errors in quadrature.

The uncertainty on the total integrated luminosity, for the 2015 data was determined to be $\pm$ 2.1% [104].

9.4 Systematics uncertainty plots

In this Section the systematics uncertainty plots as functions of the three observables reported in this thesis are shown, namely $p_{\mathrm{T}}^{\mathrm{t,had}}$, $p_{\mathrm{T}}^{\mathrm{t\bar{t}}}$, $|\,p_{\mathrm{out}}^{\mathrm{t\bar{t}}}\,|$, in the three configurations.

In each distribution the uncertainty components previously described are reported.

Figures 9.1(a)–9.3(c) show the plots for the absolute distributions, while Figures 9.4(a)–9.6(c) the normalised distributions.

It can be observed from the figures that the percentage of the total uncertainties are between 8% and 20% for the absolute distributions and between 4% and 8% in almost all the normalised distributions.

The shown distributions have a different trend and a different point at which there is a reduction of the uncertainties, depending on the observable and on the configuration.

Observing the uncertainties components shown on the Figures, the JES uncertainty increases with the number of jets and is the dominant uncertainty in the 6-jet configuration. This behaviour is seen in all observables.

In the 4-jet configuration, the dominant uncertainty is given by the b-tagging. Also the signal modeling uncertainty contributes significantly to the total uncertainty especially in the tail of the distributions.

The total uncertainties are reduced for the normalised cross sections because of the cancelling out of correlated uncertainties, such as the b-tagging and the JES uncertainties as seen by comparing Figures 9.1(a)–9.3(c) with Figures 9.4(a)–9.6(c).

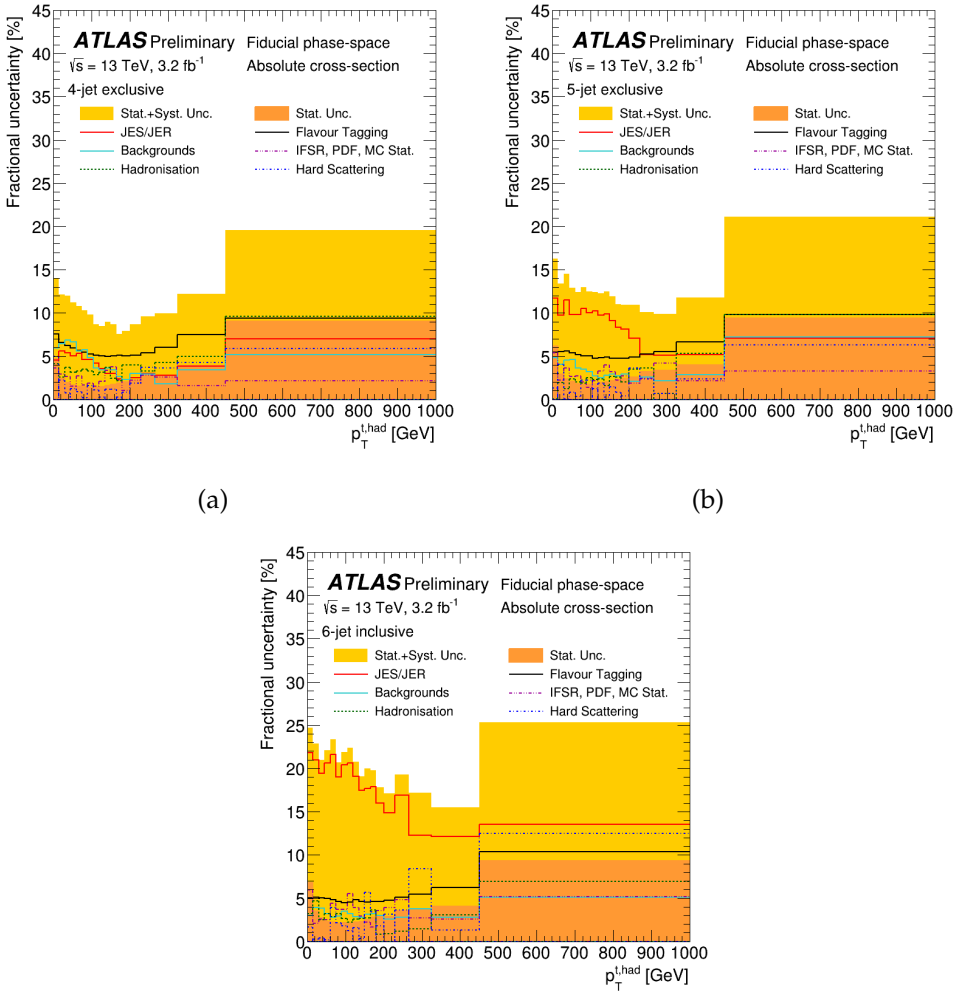

FIGURE 9.1: Uncertainties in the fiducial phase space differential cross sections as a function of $p_{\mathrm{T}}^{\mathrm{t,had}}$ for the absolute distributions in the (a) 4-jet exclusive, (b) 5-jet exclusive, and (c) 6-jet inclusive configurations.

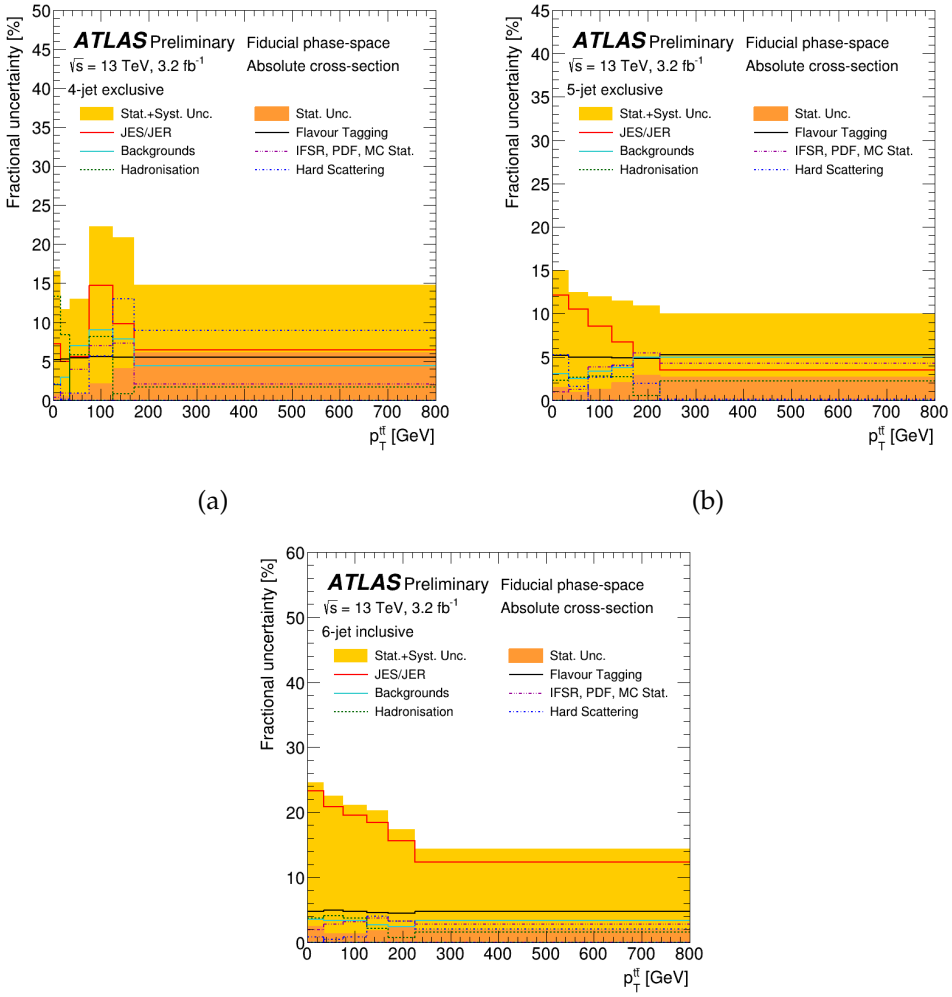

(a) (b)

(c)

FIGURE 9.2: Uncertainties in the fiducial phase space differential cross sections as a function of $p_{\mathrm{T}}^{\mathrm{t\bar{t}}}$ for the absolute distributions in the (a) 4-jet exclusive, (b) 5-jet exclusive, and (c) 6-jet inclusive configurations.

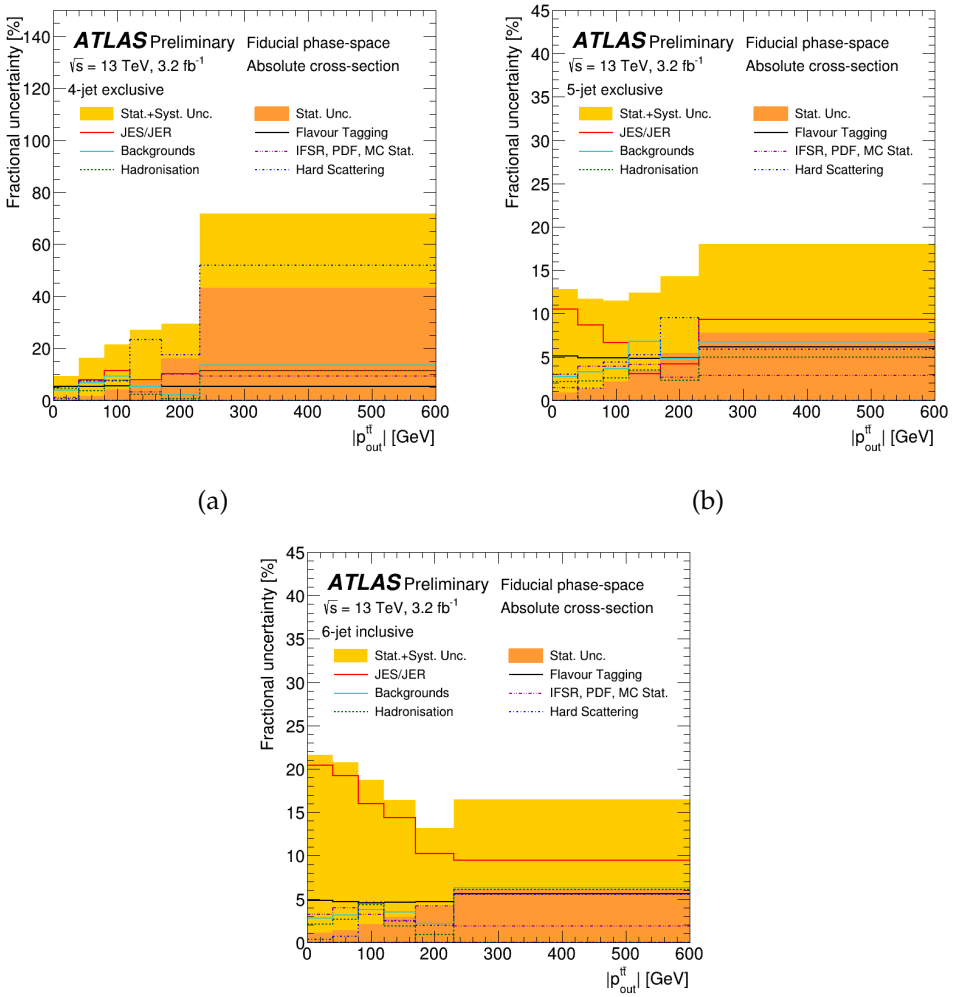

(a) (b)

(c)

FIGURE 9.3: Uncertainties in the fiducial phase space differential cross sections as a function of $|\,p_{\mathrm{out}}^{\mathrm{t\bar{t}}}\,|$ for the absolute distributions in the (a) 4-jet exclusive, (b) 5-jet exclusive, and (c) 6-jet inclusive configurations.

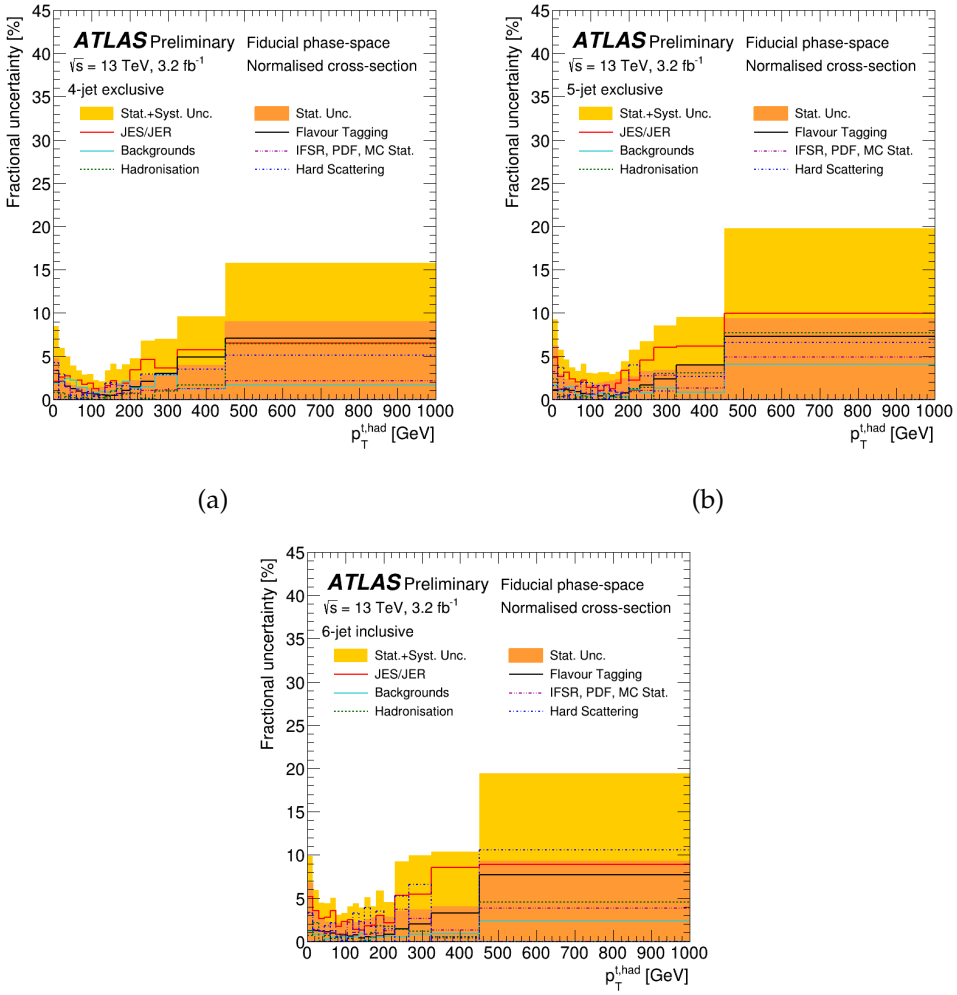

FIGURE 9.4: Uncertainties in the fiducial phase space differential cross sections as a function of $p_{\mathrm{T}}^{\mathrm{t,had}}$ for the normalised distributions in the (a) 4-jet exclusive, (b) 5-jet exclusive, and (c) 6-jet inclusive configurations.

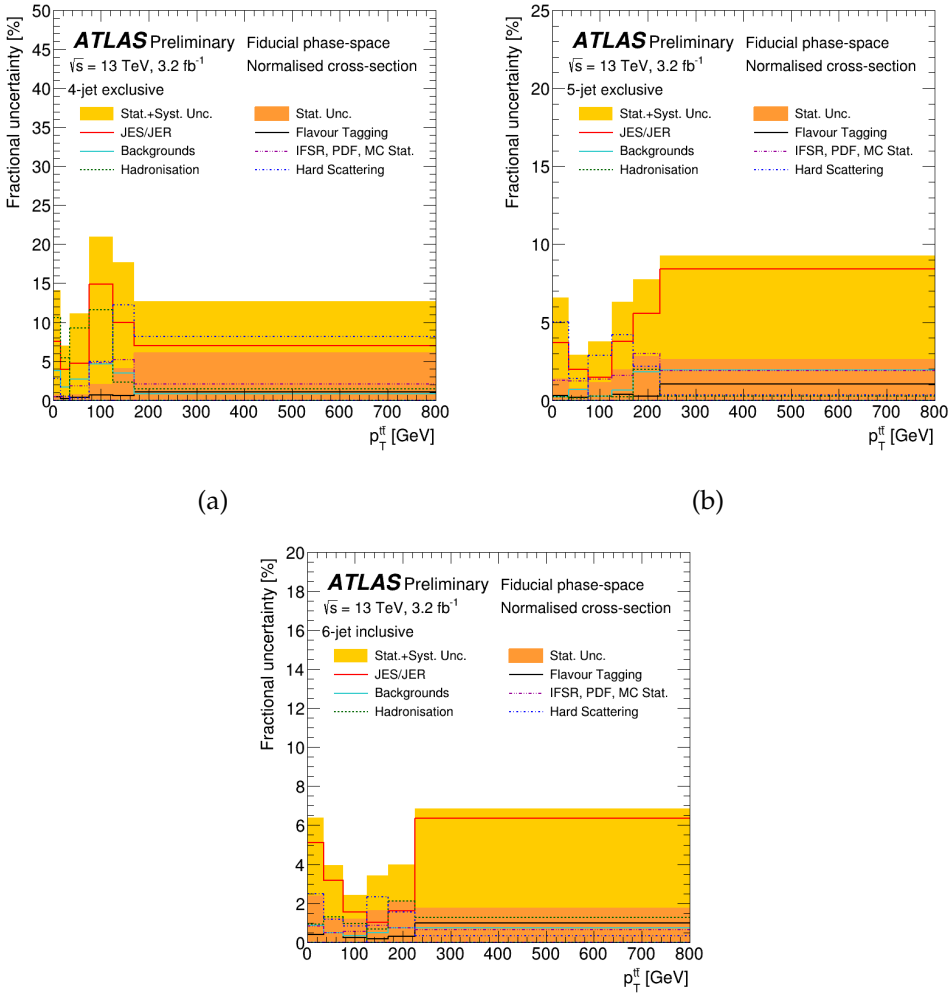

(a) (b)

(c)

FIGURE 9.5: Uncertainties in the fiducial phase space differential cross sections as a function of $p_{\mathrm{T}}^{\mathrm{t\bar{t}}}$ for the normalised distributions in the (a) 4-jet exclusive, (b) 5-jet exclusive, and (c) 6-jet inclusive configurations.

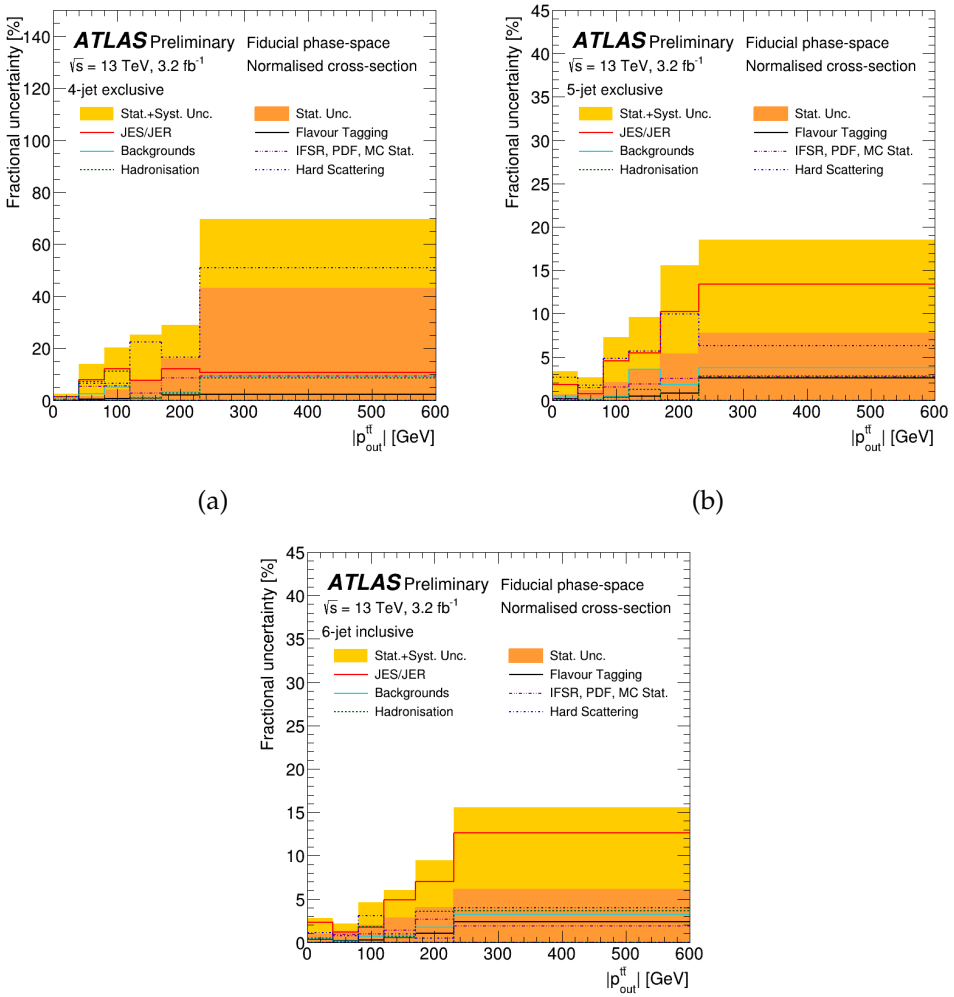

(a) (b)

(c)

FIGURE 9.6: Uncertainties in the fiducial phase space differential cross sections as a function of $|\,p_{\mathrm{out}}^{\mathrm{t\bar{t}}}\,|$ for the normalised distributions in the (a) 4-jet exclusive, (b) 5-jet exclusive, and (c) 6-jet inclusive configurations.

Chapter 10

Results

In this Chapter, the differential cross section results unfolded and compared with several MC predictions are reported as functions of $p_{\mathrm{T}}^{t,had}$, $p_{\mathrm{T}}^{t\bar{t}}$ and $|\,p_{\mathrm{out}}^{t\bar{t}}\,|$, in the three configurations.

10.1 Results and comparison with predictions

Both the absolute cross sections and the normalised cross sections are studied. The predictions used for the comparison to the data are described in Section 5.3. Only a subset of the most relevant predictions is shown in the Figures, while, a complete list of MC predictions is tested and shown in the χ_2 Tables; these are used to evaluate and to quantify the agreement level of the measured differential cross sections. For this purpose, a RIVET routine is provided that mimics the particle level fiducial phase space; its results are shown in Appendix E.

The χ_2 values are obtained by using full covariance matrices of the experimental uncertainties, not including the uncertainties on the theoretical predictions. From the χ_2 and the number of degrees of freedom (NDF) the p-values are then evaluated, i.e., the probability that the χ_2 is larger than or equal to the observed value.

To evaluate the χ_2 of the normalised spectra, the following relation is used:

$$\chi_2 = V_{N_{\mathrm{b}}-1}^{\mathrm{T}} \cdot Cov_{N_{\mathrm{b}}-1}^{-1} \cdot V_{N_{\mathrm{b}}-1}, \tag{10.1}$$

where N_{b} represents the number of bins, $V_{N_{\mathrm{b}}-1}$ corresponds to the vector of the difference between data and predictions and is obtained by discarding, from the total bins N_{b} one of them.

Finally, $Cov_{N_{\mathrm{b}}-1}$ is the $(N_{\mathrm{b}}-1) \times (N_{\mathrm{b}}-1)$ submatrix derived from the full covariance matrix and obtained by discarding the corresponding row or column. The invertibility of the submatrix which allows to compute the χ_2 calculation, which values do not depend on the choice of the discarded bin for the vector $V_{N_{\mathrm{b}}-1}$ and the corresponding submatrix $Cov_{N_{\mathrm{b}}-1}$.

The total covariance matrix, is calculated for each distribution in each of the three configurations.

The first covariance matrix contains both the statistical uncertainty and the systematic uncertainty from detector and background modeling. To obtain this first covariance matrix, pseudo-experiments are performed; in each pseudo-experiment, each bin of data, is varied with a Poisson distribution. Gaussian distributed shifts are coherently added, for each systematic uncertainty by scaling each bin, varied by the Poisson distribution, with the relative variation from the associated systematic uncertainty effect.

Differential cross sections are obtained by unfolding each varied reconstruction distribution with the nominal corrections and the results are used to compute the first covariance matrix.

The second covariance matrix contains theory-model uncertainties. It is obtained by summing four separate covariance matrices which correspond to the effects of the $t\bar{t}$ generator, parton shower, ISR/FSR and PDF uncertainties. To evaluate a single element of these covariance matrices, in each bin, the relative systematic uncertainty are multiplied and scaled by the measured cross section. For each contribution, the bin-to-bin correlation is set to unity. This procedure is needed for the theory-model uncertainty because they cannot be represented as a smooth variation at detector level and, therefore, cannot be calculated in the pseudo-experiment formalism of the first covariance matrix.

If the number of events in a given bin of a pseudo-experiment become negative, due to the effect of the combined systematic shifts, it is set to zero before the unfolding stage.

All covariance and correlation matrices for all the observables and configurations are reported in Appendix D; in general, the covariance matrices show a large correlation between bins, for the absolute distributions, due to the high correlation between the systematic uncertainty. Indeed, for the normalised distributions, a correlation between neighbouring bins is observed, whereas, there is anti-correlation with distant bins, due to the normalisation condition.

The differential cross sections, as a function of the $p_{\mathrm{T}}^{\mathrm{t,had}}$, absolute and normalised, are shown in Figure 10.1–10.2. In both the absolute and normalised cross sections a tendency of all the MC predictions to underestimate data at low value of the p_{T} and overestimate them at high value of the p_{T}, can be observed.

Going to higher value of the jet multiplicy, it is observed a reduction of this tendency. The agreement of the predictions with data is shown in the correpsondent χ_2 Tables 10.1 and 10.2, for the absolute and normalised distributions, respectively.

In general, a good agreement between data and predictions in the 5-jet exclusive and 6-jet inclusive configurations, is observed, for both the absolute and

normalised distributions. There is a bit tension in the 4-jet exclusive configuration. The only exception, which can me observed from the χ_2 tables is the POWHEG + HERWIG++ prediction which is inconsistent whit the measured differential cross sections in the 4- and 6-jet configurations.

The differential cross sections as a function of $p_{\mathrm{T}}^{\mathrm{t\bar{t}}}$ for the three jet configurations are shown in Figures 10.3 and 10.4 and the correspondent χ_2 values in Tables 10.3 and 10.4 for the absolute and normalised distributions, respectively.

In general a good agreement is observed between data and predictions in all configurations except fo the MC@NLO generator, which is not compatible with data in the 4-jet and 5-jet configurations. This is also shown in the χ_2 Tables. Also the POWHEG+HERWIG++ sample is shown to be not compatible with data in all the configurations. Finally, both 'radHi' calculations are not compatible with data in the absolute distributions of the 4- and 6-jet condigurations.

Finally, the $|\,p_{\mathrm{out}}^{t\bar{t}}\,|$ differential cross sections are shown in Figures 10.5 and 10.6 and the correspondent χ_2 values in Tables 10.5 and 10.6 for both absolute and normalised, respectively. The distributions confirm the mis-modelling of the MC@NLO sample for the 4- and 5-jet configurations, already observed in the $p_{\mathrm{T}}^{t\bar{t}}$ distributions. Several predictions are not compatible with the absolure cross sections in the 6-jet configuration but have a better agreement in the normalised cross sections. Is also confirmed a mis-modelling of the POWHEG+HERWIG++ prediction in the 5-jet configuration, as observed previously for the $p_{\mathrm{T}}^{t\bar{t}}$ distribution.

The discriminant power of the analysis reported in this thesis can be observed in Figure 10.7 where several predictions with different values of the fragmentation and renormaisation scales and of the h_{damp} parameter, are compared for the normalised differential cross section of the $p_{\mathrm{T}}^{t\bar{t}}$ observable in the 6-jet configuration. The Figure is composed by three pads, each one with three predictions. In the first pad 10.7(a), where three POWHEG+PYTHIA6 samples are compared, the best agreement is obtained for the 'radLo' sample, which is tuned to yield a lower amount of QCD radiation. It has the h_{damp} parameter set to the mass of the top quark and the renormalisation and factorisation scales increased of a factor 2, compared to the nominal value. Since the h_{damp} parameter is the same for all the three samples, it can be concluded that the nature of the different behaviour of the samples, come from the scale variations.

A similar conclusion can be drawn for the Figure 10.7(c) where the 'radLo' calculation show the best agreement respect to the other two samples. Then, the effect of changing h_{damp} is further demonstrated by comparing the two POWHEG+PYTHIA8 calculations shown in Figure 10.7(b), which have different values of the h_{damp} parameter.

The last result is reported in Figure 10.8 and shows the ratio of data distribution over the nominal prediction for the normalised $p_{\mathrm{T}}^{\mathrm{t,had}}$ and $p_{\mathrm{T}}^{\mathrm{t,had}}$ distributions, respectively. Each of the two figures show the ratio for the three configurations.

The differences between data and prediction shown in the Figures, is largest for the 4-jet configuration. The behaviour of the other two configuration is slightly better. Respect to the $p_{\mathrm{T}}^{\mathrm{t,had}}$, the $p_{\mathrm{T}}^{\mathrm{t\bar{t}}}$ observable shows a result less clear.

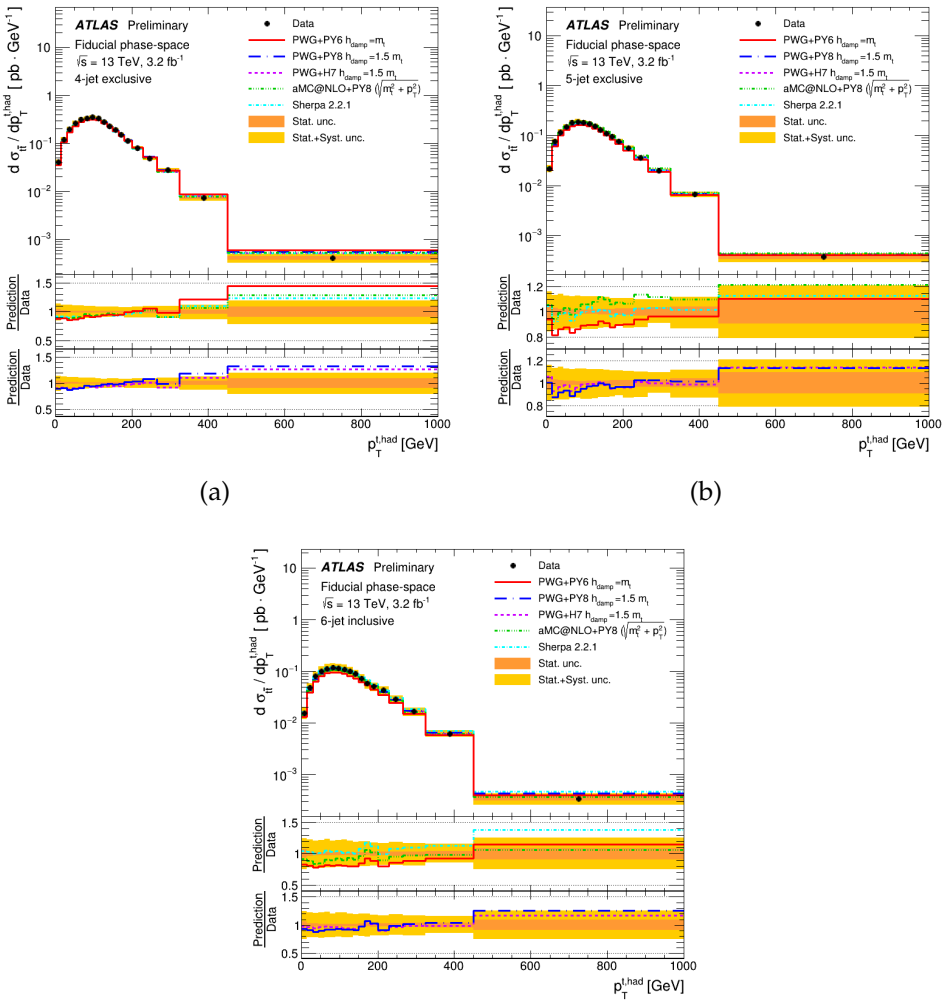

(a) (b)

(c)

FIGURE 10.1: Absolute differential cross sections in the fiducial phase space as a function of $p_{\mathrm{T}}^{\mathrm{t,had}}$: (a) in the 4-jet exclusive, (b) 5-jet exclusive and (c) 6-jet inclusive configurations. The shaded area represents the total statistical and systematic uncertainties.

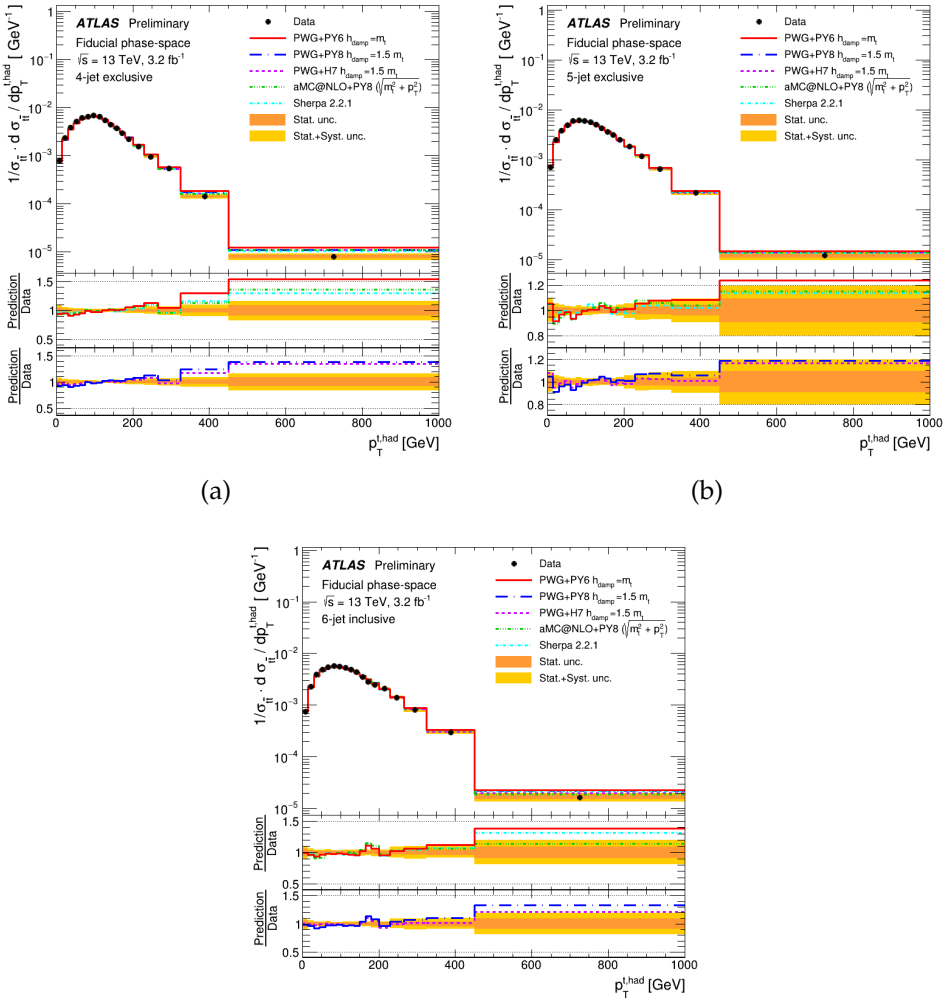

(a) (b)

(c)

FIGURE 10.2: Normalised differential cross sections in the fiducial phase space as a function of $p_{\mathrm{T}}^{\mathrm{t,had}}$: (a) in the 4-jet exclusive, (b) 5-jet exclusive and (c) 6-jet inclusive configurations. The shaded area represents the total statistical and systematic uncertainties.

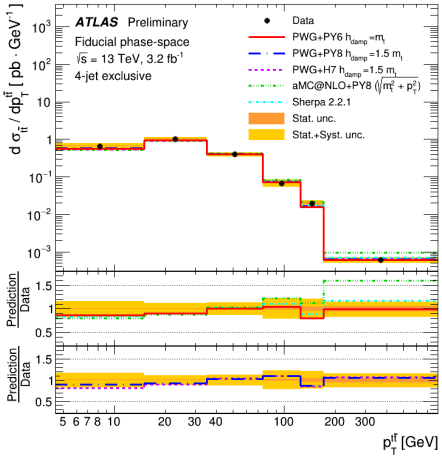

(a)

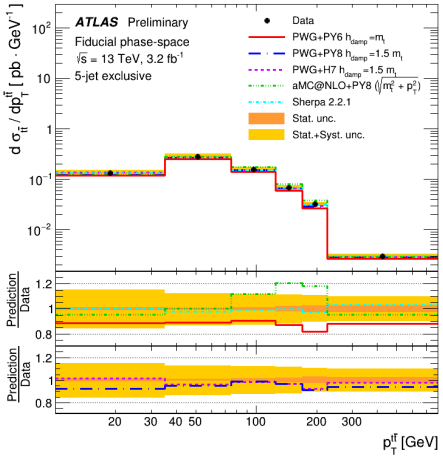

(b)

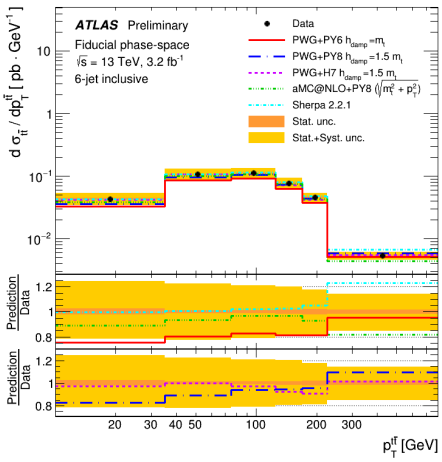

(c)

FIGURE 10.3: Absolute differential cross sections in the fiducial phase space as a function of $p_{\mathrm{T}}^{\mathrm{t\bar{t}}}$: (a) in the 4-jet exclusive, (b) 5-jet exclusive and (c) 6-jet inclusive configurations. The shaded area represents the total statistical and systematic uncertainties.

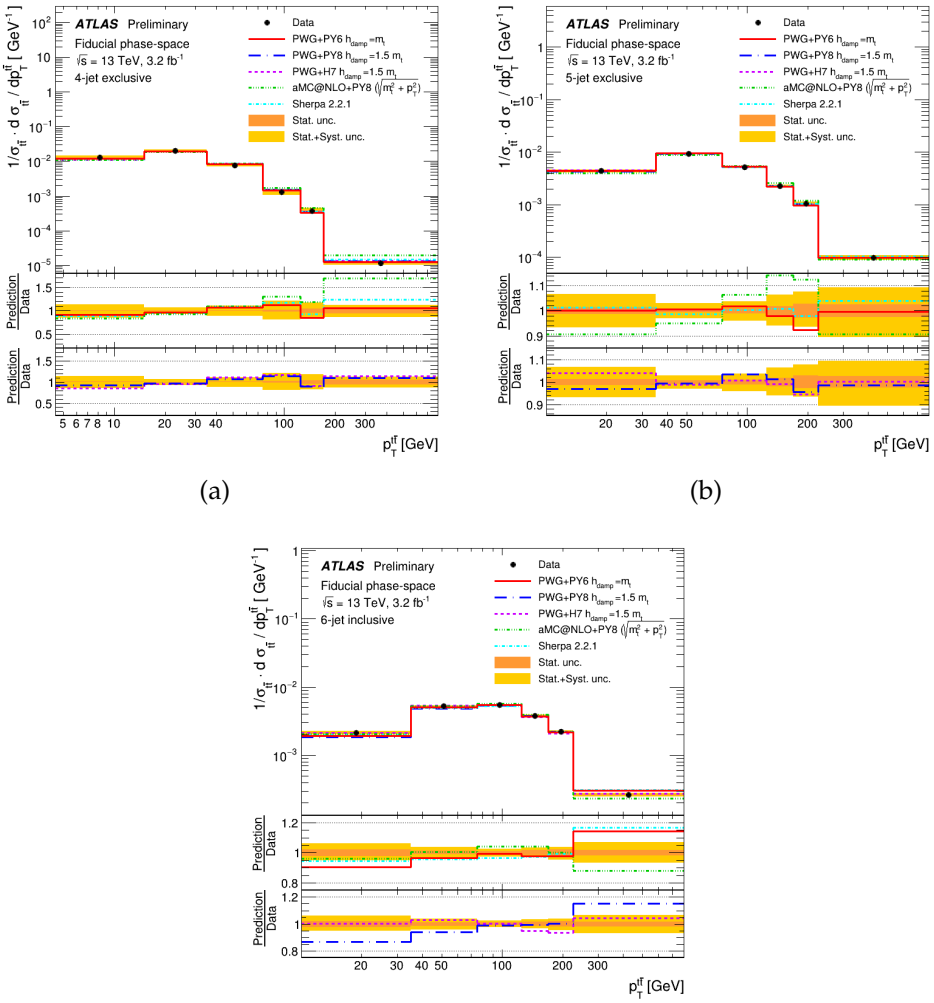

(a) (b)

(c)

FIGURE 10.4: Normalised differential cross sections in the fiducial phase space as a function of $p_{\mathrm{T}}^{t\bar{t}}$: (a) in the 4-jet exclusive, (b) 5-jet exclusive and (c) 6-jet inclusive configurations. The shaded area represents the total statistical and systematic uncertainties.

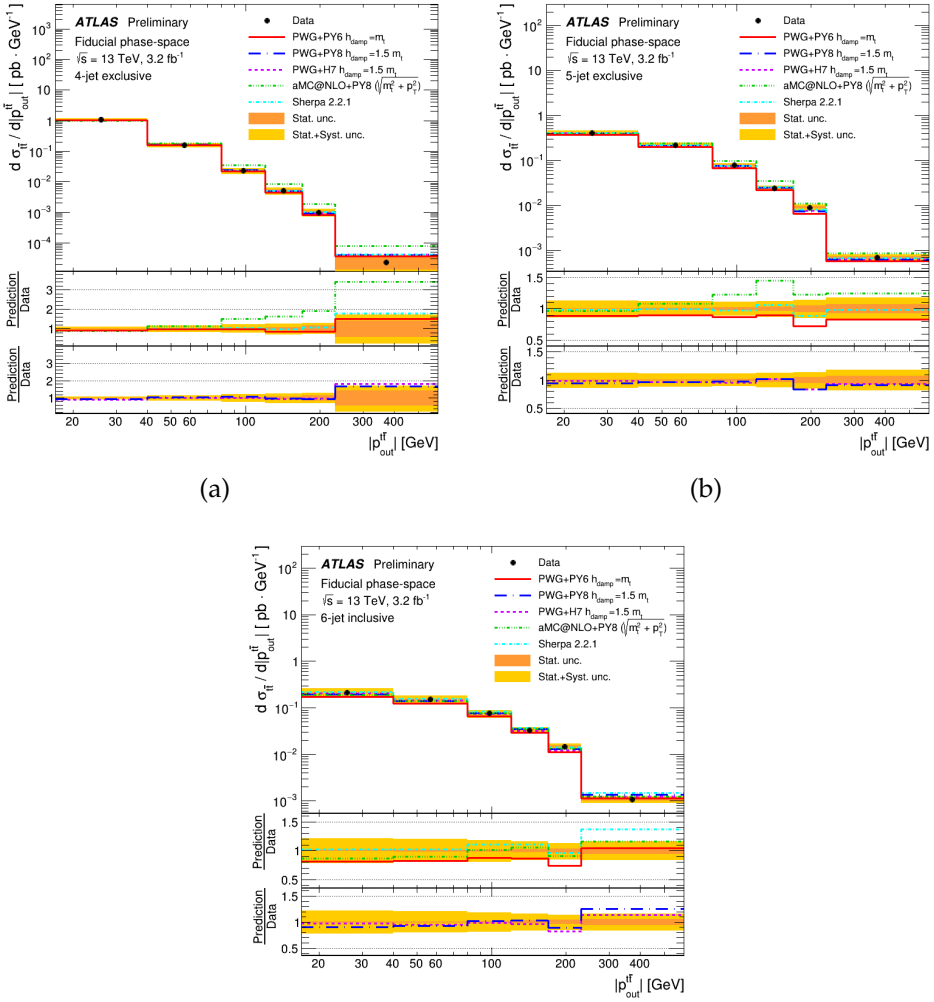

(a) (b)

(c)

FIGURE 10.5: Absolute differential cross sections in the fiducial phase space as a function of $|\,p_{\mathrm{out}}^{\mathrm{t\bar{t}}}\,|$: (a) in the 4-jet exclusive, (b) 5-jet exclusive and (c) 6-jet inclusive configurations. The shaded area represents the total statistical and systematic uncertainties.

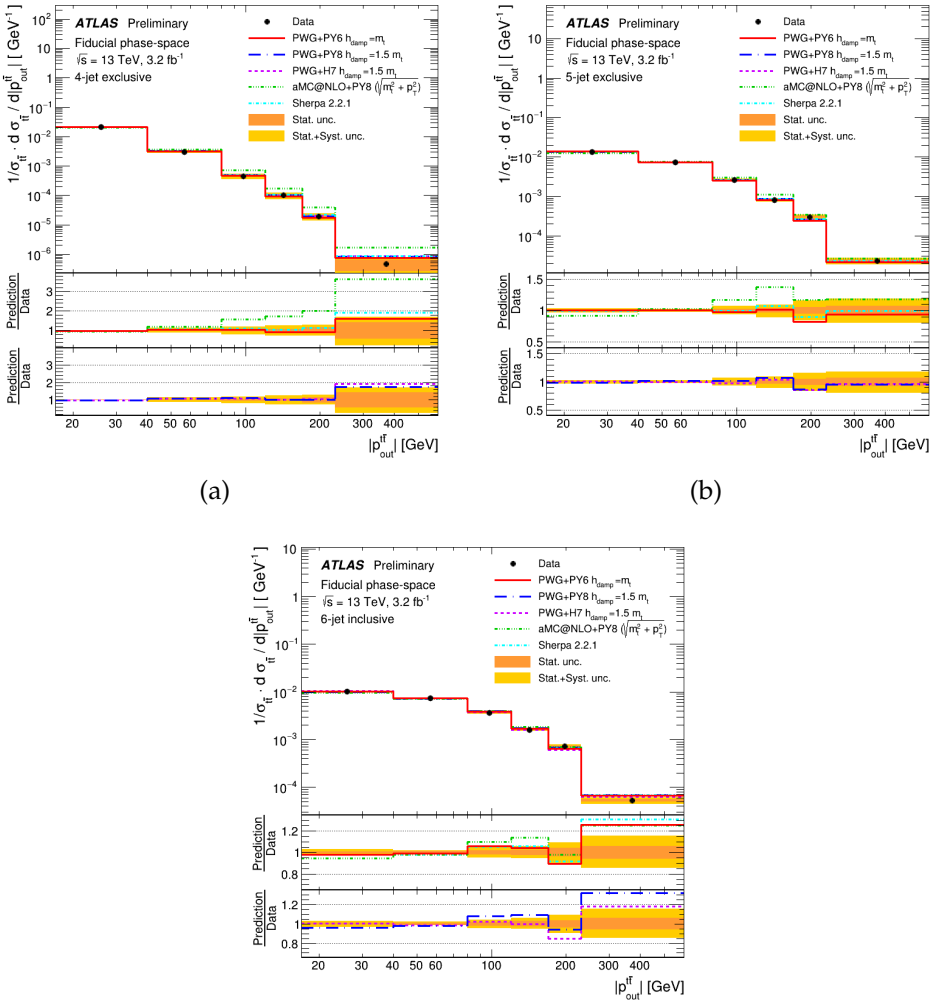

(a) (b)

(c)

FIGURE 10.6: Normalised differential cross sections in the fiducial phase space as a function of $|p_{\text{out}}^{t\bar{t}}|$: (a) in the 4-jet exclusive, (b) 5-jet exclusive and (c) 6-jet inclusive configurations. The shaded area represents the total statistical and systematic uncertainties.

	4-jet exclusive		5-jet exclusive		6-jet inclusive	
	χ^2/NDF	p-value	χ^2/NDF	p-value	χ^2/NDF	p-value
POWHEG+PYTHIA6	28.9/18	0.05	12.9/18	0.80	12.7/18	0.81
POWHEG+PYTHIA6 (radHi)	28.9/18	0.05	14.5/18	0.69	16.8/18	0.54
POWHEG+PYTHIA6 (radLo)	33.0/18	0.02	14.1/18	0.72	13.7/18	0.75
POWHEG+PYTHIA8 ($h_{\mathrm{damp}} = m_{\mathrm{t}}$)	25.8/18	0.10	14.7/18	0.68	15.3/18	0.64
POWHEG+PYTHIA8 ($h_{\mathrm{damp}} = 1.5\,m_{\mathrm{t}}$)	23.1/18	0.19	13.2/18	0.78	15.8/18	0.60
POWHEG+PYTHIA8 (radHi) ($h_{\mathrm{damp}} = 3\,m_{\mathrm{t}}$)	20.3/18	0.32	14.3/18	0.71	23.4/18	0.17
POWHEG+PYTHIA8 (radLo) ($h_{\mathrm{damp}} = 1.5\,m_{\mathrm{t}}$)	25.1/18	0.12	14.6/18	0.69	12.7/18	0.81
POWHEG+HERWIG7	21.1/18	0.28	11.9/18	0.85	12.2/18	0.84
POWHEG+HERWIG++	37.2/18	<0.01	27.9/18	0.06	38.8/18	<0.01
MC@NLO+HERWIG++	25.4/18	0.12	11.1/18	0.89	20.2/18	0.32
MC@NLO+PYTHIA8 ($H_{\mathrm{T}}/2$)	23.2/18	0.18	20.9/18	0.29	17.2/18	0.51
MC@NLO+PYTHIA8 ($\sqrt{m_{\mathrm{t}}^2 + p_{\mathrm{T}}^2}$)	25.7/18	0.11	18.9/18	0.40	22.4/18	0.21
SHERPA 2.2.1	24.2/18	0.15	18.6/18	0.42	18.0/18	0.45

TABLE 10.1: Comparison of the measured fiducial phase space absolute differential cross sections as a function of $p_{\mathrm{T}}^{\mathrm{t,had}}$ and the predictions from several MC generators in different n-jet configurations. For each prediction a χ^2 and a p-value are calculated using the covariance matrix of the measured spectrum. The number of degrees of freedom (NDF) is equal to the number of bins in the distribution.

	4-jet exclusive		5-jet exclusive		6-jet inclusive	
	χ^2/NDF	p-value	χ^2/NDF	p-value	χ^2/NDF	p-value
POWHEG+PYTHIA6	23.6/17	0.13	13.9/17	0.67	14.4/17	0.64
POWHEG+PYTHIA6 (radHi)	23.6/17	0.13	14.7/17	0.62	15.5/17	0.56
POWHEG+PYTHIA6 (radLo)	26.1/17	0.07	16.2/17	0.51	16.1/17	0.52
POWHEG+PYTHIA8 ($h_{\mathrm{damp}} = m_{\mathrm{t}}$)	23.2/17	0.14	16.9/17	0.46	17.9/17	0.40
POWHEG+PYTHIA8 ($h_{\mathrm{damp}} = 1.5\,m_{\mathrm{t}}$)	20.9/17	0.23	15.5/17	0.56	18.1/17	0.38
POWHEG+PYTHIA8 (radHi) ($h_{\mathrm{damp}} = 3\,m_{\mathrm{t}}$)	18.2/17	0.38	16.2/17	0.51	18.6/17	0.35
POWHEG+PYTHIA8 (radLo) ($h_{\mathrm{damp}} = 1.5\,m_{\mathrm{t}}$)	21.5/17	0.20	17.6/17	0.41	17.0/17	0.46
POWHEG+HERWIG7	16.9/17	0.46	12.0/17	0.80	12.6/17	0.76
POWHEG+HERWIG++	19.4/17	0.31	21.5/17	0.21	28.7/17	0.04
MC@NLO+HERWIG++	16.3/17	0.50	11.4/17	0.84	24.4/17	0.11
MC@NLO+PYTHIA8 ($H_{\mathrm{T}}/2$)	20.8/17	0.23	21.6/17	0.20	21.8/17	0.19
MC@NLO+PYTHIA8 ($\sqrt{m_{\mathrm{t}}^2 + p_{\mathrm{T}}^2}$)	21.2/17	0.22	17.8/17	0.40	27.8/17	0.05
SHERPA 2.2.1	21.7/17	0.20	20.2/17	0.26	17.2/17	0.44

TABLE 10.2: Comparison of the measured fiducial phase space normalised differential cross sections as a function of $p_{\mathrm{T}}^{\mathrm{t,had}}$ and the predictions from several MC generators in different n-jet configurations. For each prediction a χ^2 and a p-value are calculated using the covariance matrix of the measured spectrum. The number of degrees of freedom (NDF) is equal to the number of bins minus one in the distribution.

	4-jet exclusive		5-jet exclusive		6-jet inclusive	
	χ^2/NDF	p-value	χ^2/NDF	p-value	χ^2/NDF	p-value
POWHEG+PYTHIA6	7.9/6	0.25	7.1/6	0.32	7.0/6	0.32
POWHEG+PYTHIA6 (radHi)	15.8/6	0.01	6.0/6	0.42	41.1/6	<0.01
POWHEG+PYTHIA6 (radLo)	4.9/6	0.56	7.2/6	0.31	6.5/6	0.37
POWHEG+PYTHIA8 ($h_{\mathrm{damp}} = m_{\mathrm{t}}$)	7.3/6	0.29	7.0/6	0.32	8.8/6	0.19
POWHEG+PYTHIA8 ($h_{\mathrm{damp}} = 1.5\,m_{\mathrm{t}}$)	7.5/6	0.28	3.8/6	0.70	13.8/6	0.03
POWHEG+PYTHIA8 (radHi) ($h_{\mathrm{damp}} = 3\,m_{\mathrm{t}}$)	13.7/6	0.03	3.2/6	0.78	62.2/6	<0.01
POWHEG+PYTHIA8 (radLo) ($h_{\mathrm{damp}} = 1.5\,m_{\mathrm{t}}$)	5.4/6	0.49	5.9/6	0.43	6.8/6	0.34
POWHEG+HERWIG7	10.1/6	0.12	5.3/6	0.50	5.4/6	0.50
POWHEG+HERWIG++	8.4/6	0.21	30.1/6	<0.01	21.3/6	<0.01
MC@NLO+HERWIG++	99.2/6	<0.01	9.3/6	0.16	12.7/6	0.05
MC@NLO+PYTHIA8 ($H_{\mathrm{T}}/2$)	41.6/6	<0.01	34.5/6	<0.01	24.4/6	<0.01
MC@NLO+PYTHIA8 ($\sqrt{m_{\mathrm{t}}^2 + p_{\mathrm{T}}^2}$)	47.1/6	<0.01	31.5/6	<0.01	19.8/6	<0.01
SHERPA 2.2.1	13.2/6	0.04	1.8/6	0.94	24.4/6	<0.01

TABLE 10.3: Comparison of the measured fiducial phase space absolute differential cross sections as a function of $p_{\mathrm{T}}^{\mathrm{t\bar{t}}}$ and the predictions from several MC generators in different n-jet configurations. For each prediction a χ^2 and a p-value are calculated using the covariance matrix of the measured spectrum. The number of degrees of freedom (NDF) is equal to the number of bins in the distribution.

	4-jet exclusive		5-jet exclusive		6-jet inclusive	
	χ^2/NDF	p-value	χ^2/NDF	p-value	χ^2/NDF	p-value
POWHEG+PYTHIA6	4.2/5	0.52	3.2/5	0.68	4.0/5	0.54
POWHEG+PYTHIA6 (radHi)	5.1/5	0.41	6.2/5	0.29	10.2/5	0.07
POWHEG+PYTHIA6 (radLo)	6.1/5	0.30	3.9/5	0.57	5.3/5	0.38
POWHEG+PYTHIA8 ($h_{\mathrm{damp}} = m_{\mathrm{t}}$)	7.6/5	0.18	4.8/5	0.44	4.8/5	0.44
POWHEG+PYTHIA8 ($h_{\mathrm{damp}} = 1.5\,m_{\mathrm{t}}$)	5.4/5	0.36	4.1/5	0.54	6.6/5	0.26
POWHEG+PYTHIA8 (radHi) ($h_{\mathrm{damp}} = 3\,m_{\mathrm{t}}$)	6.5/5	0.26	4.0/5	0.55	11.0/5	0.05
POWHEG+PYTHIA8 (radLo) ($h_{\mathrm{damp}} = 1.5\,m_{\mathrm{t}}$)	5.2/5	0.39	6.1/5	0.30	7.9/5	0.16
POWHEG+HERWIG7	10.4/5	0.07	5.1/5	0.41	3.3/5	0.66
POWHEG+HERWIG++	18.5/5	<0.01	16.0/5	<0.01	20.2/5	<0.01
MC@NLO+HERWIG++	12.7/5	0.03	10.9/5	0.05	9.8/5	0.08
MC@NLO+PYTHIA8 ($H_{\mathrm{T}}/2$)	26.7/5	<0.01	10.1/5	0.07	8.4/5	0.13
MC@NLO+PYTHIA8 ($\sqrt{m_{\mathrm{t}}^2 + p_{\mathrm{T}}^2}$)	17.2/5	<0.01	9.9/5	0.08	8.0/5	0.16
SHERPA 2.2.1	7.4/5	0.19	1.7/5	0.89	2.2/5	0.82

TABLE 10.4: Comparison of the measured fiducial phase space normalised differential cross sections as a function of $p_{\mathrm{T}}^{\mathrm{t\bar{t}}}$ and the predictions from several MC generators in different n-jet configurations. For each prediction a χ^2 and a p-value are calculated using the covariance matrix of the measured spectrum. The number of degrees of freedom (NDF) is equal to the number of bins minus one in the distribution.

	4-jet exclusive		5-jet exclusive		6-jet inclusive	
	χ^2/NDF	p-value	χ^2/NDF	p-value	χ^2/NDF	p-value
POWHEG+PYTHIA6	4.3/6	0.64	11.0/6	0.09	10.2/6	0.12
POWHEG+PYTHIA6 (radHi)	7.6/6	0.27	7.7/6	0.26	14.4/6	0.03
POWHEG+PYTHIA6 (radLo)	2.5/6	0.87	11.4/6	0.08	15.2/6	0.02
POWHEG+PYTHIA8 ($h_{\mathrm{damp}} = m_{\mathrm{t}}$)	3.1/6	0.80	10.3/6	0.11	9.9/6	0.13
POWHEG+PYTHIA8 ($h_{\mathrm{damp}} = 1.5\,m_{\mathrm{t}}$)	3.2/6	0.78	7.3/6	0.29	10.6/6	0.10
POWHEG+PYTHIA8 (radHi) ($h_{\mathrm{damp}} = 3\,m_{\mathrm{t}}$)	5.7/6	0.46	7.2/6	0.30	25.5/6	<0.01
POWHEG+PYTHIA8 (radLo) ($h_{\mathrm{damp}} = 1.5\,m_{\mathrm{t}}$)	2.5/6	0.87	8.6/6	0.20	9.2/6	0.17
POWHEG+HERWIG7	4.9/6	0.56	6.5/6	0.36	12.4/6	0.05
POWHEG+HERWIG++	8.3/6	0.21	32.3/6	<0.01	39.5/6	<0.01
MC@NLO+HERWIG++	59.8/6	<0.01	10.3/6	0.11	22.6/6	<0.01
MC@NLO+PYTHIA8 ($H_{\mathrm{T}}/2$)	40.7/6	<0.01	39.1/6	<0.01	10.2/6	0.12
MC@NLO+PYTHIA8 ($\sqrt{m_{\mathrm{t}}^2 + p_{\mathrm{T}}^2}$)	40.7/6	<0.01	42.0/6	<0.01	10.4/6	0.11
SHERPA 2.2.1	3.7/6	0.71	5.6/6	0.46	12.8/6	0.05

TABLE 10.5: Comparison of the measured fiducial phase space absolute differential cross sections as a function of $|\,p_{\mathrm{out}}^{\mathrm{t\bar{t}}}\,|$ and the predictions from several MC generators in different n-jet configurations. For each prediction a χ^2 and a p-value are calculated using the covariance matrix of the measured spectrum. The number of degrees of freedom (NDF) is equal to the number of bins in the distribution.

	4-jet exclusive		5-jet exclusive		6-jet inclusive	
	χ^2/NDF	p-value	χ^2/NDF	p-value	χ^2/NDF	p-value
POWHEG+PYTHIA6	2.1/5	0.83	5.1/5	0.41	8.0/5	0.15
POWHEG+PYTHIA6 (radHi)	5.2/5	0.39	5.6/5	0.35	11.5/5	0.04
POWHEG+PYTHIA6 (radLo)	1.1/5	0.95	5.1/5	0.40	8.6/5	0.13
POWHEG+PYTHIA8 ($h_{\mathrm{damp}} = m_{\mathrm{t}}$)	1.4/5	0.92	6.6/5	0.25	9.0/5	0.11
POWHEG+PYTHIA8 ($h_{\mathrm{damp}} = 1.5\,m_{\mathrm{t}}$)	1.0/5	0.96	6.0/5	0.30	11.8/5	0.04
POWHEG+PYTHIA8 (radHi) ($h_{\mathrm{damp}} = 3\,m_{\mathrm{t}}$)	2.9/5	0.72	7.4/5	0.19	14.1/5	0.01
POWHEG+PYTHIA8 (radLo) ($h_{\mathrm{damp}} = 1.5\,m_{\mathrm{t}}$)	0.5/5	0.99	6.5/5	0.26	10.4/5	0.06
POWHEG+HERWIG7	2.3/5	0.80	4.6/5	0.47	5.3/5	0.39
POWHEG+HERWIG++	7.3/5	0.20	15.1/5	0.01	9.9/5	0.08
MC@NLO+HERWIG++	36.1/5	<0.01	10.6/5	0.06	6.7/5	0.24
MC@NLO+PYTHIA8 ($H_{\mathrm{T}}/2$)	46.9/5	<0.01	28.0/5	<0.01	16.0/5	<0.01
MC@NLO+PYTHIA8 ($\sqrt{m_{\mathrm{t}}^2 + p_{\mathrm{T}}^2}$)	45.5/5	<0.01	29.9/5	<0.01	15.6/5	<0.01
SHERPA 2.2.1	1.5/5	0.92	4.6/5	0.47	8.2/5	0.15

TABLE 10.6: Comparison of the measured fiducial phase space normalised differential cross sections as a function of $|\,p_{\mathrm{out}}^{\mathrm{t\bar{t}}}\,|$ and the predictions from several MC generators in different n-jet configurations. For each prediction a χ^2 and a p-value are calculated using the covariance matrix of the measured spectrum. The number of degrees of freedom (NDF) is equal to the number of bins minus one in the distribution.

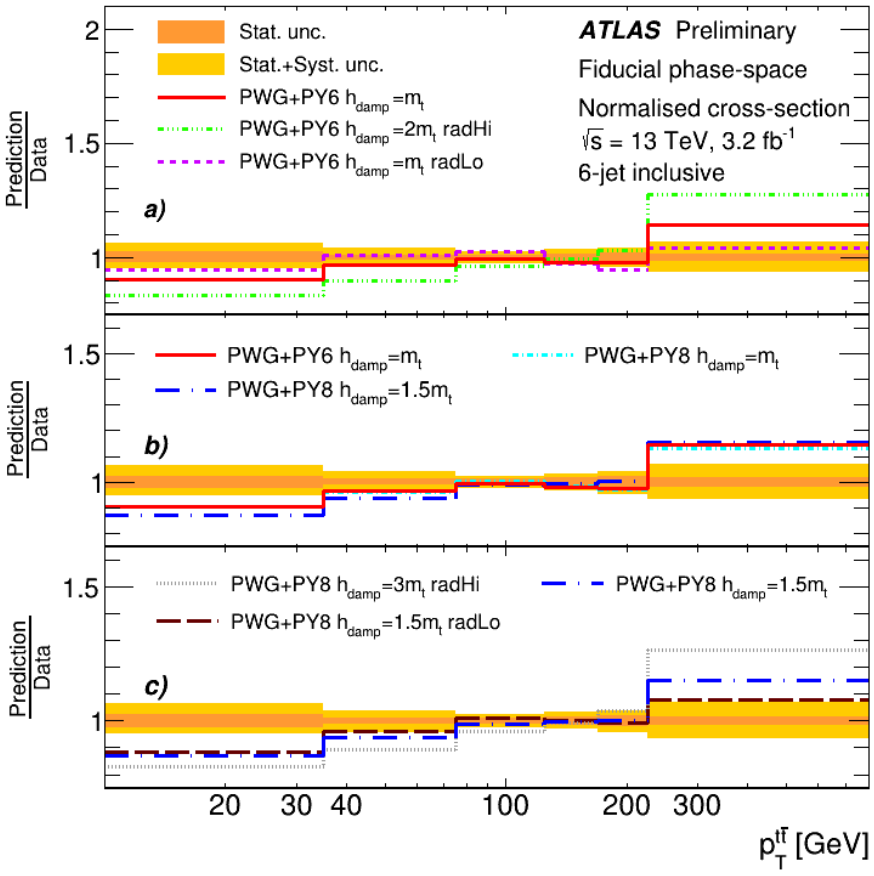

FIGURE 10.7: Normalised differential cross sections as a function of $p_{\mathrm{T}}^{\mathrm{t\bar{t}}}$ in the 6-jet inclusive configuration in the fiducial phase space.

10.1.1 Comparison with the CMS results

As already mentioned in Chapter 4, a similar measurement of the differential cross sections in different bins of jet multiplicity in the ℓ+jets channel, was performed by the CMS collaboration; the definition of the configurations by the CMS collaboration is similar to those here defined: 0 additional jets, 1 additional jets, 2 additional jets and at least 3 additional jets.

These measurements are reported here, the distributions shown are as function of the $p_{\mathrm{T}}^{t,had}$ and of the $p_{\mathrm{T}}^{t\bar{t}}$ observables, in Figures 10.9 and 10.10, respectively.

The results obtained by the two collaborations have a similar agreement and a similar trend in all the configurations. For example, a slope is observed in the 4-jet exclusive configuration of the ATLAS results as well as in the correspondent 0 additional jet configuration of the CMS measurement, for both the reported observables. Another observed common behaviour of the two measurements, for the $p_{\mathrm{T}}^{t,had}$ observable is the tendency of some of the predictions to better estimate data with the increase of the jet multiplicity.

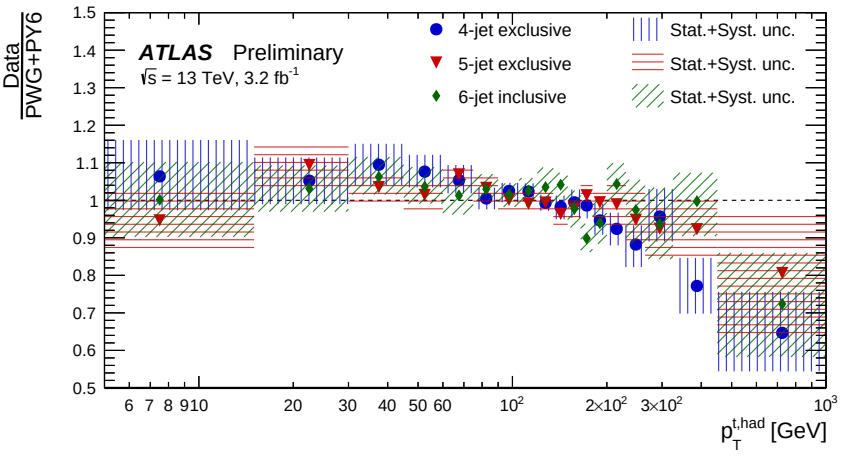

(a)

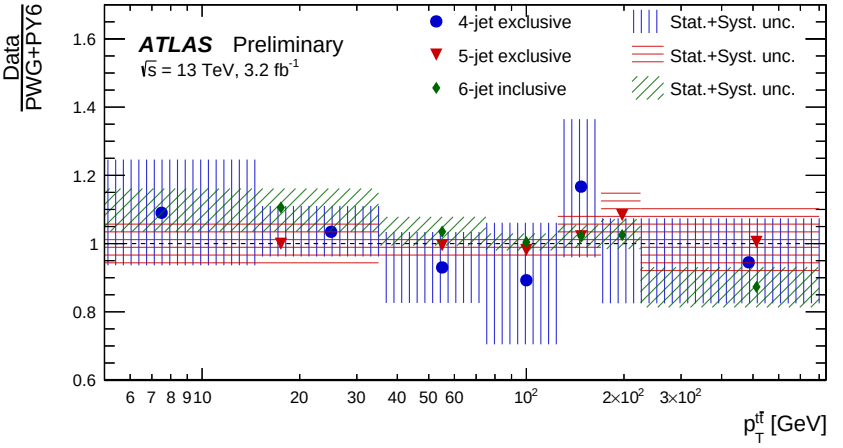

(b)

FIGURE 10.8: Normalised (a) ratio of data to the nominal prediction as a function of $p_{\mathrm{T}}^{\mathrm{t,had}}$ and (b) as function of the $p_{\mathrm{T}}^{\mathrm{t\bar{t}}}$ in the 4-jet exclusive, 5-jet exclusive and 6-jet inclusive configurations.

In general can be affirmed that the CMS results are compatible, both inclusively and exclusively, with those obtained by the ATLAS collaboration and above reported.

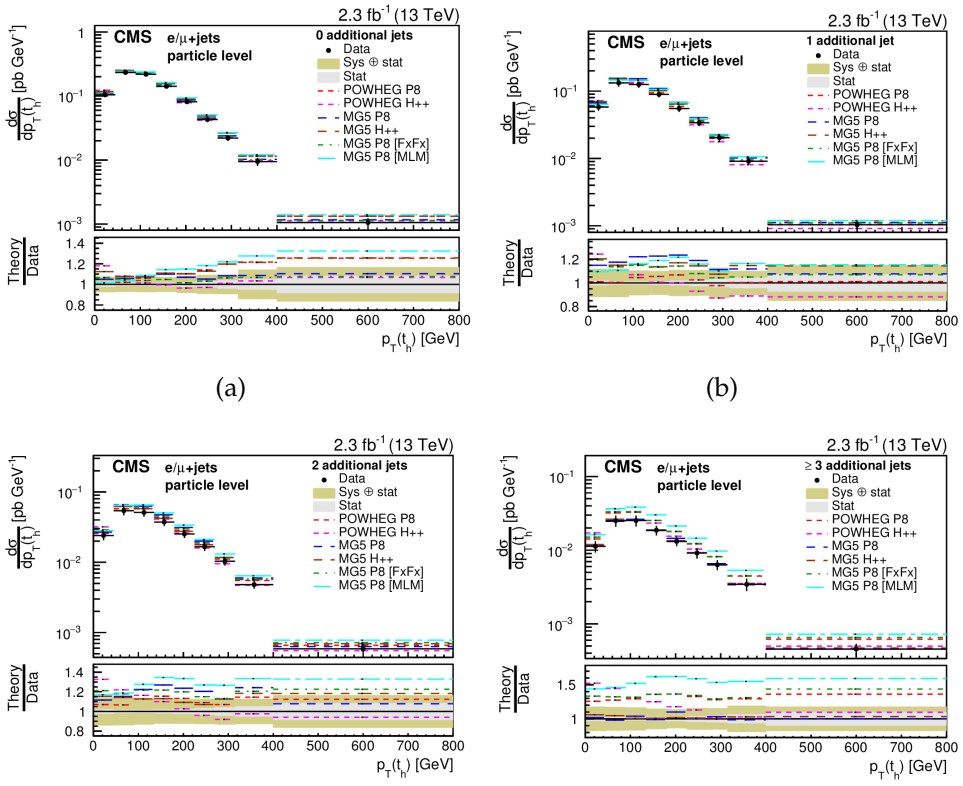

FIGURE 10.9: Absolute differential cross sections obtained by the CMS collaboration in the fiducial phase space as a function of $p_{\mathrm{T}}^{\mathrm{t,had}}$: (a) in the 0 additional jet configuration, (b) in the 1 additional jet configuration, (c) in the 2 additional jet configuration and (d) in the configuration with at least 2 additional jets.

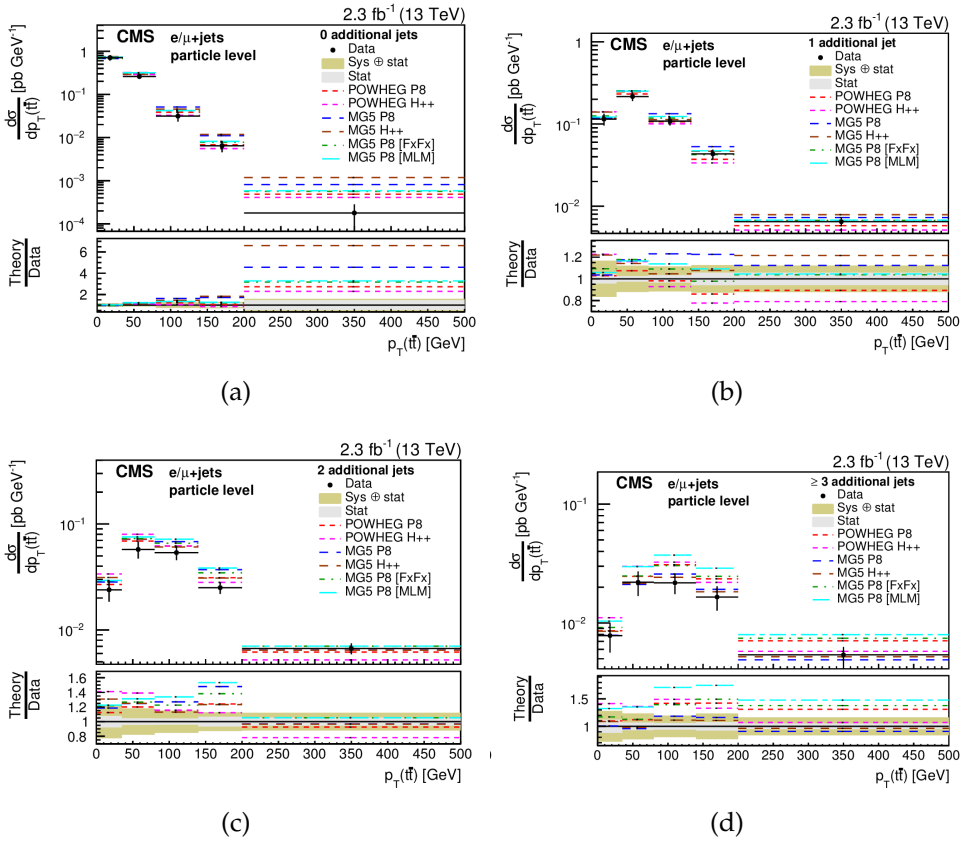

FIGURE 10.10: Absolute differential cross sections obtained by the CMS collaboration in the fiducial phase space as a function of $p_{\mathrm{T}}^{\mathrm{t\bar{t}}}$: (a) in the 0 additional jet configuration, (b) in the 1 additional jet configuration, (c) in the 2 additional jet configuration and (d) in the configuration with at least 2 additional jets.

Conclusions

In this thesis, measurements of the differential cross sections of top quark pair production in association with jets in the ℓ+jets channel are reported. In addition, test results relative to the certification of the MicroMegas chambers are presented.

The large quantity of top quark production due to the high value of the luminosity reached by the LHC, has allowed to measure the differential cross sections of top quark pair produced in association with jets with a very high precision. Moreover, the measurements will help the improvement of the MC tuning for the future MC generation.

The measurements have been performed at particle level, using data collected by the ATLAS detector during 2015 and corresponding to a total integrated luminosity of $3.2\ fb^{-1}$; after the substraction of several background components, the results have been compared with different theoretical predictions.

Differences between the data and some of the predictions have been observed and become more evident with the increasing jets multiplicity. Overall a good agreement within the uncertainties is shown for most of the MC predictions used as comparison.

Concerning the validation of the MicroMegas chamber prototype, the obtained results are in good agreement with the project requirement performances.

As future plans, for what concerns the MicroMegas chambers, tests using cosmic rays will be performed on all the chambers produced by the Italian collaboration to certify them performances before the installation on the Muon Spectrometer.

Concerning the top quark differential precision cross section measurements, the even bigger amount of data collected by the ATLAS detector during the 2016-2017 years and the relative increasing of the statistic, will allow to perform more precision measurements of the one-dimensional cross sections and to do double-differential cross sections measurements as functions of

several observables. The double-differential measurement is expected to impose stronger constraints on the gluon distribution than single-differential measurements.

Appendix A

Uncertainties tables

In this Appendix the systematic uncertainties tables are reported for all the variables described in this thesis, in the three configurarions. Tables A.1–A.10 show the systematic uncertainties tables for the absolute distributions, while, Tables A.13–A.12 the systematic uncertainties for the normalised distributions.

Bins [GeV]	0–15	15–30	30–45	45–60	60–75	75–90	90–105	105–120	120–135	135–150	150–165	165–180	180–200	200–230	230–265	265–325	325–450	450–1000
$d\sigma$ / $d p_{\mathrm{T}}^{t,had}$ [pb/GeV]	$4.06 \cdot 10^{-2}$	$1.19 \cdot 10^{-1}$	$2.00 \cdot 10^{-1}$	$2.62 \cdot 10^{-1}$	$3.10 \cdot 10^{-1}$	$3.29 \cdot 10^{-1}$	$3.48 \cdot 10^{-1}$	$3.31 \cdot 10^{-1}$	$2.82 \cdot 10^{-1}$	$2.31 \cdot 10^{-1}$	$1.89 \cdot 10^{-1}$	$1.52 \cdot 10^{-1}$	$1.15 \cdot 10^{-1}$	$7.99 \cdot 10^{-2}$	$4.87 \cdot 10^{-2}$	$2.81 \cdot 10^{-2}$	$7.24 \cdot 10^{-3}$	$4.13 \cdot 10^{-4}$
Total Uncertainty [%]	±15.6	±12.4	±12.2	±11.9	±10.6	±10.3	±9.6	±9.6	±9.7	±9.6	±9.8	±9.8	±9.9	±9.9	±9.9	±9.8	±10.1	±11.6
Statistics [%]	±4.7	±2.4	±1.9	±1.6	±1.5	±1.4	±1.3	±1.3	±1.4	±1.5	±1.7	±1.8	±2.0	±2.2	±2.7	±2.7	±3.9	±9.0
Systematics [%]	±14.9	±11.9	±11.9	±11.6	±10.2	±10.1	±9.2	±9.3	±9.3	±9.2	±9.5	±9.5	±9.7	±9.8	±9.8	±9.7	±9.5	±8.3
b-Tagged jet energy scale (JES) [%]	±0.28	±0.13	-	±0.21	±0.33	±0.19	±0.02	±0.29	±0.28	±0.87	±0.84	±0.72	±0.78	±0.83	±0.63	±0.65	±0.46	±1.14
Effective detector NP set 1 (JES) [%]	±1.23	±0.31	±0.60	±0.41	±1.25	±1.73	±1.80	±1.58	±1.55	±1.70	±1.09	±0.25	±0.51	±0.59	-	-	-	-
Effective detector NP set 2 (JES) [%]	±1.94	±1.84	±1.86	±2.88	±2.37	±2.78	±2.93	±2.85	±2.84	±2.84	±2.18	±2.81	±1.26	±1.37	±0.90	±1.37	±0.63	±2.21
Effective detector NP set 3 (JES) [%]	±0.92	±0.92	±1.26	±0.83	±1.00	±0.68	±1.09	±0.43	±0.16	±0.21	±0.45	±0.74	±0.96	±1.37	±1.31	±1.03	±3.03	±5.41
Effective detector NP set 3 (JES) [%]	±0.22	±0.38	±0.78	±0.43	±0.46	±0.44	±0.56	-	-	±0.19	±0.28	±0.51	±0.66	±1.03	±0.50	±1.88	±7.64	±2.72
Effective detector NP set 4 (JES) [%]	±4.11	±0.97	±0.83	±0.52	±0.63	±0.64	±0.32	±0.29	-	±0.22	±0.25	±0.44	±1.07	±1.25	±1.11	±1.70	±2.40	-
Effective detector NP set 4 (JES) [%]	±0.34	±0.60	±0.18	±0.32	±0.46	±0.45	±0.18	-	±0.11	±0.24	±0.49	±0.25	±0.35	±0.58	±0.44	±0.27	±0.56	±0.23
Effective detector NP set 5 (JES) [%]	±0.34	±0.30	±0.32	±0.26	±0.18	±0.27	±0.30	-	±0.15	±0.34	±0.49	±0.19	±0.45	±0.59	±0.41	±0.14	±0.36	±0.33
Effective detector NP set 5 (JES) [%]	±0.24	-	±0.27	-	-	-	-	±0.18	±0.10	±0.17	±0.12	-	-	-	-	±0.29	±0.21	-
Effective detector NP set 6 resTerm (JES) [%]	±0.26	±0.26	-	±0.22	-	±0.15	-	-	-	-	-	-	-	±0.16	±0.17	-	±0.32	±0.53
η intercalibration model (JES) [%]	±0.15	-	±0.22	±0.13	-	-	±0.20	-	-	-	-	-	-	-	-	±0.31	±0.14	±0.42
η intercalibration model (JES) [%]	±0.48	±0.38	±0.96	±0.53	±0.64	-	±0.36	±0.27	±0.27	±0.03	±0.73	±0.22	±0.15	±0.12	±0.33	-	±0.35	±0.42
η intercalibration total stat (JES) [%]	±0.89	±0.43	±0.47	±0.25	-	±0.17	±0.39	±0.69	±0.78	±0.72	±0.54	±0.81	±1.21	±0.58	-	±1.13	±0.35	±1.33
Flavour composition (JES) [%]	±0.42	±0.18	±0.26	±0.19	±0.25	±0.36	-	±0.15	-	±0.26	±0.30	-	±0.30	±0.34	±0.41	-	-	-
Flavour response (JES) [%]	±2.12	±1.73	±0.26	±0.18	±1.40	±0.68	±0.59	±0.33	±0.36	±0.23	±0.23	-	-	-	±0.46	±0.58	±0.14	±0.83
Flavour response (JES) [%]	±2.12	±1.73	±0.26	±0.18	±1.40	±0.68	±0.59	±0.54	±0.44	±1.06	±0.61	±0.56	±1.12	±0.26	±0.87	±1.17	±0.91	±2.06
Pile-up offset μ (JES) [%]	±0.33	±0.17	±0.17	±0.17	±0.47	±0.31	-	±0.31	±0.44	±0.31	±0.25	±0.45	±0.42	±0.41	±0.56	±0.51	±0.39	±1.11
Pile-up offset μ (JES) [%]	±0.70	±0.71	±1.36	±0.76	±0.69	±0.71	±0.30	-	-	-	-	-	-	-	±0.19	-	±0.25	±1.27
Pile-up offset N_{PV} (JES) [%]	±0.53	±0.23	-	-	-	±0.13	-	-	-	-	-	-	-	-	±0.19	-	-	±0.55
Pile-up offset N_{PV} (JES) [%]	±0.48	±0.17	±0.33	±0.23	-	±0.23	±0.34	-	-	-	-	-	-	-	±0.23	±0.15	-	±0.22
Pile-up offset p_T (JES) [%]	±0.45	±0.12	-	±0.21	±0.17	-	±0.21	±0.10	-	±0.14	-	±0.12	-	-	-	±0.25	-	±0.49
Pile-up offset p_T (JES) [%]	±0.33	±0.18	±0.37	±0.26	±0.31	±0.17	-	-	-	±0.13	-	±0.20	±0.44	±0.19	-	-	±0.39	-
Pile-up offset ρ topology (JES) [%]	±0.33	±0.18	±0.46	±0.28	±0.31	±0.17	-	±0.45	±0.41	±0.43	±0.39	±0.29	-	±0.19	-	±0.23	±0.21	±0.31
Pile-up offset ρ topology (JES) [%]	-	-	-	-	-	-	±0.40	-	-	-	-	-	-	±0.16	-	-	-	-
Punch-through (JES) [%]	±2.15	±0.79	±0.80	±0.61	±1.20	±0.38	±0.56	±0.99	±1.01	±1.11	±0.98	±0.86	±0.81	±0.92	±0.29	±0.68	±0.46	±1.23
Single particle high-p_T (JES) [%]	-	-	-	-	-	-	-	-	-	-	-	-	-	-	-	-	-	±0.16
Jet energy resolution [%]	-	-	-	-	-	-	-	-	-	-	-	-	-	-	-	-	-	±0.21
Jet vertex fraction [%]	±1.83	±3.55	±3.14	±2.81	±3.73	±2.94	±2.79	±2.51	±2.13	±1.52	±1.31	±1.49	±1.82	±0.94	±0.87	±1.52	±0.29	±4.55
b-Quark tagging efficiency (eigenvector 0) [%]	±4.04	±3.99	±4.07	±3.95	±3.58	±3.11	±2.83	±2.64	±2.18	±1.69	±1.44	±1.15	±0.85	±0.52	±0.25	-	±0.62	±0.51
b-Quark tagging efficiency (eigenvector 0) [%]	-3.99	-3.90	-4.02	-3.92	-3.56	-3.10	-2.84	-2.68	-2.19	-1.72	-1.46	-1.14	-0.87	-0.57	-0.26	±0.64	±0.64	±0.50
b-Quark tagging efficiency (eigenvector 0) [%]	-5.06	-4.89	-4.86	-4.73	-4.59	-4.44	-4.27	-4.21	-4.12	-4.02	-4.04	-4.00	-3.93	-3.90	-3.82	-3.84	-3.95	-4.18
b-Quark tagging efficiency (eigenvector 1) [%]	±5.16	±4.89	±4.95	±4.62	±4.67	±4.52	±4.35	±4.27	±4.19	±4.10	±4.13	±4.02	±3.99	±3.97	±3.94	±3.94	±4.04	±4.26
b-Quark tagging efficiency (eigenvector 1) [%]	±0.88	±0.89	±0.93	±0.98	±1.03	±1.12	±1.20	±1.32	±1.46	±1.62	±1.84	±2.07	±2.33	±2.74	±3.27	±3.80	±4.64	±5.35
b-Quark tagging efficiency (eigenvector 2) [%]	±1.87	±1.83	±1.84	±1.62	±1.37	±1.58	±1.46	±1.42	±1.35	±1.23	±1.10	±0.96	±0.78	±0.55	±0.25	-	±0.55	±0.93
b-Quark tagging efficiency (eigenvector 2) [%]	-1.65	-1.62	-1.63	-1.61	-1.55	-1.51	-1.45	-1.42	-1.33	-1.20	-1.09	-0.97	-0.77	-0.56	-	-0.84	-0.95	-1.18
b-Quark tagging efficiency (eigenvector 3) [%]	-	-	-	-	-	-	±0.11	±0.14	±0.18	±0.22	±0.22	±0.22	±0.23	±0.16	±0.10	±0.34	±0.55	-
b-Quark tagging efficiency (eigenvector 3) [%]	-	-	-	-	-	-	-	-	-	-	-	-	-	±0.17	-	-	-	-
b-Quark tagging efficiency (eigenvector 4) [%]	-	-	-	-	-	-	-	-	-	-	-	-	-	-	-	±0.16	±0.23	-
c-Quark tagging efficiency (eigenvector 0) [%]	±2.65	±2.62	±2.48	±2.42	±2.30	±2.08	±1.79	±1.69	±1.53	±1.32	±1.46	±1.35	±1.17	±1.08	±0.97	±0.97	±0.80	±1.14
c-Quark tagging efficiency (eigenvector 0) [%]	-2.65	-2.62	-2.49	-2.42	-2.30	-2.08	-1.73	-1.63	-1.32	-1.12	-1.36	-1.16	-1.14	-	±0.98	-	±0.81	±1.15
c-Quark tagging efficiency (eigenvector 1) [%]	±0.42	±0.41	±0.34	±0.33	±0.32	±0.28	±0.23	±0.19	±0.14	±0.11	-	-	-	-	-	±0.11	±0.13	±0.12
c-Quark tagging efficiency (eigenvector 2) [%]	±0.17	±0.17	±0.21	±0.21	±0.22	±0.24	±0.25	±0.24	±0.22	±0.21	±0.18	±0.15	±0.13	±0.12	-	±0.12	-	-
c-Quark tagging efficiency (eigenvector 3) [%]	±0.15	±0.13	±0.11	±0.10	-	-	-	-	-	-	-	-	-	-	-	-	-	-
Light-jet tagging efficiency (eigenvector 0) [%]	-3.61	-2.74	-2.39	-1.95	-1.52	-1.41	-1.31	±1.20	-1.16	-1.24	-1.40	-1.41	-1.34	±1.09	-1.17	-1.33	-1.51	-2.04
Light-jet tagging efficiency (eigenvector 0) [%]	-4.72	±3.25	±2.63	±2.20	-1.99	-1.49	-1.35	-	-1.20	-1.23	-1.43	-1.45	-1.45	-	±1.23	±1.35	±1.93	±2.12
Light-jet tagging efficiency (eigenvector 1) [%]	-	-	-	-	-	-	-	-	-	-	-	-	-	-	-	-	-0.12	-
Light-jet tagging efficiency (eigenvector 2) [%]	±0.37	±0.29	±0.25	±0.19	±0.12	±0.11	-	-	-	-	-	-	-	-	-	-	-	-
Light-jet tagging efficiency (eigenvector 2) [%]	-	-0.28	-	-0.18	-	-	-	-	-	-	-	-	-	-	-	-	-	-
Light-jet tagging efficiency (eigenvector 3) [%]	-	-	-	-	-	-	-	-	-	-	-	-	-	-	-	-	-	-
Light-jet tagging efficiency (eigenvector 4) [%]	-	-	-	-	-	-	-	-	-	-	-	-	-	-	-	-	-	-
Light-jet tagging efficiency (eigenvector 5) [%]	-	-	-	-	-	-	-	-	-	-	-	-	-	-	-	-	-	-
Light-jet tagging efficiency (eigenvector 6) [%]	-	-	-	-	-	-	-	-	-	-	-	-	-	-	-	-	-	-
Light-jet tagging efficiency (eigenvector 7) [%]	-	-	-	-	-	-	-	-	-	-	-	-	-	-	-	-	-	-
Light-jet tagging efficiency (eigenvector 8) [%]	-	-	-	-	-	-	-	-	-	-	-	-	-	-	-	-	-	-
Light-jet tagging efficiency (eigenvector 9) [%]	-	-	-	-	-	-	-	-	-	-	-	-	-	-	-	-	-	-
Light-jet tagging efficiency (eigenvector 10) [%]	-	-	-	-	-	-	-	-	-	-	-	-	-	-	-	-	-	-
Light-jet tagging efficiency (eigenvector 11) [%]	-	-	-	-	-	-	-	-	-	-	-	-	-	-	-	-	-	-
Light-jet tagging efficiency (eigenvector 12) [%]	-	-	-	-	-	-	-	-	-	-	-	-	-	-	-	-	-	-
Light-jet tagging efficiency (eigenvector 13) [%]	-	-	-	-	-	-	-	-	-	-	-	-	-	-	-	-	-	-
b-Quark tagging extrapolation [%]	-	-	-	-	-	-	-	-	-	-	-	±0.13	±0.16	±0.31	±0.83	±1.84	-3.70	+5.91
b-Quark tagging extrapolation from c-Quark [%]	±0.22	±0.15	±0.16	±0.16	±0.14	±0.16	±0.17	±0.15	+0.11 -0.12	-	-	-0.12	-0.17	-0.32	-	-1.82	-3.63	-5.79
Electron energy resolution [%]	-0.58	-	-	-	-	+0.17	-	-	-	-	-	-	-	-	-	-	-	±0.11
Electron energy scale [%]	-	-	-	-	-	-	-	-	-	-	-	-	-	-	-	-	-	-0.25
Electron trigger efficiency [%]	±0.26	±0.25	±0.25	±0.25	±0.24	±0.24	±0.24	±0.25	±0.26	±0.26	+0.27 -0.26	+0.28 -0.27	+0.28 -0.29	±0.29	±0.30	±0.32	±0.32	±0.34
Electron reconstruction efficiency [%]	±0.15	±0.15	±0.15	±0.15	±0.16	±0.16	±0.17	±0.17	±0.18	±0.19	±0.20	±0.20	±0.22	±0.22	±0.22	±0.25	±0.26	±0.29
Electron identification efficiency [%]	±0.39	±0.39	±0.38	±0.38	±0.38	±0.38	±0.40	±0.40	±0.42	±0.44	±0.46	±0.48	±0.51	±0.56	±0.63	±0.76	±0.96	±0.98
Electron isolation efficiency [%]	±0.12	±0.12	±0.11	±0.12	±0.12	±0.12	±0.12	±0.12	±0.13	+0.13 -0.14	+0.16 -0.15	+0.17 -0.16	+0.17 -0.18	±0.21	±0.26	±0.32	±0.47	±0.70
Muon energy scale [%]	-	-	-	-	-	-	-	-	-	-	-	-	-	-	-	-	-	-
Muon (MS) momentum resolution [%]	-	-	-	-	-	-	-	-	-	-	-	-	-	-	-	-	-	-
Muon (ID) momentum resolution [%]	-	-	-	-	-	-	-	-	-	-	-	-	-	-	-	-	-	-
Muon trigger efficiency stat [%]	±0.68	±0.61	±0.61	±0.60	±0.61	±0.58	±0.57	±0.57	±0.57	±0.56	±0.56	±0.55	±0.53	±0.55	±0.55	±0.55	±0.57	±0.55
Muon trigger efficiency stat [%]	-0.78	-0.63	-0.63	-0.62	-0.61	-0.60	-0.58	-0.58	-0.58	-0.58	-0.57	-0.57	-0.57	-0.57	-0.57	-0.57	-0.57	-0.57
Muon trigger efficiency syst [%]	±0.27	±0.27	±0.27	±0.26	±0.26	±0.25	±0.25	±0.24	±0.24	±0.24	±0.24	±0.24	±0.24	±0.24	±0.24	±0.24	±0.24	±0.24
Muon identification stat [%]	-	-	-	-	-	-	-	-	-	-	-	-	-	-	-	-	-	-
Muon identification syst [%]	±0.18	±0.16	±0.16	±0.16	±0.16	±0.16	±0.16	±0.16	±0.16	+0.17 -0.16	±0.17	±0.18	±0.18	±0.20	±0.22	±0.25	±0.31	+0.46 -0.45
Muon isolation efficiency stat [%]	-	-	-	-	-	-	-	-	-	-	-	-	-	-	-	-	-	-
Muon isolation efficiency syst [%]	±0.12	±0.11	±0.11	±0.11	±0.11	±0.10	±0.10	±0.10	±0.10	+0.10 -0.11	+0.11 -0.10	+0.11 -	- -0.11	±0.10	±0.10	±0.10	±0.10	+0.14 -0.13
Muon TTVA efficiency stat [%]	-	-	-	-	-	-	-	-	-	-	-	-	-	-	-	-	-	-
Muon TTVA efficiency syst [%]	-	-	-	-	-	-	-	-	-	-	-	-	-	-	-	-	-	-
E_T^{miss} Soft jet resolution para [%]	±0.21	±0.18	±0.15	±0.12	-	±0.10	±0.10	-	-	-	-	-	-	-	-	-	-	±0.15
E_T^{miss} Soft jet resolution perp [%]	±0.12	±0.11	±0.17	±0.17	±0.15	±0.10	-	-	-	-	-	-	-	-	-	-	-	±0.16
E_T^{miss} Soft jet scale [%]	-	-	-	-	-	-	-	-	-	-	-	-	-	-	-	-	-	-
Luminosity [%]	±2.04	±2.04	±2.04	±2.04	±2.04	±2.04	±2.04	±2.04	±2.04	±2.04	±2.04	±2.04	±2.04	±2.04	±2.04	±2.04	±2.04	±2.04
W+jets CA_2ex stat error [%]	-	-	-	-	-	-	-	-	-	-	-	-	-	-	-	-	-	-
W+jets CA_3ex stat error [%]	-	-	-	-	-	-	-	-	-	-	-	-	-	-	-	-	-	-
W+jets CA_4incl stat error [%]	±0.38	±0.27	±0.24	±0.21	±0.16	±0.12	±0.10	-	±0.10	±0.10	±0.10	-	-	-	-	-	±0.11	±0.15
W+jets Fc stat error [%]	±0.35	±0.34	±0.24	±0.20	±0.17	±0.12	-	-	±0.11	±0.12	±0.11	-	-	-	-	-	-	-
W+jets Fcc stat error [%]	±2.35	±2.02	±2.03	±1.88	±1.52	±1.22	±1.05	±0.93	±0.89	±0.95	±1.00	±0.82	±0.81	±0.86	±0.87	±0.87	±0.90	±1.69
W+jets Flight stat error [%]	-	-	-	-	-	-	-	-	-	-	-	-	-	-	-	-	-	-
Single top cross-section [%]	±0.93	±0.97	±0.97	±0.93	±0.89	±0.87	±0.84	±0.82	±0.82	±0.84	±0.86	±0.89	±0.89	±0.90	±0.93	±0.97	±1.16	±1.62
Z+jets cross-section [%]	±0.95	±0.76	±0.99	±1.18	±1.14	±0.92	±0.67	±0.87	±0.68	±0.34	±0.54	±0.62	±0.35	±0.45	±0.30	±0.55	±0.24	±0.24
Diboson cross-section [%]	±0.12	±0.13	±0.13	±0.12	±0.11	±0.11	±0.10	-	-	±0.10	±0.10	±0.10	±0.10	±0.10	±0.12	±0.16	±0.15	±0.50
$t\bar{t}V$ cross-section [%]	-	-	-	-	-	-	-	-	-	-	-	-	-	-	-	-	-	±0.11
Monte Carlo sample statistics [%]	±3.36	±1.43	±1.03	±0.87	±0.69	±0.69	±0.51	±0.58	±0.54	±0.54	±0.61	±0.69	±0.76	±0.77	±0.84	±1.03	±1.24	±2.09
ISR/FSR + scale [%]	-5.51	-1.67	-2.09	-3.50	-2.20	-2.99	-2.71	-3.10	-3.49	-3.03	-1.93	-3.42	-4.81	-4.10	-4.31	-3.29	-3.98	-
Alternate hard-scattering model [%]	+1.35 ±5.00	+2.55 ±2.20	+2.44 ±0.78	+1.25 ±1.25	+2.62 ±0.88	+1.48 ±0.21	+1.82 ±1.61	+1.38 ±1.09	+2.02 ±0.27	+3.33 ±1.14	+3.68 ±1.20	+2.08 ±0.25	+0.70 ±0.85	+2.05 ±1.89	+2.63 ±3.68	+3.33 ±3.64	-0.99 ±4.24	-6.82 ±5.85
Alternate parton-shower model [%]	±4.14	±2.61	±3.68	±3.15	±3.25	±3.52	±3.25	±2.89	±3.15	±3.70	±2.42	±2.13	±3.97	±4.01	±3.25	±4.28	±4.96	±9.62
Inter PDF [%]	±0.21	-	-	-	-	-	-	-	-	-	-	±0.12	-	-	-	-	-	±0.28
Intra PDF [%]	±0.14	±0.10	-	-	-	-	-	-	-	-	-	-	-	-	±0.23	±0.10	±0.15	±0.38
Fakes overall normalization [%]	±5.25	±5.85	±6.28	±6.06	±5.13	±5.32	±4.46	±3.26	±3.04	±3.23	±2.98	±2.17	±1.87	±2.60	±2.54	±1.08	±2.89	±4.21
Real lepton efficiency stat [%]	-	-	±0.10	±0.10	±0.11	±0.11	±0.12	+0.13 -0.12	+0.13 -0.12	+0.13 -0.13	+0.16 -0.15	+0.17 -0.16	+0.19 -0.17	±0.20	+0.23 -0.20	±0.26	+0.40 -0.31	±0.84 ±0.47
Fake lepton efficiency MC scale [%]	+0.56 -0.65	+0.79 -0.84	+0.81 -0.80	+0.90 -0.98	+0.74 -0.98	+0.94 -1.10	+0.78 -0.91	+0.69 -0.69	+0.57 -0.80	+0.72 -0.96	+0.73 -0.93	+0.57 -0.96	+0.65 -0.93	+0.57 -0.78	+0.59 -0.81	- -	-1.00	-0.96
Fake lepton efficiency alternate CR [%]	±0.19	±0.34	±0.31	±0.37	±0.45	±0.58	±0.50	±0.40	±0.39	±0.36	±0.28	±0.16	±0.20	±0.34	±0.13	±0.22	±0.19	±0.20

TABLE A.1: Systematic uncertainties for the absolute differential cross-section at particle-level for $pt_{\mathrm{T}}^{t,had}$ in the 4-jet exclusive configuration.

Bins [GeV]	0–15	15–30	30–45	45–60	60–75	75–90	90–105	105–120	120–135	135–150	150–165	165–180	180–200	200–230	230–265	265–325	325–450	450–1000
$d\sigma / d p_{\mathrm{T}}^{t,had}$ [pb/GeV]	$2.17 \cdot 10^{-2}$	$7.54 \cdot 10^{-2}$	$1.17 \cdot 10^{-1}$	$1.50 \cdot 10^{-1}$	$1.83 \cdot 10^{-1}$	$1.89 \cdot 10^{-1}$	$1.82 \cdot 10^{-1}$	$1.70 \cdot 10^{-1}$	$1.52 \cdot 10^{-1}$	$1.29 \cdot 10^{-1}$	$1.11 \cdot 10^{-1}$	$9.58 \cdot 10^{-2}$	$7.60 \cdot 10^{-2}$	$5.61 \cdot 10^{-2}$	$3.55 \cdot 10^{-2}$	$1.97 \cdot 10^{-2}$	$6.68 \cdot 10^{-3}$	$3.67 \cdot 10^{-4}$
Total Uncertainty [%]	±15.3	±14.1	±14.1	±14.9	±12.4	±12.9	±14.6	±12.4	±12.1	±12.6	±12.5	±12.9	±10.9	±10.9	±10.1	±9.80	±11.8	±21.1
Statistics [%]	±6.1	±2.9	±2.3	±2.0	±1.8	±1.7	±1.7	±1.8	±1.9	±2.0	±2.1	±2.3	±2.4	±2.6	±3.2	±3.3	±3.9	±9.3
Systematics [%]	±14.1	±13.9	±13.1	±13.7	±12.3	±12.9	±13.4	±12.2	±12.2	±12.0	±11.7	±11.7	±10.6	±10.6	±10.1	±9.62	±11.1	±19.7
b-Quark tagging efficiency (eigenvector 0) [%]	±13.1	±13.1	±12.3	±13.2	±11.8	±12.4	±13.2	±11.8	±11.8	±11.6	±11.3	±11.3	±10.2	±10.2	±9.77	±9.22	±10.7	±18.7
b-Quark tagging efficiency (eigenvector 1) [%]	±0.91	±0.33	-	-	±0.47	±0.45	±0.39	±0.71	±0.76	±0.80	±0.83	±1.17	±0.67	±0.96	±0.81	±0.87	±0.81	±1.91
Effective detector NP set 1 (JES) [%]	+7.02 −7.16	+5.46 −5.88	+6.96 −7.39	+5.75 −7.52	+5.93 −7.13	±7.01	+6.71 −7.61	+6.88 −7.82	+6.60 −7.72	+6.75 −7.99	+6.17 −6.48	+5.55 −6.34	+5.54 −5.35	+4.43 −6.41	+3.50 −4.28	+3.11 −3.37	+2.82 −3.82	−3.40
Effective detector NP set 2 (JES) [%]	+1.24 −1.24	+2.19 −2.19	+2.04 −2.04	+1.70 −1.70	+2.23 −2.23	+1.94 −1.94	+1.28 −1.28	+1.47 −1.47	+0.95 −0.95	+0.69 −0.69	+0.39 -	-	+0.26 −0.26	-	−0.47 −0.47	−0.80 −0.80	−0.73 −0.73	−1.52 −1.52
Effective detector NP set 3 (JES) [%]	+0.65 −1.01	+0.62 −1.25	+0.91 −1.25	+0.99 −0.71	+0.77 −0.69	+0.82 −0.88	+0.46 −0.63	+0.39 −0.33	+0.15 −0.28	-	-	+0.41 +0.32	−0.41 +0.50	−0.66 +0.29	−0.73 +0.15	−0.44 +1.21	−2.59 +2.79	−2.02
Effective detector NP set 4 (JES) [%]	−0.91 +0.30	+0.61 -	−0.75 +0.13	−0.47 +0.15	−0.39 +0.36	−0.52 +0.48	−0.35 +0.13	-	-	-	−0.33 −0.20	−0.17 -	+0.25 −0.29	+0.16 −0.36	+0.25 −0.41	+0.40 −0.24	−0.42 +0.34	−0.17 +0.28
Effective detector NP set 5 (JES) [%]	−0.31	-	−0.13	-	-	-	-	-	-	−0.16	-	+0.24	-	-	-	-	−0.50	−0.28
Effective detector NP set 6 resTerm (JES) [%]	-	+0.12	-	+0.16	-	-	-	-	-	-	-	-	+0.25	−0.15	−0.10	+0.21	+0.13	+0.85
η intercalibration model (JES) [%]	−1.16	+1.18 −1.51	+2.81 −2.21	+1.02 −1.76	+1.06 −1.82	+1.81 −1.80	+1.07 −2.26	+1.91 −2.61	+2.65 −2.66	+2.21 −2.17	+1.88 −1.95	+1.98 −1.93	+2.37 −1.96	+1.50 −2.08	+1.01 −1.24	+1.05 −0.91	+0.83 −2.04	+1.61 −0.69
η intercalibration total stat (JES) [%]	-	+0.34 −0.66	+0.79 −0.80	+0.79 −0.76	+0.96 −0.72	+0.92 −0.74	+0.62 −1.10	+0.97 −1.09	+0.94 −1.07	+1.01 −0.71	+0.81 −0.99	+0.91 −1.00	+1.22 −1.01	+0.76 −1.05	+0.97 −0.48	+1.12 −0.53	+0.64 −1.06	+1.22 −0.24
Flavour composition (JES) [%]	+5.78 −6.74	+3.68 −4.18	+4.58 −5.39	+3.61 −6.18	+3.55 −5.55	+3.12 −5.12	+3.63 −5.63	+3.66 −5.66	+3.66 −6.66	+3.97 −5.97	+3.63 −5.63	+3.74 −4.74	+3.15 −4.15	+3.28 −5.28	+3.07 −3.07	+2.48 −2.48	+2.48 −2.48	−2.15
Flavour response (JES) [%]	−1.18	−1.55	−1.44	−1.20	−1.27	−1.22	−1.50	−1.46	−1.76	−1.45	−1.44	−1.91	−1.66	−1.33	−0.84	−0.86	−1.42	+0.51
Pile-up offset μ (JES) [%]	+0.54 −0.91	+0.69 −0.40	+1.70 −0.95	+0.92 −0.30	+0.97 −0.39	+1.21 −0.40	+0.76 −0.49	+1.20 −0.23	+1.23 −0.32	+1.46 −0.37	+1.22 −0.28	+1.39 −0.27	+1.59 −0.37	+1.11 −0.27	+0.68 -	+0.89 +0.34	+0.57 -	+0.38 −0.26
Pile-up offset μ (JES) [%]	−0.91	-	−0.95	−0.47	−0.24	−0.40	−0.49	−0.29	−0.35	−0.31	−0.28	−0.24	−0.39	−0.47	-	−0.40	-	−0.31
Pile-up offset N_{PV} (JES) [%]	-	-	+0.10 −0.19	-	+0.23 -	-	−0.30 -	-	-	-	-	+0.24 −0.35	−0.16 +0.40	-	-	+0.24 -	-	+0.34 −0.15
Pile-up offset p_{T} (JES) [%]	−0.23	−0.39	−0.23	−0.15	−0.16	+0.18	-	-	-	-	+0.11	+0.13	-	-	+0.26	+0.23	-	+0.32
Pile-up offset ρ topology (JES) [%]	+0.82 +1.47	+0.36 +1.62	+0.27	+0.19 +1.62	+0.29 +1.93	+0.25 +2.03	+1.70	+2.21	+1.97	+2.02	+1.96	+1.92	+2.09	+1.38	−0.27 +0.76	+1.27	−0.28 +0.31	+0.45
Punch-through (JES) [%]	−0.94 -	−2.59 -	−2.35 -	−2.29 -	−2.35 -	−2.21 -	−2.62 -	−2.59 -	−2.92 -	−2.80 -	−2.34 -	−2.26 -	−2.04 -	−1.78 -	−1.71 -	−1.00 -	−1.79 -	−0.46 ±0.10
Single particle high-p_{T} (JES) [%]	-	-	-	-	-	-	-	-	-	-	-	-	-	-	-	-	-	-
Jet energy resolution [%]	∓4.16	∓2.60	∓1.77	∓2.32	∓1.36	∓0.64	∓1.26	∓1.34	∓1.69	∓0.60	∓1.09	∓1.27	±0.31	∓2.37	∓1.54	∓0.54	∓2.24	∓2.13
Jet vertex fraction [%]	+5.51 −5.32	+5.40 −5.27	+5.74 −5.56	+5.56 −5.57	+5.15 −5.02	+4.82 −4.72	+4.58 −4.49	+4.09 −4.04	+3.83 −3.80	+3.46 −3.41	+3.02 −2.84	+2.68 −2.66	±2.32	+2.07 −2.05	+1.64 −1.66	+1.56 −1.59	+0.80 −0.78	-
b-Quark tagging efficiency (eigenvector 0) [%]	−4.59	−4.62	−4.56	−4.40	−4.23	−4.09	−3.99	−3.89	−3.85	−3.83	−3.81	−3.80	−3.72	−3.70	−3.75	−3.69	−3.79	−3.99
b-Quark tagging efficiency (eigenvector 1) [%]	+4.68 ∓0.96	+4.73 ∓0.92	+4.64 ∓0.95	+4.48 ∓1.01	+4.30 ∓1.08	+4.16 ∓1.18	+4.06 ∓1.26	+3.96 ∓1.34	+3.91 ∓1.46	+3.87 ∓1.62	+3.82 ∓1.77	+3.80 ∓1.95	+3.73 ∓2.17	+3.70 ∓2.47	+3.61 ∓2.98	+3.52 ∓3.30	+3.60 ∓4.11	+3.92 ∓5.01
b-Quark tagging efficiency (eigenvector 2) [%]	+1.45 −1.44	+1.62 −1.41	+1.44 −1.43	+1.44 −1.43	+1.40 −1.39	+1.38 −1.35	±1.29	+1.22 −1.21	+1.15 −1.14	±1.07 −0.86	±0.85	±0.73	+0.72 −0.62	±0.29	-	±0.32	+0.32 −0.41	−0.80
b-Quark tagging efficiency (eigenvector 3) [%]	-	-	-	-	-	-	±0.12	±0.14	±0.15	+0.17 −0.16	±0.17	±0.17	±0.15	±0.12	-	±0.25	±0.51	
b-Quark tagging efficiency (eigenvector 4) [%]	-	-	-	-	-	-	-	-	-	-	-	-	-	-	-	±0.13	±0.22	
c-Quark tagging efficiency (eigenvector 0) [%]	−1.59	−1.52	−1.61	−1.60	−1.68	−1.62	−1.65	−1.46	±1.41	±1.42	±1.38	±1.28	±1.14	±1.00	−1.10	−0.89	−0.87	−1.38
c-Quark tagging efficiency (eigenvector 1) [%]	±0.28	±0.30	±0.34	±0.32	±0.28	±0.24	±0.21	±0.16	±0.14	+0.14 −0.12	-	-	-	-	−0.14	−0.90	−0.13 +0.12	±0.29
c-Quark tagging efficiency (eigenvector 2) [%]	±0.19	±0.16	±0.15	±0.19	±0.22	±0.23	±0.23	+0.21 −0.22	±0.21	±0.16	±0.15	±0.14	±0.10	-	-	-	-	±0.10
c-Quark tagging efficiency (eigenvector 3) [%]	±0.11	±0.10	±0.11	±0.10	-	-	-	-	-	-	-	-	-	-	-	-	-	
Light-jet tagging efficiency (eigenvector 0) [%]	−1.38 −1.37	−1.75 −1.82	−1.79 −1.99	−1.66 −1.72	∓1.43	∓1.48	−1.60 −1.66	−1.22 −1.24	−1.37 −1.45	−1.56 −1.70	−1.26 −1.33	−1.25 −1.29	∓1.24	−1.42 −1.52	−1.30 −1.32	−1.56 −1.58	−1.31 −1.41	−3.46 +3.51
Light-jet tagging efficiency (eigenvector 1) [%]	-	-	-	-	-	-	-	-	-	-	-	-	-	-	-	-	-	-
Light-jet tagging efficiency (eigenvector 2) [%]	±0.17	±0.17	±0.15	±0.15	±0.11	±0.10	±0.10	-	-	±0.11	-	-	-	-	-	-	-	∓0.14
Light-jet tagging efficiency (eigenvector 3) [%]	-	-	-	-	-	-	-	-	-	-	-	-	-	-	-	-	-	-
Light-jet tagging efficiency (eigenvector 4) [%]	-	-	-	-	-	-	-	-	-	-	-	-	-	-	-	-	-	∓0.13
Light-jet tagging efficiency (eigenvector 5) [%]	-	-	-	-	-	-	-	-	-	-	-	-	-	-	-	-	-	-
Light-jet tagging efficiency (eigenvector 6) [%]	-	-	-	-	-	-	-	-	-	-	-	-	-	-	-	-	-	-
Light-jet tagging efficiency (eigenvector 7) [%]	-	-	-	-	-	-	-	-	-	-	-	-	-	-	-	-	-	-
Light-jet tagging efficiency (eigenvector 8) [%]	-	-	-	-	-	-	-	-	-	-	-	-	-	-	-	-	-	-
Light-jet tagging efficiency (eigenvector 9) [%]	-	-	-	-	-	-	-	-	-	-	-	-	-	-	-	-	-	-
Light-jet tagging efficiency (eigenvector 10) [%]	-	-	-	-	-	-	-	-	-	-	-	-	-	-	-	-	-	-
Light-jet tagging efficiency (eigenvector 11) [%]	-	-	-	-	-	-	-	-	-	-	-	-	-	-	-	-	-	-
Light-jet tagging efficiency (eigenvector 12) [%]	-	-	-	-	-	-	-	-	-	-	-	-	-	-	-	-	-	-
Light-jet tagging efficiency (eigenvector 13) [%]	-	-	-	-	-	-	-	-	-	-	-	-	-	-	-	-	-	-
b-Quark tagging extrapolation [%]	-	-	-	-	-	-	-	-	-	-	±0.12	±0.17	±0.27	±0.46	±0.94	+1.58 −1.57	+3.12 −3.09	+4.24 −4.09
b-Quark tagging extrapolation from c-Quark [%]	-	±0.11	±0.15	+0.12 −0.13	±0.11	±0.10	±0.15	±0.10	-	-	±0.14	±0.11	-	-	-	-	-	-
Electron energy resolution [%]	-	-	-	-	-	-	-	-	-	-	-	-	-	-	-	-	−0.20	-
Electron energy scale [%]	+0.22 −0.14	-	-	-	-	-	-	-	-	-	-	-	-	-	-	-	-	-
Electron trigger efficiency [%]	±0.25	+0.24 −0.25	±0.25	+0.25 −0.26	±0.24	±0.24	±0.26	±0.25	±0.25	±0.25	±0.26	±0.27	±0.27	±0.28	±0.28	±0.29	±0.30	±0.39
Electron reconstruction efficiency [%]	±0.15	±0.15	±0.16	±0.16	±0.15	±0.16	±0.17	±0.17	±0.17	±0.18	±0.19	±0.19	±0.20	±0.21	±0.22	±0.22	±0.24	±0.30
Electron identification efficiency [%]	±0.38	±0.38	±0.39	±0.39	±0.38	±0.39	±0.41	±0.40	±0.41	±0.42	±0.44	±0.46	±0.48	±0.48	±0.50	±0.53	±0.58	±0.68
Electron isolation efficiency [%]	±0.12	±0.12	±0.12	+0.11 −0.13	±0.12	±0.13	±0.13	±0.14	±0.14	±0.15	±0.16	±0.17	±0.19	±0.21	±0.24	±0.29	±0.40	±0.62
Muon energy scale [%]	-	-	-	-	-	-	-	-	-	-	-	-	-	-	-	-	-	-
Muon (MS) momentum resolution [%]	-	-	-	-	-	-	-	-	-	-	-	-	-	-	-	-	-	-
Muon (ID) momentum resolution [%]	-	-	-	-	-	-	-	-	-	-	-	-	-	-	-	-	-	-
Muon trigger efficiency stat [%]	+0.61 −0.62	+0.59 −0.61	+0.56 −0.58	+0.57 −0.58	+0.58 −0.59	+0.57 −0.58	+0.56 −0.58	+0.55 −0.57	+0.55 −0.57	+0.56 −0.57	+0.56 −0.57	+0.55 −0.56	+0.55 −0.56	+0.55 −0.57	+0.56 −0.58	+0.56 −0.57	+0.57 −0.58	+0.58 −0.60
Muon trigger efficiency syst [%]	±0.26	+0.25 −0.24	±0.24	+0.25 −0.26	±0.25	+0.25 −0.24	±0.24	±0.24	±0.24	±0.24	±0.24	+0.24 −0.25	+0.24 −0.23	±0.24	±0.24	±0.24	±0.24	±0.25
Muon identification stat [%]	-	-	-	-	-	-	-	-	-	-	-	-	-	-	-	-	-	-
Muon identification syst [%]	±0.17	±0.16	±0.16	±0.16	±0.16	±0.16	±0.16	±0.16	±0.17	±0.17	+0.18 −0.17	±0.18	±0.18	+0.20 −0.19	±0.22	±0.24	+0.30 −0.29	±0.40
Muon isolation efficiency stat [%]	-	-	-	-	-	-	-	-	-	-	-	-	-	-	-	-	-	-
Muon isolation efficiency syst [%]	±0.11	+0.11 −0.10	±0.10	−0.12	+0.10 −0.11	±0.10	±0.10	±0.10	±0.10	±0.10	±0.10	±0.10	±0.10	±0.10	±0.10	±0.10	±0.11	±0.14
Muon TTVA efficiency stat [%]	-	-	-	-	-	-	-	-	-	-	-	-	-	-	-	-	-	-
Muon TTVA efficiency syst [%]	-	-	-	-	-	-	-	-	-	-	-	-	-	-	-	-	-	-
E_{T}^{miss} Soft jet resolution para [%]	-	-	-	-	-	-	-	-	-	-	-	-	-	-	-	-	-	±0.18
E_{T}^{miss} Soft jet resolution perp [%]	∓0.10	-	-	∓0.10	∓0.10	-	-	-	-	-	-	-	-	-	-	-	∓0.12	∓0.13
E_{T}^{miss} Soft jet scale [%]	-	-	-	-	-	-	-	-	-	-	-	-	-	-	-	-	-	-
Luminosity [%]	∓2.04	∓2.04	∓2.04	∓2.04	∓2.04	∓2.04	∓2.04	∓2.04	∓2.04	∓2.04	∓2.04	∓2.04	∓2.04	∓2.04	∓2.04	∓2.04	∓2.04	∓2.04
W+jets CA_2ex stat error [%]	-	-	-	-	-	-	-	-	-	-	-	-	-	-	-	-	-	-
W+jets CA_3ex stat error [%]	-	-	-	-	-	-	-	-	-	-	-	-	-	-	-	-	-	-
W+jets CA_4incl stat error [%]	∓0.11	∓0.12	∓0.12	∓0.12	∓0.10	-	-	-	-	-	-	-	-	-	-	-	∓0.12	∓0.19
W+jets Fc stat error [%]	±0.21	±0.25	±0.15	±0.14	-	±0.12	-	-	-	-	-	-	-	-	-	-	-	±0.15
W+jets Fcc stat error [%]	∓0.91	∓0.93	∓1.16	∓1.13	∓0.97	∓0.84	∓0.79	∓0.59	∓0.66	∓0.71	∓0.69	∓0.71	∓0.74	∓0.76	∓0.81	∓0.75	∓1.20	∓1.81
W+jets Flight stat error [%]	-	-	-	-	-	-	-	-	-	-	-	-	-	-	-	-	-	-
Single top cross-section [%]	±0.62	±0.69	±0.69	±0.66	±0.66	±0.66	±0.64	±0.65	±0.66	±0.67	±0.69	±0.72	±0.75	±0.78	±0.82	±0.91	±1.01	±1.84
Z+jets cross-section [%]	±1.19	±0.67	±0.60	±1.28	±0.72	±0.78	±1.11	±0.44	±0.38	±0.65	±0.69	±0.98	±0.61	±0.25	±0.83	±0.13	±0.70	±1.82
Diboson cross-section [%]	±0.33	±0.21	±0.18	±0.19	±0.18	±0.18	±0.16	±0.16	±0.17	±0.17	±0.16	±0.16	±0.18	±0.20	±0.23	±0.27	±0.43	±1.14
$t\bar{t}V$ cross-section [%]	-	-	-	-	-	-	-	-	-	-	-	-	-	-	-	-	±0.10	±0.19
Monte Carlo sample statistics [%]	±2.23	±1.14	±0.87	±0.82	±0.68	±0.65	±0.67	±0.60	±0.67	±0.81	±0.71	±0.85	±0.82	±0.88	±1.07	±1.04	±1.29	±2.90
ISR/FSR + scale [%]	−1.31 +1.90	−2.59 +1.91	−2.80 +3.50	−3.18 +2.47	−1.54 +2.03	−0.98 +1.89	−3.20 +1.24	−4.87 +2.09	−3.18 +3.22	−2.32 +3.80	−3.35 +3.14	−3.08 +2.04	+2.60	−2.72 +1.62	−6.36 +2.18	−0.32 +4.08	−4.34 +1.73	+0.79
Alternate hard-scattering model [%]	±1.31	∓4.02	-	∓0.85	∓0.34	∓2.26	∓2.22	∓1.27	∓1.89	∓0.25	∓1.43	∓0.85	±0.38	∓3.66	∓2.37	±0.68	∓2.37	∓6.27
Alternate parton-shower model [%]	-	∓1.93	∓1.27	∓2.36	∓2.01	∓1.89	∓2.53	∓2.31	∓2.34	∓1.60	∓2.64	∓2.55	±2.00	∓3.48	∓3.64	±0.66	∓5.29	∓9.82
Inter PDF [%]	±0.26	-	-	-	-	±0.15	-	∓0.13	-	-	-	±0.14	-	±0.23	-	-	±0.11	±1.06
Intra PDF [%]	±0.22	±0.10	-	±0.24	-	±0.11	-	-	-	-	-	±0.11	-	±0.12	-	±0.10	±0.21	±0.73
Fakes overall normalization [%]	±4.38	±3.69	±4.13	±4.11	±3.31	±3.05	±2.72	±2.45	±2.22	±2.50	±2.59	±2.25	±2.52	±1.68	±2.06	±1.70	±2.21	±6.13
Real lepton efficiency stat [%]	∓0.11	∓0.12	−0.12	−0.13	−0.14	−0.13	−0.14	−0.14	−0.13	−0.15	−0.17	−0.16	−0.20	−0.22	−0.25	−0.27	−0.33	−0.84
Fake lepton efficiency MC sample [%]	+0.89 −1.05	+0.72 −0.84	+0.80 −0.89	+0.70 −0.82	+0.51 −0.56	+0.53 −0.83	+0.53 −0.81	+0.52 −0.97	+0.38 −0.41	+0.32 −0.42	+0.43 −0.64	+0.46 −0.59	+0.59 −0.78	+0.30 −0.59	+0.21 −0.51	+0.23 −0.24	+0.36 −0.56	+0.45 −1.32
Fake lepton efficiency alternate CR [%]	±0.36	±0.43	±0.50	±0.44	±0.33	±0.46	±0.26	±0.13	±0.11	±0.28	±0.35	±0.16	±0.26	±0.35	±0.19	±0.35	±0.30	±0.33

TABLE A.2: Systematic uncertainties for the absolute differential cross-section at particle-level for $pt_{\mathrm{T}}^{t,had}$ in the 5-jet exclusive configuration.

Bins [GeV]	0–15	15–30	30–45	45–60	60–75	75–90	90–105	105–120	120–135	135–150	150–165	165–180	180–200	200–230	230–265	265–325	325–450	450–1000
$d\sigma$ / dp_{T}^{t} [pb/GeV]	$1.56 \cdot 10^{-2}$	$4.75 \cdot 10^{-2}$	$7.98 \cdot 10^{-2}$	$1.01 \cdot 10^{-1}$	$1.12 \cdot 10^{-1}$	$1.18 \cdot 10^{-1}$	$1.15 \cdot 10^{-1}$	$1.10 \cdot 10^{-1}$	$9.97 \cdot 10^{-2}$	$8.94 \cdot 10^{-2}$	$7.28 \cdot 10^{-2}$	$5.75 \cdot 10^{-2}$	$5.06 \cdot 10^{-2}$	$4.34 \cdot 10^{-2}$	$2.86 \cdot 10^{-2}$	$1.68 \cdot 10^{-2}$	$6.19 \cdot 10^{-3}$	$3.41 \cdot 10^{-4}$
Total Uncertainty [%]	±24.5	±22.0	±21.6	±22.7	±22.6	±20.0	±20.5	±21.4	±21.9	±19.2	±20.0	±20.1	±17.8	±17.1	±17.9	±16.6	±16.6	±20.0
Statistics [%]	±6.7	±3.4	±2.7	±2.3	±2.2	±2.1	±2.1	±2.1	±2.2	±2.3	±2.5	±2.8	±3.0	±2.8	±3.5	±3.6	±4.0	±9.2
Systematics [%]	±23.5	±22.0	±21.4	±22.0	±22.3	±20.0	±20.4	±21.3	±21.8	±19.1	±19.9	±19.8	±17.5	±16.8	±17.0	±16.7	±15.9	±23.4
	±23.5	±22.0	±21.4	±22.0	±22.3	±20.0	±20.4	±21.3	±21.8	±19.1	±19.9	±19.8	±17.5	±16.8	±17.0	±16.7	±15.9	±23.4
b-Tagged jet energy scale (JES) [%]	+0.93	+0.26	+0.12	+0.17	+0.71	+0.41	+0.54	+0.96	+0.59	+0.21	+0.68	+0.38	+0.43	+0.74	+0.45	+0.74	+0.75	+1.91
Effective detector NP set 1 (JES) [%]	+12.5	+13.5	+12.8	+13.7	+13.9	+12.6	+13.8	+13.8	+12.5	+11.6	+11.9	+12.1	+11.0	+9.76	+10.8	+8.13	+8.36	±8.10
Effective detector NP set 2 (JES) [%]	+14.2	+12.0	+13.9	+15.1	+14.6	+13.0	+12.0	+13.2	+13.0	+11.2	+10.8	+11.1	+10.3	+10.9	+10.2	+9.12	+7.47	+1.39
Effective detector NP set 3 (JES) [%]	+2.42	+3.50	+2.97	+2.86	+3.39	+2.77	+2.49	+2.23	+1.34	+2.21	+1.56	+0.94	+1.10	+0.38	+0.17	+0.19	+0.33	−2.21
Effective detector NP set 4 (JES) [%]	+2.65	+1.27	+1.11	+0.98	+1.15	+0.83	+0.65	+0.34		+0.96	+0.59	+0.22				+0.49	+0.29	−2.71
	−1.24	−1.44	−1.07	−1.17	−1.16	−1.22	−0.94	−0.48	−0.57	−0.40		+0.16	−0.28	−0.24	+0.95	+0.15	+1.09	+1.72
Effective detector NP set 5 (JES) [%]	−0.93	−0.69	−0.91	−0.44	−0.52	−0.58	−0.64	−0.22			−0.13	+0.42			+0.39	+0.21	+0.20	+0.39
	+0.81	+0.53	+0.22	+0.64	+0.64	+0.44	+0.35			+0.31	+0.29		−0.26	−0.41	+0.36	−0.47		
Effective detector NP set 6 (JES) [%]	-	−0.51	−0.22										−0.20		+0.06		+0.34	+0.54
		−0.15	−0.15	−0.19						+0.14							−0.36	
Effective detector NP set 6 restTerm (JES) [%]			−0.15					+0.27						+0.13	+0.19		+0.17	+0.70
η intercalibration model (JES) [%]	−2.21	+3.67	+2.68	+3.44	+4.06	+3.96	+3.82	+4.25	+4.14	+4.03	+3.49	+3.13	+2.66	+2.39	+3.10	+2.91	+2.84	+2.84
η intercalibration model (JES) [%]	−1.26	−3.06	−3.39	−3.49	−4.14	−4.47	−4.39	−3.92	−4.11	−3.90	−3.61	−3.59	−4.07	−3.46	−3.23	−3.84	−2.69	−3.63
η intercalibration total stat (JES) [%]	+1.71	+1.92	+1.35	+1.70	+2.37	+1.52	+1.77	+2.09	+2.01	+1.75	+1.92	+2.01	+0.90	+1.71	+1.83	+1.55	+1.20	+2.32
Flavour composition (JES) [%]	−1.84	−1.52	−2.00	−2.17	−2.08	−1.77	−1.58	−2.24	−2.71	−1.69	−1.39	−1.94	−1.74	−1.70	−1.88	−1.89	−1.14	−1.41
Flavour response (JES) [%]	+13.1	+11.1	+11.3	+11.8	+11.2	+10.2	+10.5	+11.5	+11.7	+9.86	+10.1	+10.3	+9.05	+8.78	+9.12	+8.09	+6.38	+7.20
	−13.1	−11.1	−11.3	−11.8	−11.2	−10.2	−10.5	−11.5	−11.7	−9.86	−10.1	−10.3	−9.05	−8.78	−9.12	−8.09	−6.38	−7.20
Flavour response (JES) [%]	−4.26	−2.52	−3.26	−3.18	−3.15	−3.32	−3.06	−3.52	−3.84	−3.07	−3.08	−3.38	−2.67	−2.63	−3.17	−3.05	−2.04	−2.69
Pile-up offset μ (JES) [%]	+3.26	+3.31	+1.69	+2.69	+3.45	+2.46	+2.84	+3.09	+2.91	+2.17	+2.83	+3.18	+1.95	+2.53	+3.11	+1.86	+2.11	+2.19
	−0.82	−0.64	−0.61	−0.50	−0.73	−0.62	−0.68	−0.63	−0.62	−0.54	−0.71	−0.77	−0.75	−0.63	−0.78	−0.53	−0.53	−0.54
Pile-up offset μ (JES) [%]	+0.82	+0.64	+0.61	+0.50	+0.73	+0.62	+0.68	+0.63	+0.62	+0.54	+0.71	+0.77	+0.75	+0.63	+0.78	+0.53	+0.53	+0.54
Pile-up offset N_{PV} (JES) [%]	−0.68	−0.05	−0.53	−0.03	−0.29	−0.32	−0.32	−0.47	−0.63	−0.23	−0.25	−0.37	−0.12	−0.40	−0.41	−0.18	−0.18	−0.56
		+0.44		−0.24	+0.29			+0.26	+0.15	+0.54			−0.43	+0.29		+0.62	+0.27	+0.63
Pile-up offset p_{T} (JES) [%]	−0.21	−0.04	−0.22	−0.10	−0.30	−0.29	−0.29	−0.23			+0.36				+0.11	−0.12	−0.13	+0.12
	+0.23	+0.04	+0.22	+0.10	+0.30	+0.14						+0.26	−0.50			+0.12		−0.13
Pile-up offset ρ topology (JES) [%]	+3.00	+1.27	+3.06	+3.83	+1.00	+3.70	+3.95	±4.38	+4.04	+3.79	+3.90	+3.44	+2.69	+3.36	+3.11	+2.77	+2.33	+2.70
	−1.36	−3.78	−4.76	−5.22	−4.71	−4.63	−3.96		−4.96	−4.26	−3.85	−4.15	−3.58	−3.63	−3.89	−3.45	−2.52	−3.37
Punch-through (JES) [%]	-	-	-	-	-	-	-	-	-	-	-	-	-	-	-	-	-	-
Single particle high-p_{T} (JES) [%]	-	-	-	-	-	-	-	-	-	-	-	-	-	-	-	-	-	-
Jet energy resolution [%]	±2.79	∓0.71	∓0.49	∓0.60	±0.17	±0.65	±0.37	±0.69	±0.78	±0.24	∓0.27	∓0.71	∓2.05	-	±3.40	∓2.64	-	±0.18
Jet vertex fraction [%]	+7.66	+7.83	+7.66	+7.50	+7.16	+6.81	+6.37	+5.99	+5.80	+5.40	+4.99	+4.83	+4.54	+4.14	+3.71	+3.53	+2.75	+2.39
	−7.41	−7.62	−7.27	−7.12	−6.83	−6.51	−6.11	−5.75	−5.59	−5.23	−4.88	−4.73	−4.42	−4.02	−3.65	−3.48	−2.72	−2.27
b-Quark tagging efficiency (eigenvector 0) [%]	−4.23	−4.30	−4.14	−4.01	−3.84	−3.63	−3.58	−3.50	−3.50	−3.50	−3.44	−3.44	−3.31	−3.48	−3.50	−3.53	−3.51	−3.71
	+4.48	+4.37	+4.20	+4.07	+3.90	+3.68	+3.63	+3.54	+3.55	+3.54	+3.49	+3.49	+3.36	+3.54	+3.56	+3.61	+3.62	+3.92
b-Quark tagging efficiency (eigenvector 1) [%]	+0.84	∓0.87	∓0.90	∓0.95	∓1.07	∓1.31	∓1.44	∓1.54	∓1.71	∓1.89	∓2.04	∓2.14	∓2.40	∓2.89	∓3.02	∓3.65	∓4.58	
b-Quark tagging efficiency (eigenvector 2) [%]	∓1.15	±1.16	∓1.19	±1.24	±1.21	∓1.15	∓1.10	±1.03	±0.93	±0.83	±0.76	±0.67	±0.61	±0.44	±0.21	±0.10	±0.20	∓0.77
	−1.14		−1.16				−1.01				−0.73						±0.20	
b-Quark tagging efficiency (eigenvector 3) [%]	-	-	-	-	-	-	±0.12	±0.15	±0.15	±0.15	±0.14	±0.12	±0.10	-	-	-	∓0.23	±0.49
b-Quark tagging efficiency (eigenvector 4) [%]	-	-	-	-	-	-	-	-	-	-	-	-	-	-	-	-	∓0.12	±0.20
c-Quark tagging efficiency (eigenvector 0) [%]	∓1.47	−1.37	−1.09	∓1.67	∓1.65	−1.52	∓1.49	∓1.52	∓1.49	∓1.42	∓1.46	−1.38	−1.14	−1.14	−1.17	∓1.03	±0.90	∓1.19
		−1.39	−1.09			−1.53						−1.37	−1.13	−1.13	−1.18		±0.90	
c-Quark tagging efficiency (eigenvector 1) [%]	±0.35	±0.33	±0.32	±0.32	±0.28	±0.23	±0.19	±0.17	±0.12	-	-	-	-	-	∓0.11	∓0.27	+0.19 +0.20	±0.38
c-Quark tagging efficiency (eigenvector 2) [%]	±0.10	±0.12	±0.17	±0.21	±0.21	±0.22	±0.24	±0.23	±0.23	±0.21	+0.20 −0.19	±0.15	-	-	-	-	-	∓0.14
c-Quark tagging efficiency (eigenvector 3) [%]	-	-	∓0.12	±0.10	-	-	-	-	-	-	-	-	-	-	-	-	-	-
Light-jet tagging efficiency (eigenvector 0) [%]	−1.63	−1.68	−1.84	−1.58	−1.59	−1.53	−1.36	−1.63	−2.09	−1.59	−1.35	−1.50	−1.59	−1.61	−1.63	−1.80	−1.76	−5.26
	+1.37	+1.64	+1.81	+1.54	+1.54	+1.52	+1.34	+1.64	+2.23	+1.63	+1.38	+1.49	+1.55	+1.62	+1.62	+1.85	+1.80	+5.00
Light-jet tagging efficiency (eigenvector 1) [%]	-	-	-	-	-	-	-	-	-	-	-	-	-	-	-	-	-	∓0.33
Light-jet tagging efficiency (eigenvector 2) [%]	±0.24	±0.19	±0.16	±0.13	±0.13	±0.11	-	±0.10	±0.15	-	-	-	-	-	-	-	±0.10	±0.27
Light-jet tagging efficiency (eigenvector 3) [%]	-	-	-	-	-	-	-	-	-	-	-	-	-	-	-	-	-	±0.14
Light-jet tagging efficiency (eigenvector 4) [%]	-	-	-	-	-	-	-	-	-	-	-	-	-	-	-	-	-	∓0.23
Light-jet tagging efficiency (eigenvector 5) [%]	-	-	-	-	-	-	-	-	-	-	-	-	-	-	-	-	-	∓0.13
Light-jet tagging efficiency (eigenvector 6) [%]	-	-	-	-	-	-	-	-	-	-	-	-	-	-	-	-	-	-
Light-jet tagging efficiency (eigenvector 7) [%]	-	-	-	-	-	-	-	-	-	-	-	-	-	-	-	-	-	-
Light-jet tagging efficiency (eigenvector 8) [%]	-	-	-	-	-	-	-	-	-	-	-	-	-	-	-	-	-	-
Light-jet tagging efficiency (eigenvector 9) [%]	-	-	-	-	-	-	-	-	-	-	-	-	-	-	-	-	-	-
Light-jet tagging efficiency (eigenvector 10) [%]	-	-	-	-	-	-	-	-	-	-	-	-	-	-	-	-	-	-
Light-jet tagging efficiency (eigenvector 11) [%]	-	-	-	-	-	-	-	-	-	-	-	-	-	-	-	-	-	-
Light-jet tagging efficiency (eigenvector 12) [%]	-	-	-	-	-	-	-	-	-	-	-	-	-	-	-	-	-	-
Light-jet tagging efficiency (eigenvector 13) [%]	-	-	-	-	-	-	-	-	-	-	-	-	-	-	-	-	-	-
b-Quark tagging extrapolation [%]	-	-	-	-	-	-	-	±0.10	±0.12	±0.16	±0.23	±0.33	±0.40	±0.65	±1.17	+1.80 −1.79	±1.91	+4.29 −2.88
b-Quark tagging extrapolation from c-Quark [%]	-	-	-	±0.11	±0.10	-	-	-	-	-	-	-	-	-	-	-	-	-
Electron energy resolution [%]	+0.24	-	-	-	-	-	-	-	-	-	-	-	-	-	-	-	-	-
Electron energy scale [%]	+0.20	-	-	-	-	-	-	-	-	-	-	-	-	-	-	-	-	-
Electron trigger efficiency [%]	±0.24	±0.25	±0.25	±0.25	±0.24	±0.25	±0.25	±0.26	±0.28	±0.28	±0.26	±0.26	±0.26	±0.28	±0.29	±0.30	±0.31	±0.35
Electron reconstruction efficiency [%]	±0.16	±0.17	±0.17	±0.17	±0.17	±0.17	±0.17	±0.18	±0.19	±0.19	±0.19	±0.19	±0.19	±0.21	±0.21	±0.23	±0.24	±0.28
Electron identification efficiency [%]	±0.40	±0.41	±0.41	±0.41	±0.41	±0.42	±0.42	±0.43	±0.47	±0.47	±0.45	±0.46	±0.47	±0.51	±0.55	±0.59	±0.65	±0.87
Electron isolation efficiency [%]	±0.14	±0.15	±0.15	±0.14	±0.14	±0.15	±0.15	±0.16	±0.17	±0.18	±0.18	±0.19	±0.20	±0.23	±0.25	±0.29	±0.36	±0.55
Muon energy scale [%]	-	-	-	-	-	-	-	-	-	-	-	-	-	-	-	-	-	-
Muon (MS) momentum resolution [%]	-	-	-	-	-	-	-	-	-	-	-	-	-	-	-	-	-	-
Muon (ID) momentum resolution [%]	-	-	-	-	-	-	-	-	-	-	-	-	-	-	-	-	-	-
Muon trigger efficiency stat [%]	∓0.57	∓0.57	∓0.55	∓0.56	∓0.56	∓0.55	∓0.55	∓0.55	∓0.55	∓0.55	∓0.55	∓0.56	∓0.56	∓0.55	∓0.55	∓0.54	∓0.55	∓0.58
	−0.58	−0.58	−0.57	−0.58	−0.58	−0.58	−0.58	−0.57	−0.57	−0.57	−0.57	−0.57	−0.57	−0.58	−0.55	−0.55	−0.57	−0.59
Muon trigger efficiency syst [%]	±0.25	±0.24	+0.24 −0.23	±0.24	±0.24	±0.24	+0.24 −0.23	+0.24 −0.23	±0.24	±0.24	±0.24	±0.24	±0.24	+0.24 −0.23	±0.24	±0.23	±0.24	±0.25
Muon identification stat [%]	-	-	-	-	-	-	-	-	-	-	-	-	-	-	-	-	-	-
Muon identification syst [%]	±0.17	±0.16	±0.16	±0.17	±0.17	±0.17	±0.17	±0.17	±0.18	±0.18	±0.18	±0.19	±0.19	±0.20	±0.22	±0.23	±0.26	+0.37 −0.36
Muon isolation efficiency stat [%]	-	-	-	-	-	-	-	-	-	-	-	-	-	-	-	-	-	-
Muon isolation efficiency syst [%]	±0.11	±0.10	±0.10	±0.10	±0.10	±0.10	±0.10	±0.10	±0.10	±0.10	±0.10	±0.10	±0.10	±0.10	±0.10	±0.10	±0.10	+0.14 −0.13
Muon TTVA efficiency stat [%]	-	-	-	-	-	-	-	-	-	-	-	-	-	-	-	-	-	-
Muon TTVA efficiency syst [%]	-	-	-	-	-	-	-	-	-	-	-	-	-	-	-	-	-	-
$E_{\mathrm{T}}^{\mathrm{miss}}$ Soft jet resolution para [%]	±0.13	-	-	-	-	-	-	-	-	-	-	-	-	-	-	-	-	-
$E_{\mathrm{T}}^{\mathrm{miss}}$ Soft jet resolution perp [%]	-	-	-	∓0.10	-	-	-	-	-	-	-	-	-	-	-	-	-	∓0.13
$E_{\mathrm{T}}^{\mathrm{miss}}$ Soft jet scale [%]	-	-	-	-	-	-	-	-	-	-	-	-	-	-	-	-	-	-
Luminosity [%]	∓2.04	∓2.04	∓2.04	∓2.04	∓2.04	∓2.04	∓2.04	∓2.04	∓2.04	∓2.04	∓2.04	∓2.04	∓2.04	∓2.04	∓2.04	∓2.04	∓2.04	∓2.04
W+jets CA_2ex stat error [%]	-	-	-	-	-	-	-	-	-	-	-	-	-	-	-	-	-	-
W+jets CA_3ex stat error [%]	-	-	-	-	-	-	-	-	-	-	-	-	-	-	-	-	-	-
W+jets CA_4incl stat error [%]	∓0.12	∓0.11	-	-	-	-	-	-	-	-	-	-	-	-	-	-	-	∓0.13
W+jets Fc stat error [%]	∓0.14	∓0.14	-	-	∓0.11	-	-	-	-	-	-	-	-	-	-	-	-	-
W+jets Fcc stat error [%]	∓1.05	∓0.99	∓0.83	∓0.90	∓0.80	∓0.67	∓0.73	∓0.66	∓0.77	∓0.80	∓0.84	∓0.70	∓0.71	∓0.83	∓0.81	∓0.88	∓0.79	∓1.33
W+jets Flight stat error [%]	-	-	-	-	-	-	-	-	-	-	-	-	-	-	-	-	-	-
Single top cross-section [%]	±0.52	±0.50	±0.51	±0.51	±0.49	±0.49	±0.50	±0.52	±0.53	±0.55	±0.56	±0.59	±0.63	±0.66	±0.78	±0.77	±0.94	±1.76
Z+jets cross-section [%]	±0.36	±0.66	±0.99	±0.52	±0.78	±0.91	±0.53	±0.39	±1.03	±1.31	±0.62	±0.34	±0.21	±0.59	±0.71	±0.71	±0.40	±1.68
Diboson cross-section [%]	±0.57	±0.48	±0.37	±0.38	±0.33	±0.29	±0.31	±0.31	±0.32	±0.31	±0.42	±0.54	±0.48	±0.46	±0.59	±0.55	±0.74	±1.69
$t\bar{t}V$ cross-section [%]	-	-	-	-	-	-	±0.10	±0.10	±0.11	±0.12	±0.12	±0.13	±0.14	±0.15	±0.17	±0.19	±0.23	±0.32
Monte Carlo sample statistics [%]	±2.42	±1.31	±1.05	±0.86	±0.77	±0.78	±0.74	±0.72	±0.99	±0.91	±0.84	±0.90	±0.98	±1.00	±1.17	±1.20	±1.25	±2.58
ISR/FSR + scale [%]	−1.63	−5.70	−3.33	−4.71	−4.44	−4.73	−4.87	−4.23	−3.76	−1.85	−4.20	−5.98	−6.22	−3.17	−0.17	−1.66	−3.53	−3.47
	+5.40	+1.65	+2.34	+2.32	+4.34	+3.61	+5.63	+5.49	+3.81	+2.77	+2.05	+1.39	+1.39	+3.75	+4.69	+2.49	+2.23	+3.32
Alternate hard-scattering model [%]	∓1.67	±0.26	±0.41	∓0.18	±3.89	±2.18	±1.83	±1.27	∓1.61	±0.36	±5.65	±3.43	∓1.83	±3.14	∓3.63	±8.41	±1.30	±12.5
Alternate parton-shower model [%]	∓3.24	∓4.69	∓2.50	∓3.22	∓2.89	∓3.19	∓2.67	∓2.22	∓2.57	∓2.64	∓2.69	∓3.60	∓0.81	∓0.90	∓1.19	∓1.45	∓3.06	∓6.96
Inter PDF [%]	-	∓0.12	-	±0.33	-	∓0.16	±0.11	-	±0.12	-	-	-	±0.13	-	-	±0.17	±0.15	±1.46
Intra PDF [%]	±0.10	±0.16	±0.12	±0.43	±0.13	-	±0.10	±0.10	-	-	±0.11	±0.10	-	±0.16	-	±0.16	±0.16	±2.68
Fakes overall normalization [%]	±2.52	±3.51	±3.47	±2.87	±2.35	±2.59	±3.27	±2.93	±2.43	±2.21	±2.74	±2.86	±2.69	±2.14	±2.28	±3.36	±2.16	±3.87
Real lepton efficiency stat [%]	−0.35	−0.16	−0.19	−0.15	−0.16	−0.17	−0.17	−0.19	−0.21	−0.20	−0.19	−0.21	−0.25	−0.24	−0.31	−0.28	−0.34	−1.02
	+0.15	+0.15	+0.16	+0.14	+0.15	+0.16	+0.15	+0.17	+0.18	+0.18	+0.18	+0.18	+0.19	+0.21	+0.26	+0.24	+0.28	+0.57
Fake lepton efficiency MC scale [%]	−0.17	−0.73	−0.66	−0.52	−0.54	−0.38	−0.43	−0.67	−0.53	−0.53	−0.59	−0.67	−0.72	−0.58	−0.59	−0.74	−0.58	-
		−0.83	−0.77	−0.70	−0.60	−0.41	−0.62	−0.78	−0.63	−0.58	−0.71	−0.83	−0.90	−0.82	−0.71	−0.92	−0.70	−1.50
Fake lepton efficiency alternate CR [%]	±0.81	±0.29	±0.40	±0.41	±0.42	±0.33	±0.27	±0.14	±0.10	±0.20	±0.27	±0.25	±0.31	±0.43	±0.22	-	±0.64	-

TABLE A.3: Systematic uncertainties for the absolute differential cross-section at particle-level for $pt_{\mathrm{T}}^{t,had}$ in the 6-jet inclusive configuration.

Bins [GeV]	0–15	15–35	35–75	75–125	125–170	170–800
$d\sigma$ / $dp_T^{t\bar{t}}$ [pb/GeV]	$6.58 \cdot 10^{-1}$	$1.03 \cdot 10^{0}$	$4.00 \cdot 10^{-1}$	$6.73 \cdot 10^{-2}$	$1.95 \cdot 10^{-2}$	$6.09 \cdot 10^{-4}$
Total Uncertainty [%]	$^{+16.6}_{-17.4}$	$^{+11.7}_{-12.4}$	$^{+13.0}_{-13.8}$	$^{+22.3}_{-21.1}$	$^{+20.9}_{-21.1}$	$^{+14.8}_{-17.2}$
Statistics [%]	±0.7	±0.5	±0.8	±2.0	±4.0	±6.0
Systematics [%]	$^{+16.6}_{-17.4}$	$^{+11.7}_{-12.4}$	$^{+13.0}_{-13.8}$	$^{+22.2}_{-21.0}$	$^{+20.4}_{-20.6}$	$^{+13.4}_{-15.9}$
b-Tagged jet energy scale (JES) [%]	$^{+0.54}_{-0.53}$	$^{+0.51}_{-0.47}$	$^{+0.49}_{-0.42}$	$^{+0.51}_{-0.53}$	$^{+0.39}_{-0.70}$	$^{+0.36}_{-0.35}$
Effective detector NP set 1 (JES) [%]	$^{-2.54}_{+1.58}$	-	$^{+3.72}_{-5.59}$	$^{+8.60}_{-8.51}$	$^{+3.72}_{-4.54}$	$^{+1.32}_{-1.92}$
Effective detector NP set 2 (JES) [%]	$^{+0.74}_{-0.75}$	$^{-1.00}_{+0.23}$ $^{-0.28}$	$^{-0.90}_{+0.81}$	$^{-1.05}_{+1.28}$	$^{+0.71}_{-1.32}$	$^{+2.80}_{-2.69}$
Effective detector NP set 3 (JES) [%]	$^{-0.33}_{+0.28}$	$^{-0.14}_{-}$	$^{+0.23}_{-0.33}$	$^{+0.18}_{-0.19}$	∓ 0.87	$^{-1.78}_{+1.36}$
Effective detector NP set 4 (JES) [%]	$^{+0.22}_{-0.34}$	-	$^{-0.28}_{+0.19}$	-	$^{+0.58}_{-0.36}$	$^{-}_{-0.72}$
Effective detector NP set 5 (JES) [%]	$^{-0.26}_{+0.30}$	-	$^{+0.20}_{-0.14}$	-	$^{+0.27}$	$^{+0.31}_{-0.62}$
Effective detector NP set 6 restTerm (JES) [%]	$^{-0.17}_{+0.10}$	-	-	$^{+0.17}_{-0.13}$	$^{+0.31}$	$^{+0.11}_{-0.48}$
η intercalibration model (JES) [%]	$^{-3.37}_{+3.27}$	$^{-1.89}_{+1.24}$	$^{+2.62}_{-3.31}$	$^{+7.22}_{-6.54}$	$^{+5.68}_{-5.70}$	$^{+3.42}_{-3.75}$
η intercalibration total stat (JES) [%]	$^{-0.73}_{+0.67}$	$^{-0.41}_{+0.35}$	$^{+0.64}_{-0.61}$	$^{+1.79}_{-1.62}$	$^{+0.71}_{-1.11}$	$^{+0.89}_{-1.50}$
Flavour composition (JES) [%]	$^{-4.09}_{+3.31}$	$^{-2.75}_{+1.59}$	$^{+1.91}_{-3.24}$	$^{+8.47}_{-8.11}$	$^{+6.36}_{-6.17}$	$^{+3.65}_{-3.89}$
Flavour response (JES) [%]	$^{+1.10}_{-1.68}$	$^{+0.56}_{-1.16}$	$^{-0.84}_{+0.50}$	$^{-2.62}_{+2.42}$	$^{-2.38}_{+1.99}$	$^{-2.20}_{+1.27}$
Pile-up offset μ (JES) [%]	$^{+0.51}_{-0.57}$	$^{+0.23}_{-0.28}$	$^{-0.36}_{+0.29}$	$^{-0.70}_{+0.81}$	-	$^{-}_{-0.67}$
Pile-up offset N_{PV} (JES) [%]	$^{+0.27}$	$^{+0.19}$ -	-	-	$^{+0.25}$	$^{+0.16}_{-0.49}$
Pile-up offset p_T (JES) [%]	$^{+0.18}_{-0.15}$	-	$^{-0.37}_{+0.36}$	$^{+0.26}_{-0.12}$	$^{+0.47}_{-0.41}$	$^{+0.88}_{-1.34}$
Pile-up offset ρ topology (JES) [%]	$^{-1.38}_{+0.51}$	$^{-}_{-0.70}$	$^{+1.11}_{-1.67}$	$^{+2.72}_{-2.86}$	$^{+1.01}_{-2.30}$	$^{-}_{-0.95}$
Punch-through (JES) [%]	-	-	-	-	-	-
Single particle high-p_T (JES) [%]	-	-	-	-	-	-
Jet energy resolution [%]	∓ 3.59	∓ 3.24	∓ 1.35	± 1.14	± 0.25	-
Jet vertex fraction [%]	$^{+3.39}_{-3.35}$	$^{+2.99}_{-2.97}$	$^{+1.49}_{-1.54}$	$^{-0.15}_{+0.14}$	$^{+0.91}_{-0.95}$	$^{+1.23}_{-1.26}$
b-Quark tagging efficiency (eigenvector 0) [%]	$^{-4.32}_{+4.41}$	$^{-4.30}_{+4.38}$	$^{-4.23}_{+4.31}$	$^{-4.19}_{+4.27}$	$^{-4.21}_{+4.28}$	$^{-4.08}_{+4.15}$
b-Quark tagging efficiency (eigenvector 1) [%]	$^{-1.61}_{+1.62}$	$^{-1.62}_{+1.63}$	$^{-1.66}_{+1.67}$	$^{-1.79}_{+1.81}$	$^{-2.00}_{+2.02}$	$^{-2.34}_{+2.37}$
b-Quark tagging efficiency (eigenvector 2) [%]	$^{+1.25}_{-1.24}$	± 1.22	$^{+1.18}_{-1.17}$	$^{+1.10}_{-1.09}$	$^{+0.95}_{-0.94}$	± 0.73
b-Quark tagging efficiency (eigenvector 3) [%]	-	-	-	-	-	-
b-Quark tagging efficiency (eigenvector 4) [%]	-	-	-	-	-	-
c-Quark tagging efficiency (eigenvector 0) [%]	$^{-1.45}_{+1.47}$	$^{-1.50}_{+1.52}$	$^{-1.57}_{+1.58}$	$^{-1.81}_{+1.82}$	$^{-1.89}_{+1.90}$	$^{-1.65}_{+1.66}$
c-Quark tagging efficiency (eigenvector 1) [%]	±0.17	±0.17	±0.16	$^{+0.19}_{-0.18}$	±0.17	-
c-Quark tagging efficiency (eigenvector 2) [%]	±0.18	±0.19	±0.20	±0.21	±0.23	±0.14
c-Quark tagging efficiency (eigenvector 3) [%]	-	-	-	-	-	-
Light-jet tagging efficiency (eigenvector 0) [%]	$^{-1.07}_{+1.13}$	$^{-1.29}_{+1.39}$	$^{-1.79}_{+1.96}$	$^{-2.06}_{+2.18}$	$^{-1.89}_{+1.85}$	$^{-1.75}_{+1.93}$
Light-jet tagging efficiency (eigenvector 1) [%]	-	-	-	-	-	-
Light-jet tagging efficiency (eigenvector 2) [%]	-	-	±0.12	±0.14	±0.10	±0.10
Light-jet tagging efficiency (eigenvector 3) [%]	-	-	-	-	-	-
Light-jet tagging efficiency (eigenvector 4) [%]	-	-	-	-	-	-
Light-jet tagging efficiency (eigenvector 5) [%]	-	-	-	-	-	-
Light-jet tagging efficiency (eigenvector 6) [%]	-	-	-	-	-	-
Light-jet tagging efficiency (eigenvector 7) [%]	-	-	-	-	-	-
Light-jet tagging efficiency (eigenvector 8) [%]	-	-	-	-	-	-
Light-jet tagging efficiency (eigenvector 9) [%]	-	-	-	-	-	-
Light-jet tagging efficiency (eigenvector 10) [%]	-	-	-	-	-	-
Light-jet tagging efficiency (eigenvector 11) [%]	-	-	-	-	-	-
Light-jet tagging efficiency (eigenvector 12) [%]	-	-	-	-	-	-
Light-jet tagging efficiency (eigenvector 13) [%]	-	-	-	-	-	-
b-Quark tagging extrapolation [%]	±0.22	±0.23	±0.25	±0.33	$^{+0.47}_{-0.46}$	±0.79
b-Quark tagging extrapolation from c-Quark [%]	$^{+0.13}_{-0.12}$	±0.12	±0.12	±0.16	±0.18	±0.16
Electron energy resolution [%]	-	-	-	-	$^{-0.20}$ -	-
Electron energy scale [%]	-	-	-	-	-	-
Electron trigger efficiency [%]	±0.26	±0.26	$^{+0.25}_{-0.26}$	±0.27	$^{+0.32}_{-0.31}$	±0.32
Electron reconstruction efficiency [%]	±0.18	±0.18	±0.17	±0.18	±0.21	±0.22
Electron identification efficiency [%]	±0.44	±0.43	±0.42	±0.44	±0.51	±0.55
Electron isolation efficiency [%]	±0.16	±0.15	±0.15	±0.16	±0.20	±0.23
Muon energy scale [%]	-	-	-	-	-	-
Muon (MS) momentum resolution [%]	-	-	-	-	-	-
Muon (ID) momentum resolution [%]	-	-	-	-	-	-
Muon trigger efficiency stat [%]	$^{+0.55}_{-0.57}$	$^{+0.56}_{-0.58}$	$^{+0.59}_{-0.61}$	$^{+0.60}_{-0.62}$	$^{+0.58}_{-0.59}$	$^{+0.56}_{-0.57}$
Muon trigger efficiency syst [%]	±0.24	±0.24	±0.25	$^{+0.26}_{-0.25}$	±0.24	±0.24
Muon identification stat [%]	-	-	-	-	-	-
Muon identification syst [%]	±0.16	±0.17	±0.18	±0.19	$^{+0.19}_{-0.18}$	$^{+0.21}_{-0.20}$
Muon isolation efficiency stat [%]	-	-	-	-	-	-
Muon isolation efficiency syst [%]	±0.10	±0.10	±0.11	±0.11	$^{+0.11}_{-0.10}$	±0.10
Muon TTVA efficiency stat [%]	-	-	-	-	-	-
Muon TTVA efficiency syst [%]	-	-	-	-	-	-
E_T^{miss} Soft jet resolution para [%]	∓ 1.22	∓ 0.15	± 1.06	±0.44	∓ 0.12	±0.12
E_T^{miss} Soft jet resolution perp [%]	∓ 1.62	∓ 0.41	± 1.06	±0.31	∓ 0.79	-
E_T^{miss} Soft jet scale [%]	$^{-0.95}_{+0.88}$	$^{-0.18}_{-}$	$^{+0.62}_{-0.61}$	-	$^{-0.52}_{+0.65}$	-
Luminosity [%]	∓ 2.04	∓ 2.04	∓ 2.04	∓ 2.04	∓ 2.04	∓ 2.04
W+jets CA_2ex stat error [%]	-	-	-	-	-	-
W+jets CA_3ex stat error [%]	-	-	-	-	-	-
W+jets CA_4incl stat error [%]	∓ 0.14	∓ 0.13	∓ 0.12	∓ 0.11	∓ 0.15	∓ 0.12
W+jets Fc stat error [%]	∓ 0.12	∓ 0.13	∓ 0.12	∓ 0.11	-	-
W+jets Fcc stat error [%]	∓ 1.34	∓ 1.24	∓ 1.03	∓ 1.04	∓ 1.78	∓ 1.14
W+jets Flight stat error [%]	-	-	-	-	-	-
Single top cross-section [%]	±0.89	±0.86	±0.86	±1.05	±1.34	±1.24
Z+jets cross-section [%]	±0.65	±0.70	±0.78	±0.80	±0.55	±0.82
Diboson cross-section [%]	±0.10	±0.11	±0.11	±0.13	±0.21	±0.14
$t\bar{t}V$ cross-section [%]	-	-	-	-	-	-
Monte Carlo sample statistics [%]	±0.33	±0.23	±0.32	±0.76	±1.45	±1.89
ISR/FSR + scale [%]	$^{-}_{-2.63}$	$^{-2.52}_{+0.89}$	$^{-2.86}_{+3.93}$	$^{-4.42}_{+6.93}$	$^{-6.88}_{+7.20}$	$^{-}_{-7.83}$
Alternate hard-scattering model [%]	∓ 2.10	±0.11	±0.94	±5.69	±13.0	±8.92
Alternate parton-shower model [%]	∓ 13.3	∓ 8.38	±5.86	±8.18	∓ 0.81	∓ 1.66
Inter PDF [%]	-	-	-	-	-	∓ 0.16
Intra PDF [%]	-	-	-	±0.19	±0.26	±0.82
Fakes overall normalization [%]	±0.48	±2.43	±6.53	±8.53	±7.15	±3.73
Real lepton efficiency stat [%]	$^{-0.16}_{+0.15}$	$^{-0.15}_{+0.14}$	$^{-0.14}_{+0.13}$	$^{-0.13}_{+0.12}$	$^{-0.18}_{+0.17}$	∓ 0.14
Fake lepton efficiency MC scale [%]	$^{-0.64}_{+0.80}$	$^{+0.14}_{-0.15}$	$^{+1.66}_{-2.05}$	$^{+2.03}_{-2.99}$	$^{+1.79}_{-2.15}$	$^{+0.79}_{-0.75}$
Fake lepton efficiency alternate CR [%]	-	±0.21	±0.72	±0.68	±0.53	±0.39

TABLE A.4: Systematic uncertainties for the absolute differential cross-section at particle-level for $p_{\mathrm{T}}^{t\bar{t}}$ in the 4-jet exclusive configuration.

Bins [GeV]	0–35	35–75	75–125	125–170	170–225	225–800
$d\sigma$ / $dp_T^{t\bar{t}}$ [pb/GeV]	$1.33 \cdot 10^{-1}$	$2.83 \cdot 10^{-1}$	$1.56 \cdot 10^{-1}$	$6.78 \cdot 10^{-2}$	$3.20 \cdot 10^{-2}$	$3.00 \cdot 10^{-3}$
Total Uncertainty [%]	$^{+15.0}_{-15.8}$	$^{+12.5}_{-13.4}$	$^{+12.0}_{-12.7}$	$^{+11.5}_{-11.7}$	$^{+10.9}_{-10.3}$	$^{+10.0}_{-10.1}$
Statistics [%]	± 1.4	± 0.9	± 1.2	± 2.0	± 2.8	± 2.6
Systematics [%]	$^{+14.9}_{-15.8}$	$^{+12.5}_{-13.4}$	$^{+11.9}_{-12.7}$	$^{+11.3}_{-11.5}$	$^{+10.5}_{-9.84}$	$^{+9.65}_{-9.75}$
b-Tagged jet energy scale (JES) [%]	$^{+0.44}_{-0.47}$	$^{+0.55}_{-0.56}$	$^{+0.61}_{-0.63}$	$^{+0.47}_{-0.53}$	$^{+0.56}_{-0.50}$	$^{+0.29}_{-0.20}$
Effective detector NP set 1 (JES) [%]	$^{+8.18}_{-8.88}$	$^{+6.76}_{-7.49}$	$^{+5.66}_{-6.21}$	$^{+3.98}_{-4.72}$	$^{+2.95}_{-3.04}$	$^{-}_{-2.23}$
Effective detector NP set 2 (JES) [%]	$^{-2.05}_{+2.25}$	$^{-1.80}_{+1.77}$	$^{-0.54}_{+0.21}$	$^{+0.55}_{-0.50}$	$^{+1.00}_{-0.69}$	$^{+1.99}_{-2.29}$
Effective detector NP set 3 (JES) [%]	$^{+0.79}_{-0.68}$	$^{+0.67}_{-0.73}$	$^{-}_{-}$	$^{-0.44}_{+0.76}$	$^{-0.59}_{+0.64}$	$^{-1.28}_{+1.12}$
Effective detector NP set 4 (JES) [%]	$^{-0.61}_{+0.65}$	$^{-0.34}_{+0.27}$	$^{+0.14}_{-0.34}$	$^{+0.37}_{-0.36}$	$^{+0.23}_{-0.37}$	$^{-}_{-}$
Effective detector NP set 5 (JES) [%]	$^{+0.33}_{-0.25}$	-	∓ 0.21	-	$^{+0.17}_{-}$	$^{+0.37}_{-0.29}$
Effective detector NP set 6 restTerm (JES) [%]	$^{-0.11}_{-}$	-	-	-	-	$^{+0.17}_{-0.22}$
η intercalibration model (JES) [%]	$^{+1.52}_{-1.78}$	$^{+1.69}_{-2.05}$	$^{+2.13}_{-2.35}$	$^{+1.84}_{-1.80}$	$^{+1.43}_{-1.58}$	$^{+0.18}_{-1.14}$
η intercalibration total stat (JES) [%]	$^{+1.06}_{-0.79}$	$^{+1.03}_{-1.14}$	$^{+0.69}_{-0.92}$	$^{+0.71}_{-0.34}$	$^{+0.74}_{-0.38}$	$^{-}_{-0.27}$
Flavour composition (JES) [%]	$^{+4.90}_{-6.28}$	$^{+4.67}_{-5.64}$	$^{+4.85}_{-5.15}$	$^{+4.20}_{-4.59}$	$^{+2.60}_{-2.65}$	$^{-}_{-1.00}$
Flavour response (JES) [%]	$^{-1.19}_{+1.35}$	$^{-1.57}_{+1.32}$	$^{-1.58}_{+1.04}$	$^{-1.15}_{+0.96}$	$^{-1.10}_{+0.76}$	$^{-}_{-0.69}$
Pile-up offset μ (JES) [%]	$^{-0.28}_{+0.31}$	$^{-0.34}_{+0.28}$	$^{-0.37}_{+0.27}$	$^{-}_{-}$	$^{-}_{-}$	$^{-}_{-}$
Pile-up offset N_{PV} (JES) [%]	$^{+0.30}_{-}$	-	-	$^{+0.30}_{-}$	$^{+0.23}_{-0.16}$	$^{+0.43}_{-0.28}$
Pile-up offset p_T (JES) [%]	$^{-}_{+0.17}$	$^{-0.13}_{+0.12}$	-	± 0.12	-	$^{+0.21}_{-0.14}$
Pile-up offset ρ topology (JES) [%]	$^{+2.83}_{-3.05}$	$^{+2.34}_{-2.66}$	$^{+1.33}_{-1.91}$	$^{+1.27}_{-1.39}$	$^{+0.29}_{-1.54}$	$^{-}_{-1.17}$
Punch-through (JES) [%]	-	-	-	-	-	-
Single particle high-p_T (JES) [%]	-	-	-	-	-	-
Jet energy resolution [%]	∓ 1.89	∓ 1.68	∓ 1.03	-	∓ 0.59	∓ 2.43
Jet vertex fraction [%]	$^{+5.77}_{-5.60}$	$^{+4.95}_{-4.83}$	± 2.75	$^{+1.85}_{-1.89}$	$^{+1.80}_{-1.82}$	$^{+0.71}_{-0.60}$
b-Quark tagging efficiency (eigenvector 0) [%]	$^{-4.21}_{+4.29}$	$^{-4.05}_{+4.12}$	$^{-3.92}_{+3.98}$	$^{-3.85}_{+3.90}$	$^{-3.85}_{+3.90}$	$^{-3.90}_{+3.95}$
b-Quark tagging efficiency (eigenvector 1) [%]	$^{-1.61}_{+1.63}$	$^{-1.62}_{+1.64}$	$^{-1.60}_{+1.61}$	$^{-1.50}_{+1.51}$	$^{-1.51}_{+1.52}$	$^{-2.42}_{+2.44}$
b-Quark tagging efficiency (eigenvector 2) [%]	$^{+1.22}_{-1.21}$	± 1.11	± 0.96	$^{+0.98}_{-0.97}$	± 1.05	± 0.58
b-Quark tagging efficiency (eigenvector 3) [%]	± 0.10	± 0.10	-	-	± 0.13	-
b-Quark tagging efficiency (eigenvector 4) [%]	-	-	-	-	-	-
c-Quark tagging efficiency (eigenvector 0) [%]	$^{-1.36}_{+1.37}$	$^{-1.39}_{+1.40}$	$^{-1.41}_{+1.42}$	$^{-1.63}_{+1.65}$	$^{-1.52}_{+1.53}$	$^{-1.57}_{+1.59}$
c-Quark tagging efficiency (eigenvector 1) [%]	± 0.13	± 0.13	± 0.14	± 0.20	± 0.20	± 0.20
c-Quark tagging efficiency (eigenvector 2) [%]	± 0.18	± 0.17	± 0.12	± 0.15	± 0.22	± 0.25
c-Quark tagging efficiency (eigenvector 3) [%]	-	-	-	-	-	-
Light-jet tagging efficiency (eigenvector 0) [%]	$^{-1.51}_{+1.55}$	$^{-1.31}_{+1.32}$	$^{-1.62}_{+1.74}$	$^{-1.60}_{+1.65}$	$^{-1.46}_{+1.44}$	$^{-1.40}_{+1.55}$
Light-jet tagging efficiency (eigenvector 1) [%]	-	-	-	-	-	± 0.18
Light-jet tagging efficiency (eigenvector 2) [%]	-	-	-	± 0.10	± 0.12	± 0.10
Light-jet tagging efficiency (eigenvector 3) [%]	-	-	-	-	-	-
Light-jet tagging efficiency (eigenvector 4) [%]	-	-	-	-	-	-
Light-jet tagging efficiency (eigenvector 5) [%]	-	-	-	-	-	-
Light-jet tagging efficiency (eigenvector 6) [%]	-	-	-	-	-	-
Light-jet tagging efficiency (eigenvector 7) [%]	-	-	-	-	-	-
Light-jet tagging efficiency (eigenvector 8) [%]	-	-	-	-	-	-
Light-jet tagging efficiency (eigenvector 9) [%]	-	-	-	-	-	-
Light-jet tagging efficiency (eigenvector 10) [%]	-	-	-	-	-	-
Light-jet tagging efficiency (eigenvector 11) [%]	-	-	-	-	-	-
Light-jet tagging efficiency (eigenvector 12) [%]	-	-	-	-	-	-
Light-jet tagging efficiency (eigenvector 13) [%]	-	-	-	-	-	-
b-Quark tagging extrapolation [%]	± 0.21	$^{+0.24}_{-0.23}$	± 0.33	$^{+0.43}_{-0.44}$	± 0.35	$^{+0.73}_{-0.74}$
b-Quark tagging extrapolation from c-Quark [%]	-	-	± 0.10	$^{+0.12}_{-0.14}$	-	± 0.18
Electron energy resolution [%]	-	-	-	-	-	-
Electron energy scale [%]	-	-	-	-	-	-
Electron trigger efficiency [%]	$^{+0.24}_{-0.25}$	± 0.25	± 0.26	$^{+0.27}_{-0.28}$	± 0.28	± 0.30
Electron reconstruction efficiency [%]	± 0.17	± 0.17	± 0.18	± 0.19	± 0.20	± 0.23
Electron identification efficiency [%]	± 0.40	± 0.41	± 0.44	± 0.46	± 0.49	± 0.61
Electron isolation efficiency [%]	± 0.14	± 0.15	± 0.16	$^{+0.17}_{-0.18}$	± 0.20	± 0.30
Muon energy scale [%]	-	-	-	-	-	-
Muon (MS) momentum resolution [%]	-	-	-	-	-	-
Muon (ID) momentum resolution [%]	-	-	-	-	-	-
Muon trigger efficiency stat [%]	$^{+0.56}_{-0.57}$	$^{+0.56}_{-0.58}$	$^{+0.56}_{-0.58}$	$^{+0.56}_{-0.58}$	$^{+0.57}_{-0.59}$	$^{+0.58}_{-0.59}$
Muon trigger efficiency syst [%]	± 0.24	± 0.24	± 0.24	$^{+0.24}_{-0.26}$	± 0.25	$^{+0.25}_{-0.24}$
Muon identification stat [%]	-	-	-	-	-	-
Muon identification syst [%]	± 0.17	± 0.17	± 0.17	$^{+0.19}_{-0.18}$	$^{+0.20}_{-0.19}$	± 0.24
Muon isolation efficiency stat [%]	-	-	-	-	-	-
Muon isolation efficiency syst [%]	± 0.10	± 0.10	$^{+0.11}_{-0.10}$	$^{-}_{-0.12}$	$^{+0.10}_{-0.11}$	± 0.11
Muon TTVA efficiency stat [%]	-	-	-	-	-	-
Muon TTVA efficiency syst [%]	-	-	-	-	-	-
E_T^{miss} Soft jet resolution para [%]	-	-	± 0.21	-	± 0.21	-
E_T^{miss} Soft jet resolution perp [%]	∓ 0.22	-	-	-	∓ 0.19	∓ 0.23
E_T^{miss} Soft jet scale [%]	-	-	-	-	-	-
Luminosity [%]	∓ 2.04	∓ 2.04	∓ 2.04	∓ 2.04	∓ 2.04	∓ 2.04
W+jets CA_2ex stat error [%]	-	-	-	-	-	-
W+jets CA_3ex stat error [%]	-	-	-	-	-	-
W+jets CA_4incl stat error [%]	-	-	-	∓ 0.13	∓ 0.16	∓ 0.20
W+jets Fc stat error [%]	-	-	-	∓ 0.13	-	-
W+jets Fcc stat error [%]	∓ 0.73	∓ 0.59	∓ 0.70	∓ 1.24	∓ 1.76	∓ 2.02
W+jets Flight stat error [%]	-	-	-	-	-	-
Single top cross-section [%]	± 0.67	± 0.66	± 0.68	± 0.78	± 0.89	± 0.99
Z+jets cross-section [%]	± 0.57	± 0.57	± 0.89	± 0.95	± 0.70	± 0.93
Diboson cross-section [%]	± 0.12	± 0.12	± 0.19	± 0.26	± 0.34	± 0.78
$t\bar{t}V$ cross-section [%]	-	-	-	-	-	± 0.11
Monte Carlo sample statistics [%]	± 0.50	± 0.31	± 0.47	± 0.74	± 1.01	± 0.92
ISR/FSR + scale [%]	$^{-1.38}_{+0.79}$	$^{-1.36}_{+1.19}$	$^{-4.34}_{+3.79}$	$^{-3.36}_{+3.95}$	$^{-3.32}_{+5.35}$	$^{-3.15}_{+4.15}$
Alternate hard-scattering model [%]	∓ 5.24	∓ 1.61	± 2.66	± 4.00	± 1.97	± 0.12
Alternate parton-shower model [%]	∓ 2.28	∓ 2.65	∓ 2.78	∓ 2.74	∓ 0.56	∓ 2.26
Inter PDF [%]	-	-	-	-	-	± 0.23
Intra PDF [%]	-	-	-	-	± 0.10	± 0.34
Fakes overall normalization [%]	± 2.79	± 2.18	± 2.96	± 3.27	± 4.40	± 4.19
Real lepton efficiency stat [%]	$^{-0.15}_{+0.14}$	$^{-0.15}_{+0.14}$	$^{-0.16}_{+0.15}$	$^{-0.18}_{+0.17}$	$^{-0.24}_{+0.21}$	$^{-0.35}_{+0.28}$
Fake lepton efficiency MC scale [%]	$^{+0.53}_{-0.68}$	$^{+0.41}_{-0.51}$	$^{+0.62}_{-0.74}$	$^{+0.48}_{-0.59}$	$^{+0.72}_{-0.93}$	$^{+0.54}_{-0.60}$
Fake lepton efficiency alternate CR [%]	± 0.38	± 0.32	± 0.33	± 0.27	± 0.12	± 0.11

TABLE A.5: Systematic uncertainties for the absolute differential cross-section at particle-level for $p_{\mathrm{T}}^{t\bar{t}}$ in the 5-jet exclusive configuration.

Bins [GeV]	0–35	35–75	75–125	125–170	170–225	225–800
$d\sigma$ / $dp_T^{t\bar{t}}$ [pb/GeV]	$4.34 \cdot 10^{-2}$	$1.07 \cdot 10^{-1}$	$1.12 \cdot 10^{-1}$	$7.76 \cdot 10^{-2}$	$4.58 \cdot 10^{-2}$	$5.39 \cdot 10^{-3}$
Total Uncertainty [%]	$^{+24.6}_{-21.5}$	$^{+22.5}_{-22.4}$	$^{+21.1}_{-21.0}$	$^{+20.3}_{-19.6}$	$^{+17.4}_{-19.2}$	$^{+14.4}_{-15.1}$
Statistics [%]	±2.4	±1.3	±1.3	±1.7	±2.1	±1.8
Systematics [%]	$^{+24.5}_{-21.3}$	$^{+22.4}_{-22.3}$	$^{+21.1}_{-21.0}$	$^{+20.2}_{-19.5}$	$^{+17.3}_{-19.0}$	$^{+14.3}_{-14.9}$
b-Tagged jet energy scale (JES) [%]	$^{+0.75}_{-0.41}$	$^{+0.70}_{-0.63}$	$^{+0.56}_{-0.65}$	$^{+0.66}_{-0.57}$	$^{+0.70}_{-0.89}$	$^{+0.36}_{-0.26}$
Effective detector NP set 1 (JES) [%]	$^{+15.8}_{-12.4}$	$^{+14.2}_{-13.5}$	$^{+13.1}_{-12.5}$	$^{+12.1}_{-11.3}$	$^{+9.86}_{-11.0}$	$^{+7.82}_{-8.29}$
Effective detector NP set 2 (JES) [%]	$^{-3.41}_{+3.52}$	$^{-3.38}_{+3.28}$	$^{-2.42}_{+2.40}$	$^{-1.80}_{+1.57}$	$^{-1.58}_{+0.92}$	$^{+0.54}_{-0.48}$
Effective detector NP set 3 (JES) [%]	$^{+1.40}_{-1.47}$	$^{+1.15}_{-1.13}$	$^{+0.72}_{-0.67}$	$^{-}_{-0.42}$	$^{-}_{-0.20}$	$^{-0.66}_{+0.72}$
Effective detector NP set 4 (JES) [%]	$^{-0.93}_{+0.74}$	$^{-0.63}_{+0.62}$	$^{-0.21}_{+0.17}$	-	±0.12	-
Effective detector NP set 5 (JES) [%]	$^{+0.13}_{-0.14}$	-	-	-	$^{-}_{-0.23}$	$^{+0.27}_{-0.11}$
Effective detector NP set 6 restTerm (JES) [%]	-	-	-	-	$^{+0.15}_{-0.20}$	$^{+0.21}_{-0.18}$
η intercalibration model (JES) [%]	$^{+3.73}_{-3.39}$	$^{+3.59}_{-3.98}$	$^{+3.72}_{-4.03}$	$^{+3.61}_{-3.80}$	$^{+3.29}_{-4.18}$	$^{+2.85}_{-3.14}$
η intercalibration total stat (JES) [%]	$^{+2.33}_{-1.63}$	$^{+1.96}_{-2.19}$	$^{+1.64}_{-1.92}$	$^{+1.77}_{-1.73}$	$^{+1.77}_{-2.19}$	$^{+1.45}_{-1.40}$
Flavour composition (JES) [%]	$^{+12.7}_{-10.4}$	$^{+11.2}_{-11.4}$	±11.2	$^{+11.0}_{-10.6}$	$^{+9.79}_{-10.2}$	$^{+7.36}_{-7.71}$
Flavour response (JES) [%]	$^{-3.00}_{+3.43}$	$^{-3.34}_{+2.66}$	$^{-3.10}_{+2.73}$	$^{-3.29}_{+3.00}$	$^{-3.72}_{+2.47}$	$^{-2.46}_{+2.28}$
Pile-up offset μ (JES) [%]	$^{-0.78}_{+0.79}$	$^{-0.71}_{+0.58}$	$^{-0.53}_{+0.54}$	$^{-0.76}_{+0.43}$	$^{-0.70}_{+0.56}$	$^{-0.27}_{+0.25}$
Pile-up offset N_{PV} (JES) [%]	$^{-0.16}_{+0.18}$	$^{-0.42}_{+0.35}$	$^{-0.28}_{+0.26}$	-	$^{-0.30}_{+0.33}$	-
Pile-up offset p_T (JES) [%]	$^{-0.10}_{+0.19}$	$^{-0.24}_{-}$	$^{-}_{+0.19}$	-	-	-
Pile-up offset ρ topology (JES) [%]	$^{+5.17}_{-4.98}$	$^{+4.53}_{-4.99}$	$^{+3.76}_{-4.36}$	$^{+3.76}_{-3.92}$	$^{+3.16}_{-4.35}$	$^{+2.21}_{-2.75}$
Punch-through (JES) [%]	-	-	-	-	-	-
Single particle high-p_T (JES) [%]	-	-	-	-	-	-
Jet energy resolution [%]	±0.45	∓0.52	±0.29	±0.33	±0.50	∓1.20
Jet vertex fraction [%]	$^{+7.46}_{-7.11}$	$^{+7.19}_{-6.85}$	$^{+6.29}_{-6.03}$	$^{+5.19}_{-5.05}$	$^{+4.51}_{-4.37}$	$^{+3.63}_{-3.56}$
b-Quark tagging efficiency (eigenvector 0) [%]	$^{-3.72}_{+3.77}$	$^{-3.78}_{+3.83}$	$^{-3.71}_{+3.76}$	$^{-3.61}_{+3.66}$	$^{-3.55}_{+3.59}$	$^{-3.49}_{+3.53}$
b-Quark tagging efficiency (eigenvector 1) [%]	$^{-1.50}_{+1.52}$	$^{-1.51}_{+1.52}$	$^{-1.55}_{+1.57}$	$^{-1.59}_{+1.61}$	∓1.60	$^{-2.35}_{+2.36}$
b-Quark tagging efficiency (eigenvector 2) [%]	±1.03	±1.00	$^{+0.92}_{-0.91}$	±0.84	±0.83	±0.43
b-Quark tagging efficiency (eigenvector 3) [%]	-	-	-	-	-	-
b-Quark tagging efficiency (eigenvector 4) [%]	-	-	-	-	-	-
c-Quark tagging efficiency (eigenvector 0) [%]	∓1.57	∓1.56	∓1.47	$^{-1.30}_{+1.29}$	$^{-1.31}_{+1.30}$	∓1.22
c-Quark tagging efficiency (eigenvector 1) [%]	±0.11	±0.10	±0.11	±0.12	±0.15	±0.10
c-Quark tagging efficiency (eigenvector 2) [%]	±0.20	±0.19	±0.14	±0.13	±0.16	±0.15
c-Quark tagging efficiency (eigenvector 3) [%]	-	-	-	-	-	-
Light-jet tagging efficiency (eigenvector 0) [%]	$^{-1.56}_{+1.53}$	$^{-1.91}_{+1.97}$	$^{-1.75}_{+1.74}$	$^{-1.54}_{+1.55}$	$^{-1.42}_{+1.41}$	$^{-1.45}_{+1.44}$
Light-jet tagging efficiency (eigenvector 1) [%]	-	-	-	-	-	-
Light-jet tagging efficiency (eigenvector 2) [%]	-	-	-	-	-	±0.10
Light-jet tagging efficiency (eigenvector 3) [%]	-	-	-	-	-	-
Light-jet tagging efficiency (eigenvector 4) [%]	-	-	-	-	-	-
Light-jet tagging efficiency (eigenvector 5) [%]	-	-	-	-	-	-
Light-jet tagging efficiency (eigenvector 6) [%]	-	-	-	-	-	-
Light-jet tagging efficiency (eigenvector 7) [%]	-	-	-	-	-	-
Light-jet tagging efficiency (eigenvector 8) [%]	-	-	-	-	-	-
Light-jet tagging efficiency (eigenvector 9) [%]	-	-	-	-	-	-
Light-jet tagging efficiency (eigenvector 10) [%]	-	-	-	-	-	-
Light-jet tagging efficiency (eigenvector 11) [%]	-	-	-	-	-	-
Light-jet tagging efficiency (eigenvector 12) [%]	-	-	-	-	-	-
Light-jet tagging efficiency (eigenvector 13) [%]	-	-	-	-	-	-
b-Quark tagging extrapolation [%]	$^{+0.25}_{-0.24}$	±0.27	$^{+0.34}_{-0.33}$	$^{+0.40}_{-0.39}$	±0.37	$^{+1.00}_{-1.02}$
b-Quark tagging extrapolation from c-Quark [%]	-	-	-	-	-	-
Electron energy resolution [%]	-	-	-	-	-	-
Electron energy scale [%]	-	-	-	-	-	-
Electron trigger efficiency [%]	±0.24	±0.25	±0.26	±0.27	±0.27	±0.30
Electron reconstruction efficiency [%]	±0.16	±0.17	±0.18	±0.19	±0.19	±0.23
Electron identification efficiency [%]	±0.39	±0.42	±0.43	±0.45	±0.48	±0.61
Electron isolation efficiency [%]	±0.14	±0.15	±0.16	±0.17	±0.20	±0.31
Muon energy scale [%]	-	-	-	-	-	-
Muon (MS) momentum resolution [%]	-	-	-	-	-	-
Muon (ID) momentum resolution [%]	-	-	-	-	-	-
Muon trigger efficiency stat [%]	$^{+0.56}_{-0.57}$	$^{+0.55}_{-0.57}$	$^{+0.56}_{-0.57}$	$^{+0.56}_{-0.57}$	$^{+0.55}_{-0.57}$	$^{+0.55}_{-0.56}$
Muon trigger efficiency syst [%]	$^{+0.24}_{-0.23}$	±0.24	±0.24	±0.24	±0.24	$^{+0.24}_{-0.23}$
Muon identification stat [%]	-	-	-	-	-	-
Muon identification syst [%]	±0.17	±0.17	±0.17	±0.18	±0.19	$^{+0.24}_{-0.23}$
Muon isolation efficiency stat [%]	-	-	-	-	-	-
Muon isolation efficiency syst [%]	±0.10	±0.10	±0.10	±0.10	±0.10	±0.10
Muon TTVA efficiency stat [%]	-	-	-	-	-	-
Muon TTVA efficiency syst [%]	-	-	-	-	-	-
E_T^{miss} Soft jet resolution para [%]	-	-	±0.23	∓0.21	-	±0.18
E_T^{miss} Soft jet resolution perp [%]	±0.21	∓0.21	-	∓0.11	∓0.16	-
E_T^{miss} Soft jet scale [%]	$^{+0.33}_{-}$	-	-	-	$^{-}_{-0.23}$	-
Luminosity [%]	∓2.04	∓2.04	∓2.04	∓2.04	∓2.04	∓2.04
W+jets CA_2ex stat error [%]	-	-	-	-	-	-
W+jets CA_3ex stat error [%]	-	-	-	-	-	-
W+jets CA_4incl stat error [%]	-	-	-	-	-	∓0.11
W+jets Fc stat error [%]	-	-	-	-	-	-
W+jets Fcc stat error [%]	∓0.53	∓0.70	∓0.73	∓0.74	∓0.78	∓1.22
W+jets Flight stat error [%]	-	-	-	-	-	-
Single top cross-section [%]	±0.58	±0.56	±0.56	±0.58	±0.59	±0.65
Z+jets cross-section [%]	±0.22	±0.44	±0.84	±0.79	±0.67	±0.92
Diboson cross-section [%]	±0.26	±0.24	±0.30	±0.39	±0.51	±0.91
$t\bar{t}V$ cross-section [%]	-	-	±0.10	±0.13	±0.15	±0.20
Monte Carlo sample statistics [%]	±0.84	±0.52	±0.47	±0.61	±0.73	±0.59
ISR/FSR + scale [%]	$^{-4.93}_{+1.78}$	$^{-3.34}_{+2.76}$	$^{-3.11}_{+3.15}$	$^{-3.67}_{+3.65}$	$^{-3.92}_{+3.20}$	$^{-3.10}_{+2.69}$
Alternate hard-scattering model [%]	∓0.85	±0.46	±0.82	±4.04	±3.26	±2.01
Alternate parton-shower model [%]	∓3.71	∓4.08	∓3.74	∓2.14	∓0.74	∓1.58
Inter PDF [%]	-	-	±0.11	-	±0.13	-
Intra PDF [%]	-	-	±0.15	-	±0.12	-
Fakes overall normalization [%]	±3.23	±3.02	±2.95	±2.30	±2.00	±2.73
Real lepton efficiency stat [%]	$^{-0.17}_{+0.16}$	$^{-0.16}_{+0.15}$	$^{-0.17}_{+0.16}$	$^{-0.22}_{+0.19}$	∓0.19	$^{-0.37}_{+0.28}$
Fake lepton efficiency MC scale [%]	$^{+0.90}_{-1.12}$	$^{+0.68}_{-0.90}$	$^{+0.66}_{-0.74}$	$^{+0.31}_{-0.44}$	$^{+0.32}_{-0.44}$	$^{+0.34}_{-0.37}$
Fake lepton efficiency alternate CR [%]	±0.53	±0.28	±0.34	±0.30	±0.11	±0.19

TABLE A.6: Systematic uncertainties for the absolute differential cross-section at particle-level for $p_{\mathrm{T}}^{t\bar{t}}$ in the 6-jet inclusive configuration.

Bins [GeV]	0–40	40–80	80–120	120–170	170–230	230–600
$\mathrm{d}\sigma$ / $\mathrm{d}\lvert p_{out}^{t\bar{t}}\rvert$ [pb/GeV]	$1.09 \cdot 10^{0}$	$1.56 \cdot 10^{-1}$	$2.28 \cdot 10^{-2}$	$5.15 \cdot 10^{-3}$	$9.83 \cdot 10^{-4}$	$2.35 \cdot 10^{-5}$
Total Uncertainty [%]	$^{+9.24}_{-9.81}$	$^{+16.4}_{-16.1}$	$^{+21.5}_{-21.8}$	$^{+27.2}_{-29.1}$	$^{+29.4}_{-28.0}$	$^{+71.9}_{-77.4}$
Statistics [%]	± 0.4	± 1.4	± 3.9	± 7.2	$\pm 15.$	$\pm 43.$
Systematics [%]	$^{+9.23}_{-9.80}$	$^{+16.3}_{-16.0}$	$^{+21.1}_{-21.4}$	$^{+26.1}_{-28.1}$	$^{+24.1}_{-22.4}$	$^{+57.0}_{-63.7}$
b-Tagged jet energy scale (JES) [%]	$^{+0.48}_{-0.47}$	$^{+0.68}_{-0.42}$	$^{+0.69}_{-0.71}$	$^{+0.45}_{-1.68}$	$^{+1.20}_{-}$	$^{-}_{-1.70}$
Effective detector NP set 1 (JES) [%]	$^{+0.30}_{-1.80}$	$^{+5.05}_{-5.93}$	$^{+6.13}_{-7.54}$	$^{+2.84}_{-3.07}$	$^{+2.40}_{-3.49}$	$^{-0.48}_{+0.43}$
Effective detector NP set 2 (JES) [%]	-	$^{-}_{+0.37}$	$^{-}_{-0.46}$	$^{+2.47}_{-3.12}$	$^{+2.90}_{-3.27}$	$^{+1.96}_{-6.02}$
Effective detector NP set 3 (JES) [%]	-	-	$^{-0.48}_{+0.27}$	$^{-1.98}_{+1.38}$	$^{-1.80}_{+1.56}$	$^{-5.13}_{+1.50}$
Effective detector NP set 4 (JES) [%]	-	-	$^{+0.33}_{-0.42}$	$^{+0.25}_{-0.77}$	$^{+1.39}_{-1.31}$	$^{-}_{-2.31}$
Effective detector NP set 5 (JES) [%]	-	-	$^{-}_{-}$	$^{-}_{-0.55}$	$^{+0.58}_{-0.19}$	$^{+0.67}_{-1.92}$
Effective detector NP set 6 restTerm (JES) [%]	-	-	$^{+0.14}_{-0.25}$	$^{+0.34}_{-0.80}$	$^{+0.18}_{-0.43}$	$^{+0.55}_{-1.94}$
η intercalibration model (JES) [%]	$^{-0.64}_{-}$	$^{+4.14}_{-3.79}$	$^{+6.05}_{-7.77}$	$^{+3.76}_{-4.58}$	$^{+3.89}_{-3.88}$	$^{+5.70}_{-6.56}$
η intercalibration total stat (JES) [%]	-	$^{+0.80}_{-0.71}$	$^{+1.06}_{-1.84}$	$^{-}_{-1.87}$	$^{+0.90}_{-1.31}$	$^{+1.16}_{-3.18}$
Flavour composition (JES) [%]	$^{-1.37}_{+0.29}$	$^{+4.06}_{-4.66}$	$^{+7.19}_{-7.93}$	$^{+4.89}_{-5.22}$	$^{+3.52}_{-6.27}$	$^{+2.66}_{-1.41}$
Flavour response (JES) [%]	$^{+0.14}_{-0.64}$	$^{-1.14}_{+0.91}$	$^{-2.94}_{+1.50}$	$^{-0.90}_{+0.99}$	$^{-1.37}_{+1.52}$	$^{-4.18}_{+1.46}$
Pile-up offset μ (JES) [%]	-	$^{-0.35}_{+0.27}$	$^{-0.91}_{+0.31}$	$^{-}_{-0.37}$	$^{-0.23}_{-}$	$^{-}_{-1.76}$
Pile-up offset N_{PV} (JES) [%]	$^{+0.16}_{-}$	-	$^{+0.23}_{-}$	$^{+0.27}_{-0.70}$	$^{+0.31}_{-}$	$^{-}_{-1.18}$
Pile-up offset p_T (JES) [%]	-	$^{-}_{+0.13}$	$^{+0.26}_{-0.16}$	$^{+0.61}_{-1.04}$	$^{+1.38}_{-1.29}$	$^{-}_{-2.49}$
Pile-up offset ρ topology (JES) [%]	$^{-}_{-0.56}$	$^{+1.19}_{-1.73}$	$^{+1.55}_{-3.33}$	$^{-}_{-0.75}$	$^{+0.87}_{-1.28}$	$^{+0.96}_{-1.38}$
Punch-through (JES) [%]	-	-	-	-	-	-
Single particle high-p_T (JES) [%]	-	-	-	-	-	-
Jet energy resolution [%]	∓ 2.64	∓ 0.51	± 0.69	∓ 1.85	± 7.08	∓ 9.10
Jet vertex fraction [%]	$^{+2.65}_{-2.64}$	$^{+0.47}_{-0.53}$	$^{-0.65}_{+0.70}$	$^{+1.12}_{-1.14}$	$^{+0.22}_{-0.55}$	$^{+0.31}_{-0.40}$
b-Quark tagging efficiency (eigenvector 0) [%]	$^{-4.29}_{+4.37}$	$^{-4.17}_{+4.24}$	$^{-4.04}_{+4.11}$	$^{-4.00}_{+4.05}$	$^{-4.04}_{+4.11}$	$^{-3.42}_{+3.48}$
b-Quark tagging efficiency (eigenvector 1) [%]	$^{-1.63}_{+1.64}$	$^{-1.72}_{+1.74}$	$^{-1.99}_{+2.01}$	$^{-2.22}_{+2.24}$	$^{-2.88}_{+2.92}$	$^{-2.65}_{+2.66}$
b-Quark tagging efficiency (eigenvector 2) [%]	$^{+1.21}_{-1.20}$	$^{+1.14}_{-1.13}$	± 0.96	± 0.79	± 0.50	± 0.24
b-Quark tagging efficiency (eigenvector 3) [%]	-	-	$^{+0.12}_{-0.13}$	-	-	-
b-Quark tagging efficiency (eigenvector 4) [%]	-	-	-	-	-	-
c-Quark tagging efficiency (eigenvector 0) [%]	$^{-1.53}_{+1.54}$	$^{-1.61}_{+1.62}$	$^{-1.90}_{+1.91}$	$^{-2.04}_{+2.05}$	$^{-1.50}_{+1.49}$	$^{-2.15}_{+2.20}$
c-Quark tagging efficiency (eigenvector 1) [%]	± 0.17	± 0.16	± 0.14	-	-	∓ 0.11
c-Quark tagging efficiency (eigenvector 2) [%]	± 0.19	± 0.19	± 0.22	± 0.22	± 0.11	-
c-Quark tagging efficiency (eigenvector 3) [%]	-	-	-	-	-	-
Light-jet tagging efficiency (eigenvector 0) [%]	$^{-1.43}_{+1.55}$	$^{-1.77}_{+1.89}$	$^{-1.98}_{+1.99}$	$^{-1.58}_{+1.57}$	$^{-0.26}_{+0.24}$	$^{-1.45}_{+1.41}$
Light-jet tagging efficiency (eigenvector 1) [%]	-	-	-	-	-	± 0.28
Light-jet tagging efficiency (eigenvector 2) [%]	-	± 0.11	-	-	-	-
Light-jet tagging efficiency (eigenvector 3) [%]	-	-	-	-	-	-
Light-jet tagging efficiency (eigenvector 4) [%]	-	-	-	-	-	-
Light-jet tagging efficiency (eigenvector 5) [%]	-	-	-	-	-	-
Light-jet tagging efficiency (eigenvector 6) [%]	-	-	-	-	-	-
Light-jet tagging efficiency (eigenvector 7) [%]	-	-	-	-	-	-
Light-jet tagging efficiency (eigenvector 8) [%]	-	-	-	-	-	-
Light-jet tagging efficiency (eigenvector 9) [%]	-	-	-	-	-	-
Light-jet tagging efficiency (eigenvector 10) [%]	-	-	-	-	-	-
Light-jet tagging efficiency (eigenvector 11) [%]	-	-	-	-	-	-
Light-jet tagging efficiency (eigenvector 12) [%]	-	-	-	-	-	-
Light-jet tagging efficiency (eigenvector 13) [%]	-	-	-	-	-	-
b-Quark tagging extrapolation [%]	± 0.24	$^{+0.28}_{-0.29}$	± 0.42	± 0.62	$^{+1.16}_{-1.15}$	$^{+1.48}_{-1.49}$
b-Quark tagging extrapolation from c-Quark [%]	± 0.12	$^{+0.11}_{-0.12}$	± 0.18	± 0.17	$^{+0.11}_{-0.10}$	$^{+0.20}_{-0.21}$
Electron energy resolution [%]	-	-	-	$^{-}_{-0.21}$	$^{-}_{+0.19}$	$^{-0.28}_{-}$
Electron energy scale [%]	-	-	-	-	$^{-}_{+0.25}$	$^{-}_{+0.13}$
Electron trigger efficiency [%]	± 0.26	$^{+0.26}_{-0.27}$	± 0.28	± 0.33	± 0.38	± 0.30
Electron reconstruction efficiency [%]	± 0.18	± 0.18	± 0.18	± 0.22	± 0.24	± 0.21
Electron identification efficiency [%]	± 0.43	± 0.43	± 0.46	± 0.54	± 0.64	± 0.51
Electron isolation efficiency [%]	$^{+0.16}_{-0.15}$	$^{+0.15}_{-0.16}$	± 0.17	± 0.21	$^{+0.27}_{-0.26}$	± 0.21
Muon energy scale [%]	-	-	-	-	-	-
Muon (MS) momentum resolution [%]	-	-	-	-	-	-
Muon (ID) momentum resolution [%]	-	-	-	-	-	$^{+0.72}_{-}$
Muon trigger efficiency stat [%]	$^{+0.57}_{-0.59}$	$^{+0.59}_{-0.61}$	$^{+0.60}_{-0.62}$	$^{+0.56}_{-0.57}$	$^{+0.51}_{-0.53}$	$^{+0.63}_{-0.65}$
Muon trigger efficiency syst [%]	$^{+0.25}_{-0.24}$	$^{+0.25}_{-0.26}$	$^{+0.26}_{-0.25}$	$^{+0.24}_{-0.23}$	± 0.23	± 0.25
Muon identification stat [%]	-	-	-	-	-	-
Muon identification syst [%]	± 0.17	± 0.18	± 0.19	± 0.18	± 0.19	± 0.21
Muon isolation efficiency stat [%]	-	-	-	-	-	-
Muon isolation efficiency syst [%]	$^{+0.11}_{-0.10}$	$^{+0.10}_{-0.11}$	± 0.11	$^{+0.11}_{-0.10}$	± 0.10	± 0.11
Muon TTVA efficiency stat [%]	-	-	-	-	-	-
Muon TTVA efficiency syst [%]	-	-	-	-	-	-
E_T^{miss} Soft jet resolution para [%]	-	± 0.31	∓ 0.28	± 1.11	± 0.93	∓ 2.13
E_T^{miss} Soft jet resolution perp [%]	∓ 0.14	± 0.18	-	-	± 0.77	∓ 1.99
E_T^{miss} Soft jet scale [%]	-	-	-	$^{-0.44}_{+0.39}$	$^{+0.90}_{-0.71}$	$^{-1.58}_{-}$
Luminosity [%]	∓ 2.04	∓ 2.04	∓ 2.04	∓ 2.04	∓ 2.04	∓ 2.04
W+jets CA_2ex stat error [%]	-	-	-	-	-	-
W+jets CA_3ex stat error [%]	-	-	-	-	-	-
W+jets CA_4incl stat error [%]	∓ 0.13	∓ 0.11	∓ 0.10	∓ 0.16	-	∓ 0.13
W+jets Fc stat error [%]	∓ 0.13	-	-	-	-	-
W+jets Fcc stat error [%]	∓ 1.20	∓ 1.09	∓ 1.18	∓ 1.91	∓ 0.63	∓ 1.70
W+jets Flight stat error [%]	-	-	-	-	-	-
Single top cross-section [%]	± 0.87	± 0.97	± 1.23	± 1.37	± 1.16	± 0.91
Z+jets cross-section [%]	± 0.72	± 0.75	± 0.78	± 0.88	± 1.22	± 0.18
Diboson cross-section [%]	± 0.11	± 0.12	± 0.18	± 0.22	-	± 0.23
$t\bar{t}V$ cross-section [%]	-	-	-	-	-	± 0.10
Monte Carlo sample statistics [%]	± 0.20	± 0.52	± 1.36	± 2.64	± 5.49	± 9.02
ISR/FSR + scale [%]	$^{-2.55}_{+1.16}$	$^{-5.79}_{+7.50}$	$^{-3.47}_{+7.60}$	$^{-9.36}_{+1.91}$	$^{-2.28}_{+7.83}$	$^{-}_{-26.5}$
Alternate hard-scattering model [%]	∓ 0.59	± 7.34	± 7.33	± 23.4	± 17.4	± 52.0
Alternate parton-shower model [%]	∓ 4.50	± 3.62	± 7.61	∓ 2.34	∓ 0.67	∓ 11.5
Inter PDF [%]	-	-	± 0.12	-	∓ 0.25	∓ 0.47
Intra PDF [%]	-	± 0.13	± 0.18	± 0.26	± 3.43	± 1.72
Fakes overall normalization [%]	± 3.48	± 6.25	± 8.78	± 4.42	± 0.77	± 12.7
Real lepton efficiency stat [%]	$^{-0.15}_{+0.14}$	$^{-0.14}_{+0.13}$	$^{-0.16}_{+0.13}$	$^{-0.22}_{+0.20}$	$^{-0.19}_{+0.18}$	-
Fake lepton efficiency MC scale [%]	$^{+0.48}_{-0.61}$	$^{+1.61}_{-1.95}$	$^{+2.15}_{-3.15}$	$^{+0.64}_{-0.86}$	$^{+0.25}_{-0.45}$	$^{+3.67}_{-5.59}$
Fake lepton efficiency alternate CR [%]	± 0.30	± 0.71	± 0.89	± 0.45	-	± 0.98

TABLE A.7: Systematic uncertainties for the absolute differential cross-section at particle-level for $\lvert p_{out}^{t\bar{t}} \rvert$ in the 4-jet exclusive configuration.

Bins [GeV]	0–40	40–80	80–120	120–170	170–230	230–600
$d\sigma$ / $d\lvert p_{out}^{t\bar{t}}\rvert$ [pb/GeV]	$1.71 \cdot 10^{0}$	$5.36 \cdot 10^{-1}$	$1.79 \cdot 10^{-1}$	$6.32 \cdot 10^{-2}$	$2.48 \cdot 10^{-2}$	$1.79 \cdot 10^{-3}$
Total Uncertainty [%]	$^{+9.65}_{-10.6}$	$^{+15.2}_{-15.0}$	$^{+15.4}_{-15.7}$	$^{+12.7}_{-14.2}$	$^{+11.0}_{-12.2}$	$^{+15.0}_{-16.0}$
Statistics [%]	± 0.3	± 0.7	± 1.3	± 2.0	± 3.1	± 4.7
Systematics [%]	$^{+9.65}_{-10.6}$	$^{+15.1}_{-15.0}$	$^{+15.3}_{-15.6}$	$^{+12.5}_{-14.0}$	$^{+10.5}_{-11.7}$	$^{+14.2}_{-15.2}$
b-Tagged jet energy scale (JES) [%]	$^{+0.48}_{-0.47}$	$^{+0.65}_{-0.56}$	$^{+0.67}_{-0.71}$	$^{+0.65}_{-0.78}$	$^{+0.58}_{-0.53}$	$^{+0.50}_{-0.41}$
Effective detector NP set 1 (JES) [%]	$^{+3.35}_{-4.39}$	$^{+8.39}_{-8.59}$	$^{+8.27}_{-8.64}$	$^{+5.67}_{-6.78}$	$^{+3.93}_{-5.47}$	$^{+2.49}_{-3.78}$
Effective detector NP set 2 (JES) [%]	$^{-0.77}_{+0.70}$	$^{-1.12}_{+1.18}$	$^{-0.71}_{+0.44}$	$^{+0.69}_{-0.97}$	$^{+0.90}_{-1.23}$	$^{+2.65}_{-2.09}$
Effective detector NP set 3 (JES) [%]	$^{+0.19}_{-0.26}$	$^{+0.27}_{-0.29}$	$^{-0.26}_{+0.16}$	$^{-0.81}_{+0.66}$	$^{-1.11}_{+1.00}$	$^{-1.46}_{+1.41}$
Effective detector NP set 4 (JES) [%]	$^{-0.19}_{-}$	-	$^{+0.18}_{-0.26}$	$^{+0.38}_{-0.50}$	$^{+0.25}_{-0.36}$	$^{+0.11}_{-0.57}$
Effective detector NP set 5 (JES) [%]	-	-	-	-	$^{+0.16}_{-}$	$^{+0.15}_{-0.20}$
Effective detector NP set 6 restTerm (JES) [%]	-	-	$^{+0.17}_{-0.16}$	$^{+0.13}_{-0.17}$	$^{+0.16}_{-0.31}$	$^{+0.25}_{-0.20}$
η intercalibration model (JES) [%]	$^{+0.40}_{-0.90}$	$^{+3.31}_{-3.25}$	$^{+3.61}_{-3.79}$	$^{+2.11}_{-2.83}$	$^{+1.66}_{-2.56}$	$^{+1.68}_{-1.67}$
η intercalibration total stat (JES) [%]	$^{+0.38}_{-0.41}$	$^{+1.27}_{-1.26}$	$^{+1.34}_{-1.50}$	$^{+0.64}_{-1.06}$	$^{+0.96}_{-1.26}$	$^{+1.06}_{-0.29}$
Flavour composition (JES) [%]	$^{+1.52}_{-2.43}$	$^{+7.07}_{-7.28}$	$^{+7.78}_{-7.97}$	$^{+5.62}_{-6.74}$	$^{+3.47}_{-4.31}$	$^{+1.89}_{-2.47}$
Flavour response (JES) [%]	$^{-0.62}_{+0.20}$	$^{-2.04}_{+1.72}$	$^{-2.69}_{+2.19}$	$^{-1.97}_{+1.25}$	$^{-2.14}_{+1.44}$	$^{-1.13}_{+0.79}$
Pile-up offset μ (JES) [%]	-	$^{+0.39}_{-0.44}$	$^{+0.38}_{-0.53}$	$^{+0.13}_{-0.34}$	$^{+0.21}_{-0.32}$	-
Pile-up offset N_{PV} (JES) [%]	-	$^{-0.10}_{+0.17}$	-	-	-	$^{+0.32}_{-}$
Pile-up offset p_T (JES) [%]	$^{-0.13}_{-}$	-	-	$^{+0.15}_{-0.31}$	-	$^{+0.34}_{-}$
Pile-up offset ρ topology (JES) [%]	$^{+0.90}_{-1.51}$	$^{+2.35}_{-2.84}$	$^{+2.58}_{-3.19}$	$^{+1.24}_{-2.34}$	$^{+1.08}_{-2.11}$	$^{+0.50}_{-1.24}$
Punch-through (JES) [%]	-	-	-	-	-	-
Single particle high-p_T (JES) [%]	-	-	-	-	-	-
Jet energy resolution [%]	∓ 2.10	∓ 0.34	± 0.27	∓ 1.08	∓ 1.93	∓ 4.93
Jet vertex fraction [%]	$^{+3.59}_{-3.52}$	$^{+3.57}_{-3.48}$	$^{+3.13}_{-3.06}$	$^{+2.44}_{-2.43}$	$^{+2.15}_{-2.12}$	± 1.41
b-Quark tagging efficiency (eigenvector 0) [%]	$^{-4.21}_{+4.29}$	$^{-3.85}_{+3.91}$	$^{-3.60}_{+3.65}$	$^{-3.54}_{+3.58}$	$^{-3.51}_{+3.55}$	$^{-3.69}_{+3.74}$
b-Quark tagging efficiency (eigenvector 1) [%]	$^{-1.61}_{+1.63}$	$^{-1.64}_{+1.65}$	$^{-1.75}_{+1.77}$	$^{-1.92}_{+1.94}$	$^{-2.22}_{+2.24}$	$^{-3.09}_{+3.12}$
b-Quark tagging efficiency (eigenvector 2) [%]	$^{+1.17}_{-1.16}$	± 0.99	$^{+0.81}_{-0.80}$	$^{+0.72}_{-0.71}$	± 0.53	± 0.13
b-Quark tagging efficiency (eigenvector 3) [%]	-	-	-	-	-	∓ 0.11
b-Quark tagging efficiency (eigenvector 4) [%]	-	-	-	-	-	-
c-Quark tagging efficiency (eigenvector 0) [%]	$^{-1.49}_{+1.50}$	$^{-1.49}_{+1.50}$	$^{-1.49}_{+1.50}$	∓ 1.50	$^{-1.29}_{+1.28}$	$^{-1.08}_{+1.10}$
c-Quark tagging efficiency (eigenvector 1) [%]	± 0.17	± 0.14	± 0.12	-	-	∓ 0.11
c-Quark tagging efficiency (eigenvector 2) [%]	± 0.18	± 0.17	± 0.16	± 0.15	± 0.12	-
c-Quark tagging efficiency (eigenvector 3) [%]	-	-	-	-	-	-
Light-jet tagging efficiency (eigenvector 0) [%]	$^{-1.46}_{+1.54}$	$^{-1.64}_{+1.69}$	$^{-1.67}_{+1.69}$	$^{-1.53}_{+1.57}$	$^{-1.35}_{+1.50}$	$^{-1.90}_{+1.94}$
Light-jet tagging efficiency (eigenvector 1) [%]	-	-	-	-	-	-
Light-jet tagging efficiency (eigenvector 2) [%]	-	-	-	-	-	-
Light-jet tagging efficiency (eigenvector 3) [%]	-	-	-	-	-	-
Light-jet tagging efficiency (eigenvector 4) [%]	-	-	-	-	-	-
Light-jet tagging efficiency (eigenvector 5) [%]	-	-	-	-	-	-
Light-jet tagging efficiency (eigenvector 6) [%]	-	-	-	-	-	-
Light-jet tagging efficiency (eigenvector 7) [%]	-	-	-	-	-	-
Light-jet tagging efficiency (eigenvector 8) [%]	-	-	-	-	-	-
Light-jet tagging efficiency (eigenvector 9) [%]	-	-	-	-	-	-
Light-jet tagging efficiency (eigenvector 10) [%]	-	-	-	-	-	-
Light-jet tagging efficiency (eigenvector 11) [%]	-	-	-	-	-	-
Light-jet tagging efficiency (eigenvector 12) [%]	-	-	-	-	-	-
Light-jet tagging efficiency (eigenvector 13) [%]	-	-	-	-	-	-
b-Quark tagging extrapolation [%]	± 0.25	$^{+0.31}_{-0.32}$	$^{+0.46}_{-0.45}$	$^{+0.59}_{-0.58}$	± 0.80	$^{+2.09}_{-2.10}$
b-Quark tagging extrapolation from c-Quark [%]	± 0.11	-	-	± 0.10	-	-
Electron energy resolution [%]	-	-	-	-	-	$^{-0.26}_{-}$
Electron energy scale [%]	-	-	-	-	-	-
Electron trigger efficiency [%]	± 0.26	± 0.26	± 0.27	± 0.28	± 0.29	± 0.31
Electron reconstruction efficiency [%]	± 0.18	± 0.18	± 0.19	± 0.20	± 0.21	± 0.23
Electron identification efficiency [%]	± 0.43	± 0.44	± 0.47	± 0.50	± 0.53	± 0.60
Electron isolation efficiency [%]	± 0.16	$^{+0.16}_{-0.17}$	± 0.19	± 0.21	± 0.24	± 0.29
Muon energy scale [%]	-	-	-	-	-	-
Muon (MS) momentum resolution [%]	-	-	-	-	-	-
Muon (ID) momentum resolution [%]	-	-	-	-	-	-
Muon trigger efficiency stat [%]	$^{+0.56}_{-0.58}$	$^{+0.57}_{-0.58}$	$^{+0.56}_{-0.58}$	$^{+0.57}_{-0.59}$	$^{+0.56}_{-0.57}$	$^{+0.58}_{-0.59}$
Muon trigger efficiency syst [%]	± 0.24	± 0.24	± 0.24	$^{+0.25}_{-0.24}$	± 0.24	$^{+0.25}_{-0.24}$
Muon identification stat [%]	-	-	-	-	-	-
Muon identification syst [%]	± 0.17	± 0.18	± 0.19	± 0.20	± 0.20	± 0.23
Muon isolation efficiency stat [%]	-	-	-	-	-	-
Muon isolation efficiency syst [%]	± 0.10	$^{+0.10}_{-0.11}$	± 0.10	± 0.11	± 0.10	± 0.11
Muon TTVA efficiency stat [%]	-	-	-	-	-	-
Muon TTVA efficiency syst [%]	-	-	-	-	-	-
E_T^{miss} Soft jet resolution para [%]	-	± 0.18	± 0.12	± 0.15	± 0.67	∓ 0.18
E_T^{miss} Soft jet resolution perp [%]	∓ 0.14	-	-	∓ 0.16	± 0.19	∓ 0.22
E_T^{miss} Soft jet scale [%]	-	-	-	-	$^{+0.26}_{-}$	-
Luminosity [%]	∓ 2.04	∓ 2.04	∓ 2.04	∓ 2.04	∓ 2.04	∓ 2.04
W+jets CA_2ex stat error [%]	-	-	-	-	-	-
W+jets CA_3ex stat error [%]	-	-	-	-	-	-
W+jets CA_4incl stat error [%]	∓ 0.11	-	-	∓ 0.12	∓ 0.14	∓ 0.20
W+jets Fc stat error [%]	∓ 0.11	-	-	-	-	∓ 0.11
W+jets Fcc stat error [%]	∓ 1.02	∓ 0.83	∓ 0.98	∓ 1.38	∓ 1.40	∓ 2.23
W+jets Flight stat error [%]	-	-	-	-	-	-
Single top cross-section [%]	± 0.79	± 0.71	± 0.72	± 0.78	± 0.83	± 0.94
Z+jets cross-section [%]	± 0.61	± 0.49	± 0.52	± 0.82	± 0.58	± 0.91
Diboson cross-section [%]	± 0.11	± 0.14	± 0.21	± 0.29	± 0.38	± 0.66
$t\bar{t}V$ cross-section [%]	-	-	± 0.11	± 0.14	± 0.18	± 0.25
Monte Carlo sample statistics [%]	± 0.15	± 0.28	± 0.48	± 0.76	± 1.20	± 1.51
ISR/FSR + scale [%]	$^{-2.91}_{+1.43}$	$^{-2.39}_{+4.31}$	$^{-1.32}_{+2.99}$	$^{-2.49}_{+2.33}$	$^{-1.41}_{+2.80}$	-4.84
Alternate hard-scattering model [%]	∓ 0.64	± 2.15	± 3.68	± 4.51	± 4.68	± 6.22
Alternate parton-shower model [%]	∓ 3.60	± 2.17	± 1.18	∓ 1.50	-	∓ 5.59
Inter PDF [%]	-	-	-	-	± 0.18	± 0.17
Intra PDF [%]	-	-	± 0.11	± 0.12	± 0.28	± 0.16
Fakes overall normalization [%]	± 3.15	± 3.72	± 3.82	± 4.13	± 2.16	± 5.57
Real lepton efficiency stat [%]	$^{-0.16}_{+0.14}$	$^{-0.17}_{+0.16}$	$^{-0.20}_{+0.18}$	$^{-0.22}_{+0.19}$	$^{-0.34}_{+0.27}$	$^{-0.26}_{+0.22}$
Fake lepton efficiency MC scale [%]	$^{+0.48}_{-0.60}$	$^{+0.89}_{-1.10}$	$^{+0.75}_{-1.05}$	$^{+0.76}_{-0.84}$	$^{+0.11}_{-0.18}$	$^{+0.97}_{-1.14}$
Fake lepton efficiency alternate CR [%]	± 0.33	± 0.39	± 0.30	± 0.11	± 0.24	-

TABLE A.8: Systematic uncertainties for the absolute differential cross-section at particle-level for $\lvert p_{out}^{t\bar{t}} \rvert$ in the 4-jet inclusive configuration.

Bins [GeV]	0–40	40–80	80–120	120–170	170–230	230–600
$\mathrm{d}\sigma$ / $\mathrm{d}\lvert p^{tt}_{out}\rvert$ [pb/GeV]	$4.10 \cdot 10^{-1}$	$2.20 \cdot 10^{-1}$	$7.84 \cdot 10^{-2}$	$2.44 \cdot 10^{-2}$	$9.01 \cdot 10^{-3}$	$6.89 \cdot 10^{-4}$
Total Uncertainty [%]	$^{+12.8}_{-13.7}$	$^{+11.7}_{-12.3}$	$^{+11.5}_{-11.4}$	$^{+12.4}_{-13.5}$	$^{+14.3}_{-15.3}$	$^{+18.0}_{-18.8}$
Statistics [%]	± 0.7	± 1.2	± 2.1	± 3.4	± 5.3	± 7.7
Systematics [%]	$^{+12.8}_{-13.7}$	$^{+11.7}_{-12.2}$	$^{+11.3}_{-11.1}$	$^{+11.8}_{-13.0}$	$^{+13.1}_{-14.1}$	$^{+16.1}_{-16.9}$
b-Tagged jet energy scale (JES) [%]	$^{+0.45}_{-0.51}$	$^{+0.63}_{-0.54}$	$^{+0.60}_{-0.66}$	$^{+0.62}_{-0.67}$	$^{+0.47}_{-0.57}$	$^{+0.47}_{-0.50}$
Effective detector NP set 1 (JES) [%]	$^{+6.95}_{-7.44}$	$^{+5.70}_{-6.67}$	$^{+4.03}_{-4.40}$	$^{+0.44}_{-3.75}$	$^{-}_{-0.79}$	$^{-}_{-3.15}$
Effective detector NP set 2 (JES) [%]	$^{-1.64}_{+1.60}$	$^{-0.65}_{+0.69}$	$^{+0.58}_{-0.48}$	$^{+1.15}_{-2.11}$	$^{+1.12}_{-2.66}$	$^{+1.41}_{-2.90}$
Effective detector NP set 3 (JES) [%]	$^{+0.54}_{-0.60}$	$^{+0.13}_{-0.12}$	$^{-0.62}_{+0.69}$	$^{-0.99}_{+0.96}$	$^{-1.42}_{+0.94}$	$^{-2.06}_{+2.13}$
Effective detector NP set 4 (JES) [%]	$^{-0.40}_{+0.33}$	$^{-}_{-}$	$^{+0.47}_{-0.48}$	$^{+0.26}_{-0.50}$	$^{+0.45}_{-0.67}$	$^{+0.25}_{-0.28}$
Effective detector NP set 5 (JES) [%]	-	$^{-0.12}_{+0.10}$	-	-	$^{-0.18}_{+0.11}$	$^{+0.58}_{-0.23}$
Effective detector NP set 6 restTerm (JES) [%]	-	-	$^{+0.19}_{-0.13}$	± 0.13	-	$^{+0.42}_{-}$
η intercalibration model (JES) [%]	$^{+1.62}_{-2.00}$	$^{+1.96}_{-2.12}$	$^{+2.29}_{-1.81}$	$^{+0.38}_{-2.02}$	$^{+0.55}_{-0.47}$	$^{-}_{-1.11}$
η intercalibration total stat (JES) [%]	$^{+0.92}_{-0.95}$	$^{+0.92}_{-0.87}$	$^{+0.81}_{-0.61}$	$^{-}_{-0.54}$	$^{+0.14}_{-0.54}$	$^{+0.40}_{-}$
Flavour composition (JES) [%]	$^{+4.77}_{-5.61}$	$^{+4.56}_{-5.22}$	$^{+3.68}_{-4.02}$	$^{+0.56}_{-3.19}$	$^{+0.58}_{-}$	$^{-4.09}_{+0.93}$
Flavour response (JES) [%]	$^{-1.41}_{+1.24}$	$^{-1.48}_{+1.04}$	$^{-1.16}_{+1.38}$	$^{-}_{-1.74}$	$^{-}_{-0.52}$	$^{+0.39}_{-1.38}$
Pile-up offset μ (JES) [%]	$^{-0.31}_{+0.26}$	$^{-0.24}_{+0.29}$	$^{-0.26}_{+0.23}$	$^{-}_{-0.26}$	$^{+0.26}_{-}$	$^{+0.49}_{-0.60}$
Pile-up offset N_{PV} (JES) [%]	-	$^{-0.11}_{+0.21}$	-	$^{-}_{-0.37}$	$^{+0.37}_{-0.28}$	$^{+1.22}_{-0.10}$
Pile-up offset p_T (JES) [%]	$^{-0.15}_{-}$	-	$^{+0.15}_{-0.13}$	$^{+0.25}_{-0.21}$	$^{-0.67}_{-}$	$^{+0.97}_{-}$
Pile-up offset ρ topology (JES) [%]	$^{+2.29}_{-2.59}$	$^{+1.51}_{-2.09}$	$^{+1.18}_{-1.32}$	$^{-}_{-1.88}$	$^{-}_{-0.90}$	$^{-2.39}_{+0.65}$
Punch-through (JES) [%]	-	-	-	-	-	-
Single particle high-p_T (JES) [%]	-	-	-	-	-	-
Jet energy resolution [%]	∓ 1.70	∓ 1.07	± 0.65	∓ 2.30	∓ 3.68	∓ 7.59
Jet vertex fraction [%]	$^{+4.82}_{-4.70}$	$^{+3.40}_{-3.35}$	$^{+1.62}_{-1.65}$	$^{+0.79}_{-0.80}$	$^{+0.68}_{-0.67}$	-
b-Quark tagging efficiency (eigenvector 0) [%]	$^{-4.15}_{+4.22}$	$^{-3.88}_{+3.94}$	$^{-3.76}_{+3.81}$	$^{-3.70}_{+3.74}$	$^{-3.57}_{+3.62}$	$^{-3.98}_{+4.04}$
b-Quark tagging efficiency (eigenvector 1) [%]	$^{-1.61}_{+1.62}$	$^{-1.63}_{+1.64}$	$^{-1.66}_{+1.68}$	$^{-1.72}_{+1.73}$	$^{-1.99}_{+2.00}$	$^{-2.28}_{+3.33}$
b-Quark tagging efficiency (eigenvector 2) [%]	± 1.13	$^{+1.00}_{-0.99}$	$^{+0.89}_{-0.88}$	$^{+0.90}_{-0.89}$	± 0.72	± 0.23
b-Quark tagging efficiency (eigenvector 3) [%]	-	-	-	-	± 0.13	-
b-Quark tagging efficiency (eigenvector 4) [%]	-	-	-	-	-	-
c-Quark tagging efficiency (eigenvector 0) [%]	$^{-1.38}_{+1.39}$	$^{-1.46}_{+1.47}$	$^{-1.51}_{+1.52}$	$^{-1.64}_{+1.66}$	$^{-1.51}_{+1.52}$	$^{-1.25}_{+1.28}$
c-Quark tagging efficiency (eigenvector 1) [%]	± 0.16	$^{+0.14}_{-0.13}$	± 0.17	± 0.15	-	-
c-Quark tagging efficiency (eigenvector 2) [%]	± 0.16	± 0.16	± 0.16	± 0.17	± 0.18	-
c-Quark tagging efficiency (eigenvector 3) [%]	-	-	-	-	-	-
Light-jet tagging efficiency (eigenvector 0) [%]	$^{-1.41}_{+1.44}$	$^{-1.51}_{+1.57}$	$^{-1.61}_{+1.70}$	$^{-1.55}_{+1.58}$	$^{-1.51}_{+1.96}$	$^{-2.07}_{+2.17}$
Light-jet tagging efficiency (eigenvector 1) [%]	-	-	-	-	$^{+0.15}_{-0.13}$	-
Light-jet tagging efficiency (eigenvector 2) [%]	-	-	-	± 0.10	± 0.12	-
Light-jet tagging efficiency (eigenvector 3) [%]	-	-	-	-	-	-
Light-jet tagging efficiency (eigenvector 4) [%]	-	-	-	-	-	-
Light-jet tagging efficiency (eigenvector 5) [%]	-	-	-	-	-	-
Light-jet tagging efficiency (eigenvector 6) [%]	-	-	-	-	-	-
Light-jet tagging efficiency (eigenvector 7) [%]	-	-	-	-	-	-
Light-jet tagging efficiency (eigenvector 8) [%]	-	-	-	-	-	-
Light-jet tagging efficiency (eigenvector 9) [%]	-	-	-	-	-	-
Light-jet tagging efficiency (eigenvector 10) [%]	-	-	-	-	-	-
Light-jet tagging efficiency (eigenvector 11) [%]	-	-	-	-	-	-
Light-jet tagging efficiency (eigenvector 12) [%]	-	-	-	-	-	-
Light-jet tagging efficiency (eigenvector 13) [%]	-	-	-	-	-	-
b-Quark tagging extrapolation [%]	$^{+0.26}_{-0.25}$	± 0.30	± 0.43	$^{+0.49}_{-0.48}$	± 0.48	$^{+1.94}_{-1.95}$
b-Quark tagging extrapolation from c-Quark [%]	± 0.10	± 0.10	-	± 0.16	-	-
Electron energy resolution [%]	-	-	-	-	-	$^{-0.26}_{-}$
Electron energy scale [%]	-	-	-	-	-	-
Electron trigger efficiency [%]	± 0.25	$^{+0.25}_{-0.26}$	$^{+0.27}_{-0.28}$	± 0.29	± 0.29	± 0.32
Electron reconstruction efficiency [%]	± 0.17	± 0.18	± 0.18	± 0.20	± 0.21	± 0.23
Electron identification efficiency [%]	± 0.42	± 0.43	± 0.47	± 0.51	± 0.53	± 0.60
Electron isolation efficiency [%]	± 0.16	± 0.16	± 0.18	± 0.20	± 0.23	± 0.29
Muon energy scale [%]	-	-	-	-	-	-
Muon (MS) momentum resolution [%]	-	-	-	-	-	-
Muon (ID) momentum resolution [%]	-	-	-	-	-	-
Muon trigger efficiency stat [%]	$^{+0.56}_{-0.57}$	$^{+0.56}_{-0.58}$	$^{+0.57}_{-0.59}$	$^{+0.59}_{-0.61}$	$^{+0.56}_{-0.57}$	$^{+0.62}_{-0.63}$
Muon trigger efficiency syst [%]	± 0.24	$^{+0.24}_{-0.25}$	$^{+0.25}_{-0.24}$	± 0.25	± 0.24	$^{+0.26}_{-0.25}$
Muon identification stat [%]	-	-	-	-	-	-
Muon identification syst [%]	± 0.17	± 0.18	$^{+0.19}_{-0.18}$	± 0.20	± 0.20	$^{+0.25}_{-0.24}$
Muon isolation efficiency stat [%]	-	-	-	-	-	-
Muon isolation efficiency syst [%]	± 0.10	$^{+0.10}_{-0.11}$	$^{+0.10}_{-0.11}$	± 0.11	± 0.10	± 0.12
Muon TTVA efficiency stat [%]	-	-	-	-	-	-
Muon TTVA efficiency syst [%]	-	-	-	-	-	-
E_T^{miss} Soft jet resolution para [%]	-	-	± 0.35	∓ 0.11	± 1.24	∓ 0.33
E_T^{miss} Soft jet resolution perp [%]	∓ 0.20	± 0.19	-	∓ 0.24	∓ 0.14	-
E_T^{miss} Soft jet scale [%]	-	-	-	-	-	$^{-}_{-0.42}$
Luminosity [%]	∓ 2.04	∓ 2.04	∓ 2.04	∓ 2.04	∓ 2.04	∓ 2.04
W+jets CA_2ex stat error [%]	-	-	-	-	-	-
W+jets CA_3ex stat error [%]	-	-	-	-	-	-
W+jets CA_4incl stat error [%]	-	-	-	∓ 0.18	∓ 0.21	∓ 0.32
W+jets Fc stat error [%]	-	-	-	-	-	∓ 0.25
W+jets Fcc stat error [%]	∓ 0.69	∓ 0.77	∓ 1.04	∓ 2.03	∓ 2.08	∓ 3.23
W+jets Flight stat error [%]	-	-	-	-	-	-
Single top cross-section [%]	± 0.68	± 0.70	± 0.78	± 0.88	± 1.02	± 1.15
Z+jets cross-section [%]	± 0.61	± 0.70	± 0.91	± 1.57	± 1.05	± 0.91
Diboson cross-section [%]	± 0.15	± 0.18	± 0.31	± 0.36	± 0.49	± 1.29
ttV cross-section [%]	-	-	-	-	± 0.11	± 0.16
Monte Carlo sample statistics [%]	± 0.27	± 0.44	± 0.78	± 1.29	± 2.18	± 2.67
ISR/FSR + scale [%]	$^{-2.69}_{+1.41}$	$^{-2.71}_{+3.92}$	$^{-3.13}_{+3.86}$	$^{-2.18}_{+3.92}$	$^{-1.52}_{+1.46}$	$^{-5.79}_{+0.79}$
Alternate hard-scattering model [%]	∓ 3.00	± 1.35	± 4.42	± 5.24	± 9.55	± 5.91
Alternate parton-shower model [%]	∓ 2.14	∓ 2.20	∓ 2.58	∓ 3.52	∓ 2.30	∓ 5.00
Inter PDF [%]	-	-	-	-	± 0.35	± 0.67
Intra PDF [%]	-	-	-	± 0.13	± 0.28	± 0.22
Fakes overall normalization [%]	± 2.41	± 2.91	± 3.18	± 6.06	± 4.00	± 5.50
Real lepton efficiency stat [%]	$^{-0.16}_{+0.15}$	$^{-0.16}_{+0.15}$	$^{-0.19}_{+0.17}$	$^{-0.20}_{+0.17}$	$^{-0.43}_{+0.31}$	$^{-0.30}_{+0.26}$
Fake lepton efficiency MC scale [%]	$^{+0.42}_{-0.50}$	$^{+0.59}_{-0.80}$	$^{+0.58}_{-0.70}$	$^{+1.20}_{-1.33}$	$^{+0.38}_{-0.41}$	$^{+0.35}_{-0.51}$
Fake lepton efficiency alternate CR [%]	± 0.35	± 0.27	± 0.23	± 0.16	± 0.28	∓ 0.16

TABLE A.9: Systematic uncertainties for the absolute differential cross-section at particle-level for $\lvert p^{t\bar{t}}_{out} \rvert$ in the 5-jet exclusive configuration.

Bins [GeV]	0–40	40–80	80–120	120–170	170–230	230–600
$\mathrm{d}\sigma$ / $\mathrm{d}\lvert p_{out}^{tt}\rvert$ [pb/GeV]	$2.13 \cdot 10^{-1}$	$1.52 \cdot 10^{-1}$	$7.55 \cdot 10^{-2}$	$3.34 \cdot 10^{-2}$	$1.48 \cdot 10^{-2}$	$1.08 \cdot 10^{-3}$
Total Uncertainty [%]	$^{+21.6}_{-21.8}$	$^{+20.8}_{-19.7}$	$^{+18.7}_{-19.5}$	$^{+16.4}_{-16.5}$	$^{+13.2}_{-14.9}$	$^{+16.5}_{-16.8}$
Statistics [%]	± 1.0	± 1.3	± 2.0	± 2.8	± 4.0	± 6.1
Systematics [%]	$^{+21.6}_{-21.8}$	$^{+20.8}_{-19.7}$	$^{+18.6}_{-19.3}$	$^{+16.1}_{-16.2}$	$^{+12.5}_{-14.3}$	$^{+15.3}_{-15.6}$
b-Tagged jet energy scale (JES) [%]	$^{+0.54}_{-0.44}$	$^{+0.62}_{-0.71}$	$^{+0.72}_{-0.73}$	$^{+0.69}_{-0.72}$	$^{+0.60}_{-0.58}$	$^{+0.59}_{-0.36}$
Effective detector NP set 1 (JES) [%]	$^{+13.6}_{-13.0}$	$^{+12.9}_{-11.8}$	$^{+10.4}_{-10.9}$	$^{+9.45}_{-9.17}$	$^{+6.73}_{-8.37}$	$^{+5.26}_{-4.99}$
Effective detector NP set 2 (JES) [%]	$^{-3.09}_{+2.70}$	$^{-2.01}_{+2.22}$	$^{-1.52}_{+1.10}$	-	$^{+0.63}_{-0.28}$	$^{+1.84}_{-1.60}$
Effective detector NP set 3 (JES) [%]	$^{+0.84}_{-0.94}$	± 0.60	$^{-}_{-0.21}$	$^{-0.54}_{+0.35}$	$^{-0.90}_{+1.00}$	$^{-1.05}_{+1.07}$
Effective detector NP set 4 (JES) [%]	$^{-0.57}_{+0.47}$	$^{-0.28}_{+0.22}$	-	± 0.49	-	$^{+0.13}_{-0.73}$
Effective detector NP set 5 (JES) [%]	$^{+0.14}_{-}$	-	-	-	$^{+0.32}_{-0.12}$	-
Effective detector NP set 6 restTerm (JES) [%]	-	-	± 0.14	$^{+0.10}_{-0.11}$	$^{+0.30}_{-0.44}$	$^{+0.15}_{-0.21}$
η intercalibration model (JES) [%]	$^{+3.58}_{-4.11}$	$^{+3.61}_{-3.63}$	$^{+3.57}_{-3.93}$	$^{+3.17}_{-3.22}$	$^{+2.19}_{-3.70}$	$^{+2.90}_{-2.17}$
η intercalibration total stat (JES) [%]	$^{+1.92}_{-2.04}$	$^{+1.84}_{-1.95}$	$^{+1.56}_{-1.84}$	$^{+1.27}_{-1.26}$	$^{+1.42}_{-1.69}$	$^{+1.47}_{-0.53}$
Flavour composition (JES) [%]	± 11.5	$^{+11.1}_{-10.5}$	$^{+9.49}_{-9.62}$	$^{+9.03}_{-9.23}$	$^{+5.43}_{-6.98}$	$^{+4.73}_{-4.13}$
Flavour response (JES) [%]	$^{-3.38}_{+2.89}$	$^{-3.04}_{+2.75}$	$^{-3.43}_{+2.51}$	$^{-2.19}_{+2.37}$	$^{-3.11}_{+2.31}$	$^{-1.76}_{+1.80}$
Pile-up offset μ (JES) [%]	$^{-0.63}_{+0.58}$	$^{-0.67}_{+0.51}$	$^{-0.56}_{+0.42}$	$^{-0.39}_{+0.41}$	$^{-0.67}_{+0.35}$	$^{-0.16}_{+0.13}$
Pile-up offset N_{PV} (JES) [%]	$^{-0.30}_{+0.22}$	$^{-0.16}_{+0.30}$	$^{-}_{-0.25}$	$^{-0.17}_{+0.29}$	$^{-0.31}_{+0.20}$	$^{-}_{+0.11}$
Pile-up offset p_T (JES) [%]	$^{-0.28}_{+0.12}$	$^{+0.22}_{-}$	-	$^{-}_{-0.27}$	± 0.10	$^{-}_{+0.63}$
Pile-up offset ρ topology (JES) [%]	$^{+4.21}_{-4.72}$	$^{+3.81}_{-4.22}$	$^{+3.41}_{-4.17}$	$^{+2.55}_{-2.79}$	$^{+2.22}_{-2.89}$	$^{+1.88}_{-2.16}$
Punch-through (JES) [%]	-	-	-	-	-	-
Single particle high-p_T (JES) [%]	-	-	-	-	-	-
Jet energy resolution [%]	± 0.12	± 0.33	∓ 0.61	-	∓ 1.52	∓ 3.48
Jet vertex fraction [%]	$^{+6.79}_{-6.49}$	$^{+6.03}_{-5.80}$	$^{+4.74}_{-4.60}$	$^{+3.52}_{-3.49}$	$^{+3.09}_{-3.03}$	$^{+2.14}_{-2.17}$
b-Quark tagging efficiency (eigenvector 0) [%]	$^{-3.82}_{+3.87}$	$^{-3.62}_{+3.67}$	$^{-3.47}_{+3.51}$	$^{-3.39}_{+3.43}$	$^{-3.43}_{+3.47}$	$^{-3.56}_{+3.60}$
b-Quark tagging efficiency (eigenvector 1) [%]	$^{-1.52}_{+1.53}$	$^{-1.59}_{+1.60}$	$^{-1.78}_{+1.79}$	$^{-2.03}_{+2.04}$	$^{-2.30}_{+2.32}$	$^{-3.00}_{+3.03}$
b-Quark tagging efficiency (eigenvector 2) [%]	$^{+0.96}_{-0.95}$	± 0.90	± 0.75	± 0.59	± 0.43	-
b-Quark tagging efficiency (eigenvector 3) [%]	-	-	-	-	-	∓ 0.12
b-Quark tagging efficiency (eigenvector 4) [%]	-	-	-	-	-	-
c-Quark tagging efficiency (eigenvector 0) [%]	∓ 1.45	∓ 1.45	∓ 1.39	$^{-1.34}_{+1.33}$	$^{-1.16}_{+1.14}$	∓ 0.98
c-Quark tagging efficiency (eigenvector 1) [%]	± 0.15	± 0.13	-	-	-	∓ 0.15
c-Quark tagging efficiency (eigenvector 2) [%]	± 0.17	± 0.17	± 0.16	± 0.13	-	-
c-Quark tagging efficiency (eigenvector 3) [%]	-	-	-	-	-	-
Light-jet tagging efficiency (eigenvector 0) [%]	∓ 1.69	∓ 1.68	$^{-1.62}_{+1.61}$	$^{-1.52}_{+1.58}$	∓ 1.34	$^{-1.82}_{+1.84}$
Light-jet tagging efficiency (eigenvector 1) [%]	-	-	-	-	-	-
Light-jet tagging efficiency (eigenvector 2) [%]	± 0.10	-	-	-	-	-
Light-jet tagging efficiency (eigenvector 3) [%]	-	-	-	-	-	-
Light-jet tagging efficiency (eigenvector 4) [%]	-	-	-	-	-	-
Light-jet tagging efficiency (eigenvector 5) [%]	-	-	-	-	-	-
Light-jet tagging efficiency (eigenvector 6) [%]	-	-	-	-	-	-
Light-jet tagging efficiency (eigenvector 7) [%]	-	-	-	-	-	-
Light-jet tagging efficiency (eigenvector 8) [%]	-	-	-	-	-	-
Light-jet tagging efficiency (eigenvector 9) [%]	-	-	-	-	-	-
Light-jet tagging efficiency (eigenvector 10) [%]	-	-	-	-	-	-
Light-jet tagging efficiency (eigenvector 11) [%]	-	-	-	-	-	-
Light-jet tagging efficiency (eigenvector 12) [%]	-	-	-	-	-	-
Light-jet tagging efficiency (eigenvector 13) [%]	-	-	-	-	-	-
b-Quark tagging extrapolation [%]	± 0.32	± 0.35	± 0.47	± 0.64	± 0.94	$^{+2.17}_{-2.19}$
b-Quark tagging extrapolation from c-Quark [%]	-	-	-	-	-	-
Electron energy resolution [%]	-	-	-	-	-	$^{-0.25}_{-}$
Electron energy scale [%]	-	-	-	-	-	-
Electron trigger efficiency [%]	± 0.26	± 0.26	± 0.27	± 0.27	± 0.28	± 0.31
Electron reconstruction efficiency [%]	± 0.18	± 0.18	± 0.19	± 0.19	± 0.21	± 0.24
Electron identification efficiency [%]	± 0.45	± 0.45	± 0.48	± 0.49	± 0.53	± 0.61
Electron isolation efficiency [%]	± 0.17	± 0.18	± 0.20	± 0.21	± 0.24	± 0.29
Muon energy scale [%]	-	-	-	-	-	-
Muon (MS) momentum resolution [%]	-	-	-	-	-	-
Muon (ID) momentum resolution [%]	-	-	-	-	-	-
Muon trigger efficiency stat [%]	$^{+0.55}_{-0.57}$	$^{+0.55}_{-0.57}$	$^{+0.55}_{-0.57}$	$^{+0.56}_{-0.58}$	$^{+0.56}_{-0.58}$	$^{+0.56}_{-0.57}$
Muon trigger efficiency syst [%]	± 0.24	± 0.24	± 0.24	$^{+0.25}_{-0.24}$	± 0.24	$^{+0.24}_{-0.23}$
Muon identification stat [%]	-	-	-	-	-	-
Muon identification syst [%]	± 0.18	± 0.18	$^{+0.19}_{-0.18}$	± 0.20	$^{+0.21}_{-0.20}$	$^{+0.23}_{-0.22}$
Muon isolation efficiency stat [%]	-	-	-	-	-	-
Muon isolation efficiency syst [%]	± 0.10	± 0.10	± 0.10	± 0.11	± 0.10	± 0.11
Muon TTVA efficiency stat [%]	-	-	-	-	-	-
Muon TTVA efficiency syst [%]	-	-	-	-	-	-
E_T^{miss} Soft jet resolution para [%]	-	± 0.23	-	± 0.20	± 0.34	-
E_T^{miss} Soft jet resolution perp [%]	-	∓ 0.27	± 0.15	∓ 0.13	± 0.35	∓ 0.23
E_T^{miss} Soft jet scale [%]	-	-	-	-	$^{+0.35}_{-}$	$^{-}_{-0.25}$
Luminosity [%]	∓ 2.04	∓ 2.04	∓ 2.04	∓ 2.04	∓ 2.04	∓ 2.04
W+jets CA_2ex stat error [%]	-	-	-	-	-	-
W+jets CA_3ex stat error [%]	-	-	-	-	-	-
W+jets CA_4incl stat error [%]	-	-	-	-	∓ 0.10	∓ 0.15
W+jets Fc stat error [%]	-	-	-	-	-	-
W+jets Fcc stat error [%]	∓ 0.66	∓ 0.76	∓ 0.97	∓ 0.85	∓ 1.07	∓ 1.77
W+jets Flight stat error [%]	-	-	-	-	-	-
Single top cross-section [%]	± 0.57	± 0.55	± 0.60	± 0.64	± 0.70	± 0.84
Z+jets cross-section [%]	± 0.55	± 0.64	± 0.76	± 1.14	± 0.71	± 1.95
Diboson cross-section [%]	± 0.36	± 0.34	± 0.40	± 0.67	± 0.84	± 1.14
ttV cross-section [%]	-	± 0.11	± 0.14	± 0.18	± 0.22	± 0.30
Monte Carlo sample statistics [%]	± 0.38	± 0.47	± 0.68	± 1.02	± 1.48	± 1.86
ISR/FSR + scale [%]	$^{-4.92}_{+3.15}$	$^{-3.12}_{+3.99}$	$^{-3.10}_{+3.13}$	$^{-2.91}_{+2.27}$	$^{-1.69}_{+3.89}$	$^{-}_{-4.83}$
Alternate hard-scattering model [%]	± 0.32	± 0.69	± 4.62	± 2.46	± 1.94	± 5.52
Alternate parton-shower model [%]	∓ 2.09	∓ 2.64	∓ 4.34	∓ 1.90	± 0.89	∓ 6.08
Inter PDF [%]	± 0.14	-	± 0.12	± 0.12	± 0.13	∓ 0.10
Intra PDF [%]	± 0.13	-	± 0.11	± 0.16	± 0.15	± 0.20
Fakes overall normalization [%]	± 2.45	± 2.77	± 3.41	± 2.95	± 1.24	± 5.39
Real lepton efficiency stat [%]	$^{-0.19}_{+0.18}$	$^{-0.21}_{+0.18}$	$^{-0.22}_{+0.18}$	$^{-0.23}_{+0.19}$	$^{-0.31}_{+0.24}$	$^{-0.25}_{+0.20}$
Fake lepton efficiency MC scale [%]	$^{+0.47}_{-0.58}$	$^{+0.63}_{-0.74}$	$^{+0.59}_{-0.84}$	$^{+0.53}_{-0.58}$	-	$^{+1.19}_{-1.31}$
Fake lepton efficiency alternate CR [%]	± 0.37	± 0.28	± 0.24	-	± 0.25	± 0.15

TABLE A.10: Systematic uncertainties for the absolute differential cross-section at particle-level for $\lvert p_{out}^{t\bar{t}} \rvert$ in the 6-jet inclusive configuration.

Bins [GeV]	0–40	40–80	80–120	120–170	170–230	230–600
$1/\sigma \cdot \mathrm{d}\sigma$ / $\mathrm{d}\lvert p_{out}^{tt} \rvert$	$1.35 \cdot 10^{-2}$	$7.24 \cdot 10^{-3}$	$2.58 \cdot 10^{-3}$	$8.03 \cdot 10^{-4}$	$2.97 \cdot 10^{-4}$	$2.27 \cdot 10^{-5}$
Total Uncertainty [%]	$^{+3.32}_{-3.44}$	$^{+2.67}_{-2.25}$	$^{+7.28}_{-6.69}$	$^{+9.60}_{-11.4}$	$^{+15.6}_{-16.0}$	$^{+18.5}_{-19.6}$
Statistics [%]	± 0.6	± 1.0	± 2.0	± 3.4	± 5.3	± 7.6
Systematics [%]	$^{+3.26}_{-3.37}$	$^{+2.41}_{-1.94}$	$^{+6.95}_{-6.33}$	$^{+8.88}_{-10.8}$	$^{+14.5}_{-14.9}$	$^{+16.6}_{-17.9}$
b-Tagged jet energy scale (JES) [%]	-	-	-	$^{-}_{-0.12}$	-	-
Effective detector NP set 1 (JES) [%]	$^{+1.05}_{-0.88}$	-	$^{-1.70}_{+2.36}$	$^{-5.10}_{+3.06}$	$^{-6.26}_{+6.42}$	$^{-8.49}_{+5.51}$
Effective detector NP set 2 (JES) [%]	$^{-0.72}_{+0.71}$	$^{+0.27}_{-0.18}$	$^{+1.52}_{-1.35}$	$^{+2.10}_{-2.96}$	$^{+2.07}_{-3.51}$	$^{+5.39}_{-3.75}$
Effective detector NP set 3 (JES) [%]	$^{+0.34}_{-0.37}$	-	$^{-0.82}_{+0.91}$	$^{-1.18}_{+1.19}$	$^{-1.61}_{+1.17}$	$^{-2.26}_{+2.36}$
Effective detector NP set 4 (JES) [%]	$^{-0.25}_{+0.26}$	$^{+0.16}_{-0.17}$	$^{+0.62}_{-0.54}$	$^{+0.41}_{-0.56}$	$^{+0.59}_{-0.73}$	$^{+0.40}_{-0.34}$
Effective detector NP set 5 (JES) [%]	-	$^{-0.14}_{-}$	$^{-}_{+0.17}$	-	$^{-0.20}_{+0.10}$	$^{+0.56}_{-0.25}$
Effective detector NP set 6 restTerm (JES) [%]	-	-	$^{+0.18}_{-0.11}$	$^{+0.12}_{-0.11}$	-	$^{+0.41}_{-}$
η intercalibration model (JES) [%]	-	$^{+0.26}_{-0.14}$	$^{+0.58}_{-}$	$^{-}_{-1.29}$	$^{-1.12}_{+1.54}$	$^{-2.76}_{+1.71}$
η intercalibration total stat (JES) [%]	-	-	-	$^{-}_{-1.01}$	$^{-}_{-0.70}$	$^{-}_{-0.67}$
Flavour composition (JES) [%]	$^{+0.46}_{-0.54}$	$^{+0.26}_{-0.13}$	$^{+0.25}_{-0.58}$ $^{+1.12}_{+0.28}$	$^{+0.32}_{-3.58}$ $^{+2.00}_{-}$	$^{+0.32}_{-4.03}$ $^{+5.98}_{+0.88}$	$^{+1.27}_{-8.04}$ $^{+6.35}_{+1.81}$
Flavour response (JES) [%]	-	-	-	$^{-}_{-1.48}$	$^{-}_{-1.18}$	$^{-}_{-2.45}$
Pile-up offset μ (JES) [%]	-	-	-	$^{-}_{-0.41}$	$^{+0.54}_{-0.25}$	$^{+0.76}_{-0.85}$
Pile-up offset N_{PV} (JES) [%]	-	$^{-0.10}_{+0.14}$	-	$^{-}_{-0.44}$	$^{+0.39}_{-0.35}$	$^{+1.23}_{-0.17}$
Pile-up offset p_T (JES) [%]	-	-	$^{+0.20}_{-0.17}$	$^{+0.30}_{-0.25}$	$^{+0.62}_{-}$	$^{+1.02}_{-0.12}$
Pile-up offset ρ topology (JES) [%]	$^{+0.52}_{-0.36}$	$^{-0.24}_{+0.14}$	$^{-0.56}_{+0.94}$	$^{-2.18}_{+0.36}$	$^{-2.61}_{+1.42}$	$^{-4.08}_{+2.96}$
Punch-through (JES) [%]	-	-	-	-	-	-
Single particle high-p_T (JES) [%]	-	-	-	-	-	-
Jet energy resolution [%]	∓ 0.32	± 0.31	± 2.06	∓ 0.94	∓ 2.34	∓ 6.30
Jet vertex fraction [%]	$^{+0.96}_{-0.99}$	∓ 0.40	$^{-2.11}_{+2.17}$	$^{-2.92}_{+3.05}$	$^{-3.02}_{+3.19}$	$^{-3.76}_{+4.00}$
b-Quark tagging efficiency (eigenvector 0) [%]	$^{-0.15}_{+0.14}$	± 0.12	$^{+0.25}_{-0.24}$	± 0.31	$^{+0.44}_{-0.43}$	-
b-Quark tagging efficiency (eigenvector 1) [%]	-	-	-	-	$^{-0.35}_{+0.33}$	$^{-}_{-1.67}$ $^{+1.64}$
b-Quark tagging efficiency (eigenvector 2) [%]	-	-	$^{-0.15}_{+0.16}$	$^{-0.14}_{+0.15}$	∓ 0.32	$^{-0.80}_{+0.82}$
b-Quark tagging efficiency (eigenvector 3) [%]	-	-	-	-	-	∓ 0.15
b-Quark tagging efficiency (eigenvector 4) [%]	-	-	-	-	-	-
c-Quark tagging efficiency (eigenvector 0) [%]	-	-	-	∓ 0.21	-	$^{+0.18}_{-0.16}$
c-Quark tagging efficiency (eigenvector 1) [%]	-	-	-	-	-	∓ 0.18
c-Quark tagging efficiency (eigenvector 2) [%]	-	-	-	-	-	∓ 0.12
c-Quark tagging efficiency (eigenvector 3) [%]	-	-	-	-	-	-
Light-jet tagging efficiency (eigenvector 0) [%]	-	-	$^{-0.14}_{+0.17}$	-	$^{-}_{+0.42}$	$^{-0.61}_{+0.63}$
Light-jet tagging efficiency (eigenvector 1) [%]	-	-	-	-	$^{+0.11}_{-0.10}$	-
Light-jet tagging efficiency (eigenvector 2) [%]	-	-	-	-	-	-
Light-jet tagging efficiency (eigenvector 3) [%]	-	-	-	-	-	-
Light-jet tagging efficiency (eigenvector 4) [%]	-	-	-	-	-	-
Light-jet tagging efficiency (eigenvector 5) [%]	-	-	-	-	-	-
Light-jet tagging efficiency (eigenvector 6) [%]	-	-	-	-	-	-
Light-jet tagging efficiency (eigenvector 7) [%]	-	-	-	-	-	-
Light-jet tagging efficiency (eigenvector 8) [%]	-	-	-	-	-	-
Light-jet tagging efficiency (eigenvector 9) [%]	-	-	-	-	-	-
Light-jet tagging efficiency (eigenvector 10) [%]	-	-	-	-	-	-
Light-jet tagging efficiency (eigenvector 11) [%]	-	-	-	-	-	-
Light-jet tagging efficiency (eigenvector 12) [%]	-	-	-	-	-	-
Light-jet tagging efficiency (eigenvector 13) [%]	-	-	-	-	-	-
b-Quark tagging extrapolation [%]	-	-	± 0.11	± 0.17	$^{+0.16}_{-0.17}$	$^{+1.62}_{-1.64}$
b-Quark tagging extrapolation from c-Quark [%]	-	-	-	-	-	-
Electron energy resolution [%]	-	-	-	-	-	$^{-0.18}_{-}$
Electron energy scale [%]	-	-	-	-	$^{-}_{+0.16}$	-
Electron trigger efficiency [%]	-	-	-	-	-	-
Electron reconstruction efficiency [%]	-	-	-	-	-	-
Electron identification efficiency [%]	-	-	-	-	-	± 0.16
Electron isolation efficiency [%]	-	-	-	-	-	± 0.12
Muon energy scale [%]	-	-	-	-	-	-
Muon (MS) momentum resolution [%]	-	-	-	-	-	-
Muon (ID) momentum resolution [%]	-	-	-	-	-	-
Muon trigger efficiency stat [%]	-	-	-	-	-	-
Muon trigger efficiency syst [%]	-	-	-	-	-	-
Muon identification stat [%]	-	-	-	-	-	-
Muon identification syst [%]	-	-	-	-	-	-
Muon isolation efficiency stat [%]	-	-	-	-	-	-
Muon isolation efficiency syst [%]	-	-	-	-	-	-
Muon TTVA efficiency stat [%]	-	-	-	-	-	-
Muon TTVA efficiency syst [%]	-	-	-	-	-	-
E_T^{miss} Soft jet resolution para [%]	-	-	± 0.28	∓ 0.17	± 1.18	∓ 0.39
E_T^{miss} Soft jet resolution perp [%]	∓ 0.12	± 0.26	-	∓ 0.17	-	-
E_T^{miss} Soft jet scale [%]	-	-	-	-	-	$^{+0.10}_{-0.41}$
Luminosity [%]	-	-	-	-	-	-
W+jets CA_2ex stat error [%]	-	-	-	-	-	-
W+jets CA_3ex stat error [%]	-	-	-	-	-	-
W+jets CA_4incl stat error [%]	-	-	-	-	∓ 0.12	∓ 0.23
W+jets Fc stat error [%]	-	-	-	-	-	∓ 0.16
W+jets Fcc stat error [%]	± 0.15	-	$^{-0.20}_{+0.19}$	$^{-1.19}_{+1.17}$	$^{-1.24}_{+1.22}$	$^{-2.40}_{+2.36}$
W+jets Flight stat error [%]	-	-	-	-	-	-
Single top cross-section [%]	-	-	-	± 0.17	± 0.30	± 0.43
Z+jets cross-section [%]	∓ 0.10	-	± 0.19	± 0.84	± 0.32	± 0.18
Diboson cross-section [%]	-	-	± 0.11	± 0.15	± 0.29	± 1.09
ttV cross-section [%]	-	-	-	-	-	± 0.11
Monte Carlo sample statistics [%]	± 0.22	± 0.39	± 0.75	± 1.28	± 2.16	± 2.66
ISR/FSR + scale [%]	$^{-}_{-1.05}$	$^{+1.39}_{-}$	$^{-0.41}_{+1.33}$	$^{+1.39}_{-}$	$^{+1.23}_{-1.00}$	$^{-}_{-3.15}$
Alternate hard-scattering model [%]	∓ 2.62	± 1.75	± 4.84	± 5.66	± 9.98	± 6.33
Alternate parton-shower model [%]	± 0.15	-	∓ 0.30	∓ 1.27	-	∓ 2.78
Inter PDF [%]	-	-	-	-	± 0.33	± 0.64
Intra PDF [%]	-	-	-	-	± 0.22	± 0.16
Fakes overall normalization [%]	∓ 0.40	-	± 0.33	± 3.13	± 1.13	± 2.59
Real lepton efficiency stat [%]	-	-	-	-	$^{-0.26}_{+0.15}$	$^{-0.13}_{+0.10}$
Fake lepton efficiency MC scale [%]	$^{+}_{+0.14}$	$^{-}_{-0.15}$	-	$^{+0.68}_{-0.69}$	$^{-0.13}_{+0.22}$	$^{-0.16}_{+0.12}$
Fake lepton efficiency alternate CR [%]	-	-	-	∓ 0.14	-	∓ 0.46

TABLE A.11: Systematic uncertainties for the normalised differential cross-section at particle-level for $\lvert p_{out}^{t\bar{t}} \rvert$ in the 5-jet exclusive configuration.

Bins [GeV]	0–40	40–80	80–120	120–170	170–230	230–600
$1/\sigma \cdot \mathrm{d}\sigma$ / $\mathrm{d}\lvert p_{out}^{tt} \rvert$	$1.03 \cdot 10^{-2}$	$7.40 \cdot 10^{-3}$	$3.67 \cdot 10^{-3}$	$1.62 \cdot 10^{-3}$	$7.20 \cdot 10^{-4}$	$5.27 \cdot 10^{-5}$
Total Uncertainty [%]	$^{+2.81}_{-3.39}$	$^{+2.18}_{-1.68}$	$^{+4.59}_{-4.80}$	$^{+6.00}_{-5.44}$	$^{+9.44}_{-9.87}$	$^{+15.6}_{-14.6}$
Statistics [%]	± 0.9	± 1.2	± 1.9	± 2.7	± 3.9	± 6.0
Systematics [%]	$^{+2.64}_{-3.25}$	$^{+1.76}_{-1.09}$	$^{+4.12}_{-4.35}$	$^{+5.24}_{-4.58}$	$^{+8.44}_{-8.92}$	$^{+14.3}_{-13.2}$
b-Tagged jet energy scale (JES) [%]	$^{-}_{+0.15}$	-	$^{+0.10}_{-0.14}$	$^{-}_{-0.13}$	-	$^{-}_{+0.22}$
Effective detector NP set 1 (JES) [%]	$^{+1.35}_{-1.56}$	$^{+0.73}_{-0.19}$	$^{-1.44}_{+0.79}$	$^{-2.38}_{+2.82}$	$^{-4.80}_{+3.73}$	$^{-6.11}_{+7.55}$
Effective detector NP set 2 (JES) [%]	$^{-1.12}_{+0.81}$	$^{-}_{+0.34}$	$^{+0.47}_{-0.75}$	$^{+2.21}_{-1.77}$	$^{+2.68}_{-2.11}$	$^{+3.91}_{-3.41}$
Effective detector NP set 3 (JES) [%]	$^{+0.43}_{-0.45}$	$^{+0.19}_{-0.10}$	$^{-0.42}_{+0.28}$	$^{-0.94}_{+0.86}$	$^{-1.30}_{+1.50}$	$^{-1.46}_{+1.58}$
Effective detector NP set 4 (JES) [%]	$^{-0.30}_{+0.29}$	-	$^{+0.21}_{-0.26}$	$^{+0.77}_{-0.67}$	$^{+0.34}_{-0.31}$	$^{+0.40}_{-0.91}$
Effective detector NP set 5 (JES) [%]	-	-	-	-	$^{+0.27}_{-0.10}$	-
Effective detector NP set 6 restTerm (JES) [%]	-	-	-	-	$^{+0.24}_{-0.37}$	$^{-}_{-0.14}$
η intercalibration model (JES) [%]	$^{-}_{-0.32}$	-	$^{-}_{-0.12}$	$^{-0.30}_{+0.60}$	$^{-1.25}_{+0.10}$	$^{-0.56}_{+1.69}$
η intercalibration total stat (JES) [%]	$^{+0.16}_{-0.17}$	-	$^{-0.19}_{-}$	$^{-0.47}_{+0.61}$	$^{-0.32}_{+0.18}$	$^{-0.27}_{+1.36}$
Flavour composition (JES) [%]	$^{+0.96}_{-1.30}$	$^{+0.56}_{-0.14}$	$^{-0.90}_{+0.88}$	$^{-1.31}_{+1.32}$	$^{-4.57}_{+3.83}$	$^{-5.20}_{+7.00}$
Flavour response (JES) [%]	$^{-0.24}_{+0.18}$	-	$^{-}_{-0.30}$	$^{+0.97}_{-0.31}$	$^{-}_{-0.37}$	$^{+1.42}_{-0.86}$
Pile-up offset μ (JES) [%]	-	-	-	$^{+0.21}_{-}$	-	$^{+0.44}_{-0.37}$
Pile-up offset N_{PV} (JES) [%]	-	-	$^{-}_{-0.24}$	-	-	$^{+0.14}_{-}$
Pile-up offset p_T (JES) [%]	$^{-0.22}_{-}$	$^{+0.28}_{-}$	-	$^{-}_{-0.32}$	$^{+0.16}_{-0.15}$	$^{+0.57}_{-}$
Pile-up offset ρ topology (JES) [%]	$^{+0.49}_{-0.55}$	-	$^{-0.27}_{-}$	$^{-1.10}_{+1.46}$	$^{-1.42}_{+1.35}$	$^{-1.75}_{+2.12}$
Punch-through (JES) [%]	-	-	-	-	-	-
Single particle high-p_T (JES) [%]	-	-	-	-	-	-
Jet energy resolution [%]	± 0.22	± 0.43	∓ 0.51	-	∓ 1.42	∓ 3.38
Jet vertex fraction [%]	$^{+1.01}_{-1.04}$	$^{+0.29}_{-0.32}$	$^{-0.92}_{+0.95}$	$^{-2.08}_{+2.12}$	$^{-2.48}_{+2.61}$	$^{-3.37}_{+3.52}$
b-Quark tagging efficiency (eigenvector 0) [%]	∓ 0.17	-	$^{+0.19}_{-0.18}$	$^{+0.27}_{-0.25}$	± 0.22	-
b-Quark tagging efficiency (eigenvector 1) [%]	± 0.17	-	-	$^{-0.34}_{+0.33}$	$^{-0.62}_{+0.60}$	$^{-1.33}_{+1.30}$
b-Quark tagging efficiency (eigenvector 2) [%]	± 0.12	-	-	∓ 0.24	$^{-0.40}_{+0.41}$	$^{-0.74}_{+0.75}$
b-Quark tagging efficiency (eigenvector 3) [%]	-	-	-	-	-	$^{-0.18}_{+0.17}$
b-Quark tagging efficiency (eigenvector 4) [%]	-	-	-	-	-	-
c-Quark tagging efficiency (eigenvector 0) [%]	-	-	-	-	$^{+0.25}_{-0.26}$	$^{+0.43}_{-0.41}$
c-Quark tagging efficiency (eigenvector 1) [%]	-	-	-	-	∓ 0.11	$^{-0.26}_{+0.27}$
c-Quark tagging efficiency (eigenvector 2) [%]	-	-	-	-	-	∓ 0.20
c-Quark tagging efficiency (eigenvector 3) [%]	-	-	-	-	-	-
Light-jet tagging efficiency (eigenvector 0) [%]	-	-	-	$^{+0.13}_{-}$	$^{+0.31}_{-0.30}$	$^{-0.17}_{+0.18}$
Light-jet tagging efficiency (eigenvector 1) [%]	-	-	-	-	-	-
Light-jet tagging efficiency (eigenvector 2) [%]	-	-	-	-	-	-
Light-jet tagging efficiency (eigenvector 3) [%]	-	-	-	-	-	-
Light-jet tagging efficiency (eigenvector 4) [%]	-	-	-	-	-	-
Light-jet tagging efficiency (eigenvector 5) [%]	-	-	-	-	-	-
Light-jet tagging efficiency (eigenvector 6) [%]	-	-	-	-	-	-
Light-jet tagging efficiency (eigenvector 7) [%]	-	-	-	-	-	-
Light-jet tagging efficiency (eigenvector 8) [%]	-	-	-	-	-	-
Light-jet tagging efficiency (eigenvector 9) [%]	-	-	-	-	-	-
Light-jet tagging efficiency (eigenvector 10) [%]	-	-	-	-	-	-
Light-jet tagging efficiency (eigenvector 11) [%]	-	-	-	-	-	-
Light-jet tagging efficiency (eigenvector 12) [%]	-	-	-	-	-	-
Light-jet tagging efficiency (eigenvector 13) [%]	-	-	-	-	-	-
b-Quark tagging extrapolation [%]	∓ 0.13	-	-	± 0.19	± 0.49	$^{+1.71}_{-1.75}$
b-Quark tagging extrapolation from c-Quark [%]	-	-	-	-	-	-
Electron energy resolution [%]	-	-	-	-	-	-
Electron energy scale [%]	-	-	-	-	-	-
Electron trigger efficiency [%]	-	-	-	-	-	-
Electron reconstruction efficiency [%]	-	-	-	-	-	-
Electron identification efficiency [%]	-	-	-	-	-	± 0.14
Electron isolation efficiency [%]	-	-	-	-	-	± 0.10
Muon energy scale [%]	-	-	-	-	-	-
Muon (MS) momentum resolution [%]	-	-	-	-	-	-
Muon (ID) momentum resolution [%]	-	-	-	-	-	-
Muon trigger efficiency stat [%]	-	-	-	-	-	-
Muon trigger efficiency syst [%]	-	-	-	-	-	-
Muon identification stat [%]	-	-	-	-	-	-
Muon identification syst [%]	-	-	-	-	-	-
Muon isolation efficiency stat [%]	-	-	-	-	-	-
Muon isolation efficiency syst [%]	-	-	-	-	-	-
Muon TTVA efficiency stat [%]	-	-	-	-	-	-
Muon TTVA efficiency syst [%]	-	-	-	-	-	-
E_T^{miss} Soft jet resolution para [%]	∓ 0.16	± 0.16	-	± 0.13	± 0.28	∓ 0.11
E_T^{miss} Soft jet resolution perp [%]	-	∓ 0.19	± 0.23	-	± 0.43	∓ 0.15
E_T^{miss} Soft jet scale [%]	-	-	-	-	$^{+0.38}_{-}$	$^{-}_{-0.22}$
Luminosity [%]	-	-	-	-	-	-
W+jets CA_2ex stat error [%]	-	-	-	-	-	-
W+jets CA_3ex stat error [%]	-	-	-	-	-	-
W+jets CA_4incl stat error [%]	-	-	-	-	-	-
W+jets Fc stat error [%]	-	-	-	-	-	-
W+jets Fcc stat error [%]	± 0.13	-	$^{-0.17}_{+0.16}$	-	∓ 0.27	$^{-0.97}_{+0.96}$
W+jets Flight stat error [%]	-	-	-	-	-	-
Single top cross-section [%]	-	-	-	-	± 0.11	± 0.25
Z+jets cross-section [%]	∓ 0.14	-	-	± 0.43	-	± 1.23
Diboson cross-section [%]	-	-	-	± 0.24	± 0.41	± 0.71
ttV cross-section [%]	-	-	-	-	-	± 0.17
Monte Carlo sample statistics [%]	± 0.32	± 0.43	± 0.64	± 0.99	± 1.46	± 1.84
ISR/FSR + scale [%]	$^{-}_{-1.15}$	$^{+0.74}_{-}$	$^{+0.74}_{-}$	$^{+0.94}_{-0.91}$	$^{+2.20}_{-}$	$^{-}_{-4.87}$
Alternate hard-scattering model [%]	∓ 1.13	∓ 0.76	± 3.10	± 0.97	± 0.47	± 3.99
Alternate parton-shower model [%]	± 0.48	-	∓ 1.81	± 0.68	± 3.55	∓ 3.60
Inter PDF [%]	-	-	-	-	-	∓ 0.19
Intra PDF [%]	-	-	-	-	-	-
Fakes overall normalization [%]	∓ 0.30	-	± 0.63	± 0.19	∓ 1.47	± 2.55
Real lepton efficiency stat [%]	-	-	-	-	-	-
Fake lepton efficiency MC scale [%]	-	-	$^{-}_{-0.17}$	-	$^{-0.58}_{+0.62}$	± 0.64
Fake lepton efficiency alternate CR [%]	-	-	-	∓ 0.22	-	∓ 0.13

TABLE A.12: Systematic uncertainties for the normalised differential cross-section at particle-level for $\lvert p_{out}^{t\bar{t}} \rvert$ in the 6-jet inclusive configuration.

Bins [GeV]	0–15	15–30	30–45	45–60	60–75	75–90	90–105	105–120	120–135	135–150	150–165	165–180	180–200	200–230	230–265	265–325	325–450	450–1000
$1/\sigma \cdot d\sigma / dpt^{t,had}_{T}$	$7.95 \cdot 10^{-4}$	$2.33 \cdot 10^{-3}$	$3.90 \cdot 10^{-3}$	$5.13 \cdot 10^{-3}$	$6.07 \cdot 10^{-3}$	$6.44 \cdot 10^{-3}$	$6.80 \cdot 10^{-3}$	$6.47 \cdot 10^{-3}$	$5.52 \cdot 10^{-3}$	$4.52 \cdot 10^{-3}$	$3.70 \cdot 10^{-3}$	$2.97 \cdot 10^{-3}$	$2.25 \cdot 10^{-3}$	$1.56 \cdot 10^{-3}$	$9.53 \cdot 10^{-4}$	$5.50 \cdot 10^{-4}$	$1.42 \cdot 10^{-4}$	$8.07 \cdot 10^{-6}$
Total Uncertainty [%]	$^{+8.46}_{-9.12}$	$^{+5.03}_{-5.60}$	$^{+3.90}_{-5.09}$	$^{+3.98}_{-4.75}$	$^{+3.94}_{-4.26}$	$^{+3.89}_{-4.07}$	$^{+3.96}_{-4.16}$	$^{+3.93}_{-4.24}$	$^{+4.01}_{-4.21}$	$^{+4.01}_{-4.27}$	$^{+4.14}_{-4.44}$	$^{+4.33}_{-4.53}$	$^{+4.86}_{-5.06}$	$^{+4.96}_{-4.96}$	$^{+5.41}_{-5.72}$	$^{+5.97}_{-5.61}$	$^{+6.53}_{-6.70}$	$^{+15.8}_{-16.0}$
Statistics [%]	±4.6	±2.4	±1.8	±1.6	±1.4	±1.3	±1.2	±1.3	±1.4	±1.5	±1.6	±1.8	±2.0	±2.1	±2.7	±2.7	±3.9	±8.9
Systematics [%]	$^{+7.28}_{-7.88}$	$^{+5.03}_{-5.23}$	$^{+3.62}_{-4.62}$	$^{+3.54}_{-4.16}$	$^{+3.94}_{-3.92}$	$^{+3.85}_{-3.93}$	$^{+3.93}_{-3.93}$	$^{+3.83}_{-4.03}$	$^{+3.89}_{-3.97}$	$^{+3.93}_{-4.02}$	$^{+3.96}_{-4.04}$	$^{+3.95}_{-4.02}$	$^{+4.48}_{-4.66}$	$^{+4.58}_{-4.57}$	$^{+5.17}_{-5.00}$	$^{+5.52}_{-5.04}$	$^{+5.53}_{-5.63}$	$^{+12.9}_{-14.2}$
b-Tagged jet energy scale (JES) [%]	$^{-0.59}$	$^{+0.59}$	$^{-0.03}$	$^{-0.07}$	$^{+0.32}$	$^{-0.31}$	$^{+1.28}$	±0.14	$^{+0.17}$	$^{+0.30}$	$^{+0.32}$	$^{+0.44}$	$^{+0.19}$	$^{+0.91}$	$^{+0.71}$	$^{+0.23}$	$^{+0.23}$	$^{+1.13}$
Effective detector NP set 1 (JES) [%]	$^{-1.59}_{-1.75}$	$^{+0.76}_{+0.23}$	$^{+0.52}_{-0.67}$	$^{+0.42}_{-0.39}$	$^{+0.26}_{+0.25}$	$^{+0.14}_{+0.25}$	$^{+0.72}$	$^{+0.79}_{+0.79}$	$^{+0.57}_{+0.57}$	$^{+0.40}_{+0.54}$	$^{+0.41}_{+0.69}$	$^{+0.19}_{+0.24}$	$^{+0.28}$	$^{+0.38}_{-0.48}$	$^{+0.15}_{-0.49}$	$^{-0.17}_{-1.38}$	$^{-1.61}$	$^{-0.66}_{-2.83}$
Effective detector NP set 2 (JES) [%]	$^{+0.42}_{+0.28}$	$^{+0.97}_{+0.64}$	$^{+1.01}_{+0.83}$	$^{+0.78}_{+0.69}$	$^{+0.95}_{+0.52}$	$^{+0.83}_{+0.50}$	$^{+1.04}_{+0.63}$	$^{+0.38}$	$^{+0.11}$	$^{-0.26}_{-0.13}$	$^{-0.59}_{-0.21}$	$^{-0.32}_{-0.45}$	$^{-0.91}_{-0.62}$	$^{-1.42}_{-0.97}$	$^{-1.26}_{-0.44}$	$^{-2.05}_{-1.82}$	$^{-3.00}_{-1.58}$	$^{-5.46}_{-2.66}$
Effective detector NP set 3 (JES) [%]	$^{-0.20}_{-0.30}$	$^{-0.95}_{-0.55}$	±0.83	$^{-0.51}_{-0.28}$	$^{-0.62}_{-0.42}$	$^{-0.63}_{-0.36}$	$^{-0.30}_{-0.13}$	$^{-0.16}$	$^{+0.16}$	$^{+0.20}_{\pm0.28}$	$^{+0.53}_{+0.33}$	$^{+0.27}_{+0.30}$	$^{+0.46}_{\pm0.39}$	$^{+1.09}_{+0.62}$	$^{+1.26}_{+0.48}$	$^{+1.72}_{+0.52}$	$^{+2.42}_{+0.10}$	$^{+2.66}_{-0.19}$
Effective detector NP set 4 (JES) [%]	$^{+0.03}_{+0.03}$	$^{+0.36}$	$^{+0.43}$	$^{+0.32}$	$^{+0.24}$	$^{+0.33}$	$^{+0.37}$	$^{-}$	$^{-0.19}$	$^{-}$	$^{-0.13}$	$^{-0.13}$	$^{-}$	$^{-0.53}$	$^{-0.35}$	$^{+0.14}$	$^{+0.16}$	$^{+0.33}$
Effective detector NP set 5 (JES) [%]	$^{-0.11}$	$^{-0.32}$	$^{-}$	$^{-}$	$^{-}$	$^{-}$	$^{-}$	$^{+0.13}$	$^{-}$	$^{-}$	$^{-}$	$^{-}$	$^{-}$	$^{-}$	$^{-}$	$^{-0.33}$	$^{-0.25}$	$^{-0.37}$
Effective detector NP set 6 resTerm (JES) [%]	$^{-0.23}$	$^{-0.22}$	$^{-0.21}$	$^{-0.18}$	$^{-}$	$^{-}$	$^{+0.10}$	$^{-}$	$^{-}$	$^{-}$	$^{-}$	$^{-}$	$^{-0.21}$	$^{+0.20}$	$^{+0.20}$	$^{-}$	$^{-0.16}$	$^{+0.56}$
η intercalibration model (JES) [%]	$^{+0.14}_{+0.41}$	$^{-0.13}$	$^{+0.21}$	$^{-0.11}$	$^{-}$	$^{-0.28}$	$^{+0.30}$	$^{+0.17}$	$^{+0.18}$	$^{+0.44}$	$^{+0.64}$	$^{+0.12}$	$^{-}$	$^{-}$	$^{+0.73}$	$^{-0.33}$	$^{-0.15}$	$^{+0.32}$
η intercalibration total stat (JES) [%]	$^{-0.94}$	$^{+0.17}$ $^{-0.69}$	$^{+0.35}$ $^{-0.52}$	$^{-0.30}$	$^{-}$	$^{+0.40}$ $^{-0.22}$	$^{+0.36}$	$^{-0.13}$ $^{+0.10}$	$^{-0.22}$	$^{-0.16}$ $^{+0.21}$	$^{+0.25}$	$^{-0.26}$ $^{-}$	$^{-0.65}$ $^{+0.15}$	$^{\pm0.33}$	$^{+0.43}$	$^{-0.58}$	$^{+0.20}$ $^{+0.22}$	$^{-0.77}$
Flavour composition (JES) [%]	$^{+0.50}$	$^{+0.26}$	$^{+0.34}$	$^{+0.27}$	$^{-}$	$^{+0.44}$	$^{+0.29}$	$^{+0.41}$	$^{-0.28}$	$^{-0.22}$	$^{-0.15}$	$^{-}$	$^{-0.26}$	$^{-}$	$^{-}$	$^{-0.50}$	$^{-0.36}$	$^{+0.75}$
Flavour response (JES) [%]	$^{-1.63}$	$^{+0.41}$ $^{-1.04}$	$^{+0.25}$ $^{+0.77}$	$^{+0.25}$ $^{+0.68}$	$^{-0.89}$	$^{+0.55}$ $^{-0.18}$	$^{+0.39}$	$^{-0.23}$ $^{+0.53}$	$^{-0.36}$ $^{+0.38}$	$^{-0.23}$ $^{+0.37}$	$^{-0.17}$ $^{+0.12}$	$^{-0.37}$ $^{+0.15}$	$^{-0.33}$ $^{+0.40}$	$^{-0.32}$ $^{+0.17}$	$^{+0.64}$ $^{-}$	$^{-0.42}$ $^{+0.39}$	$^{-0.31}$ $^{+0.16}$	$^{-0.71}$
Pile-up offset μ (JES) [%]	$^{-0.45}$ $^{+0.38}$	$^{-0.31}$	$^{-0.97}$	$^{-0.36}$	$^{-0.27}$ $^{+0.16}$	$^{-0.30}$ $^{+0.16}$	$^{-}$	$^{+0.27}$ $^{-0.12}$	$^{+0.24}$	$^{+0.27}$	$^{+0.36}$	$^{+0.15}$	$^{+0.40}$	$^{+0.17}$	$^{-}$	$^{+0.39}$	$^{+0.23}$	$^{+0.23}$
Pile-up offset N_{PV} (JES) [%]	$^{-0.47}$ $^{+0.33}$	$^{-}$	$^{-}$	$^{-}$	$^{+0.14}$ $^{-}$	$^{-}$	$^{-}$	$^{+0.11}$ $^{-}$	$^{-}$	$^{-}$	$^{-}$	$^{-}$	$^{-}$	$^{-}$	$^{-}$	$^{-}$	$^{-}$	$^{-0.47}$ $^{-0.13}$
Pile-up offset p_T (JES) [%]	$^{-0.39}$ $^{+0.24}$	$^{-0.31}$ $^{+0.10}$	$^{-0.29}$ $^{+0.38}$	$^{-0.15}$ $^{+0.18}$	$^{-0.34}$ $^{+0.23}$	$^{-0.25}$ $^{-}$	$^{-}$	$^{-}$	$^{-}$	$^{+0.23}$ $^{-0.27}$	$^{-}$	$^{-}$	$^{+0.10}$ $^{-0.52}$	$^{+0.26}$ $^{-0.27}$	$^{+0.35}$ $^{-}$	$^{+0.18}$ $^{-0.81}$	$^{+0.19}$ $^{+0.29}$	$^{-0.43}$ $^{+0.41}$
Pile-up offset ρ topology (JES) [%]	$^{-1.40}$	$^{-0.20}$	$^{-0.83}$ $^{+0.48}$	$^{-0.43}$ $^{+0.15}$	$^{-0.44}$	$^{+0.37}$	$^{+0.38}$	$^{+0.42}$ $^{-0.23}$	$^{+0.38}$ $^{-0.25}$	$^{+0.40}$ $^{-0.35}$	$^{+0.36}$ $^{-0.22}$	$^{-}$	$^{-}$	$^{-0.11}$ $^{+1.06}$	$^{-0.36}$ $^{-}$	$^{-0.49}$ $^{+0.47}$	$^{-}$	$^{-1.46}$
Punch-through (JES) [%]	$^{-}$	$^{-}$	$^{-}$	$^{-}$	$^{-}$	$^{-}$	$^{-}$	$^{-}$	$^{-}$	$^{-}$	$^{-}$	$^{-}$	$^{-}$	$^{-}$	$^{-}$	$^{-}$	$^{-}$	$^{+0.16}$ $^{-0.21}$
Single particle high-p_T (JES) [%]	$^{-}$	$^{-}$	$^{-}$	$^{-}$	$^{-}$	$^{-}$	$^{-}$	$^{-}$	$^{-}$	$^{-}$	$^{-}$	$^{-}$	$^{-}$	$^{-}$	$^{-}$	$^{-}$	$^{-}$	$^{-}$
Jet energy resolution [%]	±0.48	∓1.27	∓0.84	∓0.51	∓1.45	∓0.65	∓0.49	∓0.20	±0.17	±0.81	±1.01	±0.84	±0.50	±1.40	±1.47	±0.80	±2.07	∓2.29
Jet vertex fraction [%]	$^{+1.69}_{-1.72}$	$^{+1.64}_{-1.63}$	$^{+1.71}_{-1.73}$	$^{+1.61}_{-1.65}$	$^{+1.24}_{-1.28}$	$^{+0.78}_{-0.81}$	$^{+0.51}_{-0.54}$	$^{+0.32}_{-0.35}$	$^{-0.12}_{+0.11}$	∓0.60	$^{-0.84}_{+0.86}$	$^{-1.13}_{+1.19}$	$^{-1.42}_{+1.46}$	$^{-1.74}_{+1.77}$	$^{-2.60}_{+2.69}$	$^{-2.24}_{+2.34}$	$^{-2.87}_{+3.03}$	$^{-2.75}_{+2.98}$
b-Quark tagging efficiency (eigenvector 0) [%]	$^{-0.82}_{\mp0.52}$	$^{-0.65}_{\mp0.61}$	$^{-0.60}_{\mp0.52}$	$^{-0.47}_{\mp0.44}$	$^{-0.32}_{\mp0.29}$	$^{-0.17}_{\mp0.16}$	$^{-}$	$^{-}$	±0.15	$^{+0.25}_{-0.24}$	$^{+0.24}_{-0.22}$	$^{+0.28}_{-0.20}$	$^{+0.36}_{-0.28}$	$^{+0.39}_{-0.32}$	$^{+0.47}_{-0.43}$	$^{+0.45}_{-0.44}$	$^{+0.33}_{-0.33}$	$^{-}$
b-Quark tagging efficiency (eigenvector 1) [%]	$^{-0.78}$	$^{-0.77}$	$^{-0.73}$	$^{-0.68}$	$^{-0.63}$	$^{-0.54}$	$^{+0.47}$ $^{-0.46}$	±0.35	$^{+0.22}$ $^{-0.21}$	$^{-}$	∓0.15	$^{+0.38}$	$^{+0.64}$	$^{+1.04}$	$^{+1.56}$	$^{+2.08}$	$^{+2.91}$	$^{+3.61}$
b-Quark tagging efficiency (eigenvector 2) [%]	±0.47	$^{+0.43}$	$^{+0.44}$	$^{+0.42}$	±0.37	$^{+0.32}$	$^{+0.26}$	$^{+0.22}$ $^{-0.23}$	±0.14	$^{-}$	$^{-}$	∓0.22	$^{-0.40}$	$^{-0.63}$	$^{-0.92}$	$^{-1.24}$	$^{-1.72}$	$^{-2.09}$
b-Quark tagging efficiency (eigenvector 3) [%]	±0.18	∓0.16	∓0.14	∓0.11	$^{-}$	$^{-}$	$^{-}$	$^{-}$	±0.10	$^{+0.13}$ $^{-0.14}$	$^{+0.15}$ $^{-0.14}$	$^{-0.14}$ $^{-0.13}$	$^{+0.41}$ $^{-0.14}$	$^{+0.64}$ $^{-}$	$^{+0.94}$ $^{-}$	$^{+1.26}$ $^{+0.19}$	$^{+1.78}$ ±0.42	$^{+2.16}$ ∓0.63
b-Quark tagging efficiency (eigenvector 4) [%]	$^{-}$	$^{-}$	$^{-}$	$^{-}$	$^{-}$	$^{-}$	$^{-}$	$^{-}$	$^{-}$	$^{-}$	$^{-}$	$^{-}$	$^{-}$	$^{-}$	$^{-}$	$^{-}$	±0.13	∓0.20
c-Quark tagging efficiency (eigenvector 0) [%]	$^{-0.51}$	$^{-0.68}$	$^{-0.34}$	$^{-0.38}$	∓0.35	∓0.23	∓0.15	$^{-}$	$^{-}$	$^{-}$	±0.19	±0.37	$^{+0.39}$	$^{+0.47}$	$^{+0.58}$	$^{+0.58}$	$^{+0.75}$	$^{+0.49}$
c-Quark tagging efficiency (eigenvector 1) [%]	±0.25	±0.23	∓0.17	∓0.16	±0.15	$^{+0.13}$ $^{-0.10}$	$^{-}$	$^{-}$	$^{-}$	$^{-}$	$^{-}$	∓0.13	$^{-0.29}$	$^{-0.76}$	$^{-0.96}$	$^{-1.20}$	$^{-1.50}$	$^{-1.46}$
c-Quark tagging efficiency (eigenvector 2) [%]	$^{-}$	$^{-}$	$^{-0.16}$	$^{-}$	$^{-}$	$^{-}$	$^{-}$	$^{-}$	$^{-}$	$^{-}$	$^{-}$	$^{-}$	$^{-0.49}$ $^{+0.17}$	∓0.20	∓0.22	∓0.29 $^{-}$	$^{-0.31}$ ±0.16	∓0.29 ±0.18	±0.16
c-Quark tagging efficiency (eigenvector 3) [%]	∓0.10	$^{-}$	$^{-}$	$^{-}$	$^{-}$	$^{-}$	$^{-}$	$^{-}$	$^{-}$	$^{-}$	$^{-}$	$^{-}$	$^{-}$	$^{-}$	$^{-}$	$^{-}$	$^{-}$	$^{-}$
Light-jet tagging efficiency (eigenvector 0) [%]	$^{-2.17}$ $^{+3.06}$	$^{-1.27}$ $^{+1.62}$	$^{-0.91}$ $^{+1.01}$	$^{-0.47}$ $^{+0.58}$	$^{-}$	$^{-}$	$^{+0.18}$ $^{-0.24}$	$^{+0.29}$ $^{-0.39}$	$^{+0.33}$ $^{-0.39}$	$^{+0.25}$ $^{-0.30}$	$^{+0.24}$ $^{-0.16}$	$^{-}$	$^{+0.24}$ $^{-0.15}$	$^{+0.40}$ $^{-0.49}$	$^{+0.31}$ $^{-0.36}$	$^{+0.16}$ $^{-0.24}$	$^{+0.20}$	$^{-0.56}$ $^{+0.51}$
Light-jet tagging efficiency (eigenvector 1) [%]	$^{-}$	$^{-}$	$^{-}$	$^{-}$	$^{-}$	$^{-}$	$^{-}$	$^{-}$	$^{-}$	$^{-}$	$^{-}$	$^{-}$	$^{-}$	$^{-}$	$^{-}$	$^{-}$	$^{-}$	$^{-}$
Light-jet tagging efficiency (eigenvector 2) [%]	±0.27	±0.19	±0.16	$^{-}$	$^{-}$	$^{-}$	$^{-}$	$^{-}$	$^{-}$	$^{-}$	$^{-}$	$^{-}$	$^{-}$	$^{-}$	$^{-}$	∓0.11	±0.16	∓0.11
Light-jet tagging efficiency (eigenvector 3) [%]	$^{-}$	$^{-}$	$^{-}$	$^{-}$	$^{-}$	$^{-}$	$^{-}$	$^{-}$	$^{-}$	$^{-}$	$^{-}$	$^{-}$	$^{-}$	$^{-}$	$^{-}$	$^{-}$	$^{-}$	$^{-}$
Light-jet tagging efficiency (eigenvector 4) [%]	$^{-}$	$^{-}$	$^{-}$	$^{-}$	$^{-}$	$^{-}$	$^{-}$	$^{-}$	$^{-}$	$^{-}$	$^{-}$	$^{-}$	$^{-}$	$^{-}$	$^{-}$	$^{-}$	$^{-}$	$^{-}$
Light-jet tagging efficiency (eigenvector 5) [%]	$^{-}$	$^{-}$	$^{-}$	$^{-}$	$^{-}$	$^{-}$	$^{-}$	$^{-}$	$^{-}$	$^{-}$	$^{-}$	$^{-}$	$^{-}$	$^{-}$	$^{-}$	$^{-}$	$^{-}$	$^{-}$
Light-jet tagging efficiency (eigenvector 6) [%]	$^{-}$	$^{-}$	$^{-}$	$^{-}$	$^{-}$	$^{-}$	$^{-}$	$^{-}$	$^{-}$	$^{-}$	$^{-}$	$^{-}$	$^{-}$	$^{-}$	$^{-}$	$^{-}$	$^{-}$	$^{-}$
Light-jet tagging efficiency (eigenvector 7) [%]	$^{-}$	$^{-}$	$^{-}$	$^{-}$	$^{-}$	$^{-}$	$^{-}$	$^{-}$	$^{-}$	$^{-}$	$^{-}$	$^{-}$	$^{-}$	$^{-}$	$^{-}$	$^{-}$	$^{-}$	$^{-}$
Light-jet tagging efficiency (eigenvector 8) [%]	$^{-}$	$^{-}$	$^{-}$	$^{-}$	$^{-}$	$^{-}$	$^{-}$	$^{-}$	$^{-}$	$^{-}$	$^{-}$	$^{-}$	$^{-}$	$^{-}$	$^{-}$	$^{-}$	$^{-}$	$^{-}$
Light-jet tagging efficiency (eigenvector 9) [%]	$^{-}$	$^{-}$	$^{-}$	$^{-}$	$^{-}$	$^{-}$	$^{-}$	$^{-}$	$^{-}$	$^{-}$	$^{-}$	$^{-}$	$^{-}$	$^{-}$	$^{-}$	$^{-}$	$^{-}$	$^{-}$
Light-jet tagging efficiency (eigenvector 10) [%]	$^{-}$	$^{-}$	$^{-}$	$^{-}$	$^{-}$	$^{-}$	$^{-}$	$^{-}$	$^{-}$	$^{-}$	$^{-}$	$^{-}$	$^{-}$	$^{-}$	$^{-}$	$^{-}$	$^{-}$	$^{-}$
Light-jet tagging efficiency (eigenvector 11) [%]	$^{-}$	$^{-}$	$^{-}$	$^{-}$	$^{-}$	$^{-}$	$^{-}$	$^{-}$	$^{-}$	$^{-}$	$^{-}$	$^{-}$	$^{-}$	$^{-}$	$^{-}$	$^{-}$	$^{-}$	$^{-}$
Light-jet tagging efficiency (eigenvector 12) [%]	$^{-}$	$^{-}$	$^{-}$	$^{-}$	$^{-}$	$^{-}$	$^{-}$	$^{-}$	$^{-}$	$^{-}$	$^{-}$	$^{-}$	$^{-}$	$^{-}$	$^{-}$	$^{-}$	$^{-}$	$^{-}$
Light-jet tagging efficiency (eigenvector 13) [%]	$^{-}$	$^{-}$	$^{-}$	$^{-}$	$^{-}$	$^{-}$	$^{-}$	$^{-}$	$^{-}$	$^{-}$	$^{-}$	$^{-}$	$^{-}$	$^{-}$	$^{-}$	$^{-}$	$^{-}$	$^{-}$
b-Quark tagging extrapolation [%]	∓0.25	$^{-0.26}_{\mp0.25}$	∓0.26	∓0.26	∓0.25	∓0.25	∓0.24	∓0.24	∓0.23	$^{-0.21}_{\mp0.26}$	∓0.17	$^{-0.13}_{-0.14}$	$^{-}$	$^{-}$	±0.56	±1.56	$^{+3.42}_{-3.17}$	$^{+5.63}_{-5.54}$
b-Quark tagging extrapolation from c-Quark [%]	$^{-}$	$^{-}$	$^{-}$	$^{-}$	$^{-}$	$^{-}$	$^{-}$	$^{-}$	$^{-}$	$^{-}$	$^{-}$	$^{-}$	$^{-}$	$^{-}$	$^{-}$	$^{-}$	$^{-}$	$^{-}$
Electron energy resolution [%]	$^{-0.58}$	$^{-}$	$^{-}$	$^{-}$	$^{-}$	$^{-}$	$^{-}$	$^{-}$	$^{-}$	$^{-}$	$^{-}$	$^{-}$	$^{-}$	$^{-}$	$^{-}$	$^{-}$	$^{-}$	$^{-}$
Electron energy scale [%]	$^{-}$	$^{-}$	$^{-}$	$^{-}$	$^{-}$	$^{-}$	$^{-}$	$^{-}$	$^{-}$	$^{-}$	$^{-}$	$^{-}$	$^{-}$	$^{-}$	$^{-}$	$^{-}$	$^{-}$	$^{-}$
Electron trigger efficiency [%]	$^{-}$	$^{-}$	$^{-}$	$^{-}$	$^{-}$	$^{-}$	$^{-}$	$^{-}$	$^{-}$	$^{-}$	$^{-}$	$^{-}$	$^{-}$	$^{-}$	$^{-}$	$^{-}$	$^{-}$	$^{-}$
Electron reconstruction efficiency [%]	$^{-}$	$^{-}$	$^{-}$	$^{-}$	$^{-}$	$^{-}$	$^{-}$	$^{-}$	$^{-}$	$^{-}$	$^{-}$	$^{-}$	$^{-}$	$^{-}$	$^{-}$	$^{-}$	$^{-}$	±0.11
Electron identification efficiency [%]	$^{-}$	$^{-}$	$^{-}$	$^{-}$	$^{-}$	$^{-}$	$^{-}$	$^{-}$	$^{-}$	$^{-}$	$^{-}$	$^{-}$	$^{-}$	$^{-}$	±0.12	$^{+0.19}$ $^{-0.20}$	±0.32	$^{+0.54}$ $^{-0.55}$
Electron isolation efficiency [%]	$^{-}$	$^{-}$	$^{-}$	$^{-}$	$^{-}$	$^{-}$	$^{-}$	$^{-}$	$^{-}$	$^{-}$	$^{-}$	$^{-}$	$^{-}$	$^{-}$	$^{-}$	±0.16	$^{+0.39}$ $^{-0.31}$	±0.54
Muon energy scale [%]	$^{-}$	$^{-}$	$^{-}$	$^{-}$	$^{-}$	$^{-}$	$^{-}$	$^{-}$	$^{-}$	$^{-}$	$^{-}$	$^{-}$	$^{-}$	$^{-}$	$^{-}$	$^{-}$	$^{-}$	$^{-}$
Muon (MS) momentum resolution [%]	$^{-}$	$^{-}$	$^{-}$	$^{-}$	$^{-}$	$^{-}$	$^{-}$	$^{-}$	$^{-}$	$^{-}$	$^{-}$	$^{-}$	$^{-}$	$^{-}$	$^{-}$	$^{-}$	$^{-}$	$^{-}$
Muon (ID) momentum resolution [%]	$^{-}$	$^{-}$	$^{-}$	$^{-}$	$^{-}$	$^{-}$	$^{-}$	$^{-}$	$^{-}$	$^{-}$	$^{-}$	$^{-}$	$^{-}$	$^{-}$	$^{-}$	$^{-}$	$^{-}$	$^{-}$
Muon trigger efficiency stat [%]	±0.11	$^{-}$	$^{-}$	$^{-}$	$^{-}$	$^{-}$	$^{-}$	$^{-}$	$^{-}$	$^{-}$	$^{-}$	$^{-}$	$^{-}$	$^{-}$	$^{-}$	$^{-}$	$^{-}$	$^{-}$
Muon trigger efficiency syst [%]	$^{-}$	$^{-}$	$^{-}$	$^{-}$	$^{-}$	$^{-}$	$^{-}$	$^{-}$	$^{-}$	$^{-}$	$^{-}$	$^{-}$	$^{-}$	$^{-}$	$^{-}$	$^{-}$	$^{-}$	$^{-}$
Muon identification stat [%]	$^{-}$	$^{-}$	$^{-}$	$^{-}$	$^{-}$	$^{-}$	$^{-}$	$^{-}$	$^{-}$	$^{-}$	$^{-}$	$^{-}$	$^{-}$	$^{-}$	$^{-}$	$^{-}$	$^{-}$	$^{-}$
Muon identification syst [%]	$^{-}$	$^{-}$	$^{-}$	$^{-}$	$^{-}$	$^{-}$	$^{-}$	$^{-}$	$^{-}$	$^{-}$	$^{-}$	$^{-}$	$^{-}$	$^{-}$	$^{-}$	$^{-}$	±0.13	$^{+0.28}$ $^{-0.27}$
Muon isolation efficiency stat [%]	$^{-}$	$^{-}$	$^{-}$	$^{-}$	$^{-}$	$^{-}$	$^{-}$	$^{-}$	$^{-}$	$^{-}$	$^{-}$	$^{-}$	$^{-}$	$^{-}$	$^{-}$	$^{-}$	$^{-}$	$^{-}$
Muon isolation efficiency syst [%]	$^{-}$	$^{-}$	$^{-}$	$^{-}$	$^{-}$	$^{-}$	$^{-}$	$^{-}$	$^{-}$	$^{-}$	$^{-}$	$^{-}$	$^{-}$	$^{-}$	$^{-}$	$^{-}$	$^{-}$	$^{-}$
Muon TTVA efficiency stat [%]	$^{-}$	$^{-}$	$^{-}$	$^{-}$	$^{-}$	$^{-}$	$^{-}$	$^{-}$	$^{-}$	$^{-}$	$^{-}$	$^{-}$	$^{-}$	$^{-}$	$^{-}$	$^{-}$	$^{-}$	$^{-}$
Muon TTVA efficiency syst [%]	$^{-}$	$^{-}$	$^{-}$	$^{-}$	$^{-}$	$^{-}$	$^{-}$	$^{-}$	$^{-}$	$^{-}$	$^{-}$	$^{-}$	$^{-}$	$^{-}$	$^{-}$	$^{-}$	$^{-}$	$^{-}$
E_T^{miss} Soft jet resolution para [%]	±0.11	$^{-}$	$^{-}$	$^{-}$	$^{-}$	$^{-}$	$^{-}$	$^{-}$	$^{-}$	$^{-}$	$^{-}$	$^{-}$	$^{-}$	$^{-}$	$^{-}$	$^{-}$	$^{-}$	$^{-}$
E_T^{miss} Soft jet resolution perp [%]	$^{-}$	$^{-}$	$^{-}$	$^{-}$	$^{-}$	$^{-}$	$^{-}$	$^{-}$	$^{-}$	$^{-}$	$^{-}$	$^{-}$	$^{-}$	$^{-}$	$^{-}$	$^{-}$	$^{-}$	$^{-}$
E_T^{miss} Soft jet scale [%]	$^{-}$	$^{-}$	$^{-}$	$^{-}$	$^{-}$	$^{-}$	$^{-}$	$^{-}$	$^{-}$	$^{-}$	$^{-}$	$^{-}$	$^{-}$	$^{-}$	$^{-}$	$^{-}$	$^{-}$	$^{-}$
Luminosity [%]	$^{-}$	$^{-}$	$^{-}$	$^{-}$	$^{-}$	$^{-}$	$^{-}$	$^{-}$	$^{-}$	$^{-}$	$^{-}$	$^{-}$	$^{-}$	$^{-}$	$^{-}$	$^{-}$	$^{-}$	$^{-}$
W+jets CA_2ex stat error [%]	$^{-}$	$^{-}$	$^{-}$	$^{-}$	$^{-}$	$^{-}$	$^{-}$	$^{-}$	$^{-}$	$^{-}$	$^{-}$	$^{-}$	$^{-}$	$^{-}$	$^{-}$	$^{-}$	$^{-}$	$^{-}$
W+jets CA_3ex stat error [%]	$^{-}$	$^{-}$	$^{-}$	$^{-}$	$^{-}$	$^{-}$	$^{-}$	$^{-}$	$^{-}$	$^{-}$	$^{-}$	$^{-}$	$^{-}$	$^{-}$	$^{-}$	$^{-}$	$^{-}$	$^{-}$
W+jets CA_4incl stat error [%]	∓0.25	∓0.14	∓0.11	$^{-}$	$^{-}$	$^{-}$	$^{-}$	$^{-}$	$^{-}$	$^{-}$	$^{-}$	$^{-}$	$^{-}$	$^{-}$	$^{-}$	$^{-}$	$^{-}$	$^{-}$
W+jets Fc stat error [%]	∓0.23	∓0.21	∓0.11	$^{-}$	$^{-}$	$^{-}$	$^{-}$	$^{-}$	$^{-}$	$^{-}$	$^{-}$	$^{-}$	$^{-}$	$^{-}$	$^{-}$	$^{-}$	$^{-}$	$^{-}$
W+jets Fcc stat error [%]	$^{+1.37}$ $^{+1.14}$	$^{+0.94}$ $^{+0.82}$	$^{+0.85}$ $^{+0.83}$	$^{+0.69}$ $^{+0.68}$	$^{+0.33}$ $^{+0.32}$	$^{-}$	±0.13	$^{+0.25}$ $^{-0.25}$	$^{+0.30}$ $^{-0.29}$	$^{+0.24}$ $^{-0.23}$	$^{+0.19}$ $^{-0.18}$	$^{+0.26}$ $^{-0.35}$	$^{+0.37}$ $^{-0.36}$	$^{+0.43}$ $^{-0.32}$	±0.31	$^{+0.32}$ $^{-0.31}$	$^{+0.29}$ $^{-0.28}$	$^{+0.51}$ $^{+0.50}$
W+jets Flight stat error [%]	$^{-}$	$^{-}$	$^{-}$	$^{-}$	$^{-}$	$^{-}$	$^{-}$	$^{-}$	$^{-}$	$^{-}$	$^{-}$	$^{-}$	$^{-}$	$^{-}$	$^{-}$	$^{-}$	$^{-}$	$^{-}$

Bins [GeV]	0–15	15–30	30–45	45–60	60–75	75–90	90–105	105–120	120–135	135–150	150–165	165–180	180–200	200–230	230–265	265–325	325–450	450–1000
$1/\sigma \cdot d\sigma / dpt^{t,had}_{T}$	$7.18 \cdot 10^{-4}$	$2.49 \cdot 10^{-3}$	$3.85 \cdot 10^{-3}$	$4.94 \cdot 10^{-3}$	$6.05 \cdot 10^{-3}$	$6.23 \cdot 10^{-3}$	$6.01 \cdot 10^{-3}$	$5.62 \cdot 10^{-3}$	$5.02 \cdot 10^{-3}$	$4.25 \cdot 10^{-3}$	$3.65 \cdot 10^{-3}$	$3.16 \cdot 10^{-3}$	$2.51 \cdot 10^{-3}$	$1.85 \cdot 10^{-3}$	$1.17 \cdot 10^{-3}$	$6.50 \cdot 10^{-4}$	$2.21 \cdot 10^{-4}$	$1.21 \cdot 10^{-5}$
Total Uncertainty [%]	±3.0 ±4.27	±2.1 ±3.49	±1.6 ±4.64	±1.7 ±4.57	±1.8 ±4.26	±1.8 ±4.42	±1.8 ±4.67	±1.8 ±4.63	±1.9 ±5.23	±2.0 ±5.15	±2.1 ±5.60	±2.2 ±5.96	±2.4 ±6.91	±2.5 ±6.26	±3.1 ±7.65	±3.3 ±7.94	±3.9 ±9.66	±9.3 ±19.8
Statistics [%]	±6.1	±2.8	±2.3	±2.0	±1.7	±1.6	±1.6	±1.7	±1.8	±1.9	±2.1	±2.2	±2.4	±2.5	±3.1	±3.3	±3.9	±9.3
Systematics [%]	±3.3 ±3.82	±1.85 ±3.61	±2.03 ±3.45	±1.01 ±4.11	±2.07 ±3.50	±1.68 ±3.88	±2.49 ±3.68	±1.74 ±3.71	±2.16 ±4.11	±1.72 ±4.72	±1.99 ±4.85	±2.12 ±5.40	±2.06 ±5.96	±2.09 ±5.68	±2.40 ±6.89	±2.49 ±7.41	±3.59 ±8.76	±17.3 ±17.4
b-Tagged jet energy scale (JES) [%]	+1.44 +1.36	−0.19 +0.53	−0.04 +0.49	−0.15 +0.42	+0.20 +0.16	−0.21 +0.39	− −	+0.15 −0.35	+0.22 −0.37	+0.26 −0.22	+0.29 −0.34	+0.63 −	+0.38 −	−0.43 −	+0.12 −0.24	+0.36 −	−0.46 −2.85	+1.38 −6.30
Effective detector NP set 1 (JES) [%]	+1.11 −0.28	−0.35 +1.00	+1.05 −0.82 +1.00	−0.97 +1.01	−0.55 +1.02	−0.42 +1.05	−1.66 +1.68	−0.73 +0.75	−0.75 −0.20	−0.59 −	−0.51 +0.51	+0.28 −0.37 +0.41	−0.28 +1.16 −0.68	−1.33 +0.22 −1.05	−2.21 +2.29 −1.32	−2.58 +3.47 −1.65	−2.85 +2.98 −1.28	+2.84 −3.40
Effective detector NP set 2 (JES) [%]	+0.36 +0.45	+1.30 +0.63	+1.16 +0.73	+0.83 +0.80	+1.34 +0.58	+1.96 +0.63	+0.42 +0.27	−0.40 ±0.11	− −	−0.17 −	−0.37 +0.55	−0.41 +0.31	−0.68 +0.60	−1.32 +0.87	−1.65 +0.94	−1.28 +0.63	−3.40 +1.77	−5.92 +2.81
Effective detector NP set 3 (JES) [%]	−0.79 +0.65	−1.03 +0.62	−0.69 +0.53	−0.49 +0.32	−0.47 +1.24	−0.66 +0.37	−0.41 +0.20	+0.11	+0.24	+0.21 +0.11	+0.19 +0.13	+0.55 +0.52	+0.72 +0.40	+0.24 +0.34	+1.02 +0.41	+1.37 +0.55	+1.43 +0.62	+3.02
Effective detector NP set 4 (JES) [%]	+0.85 +0.85	+0.54	−0.53 +0.11	+0.38	+0.29	+0.41	−	−	−	−0.24 −0.17	+0.13 −0.22	−0.24	−0.36	−0.43	−0.48	−0.31	−0.22 +0.42	+0.21 +0.61
Effective detector NP set 5 (JES) [%]	−0.32	−	−0.12	−	−	−	−	−	−	−	+0.13	+0.23	−	−	−	−	−0.50	+0.62
Effective detector NP set 6 resTerm (JES) [%]	−	−0.10	−	−0.12	−0.10	−0.13	−	−	−	−	−	−	+0.25	−	−	+0.20	+0.12	+0.84
η intercalibration model (JES) [%]	−1.68	−0.17 +1.41	+1.19	−0.08 +0.68	−0.06 +0.68	−	+0.27	+0.24	+0.35	+0.52	+0.27	+0.66	−	−0.16 −0.67	−	−0.63	−0.49 −	−1.41
η intercalibration total stat (JES) [%]	+0.83 −0.94	+0.48 −0.50	−0.23	+0.22	+0.16	−	−0.31	−0.64 +0.12	−0.69	−0.17	−	−	+0.36 −0.14	−0.48	+0.75 −0.18	+1.08 +0.33	−0.84	+1.31 +0.03
Flavour composition (JES) [%]	+0.97 −1.74	−0.15	+0.92 −0.22	−1.14	−0.48	+0.57	−0.23 −0.55	−0.27 −0.66	−0.20 −1.01	+0.75 −0.92	+0.55	−0.37	+0.98 −0.98	−0.47	+0.38 −2.12	−2.04	−0.21 +2.74	−5.52
Flavour response (JES) [%]	+0.21 −0.51	−0.40	+0.59 −0.59	+0.10 −0.17	+0.12 −0.13	−	−0.33	−	−0.37 +0.13	+0.35	−	−0.52	−0.27 +0.49	−	+0.55 −0.41	+0.53 −0.20	−0.52	+1.49 −0.28
Pile-up offset μ (JES) [%]	+1.18 −0.43	−	−0.12 +0.11	−	−	−0.13	−	−	−	−	−	−	−	−	+0.21 −0.12	+0.27 −	−0.43	+0.66 −0.65
Pile-up offset N_{PV} (JES) [%]	−	−	+0.11	+0.24	−	−	−	−	−	−	−	+0.29	−0.14	−	−	+0.25	−	+0.37 −0.37
Pile-up offset p_T (JES) [%]	−0.18	−0.34	−0.26 −0.18	−0.18 +0.15	−0.11	−0.21	−0.29	−	−	−	+0.17	+0.19	+0.33 +0.13	−	−0.20 ±0.31	+0.29	+0.10	−0.22 +0.38
Pile-up offset p topology (JES) [%]	+0.78 −0.30	+0.32	+0.49	+0.15	+0.25 +0.16	+0.25 +0.25	−	−	+0.42	+0.19	+0.24	+0.18	−0.11	+0.31	−0.38	−0.99	−0.49	−0.52 −1.15	−1.30
Punch-through (JES) [%]	+1.32 -	−0.36 -	−0.11 -	− -	−0.11 -	− -	−0.38 -	−0.35 -	−0.69 -	− -	−0.19 -	− -	− -	−0.47 -	+0.54 -	+1.26 -	+0.45 -	+1.82 ±0.10
Single particle high-p_T (JES) [%]	-	-	-	-	-	-	-	-	-	-	-	-	-	-	-	-	-	-
Jet energy resolution [%]	∓2.81	∓1.23	∓0.38	∓0.94	-	±0.75	±0.12	-	∓0.31	±0.79	±0.29	±0.11	±1.72	∓1.00	±0.15	±0.85	±0.86	∓0.75
Jet vertex fraction [%]	+1.62 −1.63	+1.52 −1.58	+1.84 −1.89	+1.67 −1.69	+1.26 −1.32	±0.97 −1.01	±0.73 −0.77	±0.26 −0.31	− −	∓0.34 −	−0.77 +0.62	−1.69 +1.12	−1.44 +1.47	−1.67 +1.76	−2.69 +2.16	−2.17 +2.23	−2.96 +3.08	−3.63 +3.95
b-Quark tagging efficiency (eigenvector 0) [%]	−0.61 +0.49	−0.64 +0.61	−0.57 +0.54	−0.41 +0.49	−0.23 +0.22	−	−	+0.11 −0.10	+0.16 −0.15	+0.17 −0.16	+0.20 −0.19	+0.21 −0.20	+0.29 −0.28	+0.31 −0.29	+0.25 −0.24	+0.32 −0.27	+0.22 −0.21	− −1.10
b-Quark tagging efficiency (eigenvector 1) [%]	−0.71	−0.75	−0.72	−0.66	−0.59	−0.49	−0.41 +0.25	±0.33	±0.22	−	−	+0.25 −0.17	+0.47	+0.77	+1.27 −0.73	+1.59 −0.93	+2.16 −1.34	+3.27 −1.82
b-Quark tagging efficiency (eigenvector 2) [%]	±0.41	±0.38	±0.40	±0.40	±0.36	±0.32	−0.26	±0.18	±0.11	−	−	+0.16	±0.30	±0.46	+0.74	−0.93	+1.38	+1.86
b-Quark tagging efficiency (eigenvector 3) [%]	∓0.12	∓0.12	∓0.11	−	−	−	−	−	−	−	±0.10	±0.10	−	−	−	∓0.14	±0.32	∓0.58
b-Quark tagging efficiency (eigenvector 4) [%]	-	-	-	-	-	-	-	-	-	-	-	-	-	-	-	-	±0.11	±0.20
c-Quark tagging efficiency (eigenvector 0) [%]	∓0.16	-	∓0.22	∓0.27	∓0.27 ±0.28	∓0.22	−0.21 +0.20	-	-	-	-	±0.14	+0.29 −0.28	±0.42	+0.53 −0.51	-	+0.53 −0.54	-
c-Quark tagging efficiency (eigenvector 1) [%]	±0.13	±0.15	+0.19 −0.20	±0.17	±0.13	-	-	-	-	-	-	∓0.10	±0.16	±0.15	±0.20	±0.29	±0.27	±0.44
c-Quark tagging efficiency (eigenvector 2) [%]	-	-	-	-	-	-	-	-	-	-	-	-	-	-	-	∓0.17	±0.16	∓0.27
c-Quark tagging efficiency (eigenvector 3) [%]	-	-	-	-	-	-	-	-	-	-	-	-	-	-	-	-	-	-
Light-jet tagging efficiency (eigenvector 0) [%]	−0.14	−0.28 +0.29	−0.32 +0.37	∓0.19	-	-	∓0.13	+0.24 −0.27	-	+0.17	+0.21 −0.18	+0.22 −0.23	+0.23 −0.27	-	+0.17 −0.19	-	+0.16 −0.10	−2.02 +1.96
Light-jet tagging efficiency (eigenvector 1) [%]	∓0.10	-	-	-	-	-	-	-	-	-	-	-	-	-	-	-	-	-
Light-jet tagging efficiency (eigenvector 2) [%]	-	-	-	-	-	-	-	-	-	-	-	-	-	-	-	±0.11	±0.14	∓0.22
Light-jet tagging efficiency (eigenvector 3) [%]	-	-	-	-	-	-	-	-	-	-	-	-	-	-	-	-	-	-
Light-jet tagging efficiency (eigenvector 4) [%]	-	-	-	-	-	-	-	-	-	-	-	-	-	-	-	-	-	∓0.16
Light-jet tagging efficiency (eigenvector 5) [%]	-	-	-	-	-	-	-	-	-	-	-	-	-	-	-	-	-	-
Light-jet tagging efficiency (eigenvector 6) [%]	-	-	-	-	-	-	-	-	-	-	-	-	-	-	-	-	-	-
Light-jet tagging efficiency (eigenvector 7) [%]	-	-	-	-	-	-	-	-	-	-	-	-	-	-	-	-	-	-
Light-jet tagging efficiency (eigenvector 8) [%]	-	-	-	-	-	-	-	-	-	-	-	-	-	-	-	-	-	-
Light-jet tagging efficiency (eigenvector 9) [%]	-	-	-	-	-	-	-	-	-	-	-	-	-	-	-	-	-	-
Light-jet tagging efficiency (eigenvector 10) [%]	-	-	-	-	-	-	-	-	-	-	-	-	-	-	-	-	-	-
Light-jet tagging efficiency (eigenvector 11) [%]	-	-	-	-	-	-	-	-	-	-	-	-	-	-	-	-	-	-
Light-jet tagging efficiency (eigenvector 12) [%]	-	-	-	-	-	-	-	-	-	-	-	-	-	-	-	-	-	-
Light-jet tagging efficiency (eigenvector 13) [%]	-	-	-	-	-	-	-	-	-	-	-	-	-	-	-	-	-	-
b-Quark tagging extrapolation [%]	∓0.29	∓0.30	∓0.30	−0.33 +0.32	∓0.31	−0.28 +0.29	∓0.27	∓0.28	∓0.26	±0.24	±0.21	∓0.16	-	±0.12	±0.60	+1.24 −1.23	+1.77 −2.75	+5.67 −5.77
b-Quark tagging extrapolation from c-Quark [%]	-	-	-	-	-	-	-	-	-	-	-	-	-	-	-	-	-	-
Electron energy resolution [%]	-	-	-	-	-	-	-	-	-	-	-	-	-	-	-	-	-	-
Electron energy scale [%]	+0.17 -	-	-	-	-	-	-	-	-	-	-	-	-	-	-	-	-	−0.11 +0.14
Electron trigger efficiency [%]	-	-	-	-	-	-	-	-	-	-	-	-	-	-	-	-	-	±0.12
Electron reconstruction efficiency [%]	-	-	-	-	-	-	-	-	-	-	-	-	-	-	-	-	-	±0.12
Electron identification efficiency [%]	-	-	-	-	-	-	-	-	-	-	-	-	-	-	-	±0.14	±0.24	±0.51
Electron isolation efficiency [%]	-	-	-	-	-	-	-	-	-	-	-	-	-	-	-	±0.12	±0.23	±0.45
Muon energy scale [%]	-	-	-	-	-	-	-	-	-	-	-	-	-	-	-	-	-	-
Muon (MS) momentum resolution [%]	-	-	-	-	-	-	-	-	-	-	-	-	-	-	-	-	-	-
Muon (ID) momentum resolution [%]	-	-	-	-	-	-	-	-	-	-	-	-	-	-	-	-	-	-
Muon trigger efficiency stat [%]	-	-	-	-	-	-	-	-	-	-	-	-	-	-	-	-	-	-
Muon trigger efficiency syst [%]	-	-	-	-	-	-	-	-	-	-	-	-	-	-	-	-	-	-
Muon identification stat [%]	-	-	-	-	-	-	-	-	-	-	-	-	-	-	-	-	-	-
Muon identification syst [%]	-	-	-	-	-	-	-	-	-	-	-	-	-	-	-	-	±0.11	±0.22
Muon isolation efficiency stat [%]	-	-	-	-	-	-	-	-	-	-	-	-	-	-	-	-	-	-
Muon isolation efficiency syst [%]	-	-	-	-	-	-	-	-	-	-	-	-	-	-	-	-	-	-
Muon TTVA efficiency stat [%]	-	-	-	-	-	-	-	-	-	-	-	-	-	-	-	-	-	-
Muon TTVA efficiency syst [%]	-	-	-	-	-	-	-	-	-	-	-	-	-	-	-	-	-	-
E_T^{miss} Soft jet resolution para [%]	-	-	-	-	-	-	-	-	-	-	-	-	-	-	-	-	-	±0.12
E_T^{miss} Soft jet resolution perp [%]	-	-	-	-	-	-	-	-	-	-	-	-	-	-	-	-	-	-
E_T^{miss} Soft jet scale [%]	-	-	-	-	-	-	-	-	-	-	-	-	-	-	-	-	-	-
Luminosity [%]	-	-	-	-	-	-	-	-	-	-	-	-	-	-	-	-	-	-
W+jets CA_2ex stat error [%]	-	-	-	-	-	-	-	-	-	-	-	-	-	-	-	-	-	-
W+jets CA_3ex stat error [%]	-	-	-	-	-	-	-	-	-	-	-	-	-	-	-	-	-	-
W+jets CA_4incl stat error [%]	-	-	-	-	-	-	-	-	-	-	-	-	-	-	-	-	-	∓0.10
W+jets Fc stat error [%]	∓0.12	∓0.16	-	-	-	-	-	-	-	-	-	-	-	-	-	-	-	-
W+jets Fcc stat error [%]	-	-	∓0.32	∓0.29	∓0.13	-	-	±0.24	-	+0.18 −0.17	+0.13 −0.12	+0.15 −0.14	±0.12	-	-	-	−0.37 +0.36	−0.97 +0.96
W+jets Flight stat error [%]	-	-	-	-	-	-	-	-	-	-	-	-	-	-	-	-	-	-
Single top cross-section [%]	-	-	-	-	-	-	-	-	-	-	-	-	-	-	±0.10	±0.19	±0.29	±1.11
Z+jets cross-section [%]	±0.47	-	∓0.11	±0.56	-	-	±0.40	∓0.27	∓0.32	-	-	±0.26	-	∓0.46	±0.12	∓0.57	-	±1.09
Diboson cross-section [%]	±0.13	-	-	-	-	-	-	-	-	-	-	-	-	-	-	-	±0.23	±0.94
$t\bar{t}V$ cross-section [%]	-	-	-	-	-	-	-	-	-	-	-	-	-	-	-	-	-	±0.14
Monte Carlo sample statistics [%]	±2.22	±1.12	±0.85	±0.79	±0.66	±0.62	±0.64	±0.59	±0.64	±0.78	±0.69	±0.84	±0.81	±0.86	±1.05	±1.03	±1.27	±2.89
ISR/FSR + scale [%]	+2.34 -	+0.25 −0.57	+0.97 -	−0.35	+1.33	+1.91 −0.59	−1.22	−2.09	−0.35 +0.69	+1.36 -	−0.53 +0.62	−0.45	+0.24	+0.12 −0.85	+2.59 −3.63	-	−1.54	+3.74 −1.81
Alternate hard-scattering model [%]	±1.62	∓3.73	±0.39	∓0.54	-	∓1.96	∓1.92	±1.59	∓1.59	-	∓1.12	∓0.55	±0.69	±3.98	±2.69	±0.99	±2.68	±6.59
Alternate parton-shower model [%]	±2.38	±0.36	±1.04	-	±0.28	±0.41	±0.24	-	-	±0.71	±0.36	±0.26	±0.29	∓1.21	∓1.38	±3.02	∓3.07	∓7.71
Inter PDF [%]	±0.24	-	-	∓0.11	-	±0.13	-	∓0.15	-	-	-	∓0.16	-	±0.21	-	-	-	±1.04
Intra PDF [%]	±0.11	-	-	±0.14	-	-	-	-	-	-	-	-	-	-	-	-	±0.10	±0.62
Fakes overall normalization [%]	±1.53	±0.86	±1.29	±1.27	±0.50	±0.24	-	±0.34	±0.56	±0.29	±0.20	±0.53	±0.27	±1.08	±0.72	±1.06	±0.57	±3.23
Real lepton efficiency stat [%]	-	-	-	-	-	-	-	-	-	-	-	-	-	-	-	-	−0.14 +0.15	−0.46 +0.40
Fake lepton efficiency MC scale [%]	+0.37 −0.42	+0.25 −0.20	+0.29 −0.26	+0.19 −0.18	-	+0.29 −0.28	-	-	−0.12 +0.22	−0.19 +0.21	-	-	−0.15	−0.31 -	−0.14 +0.12	−0.10 +0.39	+0.03 -	+0.03 −0.69
Fake lepton efficiency alternate CR [%]	-	±0.12	±0.19	±0.13	-	±0.15	-	∓0.17	∓0.19	-	-	∓0.14	-	-	∓0.11	-	-	-

TABLE A.14: Systematics uncertainties for the normalised differential cross-section at particle-level for $pt^{t,had}_{\mathrm{T}}$ in the 5-jet exclusive configuration.

Bins [GeV]	0–15	15–30	30–45	45–60	60–75	75–90	90–105	105–120	120–135	135–150	150–165	165–180	180–200	200–230	230–265	265–325	325–450	450–1000
$1/\sigma \cdot d\sigma$ / $dpt^{t,had}_{T}$	$7.60 \cdot 10^{-4}$	$2.31 \cdot 10^{-3}$	$3.88 \cdot 10^{-3}$	$4.93 \cdot 10^{-3}$	$5.44 \cdot 10^{-3}$	$5.73 \cdot 10^{-3}$	$5.58 \cdot 10^{-3}$	$5.35 \cdot 10^{-3}$	$4.85 \cdot 10^{-3}$	$4.35 \cdot 10^{-3}$	$3.54 \cdot 10^{-3}$	$2.80 \cdot 10^{-3}$	$2.46 \cdot 10^{-3}$	$2.11 \cdot 10^{-3}$	$1.39 \cdot 10^{-3}$	$8.16 \cdot 10^{-4}$	$3.01 \cdot 10^{-4}$	$1.66 \cdot 10^{-5}$
Total Uncertainty [%]	±9.80 +10.0	±5.93 +6.00	±4.81 +4.97	±4.87 +5.05	±3.86 +3.94	±3.88 +3.87	±3.28 +3.96	±3.03 +3.08	±3.01 +3.66	±3.55 +3.07	±3.12 +3.05	±3.85 +4.06	±5.86 +5.55	±4.56 +5.32	±5.28 +8.25	±6.96 +9.83	±10.4 +8.49	±19.4 +16.8
Statistics [%]	±6.7	±3.4	±2.6	±2.2	±2.1	±2.0	±2.0	±2.0	±2.1	±2.2	±2.4	±2.7	±2.9	±2.8	±3.4	±3.6	±3.9	±9.2
Systematics [%]	±7.91 +7.93	±4.96 +5.02	±3.99 +4.08	±4.05 +4.13	±3.48 +3.57	±3.39 +3.43	±2.89 +3.05	±2.81 +2.93	±2.72 +3.17	±3.10 +2.91	±2.91 +3.01	±2.94 +3.25	±4.98 +4.75	±4.10 +4.12	±4.52 +6.58	±6.23 +8.03	±8.3 +6.73	±16.9 +16.2
b-Tagged jet energy scale (JES) [%]	+0.90 +1.54	−0.47 +0.41	−0.06 +0.46	−0.29 +0.26	− −	−0.40 +0.23	+0.13 +1.51	+0.25 +0.40	+0.27 −0.49	− −	− −	− −	− −0.27	+0.72 −0.16	+0.72 −0.13	+0.72 +0.11	+0.13 −	+1.29 +0.28
Effective detector NP set 1 (JES) [%]	+0.41 −2.89	+1.30 −0.44	+0.66 −1.48	+1.42 −1.79	+1.64 −1.16	+0.51 −1.59	+1.55 −0.40	+1.51 −1.19	+0.40 −1.61	−0.40 +0.49	−0.19 +0.78	+0.58 −	−0.96 +1.44	−2.09 +0.83	−1.08 +1.64	−3.55 +2.67	−5.35 +3.97	−3.58 +1.92
Effective detector NP set 2 (JES) [%]	+0.24 +0.65	+1.48 +0.67	+1.10 +0.73	+0.59 +0.58	+1.31 +0.75	+0.91 +0.43	+0.62 +0.55	−0.39 −	−0.57 −	+0.37 +0.66	+0.35 +0.43	−0.92 +0.62	−0.71 +0.62	−0.34 +0.62	−1.91 +1.19	−1.62 +0.68	−2.53 +1.31	−1.30 +2.10
Effective detector NP set 3 (JES) [%]	−0.76 −0.65	−0.96 −0.62	−0.29 −0.52	−0.69 −0.57	−0.68 −0.24	−0.74 −0.32	−0.46 −0.37	− −	−0.36 +0.27	− +0.21	− −	+0.65 +0.70	+0.20 +0.21	+0.24 +0.16	+1.44 +0.56	+0.64 +0.48	+1.59 +0.7	+2.23 +1.29
Effective detector NP set 4 (JES) [%]	+0.62	+0.62	−0.53	+0.26	+0.45	+0.26	+0.17	−	−0.27	−	−	−0.12	−0.30	−0.59	+0.31	−0.65	−0.17	−0.57
Effective detector NP set 5 (JES) [%]	− −	+0.19 −0.13	+0.16 −0.13	− −	− −	− −	− −	− −	−0.23 −	−0.12 +0.16	− −	− −	−0.30 +0.10	− −0.20	+0.31 −	− −	+0.29 −0.34	+0.49 −
Effective detector NP set 6 resTerm (JES) [%]	− −2.7	− +0.12	−0.21 +0.76	− −	−0.13 −	−0.15 −	− −	+0.21 −	− −	− −	− −	− −	− −2.31	− −	− −	− −	+0.11 −0.51	+0.64 −0.61
η intercalibration model (JES) [%]	+1.04 −0.48	+0.77 −	+0.76 +0.52	− −	+0.56 −0.35	− −0.69	+0.33 −0.40	+0.71 −0.12	+0.63 −0.32	+0.53 −0.10	+0.49 −	− −0.33	− −0.79	−0.12 +0.33	− +0.48	− −0.73	−0.50 +1.77	−0.60 +0.18
η intercalibration total stat (JES) [%]	− −	− +0.35	− −0.50	− −0.30	+0.60 +0.21	−0.23 +0.19	+0.30 −	+0.32 −0.37	+0.25 −0.85	− −	+0.49 −	+0.25 −	−0.84 +0.13	− +0.17	− −	− −0.20	−0.55 +0.74	+0.75 −
Flavour composition (JES) [%]	+2.58 −3.66	+1.05 −0.84	+0.62 −0.81	+0.62 −1.33	+0.21 −0.90	+0.19 −0.96	+0.99 −0.13	−0.37 −1.27	−0.85 −1.48	−0.60 +0.58	−0.23 +0.31	− −	−0.25 +0.05	+0.05 +0.69	−0.20 +1.43	−0.20 +2.58	+0.74 +4.49	−1.97 +3.57
Flavour response (JES) [%]	−1.10 +0.86	+0.63 −	−0.97	−0.25	+0.73	−0.22	−	−0.59 +0.38	−0.72 +0.20	− +0.20	+0.22 −	−0.25 +0.47	+0.48 −0.72	+0.52 −0.15	− +0.40	−0.81	+1.13 −0.57	+0.46 −1.49
Pile-up offset μ (JES) [%]	+0.92 +0.44	− −	+0.18 −2.80	− −	−0.13 +0.22	− −	− −	+0.23 +0.23	−0.32 −	− −	+0.13 +0.12	− −	− −	− −0.14	+0.17 −0.14	− −0.22	+0.15 −0.25	+1.48 +1.85
Pile-up offset N_{PV} (JES) [%]	+0.14 −	− +0.22	− −0.30	− −0.44	+0.22 −	+0.31 −	− −	−0.23 −	− −0.39	− +0.33	+0.26 −	+0.11 −0.12	− −0.39	−0.16 −	− −	−0.21 −	−0.23 −	+0.80 −0.21
Pile-up offset p_T (JES) [%]	−0.16 +0.35	+0.20 +0.19	+0.19 +0.35	− −	−0.10 +0.24	−0.22 −	− −	− −	−0.23 −	− −	+0.39 −	+0.22 +0.22	+0.55 +0.55	− −	− −	+0.17 +0.19	+0.28 −	+0.10 +0.10
Pile-up offset ρ topology (JES) [%]	−1.26 −0.17	+0.55 −	− −0.69	+0.12 −1.06	+1.25 −0.53	− −0.45	+0.24 −	+0.66 −0.19	+0.33 −0.80	− −	+0.35 −	−0.24 −	−0.96 +0.64	−0.32 +0.59	−0.55 +0.31	−0.89 +0.77	−1.31 +1.74	−0.96 +0.91
Punch-through (JES) [%]	−	−	−	−	−	−	−	−	−	−	−	−	−	−	−	−	−	−
Single particle high-p_T (JES) [%]	−	−	−	−	−	−	−	−	−	−	−	−	−	−	−	−	−	−
Jet energy resolution [%]	±2.87	∓0.64	∓0.42	∓0.53	±0.25	∓0.57	±0.44	±0.76	±0.86	±0.31	∓0.19	∓0.64	∓1.98	−	−	±3.47	∓2.56	−	±0.25
Jet vertex fraction [%]	±2.05	+2.01	+1.85	+1.71	+1.38	+1.05	+0.64	+0.28	− −	−0.27	−0.66	−0.82	−1.09	−1.47	−1.87	−2.04	−2.79	−3.12
b-Quark tagging efficiency (eigenvector 0) [%]	−0.60	−2.05	−1.89	−1.73	−1.43	−1.08	−0.67	−0.30	−0.11	+0.26	+0.63	+0.78	+1.11	+1.54	+1.83	+2.11	+2.81	+3.39
b-Quark tagging efficiency (eigenvector 1) [%]	−0.60 ∓0.52	−0.67 ∓0.64	−0.50 ∓0.48	−0.37 ∓0.46	−0.20 ∓0.42	− −	− −	+0.15 −0.14	+0.15 −0.14	±0.15 −	+0.21 −0.19	+0.21 +0.26	+0.15 ∓0.16	±0.17 −0.65	+0.15 −0.92	±0.12 −1.28	±0.14 −1.69	− −2.82
b-Quark tagging efficiency (eigenvector 2) [%]	−0.88 +0.32	−0.85 +0.34	−0.82 +0.39	−0.77 +0.42	−0.65 ±0.39	−0.56 ±0.33	±0.42 ±0.27	−0.29 ±0.21	±0.19 ±0.11	− −	+0.14 −	∓0.29 +0.14	+0.39 ±0.20	+0.64 −0.37	+1.04 ±0.60	+1.26 −0.71	+1.87 −1.61	+2.73 −1.38
b-Quark tagging efficiency (eigenvector 3) [%]	−0.33 −	−0.37 −	−0.37 −	±0.42 −	±0.39 −	±0.33 −	−0.28 −	±0.21 ±0.10	±0.11 ±0.10	− +0.10	− −	±0.14 −	±0.20 −	+0.36 −	− −	−0.72 ±0.14	+1.05 ±0.28	+1.93 ±0.54
b-Quark tagging efficiency (eigenvector 4) [%]	−	−	−	−	−	−	−	−	−	−0.11	−	−	−	−	−	−	−	±0.17
c-Quark tagging efficiency (eigenvector 0) [%]	−	−	−	−0.27	∓0.25	∓0.12	−	∓0.12	−	−	−	−	+0.25	+0.26	+0.23	+0.37	+0.50	±0.20
c-Quark tagging efficiency (eigenvector 1) [%]	±0.24	±0.22	±0.22	−0.20 ±0.21	±0.18	±0.13	−	−	−	−	−	∓0.10	−0.32 −0.13	−0.35 ±0.16	−0.23 −0.23	−0.32 ±0.37	−0.39 ±0.30	±0.49
c-Quark tagging efficiency (eigenvector 2) [%]	−	−	−	−	−	−	−	−	−	−	−	−	+0.14 −	−	+0.21 −	±0.21	±0.25	±0.30
c-Quark tagging efficiency (eigenvector 3) [%]	−	−	−	−	−	−	−	−	−	−	−	−	−	−	−	−	−	−
Light-jet tagging efficiency (eigenvector 0) [%]	−	−	−0.17	−	−0.13	+0.14	+0.31	−	−0.42	−	+0.32	+0.17	−	−	−	−0.13	−	−3.64
Light-jet tagging efficiency (eigenvector 1) [%]	∓0.10	−	+0.12 −	−0.13 −	−	−0.15 −	−0.33 −	−	+0.54 −	−	−0.29 −	−0.19 −	−0.12 −	−	−	±0.17 ±0.17	+0.12 −	+1.83 ∓0.36
Light-jet tagging efficiency (eigenvector 2) [%]	±0.16	±0.11	−	−	−	−	−	−	−	−	−	−	−	−	−	+0.11 −	−	−
Light-jet tagging efficiency (eigenvector 3) [%]	−	−	−	−	−	−	−	−	−	−	−	−	−	−	−	−	±0.18	±0.34
Light-jet tagging efficiency (eigenvector 4) [%]	−	−	−	−	−	−	−	−	−	−	−	−	−	−	−	−	−	±0.12
Light-jet tagging efficiency (eigenvector 5) [%]	−	−	−	−	−	−	−	−	−	−	−	−	−	−	−	−	−	−0.26 +0.25
Light-jet tagging efficiency (eigenvector 6) [%]	−	−	−	−	−	−	−	−	−	−	−	−	−	−	−	−	−	∓0.12
Light-jet tagging efficiency (eigenvector 7) [%]	−	−	−	−	−	−	−	−	−	−	−	−	−	−	−	−	−	−
Light-jet tagging efficiency (eigenvector 8) [%]	−	−	−	−	−	−	−	−	−	−	−	−	−	−	−	−	−	−
Light-jet tagging efficiency (eigenvector 9) [%]	−	−	−	−	−	−	−	−	−	−	−	−	−	−	−	−	−	−
Light-jet tagging efficiency (eigenvector 10) [%]	−	−	−	−	−	−	−	−	−	−	−	−	−	−	−	−	−	−
Muon isolation efficiency stat [%]	−	−	−	−	−	−	−	−	−	−	−	−	−	−	−	−	−	−
Light-jet tagging efficiency (eigenvector 12) [%]	−	−	−	−	−	−	−	−	−	−	−	−	−	−	−	−	−	−
Light-jet tagging efficiency (eigenvector 13) [%]	−	−	−	−	−	−	−	−	−	−	−	−	−	−	−	−	−	−
b-Quark tagging extrapolation [%]	∓0.44	∓0.42	∓0.45	∓0.46	−0.42 +0.43	±0.41	∓0.40	∓0.39	∓0.37	∓0.33	∓0.26	∓0.16	−	±0.15	±0.67	±1.30	+1.40 −2.10	+5.76 −5.73
b-Quark tagging extrapolation from c-Quark [%]	−	−	−	−	−	−	−	−	−	−	−	−	−	−	−	−	−	−
Electron energy resolution [%]	+0.23 −	−	−	−	−	−	−	−	−	−	−	−	−	−	−	−	−	−
Electron energy scale [%]	−	−	−	−	−	−	−	−	−	−	−	−	−	−	−	−	−	−0.12
Electron trigger efficiency [%]	−	−	−	−	−	−	−	−	−	−	−	−	−	−	−	−	−	−
Electron reconstruction efficiency [%]	−	−	−	−	−	−	−	−	−	−	−	−	−	−	−	−	−	−
Electron identification efficiency [%]	−	−	−	−	−	−	−	−	−	−	−	−	−	−	−	±0.12	±0.18	+0.39 −0.40
Electron isolation efficiency [%]	−	−	−	−	−	−	−	−	−	−	−	−	−	−	−	±0.10	±0.16	±0.36
Muon energy scale [%]	−	−	−	−	−	−	−	−	−	−	−	−	−	−	−	−	−	−
Muon (MS) momentum resolution [%]	−	−	−	−	−	−	−	−	−	−	−	−	−	−	−	−	−	−
Muon (ID) momentum resolution [%]	−	−	−	−	−	−	−	−	−	−	−	−	−	−	−	−	−	−
Muon trigger efficiency stat [%]	−	−	−	−	−	−	−	−	−	−	−	−	−	−	−	−	−	−
Muon trigger efficiency syst [%]	−	−	−	−	−	−	−	−	−	−	−	−	−	−	−	−	−	−
Muon identification stat [%]	−	−	−	−	−	−	−	−	−	−	−	−	−	−	−	−	−	−
Muon identification syst [%]	−	−	−	−	−	−	−	−	−	−	−	−	−	−	−	−	−	±0.17
Muon isolation efficiency stat [%]	−	−	−	−	−	−	−	−	−	−	−	−	−	−	−	−	−	−
Muon isolation efficiency syst [%]	−	−	−	−	−	−	−	−	−	−	−	−	−	−	−	−	−	−
Muon TTVA efficiency stat [%]	−	−	−	−	−	−	−	−	−	−	−	−	−	−	−	−	−	−
Muon TTVA efficiency syst [%]	−	−	−	−	−	−	−	−	−	−	−	−	−	−	−	−	−	−
E_T^{miss} Soft jet resolution para [%]	−	−	−	−	−	−	−	−	−	−	−	−	−	−	−	−	−	−
E_T^{miss} Soft jet resolution perp [%]	−	−	−	−	−	−	−	−	−	−	−	−	−	−	−	−	−	−
E_T^{miss} Soft jet scale [%]	−	−	−	−	−	−	−	−	−	−	−	−	−	−	−	−	−	−
Luminosity [%]	−	−	−	−	−	−	−	−	−	−	−	−	−	−	−	−	−	−
W+jets CA_2ex stat error [%]	−	−	−	−	−	−	−	−	−	−	−	−	−	−	−	−	−	−
W+jets CA_3ex stat error [%]	−	−	−	−	−	−	−	−	−	−	−	−	−	−	−	−	−	−
W+jets CA_4incl stat error [%]	−	−	−	−	−	−	−	−	−	−	−	−	−	−	−	−	−	−
W+jets Fc stat error [%]	−	∓0.10	−	−	−	−	−	−	−	−	−	−	−	−	−	−	−	−
W+jets Fcc stat error [%]	−0.26 +0.25	∓0.19	−	∓0.10	−	±0.12	−	±0.13	−	−	−	−	−	−	−	−	−	−0.04 +0.53
W+jets Flight stat error [%]	−	−	−	−	−	−	−	−	−	−	−	−	−	−	−	−	−	−
Single top cross-section [%]	−	−	−	−	∓0.10	−	−	−	−	−	−	−	−	−	±0.18	±0.17	±0.34	±1.16
Z+jets cross-section [%]	∓0.33	−	±0.29	∓0.17	−	±0.21	∓0.15	∓0.30	±0.33	±0.61	−	∓0.35	∓0.47	∓0.10	−	−	∓0.29	±0.98
Diboson cross-section [%]	±0.14	−	−	−	−	∓0.13	±0.11	±0.11	±0.10	±0.11	−	±0.11	−	−	±0.16	±0.12	±0.30	±1.26
$t\bar{t}V$ cross-section [%]	−	−	−	−	−	−	−	−	−	−	−	−	−	−	−	−	±0.10	±0.19
Monte Carlo sample statistics [%]	±2.41	±1.29	±1.03	±0.83	±0.74	±0.75	±0.73	±0.70	±0.94	±0.87	±0.82	±0.88	±0.96	±0.97	±1.16	±1.17	±1.23	±2.56
ISR/FSR + scale [%]	+2.37 −	−1.85	+0.93 −0.93	−0.95	−0.55 +0.99	−0.84 +0.29	−0.99 +0.31	−0.33 +2.11	+0.48 −	+2.14 −0.52	−1.21	−1.86	−2.40 −	+6.77 −	+3.48 −	+2.34 −0.87	+0.39 −1.04	+0.45 −
Alternate hard-scattering model [%]	∓3.30	∓1.40	∓1.25	∓1.84	±2.17	±0.48	±0.14	±0.40	∓3.25	∓1.29	±3.89	±1.71	∓3.46	±1.42	∓5.23	±6.61	±0.37	±10.6
Alternate parton-shower model [%]	∓0.69	∓2.17	−	∓0.67	∓0.33	∓0.64	∓0.11	±0.34	−	−	∓0.12	∓1.06	±1.79	±1.71	±1.40	±1.14	±0.51	∓4.51
Inter PDF [%]	−	∓0.20	−	±0.24	−	∓0.25	−	−	−	∓0.11	−	−	−	−	∓0.12	−	−	±1.38
Intra PDF [%]	−	−	−	±0.25	−	−	−	−	−	−	−	−	−	−	−	−	−	±2.50
Fakes overall normalization [%]	∓0.21	±0.75	∓0.71	±0.12	∓0.37	∓0.14	±0.51	±0.19	∓0.30	∓0.51	−	±0.11	−	∓0.58	±0.44	±0.60	∓0.56	±1.10
Real lepton efficiency stat [%]	−	−	−	−	−	−	−	−	−	−	−	−	−	−	−	−	−0.12 −	−0.80 +0.38
Fake lepton efficiency MC stat [%]	−0.58 +0.85	+0.21 −0.16	±0.12 −0.10	−	−	−0.15 +0.26	−	+0.12 −0.11	−	−0.18 +0.28	−	+0.13 −0.16	+0.17 −0.13	−	−	+0.19 −0.24	−	−1.18
Fake lepton efficiency alternate CR [%]	±0.51	−	±0.11	±0.12	±0.13	−	−	∓0.15	∓0.18	−	−	−	−	±0.14	−	±0.34	±0.35	∓0.31

TABLE A.15: Systematic uncertainties for the normalised differential cross-section at particle-level for $pt^{t,had}_{\mathrm{T}}$ in the 6-jet inclusive configuration.

Bins [GeV]	0–15	15–35	35–75	75–125	125–170	170–800
$1/\sigma \cdot \mathrm{d}\sigma$ / $\mathrm{d}p_T^{tt}$	$1.29 \cdot 10^{-2}$	$2.01 \cdot 10^{-2}$	$7.84 \cdot 10^{-3}$	$1.32 \cdot 10^{-3}$	$3.81 \cdot 10^{-4}$	$1.19 \cdot 10^{-5}$
Total Uncertainty [%]	$^{+14.1}_{-14.3}$	$^{+7.02}_{-7.31}$	± 11.1	$^{+21.0}_{-18.8}$	$^{+17.7}_{-16.9}$	$^{+12.7}_{-13.6}$
Statistics [%]	± 0.6	± 0.3	± 0.6	± 1.9	± 4.0	± 6.0
Systematics [%]	$^{+14.0}_{-14.3}$	$^{+7.01}_{-7.30}$	± 11.1	$^{+20.9}_{-18.7}$	$^{+17.2}_{-16.4}$	$^{+11.0}_{-12.0}$
b-Tagged jet energy scale (JES) [%]	-	-	-	-	-	$^{-0.14}_{+0.12}$
Effective detector NP set 1 (JES) [%]	$^{-3.61}_{+4.21}$	$^{-2.09}_{+2.04}$	$^{+2.58}_{-3.15}$	$^{+7.40}_{-6.15}$	$^{+2.58}_{-2.07}$	$^{+0.60}_{-}$
Effective detector NP set 2 (JES) [%]	$^{+0.87}_{-0.83}$	$^{+0.36}_{-0.37}$	$^{-0.78}_{+0.73}$	$^{-0.93}_{+1.19}$	$^{+0.84}_{-1.41}$	$^{+2.93}_{-2.78}$
Effective detector NP set 3 (JES) [%]	$^{-0.28}_{+0.31}$	-	$^{+0.28}_{-0.30}$	$^{+0.23}_{-0.17}$	$^{-0.83}_{+0.90}$	$^{-1.74}_{+1.39}$
Effective detector NP set 4 (JES) [%]	$^{+0.27}_{-0.29}$	-	$^{-0.24}_{+0.25}$	-	$^{+0.62}_{-0.30}$	$^{-}_{-0.66}$
Effective detector NP set 5 (JES) [%]	$^{-0.27}_{+0.25}$	-	$^{+0.19}_{-0.18}$	-	$^{+0.23}_{-}$	$^{+0.30}_{-0.67}$
Effective detector NP set 6 restTerm (JES) [%]	$^{-0.14}_{-}$	-	-	$^{+0.20}_{-0.14}$	$^{+0.34}_{-}$	$^{+0.14}_{-0.49}$
η intercalibration model (JES) [%]	$^{-3.55}_{+3.94}$	$^{-2.08}_{+1.90}$	$^{+2.42}_{-2.68}$	$^{+7.01}_{-5.93}$	$^{+5.48}_{-5.08}$	$^{+3.22}_{-3.12}$
η intercalibration total stat (JES) [%]	$^{-0.80}_{+0.77}$	$^{-0.48}_{+0.45}$	$^{+0.56}_{-0.52}$	$^{+1.71}_{-1.52}$	$^{+0.63}_{-1.01}$	$^{+0.82}_{-1.40}$
Flavour composition (JES) [%]	$^{-3.69}_{+3.94}$	$^{-2.36}_{+2.21}$	$^{+2.32}_{-2.65}$	$^{+8.91}_{-7.55}$	$^{+6.80}_{-5.60}$	$^{+4.08}_{-3.31}$
Flavour response (JES) [%]	$^{+1.22}_{-1.32}$	$^{+0.68}_{-0.80}$	$^{-0.73}_{+0.87}$	$^{-2.51}_{+2.80}$	$^{-2.27}_{+2.36}$	$^{-2.09}_{+1.64}$
Pile-up offset μ (JES) [%]	± 0.51	$^{+0.22}_{-0.23}$	$^{-0.36}_{+0.34}$	$^{-0.70}_{+0.86}$	-	$^{-}_{-0.67}$
Pile-up offset N_{PV} (JES) [%]	-	-	-	-	-	-
Pile-up offset p_T (JES) [%]	$^{+0.27}_{-0.24}$	-	∓ 0.28	$^{+0.20}_{-0.20}$	$^{+0.56}_{-0.50}$	$^{-0.44}_{+0.97}$
Pile-up offset ρ topology (JES) [%]	$^{-1.45}_{+1.32}$	$^{-0.77}_{+0.62}$	$^{+1.04}_{-0.88}$	$^{+2.65}_{-2.09}$	$^{+0.94}_{-1.51}$	$^{-1.43}_{-}$
Punch-through (JES) [%]	-	-	-	-	-	-
Single particle high-p_T (JES) [%]	-	-	-	-	-	-
Jet energy resolution [%]	∓ 1.35	∓ 1.00	± 0.93	± 3.49	± 2.57	± 2.34
Jet vertex fraction [%]	$^{+1.08}_{-1.09}$	$^{+0.69}_{-0.70}$	∓ 0.76	$^{-2.38}_{+2.48}$	$^{-1.34}_{+1.36}$	$^{-1.02}_{+1.04}$
b-Quark tagging efficiency (eigenvector 0) [%]	-	-	-	-	-	± 0.19
b-Quark tagging efficiency (eigenvector 1) [%]	-	-	-	$^{-0.14}_{+0.13}$	$^{-0.35}_{+0.34}$	$^{-0.70}_{+0.68}$
b-Quark tagging efficiency (eigenvector 2) [%]	-	-	-	-	∓ 0.24	∓ 0.46
b-Quark tagging efficiency (eigenvector 3) [%]	-	-	-	-	-	-
b-Quark tagging efficiency (eigenvector 4) [%]	-	-	-	-	-	-
c-Quark tagging efficiency (eigenvector 0) [%]	-	-	-	$^{-0.26}_{+0.25}$	$^{-0.34}_{+0.33}$	-
c-Quark tagging efficiency (eigenvector 1) [%]	-	-	-	-	-	∓ 0.12
c-Quark tagging efficiency (eigenvector 2) [%]	-	-	-	-	-	-
c-Quark tagging efficiency (eigenvector 3) [%]	-	-	-	-	-	-
Light-jet tagging efficiency (eigenvector 0) [%]	$^{+0.42}_{-0.46}$	$^{+0.20}_{-0.21}$	$^{-0.30}_{+0.35}$	$^{-0.58}_{+0.56}$	$^{-0.40}_{+0.23}$	$^{-0.26}_{+0.31}$
Light-jet tagging efficiency (eigenvector 1) [%]	-	-	-	-	-	-
Light-jet tagging efficiency (eigenvector 2) [%]	-	-	-	-	-	-
Light-jet tagging efficiency (eigenvector 3) [%]	-	-	-	-	-	-
Light-jet tagging efficiency (eigenvector 4) [%]	-	-	-	-	-	-
Light-jet tagging efficiency (eigenvector 5) [%]	-	-	-	-	-	-
Light-jet tagging efficiency (eigenvector 6) [%]	-	-	-	-	-	-
Light-jet tagging efficiency (eigenvector 7) [%]	-	-	-	-	-	-
Light-jet tagging efficiency (eigenvector 8) [%]	-	-	-	-	-	-
Light-jet tagging efficiency (eigenvector 9) [%]	-	-	-	-	-	-
Light-jet tagging efficiency (eigenvector 10) [%]	-	-	-	-	-	-
Light-jet tagging efficiency (eigenvector 11) [%]	-	-	-	-	-	-
Light-jet tagging efficiency (eigenvector 12) [%]	-	-	-	-	-	-
Light-jet tagging efficiency (eigenvector 13) [%]	-	-	-	-	-	-
b-Quark tagging extrapolation [%]	-	-	-	-	± 0.21	± 0.54
b-Quark tagging extrapolation from c-Quark [%]	-	-	-	-	-	-
Electron energy resolution [%]	-	-	-	-	-	-
Electron energy scale [%]	-	-	-	-	-	∓ 0.10
Electron trigger efficiency [%]	-	-	-	-	-	-
Electron reconstruction efficiency [%]	-	-	-	-	-	-
Electron identification efficiency [%]	-	-	-	-	-	± 0.12
Electron isolation efficiency [%]	-	-	-	-	-	-
Muon energy scale [%]	-	-	-	-	-	-
Muon (MS) momentum resolution [%]	-	-	-	-	-	-
Muon (ID) momentum resolution [%]	-	-	-	-	-	-
Muon trigger efficiency stat [%]	-	-	-	-	-	-
Muon trigger efficiency syst [%]	-	-	-	-	-	-
Muon identification stat [%]	-	-	-	-	-	-
Muon identification syst [%]	-	-	-	-	-	-
Muon isolation efficiency stat [%]	-	-	-	-	-	-
Muon isolation efficiency syst [%]	-	-	-	-	-	-
Muon TTVA efficiency stat [%]	-	-	-	-	-	-
Muon TTVA efficiency syst [%]	-	-	-	-	-	-
E_T^{miss} Soft jet resolution para [%]	∓ 1.34	∓ 0.27	± 0.95	± 0.33	∓ 0.23	-
E_T^{miss} Soft jet resolution perp [%]	∓ 1.54	∓ 0.33	± 1.14	± 0.39	∓ 0.71	-
E_T^{miss} Soft jet scale [%]	$^{-0.92}_{+0.91}$	$^{-0.15}_{-}$	$^{+0.64}_{-0.59}$	-	$^{-0.50}_{+0.67}$	$^{+0.11}_{-}$
Luminosity [%]	-	-	-	-	-	-
W+jets CA_2ex stat error [%]	-	-	-	-	-	-
W+jets CA_3ex stat error [%]	-	-	-	-	-	-
W+jets CA_4incl stat error [%]	-	-	-	-	-	-
W+jets Fc stat error [%]	-	-	-	-	-	-
W+jets Fcc stat error [%]	∓ 0.15	-	$^{+0.15}_{-0.14}$	$^{+0.14}_{-0.13}$	$^{-0.60}_{+0.59}$	-
W+jets Flight stat error [%]	-	-	-	-	-	-
Single top cross-section [%]	-	-	-	± 0.16	± 0.44	± 0.34
Z+jets cross-section [%]	-	-	-	-	∓ 0.17	-
Diboson cross-section [%]	-	-	-	-	± 0.10	-
ttV cross-section [%]	-	-	-	-	-	-
Monte Carlo sample statistics [%]	± 0.29	± 0.15	± 0.25	± 0.74	± 1.45	± 1.89
ISR/FSR + scale [%]	$^{+0.28}_{-3.13}$	$^{+0.39}_{-1.17}$	$^{+1.80}_{-}$	$^{-1.56}_{+4.74}$	$^{-4.09}_{+5.00}$	$^{-}_{-5.07}$
Alternate hard-scattering model [%]	∓ 2.76	∓ 0.55	± 0.27	± 4.98	± 12.2	± 8.19
Alternate parton-shower model [%]	∓ 10.6	∓ 5.47	± 9.23	± 11.6	± 2.33	± 1.45
Inter PDF [%]	-	-	-	-	∓ 0.12	∓ 0.20
Intra PDF [%]	-	-	-	± 0.13	± 0.19	± 0.76
Fakes overall normalization [%]	∓ 3.38	∓ 1.50	± 2.44	± 4.35	± 3.03	∓ 0.25
Real lepton efficiency stat [%]	-	-	-	-	-	-
Fake lepton efficiency MC scale [%]	$^{-1.31}_{+1.68}$	$^{-0.54}_{+0.72}$	$^{+0.97}_{-1.19}$	$^{+1.34}_{-2.14}$	$^{+1.10}_{-1.29}$	-
Fake lepton efficiency alternate CR [%]	∓ 0.43	∓ 0.16	± 0.34	± 0.30	± 0.16	-

TABLE A.16: Systematic uncertainties for the normalised differential cross-section at particle-level for $p_{\mathrm{T}}^{t\bar{t}}$ in the 4-jet exclusive configuration.

Bins [GeV]	0–35	35–75	75–125	125–170	170–225	225–800
$1/\sigma \cdot \mathrm{d}\sigma$ / $\mathrm{d}p_T^{t\bar{t}}$	$4.40 \cdot 10^{-3}$	$9.34 \cdot 10^{-3}$	$5.14 \cdot 10^{-3}$	$2.23 \cdot 10^{-3}$	$1.06 \cdot 10^{-3}$	$9.88 \cdot 10^{-5}$
Total Uncertainty [%]	$^{+6.59}_{-6.74}$	$^{+2.93}_{-3.01}$	$^{+3.79}_{-3.99}$	$^{+6.30}_{-5.87}$	$^{+7.74}_{-6.46}$	$^{+9.29}_{-10.6}$
Statistics [%]	± 1.3	± 0.7	± 1.1	± 1.9	± 2.8	± 2.6
Systematics [%]	$^{+6.43}_{-6.58}$	$^{+2.82}_{-2.91}$	$^{+3.59}_{-3.80}$	$^{+5.96}_{-5.50}$	$^{+7.14}_{-5.73}$	$^{+8.87}_{-10.2}$
b-Tagged jet energy scale (JES) [%]	-	-	-	-	-	$^{-0.23}_{+0.33}$
Effective detector NP set 1 (JES) [%]	$^{+2.26}_{-2.48}$	$^{+0.92}_{-0.99}$	$^{-0.12}_{+0.37}$	$^{-1.70}_{+1.96}$	$^{-2.67}_{+3.76}$	$^{-6.24}_{+4.63}$
Effective detector NP set 2 (JES) [%]	$^{-1.14}_{+1.38}$	$^{-0.89}_{+0.91}$	$^{+0.37}_{-0.63}$	$^{+1.48}_{-1.34}$	$^{+1.93}_{-1.53}$	$^{+2.93}_{-3.12}$
Effective detector NP set 3 (JES) [%]	$^{+0.61}_{-0.46}$	$^{+0.48}_{-0.51}$	$^{-0.33}_{+0.17}$	$^{-0.63}_{+0.98}$	$^{-0.77}_{+0.86}$	$^{-1.46}_{+1.34}$
Effective detector NP set 4 (JES) [%]	$^{-0.47}_{+0.59}$	$^{-0.20}_{+0.21}$	$^{+0.29}_{-0.39}$	$^{+0.52}_{-0.42}$	$^{+0.38}_{-0.43}$	-
Effective detector NP set 5 (JES) [%]	$^{+0.31}_{-0.27}$	-	$^{-0.23}_{+0.20}$	-	$^{+0.15}_{-}$	$^{+0.35}_{-0.31}$
Effective detector NP set 6 restTerm (JES) [%]	∓ 0.12	-	-	-	-	$^{+0.16}_{-0.19}$
η intercalibration model (JES) [%]	$^{-0.17}_{+0.21}$	-	$^{+0.42}_{-0.36}$	-	$^{-0.26}_{+0.41}$	$^{-1.48}_{+0.86}$
η intercalibration total stat (JES) [%]	$^{+0.21}_{-}$	$^{+0.18}_{-0.28}$	-	$^{-0.13}_{+0.53}$	$^{-}_{+0.48}$	$^{-0.82}_{+0.60}$
Flavour composition (JES) [%]	$^{+0.60}_{-1.27}$	$^{+0.37}_{-0.60}$	$^{+0.55}_{-}$	$^{-}_{+0.50}$	$^{-1.60}_{+2.54}$	$^{-5.06}_{+4.66}$
Flavour response (JES) [%]	$^{+0.25}_{-}$	$^{-0.17}_{+0.23}$	-	$^{+0.24}_{-0.12}$	$^{+0.30}_{-0.32}$	$^{+0.71}_{-1.51}$
Pile-up offset μ (JES) [%]	-	-	-	$^{+0.27}_{-}$	$^{+0.16}_{-0.19}$	$^{+0.36}_{-0.34}$
Pile-up offset N_{PV} (JES) [%]	$^{+0.24}_{-}$	-	-	$^{+0.24}_{-}$	$^{+0.24}_{-0.23}$	$^{+0.44}_{-0.34}$
Pile-up offset p_T (JES) [%]	-	-	-	$^{+0.18}_{-0.16}$	$^{+0.10}_{-0.12}$	$^{+0.26}_{-0.17}$
Pile-up offset ρ topology (JES) [%]	$^{+1.07}_{-0.85}$	$^{+0.59}_{-0.45}$	$^{-0.40}_{+0.31}$	$^{-0.45}_{+0.84}$	$^{-1.42}_{+0.69}$	$^{-2.86}_{+1.73}$
Punch-through (JES) [%]	-	-	-	-	-	-
Single particle high-p_T (JES) [%]	-	-	-	-	-	-
Jet energy resolution [%]	∓ 0.53	∓ 0.32	± 0.33	± 1.36	± 0.78	∓ 1.08
Jet vertex fraction [%]	$^{+1.90}_{-1.95}$	$^{+1.12}_{-1.16}$	$^{-0.99}_{+1.00}$	$^{-1.86}_{+1.89}$	$^{-1.91}_{+1.96}$	$^{-2.96}_{+3.23}$
b-Quark tagging efficiency (eigenvector 0) [%]	$^{-0.22}_{+0.21}$	-	-	$^{+0.16}_{-0.15}$	± 0.16	$^{+0.10}_{-0.11}$
b-Quark tagging efficiency (eigenvector 1) [%]	-	-	-	± 0.14	± 0.13	$^{-0.79}_{+0.77}$
b-Quark tagging efficiency (eigenvector 2) [%]	± 0.17	-	-	-	-	$^{-0.45}_{+0.46}$
b-Quark tagging efficiency (eigenvector 3) [%]	-	-	-	-	-	-
b-Quark tagging efficiency (eigenvector 4) [%]	-	-	-	-	-	-
c-Quark tagging efficiency (eigenvector 0) [%]	-	-	-	∓ 0.20	-	∓ 0.14
c-Quark tagging efficiency (eigenvector 1) [%]	-	-	-	-	-	-
c-Quark tagging efficiency (eigenvector 2) [%]	-	-	-	-	-	-
c-Quark tagging efficiency (eigenvector 3) [%]	-	-	-	-	-	-
Light-jet tagging efficiency (eigenvector 0) [%]	-	$^{+0.15}_{-0.19}$	$^{-0.15}_{+0.21}$	∓ 0.13	-	-
Light-jet tagging efficiency (eigenvector 1) [%]	-	-	-	-	-	± 0.14
Light-jet tagging efficiency (eigenvector 2) [%]	-	-	-	-	-	-
Light-jet tagging efficiency (eigenvector 3) [%]	-	-	-	-	-	-
Light-jet tagging efficiency (eigenvector 4) [%]	-	-	-	-	-	-
Light-jet tagging efficiency (eigenvector 5) [%]	-	-	-	-	-	-
Light-jet tagging efficiency (eigenvector 6) [%]	-	-	-	-	-	-
Light-jet tagging efficiency (eigenvector 7) [%]	-	-	-	-	-	-
Light-jet tagging efficiency (eigenvector 8) [%]	-	-	-	-	-	-
Light-jet tagging efficiency (eigenvector 9) [%]	-	-	-	-	-	-
Light-jet tagging efficiency (eigenvector 10) [%]	-	-	-	-	-	-
Light-jet tagging efficiency (eigenvector 11) [%]	-	-	-	-	-	-
Light-jet tagging efficiency (eigenvector 12) [%]	-	-	-	-	-	-
Light-jet tagging efficiency (eigenvector 13) [%]	-	-	-	-	-	-
b-Quark tagging extrapolation [%]	∓ 0.10	-	-	$^{+0.12}_{-0.13}$	-	$^{+0.42}_{-0.43}$
b-Quark tagging extrapolation from c-Quark [%]	-	-	-	-	-	-
Electron energy resolution [%]	-	-	-	-	-	-
Electron energy scale [%]	-	-	-	-	-	-
Electron trigger efficiency [%]	-	-	-	-	-	-
Electron reconstruction efficiency [%]	-	-	-	-	-	-
Electron identification efficiency [%]	-	-	-	-	-	± 0.16
Electron isolation efficiency [%]	-	-	-	-	-	± 0.13
Muon energy scale [%]	-	-	-	-	-	-
Muon (MS) momentum resolution [%]	-	-	-	-	-	-
Muon (ID) momentum resolution [%]	-	-	-	-	-	-
Muon trigger efficiency stat [%]	-	-	-	-	-	-
Muon trigger efficiency syst [%]	-	-	-	-	-	-
Muon identification stat [%]	-	-	-	-	-	-
Muon identification syst [%]	-	-	-	-	-	-
Muon isolation efficiency stat [%]	-	-	-	-	-	-
Muon isolation efficiency syst [%]	-	-	-	-	-	-
Muon TTVA efficiency stat [%]	-	-	-	-	-	-
Muon TTVA efficiency syst [%]	-	-	-	-	-	-
E_T^{miss} Soft jet resolution para [%]	∓ 0.13	-	± 0.14	-	± 0.14	-
E_T^{miss} Soft jet resolution perp [%]	∓ 0.14	-	± 0.11	± 0.13	∓ 0.12	∓ 0.16
E_T^{miss} Soft jet scale [%]	-	-	-	-	-	-
Luminosity [%]	-	-	-	-	-	-
W+jets CA_2ex stat error [%]	-	-	-	-	-	-
W+jets CA_3ex stat error [%]	-	-	-	-	-	-
W+jets CA_4incl stat error [%]	-	-	-	-	-	∓ 0.10
W+jets Fc stat error [%]	-	-	-	-	-	-
W+jets Fcc stat error [%]	$^{+0.12}_{-0.11}$	$^{+0.26}_{-0.25}$	± 0.14	$^{-0.39}_{+0.38}$	$^{-0.92}_{+0.90}$	$^{-1.18}_{+1.16}$
W+jets Flight stat error [%]	-	-	-	-	-	-
Single top cross-section [%]	-	-	-	-	± 0.17	± 0.27
Z+jets cross-section [%]	∓ 0.15	∓ 0.14	± 0.17	± 0.23	-	± 0.20
Diboson cross-section [%]	-	-	-	-	± 0.13	± 0.57
$t\bar{t}V$ cross-section [%]	-	-	-	-	-	-
Monte Carlo sample statistics [%]	± 0.48	± 0.26	± 0.42	± 0.71	± 1.00	± 0.90
ISR/FSR + scale [%]	$^{+1.20}_{-1.63}$	$^{+1.21}_{-1.25}$	$^{-1.84}_{+1.28}$	$^{-0.83}_{+1.44}$	$^{-0.79}_{+2.80}$	$^{-0.61}_{+1.63}$
Alternate hard-scattering model [%]	∓ 5.04	∓ 1.41	± 2.88	± 4.22	± 2.18	± 0.33
Alternate parton-shower model [%]	± 0.22	∓ 0.15	∓ 0.28	∓ 0.24	± 1.99	± 0.25
Inter PDF [%]	-	-	-	-	-	± 0.21
Intra PDF [%]	-	-	-	-	-	± 0.28
Fakes overall normalization [%]	-	∓ 0.61	± 0.13	± 0.43	± 1.53	± 1.33
Real lepton efficiency stat [%]	-	-	-	-	-	$^{-0.18}_{+0.12}$
Fake lepton efficiency MC scale [%]	-	$^{-0.10}_{+0.12}$	$^{+0.10}_{-0.11}$	-	$^{+0.20}_{-0.29}$	-
Fake lepton efficiency alternate CR [%]	-	-	-	-	∓ 0.17	∓ 0.19

TABLE A.17: Systematic uncertainties for the normalised differential cross-section at particle-level for $p_{\mathrm{T}}^{t\bar{t}}$ in the 5-jet exclusive configuration.

Bins [GeV]	0–35	35–75	75–125	125–170	170–225	225–800
$1/\sigma \cdot \mathrm{d}\sigma \,/\, \mathrm{d}p_T^{t\bar{t}}$	$2.12 \cdot 10^{-3}$	$5.21 \cdot 10^{-3}$	$5.46 \cdot 10^{-3}$	$3.79 \cdot 10^{-3}$	$2.24 \cdot 10^{-3}$	$2.63 \cdot 10^{-4}$
Total Uncertainty [%]	$^{+6.39}_{-5.03}$	$^{+3.95}_{-4.19}$	$^{+2.44}_{-2.53}$	$^{+3.43}_{-3.21}$	$^{+3.98}_{-4.56}$	$^{+6.87}_{-6.61}$
Statistics [%]	± 2.3	± 1.2	± 1.1	± 1.6	± 2.1	± 1.7
Systematics [%]	$^{+5.88}_{-4.36}$	$^{+3.73}_{-3.98}$	$^{+2.09}_{-2.19}$	$^{+2.97}_{-2.72}$	$^{+3.30}_{-3.99}$	$^{+6.63}_{-6.35}$
b-Tagged jet energy scale (JES) [%]	-	-	-	-	-	$^{-0.23}_{+0.31}$
Effective detector NP set 1 (JES) [%]	$^{+3.40}_{-0.89}$	$^{+1.97}_{-2.17}$	$^{+0.92}_{-1.07}$	$^{+0.33}_{-}$	$^{-1.95}_{+0.65}$	∓ 3.78
Effective detector NP set 2 (JES) [%]	$^{-1.48}_{+1.65}$	$^{-1.45}_{+1.42}$	$^{-0.46}_{+0.55}$	$^{+0.16}_{-0.25}$	$^{+0.38}_{-0.90}$	$^{+2.56}_{-2.28}$
Effective detector NP set 3 (JES) [%]	$^{+1.01}_{-0.99}$	$^{+0.75}_{-0.65}$	$^{+0.33}_{-0.19}$	$^{-0.41}_{-}$	$^{-0.49}_{+0.27}$	$^{-1.04}_{+1.21}$
Effective detector NP set 4 (JES) [%]	$^{-0.66}_{+0.56}$	$^{-0.35}_{+0.44}$	-	$^{+0.15}_{-0.33}$	$^{+0.40}_{-0.30}$	$^{+0.13}_{-0.19}$
Effective detector NP set 5 (JES) [%]	$^{-}_{-0.12}$	-	$^{-0.11}_{+0.16}$	$^{-0.19}_{-}$	$^{-}_{-0.21}$	$^{+0.22}_{-}$
Effective detector NP set 6 restTerm (JES) [%]	-	-	-	-	$^{-}_{-0.13}$	$^{+0.14}_{-0.11}$
η intercalibration model (JES) [%]	$^{+0.42}_{-}$	$^{+0.11}_{-0.18}$	$^{+0.24}_{-0.23}$	-	$^{-}_{-0.39}$	$^{-0.60}_{+0.69}$
η intercalibration total stat (JES) [%]	$^{+0.56}_{-}$	$^{+0.20}_{-0.32}$	-	-	$^{-}_{-0.33}$	$^{-0.30}_{+0.47}$
Flavour composition (JES) [%]	$^{+2.06}_{-}$	$^{+0.69}_{-1.14}$	$^{+0.72}_{-0.96}$	$^{+0.52}_{-0.26}$	$^{-0.61}_{+0.16}$	$^{-2.81}_{+3.01}$
Flavour response (JES) [%]	$^{+0.70}_{-}$	$^{-}_{-0.21}$	-	$^{-0.15}_{+0.28}$	$^{-}_{-0.59}$	$^{+0.69}_{-0.40}$
Pile-up offset μ (JES) [%]	$^{-0.18}_{+0.28}$	-	-	-	-	$^{+0.33}_{-0.24}$
Pile-up offset N_{PV} (JES) [%]	-	$^{-0.18}_{+0.14}$	-	$^{-}_{-0.22}$	$^{-}_{+0.13}$	$^{+0.22}_{-0.13}$
Pile-up offset p_T (JES) [%]	-	$^{-}_{-0.18}$	-	-	$^{-}_{-0.21}$	-
Pile-up offset ρ topology (JES) [%]	$^{+1.45}_{-0.84}$	$^{+0.83}_{-0.84}$	$^{-}_{-0.19}$	$^{+0.26}_{-}$	$^{-}_{-0.49}$	$^{-1.40}_{+1.48}$
Punch-through (JES) [%]	-	-	-	-	-	-
Single particle high-p_T (JES) [%]	-	-	-	-	-	-
Jet energy resolution [%]	± 0.54	∓ 0.44	± 0.38	± 0.42	± 0.58	∓ 1.11
Jet vertex fraction [%]	$^{+1.67}_{-1.72}$	$^{+1.41}_{-1.45}$	$^{+0.56}_{-0.58}$	$^{-0.47}_{+0.45}$	$^{-1.12}_{+1.17}$	$^{-1.95}_{+2.02}$
b-Quark tagging efficiency (eigenvector 0) [%]	-	$^{-0.13}_{+0.12}$	-	-	± 0.10	$^{+0.17}_{-0.16}$
b-Quark tagging efficiency (eigenvector 1) [%]	$^{+0.19}_{-0.18}$	$^{+0.18}_{-0.17}$	$^{+0.14}_{-0.13}$	-	-	$^{-0.67}_{+0.64}$
b-Quark tagging efficiency (eigenvector 2) [%]	± 0.19	± 0.16	-	-	-	∓ 0.40
b-Quark tagging efficiency (eigenvector 3) [%]	-	-	-	-	-	-
b-Quark tagging efficiency (eigenvector 4) [%]	-	-	-	-	-	-
c-Quark tagging efficiency (eigenvector 0) [%]	∓ 0.16	∓ 0.15	-	± 0.10	-	± 0.18
c-Quark tagging efficiency (eigenvector 1) [%]	-	-	-	-	-	-
c-Quark tagging efficiency (eigenvector 2) [%]	-	-	-	-	-	-
c-Quark tagging efficiency (eigenvector 3) [%]	-	-	-	-	-	-
Light-jet tagging efficiency (eigenvector 0) [%]	-	$^{-0.27}_{+0.32}$	-	± 0.10	$^{+0.22}_{-0.23}$	$^{+0.19}_{-0.20}$
Light-jet tagging efficiency (eigenvector 1) [%]	-	-	-	-	-	-
Light-jet tagging efficiency (eigenvector 2) [%]	-	-	-	-	-	-
Light-jet tagging efficiency (eigenvector 3) [%]	-	-	-	-	-	-
Light-jet tagging efficiency (eigenvector 4) [%]	-	-	-	-	-	-
Light-jet tagging efficiency (eigenvector 5) [%]	-	-	-	-	-	-
Light-jet tagging efficiency (eigenvector 6) [%]	-	-	-	-	-	-
Light-jet tagging efficiency (eigenvector 7) [%]	-	-	-	-	-	-
Light-jet tagging efficiency (eigenvector 8) [%]	-	-	-	-	-	-
Light-jet tagging efficiency (eigenvector 9) [%]	-	-	-	-	-	-
Light-jet tagging efficiency (eigenvector 10) [%]	-	-	-	-	-	-
Light-jet tagging efficiency (eigenvector 11) [%]	-	-	-	-	-	-
Light-jet tagging efficiency (eigenvector 12) [%]	-	-	-	-	-	-
Light-jet tagging efficiency (eigenvector 13) [%]	-	-	-	-	-	-
b-Quark tagging extrapolation [%]	∓ 0.20	∓ 0.17	∓ 0.11	-	-	$^{+0.55}_{-0.57}$
b-Quark tagging extrapolation from c-Quark [%]	-	-	-	-	-	-
Electron energy resolution [%]	-	-	-	-	-	-
Electron energy scale [%]	-	-	-	-	-	-
Electron trigger efficiency [%]	-	-	-	-	-	-
Electron reconstruction efficiency [%]	-	-	-	-	-	-
Electron identification efficiency [%]	-	-	-	-	-	$^{+0.13}_{-0.14}$
Electron isolation efficiency [%]	-	-	-	-	-	± 0.12
Muon energy scale [%]	-	-	-	-	-	-
Muon (MS) momentum resolution [%]	-	-	-	-	-	-
Muon (ID) momentum resolution [%]	-	-	-	-	-	-
Muon trigger efficiency stat [%]	-	-	-	-	-	-
Muon trigger efficiency syst [%]	-	-	-	-	-	-
Muon identification stat [%]	-	-	-	-	-	-
Muon identification syst [%]	-	-	-	-	-	-
Muon isolation efficiency stat [%]	-	-	-	-	-	-
Muon isolation efficiency syst [%]	-	-	-	-	-	-
Muon TTVA efficiency stat [%]	-	-	-	-	-	-
Muon TTVA efficiency syst [%]	-	-	-	-	-	-
E_T^{miss} Soft jet resolution para [%]	-	-	± 0.17	∓ 0.28	-	± 0.11
E_T^{miss} Soft jet resolution perp [%]	± 0.29	∓ 0.13	-	-	-	-
E_T^{miss} Soft jet scale [%]	$^{+0.36}_{-}$	-	-	-	$^{-}_{-0.23}$	-
Luminosity [%]	-	-	-	-	-	-
W+jets CA_2ex stat error [%]	-	-	-	-	-	-
W+jets CA_3ex stat error [%]	-	-	-	-	-	-
W+jets CA_4incl stat error [%]	-	-	-	-	-	-
W+jets Fc stat error [%]	-	-	-	-	-	-
W+jets Fcc stat error [%]	$^{+0.27}_{-0.26}$	± 0.10	-	-	-	∓ 0.41
W+jets Flight stat error [%]	-	-	-	-	-	-
Single top cross-section [%]	-	-	-	-	-	-
Z+jets cross-section [%]	∓ 0.48	∓ 0.26	± 0.13	-	-	± 0.21
Diboson cross-section [%]	∓ 0.16	∓ 0.19	∓ 0.13	-	-	± 0.48
$t\bar{t}V$ cross-section [%]	-	-	-	-	-	-
Monte Carlo sample statistics [%]	± 0.82	± 0.46	± 0.42	± 0.58	± 0.71	± 0.54
ISR/FSR + scale [%]	$^{-}_{-1.51}$	$^{+0.12}_{-0.21}$	$^{+0.36}_{-}$	$^{-0.20}_{+0.64}$	$^{-0.46}_{+0.20}$	$^{+0.38}_{-0.29}$
Alternate hard-scattering model [%]	∓ 2.48	∓ 1.18	∓ 0.83	± 2.32	± 1.56	± 0.33
Alternate parton-shower model [%]	∓ 0.93	∓ 1.31	∓ 0.96	± 0.68	± 2.12	± 1.26
Inter PDF [%]	∓ 0.14	-	-	-	-	-
Intra PDF [%]	-	-	-	-	-	-
Fakes overall normalization [%]	± 0.49	± 0.29	± 0.22	∓ 0.41	∓ 0.70	-
Real lepton efficiency stat [%]	-	-	-	-	-	$^{-0.15}_{-}$
Fake lepton efficiency MC scale [%]	$^{+0.37}_{-0.47}$	$^{+0.15}_{-0.25}$	$^{+0.13}_{-}$	∓ 0.21	∓ 0.20	$^{-0.18}_{+0.28}$
Fake lepton efficiency alternate CR [%]	± 0.24	-	-	-	∓ 0.17	-

TABLE A.18: Systematic uncertainties for the normalised differential cross-section at particle-level for $p_{\mathrm{T}}^{t\bar{t}}$ in the 6-jet inclusive configuration.

Bins [GeV]	0–40	40–80	80–120	120–170	170–230	230–600
$1/\sigma \cdot \mathrm{d}\sigma$ / $\mathrm{d}\lvert p_{out}^{tt} \rvert$	$2.13 \cdot 10^{-2}$	$3.06 \cdot 10^{-3}$	$4.46 \cdot 10^{-4}$	$1.01 \cdot 10^{-4}$	$1.92 \cdot 10^{-5}$	$4.60 \cdot 10^{-7}$
Total Uncertainty [%]	$^{+2.44}_{-2.65}$	$^{+14.0}_{-12.6}$	$^{+20.3}_{-19.7}$	$^{+25.1}_{-26.0}$	$^{+29.0}_{-27.5}$	$^{+69.7}_{-75.7}$
Statistics [%]	± 0.2	± 1.3	± 3.9	± 7.1	$\pm 15.$	$\pm 43.$
Systematics [%]	$^{+2.43}_{-2.64}$	$^{+13.9}_{-12.5}$	$^{+19.9}_{-19.2}$	$^{+23.9}_{-24.8}$	$^{+23.6}_{-21.7}$	$^{+54.2}_{-61.6}$
b-Tagged jet energy scale (JES) [%]	-	-	$^{+0.18}_{-0.23}$	$^{-}_{-1.21}$	$^{+0.73}_{-}$	$^{-}_{-2.20}$
Effective detector NP set 1 (JES) [%]	$^{-0.72}_{+0.66}$	$^{+3.97}_{-3.57}$	$^{+5.03}_{-5.22}$	$^{+1.78}_{-0.63}$	$^{+1.34}_{-1.07}$	$^{-1.51}_{+2.95}$
Effective detector NP set 2 (JES) [%]	-	$^{-0.32}_{+0.30}$	$^{-}_{-0.43}$	$^{+2.58}_{-3.18}$	$^{+3.01}_{-3.34}$	$^{+2.07}_{-6.09}$
Effective detector NP set 3 (JES) [%]	-	-	$^{-0.43}_{+0.30}$	$^{-1.93}_{+1.40}$	$^{-1.75}_{+1.58}$	$^{-5.08}_{+1.52}$
Effective detector NP set 4 (JES) [%]	-	-	$^{+0.37}_{-0.36}$	$^{+0.29}_{-0.71}$	$^{+1.43}_{-1.25}$	$^{-}_{-2.27}$
Effective detector NP set 5 (JES) [%]	-	-	-	$^{-}_{-0.60}$	$^{+0.58}_{-0.23}$	$^{+0.66}_{-1.96}$
Effective detector NP set 6 restTerm (JES) [%]	-	-	$^{+0.18}_{-0.26}$	$^{+0.37}_{-0.82}$	$^{+0.21}_{-0.45}$	$^{+0.58}_{-1.96}$
η intercalibration model (JES) [%]	$^{-0.76}_{+0.67}$	$^{+4.01}_{-3.23}$	$^{+5.91}_{-7.23}$	$^{+3.63}_{-4.02}$	$^{+3.75}_{-3.32}$	$^{+5.57}_{-6.01}$
η intercalibration total stat (JES) [%]	$^{-0.13}_{+0.14}$	$^{+0.74}_{-0.63}$	$^{+1.00}_{-1.76}$	$^{-}_{-1.79}$	$^{+0.84}_{-1.23}$	$^{+1.10}_{-3.10}$
Flavour composition (JES) [%]	$^{-0.89}_{+0.82}$	$^{+4.56}_{-4.15}$	$^{+7.71}_{-7.44}$	$^{+5.39}_{-4.72}$	$^{+4.02}_{-5.76}$	$^{+3.15}_{-0.88}$
Flavour response (JES) [%]	$^{+0.23}_{-0.25}$	$^{-1.05}_{+1.31}$	$^{-2.85}_{+1.90}$	$^{-0.81}_{+1.39}$	$^{-1.28}_{+1.91}$	$^{-4.09}_{+1.85}$
Pile-up offset μ (JES) [%]	-	$^{-0.36}_{+0.34}$	$^{-0.92}_{+0.37}$	$^{-}_{-0.38}$	$^{-0.24}_{+0.10}$	$^{-}_{-1.70}$
Pile-up offset N_{PV} (JES) [%]	-	-	$^{+0.24}_{-}$	$^{+0.11}_{-0.64}$	$^{+0.37}_{-}$	$^{-}_{-1.12}$
Pile-up offset p_T (JES) [%]	-	-	$^{+0.34}_{-0.24}$	$^{+0.70}_{-1.12}$	$^{+1.47}_{-1.38}$	$^{-}_{-2.57}$
Pile-up offset ρ topology (JES) [%]	∓ 0.20	$^{+1.15}_{-0.96}$	$^{+1.51}_{-2.58}$	$^{-0.35}_{-}$	$^{+0.83}_{-0.51}$	$^{+0.92}_{-0.61}$
Punch-through (JES) [%]	-	-	-	-	-	-
Single particle high-p_T (JES) [%]	-	-	-	-	-	-
Jet energy resolution [%]	∓ 0.35	± 1.82	± 3.05	± 0.44	± 9.60	∓ 6.97
Jet vertex fraction [%]	$^{+0.34}_{-0.35}$	$^{-1.79}_{+1.81}$	$^{-2.89}_{+3.07}$	$^{-1.15}_{+1.18}$	$^{-2.03}_{+1.99}$	∓ 1.94
b-Quark tagging efficiency (eigenvector 0) [%]	-	$^{+0.11}_{-0.10}$	$^{+0.23}_{-0.22}$	± 0.28	± 0.23	$^{+0.88}_{-0.83}$
b-Quark tagging efficiency (eigenvector 1) [%]	-	-	∓ 0.33	$^{-0.57}_{+0.56}$	$^{-1.24}_{+1.23}$	$^{-1.01}_{+0.97}$
b-Quark tagging efficiency (eigenvector 2) [%]	-	-	∓ 0.23	$^{-0.39}_{+0.40}$	$^{-0.69}_{+0.70}$	$^{-0.94}_{+0.96}$
b-Quark tagging efficiency (eigenvector 3) [%]	-	-	-	-	-	∓ 0.18
b-Quark tagging efficiency (eigenvector 4) [%]	-	-	-	-	-	-
c-Quark tagging efficiency (eigenvector 0) [%]	-	-	$^{-0.36}_{+0.34}$	$^{-0.49}_{+0.48}$	-	$^{-0.61}_{+0.62}$
c-Quark tagging efficiency (eigenvector 1) [%]	-	-	-	∓ 0.17	∓ 0.18	∓ 0.28
c-Quark tagging efficiency (eigenvector 2) [%]	-	-	-	-	-	∓ 0.12
c-Quark tagging efficiency (eigenvector 3) [%]	-	-	-	-	-	-
Light-jet tagging efficiency (eigenvector 0) [%]	-	$^{-0.29}_{+0.28}$	$^{-0.49}_{+0.38}$	-	$^{+1.24}_{-1.33}$	$^{-}_{-0.18}$
Light-jet tagging efficiency (eigenvector 1) [%]	-	-	-	-	-	± 0.25
Light-jet tagging efficiency (eigenvector 2) [%]	-	-	-	-	-	∓ 0.19
Light-jet tagging efficiency (eigenvector 3) [%]	-	-	-	-	-	-
Light-jet tagging efficiency (eigenvector 4) [%]	-	-	-	-	-	-
Light-jet tagging efficiency (eigenvector 5) [%]	-	-	-	-	-	-
Light-jet tagging efficiency (eigenvector 6) [%]	-	-	-	-	-	-
Light-jet tagging efficiency (eigenvector 7) [%]	-	-	-	-	-	-
Light-jet tagging efficiency (eigenvector 8) [%]	-	-	-	-	-	-
Light-jet tagging efficiency (eigenvector 9) [%]	-	-	-	-	-	-
Light-jet tagging efficiency (eigenvector 10) [%]	-	-	-	-	-	-
Light-jet tagging efficiency (eigenvector 11) [%]	-	-	-	-	-	-
Light-jet tagging efficiency (eigenvector 12) [%]	-	-	-	-	-	-
Light-jet tagging efficiency (eigenvector 13) [%]	-	-	-	-	-	-
b-Quark tagging extrapolation [%]	-	-	$^{+0.16}_{-0.17}$	± 0.37	$^{+0.91}_{-0.90}$	$^{+1.22}_{-1.24}$
b-Quark tagging extrapolation from c-Quark [%]	-	-	-	-	-	-
Electron energy resolution [%]	-	-	-	-	-	$^{-0.18}_{-}$
Electron energy scale [%]	-	-	-	-	$^{-}_{+0.28}$	$^{-0.14}_{+0.16}$
Electron trigger efficiency [%]	-	-	-	-	± 0.12	-
Electron reconstruction efficiency [%]	-	-	-	-	-	-
Electron identification efficiency [%]	-	-	-	± 0.10	± 0.21	-
Electron isolation efficiency [%]	-	-	-	-	± 0.11	-
Muon energy scale [%]	-	-	-	-	-	-
Muon (MS) momentum resolution [%]	-	-	-	-	-	-
Muon (ID) momentum resolution [%]	-	-	-	-	$^{-}_{-0.21}$	$^{+0.68}_{-}$
Muon trigger efficiency stat [%]	-	-	-	-	-	-
Muon trigger efficiency syst [%]	-	-	-	-	-	-
Muon identification stat [%]	-	-	-	-	-	-
Muon identification syst [%]	-	-	-	-	-	-
Muon isolation efficiency stat [%]	-	-	-	-	-	-
Muon isolation efficiency syst [%]	-	-	-	-	-	-
Muon TTVA efficiency stat [%]	-	-	-	-	-	-
Muon TTVA efficiency syst [%]	-	-	-	-	-	-
E_T^{miss} Soft jet resolution para [%]	-	± 0.21	∓ 0.38	± 1.01	± 0.84	∓ 2.22
E_T^{miss} Soft jet resolution perp [%]	-	± 0.28	± 0.12	± 0.12	± 0.87	∓ 1.89
E_T^{miss} Soft jet scale [%]	-	-	-	$^{-0.41}_{+0.40}$	$^{+0.94}_{-0.70}$	$^{-1.55}_{-}$
Luminosity [%]	-	-	-	-	-	-
W+jets CA_2ex stat error [%]	-	-	-	-	-	-
W+jets CA_3ex stat error [%]	-	-	-	-	-	-
W+jets CA_4incl stat error [%]	-	-	-	-	-	-
W+jets Fc stat error [%]	-	-	-	-	± 0.12	± 0.11
W+jets Fcc stat error [%]	-	-	-	$^{-0.73}_{+0.71}$	$^{+0.56}_{-0.55}$	$^{-0.52}_{+0.50}$
W+jets Flight stat error [%]	-	-	-	-	-	-
Single top cross-section [%]	-	-	± 0.33	± 0.47	± 0.26	-
Z+jets cross-section [%]	-	-	-	± 0.15	± 0.48	∓ 0.54
Diboson cross-section [%]	-	-	-	± 0.10	-	± 0.12
ttV cross-section [%]	-	-	-	-	-	-
Monte Carlo sample statistics [%]	-	± 0.49	± 1.36	± 2.64	± 5.49	± 9.02
ISR/FSR + scale [%]	$^{+0.47}_{-0.92}$	$^{-2.85}_{+5.29}$	$^{-0.46}_{+5.39}$	$^{-}_{-6.54}$	$^{+5.61}_{-}$	$^{+1.88}_{-28.0}$
Alternate hard-scattering model [%]	∓ 1.30	± 6.57	± 6.56	± 22.5	± 16.6	± 50.9
Alternate parton-shower model [%]	∓ 1.32	± 7.07	± 11.1	± 0.90	± 2.63	∓ 8.60
Inter PDF [%]	-	∓ 0.13	-	-	∓ 0.28	∓ 0.50
Intra PDF [%]	-	-	± 0.12	± 0.21	± 3.37	± 1.66
Fakes overall normalization [%]	∓ 0.44	± 2.22	± 4.66	± 0.46	∓ 3.05	± 8.46
Real lepton efficiency stat [%]	-	-	-	-	-	-
Fake lepton efficiency MC scale [%]	$^{-0.17}_{+0.22}$	$^{+0.94}_{-1.12}$	$^{+1.47}_{-2.33}$	-	$^{-0.40}_{+0.39}$	$^{+2.98}_{-4.79}$
Fake lepton efficiency alternate CR [%]	-	± 0.34	± 0.52	-	∓ 0.44	± 0.61

TABLE A.19: Systematic uncertainties for the normalised differential cross-section at particle-level for $\lvert p_{out}^{t\bar{t}} \rvert$ in the 4-jet exclusive configuration.

Bins [GeV]	0–40	40–80	80–120	120–170	170–230	230–600
$1/\sigma \cdot \mathrm{d}\sigma \,/\, \mathrm{d}\lvert p_{out}^{t\bar{t}} \rvert$	$1.67 \cdot 10^{-2}$	$5.23 \cdot 10^{-3}$	$1.75 \cdot 10^{-3}$	$6.17 \cdot 10^{-4}$	$2.42 \cdot 10^{-4}$	$1.75 \cdot 10^{-5}$
Total Uncertainty [%]	$^{+3.15}_{-3.34}$	$^{+7.80}_{-7.07}$	$^{+8.38}_{-8.05}$	$^{+5.84}_{-6.36}$	$^{+6.78}_{-6.92}$	$^{+11.2}_{-11.5}$
Statistics [%]	± 0.2	± 0.7	± 1.3	± 2.0	± 3.1	± 4.7
Systematics [%]	$^{+3.14}_{-3.33}$	$^{+7.76}_{-7.03}$	$^{+8.26}_{-7.92}$	$^{+5.41}_{-5.97}$	$^{+5.90}_{-6.06}$	$^{+10.0}_{-10.3}$
b-Tagged jet energy scale (JES) [%]	-	-	$^{+0.13}_{-0.19}$	$^{+0.11}_{-0.26}$	-	-
Effective detector NP set 1 (JES) [%]	$^{-1.38}_{+1.31}$	$^{+3.42}_{-3.13}$	$^{+3.31}_{-3.19}$	$^{+0.83}_{-1.22}$	$^{-0.83}_{+0.16}$	$^{-2.21}_{+1.95}$
Effective detector NP set 2 (JES) [%]	-	$^{-0.37}_{+0.48}$	$^{-}_{-0.24}$	$^{+1.46}_{-1.65}$	$^{+1.67}_{-1.91}$	$^{+3.44}_{-2.76}$
Effective detector NP set 3 (JES) [%]	-	$^{+0.15}_{-0.10}$	$^{-0.39}_{+0.35}$	$^{-0.94}_{+0.85}$	$^{-1.24}_{+1.19}$	$^{-1.58}_{+1.60}$
Effective detector NP set 4 (JES) [%]	-	-	$^{+0.31}_{-0.29}$	$^{+0.50}_{-0.53}$	$^{+0.38}_{-0.39}$	$^{+0.24}_{-0.60}$
Effective detector NP set 5 (JES) [%]	-	-	-	-	$^{+0.14}_{-}$	$^{+0.13}_{-0.23}$
Effective detector NP set 6 restTerm (JES) [%]	-	-	$^{+0.17}_{-0.14}$	$^{+0.13}_{-0.16}$	$^{+0.16}_{-0.30}$	$^{+0.25}_{-0.19}$
η intercalibration model (JES) [%]	$^{-0.88}_{+0.78}$	$^{+1.98}_{-1.61}$	$^{+2.28}_{-2.15}$	$^{+0.81}_{-1.18}$	$^{+0.36}_{-0.90}$	$^{+0.38}_{-}$
η intercalibration total stat (JES) [%]	$^{-0.26}_{+0.28}$	$^{+0.61}_{-0.57}$	$^{+0.68}_{-0.81}$	$^{-}_{-0.37}$	$^{+0.30}_{-0.58}$	$^{+0.40}_{-}$
Flavour composition (JES) [%]	$^{-1.67}_{+1.59}$	$^{+3.70}_{-3.45}$	$^{+4.39}_{-4.17}$	$^{+2.30}_{-2.88}$	$^{+0.21}_{-0.35}$	$^{-1.31}_{+1.55}$
Flavour response (JES) [%]	$^{+0.50}_{-0.49}$	$^{-0.93}_{+1.01}$	$^{-1.59}_{+1.47}$	$^{-0.86}_{+0.55}$	$^{-1.03}_{+0.73}$	-
Pile-up offset μ (JES) [%]	$^{+0.11}_{-}$	∓ 0.24	$^{-0.33}_{+0.23}$	-	-	$^{+0.23}_{-0.29}$
Pile-up offset N_{PV} (JES) [%]	-	$^{-0.12}_{+0.13}$	-	-	-	$^{+0.30}_{-}$
Pile-up offset p_T (JES) [%]	-	-	$^{+0.14}_{-0.16}$	$^{+0.22}_{-0.37}$	-	$^{+0.33}_{-}$
Pile-up offset ρ topology (JES) [%]	$^{-0.42}_{+0.43}$	$^{+1.01}_{-0.92}$	$^{+1.24}_{-1.29}$	$^{-}_{-0.42}$	$^{-}_{-0.23}$	$^{-0.80}_{+0.69}$
Punch-through (JES) [%]	-	-	-	-	-	-
Single particle high-p_T (JES) [%]	-	-	-	-	-	-
Jet energy resolution [%]	∓ 0.54	± 1.24	± 1.86	± 0.48	∓ 0.38	∓ 3.42
Jet vertex fraction [%]	-	-	$^{-0.33}_{+0.36}$	$^{-1.00}_{+1.02}$	$^{-1.28}_{+1.34}$	$^{-2.00}_{+2.07}$
b-Quark tagging efficiency (eigenvector 0) [%]	$^{-0.15}_{+0.14}$	$^{+0.22}_{-0.21}$	$^{+0.47}_{-0.46}$	$^{+0.54}_{-0.53}$	$^{+0.57}_{-0.56}$	$^{+0.38}_{-0.37}$
b-Quark tagging efficiency (eigenvector 1) [%]	-	-	-	$^{-0.27}_{+0.26}$	$^{-0.57}_{+0.55}$	$^{-1.45}_{+1.42}$
b-Quark tagging efficiency (eigenvector 2) [%]	-	-	$^{-0.26}_{+0.27}$	$^{-0.35}_{+0.36}$	$^{-0.54}_{+0.55}$	$^{-0.93}_{+0.94}$
b-Quark tagging efficiency (eigenvector 3) [%]	-	-	-	-	-	∓ 0.18
b-Quark tagging efficiency (eigenvector 4) [%]	-	-	-	-	-	-
c-Quark tagging efficiency (eigenvector 0) [%]	-	-	-	-	$^{+0.19}_{-0.20}$	$^{+0.40}_{-0.38}$
c-Quark tagging efficiency (eigenvector 1) [%]	-	-	-	-	∓ 0.13	∓ 0.27
c-Quark tagging efficiency (eigenvector 2) [%]	-	-	-	-	-	∓ 0.19
c-Quark tagging efficiency (eigenvector 3) [%]	-	-	-	-	-	-
Light-jet tagging efficiency (eigenvector 0) [%]	-	$^{-0.13}_{+0.10}$	$^{-0.15}_{+0.10}$	-	$^{+0.16}_{-}$	$^{-0.38}_{+0.34}$
Light-jet tagging efficiency (eigenvector 1) [%]	-	-	-	-	-	-
Light-jet tagging efficiency (eigenvector 2) [%]	-	-	-	-	-	-
Light-jet tagging efficiency (eigenvector 3) [%]	-	-	-	-	-	-
Light-jet tagging efficiency (eigenvector 4) [%]	-	-	-	-	-	-
Light-jet tagging efficiency (eigenvector 5) [%]	-	-	-	-	-	-
Light-jet tagging efficiency (eigenvector 6) [%]	-	-	-	-	-	-
Light-jet tagging efficiency (eigenvector 7) [%]	-	-	-	-	-	-
Light-jet tagging efficiency (eigenvector 8) [%]	-	-	-	-	-	-
Light-jet tagging efficiency (eigenvector 9) [%]	-	-	-	-	-	-
Light-jet tagging efficiency (eigenvector 10) [%]	-	-	-	-	-	-
Light-jet tagging efficiency (eigenvector 11) [%]	-	-	-	-	-	-
Light-jet tagging efficiency (eigenvector 12) [%]	-	-	-	-	-	-
Light-jet tagging efficiency (eigenvector 13) [%]	-	-	-	-	-	-
b-Quark tagging extrapolation [%]	-	-	± 0.14	± 0.27	$^{+0.48}_{-0.49}$	$^{+1.77}_{-1.79}$
b-Quark tagging extrapolation from c-Quark [%]	-	-	-	-	-	-
Electron energy resolution [%]	-	-	-	-	-	-
Electron energy scale [%]	-	-	-	-	-	-
Electron trigger efficiency [%]	-	-	-	-	-	-
Electron reconstruction efficiency [%]	-	-	-	-	-	-
Electron identification efficiency [%]	-	-	-	-	-	± 0.16
Electron isolation efficiency [%]	-	-	-	-	-	± 0.12
Muon energy scale [%]	-	-	-	-	-	-
Muon (MS) momentum resolution [%]	-	-	-	-	-	-
Muon (ID) momentum resolution [%]	-	-	-	-	-	-
Muon trigger efficiency stat [%]	-	-	-	-	-	-
Muon trigger efficiency syst [%]	-	-	-	-	-	-
Muon identification stat [%]	-	-	-	-	-	-
Muon identification syst [%]	-	-	-	-	-	-
Muon isolation efficiency stat [%]	-	-	-	-	-	-
Muon isolation efficiency syst [%]	-	-	-	-	-	-
Muon TTVA efficiency stat [%]	-	-	-	-	-	-
Muon TTVA efficiency syst [%]	-	-	-	-	-	-
E_T^{miss} Soft jet resolution para [%]	-	± 0.10	-	-	± 0.59	∓ 0.26
E_T^{miss} Soft jet resolution perp [%]	-	± 0.14	± 0.13	-	± 0.28	∓ 0.13
E_T^{miss} Soft jet scale [%]	-	-	-	-	$^{+0.29}_{-}$	-
Luminosity [%]	-	-	-	-	-	-
W+jets CA_2ex stat error [%]	-	-	-	-	-	-
W+jets CA_3ex stat error [%]	-	-	-	-	-	-
W+jets CA_4incl stat error [%]	-	-	-	-	-	-
W+jets Fc stat error [%]	-	-	-	-	-	-
W+jets Fcc stat error [%]	-	± 0.17	-	$^{-0.38}_{+0.37}$	$^{-0.40}_{+0.39}$	$^{-1.24}_{+1.21}$
W+jets Flight stat error [%]	-	-	-	-	-	-
Single top cross-section [%]	-	-	-	-	-	± 0.16
Z+jets cross-section [%]	-	-	-	± 0.23	-	± 0.32
Diboson cross-section [%]	-	-	-	± 0.15	± 0.23	± 0.52
ttV cross-section [%]	-	-	-	-	± 0.12	± 0.20
Monte Carlo sample statistics [%]	-	± 0.26	± 0.47	± 0.76	± 1.20	± 1.50
ISR/FSR + scale [%]	$^{-}_{-0.70}$	$^{+2.11}_{-}$	$^{+1.39}_{-}$	-	$^{+1.30}_{-}$	$^{-}_{-3.72}$
Alternate hard-scattering model [%]	∓ 1.13	± 1.64	± 3.17	± 3.99	± 4.17	± 5.69
Alternate parton-shower model [%]	∓ 1.64	± 4.24	± 3.23	± 0.49	± 2.07	∓ 3.67
Inter PDF [%]	-	-	-	-	± 0.13	± 0.12
Intra PDF [%]	-	-	-	-	± 0.22	± 0.10
Fakes overall normalization [%]	∓ 0.19	± 0.36	± 0.45	± 0.75	∓ 1.15	± 2.14
Real lepton efficiency stat [%]	-	-	-	-	$^{-0.17}_{+0.11}$	-
Fake lepton efficiency MC scale [%]	$^{-0.10}_{+0.14}$	$^{+0.29}_{-0.36}$	$^{+0.16}_{-0.30}$	$^{+0.16}_{-}$	$^{-0.47}_{+0.55}$	$^{+0.38}_{-0.40}$
Fake lepton efficiency alternate CR [%]	-	-	-	∓ 0.21	-	∓ 0.26

TABLE A.20: Systematic uncertainties for the normalised differential cross-section at particle-level for $\lvert p_{out}^{t\bar{t}} \rvert$ in the 4-jet inclusive configuration.

Appendix B

Closure tests

To perform the closure tests, the nominal $t\bar{t}$ sample POWHEG+PYTHIA6 is used. From this sample, two statistically indipendent sub-samples are generated. Each event of the nominal sample is assigned randomly to one of the sub-samples. One of the two sub-sample is used as pseudo-data and the other one is used to fill the migration matrix. Then, the pseudo-data subsample is unfolded using the other sample to apply the unfolding corrections. The distributions of the unfolded pesudo-data spectra are shown for all the configurations of additional jets; in Figures B.1–B.3 for the absolute distributions and in Figures B.4–B.6 for the normalised distributions. The distributions show a good closure within the statistical uncertainties.

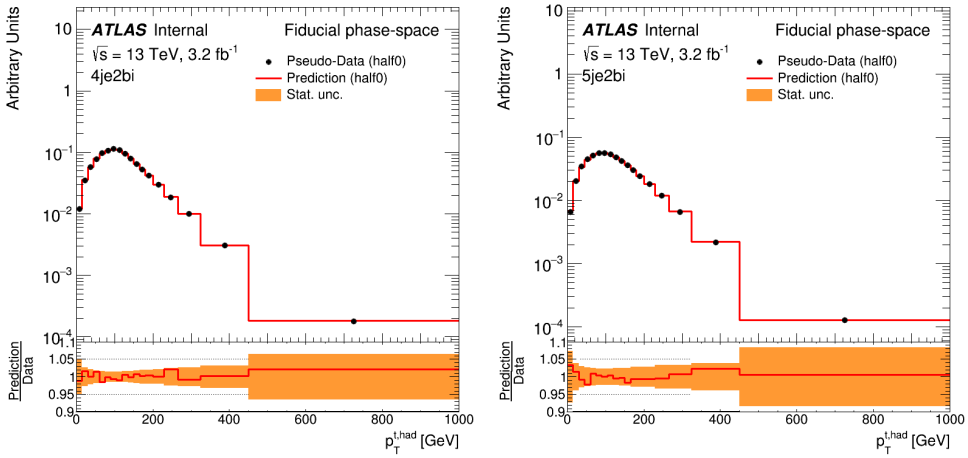

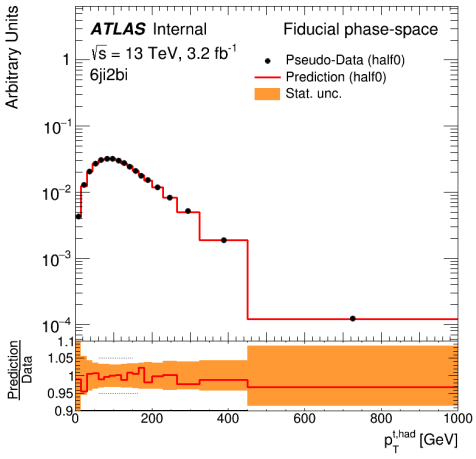

FIGURE B.1: Unfolding closure in terms of absolute differential cross-sections as a function of the $p_{\mathrm{T}}^{\mathrm{t,had}}$ in the (a) 4-jet exclusive, (b) 5-jet exclusive and (c) 6-jet inclusive configurations. The shaded area represents MC statistical uncertainties.

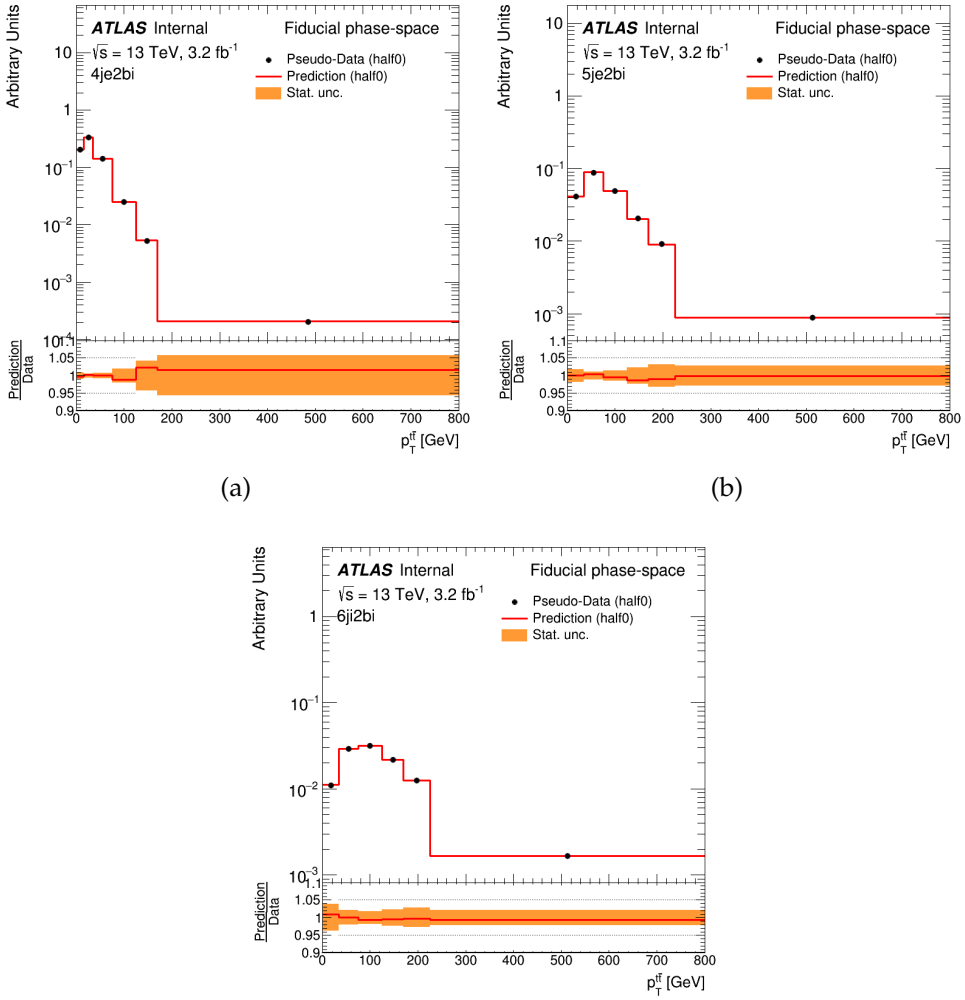

(a) (b)

(c)

FIGURE B.2: Unfolding closure in terms of absolute differential cross-sections as a function of the $p_{\mathrm{T}}^{\mathrm{t\bar{t}}}$ in the (a) 4-jet exclusive, (b) 5-jet exclusive and (c) 6-jet inclusive configurations. The shaded area represents MC statistical uncertainties.

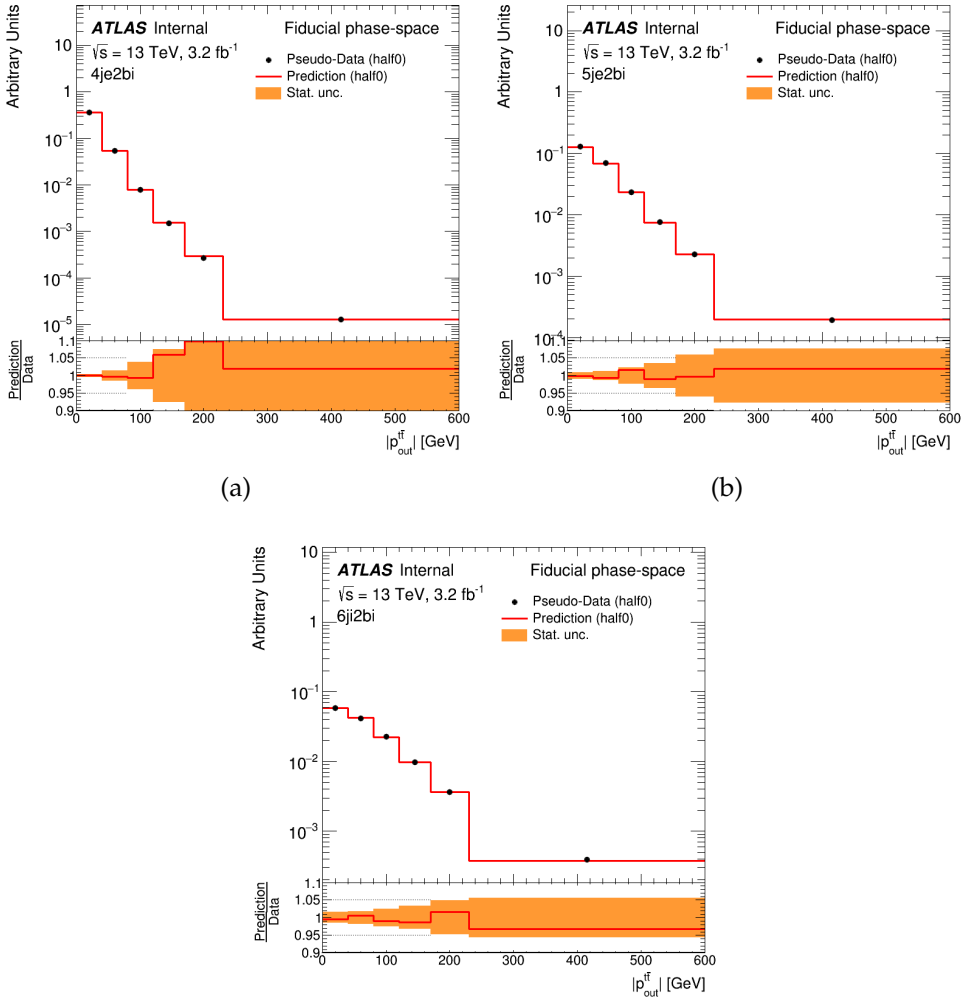

FIGURE B.3: Unfolding closure in terms of absolute differential cross-sections as a function of the $p_{\mathrm{out}}^{\mathrm{t\bar{t}}}$ in the (a) 4-jet exclusive, (b) 5-jet exclusive and (c) 6-jet inclusive configuration. The shaded area represents MC statistical uncertainties.

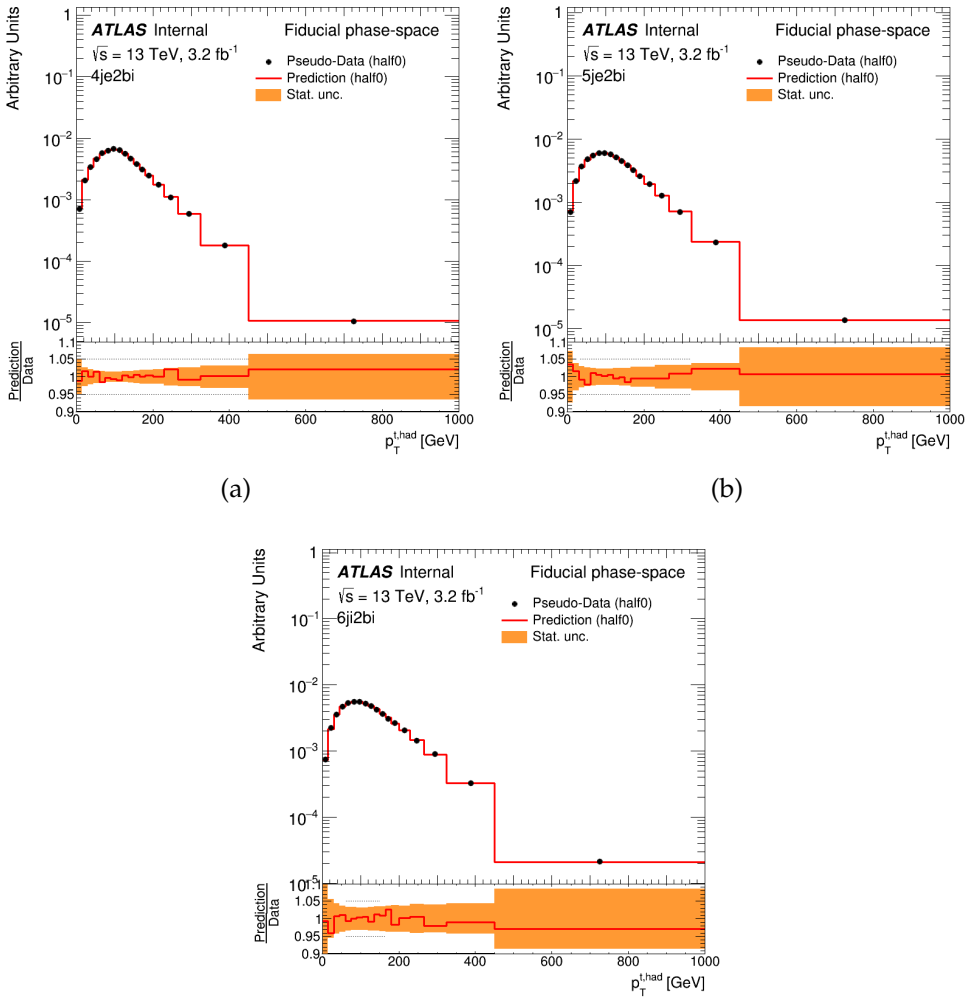

(a) (b)

(c)

FIGURE B.4: Unfolding closure in terms of normalised differential cross-sections as a function of the $p_{\mathrm{T}}^{\mathrm{t,had}}$ in the (a) 4-jet exclusive, (b) 5-jet exclusive and (c) 6-jet inclusive configurations. The shaded area represents MC statistical uncertainties.

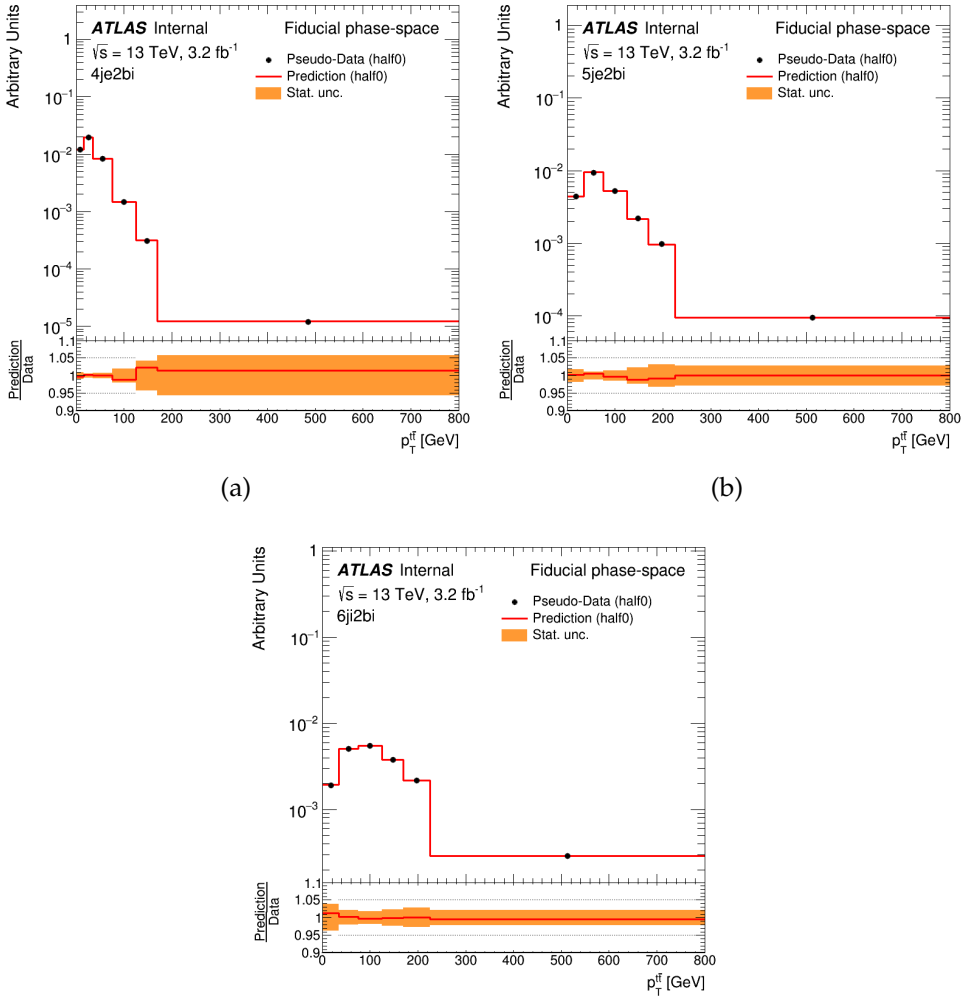

FIGURE B.5: Unfolding closure in terms of normalised differential cross-sections as a function of the $p_{\mathrm{T}}^{\mathrm{t\bar{t}}}$ in the (a) 4-jet exclusive, (b) 5-jet exclusive and (c) 6-jet inclusive configurations. The shaded area represents MC statistical uncertainties.

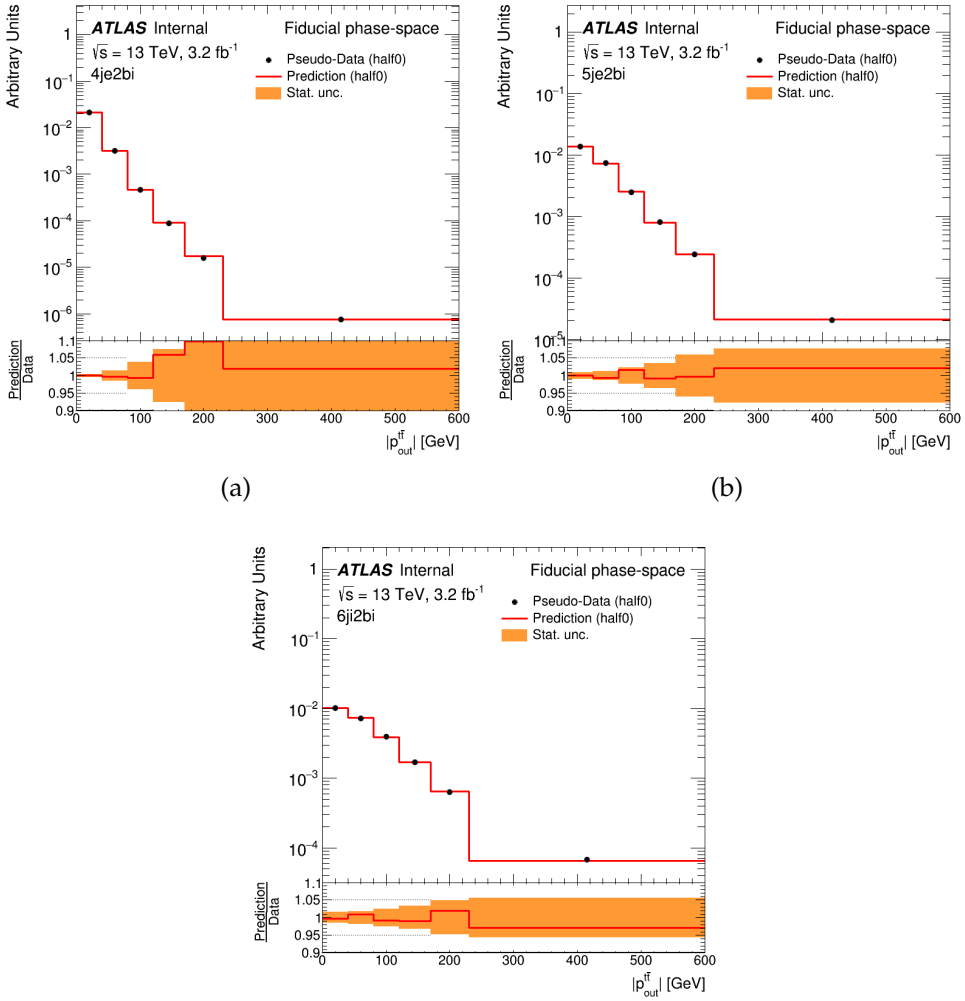

FIGURE B.6: Unfolding closure in terms of normalised differential cross-sections as a function of the $p_{\mathrm{out}}^{\mathrm{t\bar{t}}}$ in the (a) 4-jet exclusive, (b) 5-jet exclusive and (c) 6-jet inclusive configuration. The shaded area represents MC statistical uncertainties.

Appendix C

Stress tests

The second kind of test performed to check the stability of the unfolded method is the stress test. This test has the task to check if the choice of the Monte Carlo sample used for the training of the unfolding could introduce a bias during the procedure of the unfolding itself. This check is performed by reweighting the MC sample in order to change the shapes of the distributions and use this reweighted sample as peudo-data. Then, the reweighted sample is unfolded using, for the corrections and the response matrix, the nominal MC sample; after the unfolding, the result is compared with the reweighted MC sample. The stress tests are closure if the reweighted sample is within the statistical uncertainties. Non closure would indicate that the unfolding introduces a bias. The stress tests are performed using all corrections under realistic conditions. These conditions are defined as a variation of the spectra by doing a parametric reweight bin-by-bin proportional to the data MC ratio. The closure was tested including efficiency corrections and using a multiplication factor 1 applied to the stress factors.

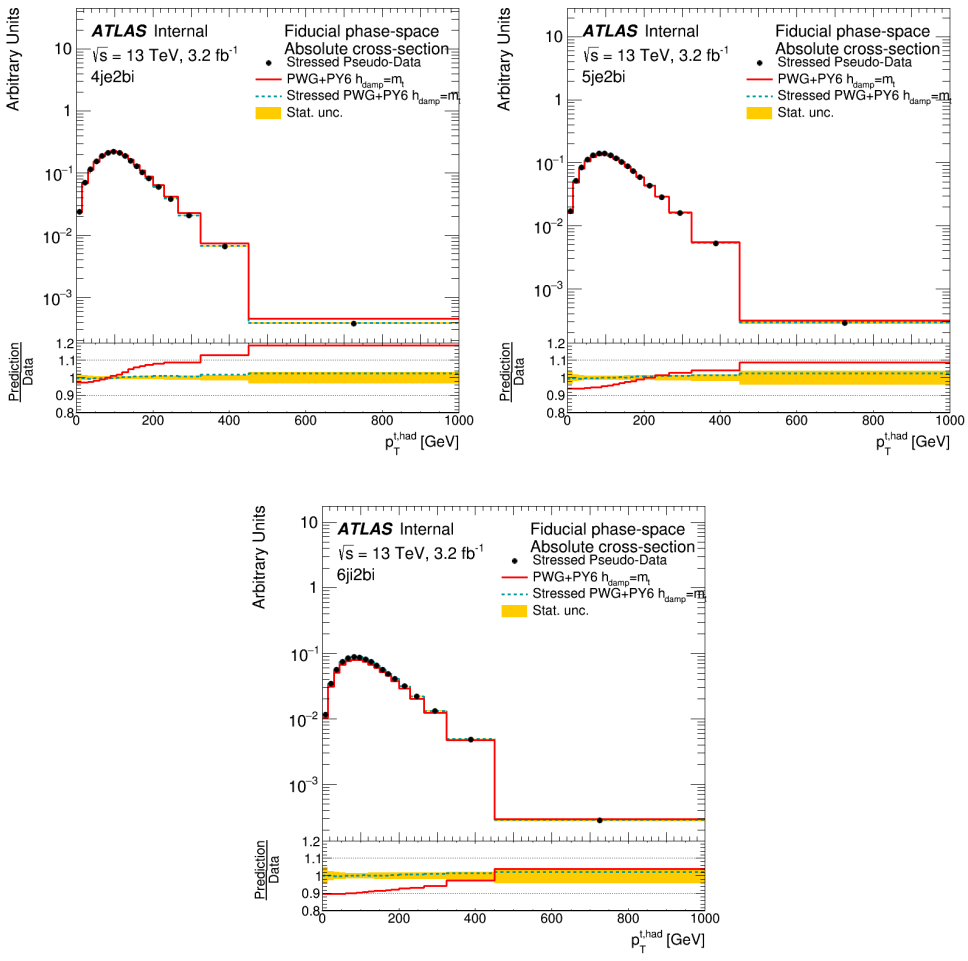

FIGURE C.1: Stress test using for the absolute cross section as a function of the $p_{\mathrm{T}}^{\mathrm{t,had}}$ applying a stress similar to the data-Monte Carlo difference in the (a) 4-jet exclusive, (b) 5-jet exclusive and (c) 6-jet inclusive configurations. The y-axis is the number of events divided by the bin width. The efficiency correction has been applied.

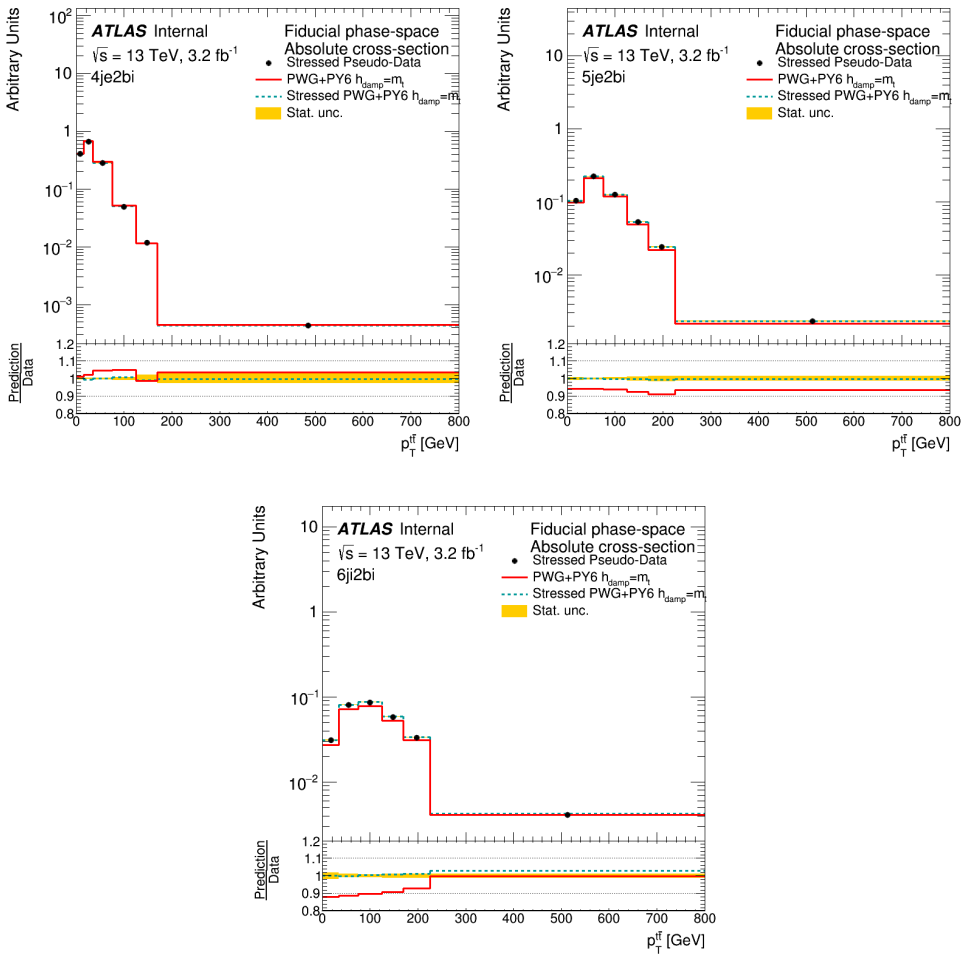

FIGURE C.2: Stress test using for the absolute cross section as a function of the $p_{\mathrm{T}}^{\mathrm{t\bar{t}}}$ applying a stress similar to the data-Monte Carlo difference in the (a) 4-jet exclusive, (b) 5-jet exclusive and (c) 6-jet inclusive configurations. The y-axis is the number of events divided by the bin width. The efficiency correction has been applied.

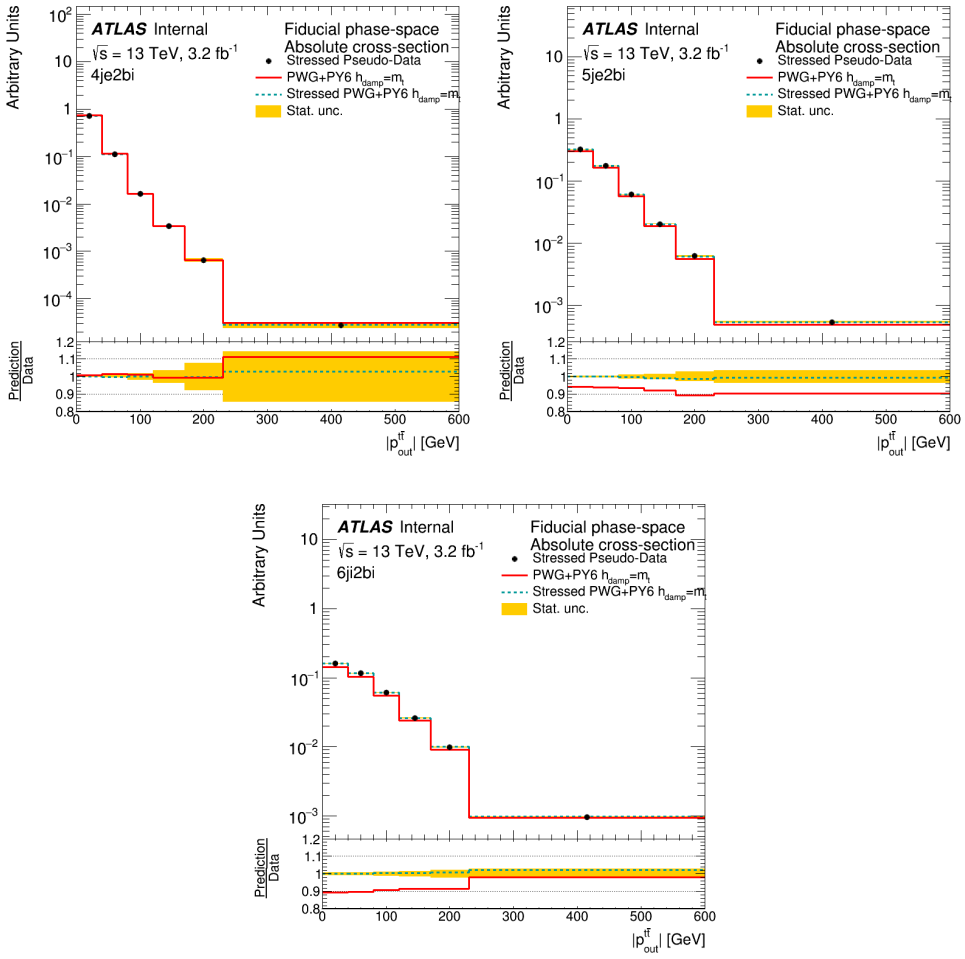

FIGURE C.3: Stress test using for the absolute cross section as a function of the $p_{\text{out}}^{\text{t}\bar{\text{t}}}$ applying a stress similar to the data-Monte Carlo difference in the (a) 4-jet exclusive, (b) 5-jet exclusive and (c) 6-jet inclusive configurations. The y-axis is the number of events divided by the bin width. The efficiency correction has been applied.

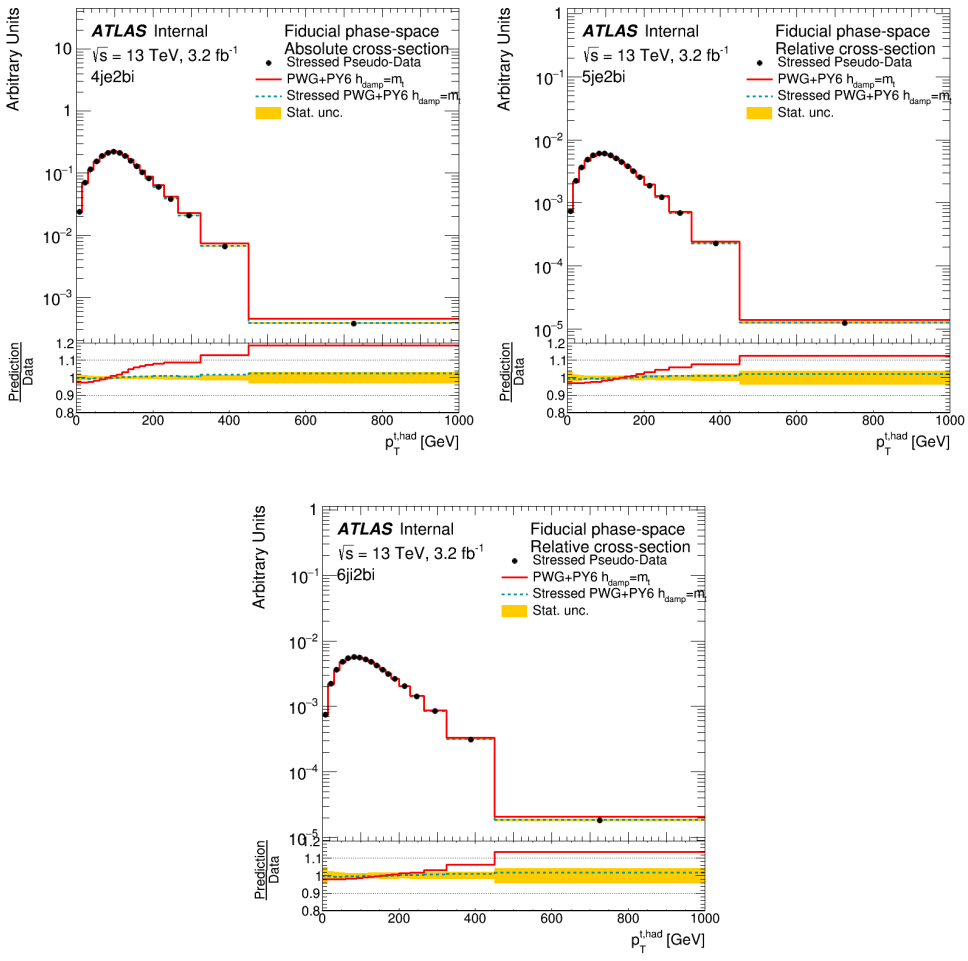

FIGURE C.4: Stress test using for the normalised cross section as a function of the $p_{\mathrm{T}}^{\mathrm{t,had}}$ applying a stress similar to the data-Monte Carlo difference in the (a) 4-jet exclusive, (b) 5-jet exclusive and (c) 6-jet inclusive configurations. The y-axis is the number of events divided by the bin width. The efficiency correction has been applied.

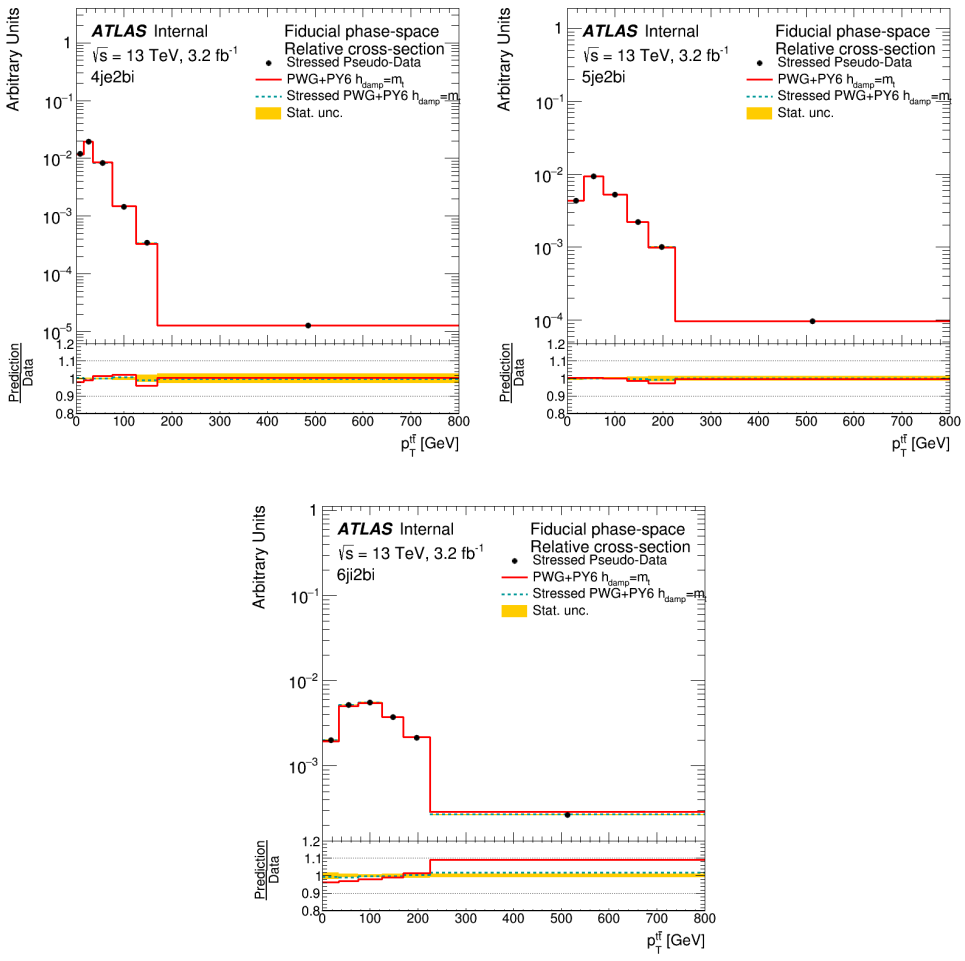

FIGURE C.5: Stress test using for the normalised cross section as a function of the $p_{\mathrm{T}}^{\mathrm{t\bar{t}}}$ applying a stress similar to the data-Monte Carlo difference in the (a) 4-jet exclusive, (b) 5-jet exclusive and (c) 6-jet inclusive configurations. The y-axis is the number of events divided by the bin width. The efficiency correction has been applied.

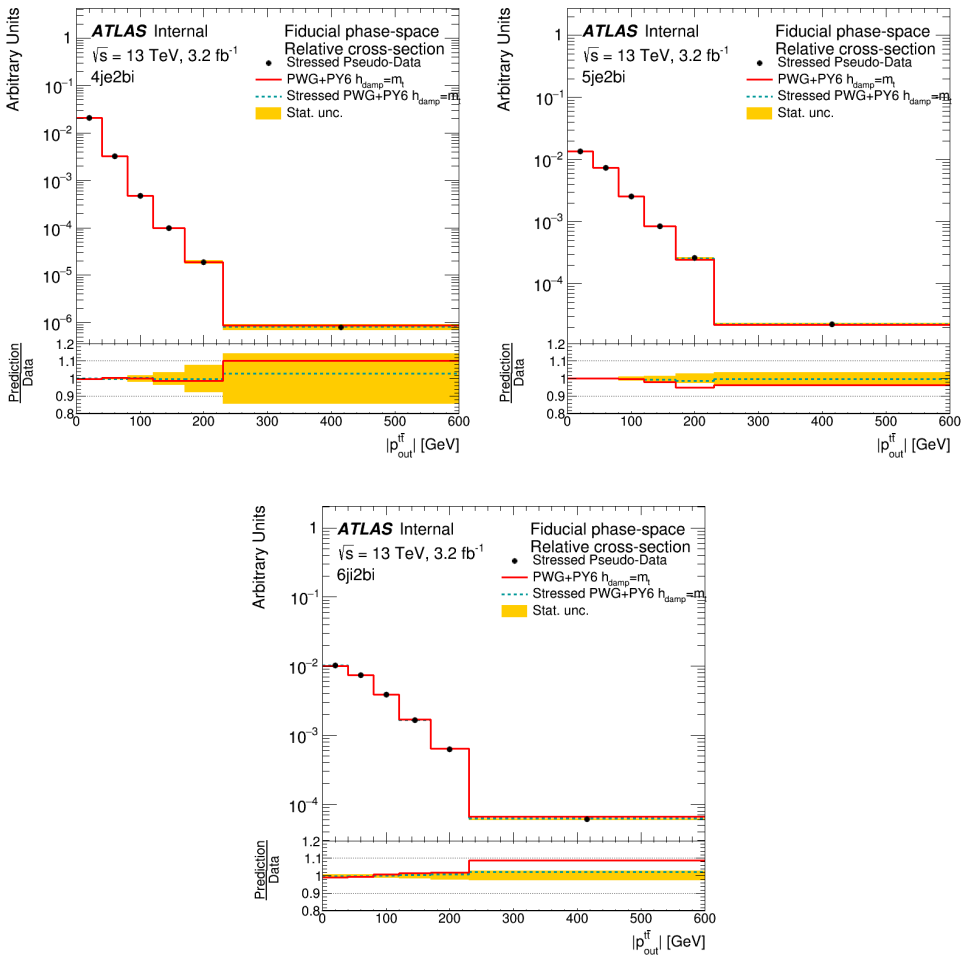

FIGURE C.6: Stress test using for the normalised cross section as a function of the $p_{\mathrm{out}}^{\mathrm{t\bar{t}}}$ applying a stress similar to the data-Monte Carlo difference in the (a) 4-jet exclusive, (b) 5-jet exclusive and (c) 6-jet inclusive configurations. The y-axis is the number of events divided by the bin width. The efficiency correction has been applied.

Appendix D

Covariance and correlation matrices

In this Appendix the covariance and correlations tables for all the variables, in the three configurarions are reported. Tables D.1–D.6 show the covariance matrices both for the absolute and normalised distributions, respectively, while, Tables D.7–D.12 the correlation matrices for both the absolute and normalised distributions, respectively.

bin [GeV]	0-15	15-30	30-45	45-60	60-75	75-90	90-105	105-120	120-135	135-150	150-165	165-180	180-200	200-230	230-265	265-325	325-450	450-1000
0-15	3.39e-05	6.93e-05	1.06e-04	1.40e-04	1.58e-04	1.57e-04	1.60e-04	1.36e-04	1.10e-04	9.49e-05	6.97e-05	4.91e-05	4.11e-05	2.97e-05	1.86e-05	1.03e-05	3.06e-06	2.88e-07
15-30	6.93e-05	2.02e-04	3.08e-04	3.81e-04	4.38e-04	4.45e-04	4.44e-04	3.71e-04	2.99e-04	2.47e-04	1.85e-04	1.31e-04	1.02e-04	6.97e-05	4.27e-05	2.22e-05	6.27e-06	6.46e-07
30-45	1.06e-04	3.08e-04	5.47e-04	6.59e-04	7.33e-04	7.53e-04	7.32e-04	6.10e-04	4.97e-04	4.07e-04	2.99e-04	2.16e-04	1.71e-04	1.19e-04	7.08e-05	3.63e-05	1.07e-05	1.09e-06
45-60	1.40e-04	3.81e-04	6.59e-04	8.63e-04	9.50e-04	9.49e-04	9.25e-04	7.83e-04	6.42e-04	5.27e-04	3.86e-04	2.76e-04	2.21e-04	1.56e-04	9.17e-05	4.76e-05	1.44e-05	1.41e-06
60-75	1.58e-04	4.38e-04	7.33e-04	9.50e-04	1.13e-03	1.11e-03	1.07e-03	9.19e-04	7.60e-04	6.19e-04	4.48e-04	3.24e-04	2.65e-04	1.80e-04	1.02e-04	5.54e-05	1.59e-05	1.64e-06
75-90	1.57e-04	4.45e-04	7.53e-04	9.49e-04	1.11e-03	1.16e-03	1.10e-03	9.23e-04	7.70e-04	6.34e-04	4.61e-04	3.34e-04	2.69e-04	1.84e-04	1.05e-04	5.54e-05	1.63e-05	1.66e-06
90-105	1.60e-04	4.44e-04	7.32e-04	9.25e-04	1.07e-03	1.10e-03	1.13e-03	9.41e-04	7.56e-04	6.35e-04	4.71e-04	3.34e-04	2.70e-04	1.87e-04	1.13e-04	6.02e-05	1.70e-05	1.74e-06
105-120	1.36e-04	3.71e-04	6.10e-04	7.83e-04	9.19e-04	9.23e-04	9.41e-04	8.45e-04	6.85e-04	5.58e-04	4.11e-04	2.99e-04	2.44e-04	1.67e-04	9.69e-05	5.43e-05	1.49e-05	1.51e-06
120-135	1.10e-04	2.99e-04	4.97e-04	6.42e-04	7.60e-04	7.70e-04	7.56e-04	6.85e-04	5.97e-04	4.86e-04	3.46e-04	2.54e-04	2.12e-04	1.45e-04	8.14e-05	4.65e-05	1.30e-05	1.30e-06
135-150	9.49e-05	2.47e-04	4.07e-04	5.27e-04	6.19e-04	6.34e-04	6.35e-04	5.58e-04	4.86e-04	4.28e-04	3.07e-04	2.15e-04	1.81e-04	1.29e-04	7.54e-05	4.31e-05	1.23e-05	1.21e-06
150-165	6.97e-05	1.85e-04	2.99e-04	3.86e-04	4.48e-04	4.61e-04	4.71e-04	4.11e-04	3.46e-04	3.07e-04	2.42e-04	1.70e-04	1.31e-04	9.46e-05	5.81e-05	3.25e-05	9.19e-06	8.88e-07
165-180	4.91e-05	1.31e-04	2.16e-04	2.76e-04	3.24e-04	3.34e-04	3.34e-04	2.99e-04	2.54e-04	2.15e-04	1.70e-04	1.33e-04	1.03e-04	6.87e-05	4.14e-05	2.41e-05	6.74e-06	6.52e-07
180-200	4.11e-05	1.02e-04	1.71e-04	2.21e-04	2.65e-04	2.69e-04	2.70e-04	2.44e-04	2.12e-04	1.81e-04	1.31e-04	1.03e-04	9.47e-05	6.26e-05	3.52e-05	2.23e-05	6.38e-06	6.18e-07
200-230	2.97e-05	6.97e-05	1.19e-04	1.56e-04	1.80e-04	1.84e-04	1.87e-04	1.67e-04	1.45e-04	1.29e-04	9.46e-05	6.87e-05	6.26e-05	5.08e-05	2.86e-05	1.70e-05	5.24e-06	4.81e-07
230-265	1.86e-05	4.27e-05	7.08e-05	9.17e-05	1.02e-04	1.05e-04	1.13e-04	9.69e-05	8.14e-05	7.54e-05	5.81e-05	4.14e-05	3.52e-05	2.86e-05	2.18e-05	1.11e-05	3.42e-06	3.17e-07
265-325	1.03e-05	2.22e-05	3.63e-05	4.76e-05	5.54e-05	5.54e-05	6.02e-05	5.43e-05	4.65e-05	4.31e-05	3.25e-05	2.41e-05	2.23e-05	1.70e-05	1.11e-05	8.09e-06	2.16e-06	2.05e-07
325-450	3.06e-06	6.27e-06	1.07e-05	1.44e-05	1.59e-05	1.63e-05	1.70e-05	1.49e-05	1.30e-05	1.23e-05	9.19e-06	6.74e-06	6.38e-06	5.24e-06	3.42e-06	2.16e-06	8.45e-07	6.32e-08
450-1000	2.88e-07	6.46e-07	1.09e-06	1.41e-06	1.64e-06	1.66e-06	1.74e-06	1.51e-06	1.30e-06	1.21e-06	8.88e-07	6.52e-07	6.18e-07	4.81e-07	3.17e-07	2.05e-07	6.32e-08	8.03e-09

bin [GeV]	0-15	15-30	30-45	45-60	60-75	75-90	90-105	105-120	120-135	135-150	150-165	165-180	180-200	200-230	230-265	265-325	325-450	450-1000
0-15	1.22e-05	3.01e-05	4.78e-05	6.10e-05	6.83e-05	6.95e-05	6.86e-05	6.30e-05	5.54e-05	4.49e-05	3.69e-05	2.97e-05	2.08e-05	1.66e-05	8.78e-06	3.87e-06	1.50e-06	7.55e-08
15-30	3.01e-05	1.07e-04	1.56e-04	1.94e-04	2.19e-04	2.33e-04	2.30e-04	2.06e-04	1.83e-04	1.43e-04	1.22e-04	9.73e-05	6.86e-05	5.83e-05	3.04e-05	1.26e-05	5.28e-06	3.17e-07
30-45	4.78e-05	1.56e-04	2.80e-04	3.31e-04	3.72e-04	3.81e-04	3.76e-04	3.48e-04	3.05e-04	2.52e-04	2.05e-04	1.65e-04	1.20e-04	8.86e-05	4.79e-05	2.14e-05	8.07e-06	3.85e-07
45-60	6.10e-05	1.94e-04	3.31e-04	4.24e-04	4.66e-04	4.70e-04	4.69e-04	4.31e-04	3.79e-04	3.07e-04	2.55e-04	2.06e-04	1.47e-04	1.14e-04	6.17e-05	2.64e-05	1.08e-05	5.91e-07
60-75	6.83e-05	2.19e-04	3.72e-04	4.66e-04	5.44e-04	5.44e-04	5.31e-04	4.89e-04	4.30e-04	3.53e-04	2.89e-04	2.34e-04	1.69e-04	1.28e-04	6.77e-05	2.98e-05	1.16e-05	5.84e-07
75-90	6.95e-05	2.33e-04	3.81e-04	4.70e-04	5.44e-04	5.88e-04	5.66e-04	5.05e-04	4.48e-04	3.64e-04	3.01e-04	2.42e-04	1.76e-04	1.37e-04	7.08e-05	3.10e-05	1.22e-05	6.63e-07
90-105	6.86e-05	2.30e-04	3.76e-04	4.69e-04	5.31e-04	5.66e-04	5.73e-04	5.13e-04	4.48e-04	3.63e-04	3.04e-04	2.45e-04	1.77e-04	1.41e-04	7.43e-05	3.14e-05	1.30e-05	7.16e-07
105-120	6.30e-05	2.06e-04	3.48e-04	4.31e-04	4.89e-04	5.05e-04	5.13e-04	4.89e-04	4.24e-04	3.39e-04	2.82e-04	2.28e-04	1.66e-04	1.28e-04	6.93e-05	2.98e-05	1.22e-05	6.14e-07
120-135	5.54e-05	1.83e-04	3.05e-04	3.79e-04	4.30e-04	4.48e-04	4.48e-04	4.24e-04	3.85e-04	3.04e-04	2.49e-04	2.01e-04	1.46e-04	1.16e-04	6.21e-05	2.66e-05	1.11e-05	5.81e-07
135-150	4.49e-05	1.43e-04	2.52e-04	3.07e-04	3.53e-04	3.64e-04	3.63e-04	3.39e-04	3.04e-04	2.59e-04	2.08e-04	1.64e-04	1.21e-04	9.04e-05	4.95e-05	2.22e-05	8.67e-06	4.22e-07
150-165	3.69e-05	1.22e-04	2.05e-04	2.55e-04	2.89e-04	3.01e-04	3.04e-04	2.82e-04	2.49e-04	2.08e-04	1.79e-04	1.42e-04	1.00e-04	7.89e-05	4.42e-05	1.87e-05	7.96e-06	4.41e-07
165-180	2.97e-05	9.73e-05	1.65e-04	2.06e-04	2.34e-04	2.42e-04	2.45e-04	2.28e-04	2.01e-04	1.64e-04	1.42e-04	1.20e-04	8.48e-05	6.33e-05	3.57e-05	1.54e-05	6.56e-06	3.66e-07
180-200	2.08e-05	6.86e-05	1.20e-04	1.47e-04	1.69e-04	1.76e-04	1.77e-04	1.66e-04	1.46e-04	1.21e-04	1.00e-04	8.48e-05	6.74e-05	4.60e-05	2.56e-05	1.17e-05	4.76e-06	2.68e-07
200-230	1.66e-05	5.83e-05	8.86e-05	1.14e-04	1.28e-04	1.37e-04	1.41e-04	1.28e-04	1.16e-04	9.04e-05	7.89e-05	6.33e-05	4.60e-05	4.35e-05	2.21e-05	8.78e-06	4.27e-06	2.77e-07
230-265	8.78e-06	3.04e-05	4.79e-05	6.17e-05	6.77e-05	7.08e-05	7.43e-05	6.93e-05	6.21e-05	4.95e-05	4.42e-05	3.57e-05	2.56e-05	2.21e-05	1.53e-05	5.32e-06	2.65e-06	1.80e-07
265-325	3.87e-06	1.26e-05	2.14e-05	2.64e-05	2.98e-05	3.10e-05	3.14e-05	2.98e-05	2.66e-05	2.22e-05	1.87e-05	1.54e-05	1.17e-05	8.78e-06	5.32e-06	3.20e-06	1.06e-06	7.04e-08
325-450	1.50e-06	5.28e-06	8.07e-06	1.08e-05	1.16e-05	1.22e-05	1.30e-05	1.22e-05	1.11e-05	8.67e-06	7.96e-06	6.56e-06	4.76e-06	4.27e-06	2.65e-06	1.06e-06	6.90e-07	4.53e-08
450-1000	7.55e-08	3.17e-07	3.85e-07	5.91e-07	5.84e-07	6.63e-07	7.16e-07	6.14e-07	5.81e-07	4.22e-07	4.41e-07	3.66e-07	2.68e-07	2.77e-07	1.80e-07	7.04e-08	4.53e-08	6.30e-09

bin [GeV]	0-15	15-30	30-45	45-60	60-75	75-90	90-105	105-120	120-135	135-150	150-165	165-180	180-200	200-230	230-265	265-325	325-450	450-1000
0-15	1.49e-05	3.76e-05	5.98e-05	8.07e-05	9.13e-05	9.01e-05	8.72e-05	8.60e-05	7.62e-05	6.00e-05	4.98e-05	4.02e-05	3.16e-05	2.65e-05	1.80e-05	8.78e-06	2.88e-06	1.98e-07
15-30	3.76e-05	1.12e-04	1.74e-04	2.31e-04	2.56e-04	2.57e-04	2.48e-04	2.43e-04	2.14e-04	1.70e-04	1.40e-04	1.14e-04	9.07e-05	7.43e-05	4.85e-05	2.49e-05	8.19e-06	5.52e-07
30-45	5.98e-05	1.74e-04	2.89e-04	3.77e-04	4.14e-04	4.15e-04	4.01e-04	3.93e-04	3.47e-04	2.76e-04	2.27e-04	1.84e-04	1.48e-04	1.21e-04	7.93e-05	4.07e-05	1.31e-05	8.69e-07
45-60	8.07e-05	2.31e-04	3.77e-04	5.09e-04	5.57e-04	5.54e-04	5.35e-04	5.27e-04	4.65e-04	3.69e-04	3.03e-04	2.47e-04	1.97e-04	1.62e-04	1.06e-04	5.39e-05	1.77e-05	1.16e-06
60-75	9.13e-05	2.56e-04	4.14e-04	5.57e-04	6.45e-04	6.29e-04	6.02e-04	5.93e-04	5.24e-04	4.12e-04	3.53e-04	2.82e-04	2.23e-04	1.85e-04	1.23e-04	6.51e-05	2.00e-05	1.46e-06
75-90	9.01e-05	2.57e-04	4.15e-04	5.54e-04	6.29e-04	6.32e-04	6.01e-04	5.87e-04	5.19e-04	4.10e-04	3.46e-04	2.79e-04	2.22e-04	1.83e-04	1.20e-04	6.32e-05	2.00e-05	1.40e-06
90-105	8.72e-05	2.48e-04	4.01e-04	5.35e-04	6.02e-04	6.01e-04	5.89e-04	5.73e-04	5.01e-04	3.96e-04	3.34e-04	2.70e-04	2.15e-04	1.77e-04	1.18e-04	6.05e-05	1.94e-05	1.35e-06
105-120	8.60e-05	2.43e-04	3.93e-04	5.27e-04	5.93e-04	5.87e-04	5.73e-04	5.73e-04	5.00e-04	3.90e-04	3.26e-04	2.65e-04	2.13e-04	1.76e-04	1.17e-04	5.89e-05	1.91e-05	1.31e-06
120-135	7.62e-05	2.14e-04	3.47e-04	4.65e-04	5.24e-04	5.19e-04	5.01e-04	5.00e-04	4.48e-04	3.49e-04	2.89e-04	2.34e-04	1.87e-04	1.55e-04	1.04e-04	5.27e-05	1.70e-05	1.19e-06
135-150	6.00e-05	1.70e-04	2.76e-04	3.69e-04	4.12e-04	4.10e-04	3.96e-04	3.90e-04	3.49e-04	2.82e-04	2.28e-04	1.83e-04	1.46e-04	1.21e-04	8.07e-05	4.07e-05	1.34e-05	9.05e-07
150-165	4.98e-05	1.40e-04	2.27e-04	3.03e-04	3.53e-04	3.46e-04	3.34e-04	3.29e-04	2.89e-04	2.28e-04	2.07e-04	1.62e-04	1.24e-04	1.05e-04	7.04e-05	3.92e-05	1.16e-05	9.21e-07
165-180	4.02e-05	1.14e-04	1.84e-04	2.47e-04	2.82e-04	2.79e-04	2.70e-04	2.65e-04	2.34e-04	1.83e-04	1.62e-04	1.32e-04	1.02e-04	8.34e-05	5.61e-05	3.04e-05	9.47e-06	7.12e-07
180-200	3.16e-05	9.07e-05	1.48e-04	1.97e-04	2.23e-04	2.22e-04	2.15e-04	2.13e-04	1.87e-04	1.46e-04	1.24e-04	1.02e-04	8.59e-05	6.75e-05	4.33e-05	2.38e-05	7.44e-06	5.21e-07
200-230	2.65e-05	7.43e-05	1.21e-04	1.62e-04	1.85e-04	1.83e-04	1.77e-04	1.76e-04	1.55e-04	1.21e-04	1.05e-04	8.34e-05	6.75e-05	5.84e-05	3.77e-05	2.00e-05	6.16e-06	4.62e-07
230-265	1.80e-05	4.85e-05	7.93e-05	1.06e-04	1.23e-04	1.20e-04	1.18e-04	1.17e-04	1.04e-04	8.07e-05	7.04e-05	5.61e-05	4.33e-05	3.77e-05	2.79e-05	1.32e-05	4.23e-06	3.28e-07
265-325	8.78e-06	2.49e-05	4.07e-05	5.39e-05	6.51e-05	6.32e-05	6.05e-05	5.89e-05	5.27e-05	4.07e-05	3.92e-05	3.04e-05	2.38e-05	2.00e-05	1.32e-05	8.99e-06	2.22e-06	2.10e-07
325-450	2.88e-06	8.19e-06	1.31e-05	1.77e-05	2.00e-05	2.00e-05	1.94e-05	1.91e-05	1.70e-05	1.34e-05	1.16e-05	9.47e-06	7.44e-06	6.16e-06	4.23e-06	2.22e-06	8.64e-07	5.80e-08
450-1000	1.98e-07	5.52e-07	8.69e-07	1.16e-06	1.46e-06	1.40e-06	1.35e-06	1.31e-06	1.19e-06	9.05e-07	9.21e-07	7.12e-07	5.21e-07	4.62e-07	3.28e-07	2.10e-07	5.80e-08	7.85e-09

TABLE D.1: Covariance matrix of the absolute cross-section as function of $p_{\mathrm{T}}^{\mathrm{t,had}}$ in the 4-jet exclusive (top) , 5-jet exclusive (centre) and 6-jet inclusive (bottom) configurations, accounting for the statistical and systematic uncertainties.

bin [GeV]	0-15	15-35	35-75	75-125	125-170	170-800
0-15	1.25e-02	1.27e-02	2.41e-03	3.36e-04	5.59e-05	2.64e-06
15-35	1.27e-02	1.47e-02	4.00e-03	6.18e-04	9.67e-05	3.55e-06
35-75	2.41e-03	4.00e-03	2.88e-03	7.16e-04	1.37e-04	3.28e-06
75-125	3.36e-04	6.18e-04	7.16e-04	2.20e-04	4.64e-05	1.04e-06
125-170	5.59e-05	9.67e-05	1.37e-04	4.64e-05	1.60e-05	3.46e-07
170-800	2.64e-06	3.55e-06	3.28e-06	1.04e-06	3.46e-07	1.06e-08
bin [GeV]	0-35	35-75	75-125	125-170	170-225	225-800
0-35	4.24e-04	7.27e-04	3.56e-04	1.35e-04	4.85e-05	2.43e-06
35-75	7.27e-04	1.35e-03	6.51e-04	2.38e-04	8.78e-05	4.81e-06
75-125	3.56e-04	6.51e-04	3.68e-04	1.41e-04	5.34e-05	3.32e-06
125-170	1.35e-04	2.38e-04	1.41e-04	6.03e-05	2.19e-05	1.41e-06
170-225	4.85e-05	8.78e-05	5.34e-05	2.19e-05	1.08e-05	6.93e-07
225-800	2.43e-06	4.81e-06	3.32e-06	1.41e-06	6.93e-07	8.40e-08
bin [GeV]	0-35	35-75	75-125	125-170	170-225	225-800
0-35	9.64e-05	2.29e-04	2.25e-04	1.44e-04	7.68e-05	7.18e-06
35-75	2.29e-04	5.59e-04	5.48e-04	3.48e-04	1.86e-04	1.75e-05
75-125	2.25e-04	5.48e-04	5.47e-04	3.49e-04	1.86e-04	1.76e-05
125-170	1.44e-04	3.48e-04	3.49e-04	2.35e-04	1.25e-04	1.16e-05
170-225	7.68e-05	1.86e-04	1.86e-04	1.25e-04	6.86e-05	6.26e-06
225-800	7.18e-06	1.75e-05	1.76e-05	1.16e-05	6.26e-06	6.35e-07

TABLE D.2: Covariance matrix of the absolute cross-section as function of $p_{\mathrm{T}}^{\mathrm{t\bar{t}}}$ in the 4-jet exclusive (top), 5-jet exclusive (centre) and 6-jet inclusive (bottom) configurations, accounting for the statistical and systematic uncertainties.

bin [GeV]	0-40	40-80	80-120	120-170	170-230	230-600
0-40	1.02e-02	1.60e-03	2.74e-04	5.11e-05	3.94e-06	6.24e-07
40-80	1.60e-03	6.55e-04	1.18e-04	2.76e-05	4.02e-06	2.94e-07
80-120	2.74e-04	1.18e-04	2.46e-05	4.66e-06	6.86e-07	4.81e-08
120-170	5.11e-05	2.76e-05	4.66e-06	2.07e-06	2.65e-07	1.93e-08
170-230	3.94e-06	4.02e-06	6.86e-07	2.65e-07	8.27e-08	2.53e-09
230-600	6.24e-07	2.94e-07	4.81e-08	1.93e-08	2.53e-09	3.48e-10
bin [GeV]	0-40	40-80	80-120	120-170	170-230	230-600
0-40	2.88e-02	1.15e-02	3.62e-03	1.16e-03	3.51e-04	3.56e-05
40-80	1.15e-02	6.51e-03	2.19e-03	6.35e-04	1.87e-04	1.44e-05
80-120	3.62e-03	2.19e-03	7.68e-04	2.21e-04	6.59e-05	4.81e-06
120-170	1.16e-03	6.35e-04	2.21e-04	7.13e-05	2.13e-05	1.75e-06
170-230	3.51e-04	1.87e-04	6.59e-05	2.13e-05	7.93e-06	5.60e-07
230-600	3.56e-05	1.44e-05	4.81e-06	1.75e-06	5.60e-07	8.11e-08
bin [GeV]	0-40	40-80	80-120	120-170	170-230	230-600
0-40	2.61e-03	1.22e-03	3.19e-04	7.91e-05	1.60e-05	7.27e-07
40-80	1.22e-03	5.97e-04	1.63e-04	4.15e-05	8.50e-06	4.89e-07
80-120	3.19e-04	1.63e-04	5.43e-05	1.34e-05	2.58e-06	1.92e-07
120-170	7.91e-05	4.15e-05	1.34e-05	6.51e-06	1.54e-06	1.38e-07
170-230	1.60e-05	8.50e-06	2.58e-06	1.54e-06	8.96e-07	4.72e-08
230-600	7.27e-07	4.89e-07	1.92e-07	1.38e-07	4.72e-08	1.15e-08
bin [GeV]	0-40	40-80	80-120	120-170	170-230	230-600
0-40	2.15e-03	1.42e-03	6.37e-04	2.42e-04	8.51e-05	5.47e-06
40-80	1.42e-03	9.56e-04	4.29e-04	1.62e-04	5.70e-05	3.81e-06
80-120	6.37e-04	4.29e-04	2.11e-04	7.64e-05	2.68e-05	2.08e-06
120-170	2.42e-04	1.62e-04	7.64e-05	3.04e-05	1.03e-05	7.45e-07
170-230	8.51e-05	5.70e-05	2.68e-05	1.03e-05	4.31e-06	2.67e-07
230-600	5.47e-06	3.81e-06	2.08e-06	7.45e-07	2.67e-07	3.54e-08

TABLE D.3: Covariance matrix of the absolute cross-section as function of $p_{\mathrm{out}}^{\mathrm{t\bar{t}}}$ respectively in the 4-jet exclusive, 4-jet inclusive, 5-jet exclusive and 6-jet inclusive configurations, accounting for the statistical and systematic uncertainties.

bin [GeV]	0-15	15-30	30-45	45-60	60-75	75-90	90-105	105-120	120-135	135-150	150-165	165-180	180-200	200-230	230-265	265-325	325-450	450-1000
0-15	5.06e-09	5.94e-09	5.25e-09	5.58e-09	4.82e-09	3.76e-09	2.13e-09	1.66e-10	1.90e-11	2.47e-09	1.91e-09	-7.74e-10	7.16e-10	-3.62e-10	1.45e-10	-3.89e-12	8.93e-11	1.72e-11
15-30	5.94e-09	1.94e-08	1.83e-08	1.31e-08	1.39e-08	1.33e-08	1.04e-08	1.30e-09	-1.65e-09	2.93e-09	1.96e-09	-4.21e-09	-1.48e-09	-3.57e-09	-1.20e-09	-1.18e-09	-2.80e-10	2.53e-11
30-45	5.25e-09	1.83e-08	3.75e-08	2.89e-08	2.07e-08	1.95e-08	1.22e-08	-3.03e-09	-8.01e-09	-4.45e-09	-4.32e-09	-9.35e-09	-6.27e-09	-6.06e-09	-2.42e-09	-2.73e-09	-5.47e-10	5.95e-12
45-60	5.58e-09	1.31e-08	2.89e-08	4.16e-08	2.94e-08	1.90e-08	7.15e-09	-4.29e-09	-8.08e-09	-7.72e-09	-9.29e-09	-1.23e-08	-8.64e-09	-7.01e-09	-4.59e-09	-3.94e-09	-7.27e-10	-1.57e-11
60-75	4.82e-09	1.39e-08	2.07e-08	2.94e-08	4.68e-08	2.46e-08	6.34e-09	6.84e-11	-3.69e-09	-6.72e-09	-1.08e-08	-1.32e-08	-7.33e-09	-8.77e-09	-7.03e-09	-4.56e-09	-1.18e-09	-2.22e-11
75-90	3.76e-09	1.33e-08	1.95e-08	1.90e-08	2.46e-08	3.26e-08	1.42e-08	-3.74e-09	-5.64e-09	-3.93e-09	-6.34e-09	-9.98e-09	-7.42e-09	-6.99e-09	-4.23e-09	-3.67e-09	-8.62e-10	-2.35e-11
90-105	2.13e-09	1.04e-08	1.22e-08	7.15e-09	6.34e-09	1.42e-08	2.73e-08	8.29e-09	-2.24e-09	2.34e-09	2.88e-09	-3.22e-09	-2.52e-09	-4.07e-09	-1.07e-09	-1.78e-09	-6.81e-10	-2.42e-11
105-120	1.66e-10	1.30e-09	-3.03e-09	-4.29e-09	6.84e-11	-3.74e-09	8.29e-09	2.01e-08	9.87e-09	4.82e-09	4.88e-09	2.83e-09	2.85e-09	-3.51e-10	-5.32e-10	-9.73e-11	-3.71e-10	-1.47e-11
120-135	1.90e-11	-1.65e-09	-8.01e-09	-8.08e-09	-3.69e-09	-5.64e-09	-2.24e-09	9.87e-09	1.56e-08	1.14e-08	5.73e-09	3.34e-09	5.11e-09	2.10e-09	9.14e-10	9.52e-10	8.54e-11	-2.01e-12
135-150	2.47e-09	2.93e-09	-4.45e-09	-7.72e-09	-6.72e-09	-3.93e-09	2.34e-09	4.82e-09	1.14e-08	2.37e-08	1.85e-08	5.87e-09	8.85e-09	5.02e-09	4.43e-09	2.64e-09	7.57e-10	5.31e-11
150-165	1.91e-09	1.96e-09	-4.32e-09	-9.29e-09	-1.08e-08	-6.34e-09	2.88e-09	4.88e-09	5.73e-09	1.85e-08	2.29e-08	1.09e-08	9.01e-09	5.62e-09	5.43e-09	3.21e-09	8.97e-10	7.07e-11
165-180	-7.74e-10	-4.21e-09	-9.35e-09	-1.23e-08	-1.32e-08	-9.98e-09	-3.22e-09	2.83e-09	3.34e-09	5.87e-09	1.09e-08	1.19e-08	7.64e-09	4.20e-09	3.40e-09	2.62e-09	6.42e-10	3.95e-11
180-200	7.16e-10	-1.48e-09	-6.27e-09	-8.64e-09	-7.33e-09	-7.42e-09	-2.52e-09	2.85e-09	5.11e-09	8.85e-09	9.01e-09	7.64e-09	1.07e-08	5.08e-09	3.41e-09	2.73e-09	7.67e-10	5.50e-11
200-230	-3.62e-10	-3.57e-09	-6.06e-09	-7.01e-09	-8.77e-09	-6.99e-09	-4.07e-09	-3.51e-10	2.10e-09	5.02e-09	5.62e-09	4.20e-09	5.08e-09	5.79e-09	3.16e-09	2.09e-09	7.08e-10	4.02e-11
230-265	1.45e-10	-1.20e-09	-2.42e-09	-4.59e-09	-7.03e-09	-4.23e-09	-1.07e-09	-5.32e-10	9.14e-10	4.43e-09	5.43e-09	3.40e-09	3.41e-09	3.16e-09	3.96e-09	1.77e-09	5.77e-10	3.61e-11
265-325	-3.89e-12	-1.18e-09	-2.73e-09	-3.94e-09	-4.56e-09	-3.67e-09	-1.78e-09	-9.73e-11	9.52e-10	2.64e-09	3.21e-09	2.62e-09	2.73e-09	2.09e-09	1.77e-09	1.68e-09	4.03e-10	3.00e-11
325-450	8.93e-11	-2.80e-10	-5.47e-10	-7.27e-10	-1.18e-09	-8.62e-10	-6.81e-10	-3.71e-10	8.54e-11	7.57e-10	8.97e-10	6.42e-10	7.67e-10	7.08e-10	5.77e-10	4.03e-10	2.02e-10	1.14e-11
450-1000	1.72e-11	2.53e-11	5.95e-12	-1.57e-11	-2.22e-11	-2.35e-11	-2.42e-11	-1.47e-11	-2.01e-12	5.31e-11	7.07e-11	3.95e-11	5.50e-11	4.02e-11	3.61e-11	3.00e-11	1.14e-11	1.97e-12

bin [GeV]	0-15	15-30	30-45	45-60	60-75	75-90	90-105	105-120	120-135	135-150	150-165	165-180	180-200	200-230	230-265	265-325	325-450	450-1000
0-15	4.53e-09	3.93e-09	2.66e-09	4.77e-09	4.31e-09	4.36e-09	4.08e-09	3.08e-09	1.17e-09	2.88e-10	-1.22e-10	-8.51e-10	-2.06e-09	7.06e-10	3.61e-10	-1.36e-10	4.15e-11	1.95e-11
15-30	3.93e-09	2.10e-08	1.00e-08	9.90e-09	8.41e-09	1.72e-08	1.46e-08	9.14e-09	6.47e-09	-2.71e-09	6.65e-10	-2.16e-09	-3.44e-09	4.73e-09	1.09e-09	-8.24e-10	-2.63e-11	4.15e-11
30-45	2.66e-09	1.00e-08	2.91e-08	1.89e-08	1.35e-08	1.63e-08	1.42e-08	9.35e-09	3.30e-09	1.83e-09	-2.63e-09	-5.80e-09	-7.08e-09	-3.68e-09	-3.70e-09	-2.94e-09	-1.13e-09	-5.08e-11
45-60	4.77e-09	9.90e-09	1.89e-08	3.67e-08	1.99e-08	1.13e-08	1.28e-08	6.47e-09	2.33e-09	-3.13e-09	-4.80e-09	-7.54e-09	-1.08e-08	-4.04e-09	-5.05e-09	-4.44e-09	-1.37e-09	-6.45e-11
60-75	4.31e-09	8.41e-09	1.35e-08	1.99e-08	3.87e-08	2.27e-08	1.11e-08	1.16e-08	2.36e-09	2.56e-09	-3.47e-09	-6.19e-09	-7.79e-09	-5.07e-09	-2.61e-09	-2.38e-09	-1.45e-09	-1.02e-10
75-90	4.36e-09	1.72e-08	1.63e-08	1.13e-08	2.27e-08	5.23e-08	3.32e-08	2.07e-08	1.06e-08	6.05e-09	3.33e-09	-2.81e-09	-2.27e-09	3.61e-09	1.29e-09	-1.11e-09	-7.30e-10	-1.12e-11
90-105	4.08e-09	1.46e-08	1.42e-08	1.28e-08	1.11e-08	3.32e-08	4.39e-08	2.79e-08	1.11e-08	5.25e-09	4.13e-09	-1.05e-09	-3.44e-09	5.25e-09	1.24e-09	-2.00e-09	-5.75e-10	-1.59e-11
105-120	3.08e-09	9.14e-09	9.35e-09	6.47e-09	1.16e-08	2.07e-08	2.79e-08	4.24e-08	2.02e-08	7.45e-09	4.49e-09	1.21e-09	-9.72e-10	5.01e-09	3.47e-09	2.35e-11	-7.14e-11	-6.37e-12
120-135	1.17e-09	6.47e-09	3.30e-09	2.33e-09	2.36e-09	1.06e-08	1.11e-08	2.02e-08	2.57e-08	8.21e-09	1.88e-09	-3.53e-10	-1.27e-09	5.35e-09	5.93e-10	-8.61e-10	-1.30e-11	-1.00e-11
135-150	2.88e-10	-2.71e-09	1.83e-09	-3.13e-09	2.56e-09	6.05e-09	5.25e-09	7.45e-09	8.21e-09	1.82e-08	6.55e-09	4.74e-11	8.02e-10	8.42e-10	1.69e-09	8.70e-10	5.89e-11	4.45e-12
150-165	-1.22e-10	6.65e-10	-2.63e-09	-4.80e-09	-3.47e-09	3.33e-09	4.13e-09	4.49e-09	1.88e-09	6.55e-09	1.19e-08	6.24e-09	2.21e-09	4.42e-09	3.64e-09	1.55e-09	6.44e-10	5.98e-11
165-180	-8.51e-10	-2.16e-09	-5.80e-09	-7.54e-09	-6.19e-09	-2.81e-09	-1.05e-09	1.21e-09	-3.53e-10	4.74e-11	6.24e-09	1.08e-08	6.19e-09	3.01e-09	3.81e-09	2.13e-09	7.94e-10	6.29e-11
180-200	-2.06e-09	-3.44e-09	-7.08e-09	-1.08e-08	-7.79e-09	-2.27e-09	-3.44e-09	-9.72e-10	-1.27e-09	8.02e-10	2.21e-09	6.19e-09	1.20e-08	3.90e-09	3.77e-09	2.88e-09	9.14e-10	8.34e-11
200-230	7.06e-10	4.73e-09	-3.68e-09	-4.04e-09	-5.07e-09	3.61e-09	5.25e-09	5.01e-09	5.35e-09	8.42e-10	4.42e-09	3.01e-09	3.90e-09	1.24e-08	5.74e-09	2.43e-09	1.31e-09	1.27e-10
230-265	3.61e-10	1.09e-09	-3.70e-09	-5.05e-09	-2.61e-09	1.29e-09	1.24e-09	3.47e-09	5.93e-10	1.69e-09	3.64e-09	3.81e-09	3.77e-09	5.74e-09	8.39e-09	3.41e-09	1.31e-09	1.29e-10
265-325	-1.36e-10	-8.24e-10	-2.94e-09	-4.44e-09	-2.38e-09	-1.11e-09	-2.00e-09	-2.35e-11	-8.61e-10	8.70e-10	1.55e-09	2.13e-09	2.88e-09	2.43e-09	3.41e-09	3.04e-09	8.00e-10	8.09e-11
325-450	4.15e-11	-2.63e-11	-1.13e-09	-1.37e-09	-1.45e-09	-7.30e-10	-5.75e-10	-7.14e-11	-1.30e-11	5.89e-11	6.44e-10	7.94e-10	9.14e-10	1.31e-09	1.31e-09	8.00e-10	4.66e-10	3.62e-11
450-1000	1.95e-11	4.15e-11	-5.08e-11	-6.45e-11	-1.02e-10	-1.12e-11	-1.59e-11	-6.37e-12	-1.00e-11	4.45e-12	5.98e-11	6.29e-11	8.34e-11	1.27e-10	1.29e-10	8.09e-11	3.62e-11	6.25e-12

bin [GeV]	0-15	15-30	30-45	45-60	60-75	75-90	90-105	105-120	120-135	135-150	150-165	165-180	180-200	200-230	230-265	265-325	325-450	450-1000
0-15	6.30e-09	3.97e-09	3.51e-09	8.88e-09	1.01e-08	6.00e-09	3.47e-09	6.13e-09	8.78e-09	8.54e-10	1.57e-09	5.99e-10	-2.79e-10	-9.29e-10	1.93e-09	-7.25e-10	-9.66e-10	-2.22e-13
15-30	3.97e-09	1.99e-08	1.34e-08	1.53e-08	1.43e-08	1.21e-08	6.90e-09	7.37e-09	6.40e-09	1.04e-09	2.54e-09	1.84e-09	3.80e-09	-3.02e-11	5.86e-10	4.87e-10	-1.43e-09	1.07e-12
30-45	3.51e-09	1.34e-08	3.67e-08	3.05e-08	1.91e-08	1.91e-08	9.61e-09	9.85e-09	1.31e-08	-2.57e-09	-2.99e-10	-2.16e-09	-1.90e-10	-5.35e-09	-3.85e-09	-1.90e-09	-3.18e-09	-9.47e-11
45-60	8.88e-09	1.53e-08	3.05e-08	6.26e-08	4.44e-08	2.86e-08	1.29e-08	2.09e-08	2.84e-08	-2.52e-09	2.80e-09	1.09e-09	2.28e-09	-6.86e-09	-3.21e-09	-2.43e-09	-5.02e-09	-9.07e-11
60-75	1.01e-08	1.43e-08	1.91e-08	4.44e-08	6.40e-08	3.23e-08	9.15e-09	1.88e-08	3.32e-08	3.56e-09	8.06e-09	1.09e-09	1.51e-09	-6.04e-09	1.14e-09	-1.53e-09	-4.32e-09	-5.09e-11
75-90	6.00e-09	1.21e-08	1.91e-08	2.86e-08	3.23e-08	4.69e-08	1.42e-08	9.02e-09	1.34e-08	-3.14e-09	-1.26e-09	-3.86e-09	-1.49e-09	-7.34e-09	-7.28e-09	-4.46e-09	-4.09e-09	-1.76e-10
90-105	3.47e-09	6.90e-09	9.61e-09	1.29e-08	9.15e-09	1.48e-08	2.85e-08	1.41e-08	7.66e-10	-3.07e-09	-1.74e-09	-1.03e-09	-2.83e-09	-4.57e-09	-1.55e-09	-3.35e-09	-2.10e-09	-1.32e-10
105-120	6.13e-09	7.37e-09	9.85e-09	2.09e-08	1.88e-08	9.02e-09	1.41e-08	3.80e-08	2.35e-08	-5.25e-09	-3.85e-09	2.02e-09	-2.60e-09	-3.30e-09	2.05e-09	-4.08e-09	-3.21e-09	-1.00e-10
120-135	8.78e-09	6.40e-09	1.31e-08	2.84e-08	3.32e-08	1.34e-08	7.66e-10	2.35e-08	5.75e-08	1.06e-08	1.22e-08	4.44e-09	6.31e-09	-1.86e-11	1.02e-08	3.02e-09	-2.79e-09	1.84e-10
135-150	8.54e-10	1.04e-09	-2.57e-09	-2.52e-09	3.56e-09	-3.14e-09	-3.07e-09	-5.25e-09	1.06e-08	2.63e-08	1.77e-08	3.13e-09	5.84e-09	5.18e-09	9.56e-09	5.28e-09	1.44e-09	1.43e-10
150-165	1.57e-09	2.54e-09	-2.99e-10	2.80e-09	8.06e-09	-3.86e-09	-1.74e-09	-3.85e-09	1.22e-08	1.77e-08	3.76e-08	1.55e-08	1.46e-08	7.11e-09	1.53e-08	1.08e-08	2.06e-09	3.21e-10
165-180	5.99e-10	1.84e-09	-2.16e-09	1.09e-09	1.09e-09	-1.59e-09	-1.03e-09	2.02e-09	4.44e-09	3.13e-09	1.55e-08	1.68e-08	1.24e-08	3.54e-09	7.94e-09	5.45e-09	1.08e-09	1.66e-10
180-200	-2.79e-10	3.80e-09	-1.90e-10	2.28e-09	1.51e-09	-1.26e-09	-2.83e-09	-2.60e-09	6.31e-09	5.84e-09	1.46e-08	1.24e-08	2.28e-08	8.12e-09	7.86e-09	9.06e-09	1.65e-09	2.53e-10
200-230	-9.29e-10	-3.02e-11	-5.35e-09	-6.86e-09	-6.04e-09	-7.34e-09	-4.57e-09	-3.30e-09	-1.86e-11	5.18e-09	7.11e-09	3.54e-09	8.12e-09	1.15e-08	7.39e-09	4.78e-09	1.69e-09	1.68e-10
230-265	1.93e-09	5.86e-10	-3.85e-09	-3.21e-09	1.14e-09	-7.28e-09	-1.55e-09	2.05e-09	1.02e-08	9.56e-09	1.53e-08	7.94e-09	7.86e-09	7.39e-09	1.77e-08	6.12e-09	1.84e-09	2.57e-10
265-325	-7.25e-10	4.87e-10	-1.90e-09	-2.43e-09	-1.53e-09	-1.46e-09	-1.35e-09	4.08e-09	3.02e-09	5.28e-09	1.08e-08	5.45e-09	9.06e-09	4.78e-09	6.12e-09	7.29e-09	1.42e-09	1.88e-10
325-450	-9.66e-10	-1.43e-09	-3.18e-09	-5.02e-09	-4.32e-09	-4.09e-09	-2.10e-09	-3.21e-09	-2.79e-09	1.44e-09	2.06e-09	1.08e-09	1.65e-09	1.69e-09	1.84e-09	1.42e-09	1.10e-09	4.73e-11
450-1000	-2.22e-13	1.07e-12	-9.47e-11	-9.07e-11	-5.09e-11	-1.76e-10	-1.32e-10	-1.00e-10	1.84e-10	1.43e-10	3.21e-10	1.66e-10	2.53e-10	1.68e-10	2.57e-10	1.88e-10	4.73e-11	1.16e-11

TABLE D.4: Covariance matrix of the normalised cross-section as function of $p_{\mathrm{T}}^{\mathrm{t,had}}$ in the 4-jet exclusive (top), 5-jet exclusive (centre) and 6-jet inclusive (bottom) configurations, accounting for the statistical and systematic uncertainties.

bin [GeV]	0-15	15-35	35-75	75-125	125-170	170-800
0-15	3.26e-06	2.48e-06	4.49e-07	2.42e-08	-1.21e-09	2.22e-10
15-35	2.48e-06	1.96e-06	3.92e-07	6.29e-09	-1.12e-08	-5.79e-11
35-75	4.49e-07	3.92e-07	8.25e-07	2.22e-07	2.54e-08	4.55e-10
75-125	2.42e-08	6.29e-09	2.22e-07	7.44e-08	1.25e-08	2.33e-10
125-170	-1.21e-09	-1.12e-08	2.54e-08	1.25e-08	4.39e-09	8.45e-11
170-800	2.22e-10	-5.79e-11	4.55e-10	2.33e-10	8.45e-11	2.76e-12

bin [GeV]	0-35	35-75	75-125	125-170	170-225	225-800
0-35	8.76e-08	6.91e-08	2.61e-08	8.75e-09	-2.59e-09	-1.21e-09
35-75	6.91e-08	8.12e-08	1.52e-08	-2.89e-09	-6.16e-09	-1.54e-09
75-125	2.61e-08	1.52e-08	3.99e-08	2.11e-08	6.67e-09	3.26e-10
125-170	8.75e-09	-2.89e-09	2.11e-08	1.92e-08	6.85e-09	6.08e-10
170-225	-2.59e-09	-6.16e-09	6.67e-09	6.85e-09	5.92e-09	5.23e-10
225-800	-1.21e-09	-1.54e-09	3.26e-10	6.08e-10	5.23e-10	9.84e-11

bin [GeV]	0-35	35-75	75-125	125-170	170-225	225-800
0-35	1.31e-08	1.66e-08	7.54e-09	3.52e-09	-3.06e-10	-1.02e-09
35-75	1.66e-08	4.94e-08	2.08e-08	-4.24e-10	-3.59e-09	-3.01e-09
75-125	7.54e-09	2.08e-08	1.98e-08	3.02e-09	-7.81e-10	-1.54e-09
125-170	3.52e-09	-4.24e-10	3.02e-09	1.63e-08	6.07e-09	3.40e-10
170-225	-3.06e-10	-3.59e-09	-7.81e-10	6.07e-09	9.18e-09	7.97e-10
225-800	-1.02e-09	-3.01e-09	-1.54e-09	3.40e-10	7.97e-10	3.97e-10

TABLE D.5: Covariance matrix of the normalised cross-section as function of $p_{\mathrm{T}}^{\mathrm{t\bar{t}}}$ in the 4-jet exclusive (top), 5-jet exclusive (centre) and 6-jet inclusive (bottom) configurations, accounting for the statistical and systematic uncertainties.

bin [GeV]	0-40	40-80	80-120	120-170	170-230	230-600
0-40	2.89e-07	5.14e-08	2.84e-09	5.56e-09	7.17e-10	-1.07e-11
40-80	5.14e-08	1.69e-07	3.45e-08	7.04e-09	1.22e-09	7.45e-12
80-120	2.84e-09	3.45e-08	8.09e-09	1.20e-09	2.14e-10	2.63e-12
120-170	5.56e-09	7.04e-09	1.20e-09	6.91e-10	8.99e-11	2.06e-13
170-230	7.17e-10	1.22e-09	2.14e-10	8.99e-11	3.15e-11	-7.04e-14
230-600	-1.07e-11	7.45e-12	2.63e-12	2.06e-13	-7.04e-14	5.09e-14
bin [GeV]	0-40	40-80	80-120	120-170	170-230	230-600
0-40	3.16e-07	-3.83e-08	-2.20e-08	-3.02e-09	3.48e-09	6.47e-10
40-80	-3.83e-08	1.59e-07	5.42e-08	8.09e-09	2.12e-09	1.38e-10
80-120	-2.20e-08	5.42e-08	2.13e-08	3.90e-09	9.63e-10	5.88e-11
120-170	-3.02e-09	8.09e-09	3.90e-09	1.46e-09	3.60e-10	3.12e-11
170-230	3.48e-09	2.12e-09	9.63e-10	3.60e-10	2.86e-10	1.99e-11
230-600	6.47e-10	1.38e-10	5.88e-11	3.12e-11	1.99e-11	4.53e-12
bin [GeV]	0-40	40-80	80-120	120-170	170-230	230-600
0-40	8.02e-08	-1.46e-08	-3.19e-08	-1.41e-08	-6.45e-09	-6.92e-10
40-80	-1.46e-08	1.14e-08	3.68e-09	-7.41e-11	-2.14e-10	-3.27e-12
80-120	-3.19e-08	3.68e-09	1.80e-08	4.40e-09	1.88e-09	2.12e-10
120-170	-1.41e-08	-7.41e-11	4.40e-09	4.68e-09	1.61e-09	1.66e-10
170-230	-6.45e-09	-2.14e-10	1.88e-09	1.61e-09	1.32e-09	8.52e-11
230-600	-6.92e-10	-3.27e-12	2.12e-10	1.66e-10	8.52e-11	1.60e-11
bin [GeV]	0-40	40-80	80-120	120-170	170-230	230-600
0-40	1.29e-07	1.60e-08	-4.51e-09	-2.17e-08	-1.40e-08	-1.46e-09
40-80	1.60e-08	2.11e-08	2.42e-09	-2.32e-09	-1.57e-09	-3.74e-11
80-120	-4.51e-09	2.42e-09	2.97e-08	7.87e-09	5.73e-09	9.15e-10
120-170	-2.17e-08	-2.32e-09	7.87e-09	1.08e-08	5.23e-09	6.52e-10
170-230	-1.40e-08	-1.57e-09	5.73e-09	5.23e-09	5.91e-09	4.90e-10
230-600	-1.46e-09	-3.74e-11	9.15e-10	6.52e-10	4.90e-10	8.29e-11

TABLE D.6: Covariance matrix of the normalised cross-section as function of $p_{\mathrm{out}}^{\mathrm{t\bar{t}}}$ in the 4-jet exclusive, 4-jet inclusive, 5-jet exclusive and 6-jet inclusive configurations, accounting for the statistical and systematic uncertainties.

bin [GeV]	0-15	15-30	30-45	45-60	60-75	75-90	90-105	105-120	120-135	135-150	150-165	165-180	180-200	200-230	230-265	265-325	325-450	450-1000
0-15	**1.00**	0.84	0.78	0.82	0.81	0.79	0.81	0.80	0.77	0.79	0.76	0.72	0.72	0.71	0.67	0.61	0.55	0.54
15-30	0.84	**1.00**	0.92	0.91	0.92	0.92	0.93	0.90	0.86	0.84	0.83	0.79	0.74	0.68	0.63	0.54	0.46	0.49
30-45	0.78	0.92	**1.00**	0.96	0.93	0.94	0.93	0.90	0.87	0.84	0.81	0.79	0.74	0.71	0.64	0.54	0.48	0.51
45-60	0.82	0.91	0.96	**1.00**	0.96	0.95	0.93	0.92	0.89	0.87	0.84	0.81	0.77	0.74	0.66	0.56	0.52	0.52
60-75	0.81	0.92	0.93	0.96	**1.00**	0.97	0.94	0.94	0.92	0.89	0.85	0.83	0.80	0.74	0.64	0.57	0.50	0.53
75-90	0.79	0.92	0.94	0.95	0.97	**1.00**	0.96	0.93	0.92	0.90	0.86	0.84	0.80	0.75	0.65	0.56	0.50	0.53
90-105	0.81	0.93	0.93	0.93	0.94	0.96	**1.00**	0.96	0.92	0.91	0.90	0.86	0.82	0.78	0.72	0.63	0.54	0.57
105-120	0.80	0.90	0.90	0.92	0.94	0.93	0.96	**1.00**	0.97	0.93	0.91	0.89	0.86	0.80	0.71	0.65	0.55	0.57
120-135	0.77	0.86	0.87	0.89	0.92	0.92	0.92	0.97	**1.00**	0.96	0.91	0.90	0.89	0.83	0.71	0.67	0.57	0.59
135-150	0.79	0.84	0.84	0.87	0.89	0.90	0.91	0.93	0.96	**1.00**	0.95	0.90	0.90	0.87	0.78	0.73	0.64	0.65
150-165	0.76	0.83	0.81	0.84	0.85	0.86	0.90	0.91	0.91	0.95	**1.00**	0.95	0.87	0.85	0.80	0.73	0.64	0.63
165-180	0.72	0.79	0.79	0.81	0.83	0.84	0.86	0.89	0.90	0.90	0.95	**1.00**	0.92	0.83	0.76	0.73	0.63	0.62
180-200	0.72	0.74	0.74	0.77	0.80	0.80	0.82	0.86	0.89	0.90	0.87	0.92	**1.00**	0.90	0.78	0.81	0.71	0.71
200-230	0.71	0.68	0.71	0.74	0.74	0.75	0.78	0.80	0.83	0.87	0.85	0.83	0.90	**1.00**	0.86	0.84	0.80	0.75
230-265	0.67	0.63	0.64	0.66	0.64	0.65	0.72	0.71	0.71	0.78	0.80	0.76	0.78	0.86	**1.00**	0.83	0.79	0.75
265-325	0.61	0.54	0.54	0.56	0.57	0.56	0.63	0.65	0.67	0.73	0.73	0.73	0.81	0.84	0.83	**1.00**	0.82	0.80
325-450	0.55	0.46	0.48	0.52	0.50	0.50	0.54	0.55	0.57	0.64	0.64	0.63	0.71	0.80	0.79	0.82	**1.00**	0.77
450-1000	0.54	0.49	0.51	0.52	0.53	0.53	0.57	0.57	0.59	0.65	0.63	0.62	0.71	0.75	0.75	0.80	0.77	**1.00**

bin [GeV]	0-15	15-30	30-45	45-60	60-75	75-90	90-105	105-120	120-135	135-150	150-165	165-180	180-200	200-230	230-265	265-325	325-450	450-1000
0-15	**1.00**	0.83	0.82	0.85	0.84	0.82	0.82	0.82	0.81	0.80	0.79	0.77	0.72	0.72	0.64	0.62	0.51	0.27
15-30	0.83	**1.00**	0.90	0.91	0.91	0.93	0.93	0.90	0.90	0.86	0.88	0.86	0.81	0.85	0.75	0.67	0.61	0.38
30-45	0.82	0.90	**1.00**	0.96	0.95	0.94	0.94	0.94	0.93	0.93	0.91	0.90	0.87	0.80	0.73	0.71	0.58	0.29
45-60	0.85	0.91	0.96	**1.00**	0.97	0.94	0.95	0.94	0.93	0.92	0.92	0.91	0.86	0.83	0.76	0.71	0.62	0.36
60-75	0.84	0.91	0.95	0.97	**1.00**	0.96	0.95	0.95	0.94	0.94	0.92	0.91	0.88	0.82	0.74	0.71	0.60	0.32
75-90	0.82	0.93	0.94	0.94	0.96	**1.00**	0.97	0.94	0.94	0.93	0.93	0.91	0.88	0.86	0.75	0.71	0.60	0.35
90-105	0.82	0.93	0.94	0.95	0.95	0.97	**1.00**	0.97	0.96	0.94	0.95	0.93	0.90	0.89	0.79	0.73	0.65	0.38
105-120	0.82	0.90	0.94	0.94	0.95	0.94	0.97	**1.00**	0.98	0.95	0.95	0.94	0.91	0.88	0.80	0.75	0.66	0.35
120-135	0.81	0.90	0.93	0.93	0.94	0.94	0.96	0.98	**1.00**	0.96	0.95	0.93	0.90	0.89	0.81	0.75	0.68	0.38
135-150	0.80	0.86	0.93	0.92	0.94	0.93	0.94	0.95	0.96	**1.00**	0.96	0.93	0.92	0.85	0.78	0.77	0.65	0.33
150-165	0.79	0.88	0.91	0.92	0.92	0.93	0.95	0.95	0.95	0.96	**1.00**	0.97	0.91	0.89	0.84	0.78	0.72	0.42
165-180	0.77	0.86	0.90	0.91	0.91	0.91	0.93	0.94	0.93	0.93	0.97	**1.00**	0.94	0.88	0.83	0.78	0.72	0.43
180-200	0.72	0.81	0.87	0.86	0.88	0.88	0.90	0.91	0.90	0.92	0.91	0.94	**1.00**	0.85	0.80	0.80	0.70	0.41
200-230	0.72	0.85	0.80	0.83	0.82	0.86	0.89	0.88	0.89	0.85	0.89	0.88	0.85	**1.00**	0.86	0.74	0.78	0.54
230-265	0.64	0.75	0.73	0.76	0.74	0.75	0.79	0.80	0.81	0.78	0.84	0.83	0.80	0.86	**1.00**	0.76	0.81	0.59
265-325	0.62	0.67	0.71	0.71	0.71	0.71	0.73	0.75	0.75	0.77	0.78	0.78	0.80	0.74	0.76	**1.00**	0.72	0.51
325-450	0.51	0.61	0.58	0.62	0.60	0.60	0.65	0.66	0.68	0.65	0.72	0.72	0.70	0.78	0.81	0.72	**1.00**	0.69
450-1000	0.27	0.38	0.29	0.36	0.32	0.35	0.38	0.35	0.38	0.33	0.42	0.43	0.41	0.54	0.59	0.51	0.69	**1.00**

bin [GeV]	0-15	15-30	30-45	45-60	60-75	75-90	90-105	105-120	120-135	135-150	150-165	165-180	180-200	200-230	230-265	265-325	325-450	450-1000
0-15	**1.00**	0.92	0.91	0.92	0.93	0.93	0.93	0.93	0.93	0.92	0.90	0.90	0.88	0.90	0.88	0.76	0.81	0.58
15-30	0.92	**1.00**	0.97	0.97	0.95	0.96	0.96	0.96	0.95	0.96	0.92	0.94	0.92	0.92	0.86	0.78	0.83	0.59
30-45	0.91	0.97	**1.00**	0.98	0.96	0.97	0.97	0.97	0.96	0.97	0.93	0.94	0.94	0.93	0.88	0.79	0.83	0.58
45-60	0.92	0.97	0.98	**1.00**	0.97	0.98	0.98	0.98	0.97	0.97	0.93	0.95	0.94	0.94	0.89	0.79	0.84	0.58
60-75	0.93	0.95	0.96	0.97	**1.00**	0.98	0.98	0.97	0.97	0.96	0.97	0.96	0.95	0.95	0.91	0.85	0.85	0.65
75-90	0.93	0.96	0.97	0.98	0.98	**1.00**	0.99	0.97	0.98	0.97	0.96	0.96	0.95	0.95	0.90	0.84	0.86	0.63
90-105	0.93	0.96	0.97	0.98	0.98	0.99	**1.00**	0.99	0.98	0.97	0.96	0.97	0.96	0.96	0.92	0.83	0.86	0.63
105-120	0.93	0.96	0.97	0.98	0.97	0.97	0.99	**1.00**	0.99	0.97	0.95	0.96	0.96	0.96	0.92	0.82	0.86	0.62
120-135	0.93	0.95	0.96	0.97	0.97	0.98	0.98	0.99	**1.00**	0.98	0.95	0.96	0.95	0.96	0.93	0.83	0.87	0.64
135-150	0.92	0.96	0.97	0.97	0.96	0.97	0.97	0.97	0.98	**1.00**	0.94	0.95	0.93	0.94	0.91	0.81	0.86	0.61
150-165	0.90	0.92	0.93	0.93	0.97	0.96	0.96	0.95	0.95	0.94	**1.00**	0.98	0.93	0.95	0.93	0.91	0.87	0.73
165-180	0.90	0.94	0.94	0.95	0.96	0.96	0.97	0.96	0.96	0.95	0.98	**1.00**	0.96	0.95	0.92	0.88	0.89	0.70
180-200	0.88	0.92	0.94	0.94	0.95	0.95	0.96	0.96	0.95	0.93	0.93	0.96	**1.00**	0.95	0.88	0.85	0.86	0.64
200-230	0.90	0.92	0.93	0.94	0.95	0.95	0.96	0.96	0.96	0.94	0.95	0.95	0.95	**1.00**	0.93	0.87	0.87	0.69
230-265	0.88	0.86	0.88	0.89	0.91	0.90	0.92	0.92	0.93	0.91	0.93	0.92	0.88	0.93	**1.00**	0.83	0.86	0.70
265-325	0.76	0.78	0.79	0.79	0.85	0.84	0.83	0.82	0.83	0.81	0.91	0.88	0.85	0.87	0.83	**1.00**	0.80	0.79
325-450	0.81	0.83	0.83	0.84	0.85	0.86	0.86	0.86	0.87	0.86	0.87	0.89	0.86	0.87	0.86	0.80	**1.00**	0.71
450-1000	0.58	0.59	0.58	0.58	0.65	0.63	0.63	0.62	0.64	0.61	0.73	0.70	0.64	0.69	0.70	0.79	0.71	**1.00**

TABLE D.7: Correlation matrix of the absolute cross-section as function of $p_{\mathrm{T}}^{\mathrm{t,had}}$ in the 4-jet exclusive (top) , 5-jet exclusive (centre) and 6-jet inclusive (bottom) configurations, accounting for the statistical and systematic uncertainties.

bin [GeV]	0-15	15-35	35-75	75-125	125-170	170-800
0-15	**1.00**	0.94	0.41	0.21	0.13	0.24
15-35	0.94	**1.00**	0.62	0.35	0.20	0.29
35-75	0.41	0.62	**1.00**	0.90	0.64	0.60
75-125	0.21	0.35	0.90	**1.00**	0.79	0.68
125-170	0.13	0.20	0.64	0.79	**1.00**	0.84
170-800	0.24	0.29	0.60	0.68	0.84	**1.00**
bin [GeV]	0-35	35-75	75-125	125-170	170-225	225-800
0-35	**1.00**	0.96	0.90	0.84	0.71	0.41
35-75	0.96	**1.00**	0.92	0.83	0.72	0.45
75-125	0.90	0.92	**1.00**	0.94	0.84	0.60
125-170	0.84	0.83	0.94	**1.00**	0.86	0.63
170-225	0.71	0.72	0.84	0.86	**1.00**	0.73
225-800	0.41	0.45	0.60	0.63	0.73	**1.00**
bin [GeV]	0-35	35-75	75-125	125-170	170-225	225-800
0-35	**1.00**	0.99	0.98	0.96	0.95	0.92
35-75	0.99	**1.00**	0.99	0.96	0.95	0.93
75-125	0.98	0.99	**1.00**	0.97	0.96	0.94
125-170	0.96	0.96	0.97	**1.00**	0.98	0.95
170-225	0.95	0.95	0.96	0.98	**1.00**	0.95
225-800	0.92	0.93	0.94	0.95	0.95	**1.00**

TABLE D.8: Correlation matrix of the absolute cross-section as function of $p_{\mathrm{T}}^{\mathrm{t\bar{t}}}$ in the 4-jet exclusive (top), 5-jet exclusive (centre) and 6-jet inclusive (bottom) configurations, accounting for the statistical and systematic uncertainties.

bin [GeV]	0-40	40-80	80-120	120-170	170-230	230-600
0-40	**1.00**	0.61	0.55	0.35	0.13	0.33
40-80	0.61	**1.00**	0.93	0.75	0.54	0.62
80-120	0.55	0.93	**1.00**	0.65	0.48	0.53
120-170	0.35	0.75	0.65	**1.00**	0.64	0.73
170-230	0.13	0.54	0.48	0.64	**1.00**	0.48
230-600	0.33	0.62	0.53	0.73	0.48	**1.00**
bin [GeV]	0-40	40-80	80-120	120-170	170-230	230-600
0-40	**1.00**	0.85	0.78	0.81	0.74	0.74
40-80	0.85	**1.00**	0.98	0.93	0.82	0.63
80-120	0.78	0.98	**1.00**	0.95	0.84	0.62
120-170	0.81	0.93	0.95	**1.00**	0.89	0.74
170-230	0.74	0.82	0.84	0.89	**1.00**	0.71
230-600	0.74	0.63	0.62	0.74	0.71	**1.00**
bin [GeV]	0-40	40-80	80-120	120-170	170-230	230-600
0-40	**1.00**	0.97	0.85	0.61	0.33	0.13
40-80	0.97	**1.00**	0.91	0.67	0.37	0.18
80-120	0.85	0.91	**1.00**	0.71	0.37	0.23
120-170	0.61	0.67	0.71	**1.00**	0.64	0.51
170-230	0.33	0.37	0.37	0.64	**1.00**	0.46
230-600	0.13	0.18	0.23	0.51	0.46	**1.00**
bin [GeV]	0-40	40-80	80-120	120-170	170-230	230-600
0-40	**1.00**	0.99	0.94	0.94	0.88	0.62
40-80	0.99	**1.00**	0.96	0.95	0.89	0.65
80-120	0.94	0.96	**1.00**	0.95	0.89	0.76
120-170	0.94	0.95	0.95	**1.00**	0.89	0.71
170-230	0.88	0.89	0.89	0.89	**1.00**	0.68
230-600	0.62	0.65	0.76	0.71	0.68	**1.00**

TABLE D.9: Correlation matrix of the absolute cross-section as function of $p_{\mathrm{out}}^{\mathrm{t\bar{t}}}$ respectively in the 4-jet exclusive, 4-jet inclusive, 5-jet exclusive and 6-jet inclusive configurations, accounting for the statistical and systematic uncertainties.

bin [GeV]	0-15	15-30	30-45	45-60	60-75	75-90	90-105	105-120	120-135	135-150	150-165	165-180	180-200	200-230	230-265	265-325	325-450	450-1000
0-15	**1.00**	0.60	0.38	0.39	0.33	0.30	0.17	0.02	0.02	0.24	0.17	-0.12	0.08	-0.07	0.01	-0.02	0.06	0.16
15-30	0.60	**1.00**	0.67	0.46	0.47	0.53	0.46	0.09	-0.08	0.14	0.09	-0.28	-0.11	-0.35	-0.15	-0.22	-0.16	0.11
30-45	0.38	0.67	**1.00**	0.73	0.50	0.56	0.39	-0.10	-0.32	-0.15	-0.16	-0.45	-0.33	-0.42	-0.21	-0.35	-0.21	0.02
45-60	0.39	0.46	0.73	**1.00**	0.67	0.51	0.20	-0.15	-0.31	-0.24	-0.31	-0.56	-0.42	-0.44	-0.36	-0.47	-0.25	-0.06
60-75	0.33	0.47	0.50	0.67	**1.00**	0.64	0.17	0.01	-0.14	-0.21	-0.34	-0.56	-0.34	-0.54	-0.52	-0.52	-0.39	-0.09
75-90	0.30	0.53	0.56	0.51	0.64	**1.00**	0.48	-0.13	-0.25	-0.15	-0.25	-0.52	-0.41	-0.51	-0.38	-0.50	-0.36	-0.10
90-105	0.17	0.46	0.39	0.20	0.17	0.48	**1.00**	0.36	-0.10	0.10	0.12	-0.17	-0.15	-0.33	-0.11	-0.26	-0.30	-0.12
105-120	0.02	0.09	-0.10	-0.15	0.01	-0.13	0.36	**1.00**	0.55	0.21	0.24	0.20	0.19	-0.04	-0.05	-0.01	-0.18	-0.09
120-135	0.02	-0.08	-0.32	-0.31	-0.14	-0.25	-0.10	0.55	**1.00**	0.58	0.31	0.25	0.39	0.22	0.13	0.18	0.05	-0.00
135-150	0.24	0.14	-0.15	-0.24	-0.21	-0.15	0.10	0.21	0.58	**1.00**	0.80	0.35	0.56	0.43	0.47	0.42	0.35	0.25
150-165	0.17	0.09	-0.16	-0.31	-0.34	-0.25	0.12	0.24	0.31	0.80	**1.00**	0.66	0.58	0.48	0.57	0.52	0.42	0.33
165-180	-0.12	-0.28	-0.45	-0.56	-0.56	-0.52	-0.17	0.20	0.25	0.35	0.66	**1.00**	0.68	0.49	0.49	0.58	0.41	0.26
180-200	0.08	-0.11	-0.33	-0.42	-0.34	-0.41	-0.15	0.19	0.39	0.56	0.58	0.68	**1.00**	0.65	0.54	0.65	0.53	0.40
200-230	-0.07	-0.35	-0.42	-0.44	-0.54	-0.51	-0.33	-0.04	0.22	0.43	0.48	0.49	0.65	**1.00**	0.67	0.67	0.67	0.39
230-265	0.01	-0.15	-0.21	-0.36	-0.52	-0.38	-0.11	-0.05	0.13	0.47	0.57	0.49	0.54	0.67	**1.00**	0.68	0.65	0.41
265-325	-0.02	-0.22	-0.35	-0.47	-0.52	-0.50	-0.26	-0.01	0.18	0.42	0.52	0.58	0.65	0.67	0.68	**1.00**	0.70	0.54
325-450	0.06	-0.16	-0.21	-0.25	-0.39	-0.36	-0.30	-0.18	0.05	0.35	0.42	0.41	0.53	0.67	0.65	0.70	**1.00**	0.58
450-1000	0.16	0.11	0.02	-0.06	-0.09	-0.10	-0.12	-0.09	-0.00	0.25	0.33	0.26	0.40	0.39	0.41	0.54	0.58	**1.00**

bin [GeV]	0-15	15-30	30-45	45-60	60-75	75-90	90-105	105-120	120-135	135-150	150-165	165-180	180-200	200-230	230-265	265-325	325-450	450-1000
0-15	**1.00**	0.40	0.25	0.37	0.33	0.30	0.30	0.22	0.11	0.04	-0.03	-0.14	-0.28	0.09	0.05	-0.04	0.01	0.10
15-30	0.40	**1.00**	0.43	0.37	0.31	0.53	0.49	0.31	0.28	-0.14	0.03	-0.15	-0.22	0.27	0.07	-0.11	-0.02	0.10
30-45	0.25	0.43	**1.00**	0.58	0.41	0.43	0.40	0.26	0.12	0.09	-0.16	-0.35	-0.39	-0.20	-0.24	-0.31	-0.30	-0.13
45-60	0.37	0.37	0.58	**1.00**	0.54	0.28	0.33	0.15	0.07	-0.13	-0.25	-0.40	-0.52	-0.20	-0.28	-0.41	-0.34	-0.14
60-75	0.33	0.31	0.41	0.54	**1.00**	0.51	0.28	0.27	0.07	0.09	-0.17	-0.31	-0.37	-0.25	-0.13	-0.22	-0.34	-0.21
75-90	0.30	0.53	0.43	0.28	0.51	**1.00**	0.70	0.43	0.29	0.19	0.13	-0.13	-0.11	0.13	0.07	-0.10	-0.14	-0.02
90-105	0.30	0.49	0.40	0.33	0.28	0.70	**1.00**	0.65	0.34	0.18	0.17	-0.06	-0.16	0.23	0.06	-0.18	-0.13	-0.03
105-120	0.22	0.31	0.26	0.15	0.27	0.43	0.65	**1.00**	0.62	0.27	0.20	0.06	-0.04	0.23	0.18	-0.01	-0.01	-0.01
120-135	0.11	0.28	0.12	0.07	0.07	0.29	0.34	0.62	**1.00**	0.39	0.12	-0.03	-0.07	0.30	0.03	-0.11	-0.01	-0.02
135-150	0.04	-0.14	0.09	-0.13	0.09	0.19	0.18	0.27	0.39	**1.00**	0.44	-0.00	0.05	0.06	0.14	0.12	0.03	0.02
150-165	-0.03	0.03	-0.16	-0.25	-0.17	0.13	0.17	0.20	0.12	0.44	**1.00**	0.55	0.19	0.37	0.37	0.27	0.29	0.23
165-180	-0.14	-0.15	-0.35	-0.40	-0.31	-0.13	-0.06	0.06	-0.03	-0.00	0.55	**1.00**	0.55	0.28	0.41	0.39	0.36	0.25
180-200	-0.28	-0.22	-0.39	-0.52	-0.37	-0.11	-0.16	-0.04	-0.07	0.05	0.19	0.55	**1.00**	0.34	0.38	0.48	0.39	0.30
200-230	0.09	0.27	-0.20	-0.20	-0.25	0.13	0.23	0.23	0.30	0.06	0.37	0.28	0.34	**1.00**	0.57	0.40	0.54	0.47
230-265	0.05	0.07	-0.24	-0.28	-0.13	0.07	0.06	0.18	0.03	0.14	0.37	0.41	0.38	0.57	**1.00**	0.68	0.65	0.57
265-325	-0.04	-0.11	-0.31	-0.41	-0.22	-0.10	-0.18	-0.01	-0.11	0.12	0.27	0.39	0.48	0.40	0.68	**1.00**	0.67	0.60
325-450	0.01	-0.02	-0.30	-0.34	-0.34	-0.14	-0.13	-0.01	-0.01	0.03	0.29	0.36	0.39	0.54	0.65	0.67	**1.00**	0.67
450-1000	0.10	0.10	-0.13	-0.14	-0.21	-0.02	-0.03	-0.01	-0.02	0.02	0.23	0.25	0.30	0.47	0.57	0.60	0.67	**1.00**

bin [GeV]	0-15	15-30	30-45	45-60	60-75	75-90	90-105	105-120	120-135	135-150	150-165	165-180	180-200	200-230	230-265	265-325	325-450	450-1000
0-15	**1.00**	0.35	0.21	0.43	0.49	0.34	0.27	0.38	0.44	0.07	0.13	0.07	-0.02	-0.10	0.19	-0.09	-0.34	0.00
15-30	0.35	**1.00**	0.49	0.42	0.40	0.39	0.28	0.26	0.18	0.06	0.12	0.13	0.19	0.00	0.04	0.05	-0.29	0.01
30-45	0.21	0.49	**1.00**	0.63	0.37	0.43	0.30	0.25	0.26	-0.06	0.02	-0.06	0.01	-0.25	-0.14	-0.10	-0.48	-0.13
45-60	0.43	0.42	0.63	**1.00**	0.69	0.51	0.31	0.42	0.46	-0.05	0.09	0.06	0.07	-0.25	-0.08	-0.10	-0.59	-0.10
60-75	0.49	0.40	0.37	0.69	**1.00**	0.58	0.21	0.36	0.53	0.10	0.20	0.06	0.06	-0.20	0.06	-0.05	-0.50	-0.05
75-90	0.34	0.39	0.43	0.51	0.58	**1.00**	0.41	0.19	0.23	-0.07	-0.07	-0.04	-0.02	-0.30	-0.24	-0.21	-0.54	-0.22
90-105	0.27	0.28	0.30	0.31	0.21	0.41	**1.00**	0.42	0.02	-0.12	-0.05	-0.04	-0.11	-0.25	-0.07	-0.23	-0.39	-0.21
105-120	0.38	0.26	0.25	0.42	0.36	0.19	0.42	**1.00**	0.50	-0.16	-0.08	0.10	-0.09	-0.14	0.10	-0.23	-0.49	-0.14
120-135	0.44	0.18	0.26	0.46	0.53	0.23	0.02	0.50	**1.00**	0.29	0.29	0.15	0.18	0.02	0.35	0.17	-0.32	0.24
135-150	0.07	0.06	-0.06	-0.05	0.10	-0.07	-0.12	-0.16	0.29	**1.00**	0.56	0.13	0.24	0.29	0.44	0.38	0.27	0.25
150-165	0.13	0.12	0.02	0.09	0.20	-0.07	-0.05	-0.08	0.29	0.56	**1.00**	0.61	0.51	0.34	0.59	0.66	0.31	0.49
165-180	0.07	0.13	-0.06	0.06	0.06	-0.04	-0.04	0.10	0.15	0.13	0.61	**1.00**	0.65	0.25	0.45	0.49	0.24	0.38
180-200	-0.02	0.19	0.01	0.07	0.06	-0.02	-0.11	-0.09	0.18	0.24	0.51	0.65	**1.00**	0.50	0.39	0.70	0.32	0.50
200-230	-0.10	0.00	-0.25	-0.25	-0.20	-0.30	-0.25	-0.14	0.02	0.29	0.34	0.25	0.50	**1.00**	0.51	0.52	0.47	0.46
230-265	0.19	0.04	-0.14	-0.08	0.06	-0.24	-0.07	0.10	0.35	0.44	0.59	0.45	0.39	0.51	**1.00**	0.53	0.40	0.56
265-325	-0.09	0.05	-0.10	-0.10	-0.05	-0.21	-0.23	-0.23	0.17	0.38	0.66	0.49	0.70	0.52	0.53	**1.00**	0.49	0.64
325-450	-0.34	-0.29	-0.48	-0.59	-0.50	-0.54	-0.39	-0.49	-0.32	0.27	0.31	0.24	0.32	0.47	0.40	0.49	**1.00**	0.42
450-1000	0.00	0.01	-0.13	-0.10	-0.05	-0.22	-0.21	-0.14	0.24	0.25	0.49	0.38	0.50	0.46	0.56	0.64	0.42	**1.00**

TABLE D.10: Correlation matrix of the normalised cross-section as function of $p_{\mathrm{T}}^{\mathrm{t,had}}$ in the 4-jet exclusive (top), 5-jet exclusive (centre) and 6-jet inclusive (bottom) configurations, accounting for the statistical and systematic uncertainties.

bin [GeV]	0-15	15-35	35-75	75-125	125-170	170-800
0-15	**1.00**	0.98	0.29	0.06	-0.01	0.08
15-35	0.98	**1.00**	0.32	0.03	-0.12	-0.02
35-75	0.29	0.32	**1.00**	0.89	0.42	0.30
75-125	0.06	0.03	0.89	**1.00**	0.70	0.51
125-170	-0.01	-0.12	0.42	0.70	**1.00**	0.76
170-800	0.08	-0.02	0.30	0.51	0.76	**1.00**

bin [GeV]	0-35	35-75	75-125	125-170	170-225	225-800
0-35	**1.00**	0.81	0.45	0.22	-0.10	-0.40
35-75	0.81	**1.00**	0.28	-0.07	-0.28	-0.54
75-125	0.45	0.28	**1.00**	0.75	0.43	0.16
125-170	0.22	-0.07	0.75	**1.00**	0.64	0.44
170-225	-0.10	-0.28	0.43	0.64	**1.00**	0.69
225-800	-0.40	-0.54	0.16	0.44	0.69	**1.00**

bin [GeV]	0-35	35-75	75-125	125-170	170-225	225-800
0-35	**1.00**	0.66	0.47	0.25	-0.02	-0.47
35-75	0.66	**1.00**	0.65	-0.02	-0.16	-0.68
75-125	0.47	0.65	**1.00**	0.18	-0.05	-0.53
125-170	0.25	-0.02	0.18	**1.00**	0.50	0.14
170-225	-0.02	-0.16	-0.05	0.50	**1.00**	0.41
225-800	-0.47	-0.68	-0.53	0.14	0.41	**1.00**

TABLE D.11: Correlation matrix of the normalised cross-section as function of $p_{\mathrm{T}}^{\mathrm{t\bar{t}}}$ in the 4-jet exclusive (top), 5-jet exclusive (centre) and 6-jet inclusive (bottom) configurations, accounting for the statistical and systematic uncertainties.

bin [GeV]	0-40	40-80	80-120	120-170	170-230	230-600
0-40	**1.00**	0.24	0.07	0.40	0.24	-0.10
40-80	0.24	**1.00**	0.93	0.65	0.53	0.09
80-120	0.07	0.93	**1.00**	0.50	0.42	0.15
120-170	0.40	0.65	0.50	**1.00**	0.61	0.05
170-230	0.24	0.53	0.42	0.61	**1.00**	-0.04
230-600	-0.10	0.09	0.15	0.05	-0.04	**1.00**
bin [GeV]	0-40	40-80	80-120	120-170	170-230	230-600
0-40	**1.00**	-0.17	-0.26	-0.14	0.37	0.53
40-80	-0.17	**1.00**	0.93	0.53	0.31	0.18
80-120	-0.26	0.93	**1.00**	0.70	0.39	0.21
120-170	-0.14	0.53	0.70	**1.00**	0.55	0.40
170-230	0.37	0.31	0.39	0.55	**1.00**	0.56
230-600	0.53	0.18	0.21	0.40	0.56	**1.00**
bin [GeV]	0-40	40-80	80-120	120-170	170-230	230-600
0-40	**1.00**	-0.48	-0.83	-0.72	-0.63	-0.60
40-80	-0.48	**1.00**	0.25	-0.01	-0.06	-0.02
80-120	-0.83	0.25	**1.00**	0.46	0.38	0.37
120-170	-0.72	-0.01	0.46	**1.00**	0.65	0.61
170-230	-0.63	-0.06	0.38	0.65	**1.00**	0.58
230-600	-0.60	-0.02	0.37	0.61	0.58	**1.00**
bin [GeV]	0-40	40-80	80-120	120-170	170-230	230-600
0-40	**1.00**	0.30	-0.07	-0.57	-0.50	-0.44
40-80	0.30	**1.00**	0.09	-0.15	-0.15	-0.02
80-120	-0.07	0.09	**1.00**	0.43	0.43	0.58
120-170	-0.57	-0.15	0.43	**1.00**	0.65	0.67
170-230	-0.50	-0.15	0.43	0.65	**1.00**	0.70
230-600	-0.44	-0.02	0.58	0.67	0.70	**1.00**

TABLE D.12: Correlation matrix of the normalised cross-section as function of $p_{\mathrm{out}}^{\mathrm{t\bar{t}}}$ in the 4-jet exclusive, 4-jet inclusive, 5-jet exclusive and 6-jet inclusive configurations, accounting for the statistical and systematic uncertainties.

Appendix E

Rivet routine

This appendix summarizes the validation of the RIVET routine. Figure E.1 shows a comparison between the nominal MC prediction by POWHEG+PYTHIA, after unfolding (red) to POWHEG+PYTHIA using the RIVET routine (blue) in all measured absolute cross section observables. A closure in the fiducial phase space at particle level is observed and hence validates the RIVET routine. The possibility to compare the measurements to different model predictions without the need of running the full ATLAS simulation is therefore established.

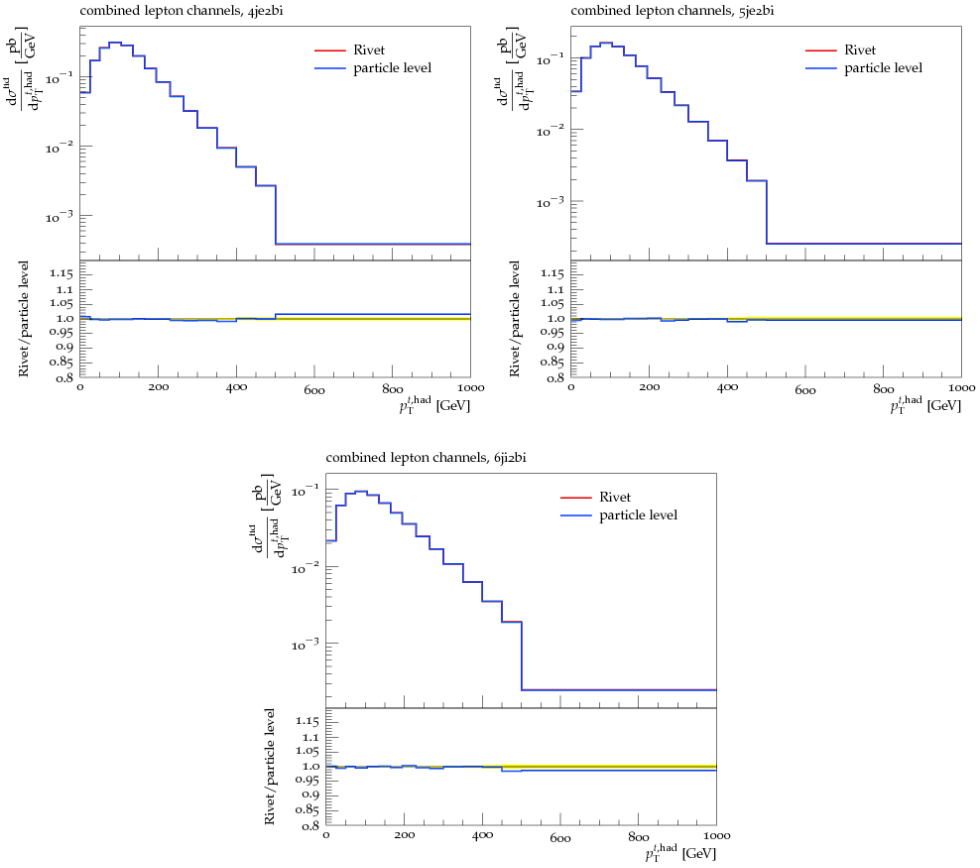

FIGURE E.1: Comparison between the unfolded POWHEG+PYTHIA MC (red) and the RIVET predictions (blue) for the $p_{\mathrm{T}}^{\mathrm{t,had}}$ in the 4 jets exclusive, 5 jets exclusive and 6 jets inclusive configurations using the absolute cross-section.

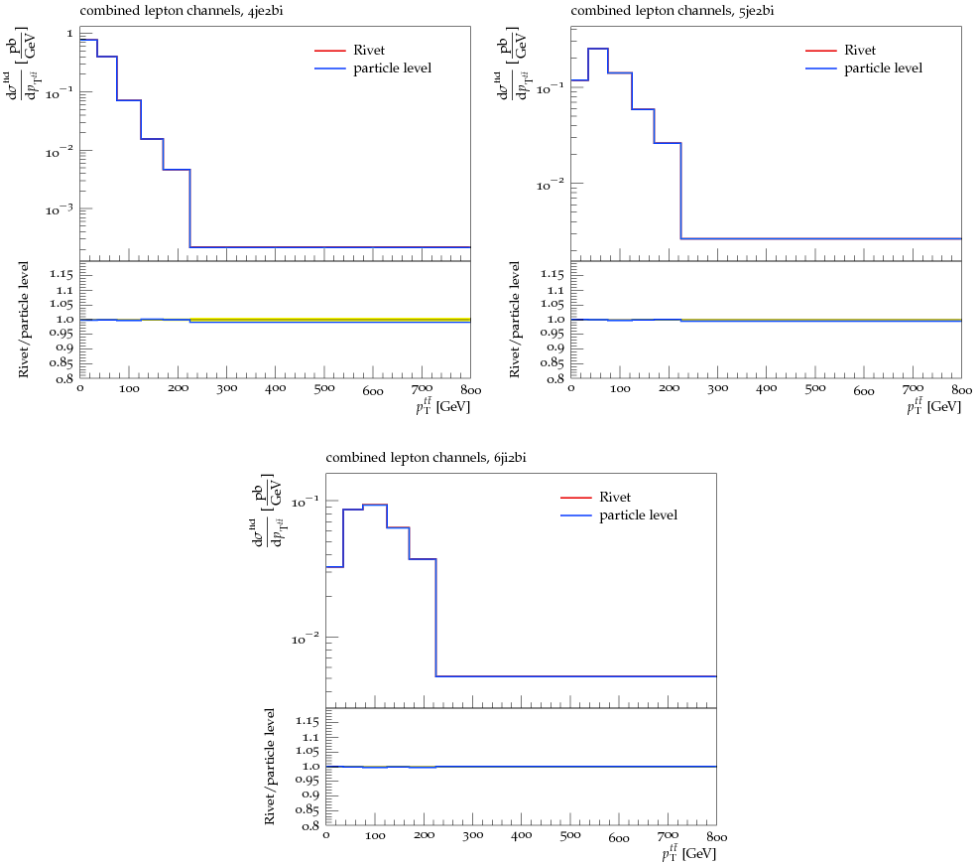

FIGURE E.2: Comparison between the unfolded POWHEG+PYTHIA MC (red) and the RIVET predictions (blue) for the $p_T^{t\bar{t}}$ in the 4 jets exclusive, 5 jets exclusive and 6 jets inclusive configurations using the absolute cross-section.

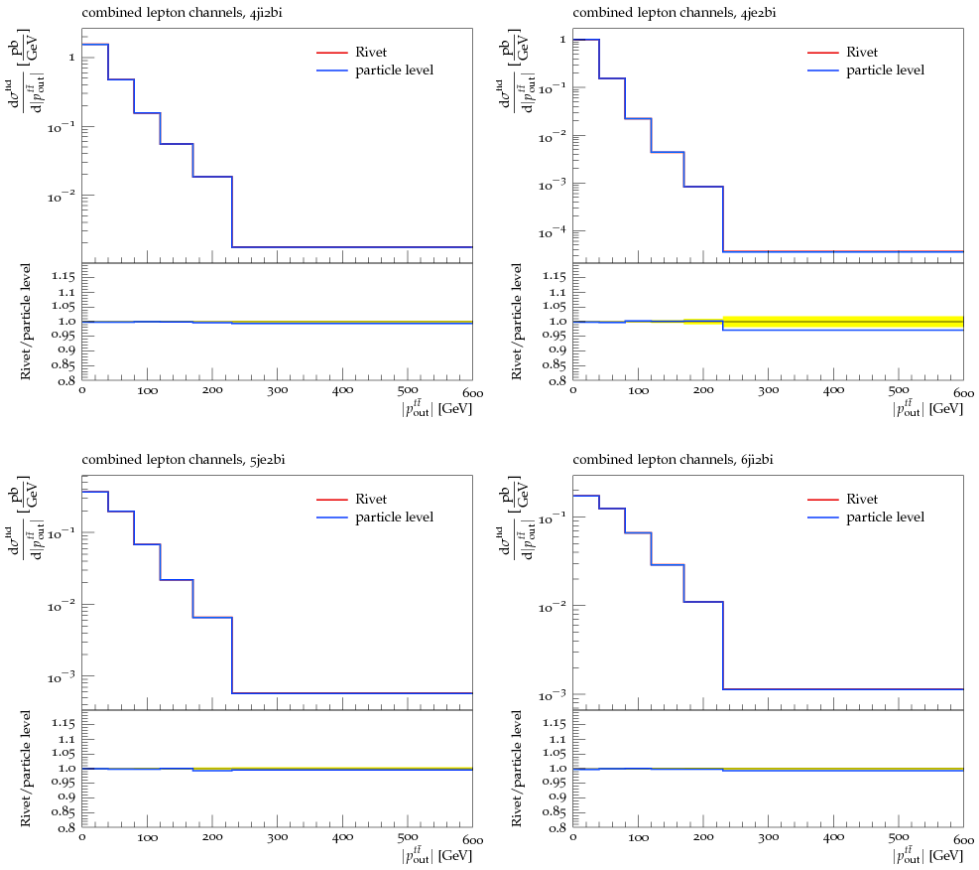

FIGURE E.3: Comparison between the unfolded POWHEG+PYTHIA MC (red) and the RIVET predictions (blue) for the $p_{\mathrm{out}}^{\mathrm{t\bar{t}}}$ in the 4 jets exclusive, 5 jets exclusive and 6 jets inclusive configurations using the absolute cross-section.

Appendix F

Unfolding iterations stability check

The number of iterations used for the unfolding is 4. Because this number was not optimised for the round of the analysis reported in this thesis, it is important to check that this value is reasonable. The higher the number of iterations, the less regularized the unfolding is (so the more similar to an unregularized unfolding) and so the bias should decrease with the number of iterations while the statistical uncertainty should increase with the number of iterations. It can be seen in Figures F.1–F.3 for the $p_{\mathrm{T}}^{t\bar{t}}$ variable in 4 jets exclusive, 5 jets exclusive and 6 jets inclusive configurations that the data unfolded results compared to the previous iteration behaves as expected and also that the change is not very large.

In order to quantify the effect, the χ^2 of these residuals, was computed and is shown in Figures F.4–F.6. Also the χ^2 for the $p_{\mathrm{T}}^{t\bar{t}}$ variable is small and has a stable distribution in all the three configurations considered. Finally, as expected, the statistical uncertainty increases with the number of iterations as shown in Figures F.7–F.9 respectively for the 4 jets exclusive, 5 jets exclusive and 6 jets inclusive configurations.

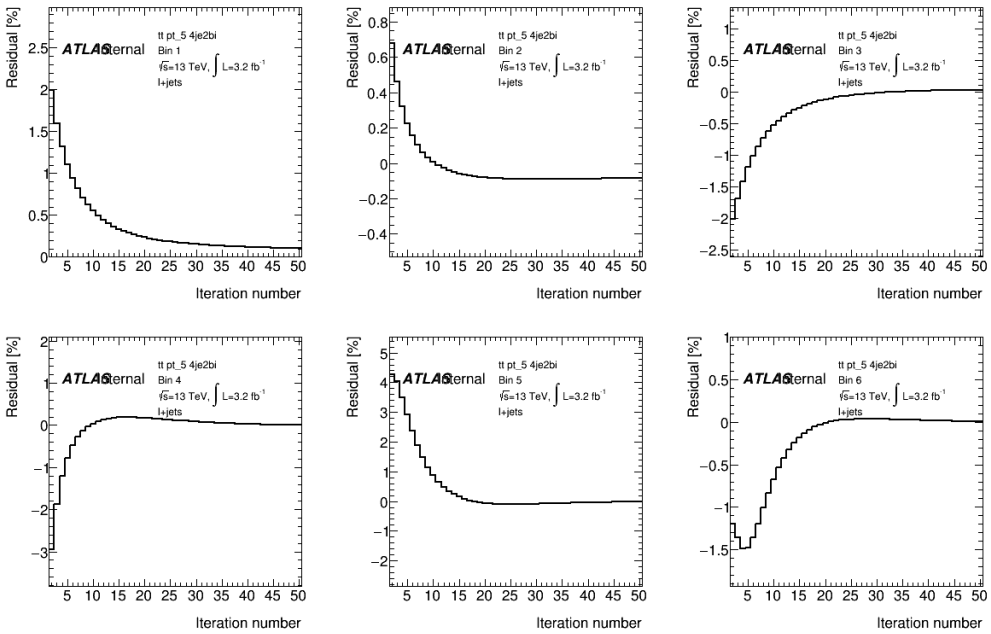

FIGURE F.1: Residuals (w.r.t. previous iteration) as a function of the N_{iter} in $p_{\text{T}}^{t\bar{t}}$ bins for the 4 jets exclusive configuration.

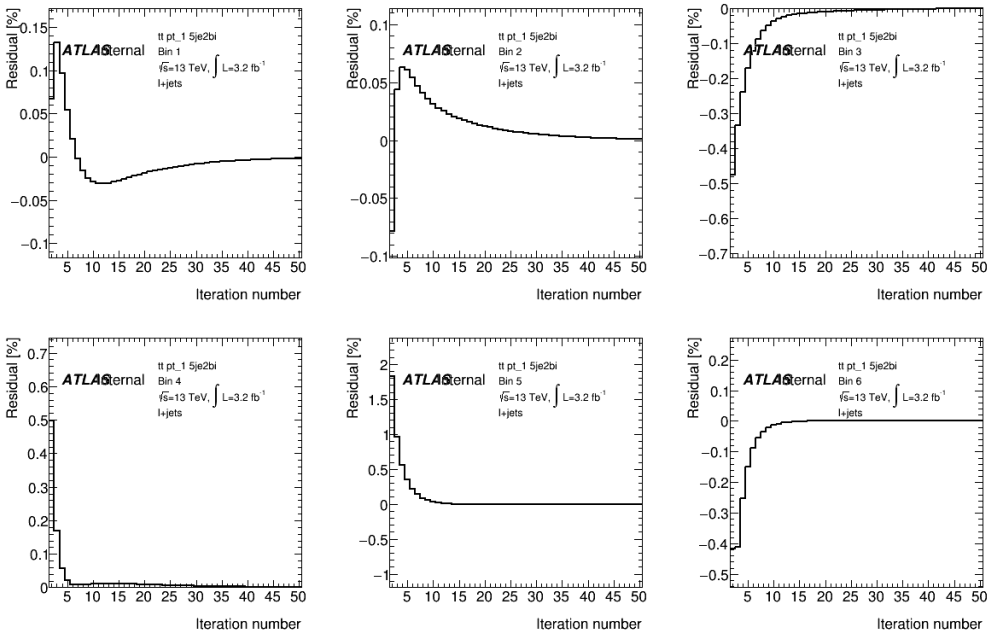

FIGURE F.2: Residuals (w.r.t. previous iteration) as a function of the N_{iter} in $p_{\text{T}}^{t\bar{t}}$ bins for the 5 jets exclusive configuration.

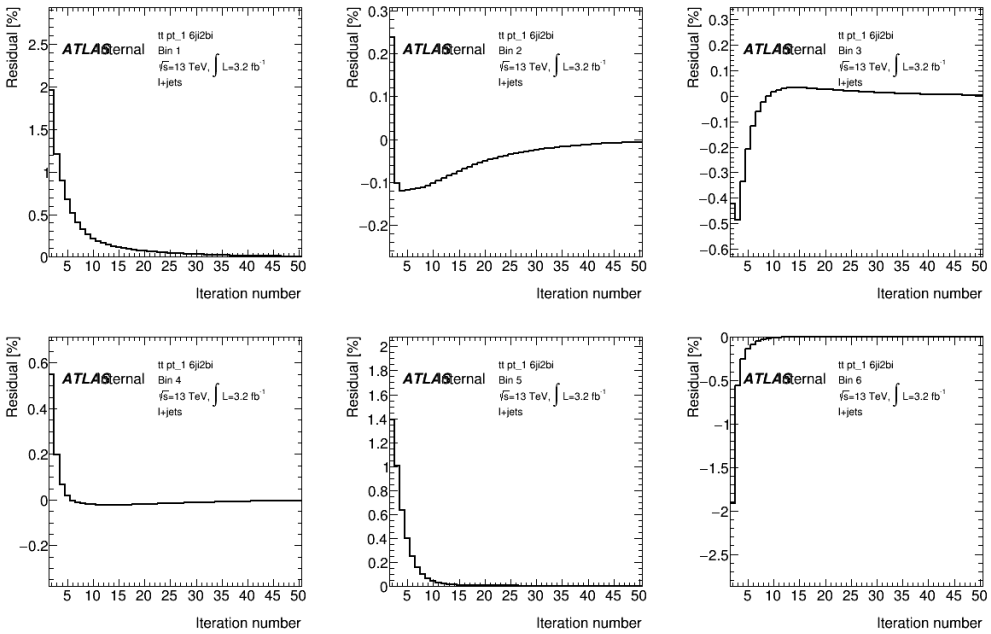

FIGURE F.3: Residuals (w.r.t. previous iteration) as a function of the N_{iter} in $p_{\text{T}}^{t\bar{t}}$ bins for the 6 jets inclusive configuration.

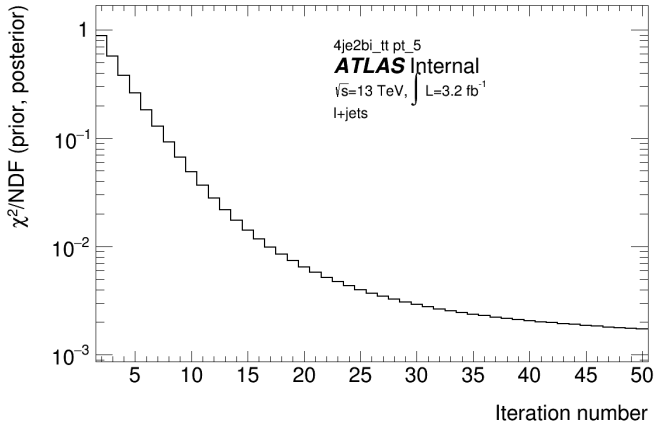

FIGURE F.4: The χ^2 test between the unfolded result in n-th iteration and the prior (result from the previous iteration) for the $p_{\text{T}}^{t\bar{t}}$ in 4 jets exclusive configuration.

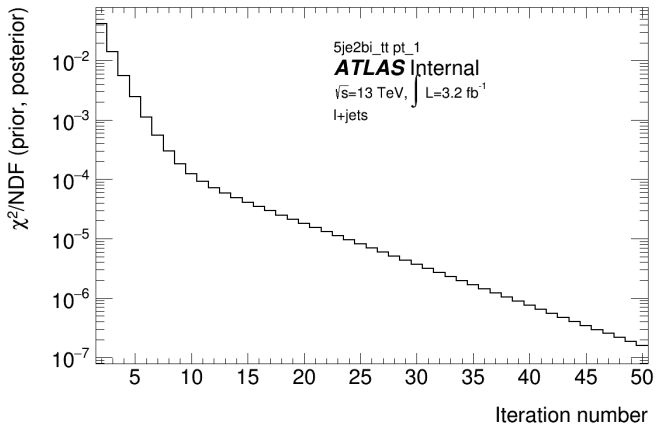

FIGURE F.5: The χ^2 test between the unfolded result in n-th iteration and the prior (result from the previous iteration) for the $p_{\mathrm{T}}^{t\bar{t}}$ in 5 jets exclusive configuration.

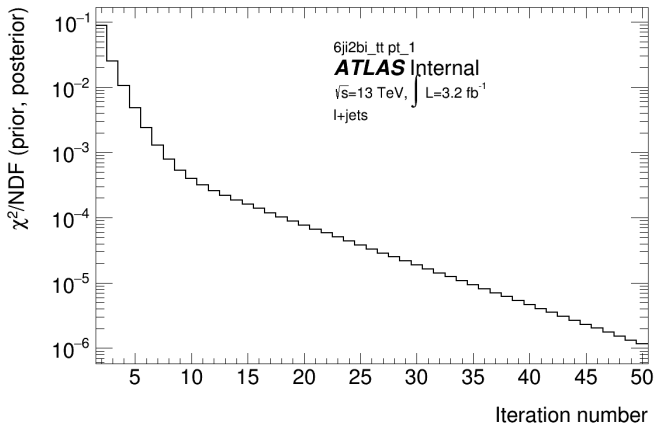

FIGURE F.6: The χ^2 test between the unfolded result in n-th iteration and the prior (result from the previous iteration) for the $p_{\mathrm{T}}^{t\bar{t}}$ in 6 jets inclusive configuration.

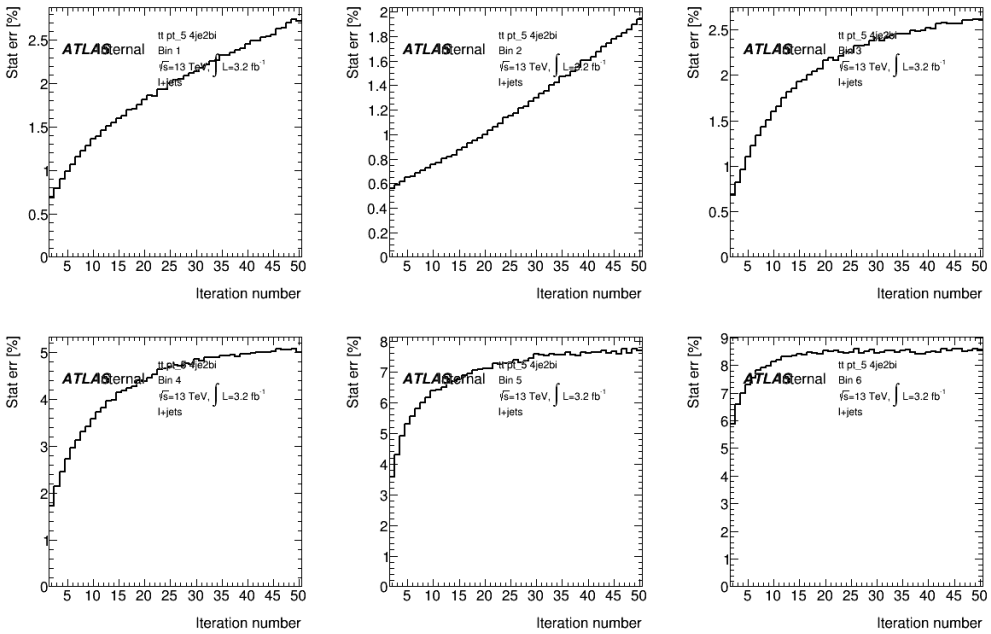

FIGURE F.7: Statistical error as a function of the N_{iter} in $p_{\text{T}}^{t\bar{t}}$ bins in 4 jets exclusive configuration.

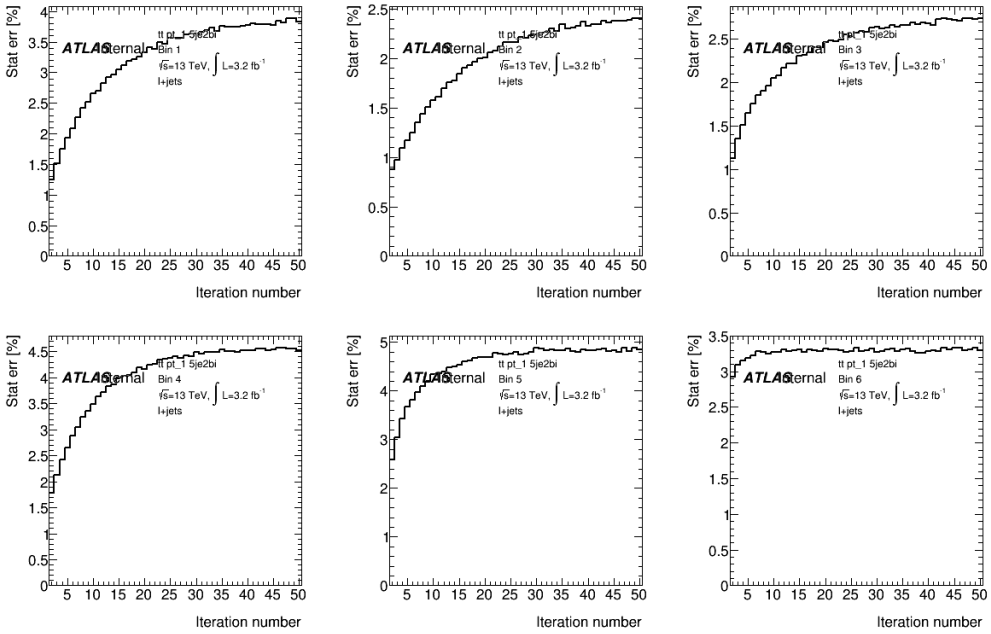

FIGURE F.8: Statistical error as a function of the N_{iter} in $p_{\text{T}}^{t\bar{t}}$ bins in 5 jets exclusive configuration.

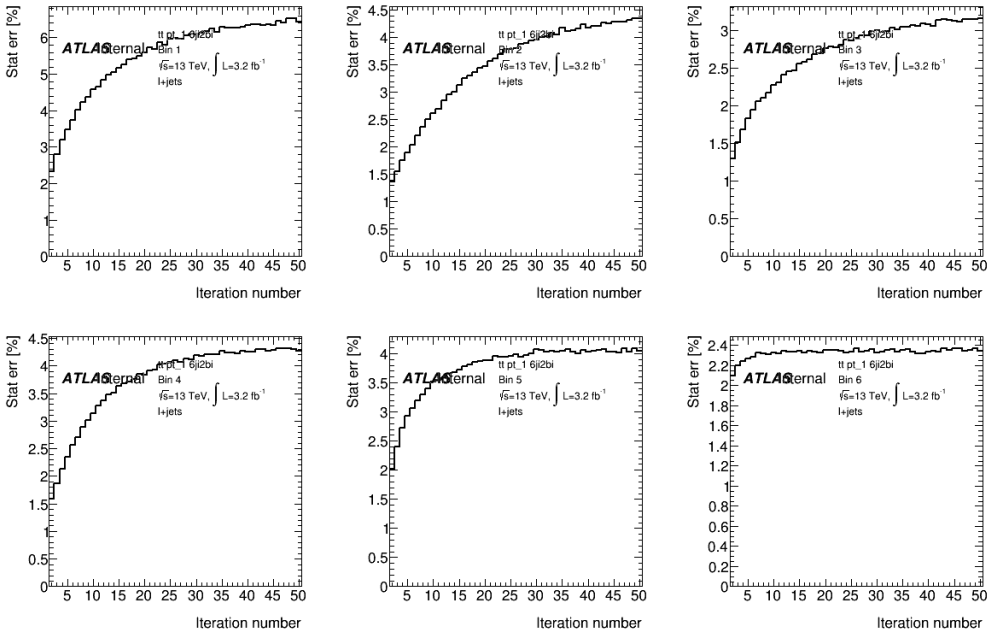

FIGURE F.9: Statistical error as a function of the N_{iter} in $p_{\mathrm{T}}^{t\bar{t}}$ bins in 6 jets inclusive configuration.

Bibliography

[1] Chen-Ning Yang and Robert L. Mills. "Conservation of Isotopic Spin and Isotopic Gauge Invariance". In: *Phys. Rev.* 96 (1954). DOI: 10.1103/PhysRev.96.191.

[2] T. Muta. "Foundations of quantum chromodynamics: An Introduction to perturbative methods in gauge theories". In: *World Sci. Lect. Notes Phys.* 5 (1987).

[3] Donald Hill Perkins. *Introduction to high-energy physics; 4th ed.* Cambridge Univ. Press, 2000. DOI: https://doi.org/10.1017/CBO9780511809040.

[4] F. Halzen and Alan D. Martin. *QUARKS AND LEPTONS: AN INTRODUCTORY COURSE IN MODERN PARTICLE PHYSICS*. 1984. URL: http://stacks.iop.org/0031-9112/36/i=2/a=033.

[5] Nicola Cabibbo. "Unitary Symmetry and Leptonic Decays". In: *Phys. Rev. Lett.* (1963). DOI: 10.1103/PhysRevLett.10.531.

[6] Makoto Kobayashi and Toshihide Maskawa. "CP Violation in the Renormalizable Theory of Weak Interaction". In: *Prog. Theor. Phys.* (1973). DOI: 10.1143/PTP.49.652.

[7] Jeffrey Goldstone, Abdus Salam, and Steven Weinberg. "Broken Symmetries". In: *Phys. Rev.* (1962). DOI: 10.1103/PhysRev.127.965.

[8] The ATLAS collaboration. "Observation of a new particle in the search for the Standard Model Higgs boson with the ATLAS detector at the LHC". In: *Phys. Lett.* (2012). DOI: 10.1016/j.physletb.2012.08.020.

[9] The CMS collaboration. "Observation of a new boson at a mass of 125 GeV with the CMS experiment at the LHC". In: *Phys. Lett.* (2012). DOI: 10.1016/j.physletb.2012.08.021.

[10] The ATLAS collaboration. "Measurements of the Higgs boson production and decay rates and constraints on its couplings from a combined ATLAS and CMS analysis of the LHC pp collision data at $\sqrt{s} =$ 7 and 8 TeV". In: *JHEP* (2016). DOI: 10.1007/JHEP08(2016)045.

[11] The CMS ATLAS CDF and D0 collaborations. "First combination of Tevatron and LHC measurements of the top-quark mass". In: (2014). arXiv: 1403.4427.

[12] The CDF collaboration. "Observation of Top Quark Production in $p\overline{p}$ Collisions with the Collider Detector at Fermilab". In: *Phys. Rev. Lett.* (1995). DOI: 10.1103/PhysRevLett.74.2626.

[13] The D0 collaboration. "Observation of the Top Quark". In: *Phys. Rev. Lett.* (1995). DOI: 10.1103/PhysRevLett.74.2632.

[14] A. D. Martin et al. "Parton distributions for the LHC". In: *Eur. Phys. J.* (2009). DOI: 10.1140/epjc/s10052-009-1072-5.

[15] J. Pumplin et al. "New generation of parton distributions with uncertainties from global QCD analysis". In: *JHEP* (2002). DOI: 10.1088/1126-6708/2002/07/012.

[16] John C. Collins, Davison E. Soper, and George F. Sterman. "Factorization of Hard Processes in QCD". In: *Adv. Ser. Direct. High Energy Phys.* (1989). DOI: 10.1142/9789814503266_0001.

[17] The CDF collaboration. "Combination of CDF top quark pair production cross-section measurements with up to 4.6 fb^{-1}". In: (2009).

[18] The D0 collaboration. "Measurement of the $t\bar{t}$ production cross section using dilepton events in $p\bar{p}$ collisions". In: *Phys. Lett.* B704 (2011). DOI: 10.1016/j.physletb.2011.09.046.

[19] Michal Czakon and Alexander Mitov. "Top++: A Program for the Calculation of the Top-Pair Cross-Section at Hadron Colliders". In: *Comput. Phys. Commun.* 185 (2014). DOI: 10.1016/j.cpc.2014.06.021.

[20] The CMS collaboration. "Measurement of the $t\bar{t}$ production cross section using events in the eμ final state in pp collisions at $\sqrt{s} = 13$ TeV". In: *Eur. Phys. J.* C77 (2017). DOI: 10.1140/epjc/s10052-017-4718-8.

[21] The ATLAS collaboration. "Measurement of the $t\bar{t}$ production cross-section using $e\mu$ events with b-tagged jets in pp collisions at $\sqrt{s}$=13 TeV with the ATLAS detector". In: *Phys. Lett.* B761 (2016). DOI: 10.1016/j.physletb.2016.08.019.

[22] The CDF collaboration. "First Measurement of the t anti-t Differential Cross Section d sigma/dM(t anti-t) in p anti-p Collisions at s**(1/2)=1.96-TeV". In: *Phys. Rev. Lett.* 102 (2009). DOI: 10.1103/PhysRevLett.102.222003.

[23] The D0 collaboration. "Dependence of the $t\bar{t}$ production cross section on the transverse momentum of the top quark". In: *Phys. Lett.* B693 (2010). DOI: 10.1016/j.physletb.2010.09.011.

[24] The CDF collaboration. "Observation of Electroweak Single Top-Quark Production". In: *Phys. Rev. Lett.* 103 (2009). DOI: 10.1103/PhysRevLett.103.092002.

[25] LEP Electroweak Working Group. "Precision Electroweak Measurements and Constraints on the Standard Model". In: (2010). arXiv: 1012.2367 [hep-ex].

[26] The ATLAS collaboration. "Direct top-quark decay width measurement in the $t\bar{t}$ lepton+jets channel at $\sqrt{s} = 8\mathrm{TeV}$ with the ATLAS experiment". In: (2017). arXiv: 1709.04207 [hep-ex].

[27] The ATLAS collaboration. "Measurements of charge and CP asymmetries in b-hadron decays using top-quark events collected by the ATLAS detector in pp collisions at $\sqrt{s} = 8$ TeV". In: *JHEP* 02 (2017). DOI: 10.1007/JHEP02(2017)071.

[28] The CMS collaboration. "Measurement of the charge asymmetry in top quark pair production in pp collisions at $\sqrt{(s)} = 8$ TeV using a

template method". In: *Phys. Rev.* D93.3 (2016). DOI: 10.1103/PhysRevD.93.034014.

[29] The ATLAS collaboration. "Measurements of top quark spin observables in $t\bar{t}$ events using dilepton final states in $\sqrt{s} = 8$ TeV pp collisions with the ATLAS detector". In: *JHEP* 03 (2017). DOI: 10.1007/JHEP03(2017)113.

[30] The LHC Study Group. "Large Hadron Collider: LHC - The Large Hadron Collider - Accelerator project - The LHC Study group". URL: https://cds.cern.ch/record/87244.

[31] The LHC Study Group. *The Large Hadron Collider: conceptual design*. Tech. rep. CERN-AC-95-05-LHC. 1995. URL: https://cds.cern.ch/record/291782.

[32] The ALICE collaboration. "The ALICE experiment at the CERN LHC". In: *JINST* 3 (2008). DOI: 10.1088/1748-0221/3/08/S08002.

[33] The ATLAS collaboration. "The ATLAS Experiment at the CERN Large Hadron Collider". In: *JINST* 3 (2008). DOI: 10.1088/1748-0221/3/08/S08003.

[34] The CMS collaboration. "The CMS Experiment at the CERN LHC". In: *JINST* 3 (2008). DOI: 10.1088/1748-0221/3/08/S08004.

[35] The LHCb collaboration. "The LHCb Detector at the LHC". In: *JINST* 3 (2008). DOI: 10.1088/1748-0221/3/08/S08005.

[36] The TOTEM collaboration. "The TOTEM experiment at the CERN Large Hadron Collider". In: *JINST* 3 (2008). DOI: 10.1088/1748-0221/3/08/S08007.

[37] The LHCf collaboration. "The LHCf detector at the CERN Large Hadron Collider". In: *JINST* 3 (2008). DOI: 10.1088/1748-0221/3/08/S08006.

[38] The MoEDAL collaboration. "The MoEDAL Experiment at the LHC - a New Light on the Terascale Frontier". In: *J. Phys. Conf. Ser.* 631.1 (2015). DOI: 10.1088/1742-6596/631/1/012014.

[39] The ATLAS collaboration. "ATLAS: Detector and physics performance technical design report. Volume 1". In: (1999).

[40] The ATLAS collaboration. "The ATLAS Inner Detector commissioning and calibration". In: *Eur. Phys. J.* C70 (2010). DOI: 10.1140/epjc/s10052-010-1366-7.

[41] The ATLAS collaboration. "The upgraded Pixel detector and the commissioning of the Inner Detector tracking of the ATLAS experiment for Run-2 at the Large Hadron Collider". In: *PoS* EPS-HEP2015 (2015). eprint: 1608.07850.

[42] The ATLAS collaboration. "Operation and performance of the ATLAS semiconductor tracker". In: *JINST* 9 (2014). DOI: 10.1088/1748-0221/9/08/P08009.

[43] The ATLAS collaboration. *ATLAS Transition Radiation Tracker (TRT): Straw Tube Gaseous Detectors at High Rates*. Tech. rep. CERN, 2013. URL: https://cds.cern.ch/record/1537991.

[44] The ATLAS collaboration. *The Run-2 ATLAS Trigger System*. Tech. rep. CERN, 2016. URL: https://cds.cern.ch/record/2133909.

[45] The ATLAS collaboration. *ATLAS Future Upgrade*. Tech. rep. CERN, 2016. URL: https://cds.cern.ch/record/2195333.

[46] The ATLAS collaboration. *New Small Wheel Technical Design Report*. Tech. rep. CERN-LHCC-2013-006. ATLAS-TDR-020. 2013. URL: https://cds.cern.ch/record/1552862.

[47] The ATLAS collaboration. "MICROMEGAS: a high-granularity position-sensitive gaseous detector for high particle-flux environments". In: *Nuclear Instruments and Methods in Physics Research Section A: Accelerators, Spectrometers, Detectors and Associated Equipment* 376.1 (1996). DOI: http://dx.doi.org/10.1016/0168-9002(96)00175-1.

[48] The ATLAS collaboration. "Measurements of top-quark pair differential cross-sections in the lepton+jets channel in pp collisions at $\sqrt{s}$=13 TeV using the ATLAS detector". In: (2017). arXiv: 1708.00727 [hep-ex].

[49] The ATLAS collaboration. "Measurements of top quark pair relative differential cross-sections with ATLAS in pp collisions at $\sqrt{s} = 7$ TeV". In: *Eur. Phys. J.* C73.1 (2013). DOI: 10.1140/epjc/s10052-012-2261-1.

[50] The ATLAS collaboration. "Differential top-antitop cross-section measurements as a function of observables constructed from final-state particles using pp collisions at $\sqrt{s} = 7$ TeV in the ATLAS detector". In: *JHEP* 06 (2015). DOI: 10.1007/JHEP06(2015)100.

[51] The ATLAS collaboration. "Measurements of top-quark pair differential cross-sections in the lepton+jets channel in pp collisions at $\sqrt{s} = 8$ TeV using the ATLAS detector". In: *Eur. Phys. J.* C76.10 (2016), p. 538. DOI: 10.1140/epjc/s10052-016-4366-4. arXiv: 1511.04716 [hep-ex].

[52] The ATLAS collaboration. "Measurement of $t\bar{t}$ production with a veto on additional central jet activity in pp collisions at sqrt(s) = 7 TeV using the ATLAS detector". In: *Eur. Phys. J.* C72 (2012). DOI: 10.1140/epjc/s10052-012-2043-9.

[53] The ATLAS collaboration. "Measurement of jet activity in top quark events using the $e\mu$ final state with two b-tagged jets in pp collisions at $\sqrt{s} = 8$ TeV with the ATLAS detector". In: *JHEP* 09 (2016). DOI: 10.1007/JHEP09(2016)074.

[54] The ATLAS collaboration. "Measurement of jet activity produced in top-quark events with an electron, a muon and two b-tagged jets in the final state in pp collisions at $\sqrt{s} = 13$ TeV with the ATLAS detector". In: *Eur. Phys. J.* C77.4 (2017). DOI: 10.1140/epjc/s10052-017-4766-0.

[55] The CMS collaboration. "Measurement of differential cross sections for top quark pair production using the lepton+jets final state in proton-proton collisions at 13 TeV". In: *Phys. Rev.* D95.9 (2017). DOI: 10.1103/PhysRevD.95.092001.

[56] The ATLAS collaboration. *Studies on top-quark Monte Carlo modelling for Top2016*. Tech. rep. ATL-PHYS-PUB-2016-020. CERN, 2016. URL: https://cds.cern.ch/record/2216168.

[57] The ATLAS collaboration. "Luminosity determination in pp collisions at $\sqrt{s}$ = 8 TeV using the ATLAS detector at the LHC". In: *Eur. Phys. J.* C76.12 (2016). DOI: 10.1140/epjc/s10052-016-4466-1.

[58] Stefano Frixione, Paolo Nason, and Carlo Oleari. "Matching NLO QCD computations with Parton Shower simulations: the POWHEG method". In: *JHEP* 11 (2007), p. 070. DOI: 10.1088/1126-6708/2007/11/070. arXiv: 0709.2092 [hep-ph].

[59] J. Alwall et al. "The automated computation of tree-level and next-to-leading order differential cross sections, and their matching to parton shower simulations". In: *JHEP* 07 (2014). DOI: 10.1007/JHEP07(2014)079.

[60] Torbjorn Sjostrand, Stephen Mrenna, and Peter Z. Skands. "A Brief Introduction to PYTHIA 8.1". In: *Comput. Phys. Commun.* 178 (2008), pp. 852–867. DOI: 10.1016/j.cpc.2008.01.036.

[61] M. Bahr et al. "Herwig++ Physics and Manual". In: *Eur. Phys. J.* C58 (2008). DOI: 10.1140/epjc/s10052-008-0798-9.

[62] S. Agostinelli et all. "Geant4-a simulation toolkit". In: *Nuclear Instruments and Methods in Physics Research Section A: Accelerators, Spectrometers, Detectors and Associated Equipment* 506.3 (2003). ISSN: 0168-9002. DOI: https://doi.org/10.1016/S0168-9002(03)01368-8.

[63] The ATLAS collaboration. *Fast Simulation for ATLAS: Atlfast-II and ISF*. Tech. rep. ATL-SOFT-PROC-2012-065. Geneva: CERN, 2012. URL: https://cds.cern.ch/record/1458503.

[64] B. Andersson et al. "Parton fragmentation and string dynamics". In: *Physics Reports* 97.2 (1983). DOI: https://doi.org/10.1016/0370-1573(83)90080-7.

[65] B.R. Webber. "A QCD model for jet fragmentation including soft gluon interference". In: *Nuclear Physics B* 238.3 (1984). DOI: https://doi.org/10.1016/0550-3213(84)90333-X.

[66] T. Gleisberg et al. "Event generation with SHERPA 1.1". In: *JHEP* 02 (2009). DOI: 10.1088/1126-6708/2009/02/007.

[67] The ATLAS collaboration. *Simulation of top quark production for the ATLAS experiment at sqrt(s) = 13 TeV*. Tech. rep. ATL-PHYS-PUB-2016-004. CERN, 2016. URL: https://cds.cern.ch/record/2120417.

[68] Stefano Frixione, Paolo Nason, and Carlo Oleari. "Matching NLO QCD computations with parton shower simulations: the POWHEG method". In: *Journal of High Energy Physics* 2007.11 (2007). URL: http://stacks.iop.org/1126-6708/2007/i=11/a=070.

[69] Hung-Liang Lai et al. "New parton distributions for collider physics". In: *Phys. Rev.* D 82 (2010). DOI: 10.1103/PhysRevD.82.074024.

[70] Torbjörn Sjöstrand, Stephen Mrenna, and Peter Skands. "PYTHIA 6.4 physics and manual". In: *Journal of High Energy Physics* 2006 (2006), p. 026. URL: http://stacks.iop.org/1126-6708/2006/i=05/a=026.

[71] Peter Z. Skands. "Tuning Monte Carlo generators: The Perugia tunes". In: *Phys. Rev. D* 82 (7 2010). DOI: 10.1103/PhysRevD.82.074018.

[72] Daniel Stump et al. "Inclusive jet production, parton distributions, and the search for new physics". In: *Journal of High Energy Physics* 2003.10 (2003), p. 046. URL: http://stacks.iop.org/1126-6708/2003/i=10/a=046.

[73] The ATLAS collaboration. *ATLAS Run 1 Pythia8 tunes*. Tech. rep. ATL-PHYS-PUB-2014-021. Geneva: CERN, 2014. URL: https://cds.cern.ch/record/1966419.

[74] The ATLAS collaboration. *Studies on top-quark Monte Carlo modelling with Sherpa and MG5_aMC@NLO*. Tech. rep. ATL-PHYS-PUB-2017-007. Geneva: CERN, 2017. URL: https://cds.cern.ch/record/2261938.

[75] Stefano Frixione et al. "Single-top hadroproduction in association with a W boson". In: *JHEP* 07 (2008). DOI: 10.1088/1126-6708/2008/07/029.

[76] Nikolaos Kidonakis. "Next-to-next-to-leading-order collinear and soft gluon corrections for t-channel single top quark production". In: *Phys. Rev.* D83 (2011). DOI: 10.1103/PhysRevD.83.091503.

[77] M. Aliev et al. "HATHOR: HAdronic Top and Heavy quarks crOss section calculatoR". In: *Comput. Phys. Commun.* 182 (2011). DOI: 10.1016/j.cpc.2010.12.040.

[78] P. Kant et al. "HatHor for single top-quark production: Updated predictions and uncertainty estimates for single top-quark production in hadronic collisions". In: *Comput. Phys. Commun.* 191 (2015). DOI: 10.1016/j.cpc.2015.02.001.

[79] Tanju Gleisberg and Stefan Hoeche. "Comix, a new matrix element generator". In: *JHEP* 12 (2008). DOI: 10.1088/1126-6708/2008/12/039.

[80] Fabio Cascioli, Philipp Maierhofer, and Stefano Pozzorini. "Scattering Amplitudes with Open Loops". In: *Phys. Rev. Lett.* 108 (2012). DOI: 10.1103/PhysRevLett.108.111601.

[81] The ATLAS collaboration. *Monte Carlo Generators for the Production of a W or Z/γ^* Boson in Association with Jets at ATLAS in Run 2*. Tech. rep. ATL-PHYS-PUB-2016-003. CERN, 2016. URL: https://cds.cern.ch/record/2120133.

[82] The ATLAS collaboration. *Expected electron performance in the ATLAS experiment*. Tech. rep. ATL-PHYS-PUB-2011-006. CERN, 2011. URL: https://cds.cern.ch/record/1345327.

[83] The ATLAS collaboration. "Electron reconstruction and identification efficiency measurements with the ATLAS detector using the 2011 LHC proton–proton collision data". In: *The European Physical Journal C* 74 (2014). DOI: 10.1140/epjc/s10052-014-2941-0.

[84] The ATLAS collaboration. *Electron efficiency measurements with the ATLAS detector using the 2015 LHC proton-proton collision data*. Tech. rep. ATLAS-CONF-2016-024. CERN, 2016. URL: https://cds.cern.ch/record/2157687.

[85] The ATLAS collaboration. "Muon reconstruction performance of the ATLAS detector in proton–proton collision data at $\sqrt{s}$ =13 TeV". In:

Eur. Phys. J. C76.5 (2016), p. 292. DOI: 10.1140/epjc/s10052-016-4120-y. arXiv: 1603.05598 [hep-ex].

[86] J. Illingworth and J. Kittler. "A survey of the hough transform". In: *Computer Vision, Graphics, and Image Processing* 44 (1988). DOI: https://doi.org/10.1016/S0734-189X(88)80033-1.

[87] Matteo Cacciari, Gavin P. Salam, and Gregory Soyez. "The Anti-k(t) jet clustering algorithm". In: *JHEP* 04 (2008). DOI: 10.1088/1126-6708/2008/04/063.

[88] The ATLAS collaboration. "Performance of pile-up mitigation techniques for jets in pp collisions at $\sqrt{s} = 8$ TeV using the ATLAS detector". In: *Eur. Phys. J.* C76 (2016). DOI: 10.1140/epjc/s10052-016-4395-z.

[89] The ATLAS collaboration. *Monte Carlo Calibration and Combination of In-situ Measurements of Jet Energy Scale, Jet Energy Resolution and Jet Mass in ATLAS*. Tech. rep. ATLAS-CONF-2015-037. CERN, 2015. URL: https://cds.cern.ch/record/2044941.

[90] The ATLAS collaboration. *Tagging and suppression of pileup jets with the ATLAS detector*. Tech. rep. ATLAS-CONF-2014-018. CERN, 2014. URL: https://cds.cern.ch/record/1700870.

[91] The ATLAS collaboration. *Expected performance of the ATLAS b-tagging algorithms in Run-2*. Tech. rep. ATL-PHYS-PUB-2015-022. CERN, 2015. URL: https://cds.cern.ch/record/2037697.

[92] The ATLAS collaboration. *Expected performance of missing transverse momentum reconstruction for the ATLAS detector at $\sqrt{s} = 13$ TeV*. Tech. rep. ATL-PHYS-PUB-2015-023. CERN, 2015. URL: https://cds.cern.ch/record/2037700.

[93] Francis Halzen, Yu Seon Jeong, and C. S. Kim. "Charge Asymmetry of Weak Boson Production at the LHC and the Charm Content of the Proton". In: *Phys. Rev.* D88 (2013). DOI: 10.1103/PhysRevD.88.073013.

[94] The ATLAS collaboration. *Estimation of non-prompt and fake lepton backgrounds in final states with top quarks produced in proton-proton collisions at $\sqrt{s} = 8$ TeV with the ATLAS detector*. Tech. rep. ATLAS-CONF-2014-058. CERN, 2014. URL: https://cds.cern.ch/record/1951336.

[95] The ATLAS collaboration. "Differential top-antitop cross-section measurements as a function of observables constructed from final-state particles using pp collisions at $\sqrt{s} = 7$ TeV in the ATLAS detector". In: *JHEP* 06 (2015). DOI: 10.1007/JHEP06(2015)100.

[96] G. D'Agostini. "A multidimensional unfolding method based on Bayes' theorem". In: *Nuclear Instruments and Methods in Physics Research Section A: Accelerators, Spectrometers, Detectors and Associated Equipment* 362.2 (1995). DOI: https://doi.org/10.1016/0168-9002(95)00274-X.

[97] Jon Butterworth et al. "PDF4LHC recommendations for LHC Run II". In: *Journal of Physics G: Nuclear and Particle Physics* 43.2 (2016). URL: http://stacks.iop.org/0954-3899/43/i=2/a=023001.

[98] Johan Alwall et al. "Comparative study of various algorithms for the merging of parton showers and matrix elements in hadronic collisions". In: *Eur. Phys. J.* C53 (2008). DOI: 10.1140/epjc/s10052-007-0490-5.

[99] The ATLAS collaboration. "Measurement of the muon reconstruction performance of the ATLAS detector using 2011 and 2012 LHC proton–proton collision data". In: *Eur. Phys. J.* C74 (2014). DOI: 10.1140/epjc/s10052-014-3130-x.

[100] The ATLAS collaboration. "Electron performance measurements with the ATLAS detector using the 2010 LHC proton-proton collision data". In: *Eur. Phys. J.* C72 (2012), p. 1909. DOI: 10.1140/epjc/s10052-012-1909-1. arXiv: 1110.3174 [hep-ex].

[101] The ATLAS collaboration. "Performance of algorithms that reconstruct missing transverse momentum in $\sqrt{s} = 8$ TeV proton-proton collisions in the ATLAS detector". In: *Eur. Phys. J.* C77.4 (2017). DOI: 10.1140/epjc/s10052-017-4780-2.

[102] The ATLAS collaboration. "Jet energy measurement and its systematic uncertainty in proton-proton collisions at $\sqrt{s} = 7$ TeV with the ATLAS detector". In: *Eur. Phys. J.* C75 (2015). DOI: 10.1140/epjc/s10052-014-3190-y.

[103] The ATLAS collaboration. "Single hadron response measurement and calorimeter jet energy scale uncertainty with the ATLAS detector at the LHC". In: *Eur. Phys. J.* C73.3 (2013). DOI: 10.1140/epjc/s10052-013-2305-1.

[104] The ATLAS collaboration. *Measurement of the luminosity with the new LUCID-2 detector in 2015*. Tech. rep. ATL-COM-FWD-2016-008. CERN, 2016. URL: https://cds.cern.ch/record/2154368.

UNIVERSITÀ DELLA CALABRIA
DIPARTIMENTO DI
FISICA

STFCM
Scienze e Tecnologie Fisiche, Chimiche e dei materiali

Consiglio Nazionale delle Ricerche

Dottorato di Ricerca in
Scienze e Tecnologie Fisiche, Chimiche e dei Materiali
Convenzione Università della Calabria-Consiglio Nazionale delle Ricerche

Giudizio sull'attività di ricerca svolta dalla Dott.ssa Serena Palazzo durante il corso di dottorato presentato ed approvato nel collegio docenti del 14/05/2018

La dott.ssa Serena Palazzo ha svolto la sua attività nell' ambito della Fisica della Alte Energie.
La sua attività di ricerca ha riguardato:

- Tematiche inerenti le camere di tracciamento MicroMegas che verranno installate nel rivelatore ATLAS ad LHC , in particolare:
  a) Partecipazione alla messa a punto , sia per la parte hardware che software, della stazione di test con raggi cosmici, ai Laboratori Nazionali di Frascati, per la validazione delle camere MicroMegas prodotte in Italia.
  b) Realizzazione di un codice Montecarlo relativo alla risposta delle camere sotto irraggiamento da cosmici.
  c) Studi di qualità del prototipo "Modulo0" durante la sua costruzione ed assemblaggio ai Laboratori Nazionali di Frascati dell' INFN.
  d) Partecipazione al Test su fascio svolto al CERN nell' estate 2016 per la validazione delle prestazioni del Modulo0, ricostruzione (adattando un pre-esistente codice all' attuale set-up sperimentale) ed analisi dei dati.

  Le attività descritte sono svolte in collaborazione con ricercatrici e ricercatori della Collaborazione ATLAS-ITALIA (Gruppo Collegato di Cosenza –INFN et al). Parte di queste hanno fatto parte del "lavoro di qualifica" , della durata di un anno, richiesto dalla Collaborazione ATLAS ai nuovi membri per entrare a far parte, in caso di esito positivo, della lista degli autori.
  La dott.ssa Palazzo ha terminato, con successo, il suo lavoro di qualifica nel marzo 2016.

- Analisi dati raccolti nel rivelatore ATLAS
  Questo studio, iniziato nel II anno di dottorato, e' stato svolto nell' ambito del Top-Working group del CERN al quale partecipano ricercatrici e ricercatori del Gruppo Collegato di Cosenza-INFN. In particolare la dott.ssa Palazzo è stata coinvolta nell' analisi degli eventi raccolti nelle collisioni pp a $\sqrt{s}$ = 13 TeV per la misura della sezione d' urto differenziale del processo ttbar nel canale di decadimento leptone + jets.
  L' analisi descritta richiede, per la sua complessità, numerose conoscenze preliminari relative sia alla fisica che ai software ufficiali da utilizzare; conoscenze che sono state rapidamente acquisite dalla dott.ssa Palazzo, permettendole un successivo e significativo contributo all' analisi.
  In questa attività, tra l' altro, ha sviluppato la parte unfolding dell' analisi applicando un metodo basato sulla statistica Bayesiana.

In tutte le attività descritte i risultati ottenuti sono stati eccellenti ed ha mostrato sia un alto grado di autonomia che ottima attitudine al lavoro di gruppo.

In aggiunta Serena Palazzo ha partecipato, dando un contributo significativo, alle attività del gruppo INFN-CS per la preparazione e svolgimento delle MasterClasses ed alle attività OPT per l' esperimento ATLAS.

In conclusione, il mio giudizio sulla attività svolta nel periodo di dottorato dalla dott.ssa Serena Palazzo e' : **eccellente**

La Supervisor
(prof. ssa Laura La Rotonda)
Laura La Rotonda